Acta Geophysica

VERSITA

Institute
of Geophysics
Polish Academy
of Sciences

Springer

Statistical Mechanics in Earth Physics and Natural Hazards

PREFACE TO THE TOPICAL ISSUE

Filippos VALLIANATOS[1,2] and Luciano TELESCA[3]

[1]Technological Educational Institute of Crete,
Laboratory of Geophysics and Seismology, Crete, Greece
e-mail: fvallian@chania.teicrete.gr

[2]University College London, Institute for Risks and Disaster Reduction
London, United Kingdom

[3]National Research Council,
Institute of Methodologies for Environmental Analysis (IMAA-CNR),
Tito Scalo, Italy; e-mail: luciano.telesca@imaa.cnr.it

There is a wide range of problems in geophysics, from earthquake prediction to the driving forces of plate tectonics, where it is necessary to understand how the Earth works.

Despite the large amount of experimental data and the considerable effort undertaken, many questions about fracture and physics of earthquakes have not yet been answered. Fracture and the physics of earthquakes is a subject with many unknowns. It is true that we have a good understanding of the propagation of seismic waves through the Earth and that, given a large set of seismographic records, we are able to reconstruct *a posteriori* the history of the fault rupture. However, when we consider the physical processes which lead to the initiation of rupture with a subsequent slip and its growth through a fault system to give rise to an earthquake, then our knowledge is really limited. Not only the friction law and rupture evolution rules are largely unknown, but the role of many other processes, such as plasticity, fluid

migration, chemical reactions, *etc*., and the couplings between them, remain unclear.

One may wonder about the physics of many earthquakes in a similar way as with the physics of fractures.

How can the collective properties of the set be defined by all earthquakes in a given region?

How does seismicity, which is the structure formed by all earthquakes, depend on its elementary constituents – the earthquakes?

Which kind of dynamical process does seismicity constitute?

It may be that these collective properties are largely independent of the physics of individual earthquakes, in the same way as many of the properties of gas or solid do not depend on the constitution of its elementary units. It is natural then to consider that the physics of many earthquakes has to be studied with a different approach than the physics of one earthquake and in this sense we can consider *the use of statistical physics to be not only appropriate but necessary to understand the collective properties of earthquakes.*

Statistical physics is one of the cornerstones of contemporary physics. It establishes a remarkably useful bridge between the mechanical microscopic laws and macroscopic description using classical thermodynamics. Its foundation is based on Boltzmann's famous molecular chaos hypothesis made in 1871, which relies on nonlinear dynamics and the ergodicity hypothesis. However, many important phenomena are not consistent with this simplifying hypothesis. A non-extensive thermodynamics, which recovers the extensive classical Boltzmann–Gibbs approach as a particular case, was proposed by Tsallis (1988) and might correctly cover at least some of the known anomalies.

In Earth's physics, a significant attempt was made in a series of works (Main 1996, Main and Henderson 2000, Rundle *et al*. 2003) that use classical statistical physics to describe seismicity. Then a natural question arises: *What type of statistical physics is appropriate to commonly describe effects from fracture level to seismicity scale?* Generalizing and integrating the question *What type of statistical physics is appropriate to commonly describe the Earth's dynamics and natural hazards* is a challenge.

An answer to the above question(s) could be the application of non extensive statistical mechanics, originally introduced by Tsallis (1988). The latter is supported by the fact that this type of mechanics is the appropriate methodological tool to describe entities with fractal or multi-fractal distribution of their elements and where long-range interactions or intermittency are important, as in the Earth's systems are.

It is well known that Earth's phenomena are among the most relevant paradigms of the so-called self-organized criticality. Despite the Earth's

complexity, some of the known empirical laws are considerably simple, as, for instance, the Omori law for temporal distribution of aftershocks and the Gutenberg–Richter (GR) law for a relationship between frequency and magnitude. Furthermore, the precise dynamics is most frequently unknown for many Earth systems. The modern statistical mechanics offers a consistent theoretical framework, to address the problems of Earth physics and to understand the physics of natural hazards. To this direction, the present issue on "Statistical Mechanics in Earth Physics and Natural Hazards" is willing to contribute, not giving answers but most important reframing of the traditional but still open questions.

R e f e r e n c e s

Main, I. (1996), Statistical physics, seismogenesis, and seismic hazard, *Rev. Geophys*. **34**, 4, 433-462, DOI: 10.1029/96RG02808.

Main, I.G., G. O'Brien, and J.R. Henderson (2000), Statistical physics of earthquakes: Comparison of distribution exponents for source area and potential energy and the dynamic emergence of log-periodic energy quanta, *J. Geophys. Res*. **105**, B3, 6105-6126, DOI: 10.1029/1999JB900396.

Rundle, J.B., D.L. Turcotte, R. Shcherbakov, W. Klein, and C. Sammis (2003), Statistical physics approach to understanding the multiscale dynamics of earthquake fault systems, *Rev. Geophys*. **41**, 1019, DOI: 10.1029/2003RG 000135.

Tsallis, C. (1988), Possible generalization of Boltzmann–Gibbs statistics, *J. Stat. Phys*. **52**, 1-2, 479-487, DOI: 10.1007/BF01016429.

Nonadditive Entropy *Sq* and Nonextensive Statistical Mechanics: Applications in Geophysics and Elsewhere

Constantino TSALLIS

Centro Brasileiro de Pesquisas Fisicas and National Institute of Science and Technology for Complex Systems, Rio de Janeiro, Brazil
e-mail: tsallis@cbpf.br

Santa Fe Institute, Santa Fe, NM, USA

A b s t r a c t

The celebrated Boltzmann–Gibbs (BG) entropy, $S_{BG} = -k\sum_i p_i \ln p_i$, and associated statistical mechanics are essentially based on hypotheses such as ergodicity, *i.e.*, when ensemble averages coincide with time averages. This dynamical simplification occurs in classical systems (and quantum counterparts) whose microscopic evolution is governed by a ***positive*** largest Lyapunov exponent (LLE). Under such circumstances, relevant microscopic variables behave, from the probabilistic viewpoint, as (nearly) independent. Many phenomena exist, however, in natural, artificial and social systems (geophysics, astrophysics, biophysics, economics, and others) that violate ergodicity. To cover a (possibly) wide class of such systems, a generalization (nonextensive statistical mechanics) of the BG theory was proposed in 1988. This theory is based on nonadditive entropies such as $S_q = k \frac{1-\sum_i p_i^q}{q-1}$ ($S_1 = S_{BG}$). Here we comment some central aspects of this theory, and briefly review typical predictions, verifications and applications in geophysics and elsewhere, as illustrated through theoretical, experimental, observational, and computational results.

Key words: nonadditive entropy, nonextensive statistical mechanics, complex systems.

1. INTRODUCTION

Statistical mechanics constitutes, together with electromagnetism (basically Maxwell equations) and classical (basically Newton's law), quantum (basically Schroedinger equation), and relativistic (basically Einstein's special and general relativity) mechanics, one of the pillars of contemporary physics. As its name indicates, *statistical mechanics* is essentially constructed from two ingredients, namely *mechanics* (including the electro-magnetic forces) and *theory of probabilities* (see Fig. 1). From this level, which is to be considered as from first principles, we may construct concepts such as energy and entropy, including their operational mathematical expressions. How to find the expressions for the energy is described in all good textbooks of mechanics (classical, quantum, relativistic). What concerns a similar task for the entropy, it has proved along 140 years (since the 1860-1870's, when Clausius and Boltzmann first focused on this issue) to be a particularly delicate matter. In principle, it goes like this. Guided by thermodynamics, we
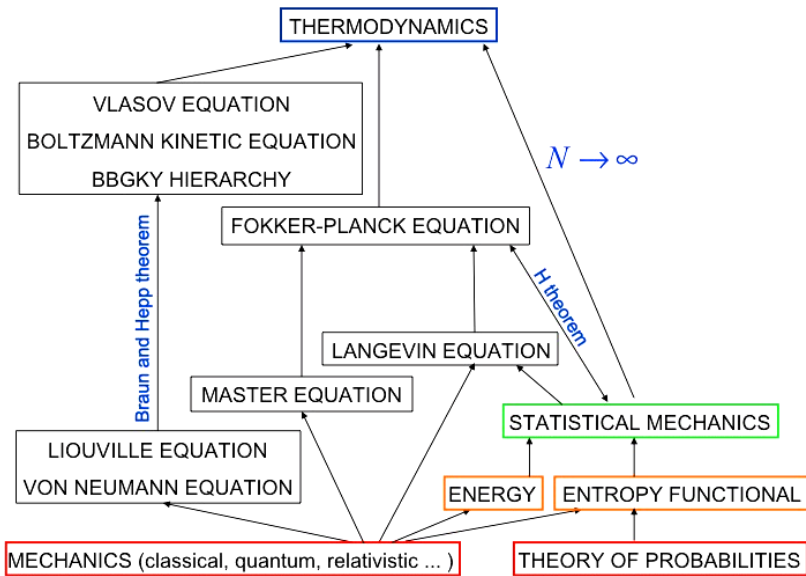

Fig. 1. Schematic and non-exhaustive connections that exist related with statistical mechanics. In red we have what we may call the first-principles or *microscopic* level, from where we can, in one or another, derive the concepts of energy and entropy (in orange). These concepts lead to statistical mechanics (in green), which, in turn, connects to thermodynamics or *macroscopic* level (in blue) for large systems. Many *mesoscopic* levels exist as well, of which we have indicated here only the most common ones. Colour version of this figure is available in electronic edition only.

would like the entropy S of a macroscopic system to be ***extensive***, *i.e.*, $S(N) \propto N (N \to \infty)$, N being the number of elements of the system. We expect this entropic extensivity to be valid for both short-and long-range interactions. For short-range interactions, it is well known that it should be so, as explained in any good textbook of thermodynamics. The question is more subtle for long-range interactions, for which the total energy U becomes nonextensive (more precisely, $U(N)$ is expected to increase faster than N for large N). But even in this case, the thermodynamic entropy should remain extensive, as lengthily argued and verified in the literature (see *e.g.*, Section 3.3.1 of Tsallis 2009a). Accepting this general thermodynamic demand, the next relevant question is what mathematical connection between S and its probabilistic expression (in terms of the admissible microscopic configurations) adequately takes into account the correlations existing between the N elements of the system in such a way that $S(N)$ is extensive. Let us illustrate this crucial point in what follows.

Assume that we have a system whose total number $W(N)$ of admissible microscopic configurations are equally probable, and satisfies

$$W(N) \propto \mu^N \ (N \to \infty, \quad \mu > 1),\tag{1}$$

Such a hypothesis corresponds to probabilistic independence (or quasi-independence) of the N elements of the system, since $W(N+1) \sim \mu W(N)$.

We know of course that the Boltzmann-Gibbs (BG) entropy is given (for discrete variables) by

$$S_{BG} = -k \sum_{i=1}^{W} p_i \ln p_i \quad \left(\sum_{i=1}^{W} p_i = 1 \right),\tag{2}$$

hence, for equal probabilities, we have

$$S_{BG} = k \ln W .\tag{3}$$

If we introduce Eq. (1) in Eq. (3), we obtain

$$S_{BG}(N) = k \ln W(N) \propto N .\tag{4}$$

In other words, the BG formula precisely yields the desired extensivity for the entropy.

Let us assume now a system whose elements are strongly correlated in such a way that the number of equally probable admissible configurations (*i.e.*, configurations whose probability is nonzero) satisfies

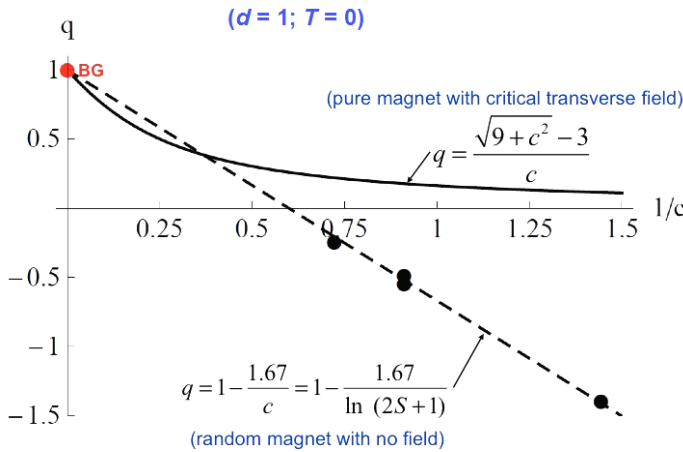$$W(N) \propto N^\rho \quad (N \to \infty, \quad \rho > 0).\tag{5}$$

Fig. 2. Dependence of q_{ent} on the central charge c of pure (Caruso and Tsallis 2008) and random (Saguia and Sarandy 2010) one-dimensional magnets undergoing quantum phase transitions at zero temperature, where the entire strongly entangled N-system is in its ground state (hence corresponding to a vanishing entropy since the ground state is a pure state), in contrast to the L-subsystem which is in a mixed state (hence corresponding to a nonvanishing entropy). For this value of q, the block nonadditive entropy S_q is extensive, whereas its additive BG entropy is nonextensive. Notice that, for the pure magnet, we have $q_{ent} \in [0, 1]$, whereas, for the random magnet, we have $q_{ent} \in (-\infty, 1]$. Both cases recover, in the $c \to \infty$ limit, the BG value $q_{ent} = 1$. These examples definitively clarify that additivity and extensivity are different properties. The only reason for which they have been confused (and still are confused in the mind of not few scientists!) is the fact that, during 140 years, the systems that have been addressed are simple, and not complex, thermodynamically speaking. For such non-pathological systems, the additive BG entropy happens to be extensive, and is naturally the one that should be used. Colour version of this figure is available in electronic edition only.

We cannot use S_{BG} in this case, since it implies $S_{BG}(N) \propto \ln N$, which violates thermodynamics. But we may consider instead the following generalized expression (Tsallis 1988):

$$S_q = k \frac{1 - \sum_{i=1}^{W} p_i^q}{q-1} = -k \sum_{i=1}^{W} p_i^q \ln_q p_i = k \sum_{i=1}^{W} p_i \ln_q \frac{1}{p_i} \quad \left(\sum_{i=1}^{W} p_i = 1 \right), \qquad (6)$$

where $\ln_q z \equiv \frac{z^{1-q}-1}{1-q}$ ($\ln_1 z = \ln z$). We straightforwardly verify the $S_1 = S_{BG}$, and also that, for equal probabilities,

$$S_q = k \ln_q W . \qquad (7)$$

If we introduce, within this entropy, expression (5), we obtain

$$S_q(N) = k \frac{[W(N)]^{1-q} - 1}{1-q} \propto N^{\rho(1-q)} . \tag{8}$$

Consequently, if we choose

$$q = 1 - \frac{1}{\rho} , \tag{9}$$

we obtain $S_{1-1/\rho}(N) \propto N$, in agreement with thermodynamics. This is the basic reason why the BG entropy must be adequately replaced in cases where strong correlations exist in the system. It is appropriate to mention here that all kinds of asymptotic mathematical behaviors can in principle exist for $W(N)$. For those, other entropic functionals become necessary in order to have extensivity. In the present work, however, we focus on Eq. (5), which represents in fact a quite wide class of natural, artificial and social systems, as we shall see later on. Verifications on other probabilistic and physical models do exist in the literature which illustrates the fact that S_q is extensive for special values of q, which characterize the universality class of the system (see Tsallis 2004, Tsallis *et al.* 2005, and Caruso and Tsallis 2008). In Fig. 2 we exhibit that special value of q for fully quantum-entangled pure and random magnetic systems.

Let us close this section by emphasizing that ***nonextensivity*** must be well distinguished from ***nonadditivity*** (Penrose 1970) Indeed, an entropy is said additive if, for two probabilistically independent systems A and B, we verify that $S(A + B) = S(A) + S(B)$. We can easily establish that

$$\frac{S_q(A+B)}{k} = \frac{S_q(A)}{k} + \frac{S_q(B)}{k} + (1-q)\frac{S_q(A)}{k}\frac{S_q(B)}{k} . \tag{10}$$

Therefore, S_{BG} is additive, whereas, for $q \neq 1$, S_q is nonadditive.

2.   EXTREMIZATION OF S_q AND q-GENERALIZED CENTRAL LIMIT THEOREMS

Let us now focus on the case where the random variable $\mathbf{x}$ is a continuous dimensionless D-dimensional one. The q-entropy is then given by[1]

---

[1]We should naturally have in mind that this type of expression cannot be used in thermo-statistics for extremely low temperatures, where the quantum nature of natural systems must be taken into account. In other words, if $p(\mathbf{x})$ is too thin, *i.e.*, too close to a Dirac delta $\delta(\mathbf{x} - \mathbf{x}_0)$, Eq. (11) will become negative ($\forall q$), which is inadmissible for entropy.

$$S_q = k \frac{1 - \int d\mathbf{x} \left[p(\mathbf{x}) \right]^q}{q - 1} = -k \int d\mathbf{x} \left[p(\mathbf{x}) \right]^q \ln_q p(\mathbf{x})$$

$$= k \int d\mathbf{x} \, p(\mathbf{x}) \ln_q \frac{1}{p(\mathbf{x})} \quad \left(\int d\mathbf{x} \, p(\mathbf{x}) = 1 \right). \tag{11}$$

We further assume that we have a ***cost function*** $E(\mathbf{x})$ (*e.g.*, the Hamiltonian of the total system in mechanical systems), and that we know the q-mean value (which characterizes the **width** of the distribution $p(\mathbf{x})$ even when its standard mean value $\langle E(\mathbf{x}) \rangle_1$ diverges (Budde *et al.* 2001, Tsallis *et al.* 2009)) of this cost function, *i.e.*,

$$\left\langle E(\mathbf{x}) \right\rangle_q \equiv \frac{\int d\mathbf{x} \, E(\mathbf{x}) \left[p(\mathbf{x}) \right]^q}{\int d\mathbf{x} \left[p(\mathbf{x}) \right]^q} . \tag{12}$$

Notice that this quantity is finite up to the same value of q for which the norm $\int d\mathbf{x} p(\mathbf{x})$ itself is finite.

If our system is a dynamical one with a physically relevant stationary state (a frequent case), this state is the one which, under the constraint (12), extremizes S_q. It is quite straightforward to verify that the maximizing distribution is as that given by Tsallis (1988), Curado and Tsallis (1991), and Tsallis *et al.* (1998)

$$p_q(\mathbf{x}) = \frac{e_q^{-\beta E(\mathbf{x})}}{\int dx \, e_q^{-\beta E(\mathbf{x})}} \quad (\beta > 0), \tag{13}$$

where $e_q^z (e_1^z = e^z)$ is the inverse function of $\ln_q z$, *i.e.*, $e_q^z \equiv [1 + (1 - q) z]_+^{\frac{1}{1-q}}$, with $[z]_+ = z$ if $z \geq 0$, and zero otherwise.

If $\mathbf{x}$ is a $D = 1$ continuous variable x, and $E(x) \propto x$, the constraint (12) becomes the value of $\langle x \rangle_q$, hence

$$p_q(x) = \frac{e_q^{-\beta_1 x}}{\int dx \, e_q^{-\beta_1 x}} \quad (\beta_1 > 0), \tag{14}$$

This distribution is normalizable for $q < 2$, and has a finite mean value $\langle x \rangle_1$ for $q < 3/2$. For $q \geq 1$ it has an infinite support, whereas it is finite for $q < 1$.

If $\langle x \rangle_q = 0$, and we happen to know $\langle x^2 \rangle_q$, this quantity becomes the constraint (12), and can be used to characterize the width. The extremization of S_q then yields

$$p_q(x) = \frac{e_q^{-\beta_2 x^2}}{\int dx \, e_q^{-\beta_2 x^2}} \quad (\beta_2 > 0), \tag{15}$$

which from now on will be referred to as q-Gaussian distribution[2]. It is normalizable for $q < 3$, and has a finite variance $\langle x^2 \rangle_1$ for $q < 5/3$[3].

For $q \geq 1$ it has an infinite support, whereas it is finite for $q < 1$. For $q > 1$, q-Gaussians asymptotically decay as power-laws (more precisely like $x^{-2/(q-1)}$). However, they are quite different from the Lévy distributions, which also decay like power-laws (the only case in which q-Gaussians and Lévy distributions coincide is for $q = 2$, which corresponds to the Cauchy–Lorentz distribution). Quite frequently, in the literature, any distribution decaying like a power-law is referred to as a "Lévy distribution", which constitutes a rather regrettable mistake.

Let us mention at this stage an interesting mesoscopic property of q-exponentials and q-Gaussians. We consider the following nonlinear diffusion-relaxation equation:

$$\frac{\partial p(x, t)}{\partial t} = D \frac{\partial^2 \left[p(x, t) \right]^{2-q}}{\partial x^2} - R \left[p(x, t) \right]^q \left(\int \mathrm{d}x \, p(x, 0) = 1 \right), \qquad (16)$$

where D and R are constant phenomenological coefficients. If $D = 0$ we have

$$p(x, t) = p(x, 0) e_q^{-Rt} (\forall x), \qquad (17)$$

which has the form of Eq. (14) with $\beta_1 = R$. If we have instead $R = 0$ we obtain (Plastino and Plastino 1995, Tsallis and Bukman 1996) the form of Eq. (15)

$$p(x, t) \propto e_q^{-\beta_2(t)x^2}, \qquad (18)$$

where β_2 is related with D. In other words, q-exponentials and q-Gaussians are exact solutions of basic nonlinear diffusion-relaxation equations. They can be shown to also provide exact stationary states of similar though inhomogenous equations (dos Santos and Tsallis 2010).

---

[2]Since long known in plasma physics under the name *suprathermal* or κ *distributions* (Rios and Galvão 2011) if $q > 1$, and equal to the Student's t-distributions (de Souza and Tsallis 1997) for special rational values of $q > 1$; for special rational values of $q < 1$, it coincides with the so-called r-distributions (de Souza and Tsallis 1997). They are also occasionally referred to as generalized Lorentzians (Treumann 1998).

[3]If x is a D-dimensional real vector, normalizability mandates that $\int_0^\infty \mathrm{d}x \, x^{D-1} e_q^{-\beta x^2}$ converges, hence $q < \frac{D+2}{D}$. If, in addition to that, the system has a density of states $\phi(x)$ which diverges like x^δ for $x \to \infty$ (a quite frequent case), then normalizability mandates $\int_0^\infty \mathrm{d}x \, x^{D-1} \phi(x) e_q^{-\beta x^2}$ converges, hence $q < \frac{D+\delta+2}{D+\delta}$. Similarly, the finiteness of the second moment mandates that $\int_0^\infty \mathrm{d}x \, x^{D+1} \phi(x) e_q^{-\beta x}$ converges, hence $q < \frac{D+\delta+4}{D+\delta+2}$.

We have briefly reminded above that these distributions appear simultaneously as those which optimize (maximize for $q > 0$, and minimize for $q < 0$), under appropriate constraints, the nonadditive entropy S_q, and as those which exactly solve nonlinear/inhomogeneous diffusion-relaxation equations. Let us conclude by mentioning another remarkable property, namely that q-Gaussians constitute attractors in the sense of the classical central limit theorem (CLT). This theorem basically states that, if we consider the sum $S_N = \sum_{i=1}^{N} X_i$ of N **independent** (or nearly independent in some sense) random variables $\{X_i\}$, each of them having a ***finite*** variance, this sum converges for $N \to \infty$, after appropriate centering and rescaling, to a Gaussian. This most important theorem can be proved in a variety of manners and under a slightly different hypothesis. One of those standard proofs uses the Fourier transform, which has been q-generalized (Umarov *et al.* 2008, 2010).

Around 2000 (Bologna *et al.* 2000), q-Gaussians have been conjectured (see details in Tsallis 2005) to be attractors in the CLT sense whenever the N random variables that are being summed are strongly correlated in a specific manner. The conjecture was recently proved in the presence of q-independent variables (Umarov *et al.* 2008, 2010). The proof presented in Umarov *et al.* (2008) is based on a q-generalization of the Fourier transform, denoted as q-Fourier transform, and the theorem is currently referred to as the q-CLT. The validity of this proof has been recently challenged by Hilhorst (2009, 2010). His criticism is constructed on the inexistence of inverse q-Fourier transform for $q > 1$, which he illustrates with counterexamples. The inverse, as used in the Umarov *et al.* (2008) paper, indeed does not exist in general, which essentially makes the proof presented in Umarov *et al.* (2008) a proof of existence, but not of uniqueness. The q-generalization of the inverse Fourier transform appears then to be a quite subtle mathematical problem if $q \neq 1$. It has nevertheless been solved recently (Jauregui and Tsallis 2011) and further considerations can be seen in Jauregui *et al.* (2010, 2011), related to q-moments (Budde *et al.* 2001, Tsallis *et al.* 2009, Rodríguez and Tsallis 2010). Work is in progress attempting to transform the existence proof in Umarov *et al.* (2008, 2010) into a uniqueness one. It is fair to say that, at the present moment, a gap exists in the complete proof (not necessarily in the thesis) of the q-CLT as it stands in Umarov *et al.* (2008). In the meanwhile, several other forms (Vignat and Plastino 2007, 2009, Hahn *et al.* 2010) of closely related q-generalized CLT's have already been published which do not use the inverse q-Fourier transform (see Fig. 3).

Probabilistic models have been formulated (Rodríguez *et al.* 2008, Hanel *et al.* 2009) which, in the $N \to \infty$ limit, yield q-Gaussians. These models are scale-invariant, which might suggest that q-independence implies (either strict or asymptotic) scale-invariance, but this is an open problem at the

	$q = 1$ [*independent*]	$q \neq 1$ (*i.e.*, $Q \equiv 2q - 1 \neq 1$) [*globally correlated*]
$\sigma_Q < \infty$ ($\alpha = 2$)	$F(x) = $ *Gaussian* $G(x)$ with same σ_1 of $f(x)$ Classic CLT	$F(x) = G_q(x) \equiv G_{(3q_1-1)/(1+q_1)}(x)$, with same σ_Q of $f(x)$ $G_q(x) \sim \begin{cases} G(x) \\ \quad \text{if } |x| \ll x_c(q,2) \\ f(x) \sim C_q/|x|^{2/(q-1)} \\ \quad \text{if } |x| \gg x_c(q,2) \end{cases}$ with $\lim_{q \to 1} x_c(q,2) = \infty$ S. Umarov *et al.*, Milan J. Math. 76, 307 (2008)
$\sigma_Q \to \infty$ ($0 < \alpha < 2$)	$F(x) = $ *Lévy distribution* $L_\alpha(x)$ with same $|x| \to \infty$ behavior $L_\alpha(x) \sim \begin{cases} G(x) \\ \quad \text{if } |x| \ll x_c(1,\alpha) \\ f(x) \sim C_\alpha/|x|^{1+\alpha} \\ \quad \text{if } |x| \gg x_c(1,\alpha) \end{cases}$ with $\lim_{\alpha \to 2} x_c(1,\alpha) = \infty$ Lévy-Gnedenko CLT	$F(x) = L_{q,\alpha}$, with same $|x| \to \infty$ asymptotic behavior $L_{q,\alpha} \sim \begin{cases} G_{\frac{2(1-q)-\alpha(1+q)}{2(1-q)-\alpha(3-q)},\,\alpha}(x) \sim C^*_{q,\alpha}/|x|^{\frac{2(1-q)-\alpha(3-q)}{2(1-q)}} \\ \quad (\textit{intermediate regime}) \\ G_{\frac{2\alpha q-\alpha+3}{\alpha+1},\,2}(x) \sim C^L_{q,\alpha}/|x|^{(1+\alpha)/(1+\alpha q-\alpha)} \\ \quad (\textit{distant regime}) \end{cases}$ S. Umarov *et al.*, J. Math. Phys. 51, 033502 (2010)

Fig. 3. Central limit theorems (CLT) for $q \geq 1$: $N^{1/[\alpha(2-q)]}$-scaled attractor $F(x)$ when summing $N \to \infty$ identical q-independent random variables with symmetric distribution $f(x)$ with $\sigma_Q \equiv \int dx\, x^2 [f(x)]^Q / \int dx\, [f(x)]^Q$ ($Q \equiv 2q - 1$). All the attractors of these theorems asymptotically decay as power-laws, except of the classical CLT. See details in Umarov *et al.* (2008, 2010). Colour version of this figure is available in electronic edition only.

present time. However, definitively, scale-invariance does not imply q-independence. Indeed, (strictly or asymptotically) scale-invariant probabilistic models are known (Moyano *et al.* 2006, Thistleton *et al.* 2009) which do not yield q-Gaussians, but other limiting distributions instead, some of which have been proved to be amazingly close to q-Gaussians (Hilhorst and Schehr 2007).

Some of the predictions, verifications and applications of this q-generalized theory are briefly reviewed in the rest of the present paper, which is based in fact on various previous books and reviews (Tsallis

2009a, b, 2011, Gell-Mann and Tsallis 2004, Boon and Tsallis 2005), parts of which are here followed/reproduced for simplicity and self-completeness.

3.   APPLICATIONS

In this section we briefly and non exhaustively review various predictions, verifications and applications of q-exponentials and q-Gaussians through analytical, experimental, observational and computational methods in natural, artificial and social systems that are available in the literature (see at http://tsallis.cat.cbpf.br/biblio.htm for full bibliography). The present list enriches the one recently presented in Tsallis (2011). Several of these applications concern, as it can be checked in what follows, geophysical phenomena, especially earthquakes and similar ones.

❑   The velocity distribution of (cells of) **_Hydra viridissima_** follows a q-Gaussian probability distribution function (PDF) with $q \simeq 3/2$ (Upadhyaya *et al*. 2001). Anomalous diffusion has been independently measured as well (Upadhyaya *et al*. 2001), and an exponent $\gamma \simeq 4/3$ has been observed (where the squared space x^2 scales with time t like t^γ). Therefore, within the error bars, the prediction $\gamma = 2/(3-q)$ (Tsallis and Bukman 1996) is verified in this system.

❑   The velocity distribution of the point defects in defect turbulence, as well as its corresponding anomalous diffusion, have been measured (Daniels *et al*. 2004). The results suggest a q-Gaussian PDF with $q \simeq 3/2$, and $\gamma \simeq 4/3$ which constitutes another verification of the prediction $\gamma = 2/(3-q)$ (Tsallis and Bukman 1996).

❑   The velocity distribution of cold atoms in a dissipative optical lattice was predicted (Lutz 2003) to be a q-Gaussian with $q = 1 + 44\frac{E_r}{U_0}$, where E_r and U_0 are parameters related to the optical lattice potential. This prediction was verified three years later, both in the laboratory and with quantum Monte Carlo techniques (Douglas *et al*. 2006, Baris Bagci and Tirnakli 2009).

❑   Computational simulations of the velocity distribution, and of the associated anomalous diffusion, during silo drainage suggest $q \simeq 3/2$ and $\gamma \simeq 4/3$ (Arevalo *et al*. 2007), once again satisfying the prediction $\gamma = 2/(3-q)$ (Tsallis and Bukman 1996).

❑   The velocity distribution in a driven-dissipative 2D dusty plasma was found to be of the q-Gaussian form, with $q = 1.08 \pm 0.01$ and $q = 1.05 \pm 0.01$ at temperatures of 30000 and 61000 K, respectively (Liu and Goree 2008).

❑ The spatial (Monte Carlo) distributions of a trapped $^{136}Ba^+$ ion cooled by various classical buffer gases at 300 K was verified to be of the q-Gaussian form, with q increasing from close to unity to about 1.9 when the mass of the molecules of the buffer increases from that of He to about 200 (De Voe 2009).

❑ The distributions of price returns and stock volumes at the New York and NASDAQ stock exchanges are well fitted by q-Gaussians and q-exponentials, respectively (Borland 2002, Duarte Queirós 2005a). The volatilities predicted within this approach fit well the real data. Various other economical and financial applications are available (Borges 2004, Mattedi et al. 2004, Borland and Bouchaud 2004, Borland 2005, Duarte Queirós 2005b, Takahashi et al. 2007, Ferrero 2011), including those associated with extreme values and risk (Ludescher et al. 2011).

❑ The Bak-Sneppen model of biological evolution exhibits a time-dependence of the spread of damage which is well approached by a q-exponential with $q < 1$ (Tamarit et al. 1998).

❑ The distributions of returns in the Ehrenfest's dog-flea model exhibit a q-Gaussian form (Bakar and Tirnakli 2010).

❑ The distributions of returns in the coherent noise model are well fitted with q-Gaussians where q is analytically obtained through $q = (2+\tau)/\tau$, τ being the exponent associated with the distribution of sizes of the events (Celikoglu et al. 2010).

❑ The distributions of returns of the avalanche sizes in the self-organized critical Olami–Feder–Christensen model, as well as in real earth-quakes exhibit a q-Gaussian form (Caruso et al. 2007).

❑ The distributions of angles in the HMF model approaches as time evolves towards a q-Gaussian form with $q \simeq 1/5$ (Moyano and Anteneodo 2006).

❑ Experimental measurements of the turbulence in pure electron plasma are analytically reproduced with $q = 1/2$ (Boghosian 1996).

❑ The relaxation in various paradigmatic spin-glass substances through neutron spin echo experiments is well reproduced by q-exponential forms with $q > 1$ (Pickup et al. 2009).

❑ The fluctuating time dependence of the width of the ozone layer over Buenos Aires (and, presumably, around the Earth) yields a q-triplet with $q_{sen} < 1 < q_{stat\ state} < q_{rel}$ (Ferri et al. 2010).

❑ Diverse properties for conservative and dissipative nonlinear dynamical systems are well described within q-statistics (Anteneodo and Tsallis 1998, Lyra and Tsallis 1998, Borges et al. 2002, Añaños and Tsallis 2004, Baldovin and Robledo 2004, Añaños et al. 2005, Tirnakli et al. 2007,

2009, Pluchino *et al*. 2008, Afsar and Tirnakli 2010, Leo *et al*. 2010, Fuentes *et al*. 2011, Frank 2011).

❑ The degree distribution of (asymptotically) scale-free networks is numerically calculated and is well approached by a *q*-exponential distribution (Thurner and Tsallis 2005).

❑ The tissue radiation response follows a *q*-exponential form (Sotolongo-Grau *et al*. 2010).

❑ The overdamped motion of interacting particles in type II superconductors is analytically shown to follow, at vanishing temperature, a *q*-Gaussian with $q = 0$. Moreover, the entropy is the nonadditive one associated with this value of *q* (Andrade *et al*. 2010).

❑ Experimental and simulated molecular spectra due to the rotational population in plasmas are frequently interpreted as two Boltzmann distributions corresponding to two different temperatures. These fittings involve three fitting parameters, namely the two temperatures and the relative proportion of each of the Boltzmann weights. It has been shown (Reis *et al*. 2011) that equally good fittings can be obtained with a single q-exponential weight, which has only two fitting parameters, namely *q* and a single temperature.

❑ High energy physics has been since more than one decade handled with *q*-statistics (Bediaga *et al*. 2000). During the last decade various phenomena, such as the flux of cosmic rays and others, have been shown to exhibit relevant nonextensive aspects (Wilk and Wlodarczyk 2009, Biró *et al*. 2009). The distributions of transverse momenta of hadronic jets outcoming from proton-proton collisions (as well as others) have been shown to exhibit *q*-exponentials with $q \simeq 1/1$. These results have been obtained at the LHC detectors CMS, ATLAS and ALICE (CMS Collaboration 2010, ALICE Collaboration *et al*. 2011, ATLAS Collaboration 2010), as well as at SPS and RHIC in Brookhaven (Shao *et al*. 2010). Predictions for the rapidities in such experiments have been advanced as well. These results stimulate an interesting possible dialog between nonextensive statistics and quantum chromodynamics (QCD).

❑ Various astrophysical systems exhibit nonextensive effects (Carvalho *et al*. 2008, Esquivel and Lazarian 2010, Livadiotis and McComas 2009, Livadiotis *et al*. 2011).

❑ Analysis of the magnetic field in the solar wind plasma using data from Voyager 1 and Voyager 2 strongly suggests nonextensive effects (Burlaga and Viñas 2005, Burlaga and Ness 2011).

❑ Various geophysical applications exhibit nonextensive effects (Tirnakli and Abe 2004, Abe *et al*. 2005, Papadimitriou *et al*. 2008, Vallianatos 2009, Balasis *et al*. 2009, Telesca 2010a, b; Vallianatos and

Sammonds 2010, Eftaxias 2010, Vallianatos 2011, Vallianatos *et al.* 2011a, b).

❑   Nonlinear generalizations of the Schroedinger, the Klein-Gordon and the Dirac equations have been impl emented which admit *q*-plane wave solutions as free particles, *i.e.*, solutions of the type $e_q^{i(kx-\omega t)}$ (Nobre *et al.* 2011), with the energy given by $E = \hbar\omega$ and the momentum given by $\vec{p} = \hbar\vec{k}$, $\forall q$. The nonlinear Schroedinger equation yields $E = p^2/2m$ ($\forall q$), and the nonlinear Klein-Gordon and Dirac equations yield the Einstein relation $E^2 = m^2c^4 + p^2c^2$ ($\forall q$).

❑   Phenomena in linguistics such as Zipf law and the frequency of words in various languages and literary styles (Montemurro 2004).

❑   Statistics of citations of scientific and technological papers (Tsallis and Portes de Albuquerque 2000, Anastasiadis *et al.* 2010).

❑   Processing of medical signals such as those emerging in epileptic crisis (Tong *et al.* 2002, Rosso *et al.* 2003).

❑   Processing of medical and other images (Portes de Albuquerque *et al.* 2004, Shi *et al.* 2009, Mohanalin *et al.* 2010).

❑   Global optimization algorithms generalizing simulated annealing and others (Tsallis and Stariolo 1996, Serra *et al.* 1997, Anastasiadis and Magoulas 2004).

❑   Diversified applications in theoretical chemistry (Mundim and Tsallis 1996, Andricioaei and Straub 1996, Hansmann *et al.* 1997, Gutterres *et al.* 1999, Straub and Andricioaei 1999, Fuks *et al.* 2001, Okamoto and Hansmann 2001, Moret *et al.* 2006, Kim and Straub 2009).

❑   Cognitive psychology in relation with learning and remembering (Tsallis *et al.* 2003, Takahashi *et al.* 2009, Wedemann *et al.* 2009).

❑   Astronomical systems (Carvalho *et al.* 2009).

The systematic study of metastable or long-living states in long-range versions of magnetic models such as the finite-spin Ising (Nobre and Tsallis 1995) and Heisenberg (Caride *et al.* 1983) ones, or in hydrogen-like atoms (Lucena *et al.* 1995, Oliveira-Neto *et al.* 2007), might provide further hints and applications.

4. FINAL REMARKS

The Boltzmann-Gibbs entropy and exponential weight have been generalized, during the last two decades, in various manners (Beck and Cohen 2003, Hanel and Thurner 2011, Tempesta 2011, Hanel *et al.* 2011; see further details in Tsallis 2009a). These various manners follow essentially from the 1988 proposal that we have focused on in this brief review. The correspond-

ing entropy is noted S_q and it is nonadditive; for a wide class of systems, it should be extensive for a special value of the index q, which reflects the nature of strong correlations that the elements of the system have. The corresponding thermostatistics is currently referred to as nonextensive statistical mechanics (the word **nonextensive** stands here to reflect the fact that those systems typically have an internal energy which grows faster than the number of elements N).

The applicability of these concepts has been illustrated in the previous section through analytical, numerical, experimental and observational results. Nevertheless, very many interesting questions still remain as opened issues. For example: Under what conditions q-independence and scale-invariance co-exist? Under what conditions the present generalized thermostatistics is compatible with classical thermodynamics? How well can be described with a q-exponential density matrix the mixed state of the block whose entropy has been discussed in Caruso and Tsallis (2008)? Further analysis of these and other points would be very welcome. Finally, since the present special issue is also dedicated to natural hazards, let us suggest that the (all important) evaluation of their risks could perhaps benefit from analysis done along the lines that have proved useful for financial systems, as illustrated in Ludescher *et al*. (2011).

References

Abe, S., N.V. Sarlis, E.S. Skordas, H. Tanaka, and P.A. Varotsos (2005), Origin of the usefulness of the natural-time representation of complex time series, *Phys. Rev. Lett*. **94**, 17, 170601, DOI: 10.1103/PhysRevLett.94.170601.

Afsar, O., and U. Tirnakli (2010), Probability densities for the sums of iterates of the sine-circle map in the vicinity of the quasiperiodic edge of chaos, *Phys. Rev. E* **82**, 4, 046210, DOI: 10.1103/PhysRevE.82.046210.

ALICE Collaboration, K. Aamodt, N. Abel, U. Abeysekara, A. Abrahantes Quintana, A. Abramyan, D. Adamová, M.M. Aggarwal, G. Aglieri Rinella, and A.G. Agocs, *et al*. (2011), Production of pions, kaons and protons in pp collisions at $\sqrt{s}$ = 900 GeV with ALICE at the LHC, *Eur. Phys. J. C* **71**, 6, 1655, DOI: 10.1140/epjc/s10052-011-1655-9.

Añaños, G.F.J., and C. Tsallis (2004), Ensemble averages and nonextensivity at the edge of chaos of one-dimensional maps, *Phys. Rev. Lett*. **93**, 2, 020601, DOI: 10.1103/PhysRevLett.93.020601.

Añaños, G.F.J., F. Baldovin, and C. Tsallis (2005), Anomalous sensitivity to initial conditions and entropy production in standard maps: Nonextensive approach, *Eur. Phys. J. B* **46**, 3, 409-417, DOI: 10.1140/epjb/e2005-00269-1.

Anastasiadis, A.D., and G.D. Magoulas (2004), Nonextensive statistical mechanics for hybrid learning of neural networks, *Physica A* **344**, 3-4, 372-382, DOI: 10.1016/j.physa.2004.06.005.

Anastasiadis, A.D., M.P. de Albuquerque, M.P. de Albuquerque, and D.B. Mussi (2010), Tsallis q-expo-nential describes the distribution of scientific citations – a new characterization of the impact, *Scientometrics* **83**, 1, 205-218, DOI: 10.1007/s11192-009-0023-0.

Andrade, Jr., J.S., G.F.T. da Silva, A.A. Moreira, F.D. Nobre, and E.M.F. Curado (2010), Thermostatistics of overdamped motion of interacting particles, *Phys. Rev. Lett*. **105**, 26, 260601, DOI: 10.1103/PhysRevLett.105.260601.

Andricioaei, I., and J.E. Straub (1996), Generalized simulated annealing algorithms using Tsallis statistics: Application to conformational optimization of a tetrapeptide, *Phys. Rev. E* **53**, 4, R3055-R3058, DOI: 10.1103/ PhysRevE.53.R3055.

Anteneodo, C., and C. Tsallis (1998), Breakdown of the exponential sensitivity to the initial conditions: Role of the range of the interaction, *Phys. Rev. Lett.* **80**, 24, 5313-5316, DOI: 10.1103/PhysRevLett.80.5313.

Arevalo, R., A. Garcimartin, and D. Maza (2007), Anomalous diffusion in silo drainage, *Eur. Phys. J. E* **23**, 191-198, DOI: 10.1140/epje/i2006-10174-1.

ATLAS Collaboration (2010), Charged-particle multiplicities in pp interactions at $\sqrt{s}$ = 900 GeV measured with the ATLAS detector at the LHC, *Phys. Letter. B* **688**, 1, 21-42, DOI: 10.1016/j.physletb.2010.03.064.

Bakar, B., and U. Tirnakli (2010), Return distributions in dog-flea model revisited, *Physica A* **389**, 17, 3382-3386, DOI: 10.1016/j.physa.2010.04.037.

Balasis, G., I.A. Daglis, C. Papadimitriou, M. Kalimeri, A. Anastasiadis, and K. Eftaxias (2009), Investigating dynamical complexity in the magnetosphere using various entropy measures, *J. Geophys. Res*. **114**, A00D06, DOI: 10.1029/2008JA014035.

Baldovin, F., and A. Robledo (2004), Nonextensive Pesin identity: Exact renormalization group analytical results for the dynamics at the edge of chaos of the logistic map, *Phys. Rev. E* **69**, 045202(R), DOI: 10.1103/ PhysRevE.69.045202.

Baris Bağci, G., and U. Tirnakli (2009), Self-organization in dissipative optical lattices, *Chaos* **19**, 3, 033113, DOI: 10.1063/1.3194107.

Beck, C., and E.G.D. Cohen (2003), Superstatistics, *Physica A* **322**, 1, 267-275, DOI: 10.1016/S0378-4371.

Bediaga, I., E.M.F. Curado, and J.M. de Miranda (2000), A nonextensive thermody-namical equilibrium approach in $e^+e^- \to$ hadrons, *Physica A* **286**, 156-163, DOI: 10.1016/S0378-4371(00)00368-X.

Biró, T.S., G. Purcsel, and K. Ürmössy (2009), Non-extensive approach to quark matter, *Eur. Phys. J. A* **40**, 3, 325-340, DOI: 10.1140/epja/i2009-10806-6.

Boghosian, B.M. (1996), Thermodynamic description of the relaxation of two-dimensional turbulence using Tsallis statistics, *Phys. Rev. E* **53**, 5, 4754-4763, DOI: 10.1103/PhysRevE.53.4754.

Bologna, M., C. Tsallis, and P. Grigolini (2000), Anomalous diffusion associated with nonlinear fractional derivative Fokker-Planck-like equation: Exact time-dependent solutions, *Phys. Rev. E* **62**, 2, 2213-2218, DOI: 10.1103/PhysRevE.62.2213.

Boon, J.P., and C. Tsallis (eds.) (2005), Nonextensive Statistical Mechanics: New Trends, New Perspectives. Special Issue, *Europhys. News* **36**, 6, DOI: 10.1051/epn:2005601.

Borges, E.P. (2004), Empirical nonextensive laws for the county distribution of total personal income and gross domestic product, *Physica A* **334**, 255-266, DOI: 10.1016/j.physa.2003.11.003.

Borges, E.P., C. Tsallis, G.F.J. Ananos, and P.M.C. de Oliveira (2002), Nonequilib-rium probabilistic dynamics at the logistic map edge of chaos, *Phys. Rev. Lett.* **89**, 254103, DOI: 10.1103/PhysRevLett.89.254103.

Borland, L. (2002), Option pricing formulas based on a non-Gaussian stock price model, *Phys. Rev. Lett.* **89**, 098701, DOI: 10.1103/PhysRevLett.89.098701.

Borland, L. (2005), Long-range memory and nonextensivity in financial markets, *Europhys. News* **36**, 6, 228-231, DOI: 10.1051/epn:2005615.

Borland, L., and J.-P. Bouchaud (2004), A non-Gaussian option pricing model with skew, *Quant. Finance* **7**, 6, 703, DOI: 10.1080/14697680701790014.

Budde, C., D. Prato, and M. Ré (2001), Superdiffusion in decoupled continuous time random walks, *Phys. Lett. A* **283**, 5-6, 309-312, DOI: 10.1016/S0375-9601(01)00234-1.

Burlaga, L.F., and N.F. Ness (2011), Transition from the sector zone to the unipolar zone in the heliosheath: Voyager 2 magnetic field observations, *Astrophys. J.* **737**, 1, 35, DOI: 10.1088/0004-637X/737/1/35.

Burlaga, L.F., and A.F. Viñas (2005), Triangle for the entropic index q of non-extensive statistical mechanics observed by Voyager 1 in the distant helio-sphere, *Physica A* **356**, 1-2, 375-384, DOI: 10.1016/j.physa.2005.06.065.

Caride, A.O., C. Tsallis, and S.I. Zanette (1983), Criticality of the anisotropic quan-tum Heisenberg model on a self-dual hierarchical lattice, *Phys. Rev. Lett.* **51**, 3, 145-147, DOI: 10.1103/PhysRevLett.51.145.

Caruso, F., and C. Tsallis (2008), Nonadditive entropy reconciles the area law in quantum systems with classical thermodynamics, *Phys. Rev. E* **78**, 2, 021102, DOI: 10.1103/PhysRevE.78.021102.

Caruso, F., A. Pluchino, V. Latora, S. Vinciguerra, and A. Rapisarda (2007), Analysis of self-organized criticality in the Olami-Feder-Christensen model and in real earthquakes, *Phys. Rev. E* **75**, 5, 055101(R), DOI: 10.1103/PhysRevE.75.055101.

Carvalho, J.C., R. Silva, J.D. do Nascimento, and J.R. de Medeiros (2008), Power law statistics and stellar rotational velocities in the Pleiades, *Europhys. Lett*. **84**, 5, 59001, DOI: 10.1209/0295-5075/84/59001.

Carvalho, J.C., J.D. do Nascimento, R. Silva, and J.R. De Medeiros (2009), Non-gaussian statistics and stellar rotational velocities of main-sequence field stars, *Astrophys. J. Lett*. **696**, 1, L48, DOI: 10.1088/0004-637X/696/1/L48.

Celikoglu, A., U. Tirnakli, and S.M. Duarte Queirós (2010), Analysis of return distributions in the coherent noise model, *Phys. Rev. E* **82**, 2, 021124, DOI: 10.1103/PhysRevE.82.021124.

CMS Collaboration (2010), Transverse-momentum and pseudorapidity distributions of charged hadrons in pp collisions at $\sqrt{s}$ = 7 TeV, *Phys. Rev. Lett*. **105**, 2, 022002, DOI: 10.1103/PhysRevLett.105.022002.

Curado, E.M.F., and C. Tsallis (1991), Generalized statistical mechanics: connection with thermodynamics, *J. Phys. A* **24**, L69-L72, DOI: 10.1088/0305-4470/24/2/004 (Corrigenda: DOI: 10.1088/0305-4470/25/4/038).

Daniels, K.E., C. Beck, and E. Bodenschatz (2004), Defect turbulence and generalized statistical mechanics, *Physica D* **193**, 1-4, 208-217, DOI: 10.1016/j.physd.2004.01.033.

De Souza, A.M.C., and C. Tsallis (1997), Student's t- and r-distributions: Unified derivation from an entropic variational principle, *Physica A*, **236**, 1-2, 52-57, DOI: 10.1016/S0378-4371(96)00395-0.

De Voe, R.G. (2009), Power-law distributions for a trapped ion interacting with a classical buffer gas, *Phys. Rev. Lett*. **102**, 6, 063001, DOI: 10.1103/PhysRevLett.102.063001.

dos Santos, B.C., and C. Tsallis (2010), Time evolution towards q-Gaussian stationary states through unified Itô-Stratonovich stochastic equation, *Phys. Rev. E* **82**, 6, 061119, DOI: 10.1103/PhysRevE.82.061119.

Douglas, P., S. Bergamini, and F. Renzoni (2006), Tunable Tsallis distributions in dissipative optical lattices, *Phys. Rev. Lett*. **96**, 11, 110601, DOI: 10.1103/PhysRevLett.96.110601.

Duarte Queirós, S.M. (2005a), On non-Gaussianity and dependence in financial in time series: A nonextensive approach, *Quant. Finance* **5**, 5, 475-487, DOI: 10.1080/14697680500244403.

Duarte Queirós, S.M. (2005b), On the emergence of a generalised Gamma distribution. Application to traded volume in financial markets, *Europhys. Lett.* **71**, 3, 339, DOI: 10.1209/epl/i2005-10109-0.

Eftaxias, K. (2010), Footprints of nonextensive Tsallis statistics, selfaffinity and universality in the preparation of the L'Aquila earthquake hidden

in a pre-seismic EM emission, *Physica A* **389**, 1, 133-140, DOI: 10.1016/ j.physa.2009.08.034.

Esquivel, A., and A. Lazarian (2010), Tsallis statistics as a tool for studying interstellar turbulence, *Astrophys. J.* **710**, 1, 125, DOI: 10.1088/0004-637X/710/1/125.

Ferrero, J.C. (2011), A statistical analysis of stratification and inequity in the income distribution, *Eur. Phys. J. B* **80**, 2, 255-261, DOI: 10.1140/epjb/e2011-11018-2.

Ferri, G.L., M.F. Reynoso Savio, and A. Plastino (2010), Tsallis *q*-triplet and the ozone layer, *Physica A* **389**, 9, 1829-1833, DOI: 10.1016/j.physa.2009.12.020.

Frank, T.D. (2011), Stochastic processes and mean field systems defined by nonlinear Markov chains: An illustration for a model of evolutionary population dynamics, *Braz. J. Phys.* **41**, 2-3, 129-134, DOI: 10.1007/s13538-011-0024-3.

Fuentes, M.A., Y. Sato, and C. Tsallis (2011), Sensitivity to initial conditions, entropy production, and escape rate at the onset of chaos, *Phys. Lett. A* **375**, 33, 2988-2991, DOI: 10.1016/j.physleta.2011.06.039.

Fuks, D., S. Dorfman, K.C. Mundim, and D.E. Ellis (2001), Stochastic molecular dynamics in simulations of metalloid impurities in metals, *Int. J. Quant. Chem.* **85**, 4-5, 354-367, DOI: 10.1002/qua.1533.

Gell-Mann, M., and C. Tsallis (eds.) (2004), *Nonextensive Entropy Interdisciplinary Applications*, Oxford University Press, New York.

Gutterres, R.F., M. Argollo de Menezes, C.E. Fellows, and O. Dulieu (1999), Generalized simulated annealing method in the analysis of atom-atom interaction, *Chem. Phys. Lett.* **300**, 1-2, 131-139, DOI: 10.1016/S0009-2614(98)01243-3.

Hahn, M.G., X. Jiang, and S. Umarov (2010), On *q*-Gaussians and exchangeability, *J. Phys. A* **43**, 16, 165208, DOI: 10.1088/1751-8113/43/16/165208.

Hanel, R., and S. Thurner (2011), A comprehensive classification of complex statistical systems and an axiomatic derivation of their entropy and distribution functions, *Europhys. Lett.* **93**, 2, 20006, DOI: 10.1209/0295-5075/93/20006.

Hanel, R., S. Thurner, and C. Tsallis (2009), Limit distributions of scale-invariant probabilistic models of correlated random variables with the *q*-Gaussian as an explicit example, *Eur. Phys. J. B* **72**, 2, 263-268, DOI: 10.1140/epjb/e2009-00330-1.

Hanel, R., S. Thurner, and M. Gell-Mann (2011), Generalized entropies and the transformation group of superstatistics, *Proc. Nat. Acad. Sci. USA* **108**, 16, 6390-6394, DOI: 10.1073/pnas.1103539108.

Hansmann, U.H.E., M. Masuya, and Y. Okamoto (1997), Characteristic temperatures of folding of a small peptide, *Proc. Natl. Acad. Sci. USA* **94**, 20, 10652-10656, DOI: 10.1073/pnas.94.20.10652.

Hilhorst, H.J. (2009), Central limit theorems for correlated variables: some critical remarks, *Braz. J. Phys*. **39**, 2A, 371-379.

Hilhorst, H.J. (2010), Note on a *q*-modified central limit theorem, *J. Stat. Mech*. **2010**, P10023, DOI: 10.1088/1742-5468/2010/10/P10023.

Hilhorst, H.J., and G. Schehr (2007), A note on *q*-Gaussians and non-Gaussians in statistical mechanics, *J. Stat. Mech*. **2007**, P06003, DOI: 10.1088/1742-5468/2007/06/P06003.

Jauregui, M., and C. Tsallis (2010), New representations of π and Dirac delta using the nonextensive-statistical-mechanics *q*-exponential function, *J. Math. Phys*. **51**, 6, 063304, DOI: 10.1063/1.3431981.

Jauregui, M., and C. Tsallis (2011), *q*-generalization of the inverse Fourier transform, *Phys. Lett. A* **375**, 21, 2085-2088, DOI: 10.1016/j.physleta.2011.04.014.

Jauregui, M., C. Tsallis, and E.M.F. Curado (2011), *q*-moments remove the degeneracy associated with the inversion of the *q*-Fourier transform, *J. Stat. Mech*. **2011**, P10016, DOI: 10.1088/1742-5468/2011/10/P10016.

Kim, J., and J.E. Straub (2009), Optimal replica exchange method combined with Tsallis weight sampling, *J. Chem. Phys*. **130**, 14, 144114, DOI: 10.1063/1.3108523.

Leo, M., R.A. Leo, and P. Tempesta (2010), Thermostatistics in the neighborhood of the π-mode solution for the Fermi-Pasta-Ulam *β* system: From weak to strong chaos, *J. Stat. Mech.* **2010**, P04021, DOI: 10.1088/1742-5468/2010/04/P04021.

Liu, B., and J. Goree (2008), Superdiffusion and non-Gaussian statistics in a driven-dissipative 2D dusty plasma, *Phys. Rev. Lett.* **100**, 5, 055003, DOI: 10.1103/PhysRevLett.100.055003.

Livadiotis, G., and D.J. McComas (2009), Beyond kappa distributions: Exploiting Tsallis statistical mechanics in space plasmas, *J. Geophys. Res*. **114**, A11105, DOI: 10.1029/2009JA014352.

Livadiotis, G., D.J. McComas, M.A. Dayeh, H.O. Funsten, and N.A. Schwadron (2011), First sky map of the inner heliosheath temperature using IBEX spectra, *Astrophys. J.* **734**, 1, DOI: 10.1088/0004-637X/734/1/1.

Lucena, L.S., L.R. da Silva, and C. Tsallis (1995), Departure from Boltzmann-Gibbs statistics makes the hydrogen-atom specific heat a computable quantity, *Phys. Rev. E* **51**, 6, 6247-6249, DOI: 10.1103/PhysRevE.51.6247.

Ludescher, J., C. Tsallis, and A. Bunde (2011), Universal behaviour of interoccurrence times between losses in financial markets: An analytical description, *Europhys. Lett.* **95**, 6, 68002, DOI: 10.1209/0295-5075/95/68002.

Lutz, E. (2003), Anomalous diffusion and Tsallis statistics in an optical lattice, *Phys. Rev. A* **67**, 5, 051402(R), DOI: 10.1103/PhysRevA.67.051402.

Lyra, M.L., and C. Tsallis (1998), Nonextensivity and multifractality in low-dimensional dissipative systems, *Phys. Rev. Lett*. **80**, 1, 53-56, DOI: 10.1103/PhysRevLett.80.53.

Mattedi, A.P., F.M. Ramos, R.R. Rosa, and R.N. Mantegna (2004), Value-at-risk and Tsallis statistics: Risk analysis of the aerospace sector, *Physica A* **344**, 3-4, 554-561, DOI: 10.1016/j.physa.2004.06.031.

Mohanalin, J., Beenamol, P.K. Kalra, and N. Kumar (2010), A novel automatic microcalcification detection technique using Tsallis entropy and a type II fuzzy index, *Comput. Math. Appl.* **60**, 8, 2426-2432, DOI: 10.1016/j.camwa.2010.08.038.

Montemurro, M.A. (2004), A generalization of the Zipf-Mandelbrot law in linguistics. **In:** M. Gell-Mann and C. Tsallis (eds.), *Nonextensive Entropy – Interdisciplinary Applications*, Oxford University Press, New York.

Moret, M.A., P.G. Pascutti, P.M. Bisch, M.S.P. Mundim, and K.C. Mundim (2006), Classical and quantum conformational analysis using Generalized Genetic Algorithm, *Physica A* **363**, 2, 260-268, DOI: 10.1016/j.physa.2005.08.062.

Moyano, L.G., and C. Anteneodo (2006), Diffusive anomalies in a long-range Hamiltonian system, *Phys. Rev. E* **74**, 021118, DOI: 10.1103/PhysRevE.74.021118.

Moyano, L.G., C. Tsallis, and M. Gell-Mann (2006), Numerical indications of a q-generalised central limit theorem, *Europhys. Lett.* **73**, 6, 813, DOI: 10.1209/epl/i2005-10487-1.

Mundim, K.C., and C. Tsallis (1996), Geometry optimization and conformational analysis through generalized simulated annealing, *Int. J. Quant. Chem*. **58**, 4, 373-381, DOI: 10.1002/(SICI)1097-461X(1996)58:4<373::AID-QUA6> 3.0.CO;2-V.

Nobre, F.D., and C. Tsallis (1995), Infinite-range Ising ferromagnet: thermodynamic limit within generalized statistical mechanics, *Physica A* **213**, 3, 337-356, DOI: 10.1016/0378-4371(94)00231-H (Erratum: DOI: 10.1016/0378-4371(95)00073-G).

Nobre, F.D., M.A. Rego-Monteiro, and C. Tsallis (2011), Nonlinear relativistic and quantum equations with a common type of solution, *Phys. Rev. Lett.* **106**, 14, 140601, DOI: 10.1103/PhysRevLett.106.140601.

Okamoto, Y., and U.H.E. Hansmann (2001), Protein folding simulations by a generalized-ensemble algorithm based on Tsallis statistics. **In***:* S. Abe and Y. Okamoto (eds.), *Nonextensive Statistical Mechanics and Its Applications*, Series Lecture Notes in Physics, Springer, Heidelberg.

Oliveira-Neto, N.M., E.M.F. Curado, F.D. Nobre, and M.A. Rego-Monteiro (2007), A simple model to describe the low-temperature behaviour of some atoms and molecules: An application to the hydrogen atom, *J. Phys. B* **40**, 11, 1975, DOI: 10.1088/0953-4075/40/11/003.

Papadimitriou, C., M. Kalimeri, and K. Eftaxias (2008), Nonextensivity and universality in the earthquake preparation process, *Phys. Rev. E* **77**, 3, 036101, DOI: 10.1103/PhysRevE.77.036101.

Penrose, O. (1970), *Foundations of Statistical Mechanics: A Deductive Treatment*, Pergamon, Oxford.

Pickup, R.M., R. Cywinski, C. Pappas, B. Farago, and P. Fouquet (2009), General-
    ized spin glass relaxation, *Phys. Rev. Lett.* **102**, 9, 097202, DOI: 10.1103/
    PhysRevLett.102.097202.

Plastino, A.R., and A. Plastino (1995), Non-extensive statistical mechanics and
    generalized Fokker-Planck equation, *Physica A* **222**, 1-4, 347-354, DOI:
    10.1016/0378-4371(95)00211-1.

Pluchino, A., A. Rapisarda, and C. Tsallis (2008), A closer look at the indications
    of q-generalized Central Limit Theorem behavior in quasi-stationary states
    of the HMF model, *Physica A* **387**, 13, 3121-3128, DOI: 10.1016/j.physa.
    2008.01.112.

Portes de Albuquerque, M., I.A. Esquef, A.R.G. Mello, and M. Portes de Albuquer-
    que (2004), Image thresholding using Tsallis entropy, *Pattern Recogn. Lett.*
    25, 9, 1059-1065, DOI: 10.1016/j.patrec.2004.03.003.

Reis, Jr., J.L., J. Amorim, and A. Dal Pino, Jr. (2011), Occupancy of rotational
    population in molecular spectra based on nonextensive statistics, *Phys.
    Rev. E* **83**, 1, 017401, DOI: 10.1103/PhysRevE.83.017401.

Rios, L.A., and R.M.O. Galvão (2011), Modulation of whistler waves in nonthermal
    plasmas, *Phys. Plasmas* **18**, 2, 022311, DOI: 10.1063/1.3556125.

Rodríguez, A., and C. Tsallis (2010), A generalization of the cumulant expansion.
    Application to a scale-invariant probabilistic model, *J. Math. Phys.* **51**, 7,
    073301, DOI: 10.1063/1.3448944 .

Rodríguez, A., V. Schwämmle, and C. Tsallis (2008), Strictly and asymptotically
    scale-invariant probabilistic models of N correlated binary random vari-
    ables having q-Gaussians as $N \to \infty$ limiting distributions, *J. Stat. Mech.*
    P09006, DOI: 10.1088/1742-5468/2008/09/P09006.

Rosso, O.A., M.T. Martin, and A. Plastino (2003), Brain electrical activity analysis
    using wavelet-based informational tools (II): Tsallis non-extensivity and
    complexity measures, *Physica A* **320**, 497-511, DOI: 10.1016/S0378-4371
    (02)01529-7.

Saguia, A., and M.S. Sarandy (2010), Nonadditive entropy for random quantum
    spin-S chains, *Phys. Lett. A* **374**, 34, 3384-3388, DOI: 10.1016/j.physleta.
    2010.06.038.

Serra, P., A.F. Stanton, and S. Kais (1997), Pivot method for global optimization,
    Phys. Rev. E **55**, 1, 1162-1165, DOI: 10.1103/PhysRevE.55.1162.

Shao, M., L. Yi, Z. Tang, H. Chen, C. Li, and Z. Xu (2010), Examination of the spe-
    cies and beam energy dependence of particle spectra using Tsallis statistics,
    J. Phys. G **37**, 8, 085104, DOI: 10.1088/0954-3899/37/8/085104.

Shi, W., Y. Miao, Z. Chen, and H. Zhang (2009), Research of automatic medical
    image segmentation algorithm based on Tsallis entropy and improved
    PCNN. **In**: *IEEE International Conference on Mechatronics and Automa-
    tion, ICMA 2009*, 1004-1008, DOI: 10.1109/ICMA.2009.5246315.

Sotolongo-Grau, O., D. Rodriguez-Perez, J.C. Antoranz, and O. Sotolongo-Costa (2010), Tissue radiation response with maximum Tsallis entropy, *Phys. Rev. Lett.* **105**, 15, 158105, DOI: 10.1103/PhysRevLett.105.158105.

Straub, J.E., and I. Andricioaei (1999), Computational methods inspired by Tsallis statistics: Monte Carlo and molecular dynamics algorithms for the simulation of classical and quantum systems, *Braz. J. Phys.* **29**, 1, 179, DOI: 10.1590/S0103-97331999000100016.

Takahashi, T., H. Oono, and M.H.B. Radford (2007), Empirical estimation of consistency parameter in intertemporal choice based on Tsallis' statistics, *Physica A* **381**, 338-342, DOI: 10.1016/j.physa.2007.03.038.

Takahashi, T., T. Hadzibeganovic, S.A. Cannas, T. Makino, H. Fukui, and S. Kitayama (2009), Cultural neuroeconomics of intertemporal choice, *Neuroendocrinol. Lett.* **30**, 2, 185-191.

Tamarit, F.A., S.A. Cannas, and C. Tsallis (1998), Sensitivity to initial conditions in the Bak-Sneppen model of biological evolution, *Eur. Phys. J. B* **1**, 4, 545-548, DOI: 10.1007/s100510050217.

Telesca, L. (2010a), Nonextensive analysis of seismic sequences, *Physica A* **389**, 9, 1911-1914, DOI: 10.1016/j.physa.2010.01.012.

Telesca, L. (2010b), Analysis of Italian seismicity by using a nonextensive approach, *Tectonophysics* **494**, 155-162, DOI: 10.1016/j.tecto.2010.09.012.

Tempesta, P. (2011), Group entropies, correlation laws, and zeta functions, *Phys. Rev. E* **84**, 021121, DOI: 10.1103/PhysRevE.84.021121.

Thistleton, W.J., J.A. Marsh, K.P. Nelson, and C. Tsallis (2009), q-Gaussian approximants mimic non-extensive statistical-mechanical expectation for many-body probabilistic model with long-range correlations, *Cent. Eur. J. Phys.* **7**, 3, 387-394, DOI: 10.2478/s11534-009-0054-4.

Thurner, S., and C. Tsallis (2005), Nonextensive aspects of self-organized scale-free gas-like networks, *Europhys. Lett.* **72**, 2, 197, DOI: 10.1209/epl/i2005-10221-1.

Tirnakli, U., and S. Abe (2004), Aging in coherent noise models and natural time, *Phys. Rev. E* **70**, 5, 056120, DOI: 10.1103/PhysRevE.70.056120.

Tirnakli, U., C. Beck, and C. Tsallis (2007), Central limit behavior of deterministic dynamical systems, *Phys. Rev. E* **75**, 4, 040106(R), DOI: 10.1103/PhysRevE.75.040106.

Tirnakli, U., C. Tsallis, and C. Beck (2009), A closer look on the time-average attractor at the edge of chaos of the logistic map, *Phys. Rev. E* **79**, 5, 056209, DOI: 10.1103/PhysRevE.79.056209.

Tong, S., A. Bezerianos, J. Paul, Y. Zhu, and N. Thakor (2002), Nonextensive entropy measure of EEG following brain injury from cardiac arrest, *Physica A* **305**, 3-4, 619-628, DOI: 10.1016/S0378-4371(01)00621-5.

Treumann, R.A. (1998), Generalized-Lorentziann path integrals, *Phys. Rev. E* **57**, 5, 5150-5153, DOI: 10.1103/PhysRevE.57.5150.

Tsallis, A.C., C. Tsallis, A.C.N. Magalhaes, and F.A. Tamarit (2003), Human and computer learning: An experimental study, *Complexus* **1**, 4, 181-189, DOI: 10.1159/000082448.

Tsallis, C. (1988), Possible generalization of Boltzmann-Gibbs statistics, *J. Stat. Phys.* **52**, 1-2, 479-487, DOI: 10.1007/BF01016429.

Tsallis, C. (2004), Nonextensive statistical mechanics: Construction and physical interpretation. **In:** M. Gell-Mann and C. Tsallis (eds.), *Nonextensive Entropy – Interdisciplinary Applications*, Oxford University Press, New York.

Tsallis, C. (2005), Nonextensive statistical mechanics, anomalous diffusion and central limit theorems, *Milan J. Math.* **73**, 1, 145-176, arXiv:cond-mat/0412132v1.

Tsallis, C. (2009a), *Introduction to Nonextensive Statistical Mechanics -Approaching a Complex World*, Springer, New York, DOI: 10.1007/978-0-387-85359-8.

Tsallis, C. (2009b), Entropy. **In:** R.A. Meyers (ed.), *Encyclopedia of Complexity and Systems Science*, Springer, Berlin.

Tsallis, C. (2011), The nonadditive entropy Sq and its applications in physics and elsewhere: Some remarks, *Entropy* **13**, 10, 1765-1804, DOI: 10.3390/e13101765.

Tsallis, C., and D.J. Bukman (1996), Anomalous diffusion in the presence of external forces: Exact time-dependent solutions and their thermostatistical basis, *Phys. Rev. E* **54**, R2197-R2200, DOI: 10.1103/PhysRevE.54.R2197.

Tsallis, C., and M.P. Portes de Albuquerque (2000), Are citations of scientific papers a case of nonextensivity?, *Eur. Phys. J. B* **13**, 777, DOI: 10.1007/s100510050097.

Tsallis, C., and D.A. Stariolo (1996), Generalized simulated annealing, *Physica A* **233**, 395-406.

Tsallis, C., R.S. Mendes, and A.R. Plastino (1998), The role of constraints within generalized nonextensive statistics, *Physica A* **261**, 3, 534-554, DOI: 10.1016/S0378-4371(98)00437-3.

Tsallis, C., M. Gell-Mann, and Y. Sato (2005), Asymptotically scale-invariant occupancy of phase space makes the entropy Sq extensive, *Proc. Natl. Acad. Sci. USA* **102**, 43, 15377-15382, DOI: 10.1073/pnas.0503807102.

Tsallis, C., A.R. Plastino, and R.F. Alvarez-Estrada (2009), Escort mean values and the characterization of power-law-decaying probability densities, *J. Math. Phys.* **50**, 4, 043303, DOI: 10.1063/1.3104063.

Umarov, S., C. Tsallis, and S. Steinberg (2008), On a q-central limit theorem consistent with nonextensive statistical mechanics, *Milan J. Math.* **76**, 307-328, DOI: 10.1007/s00032-008-0087-y.

Umarov, S., C. Tsallis, M. Gell-Mann, and S. Steinberg (2010), Generalization of symmetric α-stable Lévy distributions for $q > 1$, *J. Math. Phys.* **51**, 3, 033502, DOI: 10.1063/1.3305292.

Upadhyaya, A., J.-P. Rieu, J.A. Glazier, and Y. Sawada (2001), Anomalous diffusion and non-Gaussian velocity distribution of Hydra cells in cellular aggregates, *Physica A* **293**, 3-4, 549-558, DOI: 10.1016/S0378-4371(01) 00009-7.

Vallianatos, F. (2009), A non-extensive approach to risk assessment, *Nat. Hazards Earth Syst. Sci.* **9**, 1, 211-216, DOI: 10.5194/nhess-9-211-2009.

Vallianatos, F. (2011), A non-extensive statistical physics approach to the polarity reversals of the geomagnetic field, *Physica A* **390**, 10, 1773-1778, DOI: 10.1016/j.physa.2010.12.040.

Vallianatos, F., and P. Sammonds (2010), Is plate tectonics a case of non-extensive thermodynamics?, *Physica A* **389**, 21, 4989-4993, DOI: 10.1016/j.physa. 2010.06.056.

Vallianatos, F., E. Kokinou, and P. Sammonds (2011a), Non-extensive statistical physics approach to fault population distribution. A case study from the Southern Hellenic Arc (Central Crete), *Acta Geophys.* **59**, 4, 770-784, DOI: 10.248/s11600-011-0015-3.

Vallianatos, F., D. Triantis, and P. Sammonds (2011b), Non-extensivity of the isothermal depolarization relaxation currents in uniaxial compressed rocks, *Europhys. Lett.* **94**, 6, 68008, DOI: 10.1209/0295-5075/94/68008.

Vignat, C., and A. Plastino (2007), Central limit theorem and deformed exponentials, *J. Phys. A: Math. Theor.* **40**, 45, F969-F978, DOI: 10.1088/1751-8113/40/45/F02.

Vignat, C., and A. Plastino (2009), Geometry of the central limit theorem in the nonextensive case, *Phys. Lett. A* **373**, 20, 1713-1718, DOI: 10.1016/ j.physleta.2009.03.029.

Wedemann, R.S., R. Donangelo, and L.A.V. de Carvalho (2009), Generalized memory associativity in a network model for the neuroses, *Chaos* **19**, 015116, DOI: 10.1063/1.3099608.

Wilk, G., and Z. Wlodarczyk (2009), Power laws in elementary and heavy-ion collisions – A story of fluctuations and nonextensivity?, *Eur. Phys. J. A* **40**, 3, 299, arXiv: 0810.2939.

Non-Extensive Framework for Earthquakes: The Role of Fragments

Oscar SOTOLONGO-COSTA

Cátedra de Sistemas Complejos "Henri Poincaré", Universidad de La Habana, Habana, Cuba; e-mail: osotolongo@fisica.uh.cu

A b s t r a c t

The inclusion of fragment-asperity interaction inside tectonic plates to find a frequency magnitude relation for earthquakes, and the need for non-extensive statistics in this case is exposed. The usefulness of this formulation is shown. A comparison with seismic observations is also discussed.

Key words: non-extensivity, statistics, fragmentation.

1. INTRODUCTION

For many years, the Gutenberg–Richter (GR) law (Gutenberg and Richter 1944) has remained as a paradigm for the description of the energy distribution of earthquakes. More recently (Bak 1996), it has been argued as an illustration of self-organized criticality since it reveals a power law dependence of the cumulative number of earthquakes with energy larger than a given ε.

Some famous models, like those of Burridge and Knopoff (Burridge and Knopoff 1967) and Olami–Feder–Christensen (Olami *et al.* 1992) have focused on the mechanical phenomenology of earthquakes through simple images which capture some essentials of the nature and genesis of the seism: the relative displacement of tectonic plates in a fault and also the existence of a threshold for a catastrophic release of energy in the system.

The irregular geometry of the plate surfaces has been highlighted (De Rubeis *et al.* 1996) to deduce from numerical simulations the power-law dependence of earthquake energy distribution. The importance of a geomet-

ric viewpoint for this has also been highlighted (Herrmann *et al.* 1990), where an idealized representation of the fragmented core of a fault (gouge) was presented.

Yet, the GR law has remained as an empirical relation able to fit seismological observations in an intermediate range of magnitudes. It clearly deviates from observations for "small" and "large" magnitudes *m*. The devia-tion at small *m* is frequently justified arguing about the threshold values of the detectors to register weak earthquakes, but for "large" magnitudes it has been necessary to elaborate specific models (Lomnitz-Adler and Lomnitz 1979).

Nowadays, the lack of a clear physical image for a general description of the frequency-magnitude relation for earthquakes is evident. In this respect, a description of the phenomenon in terms of first principles is desirable.

In this paper, the model presented by Sotolongo-Costa and Posadas (Sotolongo-Costa and Posadas 2004) about fragment-asperities interaction, sometimes abbreviated as SCP model, is highlighted and the reasons for such a description are explained. Besides, the physical idea that the size distribution of fragments and their interaction is a very important factor determining the frequency-magnitude relation for earthquakes in the whole range of magnitudes is discussed. Then, the advantages of a non-extensive statistical formulation, linked to breaking phenomena and fragment size distribution, become clear since this way the non-extensivity becomes linked to stick-slip processes between tectonic plates.

2.   ENTROPY AND FRAGMENTS

The irregularity of the profiles of tectonic plates has been pointed out as a main cause of earthquakes and in the paper by De Rubeis *et al.* (1996) the GR law was obtained assuming a brownian shape of the profiles and the hypothesis that energy release is proportional to the overlap interval between the profiles. This is a very appealing explanation but the material between the fault planes is not considered there. It looks contradictory that, assuming the irregularities of the profiles and given the enormous release of energy produced by earthquakes, there are no fragments present in this description.

On the other hand, in a model presented by Herrmann *et al.* (1990) the plates are presented as planes without irregularities and the material filling the gap between the plates is composed of perfect spheres. This way, the fragmented material is considered to deaden more than to trigger earthquakes since in this case the fragments would act as roll bearings. This model does not deal with GR law but is useful to explain the fact that eventually two tectonic plates can creep on each other without producing earthquakes or the amount of heat produced by the usual friction forces.
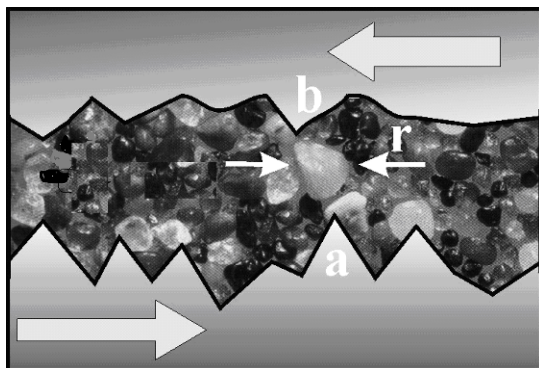
Fig. 1. Illustration of the relative motion (thick arrows) of two irregular faults in the presence of material filling the gap. This material may play the role of bearing or also of particles hindering their relative motion, as illustrated by the fragment of size *r* between the points *a* and *b*.

Yet, the irregularities of the fault planes can be combined with the distribution of (also irregular) fragments between them to develop a mechanism of triggering earthquakes, which can be essentially the same as in De Rubeis *et al.* (1996), owing to the irregular shape of the profiles and fragments.

Let us start from the situation illustrated in Fig. 1: two irregular profiles (no predetermined shape is assumed) are able to slip one with respect to the other. The motion can be hindered not only by the overlapping of two irregularities of the profiles, but also (and we assume, more probably) by the eventual relative position of several fragments.

So, tensions in the resulting structure accumulate until a displacement of one of the asperities, or even its breakage, leads to a relative displacement of the fault planes of the order of the size of the hindering fragment. Then, the release of tensions, whatever is the cause, leads to such a displacement with the subsequent liberation of energy.

Simple as it looks, this model allows a quantitative description. In this case, the leading role in the development of earthquakes is played by the fragments. The task would be to relate the size of the fragments involved in the process with the subsequent energy release, and for this it is necessary to obtain the fragment size distribution function (FSDF).

The attempt to obtain FSDF starting from first principles, particularly from the Boltzmann–Gibbs formulation of the maximum entropy (MAXENT) principle was introduced by Englman and coworkers (Englman *et al.* 1987). Yet, in that work an important feature of fragmentation, *i.e.*, the eventual presence of scaling in the size distribution of fragments, was not obtained. In many experiments, like those of Sotolongo-Costa *et al.* (1994, 1996) and

Ishii and Matsushita (1992), the presence of Pareto-like FSDF was revealed, so that the cumulative distribution function of fragments obeys a power law:

$$N(r) \approx r^{-\alpha} \, , \tag{1}$$

where $N(r)$ represents the number of fragments with size larger than r and α is the so-called scaling exponent.

   This relation is very important since it expresses the absence of any characteristic scale in the distribution, and has been reported in the distribution of moon craters, ice fields, islands (Korčak's law), *etc.* (Matsushita 1985). Besides, this is a common behavior of a whole family of distribution functions: Lévy distributions, whose role in physics is fundamental since, essentially, they exhibit the property that the behavior of a part (in distribution, of course) is similar to that of a whole. This is a fractal property! The relation between Lévy distribution and MAXENT principle will be discussed below.

   As already said, the MAXENT principle with Bolzmann–Gibbs entropy does not lead to Pareto distributions. In this case, some other considerations about the nature of fragmentation processes must enter into this approach.

   The MAXENT principle is universal and has an almost unlimited range of applications. On the other hand, Boltzmann–Gibbs entropy describes well Nature when the effective microscopic interactions and macroscopic memory are short ranged. The process of violent fractioning leads to the existence of long range interactions between all points of the object being fragmented.

   This suggests that it may be necessary to use non-extensive statistics, instead of the BG statistics. This kind of theory has already been proposed by Tsallis (Tsallis 1988), who postulated a generalized form of entropy, given by

$$S_q = k \, \frac{1 - \int_0^\infty p^q(x) \, \mathrm{d}x}{q - 1} \, . \tag{2}$$

This integral runs over all admissible values of the magnitude x, $p(x) \, \mathrm{d}x$ is the probability of the system being in a state between x and $x + \mathrm{d}x$, and q is a real number. It is straightforward to see that $S_q \xrightarrow[q \to 1]{} S$, recovering BG statistics.

   In this case S_q can be expressed through $p(\sigma)$, the probability density of finding a fragment of relative surface σ. Now the problem is to obtain FSDF applying the MAXENT principle using Tsallis entropy with adequate conditions.

   The SCP model intends to perform this task with the simplest possible assumptions. Essentially, the approach is as follows: It is assumed that the energy ε released after a slip is proportional to the size r of the hindering

fragment, *i.e.*, $\varepsilon \approx r$ or $\varepsilon \approx \sigma^{1/2}$. The process of fault slip can be considered to occur in a homogeneous fashion all along the fault so that in any plane transverse to the fault line the situation is the same. Then, to deduce the size distribution function of fragments we consider a two dimensional frame.

It is worth to say that the assumed proportionalities need not to be such and the model can be changed to consider other proportionalities between energy and fragment size. Indeed, in some papers, like those by Silva *et al*. (2006) or Telesca and Chen (2010), other proportionalities are assumed, like $\varepsilon \approx r^3$ and others, but it is not the case to detail it here.

Let us add the constraint expressing the normalization condition:

$$\int_0^\infty p(\sigma)\,\mathrm{d}\sigma = 1 \;, \tag{3}$$

and the condition about the *q*-mean value:

$$\int_0^\infty p^q(\sigma)\,\mathrm{d}\sigma = \langle \sigma \rangle_q \;. \tag{4}$$

This last constraint has also been changed by other authors as Silva *et al*. (2006), Telesca and Chen (2010) and the consequences have been discussed to some extent by Sarlis *et al*. (2010). In general, the condition for the *q*-mean value is there improved, being expressed by means of the escort distribution:

$$P_q = \frac{p^q(\sigma)}{\displaystyle\int_0^\infty p^q(\sigma)\,\mathrm{d}\sigma} \;, \tag{5}$$

arriving at similar results. The obtained frequency-magnitude relations in those works have also excellent fitting properties. The FSDF is then obtained by the method of Lagrange multipliers, *i.e.*, extremization of the entropy S_q using conditions (3) and (4).

The FSDF has the form:

$$p(\sigma)\,\mathrm{d}\sigma = \frac{(2-q)^{\frac{1}{2-q}}\,\mathrm{d}\sigma}{\left[1+(q-1)(2-q)^{\frac{q-1}{2-q}}\,\sigma\right]^{\frac{1}{q-1}}} \;, \tag{6}$$

which exhibits a power law behavior (scaling) as asymptotic limit.

This FSDF belongs to the family of Lévy distributions. Then the reason for the ubiquity of Lévy distributions in Nature becomes clearer. This has been discussed in detail in by Tsallis *et al.* (1995).

It is worth to note that the behavior obtained here should be naturally reflected in earthquake distributions if a relation between fragments and released energy does exist.

Then, introducing the proportionality of the released relative energy ε with the linear dimension of the fragments, and the definition of magnitude $m \approx \log \varepsilon$, the SCP model gives for the cumulative number of earthquakes the following relation:

$$\log\left(\frac{N_{>m}}{N}\right) \;=\; \left(\frac{2-q}{1-q}\right)\log\left[1 + a(q-1)(2-q)^{\frac{1-q}{q-2}} \times 10^{2m}\right],\qquad (7)$$

where a is the constant of proportionality between ε and r.

3. COMPARISON WITH OBSERVATIONS

The fitting of Eq. (6) with data obtained from different catalogs is quite easy to perform and, as shown in Sotolongo-Costa and Posadas (2004) the catalogs of more than 10 000 earthquakes in California, (NEIC, USA, http://neic.usgs.gov/neis/epic), more than 3000 in the Iberian Peninsula (IGN, Spain, http://www.geo.ign.es), and 300 in the Andalusian region (IAG, Spain, http://www.ugr.es/iag) were analyzed in all the range of magnitudes $m > 3$, *i.e.*, detectables, with very good results.

One can judge about the usefulness of the non-extensive formulation, focusing in the problem of large earthquakes, which are more difficult to fit.

Indeed, Lomnitz-Adler and Lomnitz (1979) have proposed a stochastic model of strain accumulation and release at plate boundaries for large earthquakes. The model leads to a generalized Gutenberg–Richter's relation in terms of the cumulative excedence of a magnitude m, $G(>m) = \left(N_{>m}\right)/N$, which tends to the original one of Gutenberg–Richter in the low magnitude range and which provides estimates of the probability of occurrence, significantly more adequate than the Gutenberg–Richter law, at high magnitudes. They have obtained a good agreement with the data of the Chinese earthquake catalogue, which contains 629 entries of earthquakes for a threshold magnitude $m = 6.0$ from 780 B.C., to 1973 A.D. It is the longest published catalogue of historical earthquakes in any region (Academia Sinica 1974).

We adjusted the constants of this equation with the Chinese catalogue and the results can be seen in Fig. 2; in this case $q = 1.69 \pm 0.02$ and the correlation factor is 0.9925.
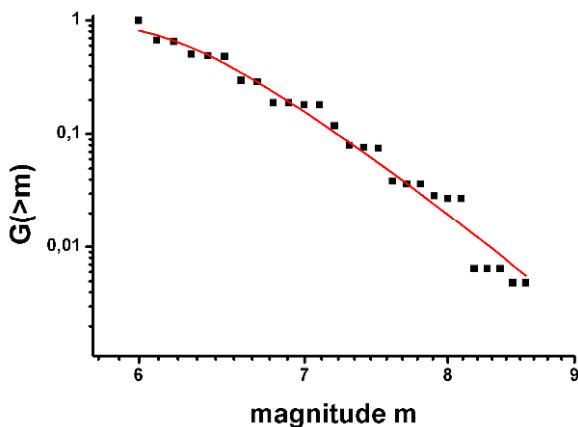
Fig. 2. Fitting of the Chinese catalogue using Eq. (6). Despite the low reliability of an old catalogue like this, the agreement is very good.

4. CONCLUSIONS

Fragments and fragmentation processes are present in enormous number of natural processes, and frequently this aspect does not receive adequate attention. This paper tries to highlight two main aspects to be taken into account:

❑ One is that frequently a simple geometrical viewpoint is able to clarify problems that are intractable by other methods. So, fractal geometry and the theory of Lévy distributions are called to play an important role in the physics of complex phenomena.

❑ The second aspect is the importance of a generalization of many concepts originated in the statistical physics of equilibrium systems, better to say the "orthodox" statistical physics. This generalization is a promising way to get a formulation of many problems that, up to now, have been poorly studied due to the inadequacy of current methods. In this paper, Tsallis entropy showed to be a promising tool to start.

This is not the definitive framework in which statistical physics could be applied to these problems. Today it is under debate if the generalized averages in Eqs. (4) and (5) are physically acceptable, since some authors (*e.g.*, Abe 2008) have pointed to the instability of the q-mean value and the difficult physical interpretation of such a q-average. Another point under debate (Abe 2010) is whether the Tsallis entropy can be defined for continuous random variables. Both arguments have been rejected by some other authors (*e.g.*, Cabo 2010, Bagci *et al*. 2010, *etc*.), and here this point will not be discussed. But what is indisputable is that Tsallis entropy successfully opened the way to the analysis of non equilibrium phenomena and complex systems.

Concerning seismicity, the starting point marked by the inclusion of fragments in a simple model for seismicity demonstrates the need to include non-extensivity in the statistics of earthquakes and provides an easier way to build intuitive models with more physics in their structure. This model provides the same physics for all the scales, and no *a priori* assumptions are needed about the shape of the profiles or fragments.

At the same time, new ways for the study of seismic processes can be sketched, like the investigation of the proportionality of the released energy and the characteristics of the fragments, evaluation of energy density, and many more problems that can be formulated in this framework.

References

Abe, S. (2008), Instability of q-expectation value, *arXiv:0806.3934v1* [cond-mat.stat-mech].

Abe, S. (2010), Essential discreteness in generalized thermostatistics with non-logarithmic entropy, *EPL* **90**, 5, 50004, DOI: 10.1209/0295-5075/90/50004.

Academia Sinica (1974), Catalogue of great earthquakes in China, 780 BC to 1973 AD, Academia Sinica, Inst. Geophys., Beijing, 31 pp. (in Chinese).

Bagci, G.B., T. Oikonomou, and U. Tirnakli (2010), Comment on "Essential discreteness in generalized thermostatistics with non-logarithmic entropy" by S. Abe, *arXiv:1006.1284v2* [cond-mat.stat-mech].

Bak, P. (1996), *How Nature Works: The Science of Self-Organised Criticality*, Copernicus Press, New York.

Burridge, R., and L. Knopoff (1967), Model and theoretical seismicity, *Bull Seismol. Soc. Am.* **57**, 3, 341-371.

Cabo, A. (2010), Is the Tsallis q-mean value instable?, *arXiv:1010.5825v1* [cond-mat.stat-mech].

De Rubeis, V., R. Hallgass, V. Loreto, G. Paladin, L. Pietronero, and P. Tosi (1996), Self-affine asperity model for earthquakes, *Phys. Rev. Lett.* **76**, 14, 2599-2602, DOI: 10.1103/PhysRevLett.76.2599.

Englman, R., N. Rivier, and Z. Jaeger (1987), Fragment-size distribution in disintegration by maximum-entropy formalism, *Philos. Mag. B* **56**, 6, 751-769, DOI: 10.1080/13642818708215309.

Gutenberg, B., and C.F. Richter (1944), Frequency of earthquakes in California, *Bull. Seimol. Soc. Am.* **34**, 4, 185-188.

Herrmann, H.J., G. Mantica, and D. Bessis (1990), Space-filling bearings, *Phys. Rev. Lett.* **65**, 26, 3223-3226, DOI: 10.1103/PhysRevLett.65.3223.

Ishii, T., and M. Matsushita (1992), Fragmentation of long thin glass rods, *J. Phys. Soc. Jpn.* **61**, 3474-3477, DOI: 10.1143/JPSJ.61.3474.

Lomnitz-Adler, J., and C. Lomnitz (1979), A modified form of the Gutenberg–Richter magnitude-frequency relation, *Bull. Seismol. Soc. Am*. **69**, 4, 1209-1214.

Matsushita, M. (1985), Fractal viewpoint of fracture and accretion, *J. Phys. Soc. Jpn*. **54**, 857-860, DOI: 10.1143/JPSJ.54.857.

Olami, Z., H.J.S. Feder, and K. Christensen (1992), Self-organized criticality in a continuous, nonconservative cellular automaton modeling earthquakes, *Phys. Rev. Lett*. **68**, 8, 1244-1247, DOI: 10.1103/PhysRevLett.68.1244.

Sarlis, N.V., E.S. Skordas, and P.A. Varotsos (2010), Nonextensivity and natural time: The case of seismicity, *Phys. Rev. E* **82**, 2, 021110, DOI: 10.1103/PhysRevE.82.021110.

Silva, R., G.S. França, C.S. Vilar, and J.S. Alcaniz (2006), Nonextensive models for earthquakes, *Phys. Rev. E* **73**, 026102, DOI: 10.1103/PhysRevE.73.026102.

Sotolongo-Costa, O., and A. Posadas (2004), Fragment-asperity interaction model for earthquakes, *Phys. Rev. Lett*. **92**, 4, 048501, DOI: 10.1103/PhysRevLett.92.048501.

Sotolongo-Costa, O., E. Lopez-Pages, F. Barreras-Toledo, and J. Marin-Antuña (1994), Scaling in drop distributions: An application in combustion, *Phys. Rev. E* **49**, 5, 4027-4030, DOI: 10.1103/PhysRevE.49.4027.

Sotolongo-Costa, O., Y. Moreno-Vega, J.J. Lloveras-González, and J.C. Antoranz (1996), Criticality in droplet fragmentation, *Phys. Rev. Lett*. **76**, 1, 42-45, DOI: 10.1103/PhysRevLett.76.42.

Telesca, L., and C.-C. Chen (2010), Nonextensive analysis of crustal seismicity in Taiwan, *Nat. Hazards Earth Syst. Sci*. **10**, 1293-1297, DOI: 10.5194/nhess-10-1293-2010.

Tsallis, C. (1988), Possible generalization of Boltzmann–Gibbs statistics, *J. Stat. Phys*. **52**, 1-2, 479-487, DOI: 10.1007/BF01016429.

Tsallis, C., S.V.F. Lévy, A.M.C. Souza, and R. Maynard (1995), Statistical-mechanical foundation of the ubiquity of Lévy distributions in nature, *Phys. Rev. Lett*. **75**, 20, 3589-3593, DOI: 10.1103/PhysRevLett.75.3589.

Earthquakes, Model Systems and Connections to q-Statistics

Ahmet CELIKOGLU and Ugur TIRNAKLI

Department of Physics, Faculty of Science,
Ege University, Izmir, Turkey
e-mails: ahmet.celikoglu@ege.edu.tr,
ugur.tirnakli@ege.edu.tr (corresponding author)

Abstract

In this work, we make an attempt to review some of the recent studies on earthquakes using either real catalogs or synthetic data coming from some model systems. A common feature of all these works is the use of q-statistics as a tool.

Key words: earthquake models, q-statistics, statistical mechanics of earthquakes.

1. INTRODUCTION

Earthquakes exhibit spatio-temporal features with complex dynamics which have been subject to active study for more than a century (Kagan and Jackson 1991, Turcotte 1997, Sornette 1999). Despite the long time period, our knowledge about earthquakes roughly consists of three empirical laws. One of them is the Gutenberg–Richter (GR) law, stating that the distribution of cumulative number of earthquakes with energy greater than E behaves as a power-law, namely,

$$N(\geq E) \sim E^{-b}, \tag{1}$$

where constant b varies from 0.8 to 1.2. This law can be better formulated by means of earthquake magnitudes m, which is defined to be $m = \log E$, as

$$N(\geq m) = 10^{a-bm} \tag{2}$$

where constant a is given by the logarithm of the number of earthquakes with magnitude greater than zero (Gutenberg and Richter 1944).

The second empirical scaling relation detected for earthquakes describes the temporal behavior of aftershock activity. This law, known as the Omori law, states that the rate of the occurrence of aftershocks after a mainshock decreases as a power law, namely

$$\frac{\mathrm{d}N}{\mathrm{d}t} = K(C+t)^{-p}, \tag{3}$$

where C and K are positive constants and p is typically between 0.7 and 1.5 (Omori 1894).

The last scaling law for earthquakes is called Bath's law (Bath 1965), which states that if one defines the difference in magnitude between a mainshock with magnitude $m_{\text{mainshock}}$ and its largest detected aftershock with magnitude $m_{\text{aftershock}}$ as

$$\Delta m = m_{\text{mainshock}} - m_{\text{aftershock}}, \tag{4}$$

this difference appears to be a constant independent of the mainshock magnitude.

Over the last decades, some properties of geophysical systems have been studied in the context of q-statistics (Tsallis 1988, 2009). This formalism seems to be a good candidate to be used for earthquake analysis since longe-range spatio-temporal correlations and complex dynamics are natural ingredients of earthquakes. In this paper we summarize some of the recent works on this line and emphasize the use of model systems for earthquakes and recent results obtained from such systems. At this point, we should mention that we prefer to leave some very interesting recent developments on the use of q-statistics in the analysis of plate tectonics (Vallianatos 2009, Vallianatos and Sammonds 2010) and fault-population (Vallianatos and Sammonds 2011) as untouched since there will be separate works in this issue analyzing these points.

2. GUTENBERG–RICHTER LAW AND SP MODEL

One of the interesting examples for the use of q-statistics is Sotolongo-Costa and Posadas (SP) model (Sotolongo-Costa and Posadas 2004). This model tries to establish a relation between Gutenberg–Richter law and general principles of physics. Earthquakes originate by relative motion of fault planes. Two planes interact with each other via fragments which are filling the gap between them and these fragments resist the motion. When the accumulated stress exceeds

breaking force of the fragments, earthquake is triggered and accumulated energy is released. They assumed that the released energy is proportional to the size of the fragment. In this regards the authors found the probability of finding a fragment with surface size σ by using nonadditive Tsallis entropy which has the following form

$$S_q = k\frac{1 - \int p^q(\sigma)\mathrm{d}\sigma}{q - 1},\tag{5}$$

where q is the entropic index. There are two conditions required for maximization of Tsallis entropy. The first one is the normalization condition of $p(\sigma)$ given by

$$\int_0^\infty p(\sigma)\mathrm{d}\sigma = 1\tag{6}$$

and the other condition

$$\int_0^\infty \sigma p^q(\sigma)\mathrm{d}\sigma = \ll\sigma\gg_q\tag{7}$$

is related to q mean value of σ. Authors have obtained the energy distribution function of earthquakes as

$$p(\varepsilon)\mathrm{d}\varepsilon = \frac{C_1\varepsilon\mathrm{d}\varepsilon}{[1 + C_2\varepsilon^2]^{1/(q-1)}}\tag{8}$$

by using the size distribution of fragments and an assumption that σ scales as r^2. In this equation, $p(\varepsilon)$ is the probability of energy, C_1 and C_2 are constants. This simple approach about fault dynamics gives rise to very interesting results. They have managed to modify the well-known GR law and establish a connection with principles of statistical physics. The modified version of GR law as a function of magnitude m has been given as

$$\log[N(> m)] = \log N + \left(\frac{2 - q}{1 - q}\right)\log\left[1 + a(q - 1)(2 - q)^{(1-q)/(q-2)}10^{2m}\right],\tag{9}$$

where a is a constant of proportionality between ε and r. The modified GR law was tested by using Iberian Peninsula, Andalucia and California catalogs. Interestingly, the value of q parameter was obtained to be approximately 1.66 for all these three catalogs (Sotolongo-Costa and Posadas 2004).

After the appearance of SP model, two different revisions have been proposed in the literature (Silva *et al.* 2006, Darooneh and Mehri 2010). These revisions focus on the definition of the expectation value and relation between energy and the linear dimension r of the fragment. Silva *et al.* approach the

problem by redefining the dependency of ε on r as $\varepsilon \sim r^3$ and q-expectation value as

$$\sigma_q = <\sigma>_q = \int_0^\infty \sigma P_q(\sigma)\mathrm{d}\sigma, \tag{10}$$

where P_q is the escort distribution (Abe 2003) given by

$$P_q = \frac{p^q(\sigma)}{\int_0^\infty p^q(\sigma)\mathrm{d}\sigma}. \tag{11}$$

The cumulative number of earthquakes (Sotolongo-Costa and Posadas 2004)

$$\frac{N_{>\varepsilon}}{N} = \int_\varepsilon^\infty p(\varepsilon)\mathrm{d}\varepsilon \tag{12}$$

used to test the validity of energy distribution function which is now given by

$$p(\varepsilon)\mathrm{d}\varepsilon = \frac{C\varepsilon^{-1/3}\mathrm{d}\varepsilon}{[1 + C'\varepsilon^{2/3}]^{1/(q-1)}} \tag{13}$$

where $N_{\varepsilon>}$ is the number of earthquakes with energy greater than ε and N is the total number of earthquakes, C and C' are constants which include proportionality constant a and parameter q. Silva et $al.$ (2006) derived new version of the modified GR law as

$$\log(N_{>m}) = \log N + \left(\frac{2-q}{1-q}\right)\log\left[1 - \left(\frac{1-q}{2-q}\right)\left(\frac{10^{2m}}{a^{2/3}}\right)\right] \tag{14}$$

by calculating the integral given in Eq. (12). This new version of the modified GR law actually amounts to make the substitution $\varepsilon \to \varepsilon^{1/3}$ in the SP model and was tested by using seismic data from Samambaia, New Madrid and Anatolian faults and it was shown that it is viable to wider detectable range of magnitude. Although these two versions of the modified GR law, very similar to each other, provide almost same q value and very good fit to the real data from different catalogs, they extremely differ from each other, especially as concerns energy density.

Recently, Darooneh and Mehri discussed the same problem again in (Darooneh and Mehri 2010). They argued that the idea of previously modified laws does not apply all over the whole magnitude regime and fractal shape of the fragments. They redefine the relation between surface size of fragments and released energy as $\varepsilon \sim \exp(\sigma^{1/a})$ inspired by the fractal nature of the fragments. The same constraints used in Silva et $al.$ (2006) have been also used in the maximization of Tsallis entropy, and the cumulative distribution of earthquakes as a function of magnitude has been derived as

$$P_>(m) = \frac{N(m)}{N} = \int_m^\infty \Pi(m)\mathrm{d}m = \exp_q(-\beta m^a), \qquad (15)$$

where $\Pi(m)$ is the escort probability of m, β is a parameter, and $\exp_q$ is the q-exponential function which is given by

$$\exp_q(x) \equiv [1 + (1-q)x]^{\frac{1}{(1-q)}} \qquad\qquad [\exp_1(x) = \exp(x)]. \qquad (16)$$

This modified version of GR law, which has q-stretch exponential form, has also been compared to the other two versions described above by using real data from Iran and California catalogs and it has been argued that this version fits the real data better than others.

At this point, it is worth mentioning that in order to better understand which version is better, one can resort to earthquake models for generating arbitrarily long synthetic time series from where a better comparison among proposed versions can be made.

3. AGING PHENOMENON

As we have already mentioned, temporal patterns of aftershocks follow an empirical law known as Omori law. This law states that the rate of the aftershocks after a mainshock decreases as power law generically given by Eq. (3). In 2004 Abe and Suzuki analyzed the temporal correlations in earthquake phenomena using California catalog by taking into account the events both inside and outside the Omori regimes (Abe and Suziki 2004). They observed that correlations among earthquakes exhibit aging inside the Omori regime and this behavior disappears outside the Omori regime. Moreover they determined the scaling function of the aging phenomenon.

In order to understand whether the earthquake models where Omori law holds, exhibit similar behavior, properties of correlation among events are studied by using Coherent Noise (CN) (Newman and Sneppen 1996, Sneppen and Newman 1997) and Olami–Feder–Christensen (OFC) (Olami *et al.* 1992, Christensen and Olami 1992) models in Tirnakli and Abe (2004) and in Tirnakli (2004), respectively. On contrary to OFC, the CN model does not have any geometric configuration space but it can still describe some important properties of real earthquakes. In CN model the system consists of N agents. The dynamics of the CN model needs an external stress which acts coherently to all agents. Each agent has a threshold value which is replaced by the new one when the applied external stress is greater than this threshold. External stress and thresholds are chosen randomly from exponential and uniform distributions, respectively. The number of replaced agents determine the size of an event. In order to provide continuity of avalanche generation, a small fraction of N agents
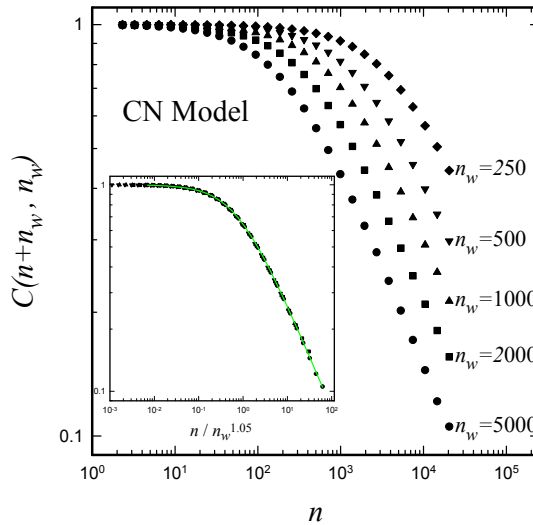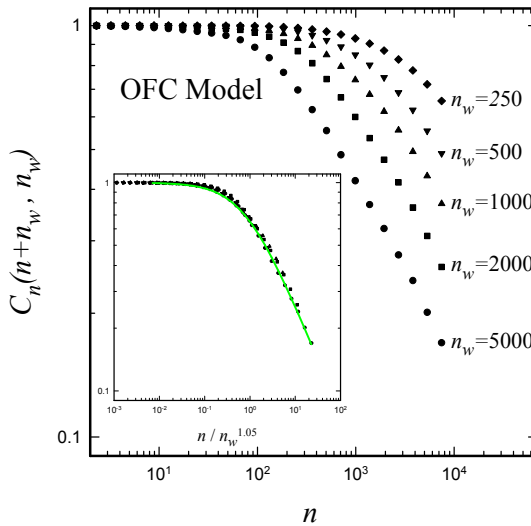
Fig. 1. The behavior of correlation function as a function of natural time n. Ensemble average is taken from 120 000 realizations. Data collapse is also given in the inset. The solid line corresponds to $\exp_q\left(0.7\, n/n_w^{1.05}\right)$ with $q \simeq 2.98$.

is also chosen randomly and new thresholds are assigned again at each time step.

Tirnakli and Abe used the same idea in Abe and Suzuki (2004) to analyze the properties of event correlations. The correlation function was defined as

$$C(n + n_w, n_w) = \frac{\langle t_{n+n_w} t_{n_w}\rangle - \langle t_{n+n_w}\rangle \langle t_{n_w}\rangle}{(\sigma_{n+n_w}^2 \sigma_{n_w}^2)^{1/2}}, \tag{17}$$

by using basic physical random variable t_n of nth aftershock with an arbitrary avalanche size, where n is the natural time of an aftershock, n_w is the natural waiting time. Since the system is nonergodic, taking the averages in Eq. (17) as the time average or the ensemble average would yield different results. In Tirnakli and Abe (2004), Tirnakli (2004), ensemble average which is obtained by using a large number of realization has been performed. The variances are given by $\sigma_m^2 = \langle t_m^2\rangle - \langle t_m\rangle^2$.

As seen in Fig. 1, since the correlation function depends on both n and n_w, it is plotted for various n_w; it is observed that aging appears inside the Omori regime, whereas it disappears outside the Omori regime. Moreover, one can propose a scaling relation of the form

$$C(n + n_w, n_w) = \tilde{C}\left(\frac{n}{n_w^{\alpha}}\right), \tag{18}$$

where α is numerically obtained as $\alpha \simeq 1.05$ and $\tilde{C}$ is a scaling function. Scaled correlation function is shown in the inset where the solid line corresponds to $\exp_q(-0.7n/n_w^{1.05})$ with $q \simeq 2.98$.

In Tirnakli (2004) one of us has reported the same behavior by using another well-known earthquake model known as OFC model (Olami *et al.* 1992, Christensen and Olami 1992). Briefly, the dynamics of the model is as follows: The model consists of discrete systems of blocks, each of them carries a stress (force) F_i. When the force F_i acting on any of the blocks, is greater than a threshold F_{th}, this block become unstable and earthquake is triggered. Each unstable block relaxes the zero and transfers a portion of own stress F_i to its neighbors, so the avalanche starts and continues until the force of all blocks becomes less than or equal to the threshold force. The measure of the size of the avalanche is given by the total number of the blocks which are relaxed during the avalanche. This mechanism is given mathematically as

$$F_i \geq F_{\text{th}} \Rightarrow \left\{ \begin{array}{l} F_i \to 0, \\ F_{nn} \to F_{nn} + \alpha F_i \end{array} \right. \tag{19}$$

where α is the conservation parameter and nn denotes neighbors of ith block. As can be seen in Fig. 2, the obtained results are very similar to that of CN model and it is evident that the scaling function given by Eq. (18) works for the OFC model as well. In this context, it should be noted that the same

Fig. 2. The behavior of correlation function as a function of natural time n. Ensemble average is taken from 20 000 realizations. Data collapse is also given in the inset. The solid line corresponds to $\exp_q\left(0.67\, n/n_w^{1.05}\right)$ with $q \simeq 2.90$.

model systems must also be studied using time averages as done for real earth-quakes in Abe and Suzuki (2004) to see whether they exhibit similar aging properties.

4. RETURN DISTRIBUTION

Another important quantity to help us to understand the physics of earthquakes is the return distribution. A return is defined as the difference between the sizes of successive avalanches, namely, if the size of an avalanche at time t is de-noted by $s(t)$ then the difference between two successive avalanches is given by $\Delta s = s(t+1) - s(t)$. Recently, we have studied the return distributions of CN Model for various model parameter values of σ which is related to the external stress distribution (Newman 1996, Newman and Sneppen 1996, Sneppen and Newman 1997) and obtained that these distributions are in the shape of q-Gaussian which is defined to be

$$P(x) = P(0)\big[1 - \beta(1-q)x^2\big]^{1/(1-q)}, \tag{20}$$

where β is a parameter. A representative case with $\sigma = 0.05$ can be seen in Fig. 3 (Celikoglu *et al.* 2010). The q-Gaussian distributions are standard distributions that naturally emerge in q-statistics. An exact relation connecting
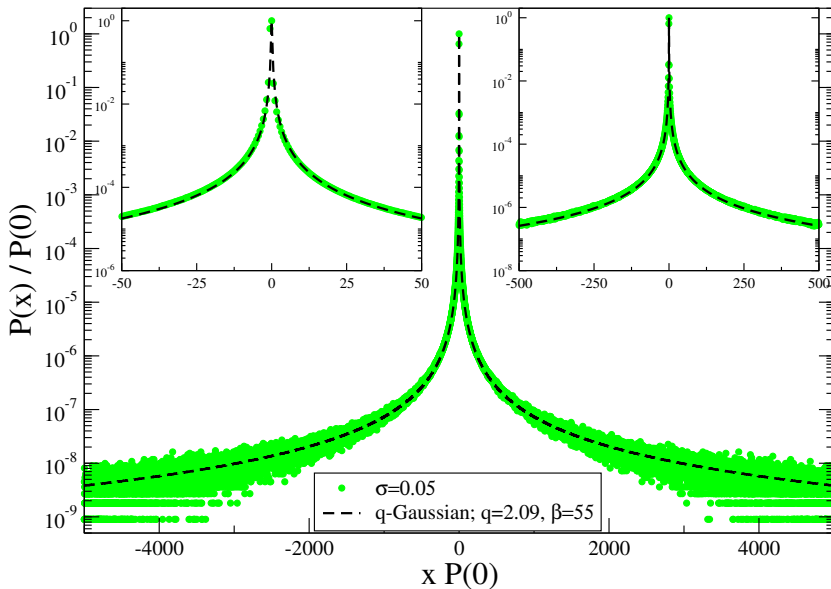
Fig. 3. Return distributions for $\sigma = 0.05$ case. Two zooms of the central part are given in the insets for better visualization.

the well-known exponent τ of avalanche size distribution to the q value of the q-Gaussian has been proposed as

$$q = \frac{\tau + 2}{\tau}. \tag{21}$$

This relation is important since it rescues q from being a fitting parameter and now one can determine *a priori* the value of q that must be used in the q-Gaussian distribution if the τ exponent of the system is known. Since the coherent noise model has the advantages both producing different τ values by varying a model parameter σ and simulating in $N \to \infty$ limit, in Celikoglu *et al.* (2010) we have checked the validity of the proposed relation for various cases and obtained clear numerical evidences on the validity of this relation. We have also studied the finite size effects by simulating directly the model dynamics with different number of agents (different N) and obtained that the return distributions deviate from q-Gaussian when N values are small. As seen in Fig. 4, when the system is getting closer to thermodynamic limit (increasing N), the return distributions better approach the q-Gaussian. An attempt was made to explain this behavior using a crossover formula, discussed in Tsallis (1988), Tsallis *et al.* (1999), Tsallis and Tirnakli (2010), of the form

$$\frac{\mathrm{d}y}{\mathrm{d}(x^2)} = -a_r y^r - (a_q - a_r) y^q \qquad [a_q \geq a_r \geq 0, q > r, y(0) = 1]. \tag{22}$$
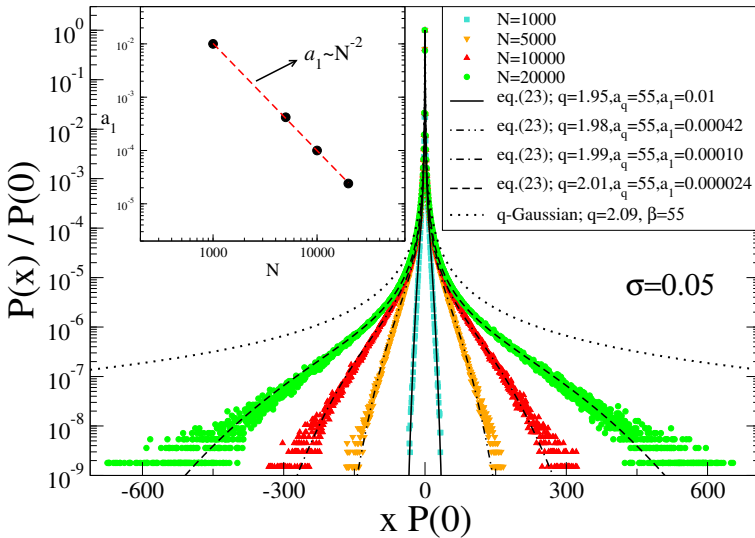
Fig. 4.   Return distributions of the various N values. In the inset, N dependence of the parameter a_1 is given. Disappearance of the finite size effects, as $N \to \infty$, is found to obey $a_1 = 11\,080 N^{-2}$.

This equation has different solutions depending on the choice of r and q values. Let us restrict ourselves to the solution of $q > 1$ and $r = 1$. In this case, the solution of the equation is given by

$$y = \left[1 - \frac{a_q}{a_1} + \frac{a_q}{a_1} e^{(q-1)a_1 x^2} \right]^{1/1-q}. \tag{23}$$

If $a_1 = 0$, the solution has the form of q-Gaussian, whereas it is Gaussian when $a_q = a_1$, in the other words, when $q \to 1$. The crossover appears between them if $a_q > a_1 > 0$ and $q > 1$. The exponential decaying part in the avalanche size distribution is dominant when the system size is small. Since this part corresponds to Gaussian shape in the return distributions and disappears as N is increasing and the crossover behavior is directly related to the system size, this mathematical model clearly demonstrates and explains the finite size effects.

The return distributions are also studied recently in a modified OFC model and same type of finite size behavior is again seen (Zhang *et al.* 2011). In this model, the authors added heterogeneity of energy transmission by redefining transmission parameter α_j as

$$\alpha_j(t) = a \frac{F_i(t) + F_j(t)}{4F_i + \sum_{j \in nn} F_j(t)}, \tag{24}$$

where F_i and F_j denote stress values at each site and a is a control parameter. In order to obtain long-range effects, a small fraction of long-range links is introduced into the lattice which is controlled by long-range parameter p_{add}. When $0.88 \leq a < 1$, the model exhibits both power law behavior and finite size scaling and it is shown that the modified OFC model exhibits self-organized criticality. The model has two different types of avalanche definition. One of them generates avalanches so that each site can topple more than once during an avalanche. The authors obtained that the return distributions of this model can also be given by the crossover formula in Eq. (23). The return distributions converge to the appropriate q-Gaussian as the system size N increases (Zhang *et al.* 2011).

5.   CONCLUSIONS

From the results of all the above-mentioned works one can conclude that q-statistics could be considered as one of the most important candidates to be used for understanding and explaining the physics of complex systems such as earthquakes. In order to better elaborate this point, works including more detailed analysis will surely be appreciated.

References

Abe, S. (2003), Geometry of escort distribution, *Phys. Rev. E* **68**, 031101, DOI: 10.1103/PhysRevE.68.031101.

Abe, S., and N. Suzuki (2004), Aging and scaling of earthquake aftershocks, *Physica A* **332**, 533-538, DOI: 10.1016/j.physa.2003.10.002.

Bath, M. (1965), Lateral inhomogeneities of upper mantle, *Tectonophysics* **2**, 6, 483-514, DOI: 10.1016/0040-1951(65)90003-X.

Celikoglu, A., U. Tirnakli, and S.M.D. Queiros (2010), Analysis of return distributions in the coherent noise model, *Phys. Rev. E* **82**, 021124, DOI: 10.1103/PhysRevE.82.021124.

Christensen, K., and Z. Olami (1992), Scaling, phase transition, and nonuniversality in a self-organized critical cellular-automaton model, *Phys. Rev. A* **46**, 4, 1829-1838, DOI: 10.1103/PhysRevA.46.1829.

Darooneh, A. H., and A. Mehri (2010), A nonextensive modification of the Gutenberg–Richter law: q-stretched exponential form, *Physica A* **389**, 509-514, DOI: 10.1016/j.physa.2009.10.006.

Gutenberg, B., and C.F. Richter (1944), Frequency of earthquakes in California, *Bull. Seismol. Soc. Am.* **34**, 185-188.

Kagan, Y.Y., and D.D. Jackson (1991), Seismic gap hypothesis: ten years after, *J. Geophys. Res.* **96**, B13, 21419-21431, DOI: 10.1029/91JB02210.

Newman, M.E.J. (1996), Self-organized criticality, evolution and the fossil extinction record, *Proc. R. Soc. London, Ser. B* **263**, 1605-1610, DOI: 10.1098/rspb.1996.0235.

Newman, M.E.J., and K. Sneppen (1996), Avalanches, scaling, and coherent noise, *Phys. Rev. E* **54**, 6, 6226-6231, DOI: 10.1103/PhysRevE.54.6226.

Olami, Z., H.J.S. Feder, and K. Christensen (1992), Self-organized criticality in a continuous, nonconservative cellular automaton modeling earthquakes, *Phys. Rev. Lett.* **68**, 1244-1248, DOI: 10.1103/PhysRevLett.68.1244.

Omori, F. (1894), On the aftershocks of earthquakes, *J. Coll. Sci. Imp. Tokyo* **7**, 111-200.

Silva, R., G.S. Franca, and J.S. Vilar (2006), Nonextensive models for earthquakes, *Phys. Rev. E* **73**, 026102, DOI: 10.1103/PhysRevE.73.026102.

Sneppen, K., and M.E.J. Newman (1997), Coherent noise, scale invariance and intermittency in large systems, *Physica D* **110**, 209-222, DOI: 10.1016/S0167-2789(97)00128-0.

Sornette, D. (1999), Earthquakes: from chemical alteration to mechanical rupture, *Phys. Rep.* **313**, 237-291, DOI: 10.1016/S0370-1573(98)00088-X.

Sotolongo-Costa, O., and A. Posadas (2004), Fragment-asperity interaction model for earthquakes, *Phys. Rev. Lett.* **92**, 048501, DOI: 10.1103/PhysRevLett.92.048501.

Tirnakli, U. (2004), Aging in earthquakes model. **In**: C. Beck, G. Benedeck, A. Rapisarda, and C. Tsallis (eds.), Complexity, *Metastability and Nonextensivity. Proc. 31st Workshop of Int. School of Solid State Physics Erice, Sicily, Italy, 20-26 July 2004*, World Scientific, Singapore, 350-354.

Tirnakli, U., and S. Abe (2004), Aging in coherent noise models and natural time, *Phys. Rev. E* **70**, 056120, DOI: 10.1103/PhysRevE.70.056120.

Tsallis, C. (1988), Possible generalization of Boltzmann–Gibbs statistics, *J. Stat. Phys.* **52**, 479-487, DOI: 10.1007/BF01016429.

Tsallis, C. (2009), *Introduction to Nonextensive Statistical Mechanics–Approaching a Complex World*, Springer, New York, DOI: 10.1007/987-0-387-85359-8.

Tsallis, C., and U. Tirnakli (2010), Nonadditive entropy and nonextensive statistical mechanics—Some central concepts and recent applications, *J. Phys. Conf. Ser.* **201**, 012001, DOI: 10.1088/1742-6596/201/1/012001.

Tsallis, C., G. Bemski, and R.S. Mendes (1999), Is re-association in folded proteins a case of nonextensivity?, *Phys. Lett. A* **257**, 93-98, DOI: 10.1016/S0375-9601(99)00270-4.

Turcotte, D.L. (1997), *Fractals and Chaos in Geology and Geophysics*, Cambridge University Press, Cambridge.

Vallianatos, F. (2009), A non-extensive approach to risk assessment, *Nat. Hazards. Earth Syst. Sci.* **9**, 211-216, DOI: 10.5194/nhess-9-211-2009.

Vallianatos, F., and P. Sammonds (2010), Is plate tectonics a case of non-extensive thermodynamics? *Physica A* **389**, 4989-4993, DOI: 10.1016/j.physa.2010.06.056.

Vallianatos, F., and P. Sammonds (2011), A non-extensive statistics of the fault-population at the Valles Marineris extensional province, Mars, *Tectonophysics* **509**, 50-54, DOI: 10.1016/j.tecto.2011.06.001.

Zhang, G.Q., U. Tirnakli, L. Wang, and T.L. Chen (2011), Self organized criticality in a modified Olami-Feder-Christensen model, *Eur. Phys. J. B* **82**, 83-89, DOI: 10.1140/epjb/e2011-10941-4.

Aftershocks in Modern Perspectives: Complex Earthquake Network, Aging, and Non-Markovianity

Sumiyoshi ABE[1] and Norikazu SUZUKI[2]

[1]Department of Physical Engineering, Mie University, Mie, Japan
e-mail: suabe@sf6.so-net.ne.jp (corresponding author)

[2]College of Science and Technology, Nihon University, Chiba, Japan

A b s t r a c t

The phenomenon of aftershocks is studied in view of science of complexity. In particular, three different concepts are examined: (i) the complex-network representation of seismicity, (ii) the event-event correlations, and (iii) the effects of long-range memory. Regarding (i), it is shown that the clustering coefficient of the complex earthquake network exhibits a peculiar behavior at and after main shocks. Regarding (ii), it is found that aftershocks experience aging, and the associated scaling holds. And regarding (iii), the scaling relation to be satisfied by a class of singular Markovian processes is violated, implying the existence of the long-range memory in processes of aftershocks.

Keywords: aftershocks, complex earthquake networks, aging, glassy dynamics, non-Markovian singular point processes.

1. INTRODUCTION

Seismicity has been attracting continuous interest of physicists from the viewpoint of complex systems science. A reason behind this stream may be due to the fact that it is characterized by two classical laws indicating how seismicity is a complex phenomenon: the Gutenberg–Richter law (Gutenberg and Richter 1949) and Omori law (Omori 1894, Utsu 1961). The former states the scaling relation between cumulative frequency of event

occurrence and released energies, and the latter tells power-law decay of occurrence of aftershocks following a main shock.

Although seismology has a long tradition, microscopic dynamics governing seismicity is still largely unknown. In such a situation, it is important to investigate the properties of correlations. In recent years, some empirical laws concerning spatiotemporal correlations have been investigated. Both 3-dimensional distance (Abe and Suzuki 2003) and time interval (calm time or inter-occurrence time) (Corral 2004, Abe and Suzuki 2005a) between two successive earthquakes were found to obey definite statistical laws that significantly deviate from Poissonian. In other words, two successive events are correlated at least at the statistical level with high significance. In addition, it is known (Steeples and Steeples 1996) that an earthquake can trigger the next one that can be more than 1000 km away. Thus, the event-event correlation length may be divergently large, indicating a strong similarity to critical phenomena. Accordingly, we propose to frame the working hypothesis that two successive events are statistically correlated. (This hypothesis is not satisfied by pairs that are not causal in terms of the propagation speed of seismic waves, for example. However, such pairs are statistically not significant if a large number of events are considered.)

In this paper, we report recent discoveries about the physics of aftershocks. Specifically, they are relevant to (i) evolution of *complex earthquake networks*, (ii) *aging* **and** *scaling*, and (iii) long-range memory, *i.e.*, the *non-Markovian nature*. All these issues are deeply concerned with correlations between aftershocks.

The present paper is organized as follows. In Section 2, first, the concept of earthquake network and the procedure of its construction are explained in detail. Then, it is shown how the clustering property of the earthquake network evolves in time before and after a main shock. In Section 3, the event-event correlations are considered. The two-point correlation function defined there is found to exhibit a peculiar non-stationary behavior, termed aging. A glassy dynamics aspect of seismicity of aftershocks is discussed. In Section 4, the non-Markovian nature of aftershocks is studied. It is shown that the scaling relation to be satisfied by a class of singular Markovian stochastic processes is violated by aftershocks. Section 5 is devoted to concluding remarks. The data analyzed in this paper is the one taken from California (http://www.data.sces.org/). However, we emphasize that the results presented here were reconfirmed by other datasets such as the Japanese one.

2. COMPLEX EARTHQUAKE NETWORK AND ITS EVOLUTION

In contemporary statistical mechanics, the concept of complex networks appears as a powerful tool for quantifying the degree of complexity of a system/phenomenon. A network tells us about basic architecture underlying

a complex system. In a recent work by Abe and Suzuki (2004a), this concept has been introduced into seismology. In Subsection 2.1, we explain the procedure of constructing an earthquake network in detail. In Subsection 2.2, we succinctly summarize the known fundamental properties of an earthquake network as a complex network. Then, in Subsection 2.3, which is the main part of this section, we discuss how time evolution of the clustering coefficient of an earthquake network can characterize aftershocks as well as a main shock.

2.1 Earthquake network and its complexity

Here, we explain the procedure of constructing an earthquake network originally presented in the work (Abe and Suzuki 2004a). First, we divide a geographical region under consideration into cubic cells. We regard a cell as a vertex of a network if earthquakes with any values of magnitude (above a certain detection threshold) occurred therein. Then, we link two vertices of successive events by an edge. If two events successively occur in the same cell, then we attach a tadpole (*i.e.*, a self-loop) to that vertex. These edges and tadpoles represent the event-event correlations in accordance with the working hypothesis mentioned in the preceding section. A useful method we employ here for practically setting up the cells and identifying a cell for each earthquake is as follows. Let θ_0 and θ_{max} be the minimal and maximal values of latitude of the whole region, respectively. Similarly, let ϕ_0 and ϕ_{max} be the minimal and maximal values of longitude. Define θ_{av} as the sum of the values of latitude of all the events divided by the number of events. The hypocenter of the ith event is denoted by (θ_i, ϕ_i, z_i), where θ_i, ϕ_i, and z_i are the values of latitude, longitude and depth, respectively. The north-south distance between (θ_0, ϕ_0) and (θ_i, ϕ_i) reads $d_i^{NS} = R(\theta_i - \theta_0)$, where $R\,(\cong 6370\text{ km})$ is the radius of the Earth. On the other hand, the east-west distance is given by $d_i^{EW} = R(\phi_i - \phi_0)\cos\theta_{av}$ (in these expressions, all the angles should be described in the unit of radian). The depth is simply $d_i^D = z_i$. Starting from the point $(\theta_0, \phi_0, z_0 \equiv 0)$, divide the region into cubic cells with a given value of the cell size $L \times L \times L$ [km^3]. Then, the cell of the ith event can be identified by making use of d_i^{NS}, d_i^{EW}, and d_i^D.

The above procedure allows us to map, in an unambiguous way, a given seismic time series to a growing stochastic network, which is an earthquake network that we have been referring to.

Several comments on the above-mentioned construction procedure are in order. First of all, it contains a single parameter: the cell size, which can be seen as the scale of coarse graining. All earthquakes occurred in a given cell

are identified. It is important to clarify how the properties of the network depend on it. This point has thoroughly been discussed in a recent work by Abe and Suzuki (2009c). Secondly, an earthquake network is a directed network. However, directedness is irrelevant to statistical analysis of connectivity (or, degree, *i.e.*, the number of edges attached to the vertex under consideration) needed for examining the scale-free property, since by construction the in-degree and out-degree are identical for each vertex except the initial and final vertices in analysis. So, they need not be distinguished. That is, vertices except the initial and final ones have the even-number values of connectivity. However, directedness is important when the period distribution (*i.e.*, the waiting event-time distribution) is considered (Abe and Suzuki 2005b). Thirdly, a full directed earthquake network should be reduced to a simple undirected network, when its small-world property is examined. There, tadpoles are removed, and each multiple edge is replaced by a single edge – see Fig. 1 (the standard small-world network (Watts and Strogatz 1998) is simple and undirected). We note that, according to our examinations, gross properties of a network do not change, although numerical values of characteristics of a network generically depend slightly on how cells are set up. Lastly, we mention that the cell size L is supposed to be typically a few kilometers or larger, in view of the smallest fault size as well as emergence of universalities of the network characteristics (Abe and Suzuki 2009c).
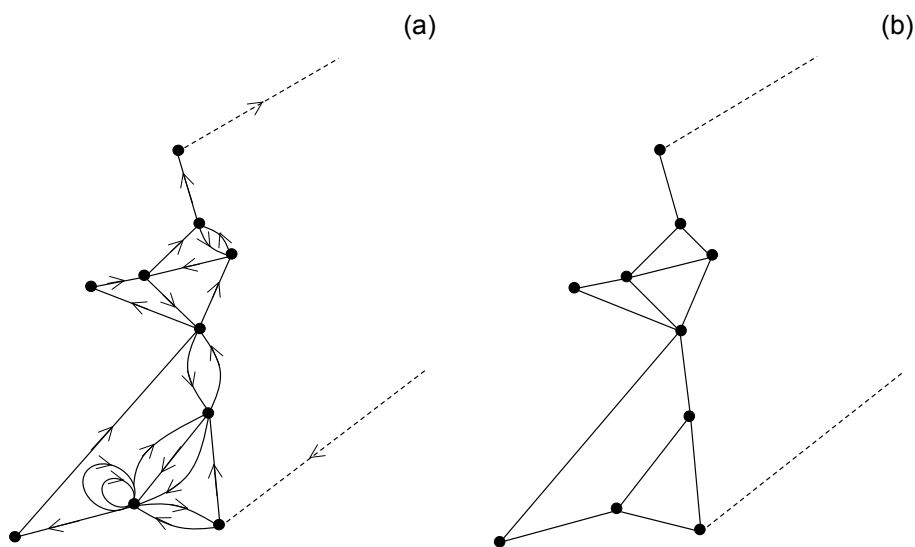
Fig. 1. Schematic descriptions of earthquake network: (a) a full directed network, and (b) its reduced undirected simple network in the small-world picture. The vertices with the dotted lines indicate the initial and final events in analysis.

2.2 Earthquake network as a complex network

In a series of our studies, we have discovered by analyzing real seismic data that an earthquake network is a complex network.

In our work (Abe and Suzuki 2004a), we have found that a full earthquake network is scale-free. That is, the probability $P(k)$ of finding vertices with connectivity, k, obeys a power law (Barabási and Albert 1999): $P(k) \sim k^{-\gamma}$, where γ is a positive constant. A remarkable empirical fact is that aftershocks following a main shock tend to return to the cell of the main shock, geographically. This makes the vertex of the main shock a hub of the earthquake network. And, consequently, the network becomes heterogeneous.

In our works (Abe and Suzuki 2004c, 2006a), we have shown that a simple network reduced from a full earthquake network is of the small-world type. Two main features of a small-world network are as follows (Watts and Strogatz 1998). One is that the average path length (*i.e.*, the number of edges between two chosen vertices) is small. The other is that the clustering coefficient is much larger than that of the Erdös–Rényi random graph (Bollobás 2001). Here, the clustering coefficient C of a simple network with N vertices is defined as follows (Watts and Strogatz 1998):

$$C = \frac{1}{N} \sum_{i=1}^{N} c_i \ .$$ (1)

In this equation, c_i appearing on the right-hand side is given by $c_i \equiv$ (number of edges of the ith vertex and its neighbors)/$[k_i (k_i - 1)/2]$, with k_i being the connectivity of the ith vertex. It is calculated also as follows. Let A be the symmetric adjacency matrix of a simple network. Its element $(A)_{ij}$ is 1 (0), if the ith and jth vertices are linked (unlinked). The diagonal elements of A are zero, since a simple network has no tadpoles. Then, c_i is also written as follows:

$$c_i = \frac{e_i}{e_i^{\max}} \ ,$$ (2)

where $e_i = (A^3)_{ii}$, and $e_i^{\max} = k_i(k_i - 1)/2$ with $k_i = \sum_{j=1}^{N} (A)_{ij}$, which is nothing but the maximum value of e_i . Coefficient c_i quantifies the tendency that two neighboring vertices of the ith vertex are linked together (*i.e.*, forming a triangle). By definition, C takes a value between 0 and 1. As pointed out by Watts and Strogatz (1998), C of a small-world network is much larger than that of the corresponding Erdös–Rényi random graph: $C \gg C_{\text{random}}$, where $C_{\text{random}} = <k>/N \ll 1$ with $<k>$ being the average value of connectivity of the random graph.

In fact, a reduced simple earthquake network has a small value of the average path length. For the number of vertices of about $27\,000$, it is less than 4 (Abe and Suzuki 2004c, 2006a). Also, C of an earthquake network is $10^3 \sim 10^4$ times larger than C_{random}. Therefore, an earthquake network is a small-world network.

In addition to scale-freeness and small-worldness, earthquake network has further remarkable properties. Among others, the hierarchical organization (Ravasz and Barabási 2003) and mixing property (Newman 2002) should be emphasized. In the work (Abe and Suzuki 2006b), it is found that an earthquake network is, in fact, hierarchically organized and possesses assortative mixing (implying that a hub tends to be linked to other hubs rather than vertices with small values of connectivity). Also, spectral analysis shows (Abe and Suzuki 2009b) that an earthquake network is locally tree-like, that is, c_i in Eq. (2) is small if the ith vertex is a hub. Furthermore, there exists finite data-size scaling for the clustering coefficient (Abe $et\ al.$ 2011).

Closing this subsection, we stress the following point. Any seismic data may be incomplete due to errors, detection threshold, and so on. However, the basic properties of an earthquake network are not affected by such incompleteness. As known in the literature (Albert $et\ al.$ 2000), complex networks are highly robust to random failure.

2.3 Evolution of clustering coefficient and aftershocks

Now, let us see, as an example of applications of an earthquake network, how aftershocks as well as a main shock can be characterized in a peculiar way (Abe and Suzuki 2007). In particular, here we discuss time evolution of the clustering coefficient C in Eq. (1) around the occurrence times of some well-known main shocks.

We construct the earthquake network from every 240-hour (10-day) interval. Here, we specifically focus our attention on two celebrated main shocks: the Joshua Tree Earthquake (M6.1 on 23 April 1992) and the Hector Mine Earthquake (M7.1 on 16 October 1999). Here, the cell size is taken to be $5 \times 5 \times 5$ km^3. The result is presented in Fig. 2. There, we see a remarkable common behavior. The clustering coefficient stays stationary before the main shock, suddenly jumps up at the main shock, and then slowly decays to return to a stationary value again with some fluctuations. In the work (Abe and Suzuki 2007), it is shown that the decay process, which takes place during the interval of aftershocks, obeys a power law. Thus, the clustering coefficient characterizes aftershocks as well as a main shock in a novel way.

The above discussion is nothing but an example of possible applications. The complex network approach to seismicity is still at an infant stage, and a lot of issues are yet to be investigated.
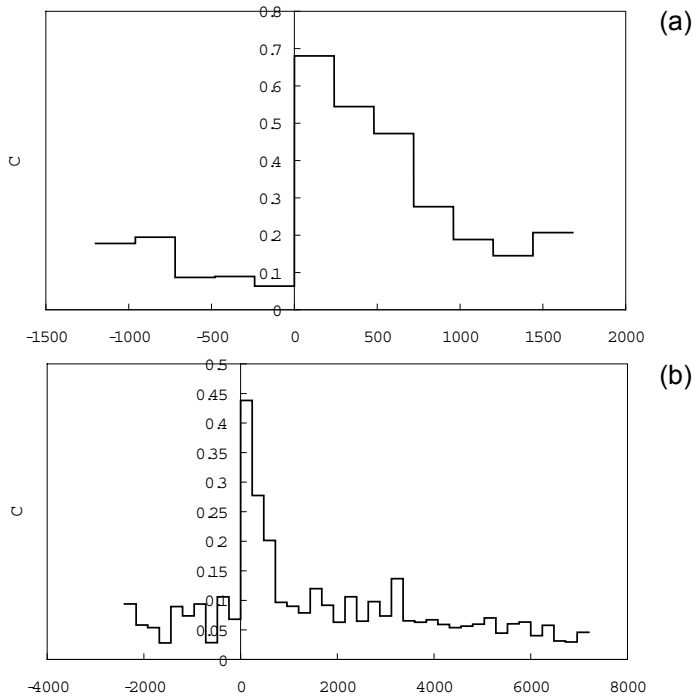
Fig. 2. Evolution of the (dimensionless) clustering coefficient for each 240 hours. The cell size is taken here as $5 \times 5 \times 5$ km^3. The origins are adjusted to the moments of the main shocks: (a) the Joshua Tree Earthquake, and (b) the Hector Mine Earthquake. The length of the total interval in (a) is shorter than that in (b). This is because another strong shock (*i.e.*, the Landers Earthquake) occurred on 28 June 1992 and made it impossible to take the aftershock sequence following the Joshua Tree Earthquake so long.

3. AGING AND SCALING: ARE AFTERSHOCKS GOVERNED BY GLASSY DYNAMICS?

Regarding aftershocks, the following two points should be noted:

(A) The stress distribution at faults has a complex landscape. A main shock instantaneously releases a huge amount of energy with quenching the disorder of the stress distribution, in analogy with super-cooling. Then, it reorganizes the stress distribution. The "system" changes its energy state from one local minimum to another. Such a transition may be regarded as an aftershock.

(B) The relaxation of the system to a stationary (or, quasi-equilibrium) state is very slow according to the power-law nature of the Omori law (Omori 1894, Utsu 1961).

Keeping (A) and (B) in mind, here we discuss the concept of event-event correlations of aftershocks. Let $\{t_0, t_1, t_2, \ldots, t_{M-1}\}$ be a sequence of the occurrence times of aftershocks, where t_0 is the occurrence time of a chosen initial event of the sequence of aftershocks. Such a sequence defines a point process, and the nth occurrence time, t_n, is a random variable labeled by the number $n(= 0, 1, 2, \ldots, M-1)$, which is referred to as **event time**. The fundamental quantity is the following **event-event correlation function** proposed in the work (Abe and Suzuki 2004b):

$$C(m, n) = \frac{<t_m\, t_n> - <t_m><t_n>}{\sqrt{\sigma_m^2\, \sigma_n^2}} \,, \tag{3}$$

where $<\cdot>$ is given by the **event-time average**: $<t_m> = (1/M)\sum_{k=0}^{M-1} t_{m+k}$, $<t_m\, t_n> = (1/M)\sum_{k=0}^{M-1} t_{m+k}\, t_{n+k}$, and $\sigma_m^2 = <t_m^2> - <t_m>^2$. If the process (*i.e.*, the sequence) is non-stationary, this quantity depends on two event times, m and n, in general. It is convenient to introduce the **waiting event time**, n_w, to rewrite Eq. (3) as

$$C(n + n_W, n_W) \,. \tag{4}$$

If the process is stationary, the quantity in Eq. (4) does not depend on n_w. Clearly, $C(n + n_w, n_w) = 1$ at $n = 0$. This quantity might have a complicated n_w-dependence, in general. However, it actually turns out to exhibit a very special n_w-dependence.

We have analyzed the event-event correlation function of the aftershocks following the Landers Earthquake ($M7.3$ on 28 June 1992) as a typical example. In Fig. 3, we present the plots of $C(n + n_w, n_w)$ for several values of n_w. A remarkable feature is observed there. The larger the n_w is, the slower the $C(n + n_w, n_w)$ decreases. No crossing of the curves occurs. This phenomenon is called aging in statistical mechanics. It implies that the system has its own clock, recording its "intrinsic internal time".

Another important point is the existence of scaling. It is possible to collapse all curves in Fig. 3 to a single curve (see Fig. 4):

$$C(n + n_W, n_W) = \tilde{C}\left[n / f(n_W)\right] \,, \tag{5}$$

where $\tilde{C}$ is a scaling function. Function $f(n_w)$ is found to have the form

$$f(n_W) = a(n_W)^\gamma + 1 \,, \tag{6}$$

where $a = 1.37 \times 10^{-6}$ and $\gamma = 1.62$ for the scaling function in Fig. 4.

In the work (Abe and Suzuki 2004b), the aftershocks associated with other main shocks are also analyzed, and the same result as the above one is
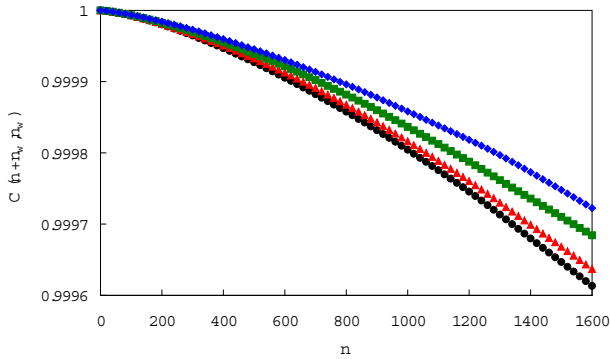
Fig. 3. The plots of the event-event correlation function with respect to the event time, n, for several values of waiting event time, n_w. The event time n runs within the interval of the aftershocks following the Landers Earthquake. $n_w = 0$ (●), 600 (▲), 1200 (■), and 1800 (◆). All quantities are dimensionless. Colour version of this figure is available in electronic edition only.
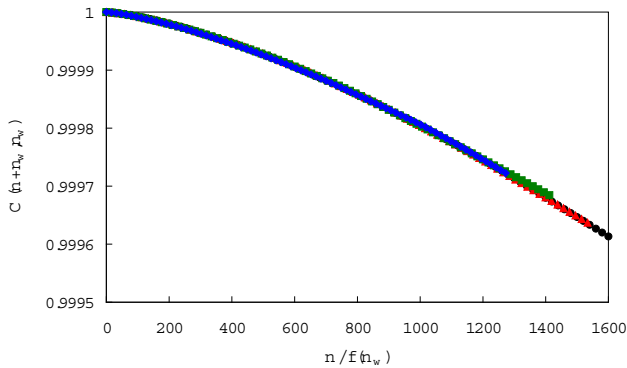

Fig. 4. The data collapse of Fig. 3 by the rescaling of the event time. All quantities are dimensionless. Colour version of this figure is available in electronic edition only.

obtained. In addition, outside of the intervals of aftershocks, the aging phenomenon is not observed. Thus, aging characterizes aftershocks.

Now, combining the aging and scaling as well as the points (A) and (B) mentioned in the beginning of this section, we conclude that the dynamics governing aftershocks is highly similar to ***glassy dynamics*** (Fischer and Hertz 1991).

4. NON-MARKOVIAN NATURE

In a Markovian process, transition of a system from one state to another can basically be understood in terms of local fluctuations. In a non-Markovian process, on the other hand, such a local picture cannot apply because of the

presence of the long-range memory, *i.e.*, temporal non-separability of events. Non-Markovianity signals the complexity of a system.

Given finite seismic data, it is generically difficult to determine if such a stochastic process is Markovian or not. However, there is a rigorous mathematical method of determining it for a class of singular point processes, which has been discussed in the problems of laser cooling of atoms (Bardou *et al.* 2002). We apply such a method to examining how the process of aftershocks is non-Markovian (Abe and Suzuki 2009a).

What is of crucial importance is the existence of the scaling relation in a class of singular Markovian processes. It is related to two basic quantities in the processes. One is the time-interval distribution, $P(t)$, of two successive aftershocks, and the other is the rate of event occurrence (*i.e.*, temporal mean density of aftershocks), $S(t) = [N(t + \Delta t) - N(t)]/\Delta t$, where $N(t)$ stands for the number of events occurred in the time interval $[0, t]$. If a process is Markovian, then holds the following equation (Bardou *et al.* 2002):

$$S(t) = P(t) + \int_0^t dt' \, P(t - t') \, S(t') \,, \tag{7}$$

which can be derived from the Kolmogorov forward equation (Barndorff-Nielsen *et al.* 2000). Since the second term on the right-hand side is a convolution integral, it is convenient to perform the Laplace transformations of the both sides. Then, we obtain

$$L[S](s) = \frac{L[P](s)}{1 - L[P](s)} \,, \tag{8}$$

where $L[f](s) \equiv \int_0^\infty dt \, e^{-st} f(t)$. Consider a singular processes, in which both P and S decay as a power law

$$P(t) \sim \frac{1}{t^{1+\mu}} \,, \tag{9}$$

$$S(t) \sim \frac{1}{t^p} \,, \tag{10}$$

for a large value of t. If the exponents, μ and p, satisfy

$$0 < \mu < 1 \,, \tag{11}$$

$$0 < p < 1 \,, \tag{12}$$

then

$$L[P](s) \sim 1 - \alpha s^\mu \,, \tag{13}$$

$$L[S](s) \sim s^{p-1} \,, \tag{14}$$

for a small value of s, where α is a positive constant. Therefore, from Eq. (8) it follows that

$$p + \mu = 1 . \qquad (15)$$

This is the scaling relation to be satisfied by singular Markovian processes with P and S obeying Eqs. (9)-(12).

Note that Eq. (10) precisely describes the Omori law for aftershocks. Therefore, a question arising is if the time-interval distribution, P, also obeys a power law for aftershocks. The answer to this question turns out to be affirmative, as we shall see below.

As in the preceding section, we analyze the aftershocks of the Landers Earthquake. We set the spatial window with size of 100 km (east-west) and 100 km (north-south), centered at the epicenter of the Landers Earthquake (34°12.00 N latitude, 116°26.22 W longitude), and 100 km in depth. We consider 600 days after the main shock, during which there occurred 34 783 events in this windowed region.

Figure 5 is the plot of $S(t)$. There, one sees that the Omori law holds well. Figure 6 is the plot of $P(t)$. One certainly recognizes the behavior in Eq. (9). However, since the scaling regime is not so large, a careful examination is needed for determining the value of the exponent μ. To do so, we employ the method of maximum likelihood estimation (Goldstein *et al.* 2004, Newman 2005).

Table 1 summarizes the result. As can be seen there, the Markovian scaling relation in Eq. (15) is violated in about 50%. Therefore, we conclude that the process of aftershocks following the Landers Earthquake is non-Markovian, possessing the long-range memory.
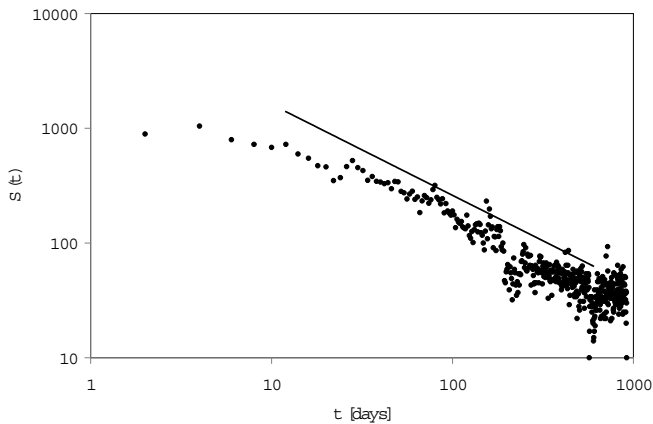

Fig. 5. The log-log plot of $S(t)$ with the inverse dimension of time. The bin size for constructing the histogram is taken to be 2 days.
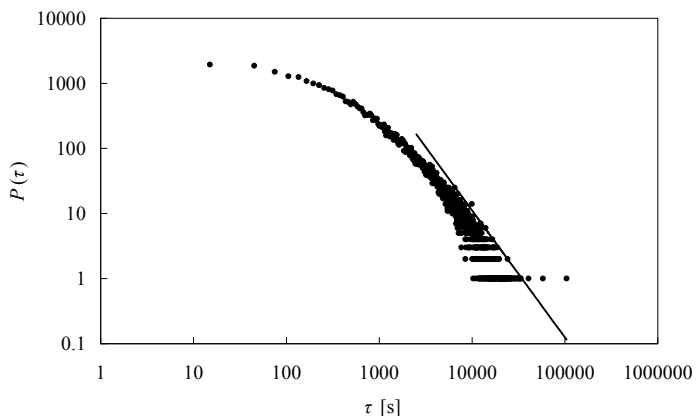
Fig. 6. The log-log plot of $P(t)$ with the inverse dimension of time. The bin size for constructing the histogram is taken to be 30 s.

Table 1

The values of p and μ for some different bin size for constructing the histograms in the case of the aftershocks following the Landers Earthquake

Bin size [days]	p	Bin size [s]	μ	$p + \mu$
0.5	0.788 ± 0.004	10	0.629 ± 0.011	1.417 ± 0.015
		20	0.873 ± 0.018	1.661 ± 0.021
		30	0.950 ± 0.017	1.738 ± 0.021
1	0.790 ± 0.004	10	0.629 ± 0.011	1.419 ± 0.015
		20	0.873 ± 0.018	1.662 ± 0.021
		30	0.950 ± 0.017	1.740 ± 0.021
1.5	0.793 ± 0.004	10	0.629 ± 0.011	1.422 ± 0.015
		20	0.873 ± 0.018	1.665 ± 0.021
		30	0.950 ± 0.017	1.743 ± 0.021
2	0.792 ± 0.004	10	0.629 ± 0.011	1.421 ± 0.015
		20	0.873 ± 0.018	1.664 ± 0.021
		30	0.950 ± 0.017	1.742 ± 0.021

Note: The errors, which are automatically calculated by the method of maximum likelihood estimation, are very small due to the large sample size.

Finally, we note that a similar result is obtained for aftershocks of other main shocks such as the Hector Mine Earthquake (Abe and Suzuki 2009a). We confidently believe that the process of aftershocks is non-Markovian, in general.

5. CONCLUDING REMARKS

To summarize, we have surveyed the recent discoveries about the nature of aftershocks in view of science of complexity. We have seen how the complex network representation can reveal the novel features of seismicity. Aging and scaling of aftershocks are certainly remarkable. It is of extreme importance to further clarify how the unknown dynamics governing aftershocks is similar to (or different from) glassy dynamics. We have also seen that processes of aftershocks are non-Markovian. All these results highlight the aspects of aftershocks as a complex phenomenon. Future investigations along these lines based on modern science will give clues to deeper understandings of the physics of seismicity.

References

Abe, S., and N. Suzuki (2003), Law for the distance between successive earthquakes, *J. Geophys. Res.* **108**, B2, 2113-2117, DOI: 10.1029/2002JB002220.

Abe, S., and N. Suzuki (2004a), Scale-free network of earthquakes, *Europhys. Lett.* **65**, 4, 581-586, DOI: 10.1209/epl/i2003-10108-1.

Abe, S., and N. Suzuki (2004b), Aging and scaling of earthquake aftershocks, *Physica A* **332**, 533-538, DOI: 10.1016/j.physa.2003.10.002.

Abe, S., and N. Suzuki (2004c), Small-world structure of earthquake network, *Physica A* **337**, 1-2, 357-362, DOI: 10.1016/j.physa.2004.01.059.

Abe, S., and N. Suzuki (2005a), Scale-free statistics of time interval between successive earthquakes, *Physica A* **350**, 2-4, 588-596, DOI: 10.1016/j.physa.2004.10.040.

Abe, S., and N. Suzuki (2005b), Scale-invariant statistics of period in directed earthquake network, *Eur. Phys. J. B* **44**, 1, 115-117, DOI: 10.1140/epjb/e2005-00106-7.

Abe, S., and N. Suzuki (2006a), Complex-network description of seismicity, *Nonlin. Processes Geophys.* **13**, 2, 145-150, DOI: 10.5194/npg-13-145-2006.

Abe, S., and N. Suzuki (2006b), Complex earthquake networks: Hierarchical organization and assortative mixing, *Phys. Rev. E* **74**, 2, 026113, DOI: 10.1103/PhysRevE.74.026113.

Abe, S., and N. Suzuki (2007), Dynamical evolution of clustering in complex network of earthquakes, *Eur. Phys. J. B* **59**, 1, 93-97, DOI: 10.1140/epjb/e2007-00259-3.

Abe, S., and N. Suzuki (2009a), Violation of the scaling relation and non-Markovian nature of earthquake aftershocks, *Physica A* **388**, 9, 1917-1920, DOI: 10.1016/j.physa.2009.01.031.

Abe, S., and N. Suzuki (2009b), Scaling relation for earthquake networks, *Physica A* **388**, 12, 2511-2514, DOI: 10.1016/j.physa.2009.02.022.

Abe, S., and N. Suzuki (2009c), Determination of the scale of coarse graining in earthquake networks, *Europhys. Lett.* **87**, 4, 48008, DOI: 10.1209/0295-5075/87/48008.

Abe, S., D. Pastén, and N. Suzuki (2011), Finite data-size scaling of clustering in earthquake networks, *Physica A* **390**, 7, 1343-1349, DOI: 10.1016/j.physa.2010.11.033.

Albert, R., H. Jeong, and A.-L. Barabási (2000), Error and attack tolerance of complex networks, *Nature* **406**, 378-382, DOI: 10.1038/35019019.

Barabási, A.-L. and R. Albert (1999), Emergence of scaling in random networks, *Science* **286**, 5439, 509-512, DOI: 10.1126/science.286.5439.509.

Bardou, F., J.-P. Bouchaud, A. Aspect, and C. Cohen-Tannoudji (2002), *Lévy Statistics and Laser Cooling. How Rare Events Bring Atoms to Rest*, Cambridge University Press, Cambridge.

Barndorff-Nielsen, O.E., F.E. Benth, and J.L. Jensen (2000), Markov jump processes with a singularity, *Adv. Appl. Probab.* **32**, 3, 779-799, DOI: 10.1239/aap/1013540244.

Bollobás, B. (2001), *Random Graphs*, 2nd ed., Cambridge Studies in Advanced Mathematics, Vol. 73, Cambridge University Press, Cambridge.

Corral, Á. (2004), Long-term clustering, scaling, and universality in the temporal occurrence of earthquakes, *Phys. Rev. Lett.* **92**, 10, 108501, DOI: 10.1103/PhysRevLett.92.108501.

Fischer, K.H., and J.A. Hertz (1991), *Spin Glasses*, Cambridge Studies in Magnetism, Vol. 1, Cambridge University Press, Cambridge.

Goldstein, M.L., S.A. Morris, and G.G. Yen (2004), Problems with fitting to the power-law distribution, *Eur. Phys. J. B* **41**, 2, 255-258, DOI: 10.1140/epjb/e2004-00316-5.

Gutenberg, B. and C.F. Richter (1949), *Seismicity of the Earth and Associated Phenomena*, Princeton University Press, Princeton.

Newman, M.E.J. (2002), Assortative mixing in networks, *Phys. Rev. Lett.* **89**, 20, 208701, DOI: 10.1103/PhysRevLett.89.208701.

Newman, M.E.J. (2005), Power laws, Pareto distributions and Zipf's law, *Contemp. Phys.* **46**, 5, 323-351, DOI: 10.1080/00107510500052444.

Omori, F. (1894), On the after-shocks of earthquakes, *J. Coll. Sci. Imp. Univ. Tokyo* **7**, 111-200.

Ravasz, E., and A.-L. Barabási (2003), Hierarchical organization in complex networks, *Phys. Rev. E* **67**, 2, 026112, DOI: 10.1103/PhysRevE.67.026112.

Steeples, D.W., and D.D. Steeples (1996), Far-field aftershocks of the 1906 earth-quake, *Bull. Seismol. Soc. Am.* **86**, 4, 921-924.

Utsu, T. (1961), A statistical study on the occurrence of aftershocks, *Geophys. Mag.* **30**, 521-605.

Watts, D.J., and S.H. Strogatz (1998), Collective dynamics of 'small-world' net-works, *Nature* **393**, 440-442, DOI: 10.1038/30918.

VERSITA

Long-Term Correlations in Earth Sciences

Armin BUNDE[1] and Sabine LENNARTZ[1,2]

[1]Institut für Theoretische Physik, Giessen, Germany
e-mail: Armin.Bunde@uni-giessen.de (corresponding author)

[2]School of Engineering and School of Geosciences,
University of Edinburgh, Edinburgh, UK

A b s t r a c t

In this article we review the occurrence and consequences of long-term memory in geophysical records like climate and seismic records, and describe similarities with financial data sets. We review several methods to detect linear and nonlinear long-term correlations, also in the presence of external trends, and show how external trends can be detected in data with long-term memory. We show as well that long-term correlations lead to a natural clustering of extreme events and discuss the implications for several geophysical data sets.

Key words: long-term correlations, extreme values, multi-fractality, trend detection.

1. INTRODUCTION

In recent years, there is growing evidence that long-term correlations play an important role in climate, physiology, and computer science as well as in the financial markets; the examples range from river floods (Hurst *et al.* 1965, Koscielny-Bunde *et al.* 2006, Livina *et al.* 2003, Mandelbrot and Wallis 1969, Mudelsee 2007), temperatures (Eichner *et al.* 2003, Király *et al.* 2006, Koscielny-Bunde *et al.* 1998, Pelletier and Turcotte 1999, Talkner and Weber 2000), and wind fields (Santhanam and Kantz 2005) to market volatilities (Liu *et al.* 1997, 1999), heart-beat intervals (Bunde *et al.* 2000, Peng *et al.* 1993)

and internet traffic (Leland *et al.* 1994). Here, we review several methods to detect long-term correlations, also in the presence of external trends, and give examples for long-term correlated climate records. We show that long-term correlations lead to a natural clustering of extreme events and discuss the implications for climate records as well as seismic and financial data. We also discuss briefly non-linear long-term correlations that play an important role in precipitation and river run-off data as well as in financial data. Finally, at the end of the article, we show how exernal trends can be detected in data with long-term memory.

2. LONG-TERM CORRELATIONS AND HOW TO DETECT THEM

Consider a record x_i of discrete numbers, where the index i runs from 1 to N. x_i may be daily, monthly or annual temperatures, precipitation data or river flows, or any other set of data consisting of N successive data points. We are interested in the fluctuations of the data around their (sometimes seasonal) mean value. Without loss of generality, we assume that the mean of the data is zero and the variance equal to one (to fulfill this requirement, climate must be seasonally detrended, as will be described below.) We call the data long-term correlated, when the corresponding autocorrelation function $C(s) = \langle x_i x_{i+s} \rangle \equiv \frac{1}{(N-s)} \sum_{i=1}^{N-s} x_i x_{i+s}$ decays, in the limit of $N \to \infty$, by a power law for $s > 0$ (see, *e.g.*, Mandelbrot and van Ness 1968),

$$C(s) \sim (1 - \gamma)s^{-\gamma}, \tag{1}$$

where γ denotes the correlation exponent, $0 < \gamma < 1$. Such correlations are named "long-term" since the mean correlation time $T = \int_0^\infty C(s)\mathrm{d}s$ diverges in the limit of infinitely long series where $N \to \infty$. For data sets with ***finite*** length N, the autocorrelation function decays for $0 < s \ll N$ as (Lennartz and Bunde 2009b)

$$C(s) = \frac{1}{1 - N^{-\gamma}} \left(\frac{(1-\gamma)(2-\gamma)}{2} s^{-\gamma} - N^{-\gamma} \right). \tag{2}$$

Accordingly, there are large finite-size effects in $C(s)$ that make it difficult to estimate the correlation exponent γ for N of the order of the length of typical climate records.

If the x_i are uncorrelated, $C(s) = 0$ for $s > 0$. More generally, if correlations exist up to a certain correlation time s_x, then $C(s) > 0$ for $s < s_x$ and $C(s) = 0$ for $s > s_x$.

Long-term correlated records also can be characterized by the power spectral density $S(f) = |x(f)|^2$, where $\{x(f)\}$, $f = 0, \ldots, N/2$, is the Fourier transform of $\{x_i\}$. With increasing frequency f, $S(f)$ decays by a power law
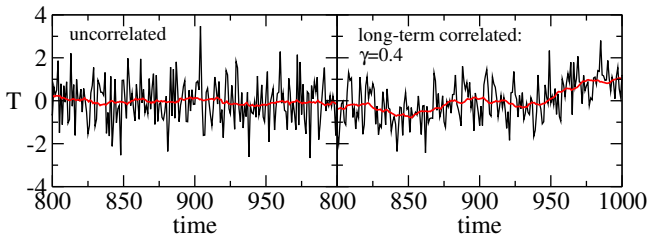
$$S(f) \sim f^{-\beta}, \tag{3}$$

Fig. 1. Comparison of an uncorrelated and a long-term correlated record with $\gamma = 0.4$. The full line is the moving average over 30 data points. Colour version of this figure is available in electronic edition only.

where $\beta > 0$ characterizes the long-term memory (Malamud and Turcotte 1999). For uncorrelated data, $\beta = 0$.

Equation (3) can be used to generate synthetic Gaussian distributed long-term correlated records, as has been described, for example, in Turcotte (1997). First one generates uncorrelated Gaussian data. Then one transforms them to Fourier space, multiplies the result by $f^{-\beta/2}$ and transforms them back to time space. By definition, the resulting $S(f)$ follows Eq. (3). We would like to note that, in a considerably more elaborate iterative procedure suggested by Schreiber and Schmitz (1996), (monofractal) long-term correlated records with any other distribution can also be generated.

Figure 1 shows parts of an uncorrelated (left) and a long-term correlated (right) record, with $\gamma = 0.4$; both series have been generated by the algorithm described above. The full line is the moving average over 30 data points. For the uncorrelated data, the moving average is close to zero, while for the long-term correlated data set, the moving average can have large deviations from the mean, forming some kind of mountain valley structure. This structure is a consequence of the power-law persistence. The mountains and valleys on the right-hand side of Fig. 1 look as if they had been generated by external trends, and one might be inclined to draw a trend-line and to extrapolate the line into the near future for some kind of prognosis. But since the data are trend-free, only a short-term prognosis utilizing the persistence can be made, and not a longer-term prognosis which often is the aim of such a regression analysis.

Alternatively, one can divide the data set in K_s equidistant windows of length s, determine in each window ν the squared sum

$$F_\nu^2(s) = \left(\sum_{i=1}^{s} x_i \right)^2, \tag{4}$$

and detect how the square root of the average of this quantity over all windows,

$$\langle F(s) \rangle = \left[\frac{1}{K_s} \sum_{\nu=1}^{K_s} F_\nu^2(s) \right]^{1/2}, \tag{5}$$

scales with the window size s. This method is called fluctuation analysis (FA). For long-term correlated data, in the limit of $N \to \infty$, $\langle F(s) \rangle$ scales as

$$\langle F(s) \rangle \sim s^{\alpha}, \tag{6}$$

where $\alpha = 1 - \gamma/2$. For uncorrelated or short-term correlated data sets, $\alpha = 1/2$. In the literature, α is often referred to as Hurst-exponent. Equation (6) represents an alternative way to determine the correlation exponent γ. For data with a finite length N, which is usually the case with climate data, one finds (Lennartz and Bunde 2009b)

$$\langle F(s) \rangle \sim s^{\alpha} (1 - (s/N)^{2-2\alpha})^{1/2}, \tag{7}$$

showing that finite size effects are strong for large s and small γ.

Since trends resemble long-term correlations and *vice versa*, there is a general problem to distinguish between trends and long-term persistence. In recent years, several methods have been developed, mostly based on the hierarchical detrended fluctuation analysis (DFAn), where long-term correlations in the presence of smooth polynomial trends of order $n-1$ can be detected (Bunde *et al.* 2000, Kantelhardt *et al.* 2001, Peng *et al.* 1993). The DFAn procedure consists of four steps (Kantelhardt *et al.* 2001). First, we determine the cumulated sum $Y(i) \equiv \sum_{k=1}^{i} x_k$, $i = 1, \dots, N$, of the record. Then we divide the profile into $N_s \equiv \mathrm{int}(N/s)$ nonoverlapping segments of equal length s. Since the length N of the series is usually not a multiple of the considered timescale s, a short part at the end of the profile may remain. In order not to disregard this part of the series, the same procedure is repeated starting from the opposite end. Thereby, $2N_s$ segments are obtained altogether. In the third step we calculate the local trend for each of the $K_s = 2N_s$ segments by fitting (least squares fit) a polynomial of order n to the data and determine the variance

$$F_{\nu}^2(s) \equiv \frac{1}{s} \sum_{i=1}^{s} [Y((\nu-1)s + i) - p_{\nu}(i)]^2 \tag{8}$$

for each segment ν. Here $p_{\nu}(i)$ is the fitting polynomial representing the local trend in the segment ν. Linear, quadratic, cubic and higher-order polynomials can be used in the fitting procedure. When linear polynomials are used, the fluctuation analysis is called DFA1, for quadratic polynomials we have DFA2, for cubic polynomials DFA3, *etc.* By definition, DFA2 removes quadratic trends in the profile $Y(i)$ and thus linear trends in the original series x_i.

In the last step, finally, one averages (as for the FA) over all segments and takes the square root to obtain the mean fluctuation function,

$$\langle F(s) \rangle \equiv \left[\frac{1}{K_s} \sum_{\nu=1}^{K_s} F_{\nu}^2(s) \right]^{1/2}. \tag{9}$$

One can show that for long-term correlated trend-free data, $\langle F(s) \rangle$ scales with the window size s as $F(s)$ in Eq. (6), *i.e.*, $\langle F(s) \rangle \sim s^\alpha$, with $\alpha = 1 - \gamma/2$, irrespective of the order of the detrending polynomial. For short-term correlated records, the exponent is $1/2$ for s above the correlation time s_x. Trends of order $n - 1$ in the original data are eliminated by DFAn, while they contribute to DFA$(n - 1)$ and DFA$(n - 2)$, *etc.*, and this allows to determine the correlation exponent γ in the presence of trends. For example, in the case of a linear trend, DFA1 is affected by the trend and will exaggerate the asymptotic exponents α, while DFA2, DFA3, *etc.* are not affected by the trend and will show, in a double logarithmic plot, the same slope α, which then gives immediately the correlation exponent γ. A further advantage of the DFAn, $n = 1, 2, 3, \ldots$, compared with the FA is that there are no pronounced finite size effects.

When γ has been obtained by DFAn, one can try to detect the trend, but there is no unique treatment available. In recent papers (Giese *et al.* 2007, Rybski and Bunde 2009, Rybski *et al.* 2006), different kinds of analysis have been elaborated and applied to estimate trends in the temperature records of the Northern Hemisphere and Siberian locations. Very recently, we have developed a quite general and easy to handle method (Lennartz and Bunde 2011) to estimate trends in long-term correlated records, that we will describe in detail in Section 7.

3. LONG-TERM CORRELATIONS IN CLIMATE RECORDS

Figure 2 shows representative results of the FA and DFAn analysis, for temperature, precipitation and river run-off data. For continental temperatures, the exponent α is around 0.65, while for island stations and sea surface temperatures the exponent is considerably higher. There is no crossover towards uncorrelated behavior at larger time scales. For the precipitation data, the exponent is close to 0.55, not being significantly larger than for uncorrelated records.

Figure 3 shows a summary of the exponent α for a large number of climate records. It is interesting to note that while the distribution of α values is quite broad for run-off, sea-surface temperature, and precipitation records, the distribution is quite narrow, located around $\alpha = 0.65$ for continental atmospheric temperature records. For the island records, the exponent is larger. The quite universal exponent $\alpha = 0.65$ for continental stations can be used as an efficient test bed for climate models (Govindan *et al.* 2002, Rybski and Bunde 2009, Vjushin *et al.* 2004).

The time window accessible by DFAn is typically $1/4$ of the length of the record. For instrumental records, the time window is thus restricted to about 50 years. For extending this limit, one has to take reconstructed records or model data, which range up to 2000y. Both have, of course, large uncertainties,
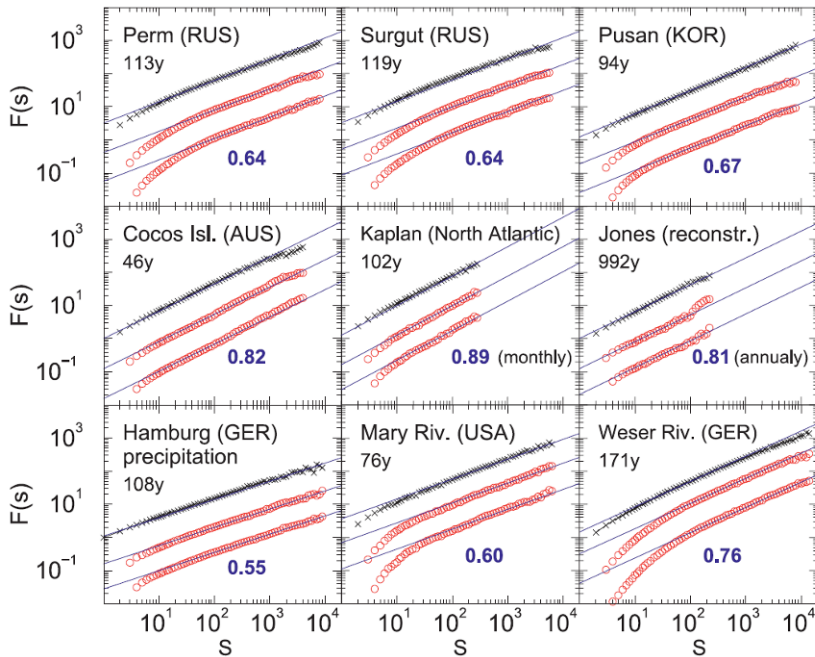
Fig. 2.   DFAn analysis of 6 temperature records, one precipitation record and 2 run-off records. Before the analysis, daily and monthly data have been seasonaly detrended. The black curves are the FA results, while the upper red curves refer to DFA1 and the lower red curves to DFA2. The blue numbers denote the asymptotic slopes of the curves. From Eichner *et al.* (2003), Kantelhardt *et al.* (2006), Monetti *et al.* (2003). Colour version of this figure is available in electronic edition only.

but it is remarkable that exactly the same kind of long-term correlations can be found in these data, thus extending the time scale where long-term memory exists to at least 500y (Rybski and Bunde 2009, Rybski *et al.* 2006).

4. LONG-TERM CORRELATIONS: CLUSTERING OF EXTREME EVENTS

Next we consider the consequences of long-term memory on the occurrence of rare events. Understanding (and predicting) the occurrence of extreme events is one of the major challenges in science (see, *e.g.*, Bunde *et al.* 2002). An important quantity here is the time interval between successive extreme events (see Fig. 4), and by understanding the statistics of these return intervals one aims to better understand the occurrence of extreme events.

Since extreme events are, by definition, very rare and the statistics of their return intervals poor, one usually studies also the return intervals between less
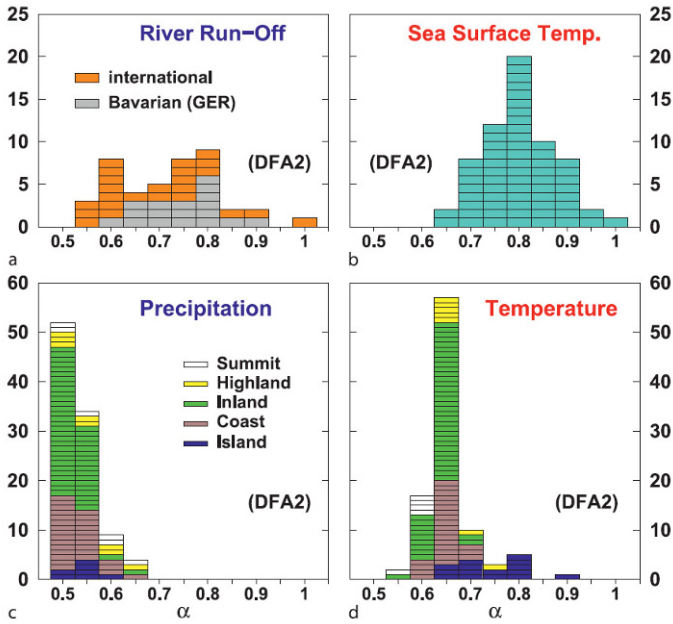
Fig. 3. Distribution of fluctuation exponents α for several kinds of climate records (from Eichner *et al.* 2003, Kantelhardt *et al.* 2006, Monetti *et al.* 2003). Colour version of this figure is available in electronic edition only.
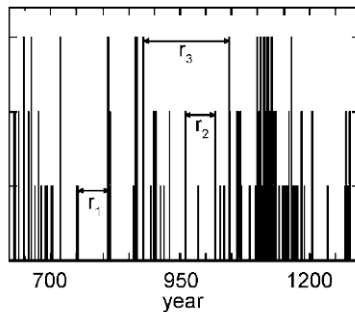

Fig. 4. Illustration of the return intervals for three equidistant threshold values q_1, q_2, q_3 for the water levels of the Nile at Roda (near Cairo, Egypt). One return interval for each threshold (quantile) q is indicated by arrows.

extreme events, where the data are above some threshold q and where the statistics is better, and hopes to find some general "scaling" relations between the return intervals at low and high thresholds, which then allows to extrapolate the results to very large, extreme thresholds (see Fig. 4).

For uncorrelated data, the return intervals are independent of each other and their probability density function (PDF) is a simple exponential, $P_q(r) = (1/R_q)\exp(-r/R_q)$. In this case, all relevant quantities can be derived from the knowledge of the mean return interval R_q. Since the return intervals are uncorrelated, a sequential ordering cannot occur. There are many cases, however, where some kind of ordering has been observed where the hazardous events cluster, for example in the floods in Central Europe during the middle ages or in the historic water levels of the Nile river which are shown in Fig. 4 for 663y. Even by eye one can realize that the events are not distributed randomly but are arranged in clusters. A similar clustering was observed for extreme floods, winter storms, and avalanches in Central Europe (see, *e.g.*, Figs. 4.4, 4.7, 4.10, and 4.13 in Pfisterer 1998, Fig. 66 in Glaser 2001, and Fig. 2 in Mudelsee *et al.* 2003). The reason for this clustering is the long-term memory.

Figure 5 shows $P_q(r)$ for long-term correlated records with $\alpha = 0.4$ (corresponding to $\gamma = 0.8$), for three values of the mean return interval R_q (which is easily obtained from the threshold q and independent of the correlations). The PDF is plotted in a scaled way, *i.e.*, $R_q P_q(r)$ as a function of r/R_q. The figure shows that all 3 curves collapse. Accordingly, when we know the functional form of the PDF for one value of R_q, we can easily deduce its functional form also for very large R_q values which due to its poor statistics cannot be obtained directly from the data. This scaling is a very important property, since it allows to make predictions also for rare events which otherwise are not accessible with meaningful statistics. When the data are shuffled, the long-term correlations are destroyed and the PDF becomes a simple exponential.

The functional form of the PDF is a quite natural extension of the uncorrelated case. The figure suggests that

$$\ln P_q(r) \sim -(r/R_q)^\gamma, \tag{10}$$

i.e., simple stretched exponential behavior (Bunde *et al.* 2003, 2005). For γ approaching 1, the long-term correlations tend to vanish and we obtain the simple exponential behavior characteristic for uncorrelated processes. For r well below R_q, however, there are deviations from the pure stretched exponential behavior. Closer inspection of the data shows that for $r/R_q \ll 1$ the decay of the PDF is characterized by a power law, with exponent $\gamma - 1$. This overall behavior does not depend crucially on the way the original data are distributed. In the cases shown here, the data had a Gaussian distribution, but similar results have been obtained also for exponential, power-law and log-normal distributions (Eichner *et al.* 2006). Indeed, the characteristic stretched exponential behavior of the PDF can also be seen in long historic and reconstructed records (Bunde *et al.* 2005).

The form of the PDF indicates that return intervals, both well below and well above their average value, are considerably more frequent for long-term
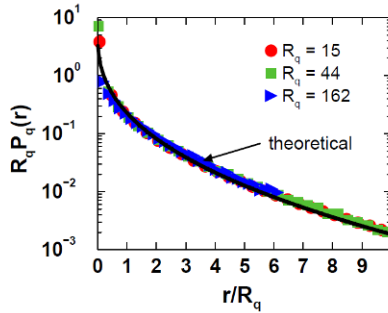
Fig. 5. Probability density function of the return intervals in long-term correlated data, for three different return periods R_q, plotted in a scaled way. The full line is a stretched exponential, with exponent $\gamma = 0.4$ (after Bunde *et al.* 2005). Colour version of this figure is available in electronic edition only.

correlated data than for uncorrelated data. The distribution does not quantify, however, if the return intervals themselves are arranged in a correlated or in an uncorrelated fashion, and if clustering of rare events may be induced by long-term correlations.

To study this question, Bunde *et al.* (2005) and Eichner *et al.* (2006) have evaluated the autocorrelation function of the return intervals in synthetic long-term correlated records. They found that also the return intervals are arranged in a long-term correlated fashion, with the same exponent as the original data. Accordingly, a large return interval is more likely to be followed by a large one than by a short one, and a small return interval is more likely to be followed by a small one than by a large one, and this leads to clustering of events above some threshold q, including extreme events.

As a consequence of the long-term memory, the probability of finding a certain return interval depends on the preceding interval. This effect can be easily seen in synthetic data sets generated numerically, but not so well in climate records where the statistics is comparatively poor. To improve the statistics, we now only distinguish between two kinds of return intervals, "small" ones (below the median) and "large" ones (above the median), and determine the mean R_q^+ and R_q^- of those return intervals following a large $(+)$ or a small $(-)$ return interval. Due to scaling, R_q^+/R_q and R_q^-/R_q are independent of q. Figure 6 shows both quantities (calculated numerically for long-term correlated Gaussian data) as a function of the correlation exponent γ. The lower dashed line is R_q^-/R_q, the upper dashed line is R_q^+/R_q. In the limit of vanishing long-term memory, for $\gamma = 1$, both quantities coincide, as expected. Figure 6 also shows R_q^+/R_q and R_q^-/R_q for 5 climate records with different values of γ. One can see that the data agree very well, within the error bars, with the theoretical curves.
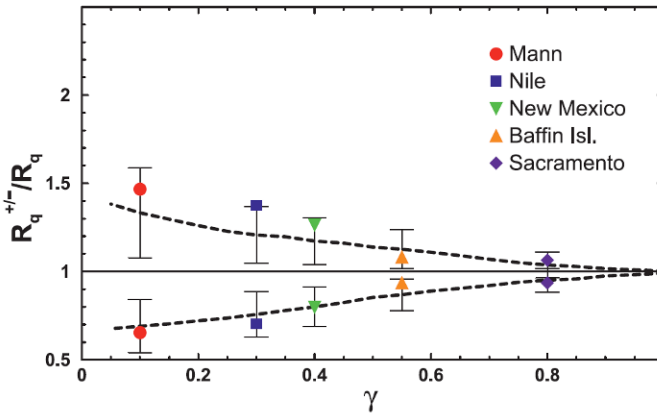
Fig. 6.   Mean of the (conditional) return intervals that either follow a return interval below the median (lower dashed line) or above the median (upper dashed line), as a function of the correlation exponent γ, for 5 long reconstructed and natural climate records. The theoretical curves are compared with the corresponding values of the climate records (from right to left): The reconstructed run-offs of the Sacramento river, the reconstructed temperatures of Baffin Island, the reconstructed precipitation record of New Mexico, the historic water levels of the Nile and one of the reconstructed temperature records of the Northern hemisphere (Mann record) (after Bunde *et al.* 2005). Colour version of this figure is available in electronic edition only.

5.   LONG-TERM CORRELATIONS IN FINANCIAL MARKETS AND SEISMIC ACTIVITY

The characteristic behavior of the return intervals, *i.e.*, long-term correlations and stretched exponential decay, can also be observed in financial markets and seismic activity. It is well known (see, *e.g.*, Liu *et al.* 1997, 1999) that the volatility of stocks and exchange rates is long-term correlated. Figure 7 shows that, as expected from the foregoing, also the return intervals between daily volatilities are long-term correlated, with roughly the same exponent γ as the original data (Yamasaki *et al.* 2005). It has further been shown in Yamasaki *et al.* (2005) that also the PDFs of the return intervals show the characteristic behavior predicted above. We come back to financial data in the next Section.

A further example where long-term correlations seem to play an important role are earthquakes in certain bounded areas (*e.g.*, California) in time regimes where the seismic activity is (quasi) stationary. It has been discovered recently by Lennartz *et al.* (2008) that the magnitudes of earthquakes in Northern and Southern California, from 1995 until 1998, are long-term correlated with an exponent around $\gamma = 0.4$, and that also the return intervals between the earthquakes are long-term correlated with the same exponent. It has been shown
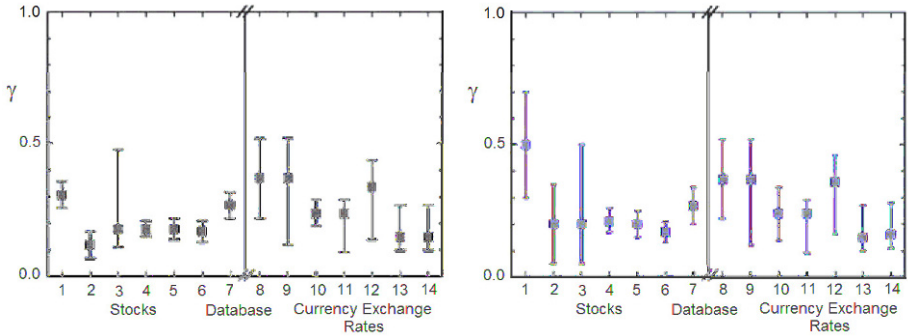
Fig. 7. Long-term correlation exponent γ for the daily volatility (left) and the corresponding return intervals (right). The studied commodities are (from left to right), the S & P 500 index, 6 stocks (IBM, DuPont, AT & T, Kodak, General Electric, Coca-Cola) and 7 currency exchange rates (US $ *versus* Japanese Yen, British Pound *versus* Swiss Franc, US $ *versus* Swedish Krona, Danish Krone *versus* Australian $, Danish Krone *versus* Norwegian Krone, US $ *versus* Canadian $ and US $ *versus* South African $). Courtesy of Lev Muchnik.

that also the PDF of the return intervals can be consistently described by the corresponding distribution of long-term correlated data ($\gamma = 0.4$), without any fit parameter. But other fits by Γ-distributions are also possible (Corral 2004). It has been emphasized by Livina *et al.* (2005) that due to the long-term correlations, large earthquakes may not be random in time but cluster. As a consequence, when the time between the last two earthquakes is well below (above) the average, one can expect the next earthquake to come earlier (later) than the average. For detailed comparison of earthquake data with the branching aftershock cascade (BASS) model, see Lennartz *et al.* (2011).

6. NON-LINEAR LONG-TERM CORRELATIONS AND MULTIFRACTAL SCALING

Many records do not exhibit a simple monofractal scaling behavior, which can be accounted for by a single scaling exponent. In some cases, there exist crossover (time-) scales s_x separating regimes with different scaling exponents, *e.g.*, long-term correlations on small scales below s_x and another type of correlations or uncorrelated behavior on larger scales above s_x. In other cases, the scaling behavior is more complicated, and different scaling exponents are required for different parts of the series. In even more complicated cases, such different scaling behavior can be observed for many interwoven fractal subsets of the time series. In this case a multitude of scaling exponents is required for a full description of the scaling behavior, and a multifractal analysis must be

applied (see, *e.g.*, Ivanov *et al.* 1999, Stanley and Meakin 1988 and literature therein).

To see this, it is meaningful to extend Eqs. (5) and (9) by considering the more general average

$$\langle F^q(s)\rangle = (1/K_s)\sum_{\nu=1}^{K_s}[F_\nu^2(s)]^{q/2} \tag{11}$$

with q between $-\infty$ and $+\infty$. For $q \ll -1$ the small fluctuations will dominate the sum, while for $q \gg 1$ the large fluctuations are dominant. It is reasonable to assume that the q-dependent average scales with s as

$$\langle F^q(s)\rangle \sim s^{q\beta(q)}, \tag{12}$$

with $\beta(2) = \alpha$. Equation (12) generalizes Eq. (6). If $\beta(q)$ is independent of q, we have $\langle F^q(s)\rangle^{1/q} \sim s^\alpha$ independent of q, and both large and small fluctuations scale the same. In this case, a single exponent is sufficient to characterize the record, which then is referred to as ***monofractal***. If $\beta(q)$ is not identical to α, we have a ***multifractal*** (Feder 1988, Mandelbrot 1977, 1982, Peitgen *et al.* 1991). In this case, the dependence of $\beta(q)$ on q characterizes the record. Instead of $\beta(q)$ one considers frequently the spectrum $f(\omega)$ that one obtains by Legendre transform of $q\beta(q)$, $\omega = \mathrm{d}(q\beta(q))/\mathrm{d}q$, $f(\omega) = q\omega - q\beta(q) + 1$. In the monofractal limit we have $f(\omega) = 1$.

For generating multifractal data sets, one considers mostly multiplicative random cascade processes, described, *e.g.*, in Feder (1988) and Peitgen *et al.* (1992). In this process, the data set is obtained in an iterative way, where the length of the record doubles in each iteration. It is possible to generate random cascades with vanishing autocorrelation function $(C(s) = 0$ for $s \geq 1)$ or with algebraically decaying autocorrelation functions $(C(s) \sim s^{-\gamma})$. Here we focus on a multiplicative random cascade with vanishing autocorrelation function, which is particularly interesting since it can be used as a model for the arithmetic returns $d_i = (P_i - P_{i-1})/P_{i-1}$ of daily stock closing prices P_i (see, *e.g.*, Bogachev *et al.* 2007). In the zero-th iteration $n = 0$, the data set, x_i, consists of one value, $x_1^{(n=0)} = 1$. In the n-th iteration, the data $x_i^{(n)}$ consist of 2^n values that are obtained from

$$x_{2l-1}^{(n)} = x_l^{(n-1)}m_{2l-1}^{(n)} \tag{13}$$

and

$$x_{2l}^{(n)} = x_l^{(n-1)}m_{2l}^{(n)}, \tag{14}$$

where the multipliers m are independent and identically distributed (i.i.d.) random numbers with zero mean and unit variance. The resulting PDF is symmetric with log-normal tails, with vanishing correlation function $C(s)$ for $s \geq 1$.

It has been shown that, in this case, the PDF of the return intervals decays by a power-law

$$P_q(r) \sim (r/R_q)^{-\delta(q)}, \tag{15}$$

where the exponent δ depends explicitly on R_q and seems to converge to a limiting curve for large data sets. Despite of the vanishing autocorrelation function of the original record, the autocorrelation function of the return intervals decays by a power law with a threshold-dependent exponent (Bogachev *et al.* 2007). Obviously, these long-term correlations have been induced by the nonlinear correlations in the multifractal data set. Extracting the return interval sequence from a data set is a nonlinear operation, and thus the return intervals are influenced by the nonlinear correlations in the original data set. Accordingly, the return intervals in data sets without linear correlations are most sensitive indicators for nonlinear correlations in the data records. The power-law dependence of $P_q(r)$ can be used for an improved risk estimation. Both power-law dependencies can be observed in financial records of the daily returns and in physiological records (heartbeat intervals) that are known to be multifractal (Bogachev *et al.* 2007, Bogachev *et al.* 2009). In the financial records, one finds a surprising universality: For fixed return periods R_q, the PDFs of the interoccurrence times do not depend on the kind of asset (kind of stocks, indices, *e.g.*, DAX or DOW JONES, commodities or exchanges rates), but only on R_Q (Bogachev and Bunde 2008). The functional form of the PDFs can be expressed analytically by generalized Pareto distributions (q-exponentials); see Ludescher *et al.* 2011.

7. DETECTION OF EXTERNAL TRENDS IN LONG-TERM CORRELATED RECORDS

This section deals with the estimation of the strength of an external trend in long-term correlated data sets. This question is relevant for the estimation of the effect of anthropogenic global warming in climate data that are known to be long-term correlated. Here we follow exclusively Lennartz and Bunde (2011). For a related method see also Lennartz and Bunde (2009a). We start with a description of the quantities of interest.

7.1 Quantities of interest

We are interested in the probability that in a Gaussian distributed record of length N, which is long-term correlated and characterized by a certain fluctuation exponent α, an increase of size Δ occurs. To determine Δ, we use the linear regression method where Δ is obtained as the slope of the regression line times N. From the regression analysis (see Fig. 8), we also obtain
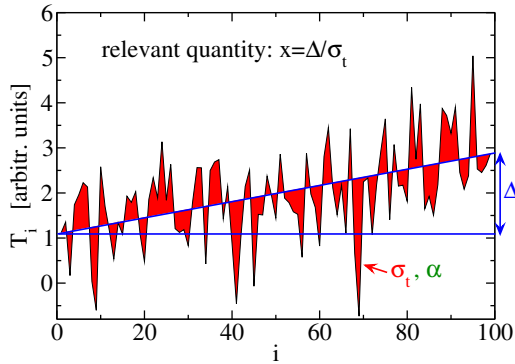
Fig. 8. Visualization of the considered quantities Δ, σ_t, and α for a data set T_i in a window of length 100. Δ is the total increase of the data T_i in the time window and is measured by a linear regression line. σ_t is the standard deviation around this regression line. The fluctuation exponent α characterizes the memory of the data T_i in this time window. The relevant quantity in which we are interested, is the dimensionless fraction Δ/σ_t when a certain value for α is measured. Colour version of this figure is available in electronic edition only.

the standard deviation σ_t around the regression line, which is a measure for the fluctuations in the considered time interval. It is important to note that in contrast to the normal standard deviation σ around the mean value, σ_t is not affected by an external trend and thus represents the natural fluctuations. In the following, we are interested in the dimensionless relative trend $x \equiv \Delta/\sigma_t$.

For determining the fluctuation exponent α in the (sub-) record, we use the DFA2 method which is able to eliminate linear trends in the data (Kantelhardt *et al.* 2001), see Section 2.

Accordingly, a given (sub-) record is characterized: (i) by its length N, (ii) by its relative trend $x = \Delta/\sigma_t$, and (iii) by its fluctuation exponent α obtained by DFA2.

To estimate the contribution of an external linear trend to an observed relative trend, we need to know the probability $P(x, \alpha; N)\mathrm{d}x$ that in a given purely long-term correlated record of length N characterized by α, a relative trend between x and $x + \mathrm{d}x$ occurs. By definition, the probability density function (PDF) $P(x, \alpha; N)$ is symmetric in x, *i.e.*, $P(x, \alpha; N) = P(-x, \alpha; N)$. From $P(x, \alpha; N)$ we then obtain the exceedance probability

$$W(x, \alpha; N) = \int_x^\infty P(x', \alpha; N)\mathrm{d}x' \qquad (16)$$

that an observed relative trend is larger than x.

An important quantity in the further analysis is the confidence interval $[-x_Q, x_Q]$, see Fig. 9. By definition, relative trends within this interval occur
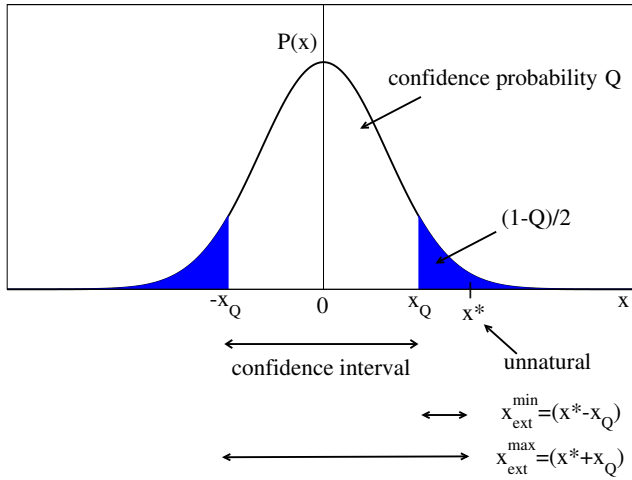
Fig. 9. Sketch of a probability density function $P(x)$. The integral over the white area defines the confidence probability Q. The lower and upper bounds $-x_Q$ and x_Q define the confidence interval $[-x_Q, x_Q]$. If an event x^* is outside this interval, it is considered unnatural. In this case, the minimum external relative trend is $x^* - x_Q$. Colour version of this figure is available in electronic edition only.

with confidence probability Q, that is,

$$Q = \int_{-x_Q}^{x_Q} P(x', \alpha; N) \mathrm{d}x'$$
$$= 1 - 2W(x_Q, \alpha; N). \tag{17}$$

Accordingly, x_Q can be obtained from the inverse function of W, that is,

$$x_Q = W^{-1}[(1 - Q)/2, \alpha; N]. \tag{18}$$

For $Q = 0.95$, for example, $[-x_Q, x_Q]$ defines the 95% confidence interval, which we will use later as a criterion to distinguish between natural and unnatural trends; see Fig. 9. In the presence of an external linear trend, the total trend is the sum of the natural trend and the external trend. If an observed relative trend x is larger than x_Q it is considered unnatural. In this case, the minimum and maximum external trends are given by

$$\Delta_{\text{ext}}^{\min} = \sigma_t(x - x_Q) \tag{19}$$

and

$$\Delta_{\text{ext}}^{\max} = \sigma_t(x + x_Q). \tag{20}$$

By definition, the uncertainty of the external trend (error bar) $(\Delta_{\text{ext}}^{\max} - \Delta_{\text{ext}}^{\min})/2$ is equal to the confidence interval times σ_t and is independent from the observed trend Δ.

7.2 Numerical estimation of the exceedance probability

In the following, we describe the numerical estimation of the exceedance probability. First, for 160 α values ranging from 0.41 to 2.00, 100 synthetic records of length 2^{21} were generated by the Fourier-filtering technique (see Section 2), respectively. With this technique, Gaussian-distributed data are generated. Here we focus on Gaussian-distributed data but would like to note that, in a considerably more elaborate iterative procedure suggested by Schreiber and Schmitz (1996), (monofractal) long-term correlated records with any other distribution can also be generated. Since we are interested in the analysis of trends in smaller records, which typically vary between 500 and 2000 data points, we extracted from the long records for each α value 25 000 subsequences of lengths $N = 500, 750, 1000, 1500$, and 2000. In each sub-record of length N, we determined (i) the local α values by DFA2 as the slope of the logarithmic fluctuation function between $s = 10$ and $s = 100$ and (ii) the relative trends $x = \Delta/\sigma_t$. It is essential to determine α in each sub-record, since the local α values of the sub-records usually differ from the global one (see, *e.g.* Rybski and Bunde 2009).

To estimate $P(x, \alpha; N)$ for fixed N we proceed as described in Fig. 10. We divide the local α values into windows of size 0.02, and focus on the most interesting regime between 0.5 and 1.5. Most natural records, where long-term memory is important, are characterized by α values in this regime. In each α window we determine the histogram $h(x)$, which after normalization yields the desired PDF $P(x, \alpha; N)$.

Figure 11 (a) shows, for $N = 1000$, the resulting $P(x, \alpha; N)$ in a semilogarithmical plot for $\alpha = 0.7 \pm 0.01$ (triangles) and $\alpha = 1.0 \pm 0.01$ (circles). Since $P(x, \alpha; N)$ is symmetric in x, only positive values of x are shown. One can see clearly that there exists a crossover x_c which depends on α (and on N; see below). For small relative trends $x < x_c$, the curves are Gaussian (dashed lines), while for large $x > x_c$, the curves follow a simple exponential (full lines). The figure also shows that the PDFs broaden with increasing fluctuation exponent α, when the mountain-valley structure of the long-term correlated record becomes more pronounced (*i.e.*, large natural trends become more likely with increasing α). From $P(x, \alpha; N)$, we obtain, by direct summation, the desired exceedance probability $W(x, \alpha; N)$; see Eq. (16).

Figure 11 (b)-(d) show $W(x, \alpha; N)$ for $N = 500, 1000$, and 2000. By definition, $W(0, \alpha; N) = 1/2$ (*i.e.*, all curves intersect at $x = 0$). As also seen in the PDF, large relative trends become more likely with an increasing fluctuation exponent α. The figure also shows that the exceedance probability exhibits a remarkable N dependence such that, for fixed α, large relative trends become more likely for small (sub-) records than for large ones. This is also reasonable: Due to the mountain-valley structure of long-term correlated
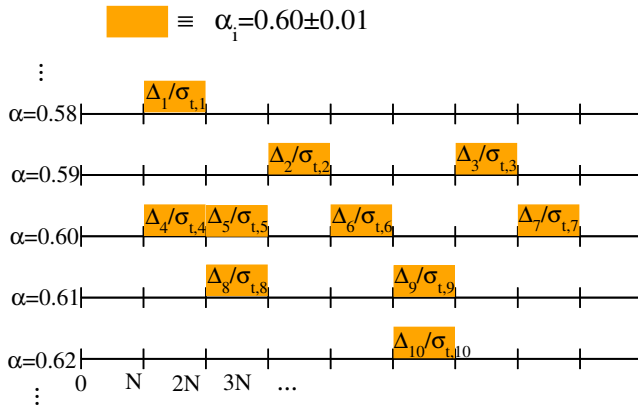
Fig. 10. Visualisation of the data generation procedure. For each global α value, we generated several long data sets (long lines), which we divided into smaller subsequences of size N. In each of these subsequences, we measured the local α value by DFA2. Next we considered only those subsequences, where the measured α value is in a certain range; for example, $\alpha = 0.60 \pm 0.01$ (marked subsequences). In all these sequences we measured the relative trend $x_i = \Delta_i/\sigma_{t,i}$ as described in Fig. 8, to obtain the histogram $h(x)$ which, after normalization, yields the desired PDF $P(x, \alpha; N)$.

data, a large trend can be seen if the sub-record starts in a valley and ends up in a mountain. In a short sub-record, it is very likely that the mountain is just the next one, and the standard deviation around the regression line will be small, resulting in a very large relative trend. Conversely, in a long sub-record, it is very likely that the mountain is not the first one; that is, between the start and the end there are several mountains and valleys in between. Thus, the standard deviation around the regression line will be large. This results in a smaller relative trend in comparison with a short sub-record.

From Fig. 11 (b)-(d), one can obtain graphically the boundary x_Q of the confidence interval. For example, for $Q = 0.99$, x_Q is obtained from the intersection of $W(x, \alpha; N)$ and $(1 - Q)/2$; see Eq. (18). For $N = 2000$ and $\alpha = 1.0$ the intersection is at $x_Q \approx 3.3$.

Using scaling theory, it is possible to derive an analytical expression for $W(x, \alpha; N)$ for $0.5 \leq \alpha \leq 1.2$. From W one can obtain an analytical expression for the bounds $x_Q(\alpha, N)$ of the confidence interval (for details, see Lennartz and Bunde 2011):

$$
x_Q(\alpha, N) = C_N \alpha^{\delta_N} \left\{ \frac{w_N^2}{2} + \ln \left(\frac{2}{1 - Q} \right) \right.
$$
$$
\left. - \ln \left(\mathrm{erf}(w_N/\sqrt{2})(\sqrt{2\pi} w_N) + 2e^{-w_N^2/2} \right) \right\}, \tag{21}
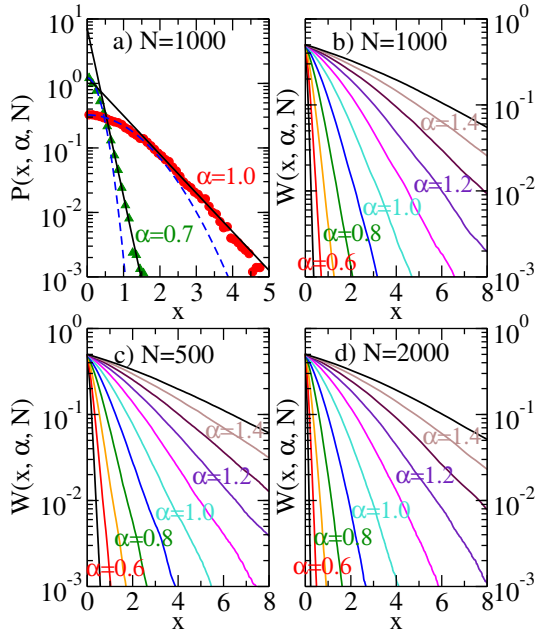$$

Fig. 11: (a) Probability density function $P(x, \alpha; N)$ of the relative temperature increase $x = \Delta/\sigma_t$ of synthetic long-term correlated records in a time window $N = 1000$. The circles represent the probability density function for $\alpha = 1.0$ and the triangles are for $\alpha = 0.7$. The dashed lines are Gaussians, which fit the data best for small arguments, while the straight lines are exponentials, which fit the data best for large arguments. (b)-(d) Cumulative probability $W(x, \alpha; N)$ for $N = 500$, 1000, and 2000 for fluctuation exponents α between 0.5 and 1.5 (from left to right). Colour version of this figure is available in electronic edition only.

where C_N, δ_N, and w_N^2 depend logarithmically on N:

$$C_N \approx C^{(0)} + C^{(1)} \ln(N), \tag{22}$$
$$\delta_N \approx \delta^{(0)} + \delta^{(1)} \ln(N), \tag{23}$$
$$w_N^2 \approx w^{(0)} + w^{(1)} \ln(N), \tag{24}$$

with $C^{(0)} \approx 2.04$, $C^{(1)} \approx -0.20$, $\delta^{(0)} \approx -0.57$, $\delta^{(1)} \approx 0.61$, $w^{(0)} \approx -6.32$, and $w^{(1)} \approx 1.41$.

Figure 12 shows the α and N dependence of the analytical expression (21) (full lines) together with the numerical results (circles) for $Q = 95\%$ (left-hand side) and $Q = 99\%$ (right-hand side). It can be seen that the agreement between the numerical and the analytical results is very good, as long as α is between 0.5 and 1.2.
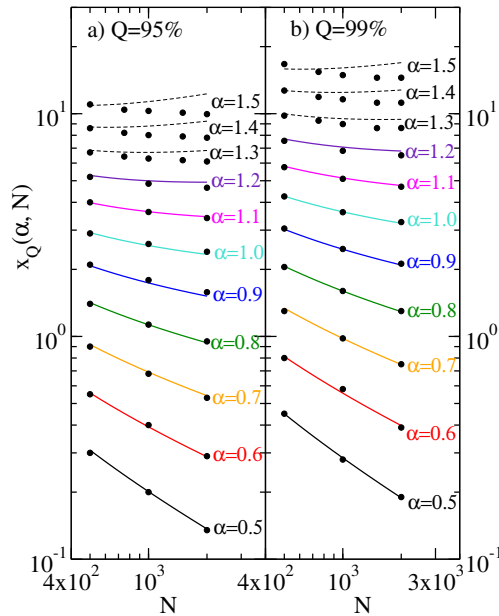
Fig. 12. Boundaries $x_Q(\alpha, N)$ from Eq. (21) of the confidence interval as a function of N for (a) $Q = 95\%$, and (b) $Q = 99\%$ for α between 0.5 and 1.2 (full lines) and between 1.3 and 1.5 (dashed lines) (from bottom to top). For comparison the numerically estimated values for $x_Q(\alpha, N)$ are also shown (full circles). One can clearly see that Eq. (21) is only a very good approximation for $\alpha \leq 1.2$ or $N \approx 500$. For larger α values and $N > 500$ one has to interpolate the numerical values. Colour version of this figure is available in electronic edition only.

7.3 Application to climate data

From Fig. 12 one can immediately obtain, in a data set of length N characterized by the DFA2 fluctuation exponent α, the boundary of the confidence intervals of interest and, by comparing x_Q with a measured relative trend $x = \Delta/\sigma_t$, one can decide if the measured trend is significant or not.

We have applied our analysis (i) to global temperature records provided by the Hadley Centre (http://www.cru.uea.ac.uk/cru/data/temperature/) (Brohan *et al.* 2006) and (ii) to representative local temperature records provided by the Potsdam Institute for Climate Impact Research (PIK). We have also considered (iii) representative precipitation records, also provided by the PIK, and (iv) representative river run-off records provided by the Water Management Authorities of Bavaria and Baden-Württemberg and the Global Runoff Data Centre (GRDC) in Koblenz (Germany). The data are listed in Tables 1 and 2. We used these data in Eichner *et al.* (2003), Kantelhardt *et al.* (2006), Koscielny-Bunde *et al.* (2006), where they are also described.

We would like to note again that, in contrast to the temperature data, precipitation and river flows show (on the time scales considered here) weak multifractal behavior with nonlinear memory (Kantelhardt *et al.* 2006, Koscielny-Bunde *et al.* 2006, Schertzer and Lovejoy 1991, Schertzer *et al.* 1997), and their data distribution differs from Gaussians. Accordingly, our assumption of monofractal behavior with a Gaussian distribution of the data is not *a priori* satisfied. However, we can argue that we can still apply our methodology, to a reasonable approximation, to these data. The reason for this is that the characteristic mountain-valley behavior in long-term correlated records is mainly due to the linear persistence being described by the fluctuation exponent α. The nonlinear correlations solely add some "bursty" behavior to it that does not show up in α but in higher moments of the fluctuation function and does not affect the mountain-valley structure. The same is true for the deviations of the distribution function from a Gaussian, as long as they are not characterized by "fat" tails. This is the case for both precipitation and river run-off data. Indeed, preliminary results of Yuan and Bunde show that Eq. (21) is a very good approximation also for exponentially and power-law distributed data.

For all records we consider only monthly data, where additional short-term dependencies have been averaged out. Other advantages of monthly data are that they are easily available on the Internet and that the seasonal trend can be eliminated in a more effective way than in daily data. In the seasonal detrending procedure, we have followed Koscielny-Bunde *et al.* (2006), Lennartz and Bunde (2009a). We have subtracted the seasonal mean value from the data and divided by the seasonal standard deviation.

Tables 1 and 2 also show, for each data set, the length N of the considered time window (full length and the last 500 months of the record), the fluctuation exponent α, and the relative trend x in this time window. When x, α, and N are known, we can easily read the desired bound of the confidence interval from Fig. 12. In the tables, we show the bounds and mark them by a cross if the observed relative trend is outside this interval and thus significant. In addition to the relative trend x, we also specify the linear trend Δ^{real} obtained by linear regression of the original monthly data set (without seasonal detrending) in the original units; for example, a temperature increase in $^\circ$ C. To obtain the upper and lower bound, $\Delta^{\text{real}}_{\text{min}}$ and $\Delta^{\text{real}}_{\text{max}}$, respectively, of the anthropogenic contribution to the observed trend Δ^{real}, we note that the fraction between the minimal (maximal) trend and the observed trend is (for large $N \gg 12$) approximately independent of the seasonal detrending; that is,

$$\frac{\Delta^{\text{real}}_{\text{min}}}{\Delta^{\text{real}}} = \frac{\Delta^{\text{ext}}_{\text{min}}}{\Delta} = \frac{x - x_Q}{x}, \qquad (25)$$

$$\frac{\Delta^{\text{real}}_{\text{max}}}{\Delta^{\text{real}}} = \frac{\Delta^{\text{ext}}_{\text{max}}}{\Delta} = \frac{x + x_Q}{x}, \qquad (26)$$

Table 1

Long global temperature records and representative local temperature, river runoff, and precipitation records; their length N in units of months, their fluctuation exponent α, the absolute increase Δ^{real} in units of $^\circ$ C for temperatures, m^3/s for river run-offs, and mm for precipitation. The measured relative trend is marked by a cross ($\times$) if the observed relative trend is outside the 95% or 99% confidence interval and is thus significant

Data set	N	α	Δ^{real}	x	x_Q 95%	x_Q 99%
Global temperatures						
Global	1908	1.02	0.69	3.59	2.40 (x)	3.60
Global land air	1908	0.81	0.80	2.49	1.00 (x)	1.30 (x)
Global sea surface	1908	1.21	0.62	3.56	5.00	7.00
Local temperatures						
Arwagh (GB)	1584	0.62	0.28	0.22	0.40	0.52
Brno (CZ)	1296	0.60	0.73	0.45	0.34 (x)	0.50
Charleston (US)	1488	0.61	0.25	0.15	0.35	0.50
Irkutsk (RU)	1416	0.52	2.09	0.85	0.20 (x)	0.28 (x)
Kiev (UA)	1308	0.64	0.74	0.27	0.43	0.61
Melbourne (AU)	1632	0.64	0.40	0.38	0.42	0.60
New York (US)	1392	0.60	2.50	1.41	0.32	0.50
Oxford (GB)	1740	0.64	0.85	0.61	0.41 (x)	0.58 (x)
Plymouth (GB)	1440	0.64	0.24	0.13	0.42	0.60
Potsdam (DE)	1284	0.63	0.83	0.48	0.46 (x)	0.60
Prague (CZ)	2616	0.65	0.35	0.08	0.40	0.53
Sonnblick (AT)	1332	0.52	1.60	0.88	0.20 (x)	0.27 (x)
Swerdlowsk (RU)	1260	0.61	1.68	0.46	0.40 (x)	0.54
Sydney (AU)	1404	0.61	1.21	0.59	0.36 (x)	0.51
Tomsk (RU)	1427	0.57	1.34	0.40	0.27 (x)	0.40 (x)
Vancouver (US)	1116	0.66	-0.70	-0.37	0.52	0.70
Wien Hohewarte (AT)	1500	0.55	1.69	0.96	0.22 (x)	0.30 (x)
River run-offs						
Barron River (Myola, AU)	948	0.96	-2.9	0.18	2.30	3.20
Danube (Orsova, RO)	1812	0.80	-1.5	-0.02	1.00	1.20
Gaula (Haga Bru, NO)	1080	0.66	8.5	0.14	0.55	0.70
Labe (Decin, CZ)	1224	0.81	-2.5	-0.03	1.10	1.50
Maas (Borgharen, NL)	960	0.85	-40	-0.27	1.46	2.00
Niger (Koulikoro, ML)	948	0.87	-198	-0.28	1.60	2.20
Susquehanna (Harrisb., US)	1152	0.63	67	0.12	0.42	0.60
Thames (Kingston, GB)	1356	0.93	14	0.46	1.89	2.70
Weser (Vlotho, DE)	2052	0.81	-37	-0.35	1.00	1.30
Zaire (Kinshasa, CD)	972	1.07	6025	1.21	3.50	4.80
Precipitation						
Albany (US)	1452	0.48	0.06	0.06	0.14	0.18
Charleston (US)	1487	0.53	-0.36	-0.19	0.21	0.28
Hamburg (DE)	1296	0.59	0.20	0.18	0.31	0.42
Irkutsk (RU)	1356	0.52	0.43	0.64	0.20 (x)	0.27 (x)
München (DE)	768	0.69	-0.24	-0.24	0.75	1.01
Norfolks Ils. (AU)	744	0.68	-1.42	-0.61	0.73	1.00
Perm (RU)	1356	0.51	0.23	0.24	0.18 (x)	0.25
Seoul (KR)	1056	0.59	0.63	0.27	0.39	0.52
Sonnblick (AT)	1289	0.61	-0.11	-0.02	0.39	0.55
Spokane (US)	1367	0.51	-0.08	-0.08	0.19	0.28

Table 2

Short global temperature records and representative local temperature, river run-off, and precipitation records; their length N in units of months, their fluctuation exponent α, the absolute increase Δ^{real} in units of $^\circ$C for temperatures, m^3/s for river run-offs, and mm for precipitation. The measured relative trend is marked by a cross $(\times)$ if the observed relative trend is outside the 95% or 99% confidence interval and is thus significant

Data set	N	α	Δ^{real}	x	x_Q 95%	x_Q 99%
Global temperatures						
Global	500	1.24	0.65	5.08	5.90	8.30
Global land air	500	1.04	0.93	4.40	3.00 (x)	4.30 (x)
Global sea surface	500	1.42	0.53	4.87	9.10	13.0
Local temperatures						
Arwagh (GB)	500	0.64	0.13	0.16	0.70	0.99
Brno (CZ)	500	0.67	0.49	0.39	0.80	1.25
Charleston (US)	500	0.63	-0.06	-0.01	0.65	0.92
Irkutsk (RU)	500	0.46	1.65	0.89	0.20 (x)	0.30 (x)
Kiev (UA)	500	0.66	0.00	-0.11	0.75	1.20
Melbourne (AU)	500	0.66	0.15	0.21	0.75	1.20
New York (US)	500	0.57	0.32	0.70	0.46 (x)	0.68 (x)
Oxford (GB)	500	0.66	0.60	0.49	0.75	1.20
Plymouth (GB)	500	0.71	0.44	0.41	0.99	1.50
Potsdam (DE)	500	0.66	0.61	0.37	0.75	1.20
Prague (CZ)	500	0.64	0.95	0.60	0.70	0.99
Sonnblick (AT)	500	0.54	1.02	0.66	0.38 (x)	0.58 (x)
Swerdlowsk (RU)	500	0.66	1.37	0.46	0.75	1.20
Sydney (AU)	500	0.56	0.59	0.61	0.42 (x)	0.62
Tomsk (RU)	500	0.56	1.33	0.53	0.42 (x)	0.62
Vancouver (US)	500	0.64	-0.64	-0.37	0.70	0.99
Wien Hohewarte (AT)	500	0.64	0.91	0.66	0.70	0.99
River run-offs						
Barron River (Myola, AU)	500	0.92	-9.7	-0.32	2.30	3.30
Danube (Orsova, RO)	500	0.83	-196	-0.09	1.60	2.20
Gaula (Haga Bru, NO)	500	0.64	-4.4	-0.18	0.70	0.99
Labe (Decin, CZ)	500	0.79	113	0.66	1.20	1.90
Maas (Borgharen, NL)	500	0.83	19	0.13	1.60	2.20
Niger (Koulikoro, ML)	500	0.87	-565	-1.15	1.50	2.60
Susquehanna (Harrisb., US)	500	0.60	25	0.11	0.55	0.80
Thames (Kingston, GB)	500	0.87	-0.1	-0.06	1.80	2.60
Weser (Vlotho, DE)	500	0.96	4.3	0.09	2.50	3.70
Zaire (Kinshasa, CD)	500	1.06	2986	0.47	3.50	5.00
Precipitation						
Albany (US)	500	0.49	0.41	0.34	0.28 (x)	0.41
Charleston (US)	500	0.51	0.05	0.02	0.31	0.49
Hamburg (DE)	500	0.66	0.22	0.20	0.75	1.20
Irkutsk (RU)	500	0.53	0.18	0.19	0.36	0.53
München (DE)	500	0.69	-0.37	-0.29	0.85	1.30
Norfolks Ils. (AU)	500	0.74	-1.96	-0.83	1.10	1.60
Perm (RU)	500	0.51	0.38	0.39	0.32 (x)	0.50
Seoul (KR)	500	0.58	0.08	0.13	0.49	0.71
Sonnblick (AT)	500	0.53	0.26	0.17	0.36	0.53
Spokane (US)	500	0.54	-0.13	-0.12	0.38	0.58

yielding

$$\Delta_{\min}^{\mathrm{real}} = \Delta^{\mathrm{real}}(1 - x_Q/x), \qquad (27)$$

$$\Delta_{\max}^{\mathrm{real}} = \Delta^{\mathrm{real}}(1 + x_Q/x). \qquad (28)$$

We have used these results to estimate the significance of trends in temperature data, which show more significant upward trends in the longer time periods than in the last 500 months. For river run-off and precipitation data, our results are not exact, but can be used as a first order approximation. For river run-offs, they do not indicate any significant trend, while in the precipitation data only very few significant trends are observed.

Finally, we would like to emphasize that, for estimating the size of a possible external trend, it is not sufficient to look only at the lower bound of the confidence interval, but the upper bound must also be considered. With increasing strength of the correlations (*i.e.*, with increasing fluctuation exponent α), the confidence interval increases and thus so does the uncertainty about the trend.

R e f e r e n c e s

Bogachev, M.I., and A. Bunde (2008), Memory effects in the statistics of interoccurence times between large events in financial markets, *Phys. Rev. E* **78**, 036114, DOI: 10.1103/PhysRevE.78.036114.

Bogachev, M.I., J.F. Eichner, and A. Bunde (2007), The effect of nonlinear correlations on the statistics of return intervals in multifractal data sets, *Phys. Rev. Lett.* **99**, 240601, DOI: 10.1103/PhysRevLett.99.240601.

Bogachev, M.I., I.S. Kireenkov, E.M. Nifontov, and A. Bunde (2009), Statistics of return intervals between large heartbeat intervals and their usability for on-line prediction of disorders, *New J. Phys.* **11**, 063036, DOI: 10.1088/1367-2630/11/6/063036.

Brohan, P., J.J. Kennedy, I. Harris, S.F.B. Tett, and P.D. Jones (2006), Uncertainty estimates in regional and global observed temperature changes: a new dataset from 1850, *J. Geophys. Res.* **111**, D12106, DOI: 10.1029/2005JD006548.

Bunde, A., S. Havlin, J.W. Kantelhardt, T. Penzel, J.-H. Peter, and K. Voigt (2000), Correlated and uncorrelated regions in heart-rate fluctuations during sleep, *Phys. Rev. Lett.* **85**, 3736, DOI: 10.1103/PhysRevLett.85.3736.

Bunde, A., J. Kropp, and H.-J. Schellnhuber (eds.) (2002), *The Science of Disasters—Climate Disruptions, Heart Attacks, and Market Crashes*, Springer, Berlin.

Bunde, A., J. Eichner, S. Havlin, and J.W. Kantelhardt (2003), The effect of long-term correlations on the return periods of rare events, *Physica A* **330**, 1, DOI: 10.1016/j.physa.2003.08.004.

Bunde, A., J. Eichner, S. Havlin, and J.W. Kantelhardt (2005), Long-term memory: A natural mechanism for the clustering of extreme events and anomal residual times in climate records, *Phys. Rev. Lett.* **94**, 048701, DOI: 10.1103/PhysRevLett.94.048701.

Corral, A. (2004), Long-term clustering, scaling, and universality in the temporal occurrence of earthquakes, *Phys. Rev. Lett.* **92**, 108501, DOI: 10.1103/PhysRevLett.92.108501.

Eichner, J.F., E. Koscielny-Bunde, A. Bunde, S. Havlin, and H.-J. Schellnhuber (2003), Power-law persistence and trends in the atmosphere: A detailed study of long temperature records, *Phys. Rev. E* **68**, 046133, DOI: 10.1103/PhysRevE.68.046133.

Eichner, J.F., J. W. Kantelhardt, A. Bunde, and S. Havlin (2006), Extreme value statistics in records with long-term persistence, *Phys. Rev. E* **73**, 016130, DOI: 10.1103/PhysRevE.73.016130.

Feder, J. (1988), *Fractals*, Plenum, New York.

Giese, E., I. Mossig, D. Rybski, and A. Bunde (2007), Long-term analysis of air temperature trends in Central Asia, *Erdkunde* **61**, 186-202.

Glaser, R. (2001), *Klimageschichte Mitteleuropas*, Wissenschaftliche Buchgesellschaft, Darmstadt.

Govindan, R.B., D. Vjushin, S. Brenner, A. Bunde, S. Havlin, and H.-J. Schellnhuber (2002), Global climate models violate scaling of the observed atmospheric variability, *Phys. Rev. Lett.* **89**, 028501, DOI: 10.1103/PhysRevLett.89.028501.

Hurst, H.E., R.P. Black, and Y.M. Simaika (1965), *Long-term Storage: An Experimental study*, Constable & Co. Ltd., London.

Ivanov, P.Ch., A.L. Goldberger, S. Havlin, M.G. Rosenblum, Z. Struzik, and H.E. Stanley (1999), Multifractality in human heartbeat dynamics, *Nature* **399**, 461-465, DOI: 10.1038/20924.

Kantelhardt, J.W., E. Koscielny-Bunde, H.H.A. Rego, A. Bunde, and S. Havlin (2001), Detecting long-range correlations with detrended fluctuation analysis, *Physica A* **295**, 441-454, DOI: 10.1016/S0378-4371(01)00144-3.

Kantelhardt, J.W., E. Koscielny-Bunde, D. Rybski, P. Braun, A. Bunde, and S. Havlin (2006), Long-term persistence and multifractality of precipitation and river runoff records, *J. Geophys. Res.* **111**, D01106, DOI: 10.1029/2005JD005881.

Király, A., I. Bartos, and I.M. Jánosi (2006), Correlation properties of daily temperature anomalies over land, *Tellus*, **58A**, 5, 593-600, DOI: 10.1111/j.1600-0870.2006.00195.x.

Koscielny-Bunde, E., A. Bunde, S. Havlin, H.E. Roman, Y. Goldreich, and H.-J. Schellnhuber (1998), Indication of a universal persistence law governing atmospheric variability, *Phys. Rev. Lett.* **81**, 3, 729-732, DOI: 10.1103/PhysRevLett.81.729.

Koscielny-Bunde, E., J.W. Kantelhardt, P. Braun, A. Bunde, and S. Havlin (2006), Long-term persistence and multifractality of river runoff records: Detrended fluctuation studies, *J. Hydrol.* **322**, 120-137, DOI: 10.1016/j.jhydrol.2005.03.004.

Leland, W.E., M.S. Taqqu, W. Willinger, and D.V. Wilson (1994), On the self-similar nature of ethernet traffic (extended version), *IEEE ACM Trans. Network.* **2**, 1-15, DOI: 10.1109/90.282603.

Lennartz, S., and A. Bunde (2009a), Trend evaluation in records with long-term memory; Application to global warming, *Geophys. Res. Lett.* **36**, L16706, DOI: 10.1029/2009GL039516.

Lennartz, S., and A. Bunde (2009b), Eliminating finite-size effects and detecting the amount of white noise in short records with long-term memory, *Phys. Rev. E* **79**, 066101, DOI: 10.1103/PhysRevE.79.066101.

Lennartz, S., and A. Bunde (2011), Distribution of natural trends in long-term correlated records: A scaling approach, *Phys. Rev. E* **84**, 021129, DOI: 10.1103/PhysRevE.84.021129.

Lennartz, S., V.N. Livina, A. Bunde, and S. Havlin (2008), Long-term memory in earthquakes and the distribution of interoccurrence times, *Europhys. Lett.* **81**, 69001, DOI: 10.1209/0295-5075/81/69001.

Lennartz, S., A. Bunde, and D.L. Turcotte (2011), Modelling seismic catalogues by cascade models: Do we need long-term magnitude correlations?, *Geophys. J. Int.* **184**, 1214-1222, DOI: 10.1111/j.1365-246X.2010.04902.x.

Liu, Y.H., P. Cizeau, M. Meyer, C.-K. Peng, and H.E. Stanley (1997), Correlations in economic time series, *Physica A* **245**, 437-440, DOI: 10.1016/S0378-4371(97)00368-3;

Liu, Y.H., P. Gopikrishnan, P. Cizeau, M. Meyer, C.-K. Peng, and H.E. Stanley (1999), Statistical properties of the volatility of price fluctuations, *Phys. Rev. E* **60**, 1390-1400, DOI: 10.1103/PhysRevE.60.1390.

Livina, V.N., Y. Ashkenazy, P. Braun, A. Monetti, A. Bunde, S. Havlin (2003), Non-linear volatility of river flux fluctuations, *Phys. Rev. E* **67**, 042101, DOI: 10.1103/PhysRevE.67.042101.

Livina, V.N., S. Havlin, and A. Bunde (2005), Memory in the occurence of earthquakes, *Phys. Rev. Lett.* **95**, 208501, DOI: 10.1103/PhysRevLett.95.208501.

Ludescher, J., C. Tsallis, and A. Bunde (2011), Universal behaviour of interoccurrence times between losses in financial markets: An analytical description, *Europhys. Lett.* **95**, 68002, DOI: 10.1209/0295-5075/95/68002.

Malamud, B.D., and D.L. Turcotte (1999), Self-affine time series: I. Generation and Analyses, *Adv. Geophys.* **40**, 1-90.

Mandelbrot, B.B. (1977), *Fractals: Form, Chance and Dimension*, Freeman, San Francisco.

Mandelbrot, B.B. (1982), *The Fractal Geometry of Nature*, Freeman, San Francisco.

Mandelbrot, B.B., and J. van Ness (1968), Fractional Brownian motions, fractional noises and applications, *SIAM Review* **10**, 422-437.

Mandelbrot, B.B., and J.R. Wallis (1969), Some long-run properties of geophysical records, *Water. Resour. Res.* **5**, 321-340, DOI: 10.1029/WR005i002p00321.

Monetti, A., S. Havlin, and A. Bunde (2003), Long-term persistence in the sea surface temperature fluctuations, *Physica A* **320**, 581-589, DOI: 10.1016/S0378-4371(02)01662-X.

Mudelsee, M. (2007), Long memory of rivers from spatial aggregation, *Water. Resour. Res.* **43**, W01202, DOI: 10.1029/2006WR005721.

Mudelsee, M., M. Börngen, G. Tetzlaff, and U. Grünwald (2003), No upward trends in the occurrence of extreme floods in central Europe, *Nature*, **425**, 166-169, DOI: 10.1038/nature01928.

Peitgen, H.-O., H. Jürgens, and D. Saupe (1991), *Chaos and Fractals*, Springer Verlag, Heidelberg.

Peitgen, H.-O., H. Jürgens, and D. Saupe (1992), *Chaos and Fractals*, Springer Verlag, New York.

Pelletier, J.D., and D.L. Turcotte (1999), Self-affine time series: II. Applications and models, *Adv. Geophys.* **40**, 91, DOI: 10.1016/S0065-2687(08)60294-0.

Peng, C.-K., J. Mietus, J.M. Hausdorff, S. Havlin, H.E. Stanley, and A.L. Goldberger (1993), Long-range anticorrelations and non-Gaussian behavior of the heartbeat, *Phys. Rev. Lett.* **70**, 1343-1346, DOI: 10.1103/PhysRevLett.70.1343.

Pfisterer, C. (1998), *Wetternachhersage. 500 Jahre Klimavariationen und Naturkatastrophen 1496-1995*, Verlag Paul Haupt, Bern.

Rybski, D., and A. Bunde (2009), On the detection of trends in long-term correlated records, *Physica A* **388**, 1687-1695, DOI: 10.1016/j.physa.2008.12.026.

Rybski, D., A. Bunde, S. Havlin, and H. von Storch (2006), Long-term persistence in climate and the detection problem, *Geophys. Res. Lett.* **33**, 6, L06718, DOI: 10.1029/2005GL025591.

Santhanam, M.S., and H. Kantz (2005), Long-range correlations and rare events in boundary layer wind fields, *Physica A* **345**, 713-721, DOI: 10.1016/j.physa.2004.07.012.

Schertzer, D., and S. Lovejoy (1991), *Nonlinear Variability in Geophysics: Scaling and Fractals*, Springer, New York.

Schertzer, D., S. Lovejoy, F. Schmitt, Y. Chigirinskaya, and D. Marsan (1997), Multi-fractal cascade dynamics and turbulent intermittency, *Fractals* **5**, 3, 427-471, DOI: 10.1142/S0218348X97000371.

Schreiber, T., and A. Schmitz (1996), Improved Surrogate Data for Nonlinearity Tests, *Phys. Rev. Lett.* **77**, 635-638, DOI: 10.1103/PhysRevLett.77.635.

Stanley, H.E., and P. Meakin (1988), Multifractal Phenomena in Physics and Chemistry, *Nature* **355**, 405-409, DOI: 10.1038/335405a0.

Talkner, P., and R.O. Weber (2000), Power spectrum and detrended fluctuation analysis: application to daily temperatures, *Phys. Rev. E* **62**, 150-160, DOI: 10.1103/PhysRevE.62.150.

Turcotte, D.L. (1997), *Fractals and Chaos in Geology and Geophysics*, 2nd edn., Cambridge Univ. Press, Cambridge.

Vjushin, D., I. Zhidkov, S. Brenner, S. Havlin, and A. Bunde (2004), Volcanic forcing improves atmosphere-ocean coupled general circulation model scaling performance, *Geophys. Res. Lett.* **31**, L10206, DOI: 10.1029/2004GL019499.

Yamasaki, K., L. Muchnik, S. Havlin, A. Bunde, and H.E. Stanley (2005), Scaling and memory in volatility return intervals in financial markets, *PNAS* **102**, 26, 9424-9428, DOI: 10.1073/pnas.0502613102.

Visibility Graph Analysis of Geophysical Time Series: Potentials and Possible Pitfalls

Reik V. DONNER[1] and Jonathan F. DONGES[1,2]

[1]Research Domain IV – Transdisciplinary Concepts & Methods,
Potsdam Institute for Climate Impact Research, Potsdam, Germany
e-mail: reik.donner@pik-potsdam.de (corresponding author)

[2]Department of Physics, Humboldt University of Berlin, Berlin, Germany
e-mail: donges@pik-potsdam.de

A b s t r a c t

Recently, complex network approaches to time series analysis have been developed and successfully applied to geophysical records. In this paper, the visibility graph approach is re-considered, which has been found useful as an alternative tool for describing the fractal properties of a time series. The interpretation of various graph-theoretical measures in the context of visibility graphs, their mutual interdependence, and their sensitivity in the presence of missing values and uncertainties (posing typical challenges in geophysical time series analysis) are thoroughly discussed. The obtained results are illustrated for some exemplary records from different fields of geosciences.

Key words: Geophysical time series, complex networks, fractals, uncertainty.

1. INTRODUCTION

Based on earlier foundations of graph theory, the investigation of the structure and dynamics of complex networks has emerged as an alternative approach to describing a variety of complex systems from a statistical mechanics perspective (Albert and Barabasi 2002). Examples include many geophysical phenomena, such as climate dynamics (*e.g.*, Tsonis and Roebber

2004, Donges *et al.* 2009), earthquake processes (*e.g.*, Abe and Suzuki 2004, Baiesi and Paczuski 2004, Davidsen *et al.* 2008, Jimenez *et al.* 2009), river morphology (Zaliapin *et al.* 2010), or soil porous architecture (Santiago *et al.* 2008), to mention only a few. In the last years, a variety of different methods has been proposed for studying time series of dynamical systems from a complex network perspective (Donner *et al.* 2010, 2011). First applications to problems from different disciplines of Earth sciences have been published (Elsner *et al.* 2009, Tang *et al.* 2010, Donner *et al.* 2011, Donges *et al.* 2011a, b), highlighting the great potential of the corresponding conceptual ideas for studying geophysical problems. Among other approaches, the so-called ***visibility graph*** (VG) has attracted considerable interest. Originally, this concept has been introduced for the analysis of mutual visibility relationships between points and obstacles in two-dimensional landscapes in the framework of computational geometry, with applications ranging from robot motion planning to architectural design and topographic descriptions of geographical space (Lozano-Perez and Wesley 1979, Nagy 1994, de Floriani *et al.* 1994, Turner *et al.* 2001).

Lacasa *et al.* (2008) adopted the VG approach to the analysis of structures in scalar, univariate time series (for a recent review, see Núñez *et al.* 2012). It has been shown that certain statistical features of the resulting complex networks are closely related with fractal and multifractal properties of the underlying time series (Lacasa *et al.* 2009, Ni *et al.* 2009). Besides the introduction of a simplifying methodological variant called horizontal visibility graphs (HVGs, see Luque *et al.* (2009), Lacasa and Toral (2010), Xie and Zhou (2011), and Gutin *et al.* (2011)), the approach has been applied so far for studying energy dissipation rates in fully developed turbulence (Liu *et al.* 2010), financial data (Ni *et al.* 2009, Yang *et al.* 2009, Qian *et al.* 2010), and different physiological time series (Lacasa *et al.* 2009, Shao 2010, Dong and Li 2010, Ahmadlou *et al.* 2010). In the geoscientific context, Elsner *et al.* (2009) studied the time series of annual US landfalling hurricane counts. Subsequently, Tang *et al.* (2010) presented a study on daily streamflow series from the US and China. Telesca and Lovallo (2012) used VGs for studying seismic activity in Italy. However, convincing results on linking the complete variety of different network properties describing the structure of VGs with specific structural features of the system under study (as it has been done for the recurrence network approach, *cf.* Donner *et al.* 2010, 2011) or, specifically, geophysical processes in some more detail are still missing.

This paper presents an attempt to a more holistic consideration of information contained in a visibility graph. For this purpose, in Section 2 the interpretation of some of the most studied properties of complex network theory is discussed for this specific type of graph. Subsequently, in Section 3 some practical issues are discussed which pose considerable challenges

to VG analysis of geophysical data, such as missing data, homo- and heteroscedastic uncertainty of observations, and time-scale uncertainty. The corresponding theoretical considerations are illustrated for some exemplary geoscientific time series in Section 4. Finally, the main findings of this work are summarized and put into context in Section 5.

2. THE VISIBILITY GRAPH APPROACH

2.1 Basic construction principle

For constructing the VG associated with a univariate time series recording values of a scalar observable x, this series is considered as a two-dimensional set of points (t_i, x_i) with $x_i = x(t_i)$. Two of such points are regarded as being mutually connected vertices of the VG if the convexity condition

$$\frac{x_i - x_k}{t_k - t_i} > \frac{x_i - x_j}{t_j - t_i}$$

(1)

is fulfilled for all time points t_k with $t_i < t_k < t_j$ (Lacasa *et al.* 2008). A schematic illustration of the corresponding construction principle of a VG is given in Fig. 1. As a special case deserving further discussions, subsequent observations that are not separated by another observation (*i.e.*, where there is no such t_k) are considered as being connected by default. Hence, VGs are always completely connected and do not decompose into disjoint subgraphs.

In contrast to other complex network approaches to time series analysis (such as recurrence networks, *cf.* Donner *et al.* 2010, 2011), the vertices i of the VG are directly related to specific points t_i in time rather than distinct locations in some (abstract) phase space of the system under study. Mathematically, the binary adjacency matrix A_{ij} of the VG is defined as $A_{ij} = 1$ (*i.e.*, the two vertices i and j are connected) if Eq. (1) holds, and $A_{ij} = 0$ otherwise. Note that A_{ij} completely describes the connectivity structure of the associated simple (*i.e.*, undirected and unweighted) graph, so that all information contained in a VG can be inferred from its adjacency matrix. The latter is invariant under certain transformations, particularly with respect to rescaling and translation of both t and x as well as the superposition of linear trends (Lacasa *et al.* 2008).

As a variant of the basic VG approach, HVGs are alternatively defined by the mutual horizontal visibility of two observations x_i and x_j made at times t_i and t_j, respectively, *i.e.*, $A_{ij} = 1$ if for all t_k with $t_i < t_k < t_j$, $x_k < \min(x_i, x_j)$, and $A_{ij} = 0$ otherwise (Luque *et al.* 2009). It should be emphasized that although their construction principles are rather different, VG and HVG capture similar kinds of properties of a time series, particularly, such associated with fractality and hierarchical organization. HVGs conserve the invariance properties of VGs with the exception of the superposition of
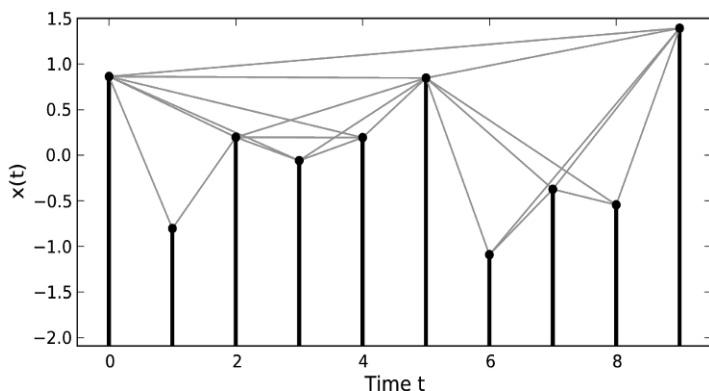
Fig. 1. Schematic illustration of the construction principle of a VG.

trends. Hence, unlike those of VGs, the properties of HVGs are potentially sensitive with respect to the presence of trends in the data under consideration. It should be noted that the construction algorithm of the HVG poses stronger constraints than that of the VG, *i.e.*, the HVG can be regarded as a subgraph of the associated VG with a lower number of edges (Luque *et al.* 2009). The advantage of the HVG is that many of the resulting network properties can be calculated analytically (Luque *et al.* 2009), such as the distributions of vertex degrees and local clustering coefficients, $p(k)$ and $p(C)$ (see below) as well as their mutual relationship, but also the probability that two observations t_i and t_j separated by $t_j - t_i = n\Delta t$ are connected and the dependence of the average path length L on the network size N. Particularly, the degree distribution $p(k)$ shows a generic behavior with one parameter allowing discrimination between uncorrelated and correlated stochastic as well as deterministic series (Lacasa and Toral 2010). Recently, the HVG algorithm has been found to be useful for periodicity detection in time series (Núñez *et al.* 2011) and describing bifurcation scenarios in terms of so-called Feigenbaum diagrams (Luque *et al.* 2011), which represent first steps towards a VG approach to deterministic dynamical systems. However, in the following, the focus of this work will be exclusively on the use of the standard VG algorithm with a particular emphasis on geophysical applications.

2.2 Interpretation of vertex characteristics

In complex networks, the relevance of individual vertices for structural as well as dynamic characteristics of the underlying system can be quantified by a variety of different measures. Most of these network-theoretical measures describe a certain notion of centrality of vertices with respect to

the entire network. Specifically, one distinguishes (among others) the following centrality measures (Albert and Barabasi 2002, Newman 2003, Boccaletti *et al.* 2006, Costa *et al.* 2007):

❑ *Degree centrality k_i* measures the number of direct connections vertex *i* has with the rest of the network:

$$k_i = \sum_j A_{ij} \,. \tag{2}$$

❑ *Closeness centrality c_i* measures the inverse mean value of the geodesic distances l_{ij} between *i* and all other vertices *j*:

$$c_i = \left(\frac{1}{N-1} \sum_{j \neq i} l_{ij} \right)^{-1} \,. \tag{3}$$

❑ *Betweenness centrality b_i* measures the average fraction of shortest paths between all other pairs *(j,k)* of vertices that contain *i*,

$$b_i = \sum_{j,k \neq i} \frac{\sigma_{jk}(i)}{\sigma_{jk}} \,. \tag{4}$$

Here, $\sigma_{jk}(i)$ is the number of shortest paths between vertices *j* and *k* that include *i*, and σ_{jk} is the total number of shortest paths between *j* and *k*.

There are further concepts of centrality, such as eigenvector centrality or local efficiency, which shall not be further discussed here.

In addition to these classical centrality measures, one is often interested in the structural organization of a network under study. Specifically, relevant information can be obtained from studying the connectivity properties in the direct neighborhood of a particular vertex. For this purpose, one commonly used measure is the *local clustering coefficient C_i*, which characterizes the fraction of neighbors of a vertex *i* that are mutually connected themselves, *i.e.*,

$$C_i = \frac{\sum_{j,k} A_{ij} A_{ik} A_{jk}}{k_i (k_i - 1)} \,. \tag{5}$$

Since the local clustering coefficient is based on three-point relationships, it characterizes a local convexity property of higher order (*i.e.*, a large value of C_i indicates a dominating convexity of the underlying time series over a given range of time). We will give some more specific comments on this point (and its implications for the relationship between local clustering coefficient and degree centrality) below.

Recent work on VGs has mainly highlighted the properties of the degree distribution $p(k)$ of networks resulting from different kind of processes

(Lacasa *et al.* 2008). Specifically, VGs obtained from periodic signals appear as a concatenation of a finite number of network motifs (given that the basic period is an integer multiple of the sampling rate), *i.e.*, have a regular structure with only a few distinct values of the vertex degree. The opposite extreme case, white noise, yields VGs appearing as exponential random graphs, *i.e.*, random networks characterized by an exponential degree distribution. In contrast, for fractal processes, $p(k)$ is generically scale-free, *i.e.*, $p(k) \sim k^{-\gamma}$ with the exponent γ being related with the Hurst exponent H of the underlying time series as $\gamma = 3 - 2H$ for fractional Brownian motion and f^β-noise, and $\gamma = 5 - 2H$ for fractional Gaussian noise (Lacasa *et al.* 2009, Ni *et al.* 2009).

Whereas closeness and betweenness have not yet been investigated for VGs, the local clustering coefficient C_i and its relationship with the degree k_i have been studied recently (Shao 2010). Particularly, it has been observed that $C(k) \sim k^{-\delta}$, pointing to a hierarchical organization of the network (Ravasz and Barabasi 2003), since vertices i with high C_i and low k_i (which are most abundant) form densely connected subgraphs, indicating a strong modular structure of the VG reflecting the temporal order of observations.

In order to understand the scale-free property of the degree distributions for VGs from fractal records, one has to note that, typically, maxima of the time series have visibility contact with more vertices than other points, *i.e.*, hubs of the network often form at maximum values of the recorded observable. To put it differently, the degree of a vertex in the VG characterizes the maximality property of the corresponding observation in comparison with its neighborhood in the time series. However, this finding is not completely general, since there can be specific conditions (*e.g.*, a concave behavior over a certain period of time) which can lead to highly connected vertices that do not coincide with local maxima, for example, in case of a Conway series (Lacasa *et al.* 2008).

For betweenness, it can be argued in a similar way that high values occur at local maxima of the underlying time series, since the associated vertices separate different parts of the series without mutual visibility contact and, thus, act as bottlenecks in the network structure, bundling a large number of shortest paths between vertices at $t < t_i$ and $t > t_i$, respectively. However, in contrast to the degree, betweenness is additionally affected by the vertex' position in the underlying time series due to a simple combinatorial effect: Considering that the majority of shortest paths that cross a vertex i connect observations before and after i with each other, there are more possible combinations of such points for i being close to the middle of the time series than for vertices close to the edges of the record. In this respect, in a VG betweenness centrality of a vertex mixes information on the local

maximality of the corresponding observation and its position within the time series.

Beyond the previous considerations for betweenness, in the case of closeness centrality the position of a vertex in the time series is even more important in comparison with the value of the underlying observable. Specifically, this measure is strongly determined by the number of vertices to its left and right, respectively. In this spirit, it can be argued that in the middle of the time series, high closeness values are more likely than at its ends. As argued above, a similar (but weaker) effect contributes to betweenness and – close to the edges of the record – also to the degree (consequently, the highest degree and betweenness values can be taken by other vertices than that corresponding to the global maximum). In contrast, the local clustering coefficient is almost unaffected except for vertices very close to the beginning and end of the time series, since direct connectivity is mainly established between vertices that correspond to observations that are not very distant in time.

The theoretical considerations made above concerning possible boundary effects are supported by the numerical results for simple Gaussian white noise shown in Fig. 2. It can be seen that for short time series (here, $N = 100$), the expected degree, closeness, and betweenness are strongly reduced towards the ends of the time series, with the most pronounced effect for the closeness. In turn, the local clustering coefficient is almost unaffected. The described impact of boundaries on the estimated vertex properties is particularly strong for short records, which are typical in geophysical applications. Specifically, degree and other centrality properties of observations close to both ends of a time series are systematically underestimated, which may artificially alter the interpretation of the corresponding results in their geophysical context. Hence, a careful treatment and interpretation of the results of VG analysis is necessary in such cases. A detailed discussion of a corresponding methodological framework is beyond the scope of this manuscript and will be addressed in a separate publication.

Taking a more detailed look at Fig. 2, some more interesting features are revealed. In particular, there are many vertices with minimum degree ($k_i = 2$), most of which correspond to local minima of the time series. (Moreover, note that not all local minima need to have $k_i = 2$.) Associated to this, many vertices have a maximum local clustering coefficient of $C_i = 1$. Specifically, this holds for most vertices with $k_i = 2$, since the two next neighbors of a local minimum *must* be mutually visible. In a similar way, local minima have zero betweenness, since all shortest paths on the VG would eventually traverse their neighbors, but *not* these specific vertices themselves. Since there are many local minima in a typical time series, one finds many vertices with minimum degree, maximum local clustering coefficient, and zero betweenness, which results in strong mutual interdependences
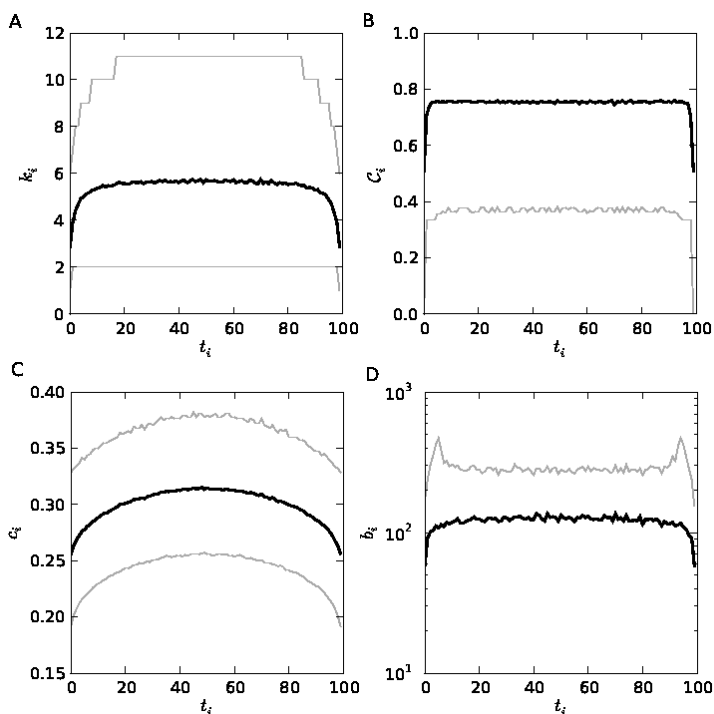
Fig. 2. Effect of the time series boundaries on vertex properties (A: degree, B: local clustering coefficient, C: closeness, D: betweenness) of VGs obtained from $N = 100$ data points of Gaussian white noise. Results have been obtained as ensemble averages over $M = 10\,000$ independent realizations (black lines). Gray lines indicate the corresponding 10% and 90% quantiles of the estimated distributions of all measures. Note that for the clustering coefficient, the 90% quantile is 1.0, whereas for degree and betweenness, the 10% quantiles are 2.0 and 0.0, respectively.

between the different vertex properties. This generic behavior is confirmed by recent numerical results on the power-law dependence of $C(k)$ for certain types of time series (Ravasz and Barabasi 2003). In a similar way, it can be argued that the mean shortest-path distance of vertices to other parts of a VG is lower for hubs (high k_i) than for low-degree vertices, which implies a systematic positive correlation between degree and closeness as well. Indeed, for the previously considered example of Gaussian white noise, we find that the mutual correlations between all four vertex characteristics are significant on by far more than 99% confidence level (Table 1). Note, however, that the different measures do not show a 1:1 correspondence, since they still quantify different aspects of connectivity. The obtained results discussed above are generic and, thus, can be expected to persist when considering other types of data such as correlated or fractal stochastic as well as deterministic series.

Rank-order correlation coefficients (Spearman's Rho) between the individual vertex characteristics obtained from VGs for Gaussian white noise ($N = 100$). The given values and their confidence intervals correspond to mean values and standard deviations obtained from $M = 10000$ independent realizations of the same process

	Degree	Clustering	Closeness	Betweenness
Degree		−0.72 +/− 0.05	0.74 +/− 0.06	0.89 +/− 0.03
Clustering	−0.72 +/− 0.05		−0.55 +/− 0.07	−0.78 +/− 0.04
Closeness	0.74 +/− 0.06	−0.55 +/− 0.07		0.70 +/− 0.06
Betweenness	0.89 +/− 0.03	−0.78 +/− 0.04	0.70 +/− 0.06	
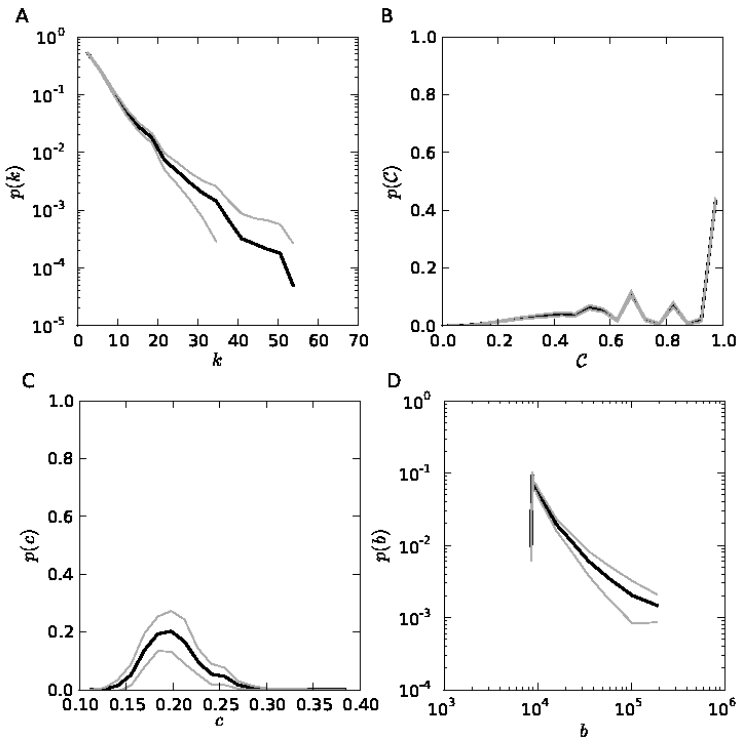
Fig. 3. Distributions of (A) degree, (B) local clustering coefficient, (C) closeness, and (D) betweenness for VGs obtained from Gaussian white noise series with $N = 1000$ data points. Black and gray lines correspond to the mean values and +/−1 standard deviation confidence levels obtained from $M = 100$ independent realizations of the process. All distributions have been estimated by grouping the obtained data into 20 bins (betweenness: equal bin size on logarithmic scale, all other quantities: equal bin size on linear scale).

With respect to the strong interdependences between different vertex measures, it is interesting to compare the general appearance of the associated distributions. For the case of Gaussian white noise, the corresponding results are shown in Fig. 3. It can be seen that the degree distribution $p(k)$ displays the expected exponential tail (Lacasa *et al.* 2008), whereas the betweenness distribution $p(b)$ has a heavy tail, which is a typical feature of many complex networks (Goh *et al.* 2001, Barthelemy 2004, Kitsak *et al.* 2007). For the clustering coefficient, a pronounced maximum close to 1 is observed, whereas closeness centrality shows a continuous unimodal distribution, the shape of which probably reflects the boundary effects discussed above.

2.3 Global network characteristics

In contrast to the previously discussed vertex properties, global network characteristics describe certain topological features of the graph as a whole. Among others, the following measures have been used recently for studying VGs as well as other types of time series networks:

❑   The *edge density* ρ measures the relative fraction of possible edges that are actually realized in the graph, *i.e.*,

$$\rho = \frac{1}{N(N-1)} \sum_{i,j} A_{ij} \, . \tag{6}$$

In contrast to other approaches to complex network based time series analysis, in a VG the edge density is a true network characteristic rather than a parameter of the method (*cf.* Donner *et al.* (2010, 2011) for the corresponding meaning for recurrence networks). Specifically, a maximum edge density of 1 would be present if the underlying time series is globally convex (*e.g.*, of regular parabolic shape), whereas low values indicate a strong fragmentation of the VG and, hence, irregularity of fluctuations of the underlying observable. It is left to the interested reader to decide (probably depending on the specific problem under study) whether the fact that very high edge densities are possible makes VG a more robust approach than others, or just a more strongly constrained one.

❑   The *global (Watts–Strogatz) clustering coefficient C* is defined as the arithmetic mean of the local clustering coefficients of all vertices in the network (Watts and Strogatz 1998), *i.e.*,

$$C = \frac{1}{N} \sum_{i,j,k} \frac{A_{ij} A_{ik} A_{jk}}{k_i (k_i - 1)} = \frac{1}{N} \sum_i C_i \, . \tag{7}$$

❑   The *transitivity T* measures the fraction of possible triangles that is actually realized in a graph, *i.e.*,

$$T = \frac{\sum_{i,j,k} A_{ij} A_{ik} A_{jk}}{\sum_{i,j,k} A_{ij} A_{ik}} . \tag{8}$$

Obviously, global clustering coefficient and transitivity characterize closely related properties of a graph; however, they can differ significantly from each other (Newman 2003, Boccaletti *et al.* 2006). Specifically, C gives equal weight to all vertices of a network, whereas T gives equal weight to all triangles. Both measures are sometimes confused in the literature, since T is sometimes alternatively referred to as the ***Barrat–Weigt clustering coefficient*** (Barrat and Weigt 2000). In the spirit of the heuristic interpretation of the local clustering coefficient (measuring the fraction of possible triangular connectivity structures centered at a given vertex), both global clustering coefficient and transitivity characterize the typical convexity properties on some intermediate time-scale, which relate to the question of how fast fluctuations in the underlying record occur.

  ❑ The ***average path length L*** gives the mean geodesic distance between all pairs of vertices in the graph, *i.e.*,

$$L = \frac{1}{N(N-1)} \sum_{i,j} l_{ij} . \tag{9}$$

It can be expected that the value of L is large when there are only few edges in the VG (low edge density) and low for a high edge density. In this spirit, average path length and edge density capture similar properties of the underlying time series. However, it is likely that the average path length is also crucially influenced by the type of the underlying time series (*e.g.*, periodic or fractal) and the associated distribution of local maxima within the record. A more detailed examination of these different effects is beyond the scope of this work, but might be an interesting task for future research.

  ❑ The ***assortativity coefficient A*** measures the strength of linear correlations between the degrees of vertices at both ends of the same edge, *i.e.*,

$$A = \frac{\frac{1}{E} \sum_{j>i} k_i k_j A_{ij} - \left[\frac{1}{E} \sum_{j>i} \frac{1}{2} \left(k_i + k_j \right) A_{ij} \right]^2}{\frac{1}{E} \sum_{j>i} \frac{1}{2} \left(k_i^2 + k_j^2 \right) A_{ij} - \left[\frac{1}{E} \sum_{j>i} \frac{1}{2} \left(k_i + k_j \right) A_{ij} \right]^2} , \tag{10}$$

where $E = \rho N(N-1)/2$ is the total number of undirected edges in the graph. In comparison with the aforementioned global network properties, A captures a more complex feature linking the local neighborhood properties of mutually connected vertices. In this spirit, a high assortativity coefficient points to a considerable degree of symmetry in the time series under study, whereas negative values rather indicate asymmetry.

A more detailed discussion and clean interpretation of the various possible network measures for VGs will surely be subject of future research. Of course, beyond the aforementioned characteristics there are multiple other measures one could also consider for describing the properties of VGs. This includes also measures characterizing the properties of individual edges as well as the distributions of small subgraphs (motifs). For a holistic characterization of a graph, C and L have attracted particular interest, since their common behavior gives rise to a mathematical evaluation of the small-world phenomenon, *i.e.*, the emergence of real-world networks with a high degree of clustering and a short average path length (Watts and Strogatz 1998).

Besides studies on the small-world effect, the assortativity of VGs has recently attracted considerable interest. Specifically, the presence of assortative behavior (*i.e.*, vertices preferentially connect to other vertices with similar degree) implies the so-called hub attraction, whereas disassortative behavior relates to hub repulsion. It has been shown that the latter is a necessary condition for the emergence of fractal structures in networks (Song *et al.* 2006). For example, for Brownian motion (a fractal stochastic process), hub repulsion is not present, and the resulting VGs are non-fractal, but show a scaling of the average path length with increasing network size as $L(N) \sim \log N$, which is typical for small-world networks. In contrast, for the Conway series (a deterministic fractal) one finds hub repulsion and $L \sim N^{-\beta}$, which implies the presence of a fractal VG (Lacasa *et al.* 2008). In this respect, the assortativity coefficient or, more specifically, the scaling of the degree correlation determines the fractality of a VG (Song *et al.* 2006, Gallos *et al.* 2008), which is an interesting and potentially relevant property when studying fractal time series.

2.4 Possible generalizations of the visibility graph approach

Besides the already well explored HVG algorithm, there are multiple further possible generalizations of the VG idea. In the following, some of the corresponding conceptual ideas shall be briefly discussed.

First, Luque *et al.* (2009) briefly discussed considering directional VGs and HVGs, where directed edges between vertices are considered according to the arrow of time, *i.e.*, the edges represent potential causal relationships between different observations, with the direction being from the cause at t_i to the effect at $t_j > t_i$. Studying such directed graphs would give information on time-reversal asymmetry of the considered time series, which could be related to non-conservative processes. A corresponding detailed discussion on detecting time series irreversibility based on HVGs has been recently provided by Lacasa *et al.* (2011). Similar considerations apply to other types of networks constructed from time series as well.

Second, one should note that VG analysis has so far only concerned convexity, *i.e.*, relationships mainly affecting the local maxima of a time series. This strategy appears useful if considering records with homogeneous distribution (*i.e.*, with some mirror symmetry in x), or if the studied observable is naturally bound from below (*e.g.*, in case of hurricane counts (Elsner *et al.* 2009), streamflows (Tang *et al.* 2010), or precipitation data). However, there could be cases where one is particularly interested in studying asymmetries between the fluctuations of an observable towards upper and lower values, respectively. In such cases, it may be worth considering the observable $y = -x$ and comparing the properties of the VGs obtained for x and y. Systematic differences between both graphs would indicate structural asymmetries, which could have interesting interpretations in terms of the underlying dynamical processes.

Finally, the trivial connection of neighboring points in time in the VG enhances the signature of structures due to autocorrelations in the record under study. Although this might be desirable for VGs and HVGs since some of their respective network properties are explicitly related with the presence of serial dependences (*e.g.*, the typical scale of the degree distribution of HVGs, *cf.* Luque *et al.* 2009), there could be situations in which one is interested in removing the corresponding effects. In such cases, it is possible to introduce a minimum time difference for two observations to be connected in the network for removing the effect of slowly decaying autodependences, which would correspond to the Theiler window in other concepts of nonlinear time series analysis (Theiler 1990, Donner *et al.* 2010).

The aforementioned conceptual ideas have not yet been explicitly studied in the scientific literature, but should eventually be considered in more detail in future work.

3.   METHODOLOGICAL CHALLENGES

Many recent publications on VG analysis of time series have particularly made use of data from model systems, which are characterized by rather ideal conditions for statistical analysis. Even for most practical applications presented so far, the properties of the data under study have allowed using this methodological approach without extensive precautions. However, when operating with data obtained in a geophysical context, features challenging basically any kind of time series analysis are often present, including missing data, heteroscedastic "noise", or even uncertainties in the time domain (the latter being particularly relevant in paleoclimatology). The explicit treatment of the resulting effects on VG properties has not yet been investigated elsewhere.

As in the previous section, in the following a corresponding study is presented for the specific case of a Gaussian white noise process as a simple,

but still illustrative example. It has to be emphasized that for "real" data characterized by a non-Gaussian probability distribution function, serial dependences, or even (multi-)fractal behavior, the resulting effects could well be much stronger than in this example. A detailed study of the interdependences between such features of the data and the resulting effects of missing data and uncertainties on VG properties is, however, beyond the scope of the presented research.

3.1 Missing data

One important problem of many observational time series – not only in geophysics – is the presence of missing data. Since existing methods of time series analysis typically require a uniform spacing in time, this problem is most often addressed by means of interpolation or sophisticated imputation of the missing observations. In general, there is a great variety of possible approaches for such gap filling, which shall not be further discussed here. Specifically, it is not always a priori clear what method performs best under the specific conditions of the data studied.

As far as VGs are concerned, the problem of missing data has not yet been explicitly addressed. Unlike many other approaches of time series analysis, VGs do not explicitly require uniform sampling. Hence, missing data could be ignored when performing a corresponding analysis. However, if it is known that there must have been an observation at a given time, it could be conceptually problematic to neglect this information in the analysis. From a broader perspective, it can be argued, however, that this argument applies to essentially all kinds of time series (except for explicitly discrete processes), since values of the considered observable (with a continuous-time variability) taken in between two subsequent observations remain always unknown, but could have a certain impact on the results of the analysis.

Looking at the issue of missing values from a complementary perspective, one can reinterpret this problem as an attack to (or just failure of) the complex network represented by the visibility graph. In complex network theory, the impact of such attacks on various types of networks has been intensively studied under the aspect of safety and robustness of infrastructures (*e.g.*, Albert *et al.* 2000, Holme *et al.* 2002). In general, one has to distinguish random failures (corresponding to randomly missing values) from intentional attacks, which typically affect the network hubs. Since for a VG, these hubs correspond to the maxima of the underlying time series, this effect is particularly relevant for certain types of censored data, *e.g.*, in case of measurement failures due to the limited detection range of a measurement device. Since is known that attacks on hubs typically have a more severe effect on the network architecture than those on other vertices, censoring can

strongly alter the properties of the resulting VGs. However, even a random removal can have notable consequences for the VG properties on both global and local scale.

In order to illustrate the effect of missing data on the properties of VGs, in the following, two different types of treatment are studied, which can be considered as opposite extreme cases. On the one hand, missing data will be simply neglected in the generation of the VG. On the other hand, since there is no information about the magnitude of the missing values, it can be a more honest solution to consider the VG as being fragmented into pieces corresponding to times before and after the missing observation, *i.e.*, regarding the VG becoming decomposed into mutually disconnected subgraphs. It should be noted, however, that the latter approach results in the emergence of additional boundaries, which again cause an enhancement of the effects discussed in Section 2.2. It should be emphasized that sophisticated gap filling by means of interpolation or imputation will be most likely a better strategy in many practical applications.
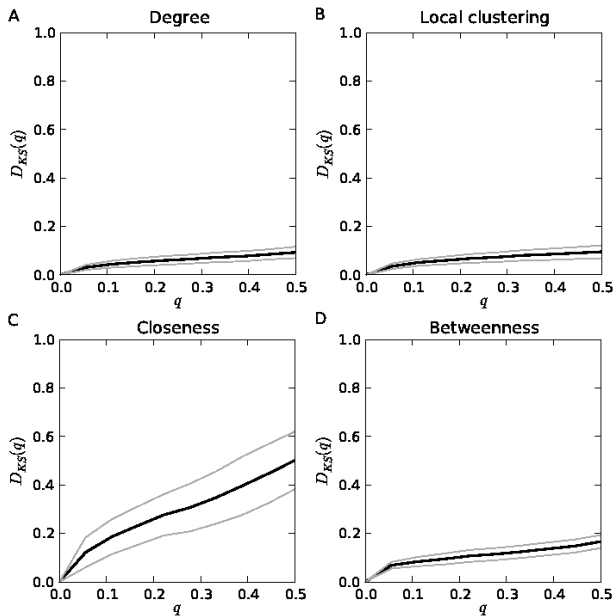
Fig. 4. Effect of random removal of a fraction q of single values from one Gaussian white noise time series with $N = 100$ on the four VG vertex measures degree (A), local clustering coefficient (B), closeness (C), and betweenness (D), measured in terms of the Kolmogorov–Smirnov test statistics D_{KS} between the distributions of the corresponding properties for original and corrupted series. Missing values are neglected. Black and gray lines correspond to mean values and +/− 1 standard deviation levels obtained from $M = 1000$ realizations of the removal process.

In the following, the impact of both treatments described above on the distributions of VG vertex properties (see Section 2.2) will be summarized for the case of a Gaussian white noise process. In order to quantify the corresponding effect, the values of the Kolmogorov–Smirnov (KS) test statistics (*i.e.*, the maximum deviation between two cumulative distribution functions) between the distributions of a given vertex property for both the original and perturbed time series are considered. For a variable fraction q of randomly selected individual observations being removed from the data, the results are shown in Figs. 4 and 5. As it can be seen, simply ignoring missing values has a considerable effect mainly on closeness centrality, whereas the changes in the distributions of degree, betweenness, and local clustering coefficient remain within a certain, possibly tolerable range. Considering a fragmentation of the VG, the impacts, however, get much more severe due to the emergence of boundary effects particularly affecting closeness (Fig. 5C).

In geophysical applications, missing data often occur not randomly independent of each other, but as blocks. When removing a given fraction of observations as one block of random positioning in the time series, the effects on the distributions of vertex properties are slightly reduced if the missing data are just ignored (Fig. 6), which becomes most clearly visible for closeness centrality again. Treating the missing values as segmentation points of the VG, this effect becomes even much more prominent (Fig. 7),
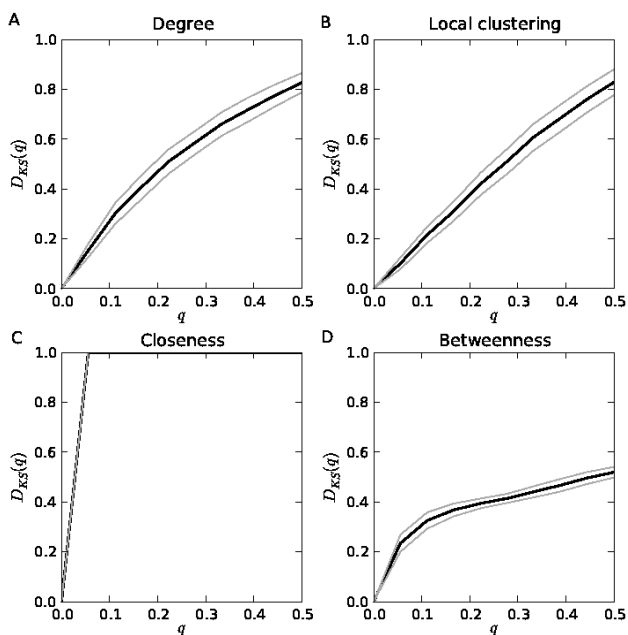
Fig. 5. As in Fig. 4, missing data are treated as additional boundaries of the time series.
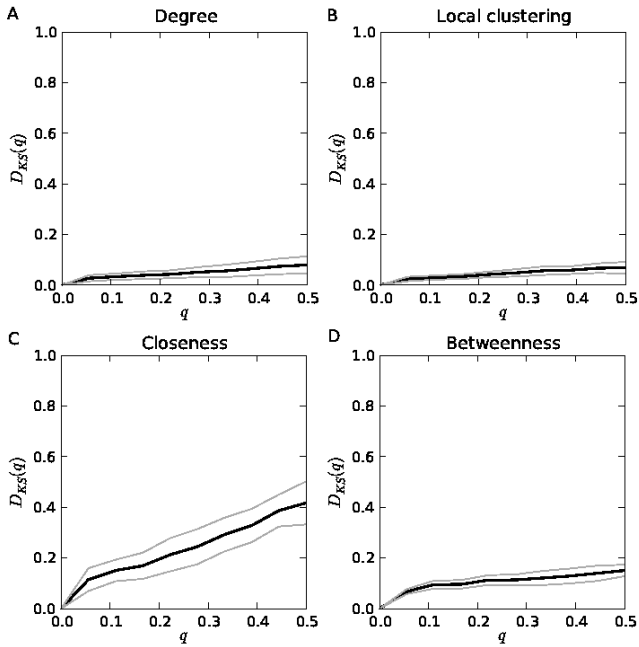
Fig. 6. As in Fig. 4, with all missing values being removed as a block.
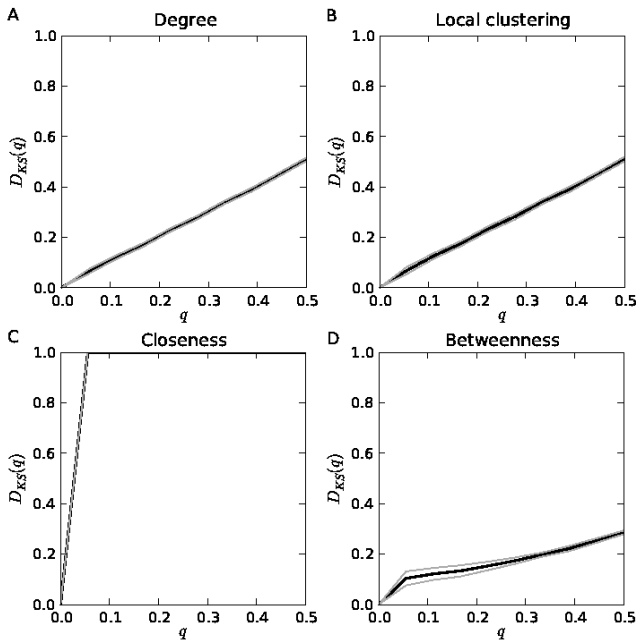
Fig. 7. As in Fig. 5, with all missing values being removed as a block.

since the considered time series just displays four end points instead of many in the case of independently removed observations. However, the modifications of the VG properties are still much stronger than for the missing blocks just being ignored. In all cases, these modifications become continuously stronger as the fraction of missing values is increased.

3.2   Homo- and heteroscedastic uncertainties

In a similar way as for the treatment of missing values in Section 3.1, the influence of measurement uncertainties on the resulting VG properties can be studied. For convenience, homoscedastic uncertainties are modeled as an additional additive Gaussian white noise component (Fig. 8), whereas the heteroscedastic case is studied by considering multiplicative noise with a reasonable, simple analytical distribution (Fig. 9). Again, it is found that in both cases the signal-to-noise ratio has a considerable effect by systematically shifting the distributions of vertex properties obtained for the original data towards those expected for the noise process. Note that since in the considered numerical example both signal and noise originated from mutually
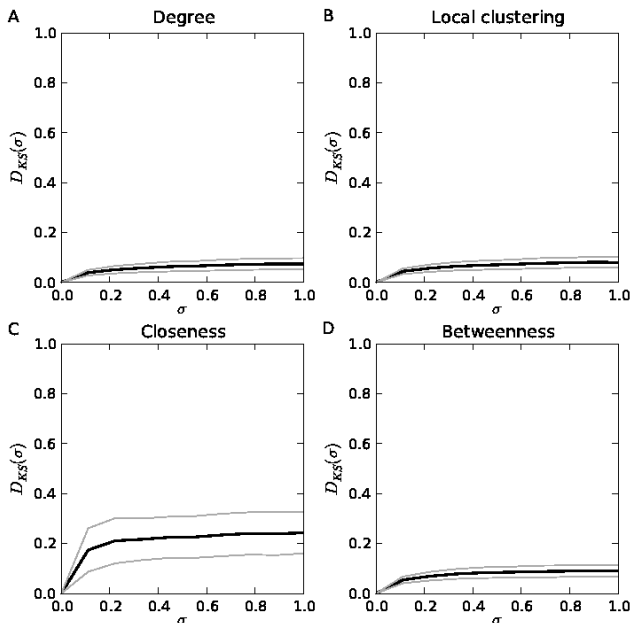
Fig. 8. Effect of additive Gaussian white noise with variance σ^2 on the four VG vertex measures: (A) degree, (B) local clustering coefficient, (C) closeness, and (D) betweenness, obtained for one uncorrelated Gaussian random process with $N = 100$. Black and gray lines correspond to mean values and +/– 1 standard deviation levels obtained from $M = 1000$ realizations of the additive noise.
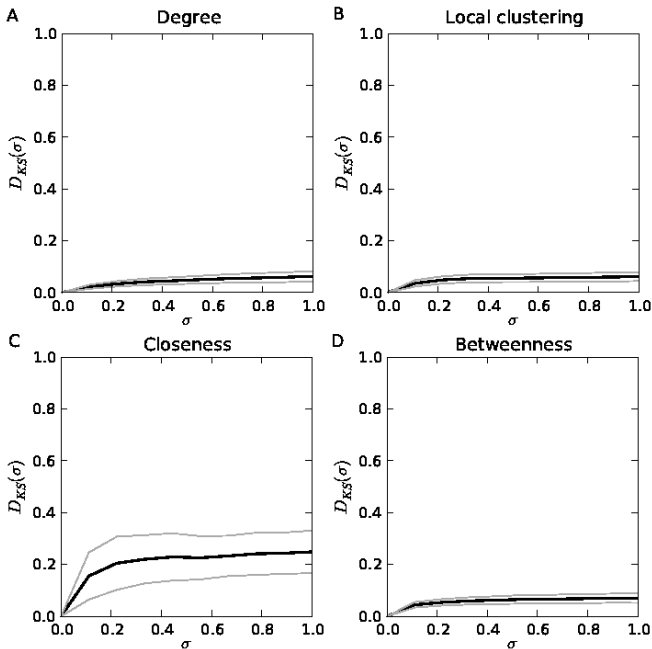
Fig. 9. As in Fig. 8 for multiplicative noise of the form $y_i = x_i \exp(-|\xi_i|)$, where $\{\xi_i\}$ is a Gaussian white noise process with zero mean and variance σ^2, mimicking the effect of heteroscedastic uncertainties on VG vertex measures.

independent Gaussian white noise processes, there is a saturation of the KS statistics for moderate noise at values corresponding to the variance of VG properties for independent realizations of the same "signal" process.

3.3   Uncertain timings

In full analogy to the case of uncertainties in the observable x, one can study the impact of uncertain timings t_i on the properties of the resulting VGs. The latter is a wide-spread problem particularly in the analysis of paleoclimate time series (Telford *et al.* 2004). Since in the construction of VGs both observable and time enter in terms of an inequality defined by a linear relationship, it is not surprising that uncertain timing can indeed have a similar effect on the VG properties as uncertainties in the measurement itself (this is distinctively different for HVGs where changes in the time coordinate do not matter as long as the order of observations is preserved). Figure 10 displays the corresponding results for a realization of Gaussian white noise originally observed with regular spacing, with the timings being artificially corrupted later as

$$\tilde{t}_i = t_i + \Delta t \left(\left| 1 - 2\eta_i \right| - 0.5 \right). \tag{11}$$
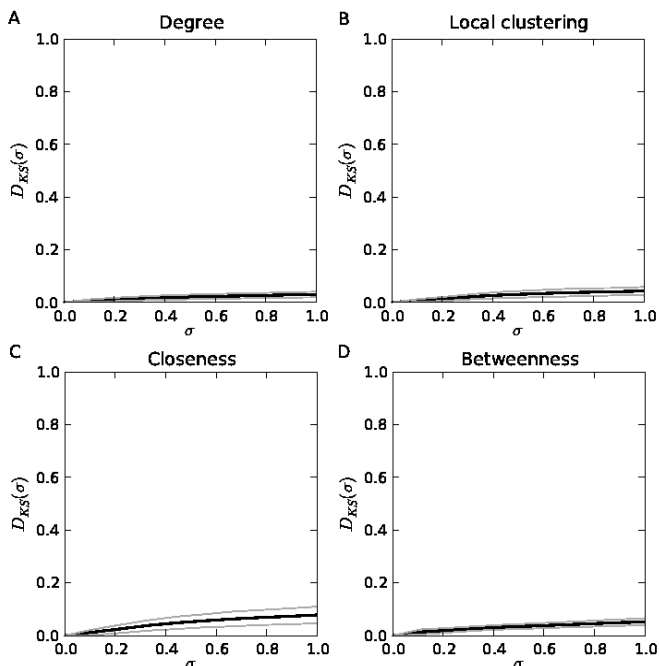
Fig. 10. As in Fig. 8 for fixed data, but uncertain timing of observations. Uncertainty in the time domain has been modeled by considering new times $\tilde{t}_i = t_i + \Delta t \left(\left| 1 - 2\eta_i \right| - 0.5 \right)$. where η_i is an uncorrelated random process with uniform distribution in [0,1].

Here, η_i are independent realizations of a random variable with uniform distribution in [0,1], and Δt is the spacing between subsequent observations in the original data set. Note that this specific form of the time-scale corruption, which allows preserving the temporal order of observations, has been inspired by the tent map as a paradigmatic nonlinear mapping often used as an illustrative example in complex systems sciences. The obtained results demonstrate that the distributions of vertex properties of a VG are indeed affected by modifications of the time-scale; however, the changes are considerably smaller than for noisy corruptions of the measurements themselves. The reason for this is that the modification used here has been restricted by the normal sampling interval, whereas the changes induced by additive and multiplicative noise considered in Section 3.2 allowed for comparably larger modifications in the data.

4.   GEOSCIENTIFIC EXAMPLES

All case studies presented in the previous chapter have considered possible origins of pitfalls of VG analysis applied to geophysical data. However, the

stochastic model chosen for illustrating the corresponding effects has been as simple as possible, not reflecting the large variety of dynamics present in geophysical systems. In the following, some examples from different geoscientific disciplines will be presented to illustrate what kind of information can be obtained from VG analysis, hence highlighting the potentials of this rather new type of analysis.

4.1 US landfalling hurricanes

The first published application of VGs to studying a problem of specific geophysical relevance has been presented by Elsner *et al.* (2009), who investigated the time series of annual US landfalling hurricanes counts (see http://www.aoml.noaa.gov/hrd/hurdat/ushurrlist.htm) since 1851. Here, this example will be recapitulated, extending the already presented analysis by corresponding information obtained from different vertex properties of the corresponding VG. It should be noted that in the present study, only data until 2005 have been used, whereas Elsner *et al.* (2009) considered a slightly extended data set.

The obtained results displayed in Fig. 11 present interesting complementary features displayed by the different vertex measures. Specifically, both degree and betweenness show a marked decay of probability towards higher values of the respective measure, which is to be expected and reflects the presence of hubs in the VG. However, while this decay is sufficiently smooth (except for numerical artifacts of the considered estimator, *cf.* the caption of Fig. 11), the degree distribution presents some interesting secondary structure at degrees between about 20 and 35. The distribution of closeness centrality is quite symmetric with a two-peaked maximum. Local clustering coefficients of 1 are most abundant as expected (correspondence to local minima of the data), whereas there is some intermediate maximum of the corresponding distribution at values of about 0.5, which reflects the typical values of this measure for vertices not coinciding with local minima of the data. In relationship with these findings, one should note the rather specific nature of hurricane count data, which are discrete by definition. It can be expected that some of the features displayed by the empirical distributions of VG vertex measures have been affected by this property.

Following the lines of the original work of Elsner *et al.* (2009), all four distributions of vertex properties have been subsequently compared with those obtained from realizations of a Poissonian random process with the same average event rate (1.8) and length ($N = 155$) as the original data. The results shown in Fig. 11 indicate that most of the observed features are indeed consistent with the assumption of a Poissonian distribution (confirming the results of Elsner *et al.*), with two marked exceptions: the doubly-peaked maximum of the closeness distribution (which could, however, result
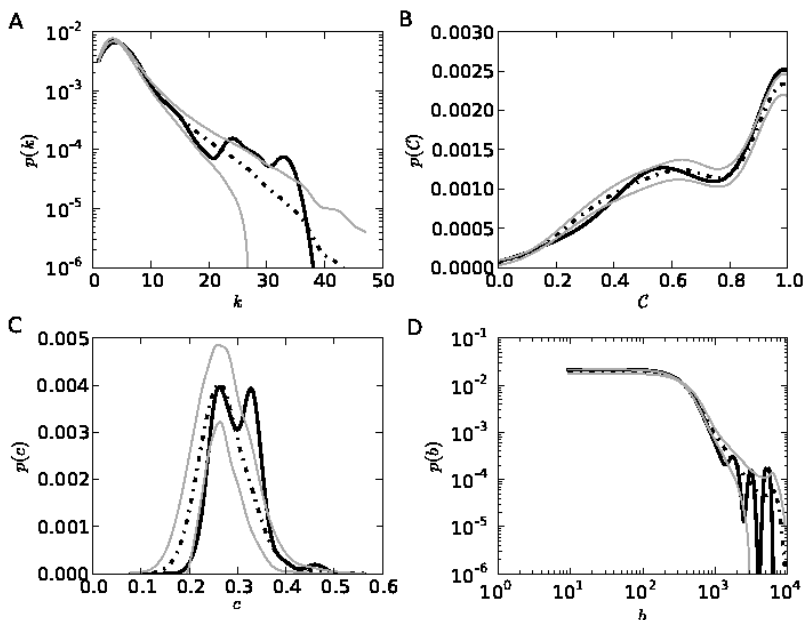
Fig. 11. Distributions of degree (A), local clustering coefficient (B), closeness centrality (C), and betweenness (D) for the VG obtained from the US annual landfalling hurricane counts since 1851 (black lines). Dashed black as well as solid gray lines indicate the mean values and 90% confidence intervals obtained from $M = 1000$ surrogate time series taken from a Poissonian distribution with the same mean event rate of 1.8 as for the observational data. All distributions have been estimated from the empirical data by means of a Gaussian kernel smoother. Note that the apparent oscillations of the betweenness distribution for high values are an artifact of this estimator in the presence of sparse data.

from the small sample size) and the secondary local maxima of the degree distribution. In contrast, the general behavior of all four distributions is well reflected by the corresponding surrogate VGs, underlining that most of the obtained results are already captured by very simple stochastic processes without assumptions on temporal correlations etc. However, further detailed work is necessary to fully explore what part of the results is eventually already predetermined by the VG algorithm, and what is a real effect of the considered data's properties.

4.2 Tide gauge records

Sea-level rise is one of the expected consequences of the ongoing global climatic change that will have the most serious societal impacts. Since detailed high-resolution data from satellite altimetry are only available for a sufficiently long observational period, tide gauge records of coastal stations

are the most reliable source of information on sea-level variability in the past century and partially even earlier times. However, similar to meteorological observations, missing data are a typical feature of tide gauge records, which makes them an ideal test case for any kind of interpolation or imputation scheme.

For illustrational purposes within the course of this study, two long-term records of relative sea-level with daily resolution have been selected, which have been obtained at Ratan (Northern Sweden) and Stockholm (data courtesy of the University of Hawaii Sea Level Center (UHSLC, Stockholm) and the Swedish Meteorological and Hydrological Institute (SMHI, Ratan), respectively). Both records cover the time interval 1916-2005 without any (Ratan), and with about 1% missing values (Stockholm), respectively. In order to remove potential influences of the annual variability component on the results of VG analysis discussed in the following, both seasonal cycle and linear long-term trends have been removed from both records before further analysis.

Since the selected data sets offer an excellent temporal resolution, it is feasible to study the properties of the associated VGs in an evolving network framework. In order to make possible further interpretations as simple as possible, running windows of size 360 days and a mutual offset of 30 days have been considered. In order to capture temporal changes in the VG properties, two commonly studied global network measures have been chosen for tracing the signatures of changing conditions in the VGs: network transitivity T and average path length L. Missing values have been ignored when obtaining the corresponding network connectivity.

The results of the corresponding analysis are summarized in Figs. 12 and 13. It can be seen that the VGs obtained from both records display strong variations with respect to their global structure as time proceeds. In order to derive a simple test distribution for identifying time intervals with VG properties that are not simply explained by statistical fluctuations (given the distribution of the entire data), surrogate time series have been resampled by randomly picking 360 individual observations from the respective record and used for calculating the properties of interest for the resulting VG. A detailed description of the corresponding resampling approach has been recently given by Donges *et al.* (2011a, b) within the framework of evolving recurrence network analysis. This simple approach reveals distinct time intervals of extraordinarily high average path length, the detailed interpretation of which (particularly regarding their magnitude and timing) clearly deserves further detailed investigations on the short-term dynamics of the data, which are beyond the scope of the present work. In contrast, the transitivity of the surrogate VGs is most often smaller than that of the networks obtained from the original data, which points to a network signature of the systematic
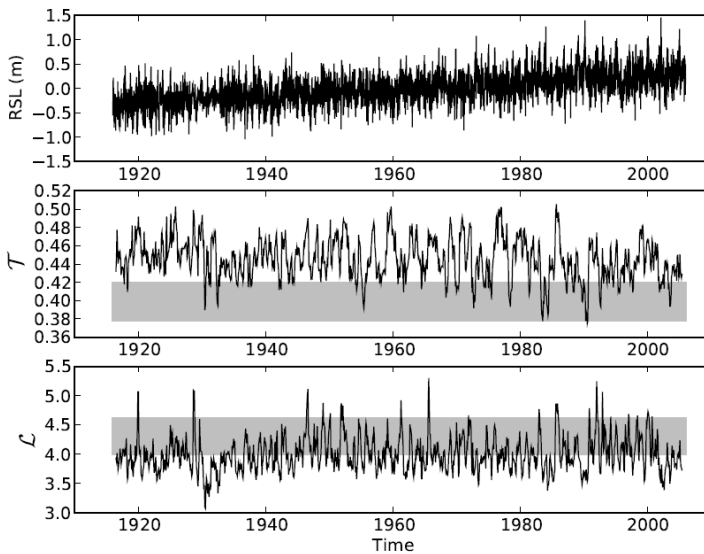
Fig. 12. Record of relative sea-level (RSL) obtained at the tide gauge of Ratan (Northern Sweden), and resulting global VG properties transitivity T and average path length L obtained from running windows of 360 days length. The gray bands represent 90% confidence levels (upper and lower 5% confidence) estimated from $M = 200$ surrogate data sets obtained by resampling the entire data set (see text for details).
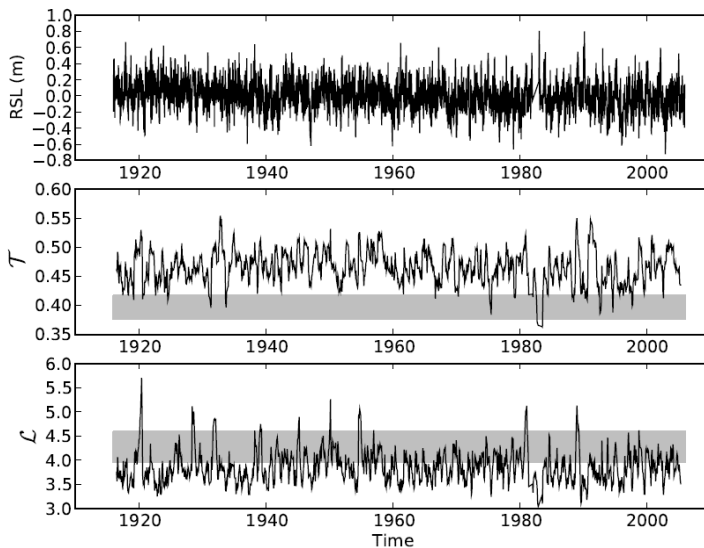

Fig. 13. As in Fig. 12 for the tide gauge of Stockholm. Missing values in the data have been ignored for analysis.
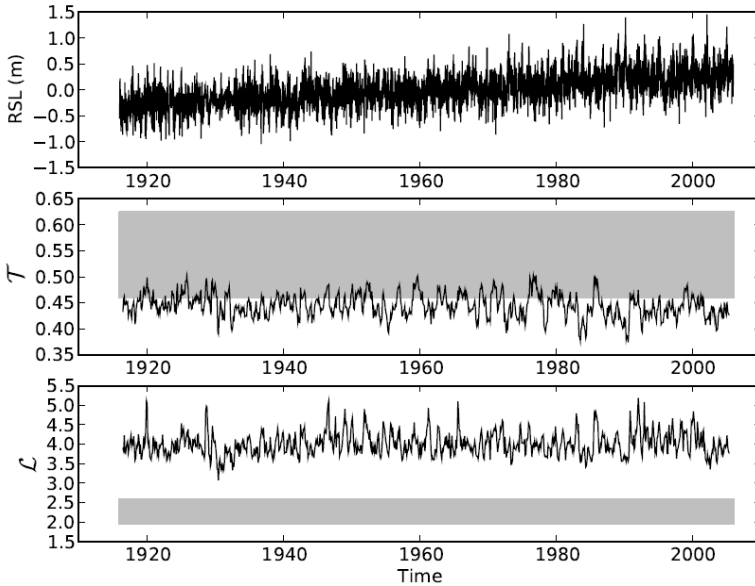
Fig. 14. As in Fig. 12 using surrogates obtained from block bootstrapping of the original data with a block length of 20 days.

destruction of temporal correlations in the data and, hence, resulting organization in the VGs. Specifically, the surrogate data represent temporally uncorrelated time series with approximately the same distribution as the original data. Therefore, coincidences between network properties of original and surrogate VGs reflect exclusively the effects of the underlying data's distribution.

Since the resampling approach described above does not take into account temporal correlation within the time series under study, it is worth investigating the changes in surrogate VG properties if these temporal structures are retained. In fact, when applying block bootstrapping for obtaining surrogate time series with a block length determined by the decorrelation time of the records (around 20 days), the resulting confidence bands of the statistical test exclude the network properties of the evolving VGs for a large part of the considered time interval (Fig. 14). A probable reason for this is that block bootstrapping using data from time periods with possibly different short-term dynamics results in rather heterogeneous surrogate VGs (due to structural breakpoints in the surrogate time series separating parts of the VG with different local properties). As a consequence, the resulting VGs are characterized by significantly higher transitivity and lower shortest path length, *i.e.*, resemble much more a small-world network than the VGs from the original data.

Looking at the obtained temporal variability of VG properties in more detail, it is found that some (but not all) of the extreme values of both L and T coincide for both considered tide gauges, which indicates the possible presence of a common signature in the recorded short-term sea-level dynamics. Specifically, the average path length displays consistent minima at about 1920, 1928 and between 1945 and 1955, whereas network transitivity has joint minima between 1930 and 1935 as well as in 1982/83. For the latter period, L also shows a distinct minimum for both records. Since maxima of L indicate a stronger fragmentation of the network under study (*i.e.*, the absence of connections between distant points in time for the specific case of a VG), the corresponding time intervals can be interpreted as characterized by a higher complexity of sea-level variability, indicating a certain loss of stability of the underlying dynamical processes. The low values of both L and T in 1982/83 coincide with one of the strongest El Nino events in the last decades. Since such strong El Niño events have a pronounced effect on sea-level at a global scale (*e.g.*, Lukas *et al.* 1984), the latter result is not surprising. In the case of VG analysis of individual tide gauge data, the observed behavior can be explained by an increasing emergence of hubs (*i.e.*, pronounced sea-level maxima eventually pointing to increased storm activity due to a general destabilization of the North Atlantic climate) connecting very distant points in time in the VG. According to the theoretical discussion on local clustering properties of VGs (Section 2.2), this explanation is consistent with both a short average path length and low transitivity.

Besides the obvious fact that these preliminary interpretations require further validation based on additional studies on a larger set of records, it has to be emphasized that given the strong constraints on network topology imposed by the VG algorithm, any attempt of interpreting corresponding findings in some detail should be accompanied by alternative methodological approaches considering the present state of knowledge.

4.3 Paleoclimate records

As a final example, the analysis of paleoclimate records by means of VGs is considered. Among the great variety of corresponding archives, one data set of oxygen isotope anomalies ($\delta^{18}O$) measured at the speleothem (stalagmite) D4 from the Dongge cave in Southeastern China is considered (Dykoski *et al.* 2005). Speleothems have proven their excellent potentials as sources of information on the variability of paleoenvironmental conditions, particularly related to changes of precipitation (*e.g.*, in the Asian monsoon system). As for other paleoclimate archives, speleothem data are often characterized by properties such as partially unknown age-depth models or even hiata (*i.e.*, interruptions of stalagmite growth). The specific record has been chosen because it has a reasonable temporal resolution, is extremely well dated, and

has already been subjected to several independent analyses by other authors. From this perspective, Dongge D4 is an excellent test case for the performance of VG analysis in the presence of age-depth uncertainties.

In order to study the effect of uncertainties in the timing of paleoclimate records on the resulting VG properties, the original age model based on piecewise linear interpolation between 45 subsequent dating points (Dykoski *et al.* 2005) has been stochastically perturbed by the following procedure:

(i)   Generate $M = 100$ independent realizations of the age model with the dating points being corrupted by Gaussian white noise with a standard deviation corresponding to the respective dating uncertainty. Check each of these perturbed age-depth models for stratigraphic consistency (*i.e.*, monotonicity of the age-depth relationship) and accept only those models that fulfill this requirement (the others have to be rejected).

(ii)   Use these perturbed age-depth models for generating $M = 100$ realizations of the ages of all $\delta^{18}O$ measurements by means of linear interpolation based on the spatial coordinates of the dating points (*cf.* Dykoski *et al.* 2005). The resulting differences in the recorded time series between original and perturbed data are visualized in Fig. 15. Note that due to the excellent dating of the considered record, original and perturbed data do not differ markedly from each other.

(iii)   For each realization, generate a VG and compute the network quantifiers of interest. Compare the results found for the original data (unperturbed age model) with the distributions obtained from this ensemble of noisy surrogates.

Note that these randomized age-depth models approximate the limits of time-scale uncertainty between the individual dating points and their effects on the resulting VG properties, but do not explicitly consider dating uncertainties. For the sake of simplicity, in the following only the distributions of the four previously studied vertex characteristics will be considered. For global network quantifiers, one could, however, proceed the same way.

The results of the described numerical analysis are shown in Fig. 16. It is interesting to note that the distributions closely resemble those obtained for the hurricane counts in Section 4.1 despite the completely different nature and structure of the respective data. This observation indicates a possibly strong influence of the construction mechanism of a VG which could restrict the possible outcomes of the performed analysis (note that similar effects are known regarding the global properties of spatially embedded networks, *cf.* Bialonski *et al.* 2010). Besides this finding, one observes that the perturbations of the age-depth model do not change the results of VG analysis
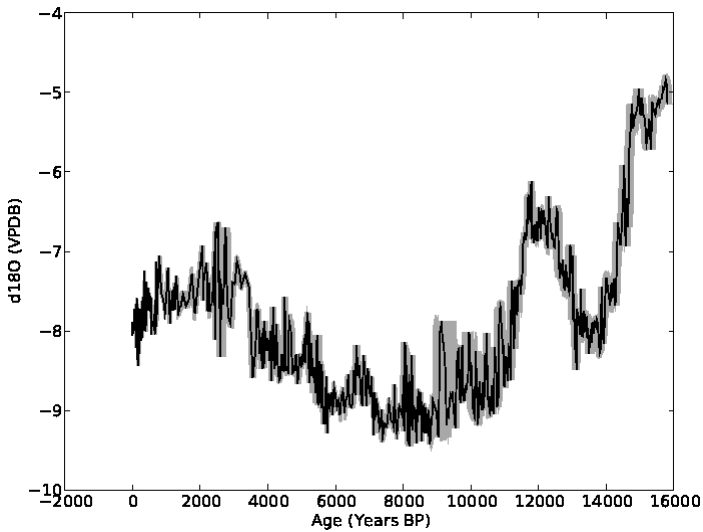
Fig. 15. Original oxygen isotope anomalies of the Dongge D4 record (black line), and standard deviation of the ensemble of $M = 100$ realizations of a perturbed age model (gray).
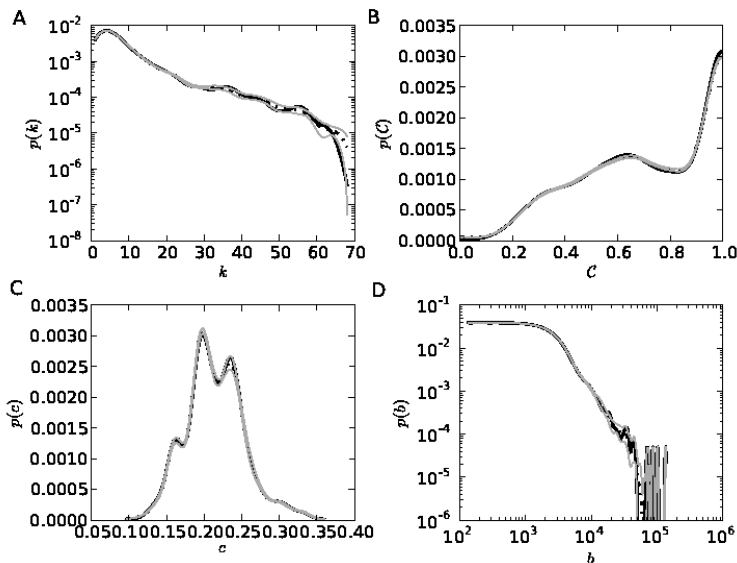

Fig. 16. Distributions of degree (A), local clustering coefficient (B), closeness centrality (C), and betweenness (D) for the VG obtained from the Dongge D4 oxygen isotope anomalies (black lines). Dashed black lines indicate the mean obtained from $M = 100$ surrogate age-depth models, solid gray lines correspond to the associated 90% confidence intervals. All distributions have been estimated from the empirical data by means of a Gaussian kernel smoother.

markedly. The reasons for this behavior are that (i) the dating is very accurate with many rather dense dating horizons, (ii) the randomized age-depth models are strongly constrained in order to retain the correct chronological (stratigraphic) order of observations, and (iii) the structure of the recorded observations does not change much along the measurement transect on the speleothem. Consequently, the influence of dating uncertainties on VG properties is limited, which renders this method a promising tool for paleoclimate time series analysis. An additional advantage is that non-uniform spacing of observations does not cause any methodological difficulties for VG construction. Moreover, in contrast to recurrence network analysis (Donges *et al.* 2011a, b), the observational data can simply be taken as they are without the need for phase space reconstruction and time-delay embedding.

5. SUMMARY

In the last years, various approaches for analyzing time series from a complex network perspective have been developed. Particularly, recurrence networks (Donner *et al.* 2010, 2011) and visibility graphs (Lacasa *et al.* 2008) have been widely used for studying the properties of various complex systems. Besides their methodological variants, both approaches are well suited, and have already been successfully applied to studying different kinds of geophysical problems. A detailed discussion of the multiplicity of complex network characteristics of visibility graphs presented in this work has highlighted the great potentials for future practical applications of this approach. Specifically, one main benefit of the visibility graph and associated methods such as horizontal visibility graphs is their algorithmic simplicity (*i.e.*, the mapping from the time series to the network domain is conceptually simple), but leads to a surprising amount of structural properties of the time series being recovered in the graph connectivity. Moreover, recent work has demonstrated and rigorously proven connections between the respective graph and time series properties for both stochastic and deterministic systems (Lacasa *et al.* 2009, Luque *et al.* 2009, 2011).

Beyond previous results, the detailed potentials and limitations of visibility graphs and related methods still need to be further explored. This work has identified some methodological limits of the original visibility graph approach which call for a careful treatment in real-world geoscientific applications. On the one hand, it has been demonstrated that a joint analysis of different network measures can provide complementary insights into the system under study compared to studying only one or two of them. Specifically, the visibility graph algorithm allows investigating particularly systems with a strong degree of stochasticity (*e.g.*, observations with strong observational noise), whereas the alternative approach of recurrence networks aims on

finding structural changes of an underlying (presumely deterministic) attractor in some reconstructed phase space (Donner *et al.* 2010), which could be hidden by measurement noise. However, the explicit interpretation of more complex local and global network characteristics in a visibility graph is less obvious than for recurrence networks and needs to be fully explored in future work prior to their wide potential application to real-world problems. On the other hand, the different resulting network measures of visibility graphs are typically not independent of each other, but display strong statistical interrelationships induced by the specific algorithm of network construction. Even more, it has been demonstrated that the visibility graph algorithm implies the presence of boundary effects resulting in a systematic downward bias of all local network properties when entering the edges of a time series. This behavior is not only distinctively different from that of other time series network approaches, but poses additional methodological challenges to be solved in future research. One has to emphasize the particular relevance of this finding for the study of short time series, which are common in geophysics. Hence, the results obtained for the geophysical examples discussed in this work demonstrate that although one has to be aware of certain intrinsic methodological problems of the visibility graph method (which need to be further addressed in future work), the results appear robust and can (under certain conditions) be meaningfully interpreted in terms of characteristic properties of the underlying time series. In this respect, one can conclude that visibility graph analysis has great potentials for future applications to geophysical data.

As a new strategy with potential relevance to many real-world applications, this work has demonstrated the use of visibility graphs in an evolving network framework. Specifically, when obtaining visibility graphs for sliding windows of a time series, there are always vertices and respective edges removed from one end of the graph, whereas new ones are added at the other end. By studying the resulting graph properties as a function of time, it is possible to detect subtle changes in the dynamical properties of the time series under study. We note that the same conceptual idea has already been successfully applied to recurrence networks (*e.g.*, for detecting dynamical transitions in paleoclimate time series; Donges *et al.* 2011a, b), but not yet within the visibility graph framework. The results obtained in this work for the example of tide gauge records suggest the broad applicability of this framework to visibility graphs as well.

The emergence of different topological features in visibility graphs as time evolves, reflecting the time evolution of the network's architecture, is an important example for the application of statistical physics concepts to this new kind of time series analysis approach. Specifically, besides the possibility of studying the relevance of variations in the network topology by

simple statistical resampling approaches, the strong link between the properties of visibility graphs and the stochastic properties of the underlying time series suggests that there could be a similar link between stochastic time series models with time-dependent coefficients and corresponding evolving network models studied in statistical physics. In this respect, studying the time evolution of network properties can provide complementary insights into the dynamics of the system under study in comparison to traditional time series analysis techniques. However, the corresponding framework still includes important open methodological questions that have to be answered in future research.

References

Abe, S., and N. Suzuki (2004), Scale-free network of earthquakes, *Europhys. Lett.* **65**, 581-586, DOI: 10.1209/epl/i2003-10108-1.

Ahmadlou, M., H. Adeli, and A. Adeli (2010), New diagnostic EEG markers of the Alzheimer's disease using visibility graphs, *J. Neural Transm.* **117**, 1099-1109, DOI: 10.1007/s00702-010-0450-3.

Albert, R., and A.-L. Barabasi (2002), Statistical mechanics of complex networks, *Rev. Mod. Phys.* **74**, 47-97, DOI: 10.1103/RevModPhys.74.47.

Albert, R., H. Jeong, and A.-L. Barabasi (2000), Error and attack tolerance of complex networks, *Nature* **406**, 378-382, DOI: 10.1038/35019019.

Baiesi, M., and M. Paczuski (2004), Scale-free networks of earthquakes and aftershocks, *Phys. Rev. E* **69**, 066106, DOI: 10.1103/PhysRevE.69.066106.

Barrat, A., and M. Weigt (2000), On the properties of small-world network models, *Eur. Phys. J. B* **13**, 547-560, DOI: 10.1007/s100510050067.

Barthelemy, M. (2004), Betweenness centrality in large complex networks, *Eur. Phys. J. B* **38**, 163-168, DOI:10.1140/epjb/e2004-00111-4.

Bialonski, S., M.-T. Horstmann, and K. Lehnertz (2010), From brain to earth and climate systems: Small-world interaction networks or not?, *Chaos* **20**, 013134, DOI: 10.1063/1.3360561.

Boccaletti, S., V. Latora, Y. Moreno, M. Chavez, and D.-U. Huang (2006), Complex networks: structure and dynamics, *Phys. Rep.* **424**, 175-308, DOI: 10.1016/j.physrep.2005.10.009.

Costa, L. da F., F.A. Rodrigues, G. Travieso, and P.R. Villas Boas (2007), Characterization of complex networks: a survey of measurements, *Adv. Phys.* **56**, 167-242, DOI: 10.1080/00018730601170527.

Davidsen, J., P. Grassberger, and M. Paczuski (2008), Networks of recurrent events, a theory of records, and an application to finding causal signatures in seismicity, *Phys. Rev. E* **77**, 066104, DOI: 10.1103/PhysRevE.77.066104.

de Floriani, L., P. Marzano, and E. Puppo (1994), Line-of-sight communication on terrain models, *Int. J. Geograph. Inform. Sci.* **8**, 329-342, DOI: 10.1080/02693799408902004.

Dong, Z., and X. Li (2010), Comment on "Network analysis of human heartbeat dynamics" [Appl. Phys. Lett. 96, 073703 (2010)], *Appl. Phys. Lett.* **96**, 266101, DOI: 10.1063/1.3458811.

Donges, J.F., Y. Zou, N. Marwan, and J. Kurths (2009), The backbone of the climate network, *Europhys. Lett.* **87**, 48007, DOI: 10.1209/0295-5075/87/48007.

Donges, J.F., R.V. Donner, K. Rehfeld, N. Marwan, M.H. Trauth, and J. Kurths (2011a), Identification of dynamical transitions in marine palaeoclimate records by recurrence network analysis, *Nonlin. Proc. Geophys.* **18**, 545-562, DOI: 10.5194/npg-18-545-2011.

Donges, J.F., R.V. Donner, M.H. Trauth, N. Marwan, H.J. Schellnhuber, and J. Kurths (2011b), Nonlinear detection of paleoclimate-variability transitions possibly related to human evolution, *Proc. Natl. Acad. Sci. USA* **108**, 20422-20427, DOI: 10.1073/pnas.1117052108.

Donner, R.V., Y. Zou, J.F. Donges, N. Marwan, and J. Kurths (2010), Recurrence networks – a novel paradigm for nonlinear time series analysis, *New J. Phys.* **12**, 033025, DOI: 10.1088/1367-2630/12/3/033025.

Donner, R.V., M. Small, J.F. Donges, N. Marwan, Y. Zou, R. Xiang, and J. Kurths (2011), Recurrence-based time series analysis by means of complex network methods, *Int. J. Bifurcation Chaos* **21**, 1019-1048, DOI: 10.1142/S0218127411029021.

Dykoski, C.A., R.L. Edwards, H. Cheng, D. Yuan, Y. Cai, M. Zhang, Y. Lin, J. Qing, Z. An, and J. Revenaugh (2005), A high-resolution, absolute dated Holocene and deglacial Asian monsoon record from Dongge Cave, China, *Earth Planet. Sci. Lett.* **233**, 71-86, DOI: 10.1016/j.epsl.2005.01.036.

Elsner, J.B., T.H. Jagger, and E.A. Fogarty (2009), Visibility network of United States hurricanes, *Geophys. Res. Lett.* **36**, L16702, DOI: 10.1029/2009GL039129.

Gallos, L.K., C. Song, and H.A. Makse (2008), Scaling of degree correlations and its influence on diffusion in scale-free networks, *Phys. Rev. Lett.* **100**, 248701, DOI: 10.1103/PhysRevLett.100.248701.

Goh, K.-I., B. Kahng, and D. Kim (2001), Universal behavior of load distribution in scale-free networks, *Phys. Rev. Lett.* **87**, 278701, DOI: 10.1103/PhysRevLett.87.278701.

Gutin, G., T. Mansour, and S. Severini (2011), A characterization of horizontal visibility graphs and combinatorics on words, *Physica A* **390**, 2421-2428, DOI: 10.1016/j.physa.2011.02.031.

Holme, P., B.J. Kim, C.N. Yoon, and S.K. Han (2002), Attack vulnerability of complex networks, *Phys. Rev. E* **65**, 056109, DOI: 10.1103/PhyRevE.65.056109.

Jimenez, A., K.F. Tiampo, A.M. Posadas, F. Luzon, and R. Donner (2009), Analysis of complex networks associated to seismic clusters near the Itoiz reservoir dam, *Eur. Phys. J. ST* **174**, 181-195, DOI: 10.1140/epjst/e2009-01099-1.

Kitsak, M., S. Havlin, G. Paul, M. Riccaboni, F. Pammolli, and H.E. Stanley (2007), Betweenness centrality of fractal and nonfractal scale-free model networks and tests on real networks, *Phys. Rev. E* **75**, 056115, DOI: 10.1103/PhysRevLett.87.278701.

Lacasa, L., and R. Toral (2010), Description of stochastic and chaotic series using visibility graphs, *Phys. Rev. E* **82**, 036120, DOI: 10.1103/PhysRevE.82.036120.

Lacasa, L., B. Luque, F. Ballesteros, J. Luque, and J.C. Nuno (2008), From time series to complex networks: The visibility graph, *Proc. Natl. Acad. Sci. USA* **105**, 4972-4975, DOI: 10.1073_pnas.0709247105.

Lacasa, L., B. Luque, J. Luque, and J.C. Nuno (2009), The visibility graph: A new method for estimating the Hurst exponent of fractional Brownian motion, *Europhys. Lett.* **86**, 30001, DOI: 10.1209/0295-5075/86/30001.

Lacasa, L., A. Núñez, E. Roldán, J.M.R. Parrondo, and B. Luque (2011), Time series irreversibility: a visibility graph approach, *arXiv:1108.1691v1* [physics.data-an].

Liu, C., W.-X. Zhou, and W.-K. Yuan (2010), Statistical properties of visibility graph of energy dissipation rates in three-dimensional fully developed turbulence, *Physica A* **389**, 2675-2681, DOI: 10.1016/j.physa.2010.02.043.

Lozano-Perez, T., and M.A. Wesley (1979), An algorithm for planning collision-free paths among polyhedral obstacles, *Comm. ACM* **22**, 560-570, DOI: 10.1145/359156.359164.

Lukas, R., S.P. Hayes, and K. Wyrtki (1984), Equatorial sea level response during the 1982-1983 El Nino, *J. Geophys. Res.* **89**, C6, 10425-10430, DOI: 10.1029/JC089iC06p10425.

Luque, B., L. Lacasa, F. Ballesteros, and J. Luque (2009), Horizontal visibility graphs: Exact results for random time series, *Phys. Rev. E* **80**, 046103, DOI: 10.1103/PhysRevE.80.046103.

Luque, B., L. Lacasa, F.J. Ballesteros, and A. Robledo (2011), Feigenbaum graphs: A complex network perspective to chaos, *PLoS One* **6**, e22411, DOI: 10.1371/journal.pone.0022411.

Luque, B., L. Lacasa, F.J. Ballesteros, and A. Robledo (2012), Analytical properties of horizontal visibility graphs in the Feigenbaum scenario, *Chaos* **22**, 013109, DOI: 10.1063/1.3676686.

Nagy, G. (1994), Terrain visibility, *Comp. Graph.* **18**, 763-773, DOI: 10.1016/0097-8493(94)90002-7.

Newman, M. (2003), The structure and function of complex networks, *SIAM Rev.* **45**, 167-256, DOI: 10.1137/S003614450342480.

Ni, X.-H., Z.-Q. Jiang, and W.-X. Zhou (2009), Degree distributions of the visibility graphs mapped from fractional Brownian motions and multifractal random walks, *Phys. Lett. A* **373**, 3822-3826, DOI: 10.1016/j.physleta.2009.08.041.

Núñez, A., L. Lacasa, E. Valero, J.P. Gómez, and B. Luque (2011), Detecting series periodicity with horizontal visibility graphs, *arXiv:1108.1693v1* [physics.data-an].

Núñez, A.M., L. Lacasa, J.P. Gomez, and B. Luque (2012), Visibility algorithms: A short review. **In:** Y. Zhang (ed.), *New Frontiers in Graph Theory*, InTech, Rijeka, 119-152.

Qian, M.-C., Z.-Q. Jiang, and W.-X. Zhou (2010), Universal and nonuniversal allometric scaling behaviors in the visibility graphs of world stock market indices, *J. Phys. A* **43**, 335002, DOI: 10.1088/1751-8113/43/33/335002.

Ravasz, E., and A.-L. Barabasi (2003), Hierarchical organization in complex networks, *Phys. Rev. E* **67**, 026112, DOI:10.1103/PhysRevE.67.026112.

Santiago, A., J.P. Cardenas, J.C. Losada, R.M. Benito, A.M. Tarquis, and F. Borondo (2008), Multiscaling of porous soils as heterogeneous complex networks, *Nonlin. Proc. Geophys.* **15**, 893-902, DOI: 10.5194/npg-15-893-2008.

Shao, Z.-G. (2010), Network analysis of human heartbeat dynamics, *Appl. Phys. Lett.* **96**, 073703, DOI: 10.1063/1.3308505.

Song, C., S. Havlin, and H.A. Makse (2006), Origins of fractality in the growth of complex networks, *Nature Phys.* **2**, 275-281, DOI: 10.1038/nphys266.

Tang, Q., J. Liu, and H. Liu (2010), Comparison of different daily streamflow series in US and China, under a viewpoint of complex networks, *Mod. Phys. Lett. B* **24**, 1541-1547, DOI: 10.1142/S0217984910023335.

Telesca, L., and M. Lovallo (2012), Analysis of seismic sequences by using the method of visibility graph, *Europhys. Lett.* **97**, 50002, DOI: 10.1209/0295-5075/97/50002.

Telford, R.J., E. Heegaard, and H.J.B. Birks (2004), All age-depth models are wrong: but how badly?, *Quat. Sci. Rev.* **23**, 1-5, DOI: 10.1016/j.quascirev.2003.11.003.

Theiler, J. (1990), Estimating fractal dimensions, *J. Opt. Soc. Am. A* **7**, 1055-1073, DOI: 10.1364/JOSAA.7.001055.

Tsonis, A.A., and P.J. Roebber (2004), The architecture of the climate network, *Physica A* **333**, 497-504, DOI: 10.1016/j.physa.2003.10.045.

Turner, A., M. Doxa, D. O'Sullivan, and A. Penn (2001), From isovists to visibility graphs: A methodology for the analysis of architectural space, *Env. Plann. B* **28**, 103-121, DOI: 10.1068/b2684.

Watts, D.J., and S.H. Strogatz (1998), Collective dynamics of 'small-world' networks, *Nature* **393**, 409-410, DOI: 10.1038/30918.

Xie, W.-J., and W.-X. Zhou (2011), Horizontal visibility graphs transformed from fractional Brownian motions: Topological properties versus the Hurst index, *Physica A* **390**, 3592-3601, DOI: 10.1016/j.physa.2011.04.020.

Yang, Y., J. Wang, H. Yang, and J. Mang (2009), Visibility graph approach to exchange rate series, *Physica A* **388**, 4431-4437, DOI: 10.1016/j.physa.2009.07.016.

Zaliapin, I., E. Foufoula-Georgiou, and M. Ghil (2010), Transport on river networks: A dynamic tree approach, *J. Geophys. Res.* **115**, F00A15, DOI: 10.1029/2009JF001281.

On the Testing of Seismicity Models

George MOLCHAN

[1]International Institute of Earthquake Prediction Theory
and Mathematical Geophysics, Russian Academy of Sciences, Moscow, Russia
e-mail: molchan@mitp.ru

[2]The Abdus Salam International Centre for Theoretical Physics,
SAND Group, Trieste, Italy

A b s t r a c t

Recently a likelihood-based methodology has been developed by the Collaboratory for the Study of Earthquake Predictability (CSEP) with a view to testing and ranking seismicity models. We analyze this approach from the standpoint of possible applications to hazard analysis. We arrive at the conclusion that model testing can be made more efficient by focusing on some integral characteristics of the seismicity distribution. This can be achieved either in the likelihood framework but with economical and physically reasonable coarsening of the phase space or by choosing a suitable measure of closeness between empirical and model seismicity rate in this space.

Keywords: statistical seismology, earthquake forecasting, earthquake likelihood models.

1. INTRODUCTION

The assessments of seismic hazard and risk are based on maps of long-term rate of damaging seismic events. There is a wide diversity of approaches to making such maps, which differ in the use of historical and low magnitude seismicity, seismotectonic regionalization, the Gutenberg–Richter law, smoothing techniques, and so on (see *e.g*., Molchan *et al.* 1997, Giardini 1999, and references therein). For this reason, the initiative of the U.S. branch of the Collaboratory for the Study of Earthquake Predictability (CSEP) is important;

its purpose is to develop a statistical methodology for objective testing and ranking of seismicity models (Field 2007). This program has been implemented as the Regional Earthquake Likelihood Models (RELM) project for California (Schorlemmer *et al.* 2010) and now the methodology is in a stage of active analysis and development (see *e.g.*, Lombardi and Marzocchi 2010, Werner *et al.* 2010, Rhoade*s et al.* 2011, Zechar *et al.* 2010).

Below we examine the RELM methodology from the point of view of possible applications to hazard analysis, *i.e.*, to the testing of long-term seismicity maps. We provide a brief description of basic elements of the methodology with a parallel discussion of its strong and weak points.

2. THE SEISMICITY MODEL

A seismicity map describes the mean rate of target events $\lambda_j = \lambda(\Delta_j)$ in subsets Δ_j of space $G \times M$. Here G denotes the region and M the magnitude range of target events. The model $\{\lambda_j\}$ is to be tested based on observations $\{v(\Delta_j) = v_j\}$, in the subsets $\{\Delta_j\}$ for a period T. In the CSEP/RELM experiments, the subsets Δ_j are standard bins of 10 km in linear size and 0.1 in magnitude; the numbers of events in bins, $\{v_j\}$, are generally low: 0, 1, 2, with the total number

$$N = \sum v_j \tag{1}$$

being a few tens of events.

The statistical analysis of maps is based on the following assumption: the variables $\{v_j\}$ are independent and Poissonian, *i.e.*,

$$P(v_j = k) = \lambda_j^k e^{-\lambda_j} / k!, \tag{2}$$

which is the H_0 hypothesis.

The H_0 hypothesis is reasonable for small time intervals. This circumstance is used by the authors of the methodology to test time-dependent forecasts. They consider $\{\lambda_j\}$ as a functions of time and at the same time extend the H_0 hypothesis to the entire phase space $G \times M \times T$ with an arbitrary T. The simplest cluster seismicity models like the Epidemic-Type Aftershock Sequence by Ogata (1998) show that the vector $\{\lambda_j(t)\}$ is stochastic and
depends on the seismicity under study up to time t. On the contrary, H_0 assumes that the time variables $\{\lambda_j(t)\}$ are independent for different t. This contradiction may cause appreciable difficulties in the testing of non-trivial time-dependent forecasts (see more in Werner and Sornette 2008, Lombardi and Marzocchi 2010).

In testing a long-term seismicity model, the H_0 hypothesis is reasonable for main shocks only, *i.e.*, the catalog needs to be declustered. This operation is not unique. Consequently, the statistical analysis should be weakly sensitive to the independence property of $\{v_j\}$ as much as possible, focusing on important parameters of the $\lambda(\Delta)$ measure.

3. TESTS

Nearly all goodness-of-fit tests of model $\{\lambda_j\}$ with data $\{v_j\}$ suggested by the RELM working group are based on the likelihood approach. The log-probability of $\{v_j\}$ under the H_0 hypothesis is

$$L = \sum l(\Delta_j),\tag{3}$$

where $l(\Delta)$ is

$$l(\Delta) = v(\Delta)\ln \lambda(\Delta) - \lambda(\Delta) - \ln v(\Delta)!\tag{4}$$

in virtue of Eq. (2); by definition, $v! = 1$ for $v = 0$.

The L-statistic (3) depends on the partition $\{\Delta_j\}$ and the model $\{\lambda(\Delta_j)\}$. The partition is an important component of the methodology, because the partition can be used to good advantage in the testing problem. The simplest examples of the partition are related to the following representation of the rate measure:

$$\lambda(\Delta) = \Lambda p(\Delta g)q(\Delta M),\tag{5}$$

where Λ is the rate of target events in G, $p(\Delta g)$ and $q(\Delta M)$ are normalized distributions of the events over space and over magnitude, respectively.

Taking the case of the trivial partition as represented by a single element $\Delta = G \times M$, we arrive at the statistic $v(\Delta) = N$. The L-statistic in this case labeled as $L(N)$ is then given by Eq. (4); the distributions of $L(N)$ and N depend on the single parameter $\Lambda = \lambda(G \times M)$, *i.e.*, N is a sufficient statistic for the analysis of Λ.

If the partition deals with magnitude only then $\Delta_j = G \times \Delta_j M$ and the L-statistic, $L(M)$, is sufficient for the analysis of the parameters $\{\Lambda q(\Delta_j M)\}$. In practice we use this partition to analyse the frequency-magnitude law.

Finally, the space partition is based on $\Delta_j = \Delta_j G \times M$; the corresponding L-statistic, $L(G)$, is sufficient for the analysis of parameters $\{\Lambda p(\Delta_j G)\}$.

The conditional distribution of $\{v_j\}$ provided $\Sigma v_j = N$ is the multinomial distribution with parameters $\{p_1,\dots,p_n; N\}$, $p_j = p(\Delta_j G)$:

$$P(v_1 = k_1,\dots,v_n = k_n \mid N) = \frac{N!}{k_1!,\dots,k_n!}p_1^{k_1},\dots,p_n^{k_n}, \qquad k_1 + \dots + k_n = N.\tag{6}$$

The respective L-statistic for the conditional distribution of $\{v_j\}$ is

$$L(G \mid N) = \sum_{j=1}^{n} v_j \ln p_j + \ln N! - \sum_{j=1}^{n} \ln(v_j!) . \qquad (7)$$

The statistics N and $L(G|N)$ enable us to perform a separate analysis of the parameters Λ and $\{p_j\}$ (see *e.g.*, Molchan and Podgaetskaya 1973, Molchan *et al.* 1997, Werner *et al.* 2010). The necessity for the separate analysis is caused by many things: the small amount of data N, catalog declustering, standardization of catalog magnitude, *etc*. (see *e.g.*, Kagan 2010, and Werner *et al.* 2011).

3.1 The significance of the *L*-test

The Monte Carlo method can be used to find the distributions of all type L-statistics under H_0. In the case $L(G|N)$ the distribution (6) corresponds to the model of N independent trials with n outcomes and probabilities $\{p_1,\ldots,p_n\}$.

The distribution of L can be used to find the observed significance level for an observed L-value, $\hat{L}$:

$$\hat{\alpha} = P\{L \leq \hat{L} \mid H_0\} .$$

In the cases L: $L(M)$, $L(G|N)$, $L(G)$ the hypothesis H_0 is rejected if $\hat{\alpha}$ is below the nominal significance level α_0 (the conventional value $\alpha_0 = 0.05$ is used). In the case of statistic N, both small and large values are suspects, so a two-sided test is used: $\min(\hat{\alpha}, 1-\hat{\alpha}) \leq \alpha_0 / 2$.

This is a standard scheme for testing any hypothesis. The key point for applications in this scheme is the choice of the test statistic.

4. WHY *L*?

To answer this question, let us discuss some peculiarities of the RELM experiment:

- ❑ In general, the number of tested models $\lambda(\Delta)$ for the same territory can be arbitrary. This is naturally due to the existence of different approaches to create such models. Some local change in a test model can be considered as a new test model. The past seismicity may only impose some integral limitation on $\lambda(\Delta)$;
- ❑ The partition $\{\Delta_j, j = 1, \ldots, n\}$ is usually very detailed, therefore n is large and the numbers of events $\{v_j\}$ are small;
- ❑ Any possible local relations between $\{\lambda_j\}$ are not used. To be specific, if the bins $\{\Delta_j\}$ are small we could assume that the λ_j are equal within some space structures.

In other words, in the RELM experiment we have to deal with the statistical problem of a large number of degrees of freedom f because usually $f = n$. The advantage of the likelihood method in such conditions is not obvious. Cox and Hinkley (1974) in their book "Theoretical Statistics" tried to formulate some general principles underlying the theory of statistical inference. One of the obstacles that impede the use of likelihood theory is worded as follows: "in considering problems with many parameters one generally focuses on a small number of components, but to do this one needs principles that are outside the **pure** likelihood theory" (Section 2.4. VIII).

In the hazard evaluation case we are interested in the accuracy of the rate measure $\lambda(\Delta)$. However, small values $\{v_j\}$ carry little information for this purpose and rejection of the $\{H_0, \lambda\}$-hypothesis does not mean that the model $\lambda(\Delta)$ is unsatisfactory. It is possible that some components of the hypothesis, *i.e.*, independence of $\{v_j\}$ or the Poisson property may be violated.

In the framework of the likelihood approach we possess a good enough tool to focus on the essentials in the rate measure. The tool in question is the partition of the phase space. For purposes of seismic risk analysis, the physically reasonable partitions with $\{v_j\}$ that are not small are preferable. The effect of small/large values of $\{v_j\}$ can be observed by examining the $L(G|N)$-statistic for $N \gg 1$.

4.1 The case of large $\{v_j\}$

Using Eq. (7) and the following the approximation

$$v! \approx (v/e)^v \sqrt{2\pi v} \tag{8}$$

for large $\{v_j\}$ and N, we can represent $L(G|N)$ as follows:

$$-N^{-1}L(G \mid N) \approx \sum_{j=1}^{n} \hat{p}_j \ln(\hat{p}_j / p_j) := \rho(\hat{P}, P), \tag{9}$$

where $x \ln x = 0$ for $x = 0$. Here, $\hat{P} = \{\hat{p}_j = v_j / N\}$ is an empirical analogue of the distribution $P = \{p_j = \lambda_j/\Lambda\}$, while $\rho(P_1, P_2)$ is the well-known Kullback–Leibler entropy distance from P_1 to P_2 (see *e.g.*, Harte and Vere-Jones 2005). This distance is non-negative but is not a metric; for example, $\rho(P_1, P_2) \neq \rho(P_2, P_1)$. It is important that $\rho(P_1, P_2) = 0$ if and only if $P_1 = P_2$.

Consistency of the L(G | N)-test

By Equation (6), we have $\hat{p}_j \to p_j^t$ as N becomes large; here $\{p_j^t\} = P^t$ is the true distribution. Consequently, $\rho(\hat{P}, P) \to \rho(P^t, P)$ for $N \gg 1$. We can use

this fact to conclude that P is the true distribution if $\rho(\hat{P}, P) \to 0$. Indeed, the relation $\rho(P^t, P) = 0$ implies $P = P^t$. In statistical terms this means that the procedure of selecting the correct model based on small values of $\rho(\hat{P}, P)$ or $|N^{-1}L(G|N)|$ is consistent (Borovkov 1984).

We remind this useful notion for the general situation. Suppose we accept the P-model when vector $\{v_j\}$ belongs to some set Ω_N. Suppose this rule guarantees that the P-probability to reject the P-model is fixed, $e.g.$, is equal to α_0. By definition, the rule is consistent if the P^t-probability to accept the P-model goes to zero as $N \to \infty$. In other words, any consistent test must reject an incorrect model almost surely as N becomes large. This natural property is highly desirable in the selection problem of the correct model.

In our case $\Omega_N = \{\rho(\hat{P}, P) < c_N\}$, where $c_N \to 0$ because the distribution of $\rho(\hat{P}, P)$, provided P is true, is concentrated close to 0 as N increases indefinitely. But then the relation $\rho(\hat{P}, P) < c_N$ is impossible for an incorrect distribution P for large enough N because the $\rho(P^t, P)$ is strictly positive.

The χ^2-test

The notion of the entropy distance from an empirical to the corresponding theoretical distribution becomes quite transparent in the case $N \gg 1$. We have $\hat{p}_j \to p_j^t$, hence

$$\ln \hat{p}_j / p_j^t \approx (\hat{p}_j - p_j^t) / p_j^t. \tag{10}$$

Using Eq. (9), we get

$$\rho(\hat{P}, P^t) \approx \sum_{j=1}^n \frac{(\hat{p}_j - p_j^t)^2}{p_j^t}. \tag{11}$$

The right-hand side of Eq. (11) is well-known as the chi-square statistic. For large N in the conditions H_0 the statistic $N\rho(\hat{P}, P^t)$ is approximately distributed as chi-square with $f = n - 1$ degrees of freedom, hence the quantity $-L(G|N) \approx N\rho(\hat{P}, P^t)$ is of the order of n.

Splitting of L(G)

Note that

$$L(G) = L(N) + L(G|N). \tag{12}$$

By Equation (4), one has $L(N) = N\varphi(\Lambda/N)$ where $\varphi(x) = \ln x - x + 1 \le 0$ and $\max \varphi(x) = \varphi(1) = 0$, $i.e.$, $L(N) > c_N$ if $|\Lambda/N - 1| > \rho$. As we have shown, the contribution of $L(G|N)$ in Eq. (12) is of order n in the case of the true

P-model. Hence, the term $L(N)$ will dominate (12), if $\{p_j\}$ is a satisfactory model but Λ is not. This circumstance emphasizes the need for separate analysis of Λ and $\{p_j\}$. In practice there are other reasons for this: the parameter Λ is very unstable because the declustering operation is not unique, and the Poisson distribution of N is questionable (Kagan 2010).

4.2 The case of small $\{v_j\}$

This case with $v_j = 0$ or 1 is typical of the RELM model experiments because of detailed space partition. As a result, one has $L(G \mid N) = N\xi_N + N\ln |\Delta| + \ln N!$ where

$$\xi_N = \frac{1}{N}\sum_{j=1}^{n} v_j \ln \dot{p}_j , \qquad v_j = 0 \ \text{or} \ 1 , \qquad \dot{p}_j = p_j/|\Delta| ,$$

and $|\Delta|$ is the bin volume. A similar representation of the likelihood function was recommended for the testing of seismicity models by Rhoades *et al.* (2011).

To analyse the situation when $N \gg 1$, the $\{v_j\}$ values and bin size are small, we have to modify the statistic ξ_N as follows:

$$\xi_N = \int \hat{p}(dg)\ln \dot{p}(g) . \tag{13}$$

Here $\hat{p}(\Delta) = v(\Delta)/N$ is the empirical distribution of the events in space, and $\dot{p}(g)$ is density of the rate model measure $p(\Delta)$. If the density is constant within the partition elements then both representation of ξ_N are identical.

The random variable ξ_N given H_0 is a sum of N independent identically distributed random variables $\ln \dot{p}(g_j)$, where g_j are random event locations in the space G with a distribution $X := x(\Delta)$; more exactly, $X = P$ for the *P*-model and $X = P^t$ for the true model. Therefore, ξ_N is approximately Gaussian with the following mean $m(X)$ and variance $\sigma^2(X)/N$:

$$m(X) = \int x(dg)\ln \dot{p}(g) , \qquad \sigma^2(X) = \int x(dg)\ln^2 \dot{p}(g) - m^2(X) .$$

Thus, the critical zone Ω_N of size approximately 95% for acceptance of model *P* looks as follows:

$$N^{-1}\xi_N > m(P) - 2\sigma(P)/\sqrt{N} . \tag{14}$$

If $m(P) = m(P^t)$, then P^t probability of Ω_N is greater than 50%. Indeed, given P^t, we have the following representation:

$$\xi_N = m(P^t) + \xi\sigma(P^t)/\sqrt{N} ,$$

where ξ is approximately a standard Gaussian variable. Substituting this relation in Eq. (14) and taking the equality $m(P) = m(P')$ into account, we have

$$P'(\Omega_N) = P\left[\xi > -2\sigma(P)/\sigma(P')\right] > P(\xi > 0) \approx 0.5 .$$

Obviously, the relation $m(P) = m(P')$ does not yield the equality $P = P'$, because this relation holds for any pair $p(\Delta)$ and $p'(\Delta) = p(\Delta) + \varepsilon\psi(\Delta)$, where ψ is orthogonal to the following functions: $\varphi_1(g) = 1$ and $\varphi_2(g) = \ln\dot{p}(g)$, i.e., $\int \psi(dg) = 0$, $\int \psi(dg)\ln\dot{p}(g) = 0$.

Hence, the likelihood approach in the case of small $\{v_j\}$ is not consistent because $P'(\Omega_N) > 0.5$ for a large enough N.

5. COMPARISON OF THE MODELS

Schorlemmer *et al.* (2007) tried to rank the tested models using pairwise comparison of the hypotheses $H^{(i)} = \{H_0, \lambda^{(i)}(\Delta)\}$. To test $H^{(1)}$ *versus* $H^{(2)}$, the statistic $R = L^{(1)} - L^{(2)}$ is used ($L^{(i)}$ is the L-statistic for the $H^{(i)}$-hypothesis). A small observed value of R under $H^{(1)}$, *i.e.*,

$$P\{R \leq \hat{R} \mid H^{(1)}\} \leq \alpha_0 ,$$

is treated as evidence for the $H^{(2)}$ model. In classical approach, the $R = L^{(1)} - L^{(2)}$ test operates with unique reference model (see the Neyman–Pearson Lemma, Cox and Hinkley 1974). On the contrary, in the CSEP/RELM approach any of tested models is considered as a reference, *i.e.*, the direction in the test procedure is lost. Therefore, the interpretation of testing results in such a case might be difficult. We now consider this point.

Proceeding as above, we shall restrict ourselves to the parameters $\{p_1,\ldots,p_n\}$ alone. The analogue of R is then the statistic $R(G|N) = L^{(1)}(G|N) - L^{(2)}(G|N)$. In virtue of Eq. (7) one has

$$N^{-1}R(G \mid N) = \sum_{j=1}^{n} \hat{p}_j \ln p_j^{(1)}/p_j^{(2)} = \sum \hat{p}_j \ln\hat{p}_j/p_j^{(2)} - \sum \hat{p}_j \ln\hat{p}_j/p_j^{(1)} ,$$

$$\text{or} \qquad N^{-1}R(G \mid N) = \rho(\hat{P}, P^{(2)}) - \rho(\hat{P}, P^{(1)}) . \qquad (15)$$

As above, $\hat{P} = \{\hat{p}_j\}$ is the empirical distribution. In contrast to the approximate relation between $L(G|N)$ and the entropy distance, Eq. (15) is exact. The fact $R(G|N) > 0$ means that the empirical distribution $\hat{P}$ is closer to $P^{(1)}$ than to $P^{(2)}$.

The linearity of $R(G|N)$ in the data $\{v_j\}$ makes it easier to estimate the distribution of this statistic (Rhoades *et al.* 2011), because for large N the quantity $N^{-1}R(G|N)$ is approximately normal and under $H^{(1)}$ has the mean

$$m = \sum_{j=1}^{n} p_j^{(1)} \ln p_j^{(1)}/p_j^{(2)} = \rho(P^{(1)}, P^{(2)}) , \tag{16}$$

and the variance σ^2/N where

$$\sigma^2 = (\sum p_j^{(1)} \ln^2 p_j^{(1)}/p_j^{(2)} - m^2) . \tag{17}$$

The following example demonstrates the difficulties arising in the $R(G|N)$ test interpretations.

Example

Let us consider a model $P^{(1)} = (p_1, p_2, \ldots, p_{n-1}, p_n)$ and the dual model $P^{(2)} = (p_n, p_2, \ldots, p_{n-1}, p_1)$; in other words, $P^{(1)}$ and $P^{(2)}$ are only different in two bins Δ_1 and Δ_n. It is convenient to use the following representation:

$$p_1^{(1)} = a + \delta , \quad p_n^{(1)} = a - \delta \quad \text{and} \quad p_1^{(2)} = a - \delta , \quad p_n^{(2)} = a + \delta ,$$

where $a > \delta$ and $a + \delta < 1$. Then

$$N^{-1}R(G \mid N) = \frac{v_1 - v_n}{N} \ln \frac{a + \delta}{a - \delta} . \tag{18}$$

Considering the case of large v_1, v_n, N we can have $R(G|N) > 0$ with $P^{(1)}$-probability greater than or equal to 0.95 for suitable parameters (a, δ, N). Indeed, according to Eqs. (16) and (17), we have with probability greater than 0.95

$$N^{-1}R(G \mid N) \geq m - 2\sigma / \sqrt{N} ,$$

where

$$m = 2\delta \ln \frac{a + \delta}{a - \delta} \quad \text{and} \quad \sigma = \sqrt{2a - 4\delta^2} \ln \frac{a + \delta}{a - \delta} .$$

The threshold $m - 2\sigma / \sqrt{N}$ is positive if $\delta^2 > 2a / (N + 4)$; for example, if $a = 0.01$, $\delta = 0.009$, and $N = 300$.

Now impose a single requirement on the true model, namely, $p_1^t = p_n^t$. Then one has $P^t(v_1 \leq v_n) = P^t(v_1 \geq v_n)$ and therefore the true distribution of the R-statistic (18) will be symmetrical. This entails instability of the inferences based on $R(G|N)$.

To show this, we proceed as follows. Suppose we observe $v_1 \leq v_n$, then we have $R(G|N) \leq 0$. Given $P^{(1)}$, the model $P^{(1)}$ will be rejected in favor of $P^{(2)}$ at confidence level 95%. That means that the relation $\rho(\hat{P}, P^{(2)}) \leq \rho(\hat{P}, P^{(1)})$ is significant under $P^{(1)}$ or briefly $(P^{(2)} \succ P^{(1)} \mid P^{(1)})$, where "$\succ$" means "better than".

Due to duality of distributions $P^{(1)}$ and $P^{(2)}$ we shall have the diametrically opposite inference, namely $(P^{(1)} \succ P^{(2)} \mid P^{(2)})$, if $v_1 \geq v_2$. Hence, in the case $v_1 = v_n$ the two models will reject each other.

The CSEP group encountered this seemingly contradictory situation empirically (Gerstenberger *et al*. 2009). Rhoads *et al*. (2011) explained it as follows: "In fact, an *R*-test rejection of model $P^{(1)}$ does not imply anything regarding the superiority of model $P^{(2)}$; it simply indicates that the observed catalogue is inconsistent with model $P^{(1)}$". The last sentence is not entirely accurate. When the $R(G|N)$ test rejects $P^{(1)}$-model relative to a reference model $P^{(2)}$, that means that $P^{(1)}$ has significant local departures from $P^{(2)}$. This does not mean, however, that $P^{(1)}$ can be far from the true distribution in the area where both models are identical, because the contribution of this area into the *R*-test is zero.

Inconsistency of the R-test

We can consider $R(G|N)$ as a possible statistic for testing the model provided $P^{(2)}$ is a reference distribution. In such a case the *R*-test will not necessarily be consistent, that is, the false model will not always be rejected as *N* becomes large.

The proof of this statement is the same as in previous Section 4.2 The key point here is the following. In the case of large $\{v_j\}$ the random variable $\xi_N = N^{-1}R(G|N)$ given (H_0, P) is approximately Gaussian with mean $m(P) = \rho(P, P^{(2)}) - \rho(P, P^{(1)})$ and variance of the type $\sigma^2(P)/N$, see Eq. (17). By arguments of Section 4.2, the *R*-test is consistent if the relation $m(P^{(1)}) = m(P^t)$ results in $P^{(1)} = P^t$. However, this is not true.

We can illustrate our assertion using the dual models $P^{(1)}$, $P^{(2)}$ (but not P^t) from our example. One has

$$m(P^t) = (p_1^t - p_n^t)\ln\frac{a+\delta}{a-\delta} \quad \text{and} \quad m(P^{(1)}) = (p_1^{(1)} - p_n^{(1)})\ln\frac{a+\delta}{a-\delta}. \qquad (19)$$

These quantities are equal if one has $p_1^t - p_n^t = p_1^{(1)} - p_n^{(1)}$ only while other bin probabilities are arbitrary.

6.   THE AREA SKILL SCORE, A_N

The area skill score test, A_N, was put forward by Zechar and Jordan (2010a, b). The test is based on the following helpful idea. Consider a family of subareas U_h of the region *G* that increases if *h* does

$$U_0 \subset U_h \subset U_{h'} \subset G, \qquad h < h'. \qquad (20)$$

For example, the family may be linked to levels of some positive function in *G*

$$U_h = \{g : u(g) \le h\}.$$

The function $u(g)$ may be specified as a prior rate of seismic events within a magnitude range.

Suppose $\hat{F}_N(h)$ gives the relative number of target events that fall in U_h for some test period. Accordingly,

$$F(h) = P(U_h) := \int_{U_h} P(\mathrm{d}g). \qquad (21)$$

is the probability of a target event falling in U_h under $\{H_0, P\}$. In this way we have reduced the problem of agreement between the data and the model to the classical problem of agreement between an empirical and a theoretical distribution. The freedom of choice for U_h allows one to focus on those elements in the models $\{P^{(i)}\}$ which are important for the investigator and to group the available observations accordingly.

The statistic A_N is defined by Zechar and Jordan (2010a) in terms of the (n, τ) diagram (Molchan 1997), but in the situation we are considering it can be represented as follows:

$$A_N - 1/2 = \int_0^\infty \left[\hat{F}_N(h) - F(h) \right] \mathrm{d}F(h). \qquad (22)$$

When N is large, the empirical distribution converges to the true distribution, $F^t(h)$, i.e., (22) $\to 0$ if $F(h) = F^t(h)$. But this is true also for any distribution of the type $F(h) = \varphi[F^t(h)]$, where $\varphi(x)$ is an arbitrary distribution on (0, 1) with mean 1/2 .This fact means that the A_N-test is not consistent. The formal way to prove the statement is the same as in Section 4.2.

Namely, the random variable $\xi_N = A_N - 1/2$ has the following representation in terms of N independent identically distributed variables $\{h_k\}$:

$$\xi_N = 1/2 - N^{-1} \sum F(h_k).$$

The distribution of h_k is $F(h)$ for the case of a P model and $F^t(h)$ for the case of the true model P^t. Thus ξ_N is asymptotically Gaussian with mean $m(P) = 0$ for the P case and

$$m(P^t) = 1/2 - \int_0^\infty F(h)\, \mathrm{d}F^t(h) = \int_0^\infty \left[F^t(h) - F(h) \right] \mathrm{d}F(h),$$

for the P^t case, while the variance of ξ_N for any model is of order $N^{-1/2}$.

We have already shown that the solution of the equation $m(P) = m(P^t)$ is not unique and is given by the formula $F(h) = \varphi[F^t(h)]$. Therefore, proceeding as in Section 4.2, we can conclude that the A-test is not consistent.

The situation can be changed by transforming Eq. (22) into a distance as follows:

$$\rho(\hat{F}, F) = \int_0^\infty |\hat{F}_N(h) - F(h)|^\alpha \, \psi[F(h)] \, dF(h),$$

where $\psi(x)$ is some weight function. The case $\alpha = 2$ with $\psi(x) = 1/x(1-x)$ or $\psi(x) = 1$ gives the well-known nonparametric ω^2-test (Bolshev and Smirnov 1983). The Kolmogorov–Smirnov (K–S) test gives us another example of distance (even a metric):

$$\rho(\hat{F}, F) = \max |\hat{F}(h) - F(h)|.$$

Rhoades *et al.* (2011) successfully applied the K–S test in the framework of the CSEP experiments.

In other words, a reasonable choice of the metric can be a natural alternative to the likelihood method. The non-trivial part of this approach consists in the choice of the sequence of subsets U_h which depend on the goals of research.

7. CONCLUSIONS

The CSEP experiment deals with testing and ranking of seismicity rate models. In this approach there is no prior limitation on the number of models, all models are a priori equally acceptable, and the number of partition elements of phase space, n, to group the data is large. Under these conditions the advantage of the likelihood (LH) method that is used as the main tool is not obvious.

We analyzed theoretically the LH method in two particular cases: (i) numbers of events $\{v_j\}$ in space bins are large, which can be of interest for testing the long-term seismicity maps, and (ii) the $\{v_j\}$ are small, which is typical of the CSEP experiments. In the second case, LH method loses a highly desirable property, namely, statistical consistency. In other words, there exist nontrivial models which cannot be classified as wrong by the LH method as the number of observations N becomes large. The same is true regarding the other tests being used under the less stringent limitations on $\{v_j\}$ (the R and the Area Skill Score tests).

The case of small $\{v_j\}$ arises from the detailed partition of the phase space, *i.e.*, when n is large. As a result, an additional undesirable property of the test methodology appears. The testing procedure is based on the rate model and on the assumption of independence of the variables $\{v_j\}$. Selection of the correct rate model is the most important part of the testing while the independence property is usually questionable. The greater n is, the more the independence property affects on the statistical conclusions. Consequently the statistical test analysis should be as weakly sensitive to this property as

possible, focusing on important elements of the rate measure. Practically this is achieved by (i) a physically reasonable coarsening of the phase space, and (ii) by choosing a suitable measure of closeness between empirical and model seismicity rate in the space. A formal realization of this idea is presented in Section 6 as a generalization of the Area Skill Score test.

R e f e r e n c e s

Bolshev, L.N., and N.V. Smirnov (1983), *Mathematical Statistical Tables*, Nauka, Moscow (in Russian).

Borovkov, A.A. (1984), *Mathematical Statistics: Estimation of Parameters, Testing Hypotheses*, Nauka, Moscow (in Russian).

Cox, D.R., and D.V. Hinkley (1974), *Theoretical Statistics*, Chapman and Hall, London.

Field, E.H. (2007), Overview of the Working Group for the development of Regional Earthquake Likelihood Models (RELM), *Seismol. Res. Lett.* **78**, 1, 7-16, DOI: 10.1785/gssrl.78.1.7.

Gerstenberger, M.C., D.A. Rhoades, M.W. Stirling, R. Brownrigg, and A. Christophersen (2009), Continued development of the New Zealand Earthquake Forecast Testing Centre, GNS Science Consultancy Report 2009/182, GNS Science, Lower Hutt.

Giardini, D. (1999), The Global Seismic Hazard Assessment Program (GSHAP) – 1992/1999, *Ann. Geophys.* **42**, 6, 957-974.

Harte, D., and D. Vere-Jones (2005), The entropy score and its uses in earthquake forecasting, *Pure Appl. Geophys*. **162**, 6-7, 1229-1253, DOI: 10.1007/s00024-004-2667-2.

Kagan, Y.Y. (2010), Statistical distributions of earthquake numbers: consequence of branching process, *Geophys. J. Inter*. **180**, 3, 1313-1328, DOI: 10.1111/j.1365-246X.2009.04487.x.

Lombardi, A.M., and W. Marzocchi (2010), The assumption of Poisson seismic-rate variability in CSEP/RELM experiments, *Bull. Seismol. Soc. Am*. **100**, 5A, 2293-2300, DOI: 10.1785/0120100012.

Molchan, G.M. (1997), Earthquake prediction as a decision-making problem, *Pure Appl. Geophys.* **149**, 1, 233-247, DOI: 10.1007/BF00945169.

Molchan, G.M., and V.M. Podgaetskaya (1973), Parameters of global seismicity, *Comput. Seismol.* **6**, 44-66 (in Russian).

Molchan, G., T. Kronrod, and G.F. Panza (1997), Multi-scale seismicity model for seismic risk, *Bull. Seismol. Soc. Am*. **87**, 5, 1220-1229.

Ogata, Y. (1998), Space-time point-process models for earthquake occurrences, *Ann. Inst. Statist. Math*. **50**, 2, 379-402, DOI: 10.1023/A:1003403601725.

Rhoades, D.A., D. Schorlemmer, M.C. Gerstenberger, A. Christophersen, J.D. Zechar, and M. Imoto (2011), Efficient testing of earthquake forecasting models, *Acta Geophys*. **59**, 4, 728-747, DOI: 10.2478/s11600-011-0013-5.

Schorlemmer, D., M.C. Gerstenberger, S. Wiemer, D.D. Jeckson, and D.A. Rhoades (2007), Earthquake likelihood model testing, *Seismol. Res. Lett.* **78**, 17-29, DOI: 10.1785/gssrl.78.1.17.

Schorlemmer, D., J.D. Zechar, M.J. Werner, E.H. Field, D.D. Jackson, T.H. Jordan, and the RELM Working Group (2010), First results of the regional earthquake likelihood models experiment, *Pure Appl. Geophys*. **167**, 8-9, DOI: 10.1007/s0024-010-0081-5.

Werner, M.J., and D. Sornette (2008), Magnitude uncertainties impact seismic rate estimates, forecasts, and predictability experiments, *J. Geophys. Res*. **113**, B08302, DOI: 10.1029/2007JB005427.

Werner, M.J, J.D. Zechar, W. Marzocchi, S. Wiemer, and the CSEP-Italy Working Group (2010), Retrospective evaluation of the five-year and ten-year CSEP-Italy earthquake forecasts, *Ann. Geophys*. **53**, 3, 11-30, DOI: 10.4401/ag-4840.

Werner, M.J., A. Helmstetter, D.D. Jackson, and Y.Y. Kagan (2011), High resolution long-term and short-term earthquake forecasts for California, *Bull. Seismol. Soc. Am*. **101**, 4, 1630-1648, DOI: 10.1785/0120090340.

Zechar, J.D., and T.H. Jordan (2010a), The area skill score statistic for evaluating earthquake predictability experiments, *Pure Appl. Geophys*. **167**, 8-9, 893-906, DOI: 10.1007/ s00024-010-0086-0.

Zechar, J.D., and T.H. Jordan (2010b), Simple smoothed seismicity earthquake forecasts for Italy, *Ann. Geophys*. **53**, 3, 99-105, DOI: 10.4401/ag-4845.

Zechar, J.D., M.C. Gerstenberger, and D.A. Rhoades (2010), Likelihood-based tests for evaluating space-rate-magnitude earthquake forecasts, *Bull. Seismol. Soc. Am*. **100**, 3, 1184-1195, DOI: 10.1785/0120090192.

A Statistical Damage Model
with Implications for Precursory Seismicity

Ya-Ting LEE[1,2], Donald L. TURCOTTE[2], John B. RUNDLE[2,3],
and Chien-Chih CHEN[1]

[1]Graduate Institute of Geophysics, National Central University, Jhongli, Taiwan
e-mails: shine2530@gmail.com (corresponding author), chencc@earth.ncu.edu.tw

[2]Department of Geology, University of California, Davis, CA, USA
e-mails: dlturcotte@ucdavis.edu, jbrundle@ucdavis.edu

[3]Department of Physics, University of California, Davis, CA, USA

A b s t r a c t

Acoustic emissions prior to rupture indicate precursory damage. Laboratory studies of frictional sliding on model faults feature accelerating rates of acoustic emissions prior to rupture. Precursory seismic emissions are not generally observed prior to earthquakes. To address the problem of precursory damage, we consider failure in a fiber-bundle model. We observe a clearly defined nucleation phase followed by a catastrophic rupture. The fibers are hypothesized to represent asperities on a fault. Two limiting behaviors are the equal load sharing $p = 0$ (stress from a failed fiber is transferred equally to all surviving fibers) and the local load sharing $p = 1$ (stress from a failed fiber is transferred to adjacent fibers). We show that precursory damage in the nucleation phase is greatly reduced in the local-load sharing limit. The local transfer of stress from an asperity concentrates nucleation, restricting precursory acoustic emissions (seismic activity).

Key words: earthquake precursors, acoustic emissions, fiber-bundle model, rupture, nucleation.

1. INTRODUCTION

A magnitude $M_w = 6.0$ earthquake occurred on the Parkfield segment of the San Andreas fault on 28 September 2004. This was the most recent in a sequence of $M \approx 6.0$ earthquakes that have occurred on this segment with mean intervals of about 30 years. In expectation of this event, a dense array of instruments were deployed to study all aspects of the earthquake. Seismometers were installed to monitor any precursory seismic activity. No precursory seismic activity was observed on or near the rupture surface. The instrument sensitivity extended down to at least an $M = 1$ earthquake (Bakun *et al*. 2005).

The object of this paper is to study the physical processes responsible for precursory seismicity. Two examples of precursory seismicity have received considerable attention. The first of these are foreshocks. Extensive statistical studies have shown that the magnitudes of most foreshocks are very nearly as large as the subsequent mainshocks (Savage and dePolo 1993). In addition, the times of occurrence of the foreshocks are quite close to the times of the mainshocks (Agnew and Jones 1991). These observations have led to the working hypothesis that a foreshock is an aftershock that had a magnitude larger than the magnitude of the original mainshock (Helmstetter and Sornette 2003). About 5% of earthquakes have foreshocks (Reasenberg 1999). No foreshocks occurred prior to the 2004 Parkfield earthquake.

A second example of observed precursory seismicity is accelerated moment release (AMR) (Bowman *et al*. 1998). There is considerable evidence that there may be an increase in the number of intermediate-sized earthquakes prior to some large earthquakes. This precursory seismicity occurs over periods of years and accelerates in frequency prior to the large earthquake. The region over which this seismicity occurs appears to scale as a correlation length which is a function of the magnitude of the large earthquake. Earthquakes associated with foreshocks and AMR occur on faults other than the fault on which the subsequent large earthquake occurs. In this paper our concern is the occurrence of precursory seismicity on the fault zone on which a large earthquake subsequently occurs. No such seismicity was observed prior the 2004 Parkfield earthquake. We propose a model for the physics of material failure associated with an earthquake.

Our understanding of the physics of material failure is largely based on laboratory experiments. The Parkfield earthquake occurred on a well defined fault, the San Andreas, that had been subject to many previous ruptures. It is generally hypothesized that fault ruptures occur when the applied shear stress exceeds the "static" coefficient of friction. Many laboratory studies of frictional sliding on model faults have been carried out (Marone 1998). Probably the most relevant in terms of precursory damage prior to failure was carried out by Weeks *et al*. (1978). A large granite block containing

a through-going saw cut was confined at pressures up to 100 MPa. Under constant stress-rate loading, fourteen violent slip events occurred. Some 8000 microseismic events also occurred. A systematic increase in the rate of microseismic events was observed prior to each major slip event. These events satisfied a power-law frequency-amplitude scaling to a good approximation.

The granite blocks constituted rigid elastic half spaces with near uniform properties. The frictional resistance of the saw cut can be attributed to "asperities" (points of contact) across the saw cut. These asperities can be assumed to have a range of scales and strengths. When an asperity fails, the stress carried by the asperity is transferred to other asperities. The physics of this stress transfer is a major focus of this paper. The precursory acoustic emissions can be associated with failure of weak "asperities" (points of contact). A major question in earthquake physics is: Why do we not observe asperity failures (small earthquakes) prior to an event such as the Parkfield earthquake?

Before presenting our model for earthquake rupture it is appropriate to discuss the relevance of these laboratory studies to earthquake ruptures. It is generally accepted that friction is the applicable rheology for faults. However, there are differences between the laboratory conditions and the conditions of a fault. In the laboratory, normal stresses are much lower and the rates of strain are much higher. In addition, the role of fluids in terms of fluid pressure and chemical healing of a fault are not duplicated. Thus caution must be exercised in relating the laboratory experiments to earthquakes.

In this paper we restrict our earthquake discussion to the precursory behavior prior to the 2004 Parkfield earthquake because of the very sensitive seismic network adjacent to the rupture which provides the best available evidence for the absence of precursory small earthquakes. We have restricted our discussion of laboratory experiments to those of Weeks *et al*. (1978) because they most closely simulate the earthquake rupture.

The basic observation we address in this paper is the absence of small earthquakes on a fault prior to a large earthquake. This is not the case for the laboratory experiments discussed above, in which a large number of microseismic events preceded rupture. In order to provide an answer to this question, we will consider a discrete model for the behavior of asperities on a rupture surface. Several discrete models for faults have been proposed. The first large-scale model was studied by Carlson and Langer (1989). These authors considered a long linear array of slider blocks; each block was attached to a constant velocity driver plate by loader springs, spring constant K_L, and was connected to the two adjacent blocks with connector springs, spring constant K_c. They used a velocity weakening friction law and considered up to 400 blocks. Slip events involved various numbers of blocks. The frequency-size distribution of events was found to satisfy power-law scaling. Many

other slider-blocks simulations have been carried out with similar results. This work has been reviewed by Turcotte (1999). A near uniform behavior is found under a wide range of conditions. This behavior is controlled by the ratio of spring constants

$$\gamma = \frac{K_C}{K_L} .$$ (1)

If γ is very small, single block failures dominate; as γ is increased a power-law frequency-size distribution of small events develops but no large events occur. The ratio of spring constants γ can be increased until the power-law distribution extends across the entire array; this is taken to be a critical point, and γ is the turning parameter. As γ is increased further, system wide events occur with a power-law distribution of small events. In the limit $\gamma \to \infty$ only system wide events occur (Turcotte *et al.* 2007). There are similarities between the large γ slider-block model and the experiments described above. However, a systematic acceleration of small slip events prior to a large event is not seen.

In this paper we will model fault rupture using a fiber-bundle model. We associate the fibers with asperities on a fault. We will consider in some detail the relation of the fiber-bundle model to the slider-block model in the Appendix. Fiber-bundle models have been widely used to model material failure (Pradhan *et al.* 2010), specifically for composite materials. Two types of fiber-bundle models have been proposed. The first is a static model in which the failure strength of each fiber is specified from a statistical distribution (Daniels 1945). There is no time dependence in this model, a fiber fails instantaneously when the stress on the fiber is equal to or greater than the prescribed failure strength. The second type of model is dynamic and time dependent. A time to failure is specified for each fiber from a statistical distribution. These failure times are strongly stress dependent (Coleman 1958).

It is also necessary to specify how the stress from a failed fiber is redistributed to other fibers. One extreme case is an equal load sharing. The stress from a failed fiber is redistributed equally to all surviving fibers. The other extreme case is a local load sharing. The stress from a failed fiber is redistributed equally to adjacent fibers. Fiber-bundle models have been reviewed by Phoenix and Newman (2009).

An important distinction between slider-block and fiber-bundle models is healing. In the standard slider-block model, the surface heals after a slip event and multiple slip events involving a block can occur. In the standard fiber-bundle model, the fiber is removed from the system when it fails and cannot carry a stress again.

Our objective is to model the failure of asperities on a fault during stress accumulation. We make the hypothesis that when an asperity fails it does not

restick and therefore we utilize the fiber-bundle model in preference to the slider-block model. Since stress accumulation on a fault is a slow process we choose the static model and specify the distribution of the strengths of the fibers (asperities). We find the variability of these strengths (coefficient of variation representing material heterogeneity) to be an important parameter. Redistribution of stress from a failed fiber is also important. Two extremes are the uniform load sharing (the load is redistributed uniformly to surviving fibers) and the local load sharing (load is redistributed to adjacent fibers). We associate the near uniform load sharing with the laboratory experiments described above due to the rigidity of the granite matrix. We associate the local load sharing with actual faults due to the damaged matrix in which they are embedded. We will show that precursory failures are fewer with local load sharing than with uniform load sharing.

There have been extensive discussions in the physics literature whether the transition from nucleation to rupture is a phase change. This work has been reviewed by Alava *et al.* (2006) and Pradhan *et al.* (2010). The thermodynamics of fiber-bundle models has been discussed by Pride and Toussaint (2002). Central to this work is the definition of temperature for the problem. Fluctuations can be introduced but they do not follow naturally from the basic fiber-bundle model.

A relevant set of laboratory experiments have been carried out by Garcimartin *et al.* (1997) and by Guarino *et al.* (1998, 1999, 2002). These authors studied the failure of circular panels (222 mm diameter, 3-5 mm thickness) of chipboard. A differential pressure across the panel was (1) increased linearly in time until failure occurred, or (2) increased instantaneously and held constant until failure occurred. The use of chipboard introduced a relatively soft material with interacting fibers similar to our fault model. Precursory micro fractures occurred. Initially, the micro fractures occurred randomly but they subsequently coalesced in the region of subsequent rupture initiation. Precursory acoustic emissions occurred similar in form to those illustrated in Fig. 4b. We conclude that the near uniform tension hoop stresses in the panels result in a near uniform stress distribution from failed fibers.

Scorretti *et al.* (2001) and Ciliberto *et al.* (2001) discussed the failure behavior of the chipboard in terms of a fiber-bundle model. They argued that the dominant feature is a random (thermal) distribution of stresses. The heterogeneous stress field is not due to thermalization but rather due to the stress interactions in the heterogeneous chipboard. Their explanation would appear also applicable to earthquakes on faults. The heterogeneous nature of the earth's crust due to distribution of faults and joints on all scales leads to a strongly heterogeneous stress field. This heterogeneous stress field masks the build up of stress during the tectonic earthquake cycle, as discussed above.

2. FIBER-BUNDLE MODEL

Our model consists of a square array of n_0 fibers, as illustrated in Fig. 1. A load F_0 is applied to the array and the mean stress on the fibers $\overline{f}$ is given by

$$\overline{f} = \frac{F}{n_0} \,. \tag{2}$$

The failure force for each fiber i, f_{fi}, is specified by a statistical distribution of failure forces. Based on many studies, we choose the Weibull distribution (Weibull 1951, Meeker and Escobar 1998). The unique property of the Weibull distribution is the scale-invariant, power-law behavior of its hazard function. The cumulative distribution function (cdf) for this distribution is given by

$$P\left(f_{fi}\right) = 1 - \exp\left[-\left(\frac{f_{fi}}{f_0}\right)^{\beta}\right], \tag{3}$$

where f_0 is a reference failure force and β is the power-law exponent. The mean $\overline{f}$, standard deviation σ, and coefficient of variation C_v of the Weibull distribution are given by
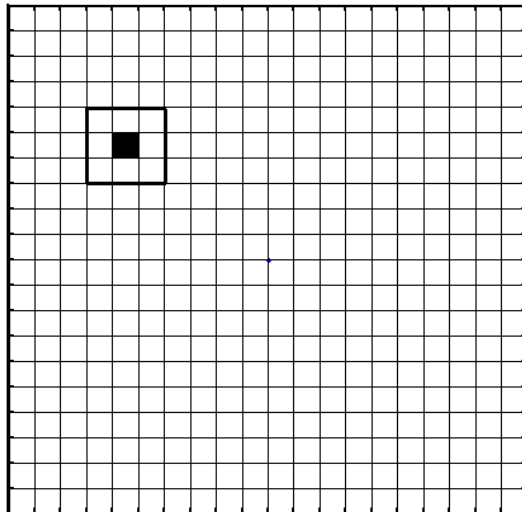
Fig. 1. Illustration of the model. A square array of fibers is considered with L fibers on a side. For the example shown $L = 20$ so the original number of fibers is $n_0 = 20^2 = 400$. The load on the fibers is increased until the weakest fiber fails, this is indicated by the solid square. A local load sharing region is defined, for the case illustrated $r = 1$ and the number of fibers in this region is n_{rd} 8 as given by Eq. (7).

$$\overline{f} = f_0 \Gamma \left(1 + 1/\beta \right) , \tag{4}$$

$$\sigma = f_0 \left\{ \Gamma \left(1 + 2/\beta \right) - \left[\Gamma \left(1 + 1/\beta \right) \right]^2 \right\}^{1/2} , \tag{5}$$

$$C_v = \frac{\sigma}{\overline{f}} = \left\{ \frac{\Gamma \left(1 + 2/\beta \right)}{\left[\Gamma \left(1 + 1/\beta \right) \right]^2} - 1 \right\}^{1/2} . \tag{6}$$

When $\beta = 1$, the Weibull distribution reduces to the exponential distribution. In the limit $\beta \to \infty$ all fibers fail at the reference failure force f_0. The applicability of the Weibull distribution to the failure of fibers has been established directly by experimental studies (Pradhan *et al*. 2010).

We determine the failure strength of the fibers is in our fiber bundle randomly. For each fiber, a random number P_i in the range 0 to 1 is chosen. Using this random number, the failure force f_{fi}/f_0 is obtained from Eq. (3). The first fiber fails at $f_{fi} = f_{f\min}$, the smallest failure stress. The force on the array is increased until $f = f_{f\min}$, and the weakest fiber fails. The failed fiber is removed from the array and the force on this fiber $f_{f\min}$ is redistributed onto the surviving fibers, the total force on the array F remains constant.

The redistributed force is divided into two parts. A fraction p is redistributed equally to all surviving fibers within a range of interaction r (Kun *et al*. 2000). The parameter p is a measure of the stiffness of the system. A stiff system has p near zero and a soft system has p near unity. If the medium in which a fault is embedded behaves elastically then the stress is redistributed according to the laws of elasticity. However, actual faults are embedded in a damaged region. Transfers of stress induce displacements on the ensemble of embedded faults. The result is that the matrix is relatively soft.

The concept of local load shearing is illustrated in Fig. 1 with $r = 1$. This local load sharing is carried out over a square region with $2r + 1$ fibers on a side. The number of fibers n_{rd} over which this fraction of the failed load is redistributed is

$$n_{rd} = \left(2r + 1 \right)^2 - 1 . \tag{7}$$

For example, in Fig. 1, $n_{rd} = 8$. Each of these n_{rd} fibers has an increase in force Δf_{lls} given by

$$\Delta f_{lls} = \frac{p f_{f\min}}{n_{rd}} . \tag{8}$$

In subsequent redistributions, some of the fibers in the local load sharing region may have been removed due to previous failures. In this case, the stress is redistributed to the surviving fibers. In terms of the fiber-bundle model, local load sharing takes into account the frictional transfer of stress to adjacent fibers when a fiber fails.

The other redistribution fraction $(1 - p)$ is distributed equally to all surviving fibers. This is uniform load sharing. For the failure of the first fiber each of the $n_0 - 1$ surviving fibers has an increase in force Δf_{els} given by

$$\Delta f_{els} = \frac{(1-p)f_{f\,min}}{(n-1)} .$$ (9)

The fibers within the square local load sharing region receive both contributions. The limit $p = 0$ is the uniform load sharing. A fiber does not interact with other fibers and when it fails its stress is redistributed equally to all other fibers. This equal redistribution of stresses would be appropriate for the granite block experiments carried out by Weeks *et al.* (1978) and discussed above. This would be a very stiff system. In order to specify our problem we require: (1) array size n_0, (2) range of interaction r, (3) measure of load sharing p, and (4) Weibull exponent β. As a measure of the applied load we consider the mean load per original fiber as given in Eq. (2). We further assume that the applied load $F(t)$ increases linearly with time t and write

$$\overline{f} = f_0 \frac{t}{t_0} ,$$ (10)

where t_0 is a reference time and f_0 is the reference failure force introduced in Eq. (3).

3. MEAN-FIELD SOLUTION

To illustrate our fiber-bundle model we first consider the mean-field (uniform-load sharing) limit $p = 0$. In this case we can obtain an analytic solution. In the mean-field limit, the forces $f(t)$ on the surviving fibers are equal. The number of surviving fibers is $n(t)$. From Eq. (3) we note that in the limit $\beta \rightarrow \infty$ all fibers fail at the reference fiber load f_0. Thus from Eq. (10) we see that the failure of the array in this limit occurs at $t = t_0$. We will obtain our solutions as a function of the nondimensional time t/t_0.

In order to quantify the failure of our fiber bundle we introduce the concept of damage mechanics (Krajcinovic 1996). The damage variable α is defined by

$$E = E_0(1-\alpha) ,$$ (11)

where E is Young's modulus during failure and E_0 is the original reference value of Young's modulus. The damage variable α quantifies the deviation from linear elasticity due to damage such as microcracks. For our fiber-bundle array with equal load sharing we have

$$\alpha = 1 - \frac{n}{n_0} .$$ (12)

This follows from the relation

$$E = E_0 \frac{n}{n_0} .$$

(13)

A primary objective of our studies is to obtain $\alpha(t/t_0)$.

We first write a force balance for the array with equal-load sharing. This is given by

$$F = n_0 \overline{f} = nf .$$

(14)

Since the fiber force f is the same for all fibers, the number of surviving fibers is related to the fiber force by Eq. (3) with the result

$$\frac{n}{n_0} = \exp\left[-\left(\frac{f}{f_0}\right)^{\beta}\right].$$

(15)

Combining Eqs. (10) and (14) gives

$$\frac{\overline{f}}{f_0} = \frac{f}{f_0} \frac{n}{n_0} = \frac{t}{t_0} .$$

(16)

Combining this with Eq. (16) gives

$$\frac{t}{t_0} = \frac{f}{f_0} \exp\left[-\left(\frac{f}{f_0}\right)^{\beta}\right].$$

(17)

This equation gives f/f_0 as a function of t/t_0. It is important to note that for each value of t/t_0 there are two values of f/f_0. This will be illustrated below. From Eqs. (12) and (16) we have

$$\alpha = 1 - \frac{n}{n_0} = 1 - \frac{t}{t_0} \frac{f_0}{f} ,$$

(18)

which can be used to obtain α as a function of t/t_0. The dependence of α on t/t_0 is given in Fig. 2 for $\beta = 2$, 6, and 10. We see that the damage increases slowly to a maximum critical value of α, α_c, at which time, t_c, the total failure occurs catastrophically. The increase in damage from $\alpha = 0$ at $t = 0$ to $\alpha = \alpha_c$ at $t = t_c$ is a nucleation phase and the increase in damage from $\alpha = \alpha_c$ to $\alpha = 1$ at $t = t_c$ is a rupture phase. This transition can be associated with a second-order phase change since $d\alpha/dt$ is continuous but $d^2\alpha/dt^2$ is discontinuous. As noted above, there are two values of α for each value of t/t_0. The upper values shown as dashed lines are not physical. When $d\alpha/dt \rightarrow \infty$ the value of α increases instantaneously, as shown by the solid lines in Fig. 2.
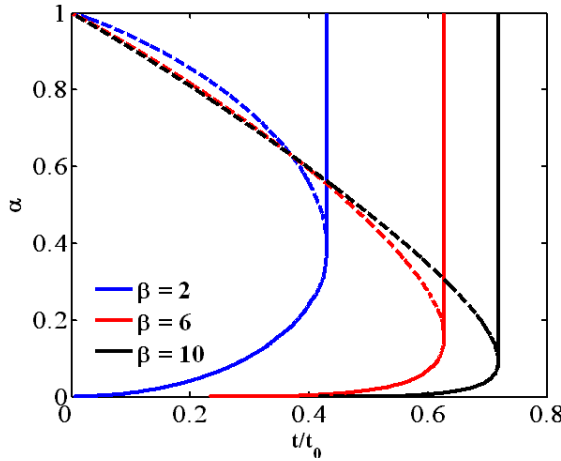
Fig. 2. The dependence of the damage variable α on the nondimensional time t/t_0 in the uniform load sharing (mean field) limit with $\beta = 2$, 6, and 10. The transition from the nucleation phase to the rupture phase occurs when $d\alpha/dt \to \infty$ with $\alpha = \alpha_c$ and $t = t_c$. The vertical lines represent the rupture phase, the dashed lines are solutions of Eq. (18) but are not physical.

We can obtain simple analytic expressions for the critical failure time t_c and the corresponding value of damage α_c. As can be seen in Fig. 2 we have $d\alpha/dt = \infty$ at this critical point. This corresponds to the condition $df/dt = \infty$ or $dt/df = 0$. Taking the derivative of Eq. (17) we obtain

$$\frac{f_0}{t_0}\frac{dt}{df} = \exp\left(-\frac{f}{f_0}\right)^{\beta}\left[1 - \beta\left(\frac{f}{f_0}\right)^{\beta}\right] = 0 , \tag{19}$$

which gives

$$\frac{f_c}{f_0} = \left(\frac{1}{\beta}\right)^{1/\beta} . \tag{20}$$

And from Eq. (17) we have

$$\frac{t_c}{t_0} = \left(\frac{1}{\beta}\right)^{\frac{1}{\beta}}\exp\left(-\frac{1}{\beta}\right) . \tag{21}$$

Combining Eqs. (18), (20), and (21) gives

$$\alpha_c = 1 - \exp\left(-\frac{1}{\beta}\right) . \tag{22}$$

For the examples considered in Fig. 2 we have for $\beta = 2$, 6, and 10, $f_c/f_0 = 0.707$, 0.742, and 0.794; $t_c/t_0 = 0.429$, 0.628, and 0.719; and $\alpha_c = 0.393$, 0.154, and 0.095.

Although we have a critical failure of the array, we do not have a propagating fracture. In the equal load sharing (mean field) limit failures are spatially random. There is no localization and nucleation of a propagating rupture.

It is also of interest to determine the energy dissipated by fiber failure. We assume that the energy dissipated is the elastic energy in the fiber just prior to failure. We associate this energy with acoustic emissions and seismic energy. Our objective is to determine the time dependence of the dissipated energy during the nucleation phase and the relative magnitudes of energy dissipated during the nucleation phase and the rupture phase.

We will again define a reference failure energy E_0 in the limit $\beta \to \infty$. In this limit all fibers fail at the reference fiber load f_0. The energy dissipated when a fiber fails at this load e_0 is given by the elastic energy in the fiber at this load

$$e_0 = \frac{A_f L_f \sigma_0^2}{2E_f} \; , \tag{23}$$

where A_f is the fiber area, L_f is the fiber length, E_f is Young's modulus of the fiber, and σ_0 is the fiber failure stress. Using the relation

$$f_0 = A_f \sigma_0 \; . \tag{24}$$

Equation (23) can be written as

$$e_0 = \frac{L_f f_0^2}{2A_f E_f} \; . \tag{25}$$

The total energy associated with the failure of the fiber bundle in the limit $\beta \to \infty$, E_0 is given by

$$E_0 = n_0 e_0 = \frac{A_f L_f \sigma_0^2 n_0}{2E_f} \; . \tag{26}$$

The energy dissipated when a fiber fails at the load f is given by

$$e_f = \frac{L_f f^2}{2A_f E_f} \; . \tag{27}$$

Using Eqs. (25) and (27) we introduce the nondimensional failure energy

$$\frac{e_f}{e_0} = \left(\frac{f}{f_0} \right)^2 \; . \tag{28}$$

We now apply this result to our mean-field fiber bundle failure. In this case all fibers have the same force $f(t)$. We next determine the cumulative energy E dissipated in the fiber bundle as it fails. We consider the nondimensional ratio E/E_0 which is given by

$$\frac{E}{E_0} = \frac{1}{n_0} \int_{t=0}^{t/t_0} \frac{e_f}{e_0} \, dn \; . \tag{29}$$

Taking the derivative of Eq. (15) we obtain

$$\frac{1}{n_0} \frac{dn}{d(f/f_0)} = \beta \left(\frac{f}{f_0}\right)^{\beta-1} \exp\left[-\left(\frac{f}{f_0}\right)^{\beta}\right]. \tag{30}$$

Substitution of Eqs. (28) and (30) into Eq. (29) gives

$$\frac{E}{E_0} = \beta \int_0^{f/f_0} \left(\frac{f}{f_0}\right)^{\beta+1} \exp\left[-\left(\frac{f}{f_0}\right)^{\beta}\right] d\left(\frac{f}{f_0}\right). \tag{31}$$

Making the substitution

$$s = \left(\frac{f}{f_0}\right)^{\beta} . \tag{32}$$

Equation (31) can be written as

$$\frac{E}{E_0} = \beta \int_0^{(f/f_0)^{\beta}} s^{\frac{2}{\beta}} e^{-s} ds = \beta \gamma \left[\left(\frac{2}{\beta}+1\right), \left(\frac{f}{f_0}\right)^{\beta}\right], \tag{33}$$

where γ is the lower incomplete gamma function (Abramowitz and Stegun 1972).

From Eqs. (17) and (31) we obtain E/E_0 as a function of t/t_0.
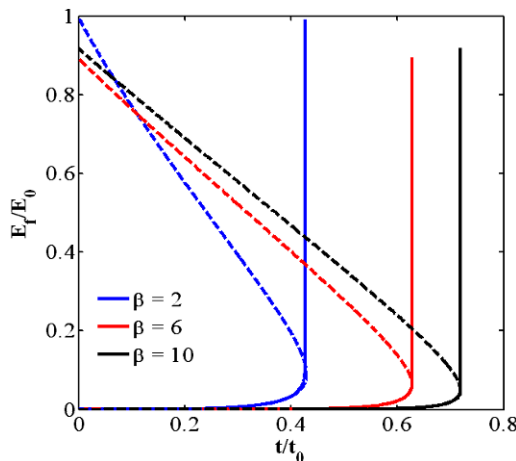
Fig. 3. Dependence of the nondimensional accumulative energy dissipated E_f/E_0 on the nondimensional time $t = t_0$ in the uniform load sharing (mean field, $p = 0$) limit with $\beta = 2$, 6, and 10. The transition from the nucleation phase to the rupture phase occurs when $dE_f/dt \rightarrow \infty$ with $E_f = E_n$ and $t = t_c$. The vertical lines represent the rupture phase, the dashed lines are solutions of Eq. (17) and (31) but are not physical.

The dependence of the cumulative energy dissipated E/E_0 on t/t_0 is given in Fig. 3 for $\beta = 2$, 6, and 10. The nucleation and rupture phases are clearly illustrated. The energy dissipated during the nucleation phase E_n is associated with precursory fiber failures or foreshocks. The energy dissipated during the rupture phase E_r is associated with the propagating rupture or main shock. For $\beta = 2$ we have $E_n/E_0 = 0.097$ and $E_r/E_0 = 0.893$ so that $E_n/E_r = 0.109$, about 10% of the energy is dissipated in the nucleation phase. For $\beta = 6$ the values are $E_n/E_0 = 0.064$, $E_r/E_0 = 0.830$, and $E_n/E_r = 0.072$. For $\beta = 10$ we have $E_n/E_0 = 0.049$, $E_r/E_0 = 0.870$, and $E_n/E_r = 0.056$.

4. SIMULATIONS

In order to understand the behavior of our model we have carried out a sequence of numerical simulations. All simulations are carried out on a square array of width 150 so that the original number of fibers is $n_0 = 150^2 = 22\,500$. Our simulations will also be restricted to the range of interaction $r = 1$. Results will be given for power-law exponents $\beta = 2$, 6, and 10 and a range of values of the redistribution parameter p. Varying the range of interaction r gives results similar to those obtained by varying the redistribution parameter p.

In Figure 4 nucleation and propagation of the rupture are illustrated for several typical examples. The distributions of failed fibers (dark areas) are given for increasing values of the damage variable. The lowest value of the damage variable, $\alpha = 0.07$ in Fig. 4a, is during the nucleation phase. The second value of the damage variable, $\alpha_c = 0.145$ in Fig. 4a, is at the critical transition from nucleation to rupture. The largest value of the damage variable, $\alpha = 0.3$ in Fig. 4a, is during the propagation phase. Note that periodic boundary conditions are assumed so that when the propagating fracture reaches the top boundary of the array its extension appears at the lower boundary. The amount of damage during the nucleation phase decreases with increasing value of p and β.

It is also of interest to study the distribution of cluster areas at the critical transition from nucleation to propagation. In Figure 5 we give the cumulative number of clusters N_{cc} with areas greater than A_c for the four examples given in Fig. 4. The cluster area A_c is taken to be the number of adjacent fibers that have failed. We compare our data in Fig. 5 with the power-law scaling relation

$$N_{cc} = CA_c^{-D/2} \; . \tag{34}$$

We find quite good scaling taking the fractal dimension $D = 4$. Hemmer and Hansen (1992) found a similar dependence for their fiber bundle studies taking $D = 3$.
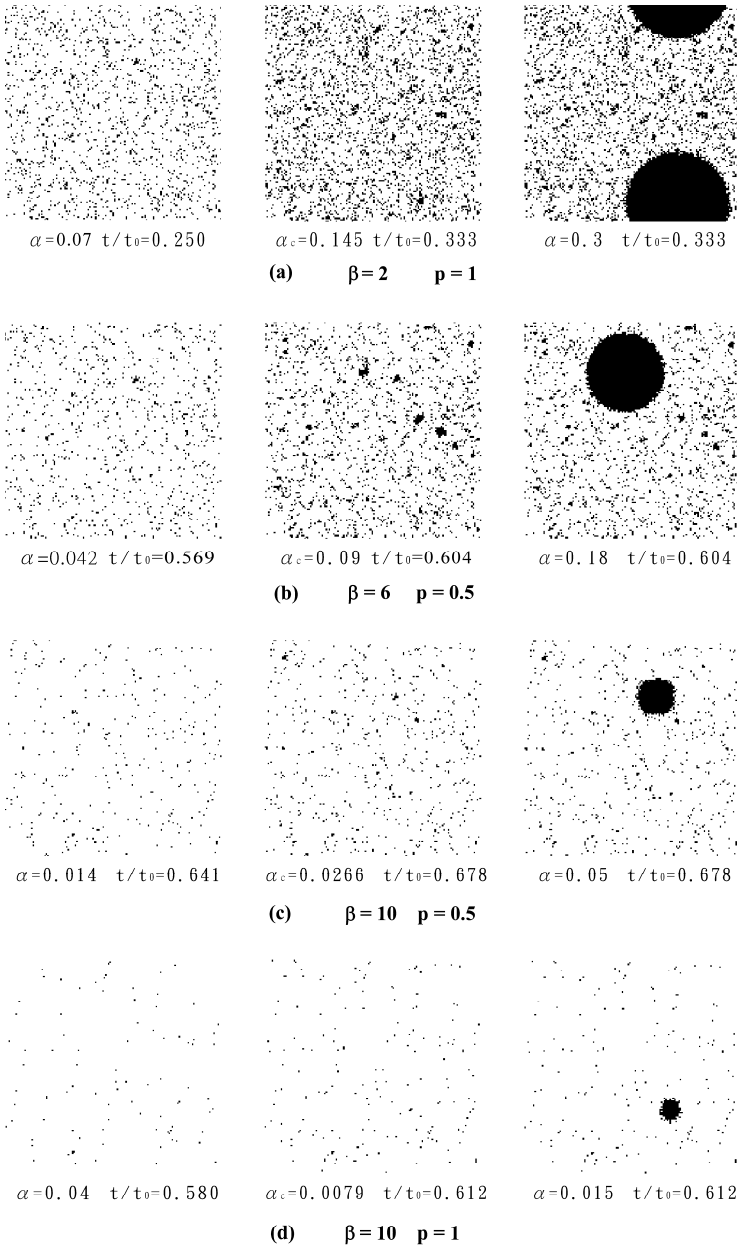
$\alpha = 0.07$ t/t$_0$=0.250 α_c=0.145 t/t$_0$=0.333 α=0.3 t/t$_0$=0.333

(a)   β = 2   p = 1

α=0.042 t/t$_0$=0.569 α_c=0.09 t/t$_0$=0.604 α=0.18 t/t$_0$=0.604

(b)   β = 6   p = 0.5

α=0.014 t/t$_0$=0.641 α_c=0.0266 t/t$_0$=0.678 α=0.05 t/t$_0$=0.678

(c)   β = 10   p = 0.5

α=0.04 t/t$_0$=0.580 α_c=0.0079 t/t$_0$=0.612 α=0.015 t/t$_0$=0.612

(d)   β = 10   p = 1

Fig. 4. Four examples of rupture nucleation and propagation are illustrated. The dark regions are failed fibers. On the left are examples during nucleation, on the center critical ($\alpha = \alpha_c$) nucleation is illustrated and on the right are examples during rupture. In all cases $n_0 = 22\,500$ and $r = 1$. Results are given for: (a) $\beta = 2$, $p = 1$, (b) $\beta = 6$, $p = 0.5$, (c) $\beta = 10$, $p = 0.5$, and (d) $\beta = 10$, $p = 1$.
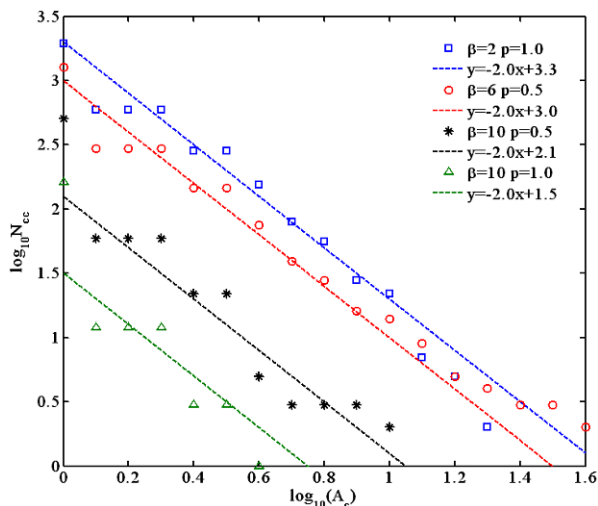
Fig. 5. Frequency-area statistics for failed clusters at the critical transition from nucleation to propagation. The cumulative numbers of clusters N_{cc} are given as a function of cluster area A_c for the four examples in Fig. 4. The straight lines are the correlation with the power-law scaling given in Eq. (32) taking $D = 4$. Colour version of this figure is available in electronic edition only.

In Figure 6 we give the dependence of the damage variable α on the nondimensional time t/t_0. Typical simulations are shown. There is some variability among simulations, but this is generally small, a few percent. The nucleation phase is delayed significantly as β is increased. This is expected since as $\beta \to \infty$ there will be no nucleation phase and the rupture will propagate at $t/t_0 = 1$. The nucleation phase has only a weak dependence on p. However, as p is increased the critical values of the damage variable α_c decrease.

In Figure 7a we give the dependence of the critical nondimensional failure time t_c/t_0 on the load sharing parameter p and in Fig. 7b we give the dependence of the corresponding critical damage parameter value α_c on p. In each case, we give results for $\beta = 2$, 6, and 10. We see that both t_c/t_0 and α_c decrease with increasing values of p.

We next determine the cumulative energy dissipated during fiber failures. During simulation, the nondimensional energy dissipated in a fiber failure E_f/E_0 is given by Eq. (28). These values are added to give the cumulative nondimensional energy dissipated E_f/E_0. These values are given as a function of nondimensional time t/t_0 in Fig. 8 for (a) $p = 0$, (b) $p = 0.5$, and (c) $p = 1.0$. In each case, results are given for $\beta = 2$, 6, and 10.

In Figure 9 we give the dependence of the ratio of energy generated in the nucleation phase E_n to the energy generated in the rupture phase E_r on the
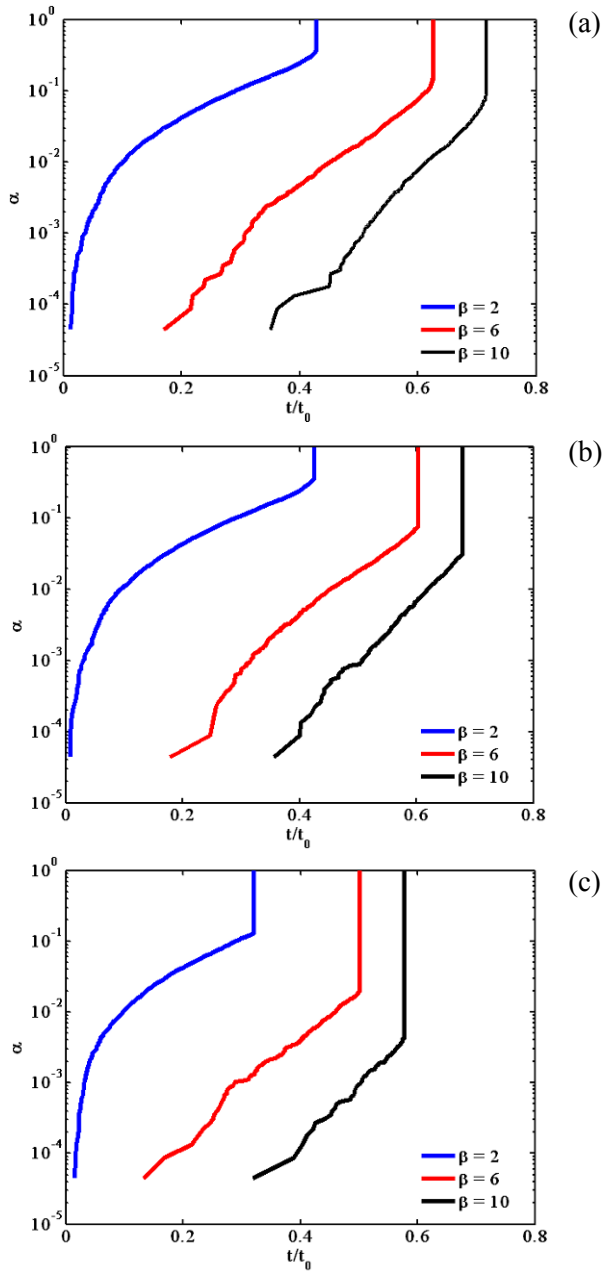
Fig. 6. Dependence of the damage variable α on the nondimensional time t/t_c. Results are given for: (a) $p = 0$, (b) $p = 0.5$, and (c) $p = 1.0$. In each case results are given for: $\beta = 2$, $\beta = 6$, and $\beta = 10$. The simulations given in (a) are basically identical to the analytical results given in Fig. 2.
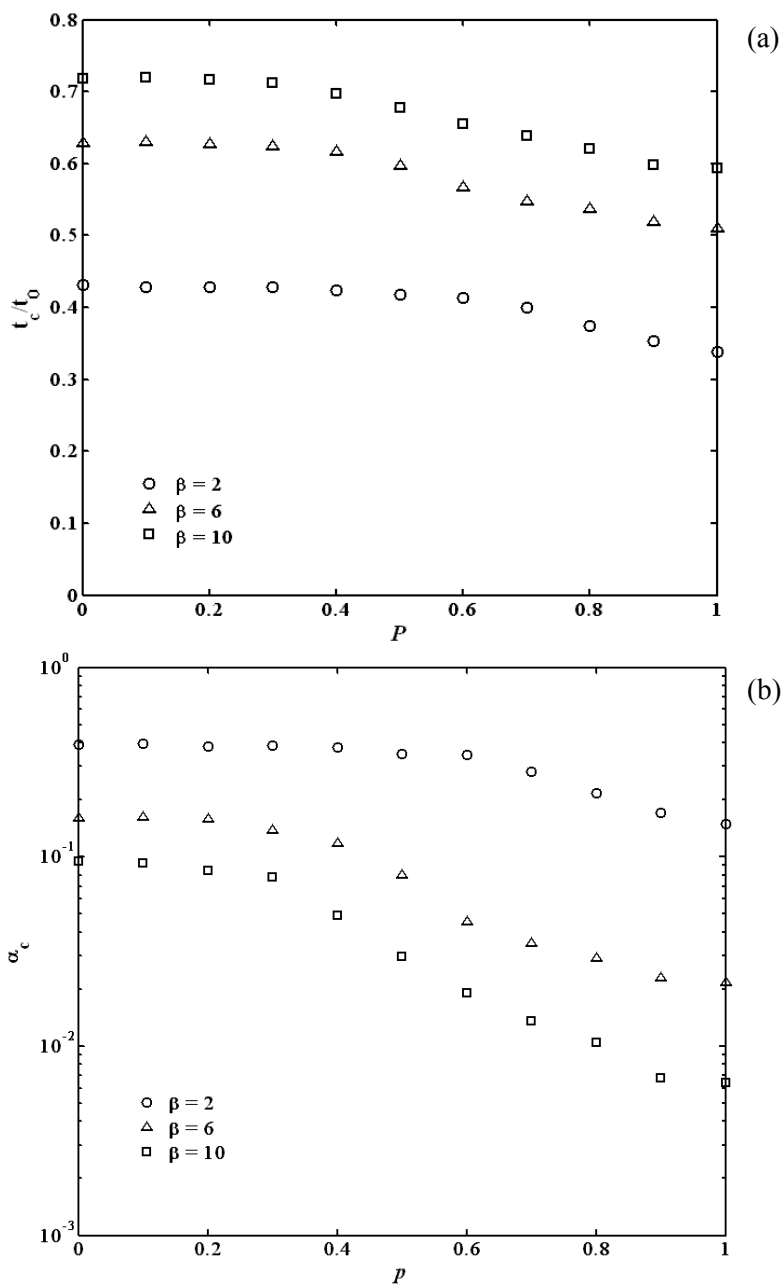
Fig. 7: (a) Dependence of the critical nondimensional failure time t_c/t_0 on the load sharing parameter p; (b) dependence of the corresponding critical damage parameters α_c on p. In both cases results are given for $\beta = 2, 6,$ and 10.
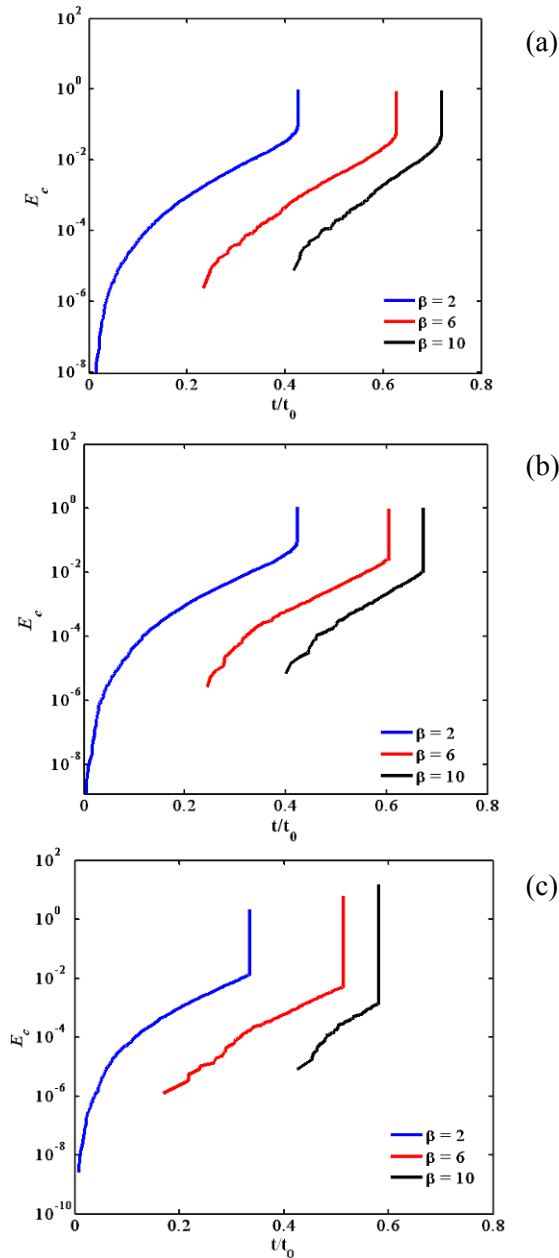
Fig. 8. Dependence of the nondimensional cumulative energy dissipated E_f/E_0 on the nondimensional time t/t_0. Results are given for: (a) $p = 0$, (b) $p = 0.5$, and (c) $p = 1.0$. In each case results are given for $\beta = 2$, 6, and 10. The simulations given in (a) are basically identical to the analytical results given in Fig. 3.
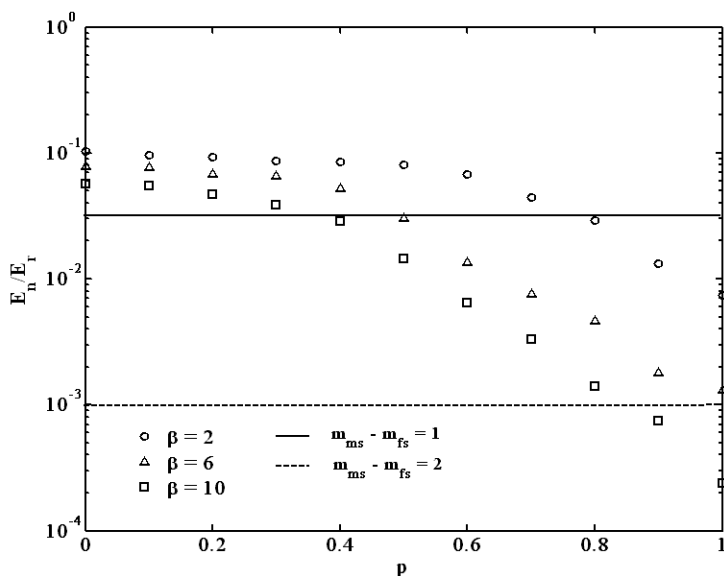
Fig. 9. Dependence of the ratio of energy generated in the nucleation phase E_n to the energy generated in the rupture phase E_r on the load sharing parameter p with $\beta = 2$, 6, and 10. We associate E_r with a main shock with magnitude m_{ms} and E_n with a single foreshock of magnitude m_{fs}. The energy ratios associated with $m_{ms} - m_{fs} = 1$ and 2 are all given.

load sharing parameter p with $\beta = 2$, 6, and 10. We associate the propagation phase with a main shock of magnitude m_{ms}, and we associate the nucleation phase with a single precursor earthquake of magnitude m_{fs}. Using the standard relation between earthquake energy and magnitude we write

$$\frac{E_n}{E_r} = 10^{-1.5(m_{ms} - m_{fs})} \quad . \tag{33}$$

We also give in Fig. 9 energy ratios corresponding to $m_{ms} - m_{fs} = 1$ and 2.

A major focus of this paper is to study the role of precursory damage prior to a propagating rupture. The objective is to provide an explanation for the absence of small earthquakes as a precursor to the 2004 Parkfield earthquake as well as other earthquakes. Figure 9 illustrates the conditions under which precursory damage is reduced. For $p = 0$ (the uniform load sharing, mean-field limit) the energy in the precursory events is about 10% of the energy generated by the propagating rupture. There is only a weak dependence on the Weibull exponent β. The stress from a failed asperity is transferred to all other asperities. This transfer enhances precursory failures and a strong nucleation phase. We associate their behavior with the laboratory experi-

ments discussed above. The rigid granite blocks transfer the stress from a failed asperity across the entire saw cut (model fault).

For the $p = 1$ (local load sharing) limit the energy in the precursory damage is reduced considerably. There is also a strong dependence on the Weibull exponent β. With $\beta = 10$ and $p = 1$ the energy in the precursory events is only 0.02% of the energy in the propagating rupture. In order to relate our results to the problem of precursory seismic activity we have also included in Fig. 9 the magnitude of a single precursory earthquake that would give the fraction of precursory energy release during the nucleation phase. For p near unity and large β, the precursory single earthquake would have a magnitude two units less than the main shock associated with the propagation phase. For the 2004 Parkfield magnitude 6.0 earthquake this would be the energy associated with a single magnitude 4 earthquake.

With $p = 1$ the force from a failed asperity is transferred to adjacent asperities. This local transfer of stress accelerates fracture nucleation reducing precursory failures. We associate this behavior with faults. The matrix around a fault is heavily damaged and this damage inhibits the transfer of stress from a failed asperity over large distances.

5. DISCUSSION

A major problem in understanding earthquake physics is the absence of a precursory build up of seismicity associated with the rupture of a major earthquake. There was no evidence for precursory seismic activity prior to the 2004 Parkfield $M_w = 6$ earthquake. A very sensitive seismic array was located adjacent to the rupture and no systematic build up of activity was observed.

In order to study this problem, we have utilized a fiber-bundle model. Breaking fibers are hypothesized to be analogous to breaking asperities on a fault zone. The behavior of the fiber-bundle model is controlled by several parameters and assumptions. First we assume a "static" model in which failure forces on each fiber are specified. We believe that this is the appropriate approach for a model of a main shock since the build up of the tectonic stress is so slow. It is also necessary to specify the statistical distribution of failure stresses. We choose the Weibull distribution given in Eq. (3) because it is the accepted distribution for the failure of fiber bundle (Phoenix and Newman 2009). It is also necessary to specify the power-law exponent β of the distribution and we consider several values.

There are alternative ways in which the force on a failed fiber is redistributed. We introduce a redistribution parameter p which is the fraction of the force that is redistributed to neighboring fibers (local load sharing). The remainder of the force $1 - p$ is redistributed to all surviving fibers (uniform load sharing). It is also necessary to specify the range of local load sharing.

We assume that the fraction of the load p is redistributed to all surviving fibers in a square region with $2r + 1$ fibers on a side as defined in Eq. (7). When $2r + 1$ is equal to the size of the square grid of fibers local load sharing $p = 1$ is equivalent to equal load sharing and $p = 0$.

In our simulations we consider only local load sharing with $r = 1$. Our focus is on the role of parameters p and β on precursory failures. Our results are clearly illustrated in Fig. 9. Precursory failures are suppressed as $p \rightarrow 1$ for relatively large β. Local load sharing leads to a weak nucleation phase and a strong rupture phase. This result is clearly illustrated in Fig. 4. Precursory activity is very low for $p = 1$ and $\beta = 10$.

In the Appendix we have related the fiber-bundle model to the slider-block model. A slider-block model without healing is similar to the fiber-bundle model. When a block slips, it does not stick. The primary parameter in the slider-block model is the ratio of spring constants defined in Eq. (1). As shown in Eq. (A21), with very weak springs, $\gamma \rightarrow 0$, we have uniform load sharing corresponding to $p = 0$ in the fiber bundle model and with very strong connector springs, $\gamma \rightarrow \infty$, we have local load sharing corresponding to $p = 1$ in the fiber-bundle model. The redistribution parameter p plays the same role in the fiber-bundle model as the spring constant ratio γ in the slider-block model.

As discussed in the Introduction, the laboratory experiments on granite blocks carried out by Weeks *et al.* (1978) also exhibited systematic precursory acoustic emissions. Again it appears to be appropriate to associate these experiments with the uniform load sharing limit. The granite blocks behaved as loader plates in a slider-block model. When an asperity failed the rigid granite block transferred the force on that asperity to all surviving asperities.

We attribute the lack of precursory seismicity prior to earthquakes to local load sharing from failed asperities. The Earth's crust in seismogenic regions is populated by faults on all scales. This complexity allows the force on a failed asperity to be transferred only to neighboring asperities, *i.e.*, local load sharing. Thus, the behavior of a fault is better approximated by the lack of precursory damage as illustrated in Fig. 4d.

APPENDIX

Slider-block model

There are strong similarities between the fiber-bundle model and the slider-block model. We will use these similarities to relate the load-sharing parameter p in our fiber-bundle model to the slider-block model. We consider

a slider-block model consisting of a two-dimensional square array of n_0 slider blocks pulled over a surface by a driver plate (Turcotte 1997). A constant pulling force F is applied to the driver plate. Each block is connected to the driver plate with a driver spring with spring constant K_L. Each block is connected to n_c adjacent blocks with connector springs with spring constants K_c. We assume that the blocks have a statistical distribution of static frictional failure strengths in analogy to the failure strengths of our fibers. The force F on the driver plate is increased from zero until the weakest block slips with a force F/n_0 on it. The extension of the connector springs x is given by

$$x = \frac{F}{n_0 K_L} . \tag{A1}$$

In order to relate the slider-block model to the fiber-bundle model we assume that the frictional force on the failed block is zero after slip.

To illustrate the behavior of this slider-block model we first consider two limiting cases: (1) no connector springs ($K_c = 0$) and (2) very strong connector springs ($K_c \gg K_L$). When a block fails with $K_c = 0$, there is no force on the block and the original force on the block xK_L is transferred equally to the $n - 1$ remaining blocks. This results in an increase in the extension of the loader springs from x to $x + \delta x$. The resulting force balance is

$$xK_L = (n-1)K_L \delta x , \tag{A2}$$

or

$$\delta x = \frac{x}{(n-1)} . \tag{A3}$$

With $K_c = 0$ and no frictional force on the failed block, the forces on the connector springs are zero so that the displacement of the failed block x_b is given by

$$x_b = x + \delta x = \frac{nx}{n-1} . \tag{A4}$$

This is the uniform-load sharing (mean field) limit. This corresponds to the $p = 0$ (uniform load sharing) limit for the fiber-bundle model.

When a block fails with $K_c \gg K_L$, the displacement of failed block is very small so that the force transmitted to this block through its loader spring remains unchanged. All loader springs transmit the same force so that there is no displacement of the driver plate and

$$\delta x = 0 . \tag{A5}$$

The load on the failed block is distributed uniformly to the n_c blocks to which it is connected by connector springs, this is local load sharing. The resulting force balance on the failed block requires

$$xK_L = n_c x_b K_c = n_c x_c K_c . \tag{A6}$$

The extension of the connector springs x_c is given by

$$x_c = \frac{xK_L}{n_c K_c} \ . \tag{A7}$$

In the limit $K_c/K_L \to \infty$ we have $x_b = x_c \to 0$. The load is redistributed locally and the driver plate does not move. This corresponds to the $p = 1$ (local load sharing) limit for the fiber-bundle model.

We now give the general result for arbitrary values of K_c and K_L. The force balance on the failed block before and after failure (slip) requires that

$$xK_L = (n-1)K_L\delta x + n_c K_c x_b \ . \tag{A8}$$

This reduces to Eqs. (A2) and (A6) in the appropriate limits. In addition, the static force balance between the force exerted by the driver spring and the force exerted by the n_c connector springs requires

$$(x + \delta x - x_b)K_L = n_c K_c x_b \ . \tag{A9}$$

Equations (A8) and (A9) can now be solved for the displacement of the loader plate δx and the displacement of the failed block x_b.

The displacement of the loader plate is given by

$$\delta x = \frac{K_L x}{n_c K_c n + K_L(n-1)} \ . \tag{A10}$$

This reduces to Eq. (A3) when $K_c = 0$ and to Eq. (A5) when $K_c \gg K_L$. The displacement of the failed block is given by

$$x_b = \frac{nK_L x}{n_c K_c n + K_L(n-1)} \ . \tag{A11}$$

This reduces to Eq. (A4) when $K_c = 0$ and to Eq. (A7) when $K_c \gg K_L$. We finally consider the partition of the load from a failed site to the surviving sites.

When a site fails the load f_f that is redistributed to other sites is given by

$$f_f = K_L x = f_{mf} + f_{LLS} \ , \tag{A12}$$

where f_{mf} is the fraction of the load redistributed uniformly (mean field) and f_{LLS} is the fraction of the load redistributed locally. The equal load sharing (mean field) component is redistributed to all surviving blocks due to the displacement δx of the drive plate. This component f_{mf} is given by

$$f_{mf} = (n-1) K_L \delta x \, , \tag{A13}$$

and using Eq. (A10) we obtain

$$f_{mf} = \frac{(n-1) K_L^2 x}{n_c K_c n + K_L (n-1)} \, . \tag{A14}$$

There is also a local load-sharing component that is redistributed to the n_c local blocks connected to the failed block by connector springs. This component f_{LLS} is given by

$$f_{LLS} = n_c x_b K_c \, , \tag{A15}$$

and using Eq. (A11) we obtain

$$f_{LLS} = \frac{n_c K_c n K_L x}{n_c K_c n + K_L (n-1)} \, . \tag{A16}$$

Adding Eqs. (A14) and (A16) gives (A12), as required.

We introduced the redistribution fraction in Eq. (7). Noting that

$$f_{LLS} = n_{rd} \Delta f_{lls} \, , \tag{A17}$$

and

$$f_f = f_{f \min} \, , \tag{A18}$$

we find

$$p = \frac{f_{LLS}}{f_f} \, . \tag{A19}$$

Introducing the ratio of spring constants defined in Eq. (1), substitution of Eqs. (A12) and (A16) in Eq. (A19) gives

$$p = \frac{n_c \gamma n}{n_c \gamma n + (n-1)} \, . \tag{A20}$$

For $n \gg 1$ we have

$$p = \frac{n_c \gamma}{n_c \gamma + 1} \, . \tag{A21}$$

This demonstrates that the local load sharing limit ($p = 1$) in the fiber bundle model corresponds to the $\gamma \to \infty$ ($K_c \gg K_L$) limit in the slider-block model and that the uniform (mean field) limit ($p = 0$) in the fiber-bundle model corresponds to the $\gamma = 0$ ($K_c = 0$) limit in the slider-block model.

R e f e r e n c e s

Abramowitz, M., and I.A. Stegun (eds.) (1972), *Handbook of Mathematical Functions with Formulas, Graphs, and Mathematical Tables*, 9th ed., Dover Publications Inc., New York, 260 pp.

Alava, M.J., P.K.V.V. Nukala, and S. Zapperi (2006), Statistical models of fracture, *Adv. Phys.* **55**, 3-4, 349-476, DOI: 10.1080/00018730300741518.

Agnew, D.C., and L.M. Jones (1991), Prediction probabilities from foreshocks, *J. Geophys. Res.* **96**, B7, 11959-11971, DOI: 10.1029/91JB00191.

Bakun, W.H., B. Aagaard, B. Dost, W.L. Ellsworth, J.L. Hardebeck, R.A. Harris, C. Ji, M.J.S. Johnston, J. Langbein, J.J. Lienkaemper, A.J. Michael, J.R. Murray, R.M. Nadeau, P.A. Reasenberg, M.S. Reichle, E.A. Roeloffs, A. Shakal, R.W. Simpson, and F. Waldhauser (2005), Implications for prediction and hazard assessment from the 2004 Parkfield earthquake, *Nature* **437**, 969-974, DOI: 10.1038/nature04067.

Bowman, D.D., G. Ouillon, C.G. Sammis, A. Sornette, and D. Sornette (1998), An observational test of the critical earthquake concept, *J. Geophys. Res.* **103**, B10, 24359-24372, DOI: 10.1029/98JB00792.

Carlson, J.M., and J.S. Langer (1989), Mechanical model of an earthquake fault, *Phys. Rev. A* **40**, 11, 6470-6484, DOI: 10.1103/PhysRevA.40.6470.

Ciliberto, S., A. Guarino, and R. Scorretti (2001), The effect of disorder on the fracture nucleation process, *Physica D* **158**, 1-4, 83-104, DOI: 10.1016/S0167-2789(01)00306-2.

Coleman, B.D. (1958), Statistics and time dependence of mechanical breakdown in fibers, *J. Appl. Phys.* **29**, 6, 968-983, DOI: 10.1063/1.1723343.

Daniels, H.E. (1945), The statistical theory of the strength of bundles of threads, *Proc. Roy. Soc. A* **183**, 995, 405-435, DOI: 10.1098/rspa.1945.0011.

Garcimartin, A., A. Guarino, L. Bellon, and S. Ciliberto (1997), Statistical properties of fracture precursors, *Phys. Rev. Lett.* **79**, 17, 3202-3205, DOI; 10.1103/PhysRevLett.79.3202.

Guarino, A., A. Garcimartin, and S. Ciliberto (1998), An experimental test of the critical behavior of fracture precursors, *Eur. Phys. J. B* **6**, 13-24, DOI: 10.1007/s100510050521.

Guarino, A., S. Ciliberto, and A. Garcimartin (1999), Failure time and microcrack nucleation, *Europhys. Lett.* **47**, 4, 456-461, DOI: 10.1209/epl/i1999-00409-9.

Guarino, A., S. Ciliberto, A. Garcimartin, M. Zei, and R. Scorretti (2002), Failure time and critical behaviour of fracture precursors in heterogeneous materials, *Eur. Phys. J. B* **26**, 2, 141-151, DOI: 10.1140/epjb/e20020075.

Helmstetter, A., and D. Sornette (2003), Foreshocks explained by cascades of triggered seismicity, *J. Geophys. Res.* **108**, B10, 2457-2466, DOI: 10.1029/2003JB002409.

Hemmer, P.C., and A. Hansen (1992), The distribution of simultaneous fiber failures in fiber bundles, *J. Appl. Mech*. **59**, 4, 909-914, DOI: 10.1115/1.2894060.

Krajcinovic, D. (1996), *Damage Mechanics*, 2nd ed., Elsevier, Amsterdam, 761 pp.

Kun, F., S. Zapperi, and H.J. Herrmann (2000), Damage in fiber bundle models, *Eur. Phys. J. B* **17**, 2, 269-279, DOI: 10.1007/PL00011084.

Marone, C. (1998), Laboratory-derived friction laws and their application to seismic faulting, *Ann. Rev. Earth Planet. Sci*. **26**, 643-696, DOI: 10.1146/annurev. earth.26.1.643.

Meeker, W.Q., and L.A. Escobar (1998), *Statistical Methods for Reliability Data*, John Wiley and Sons, New York, 680 pp.

Phoenix, S.L., and W.I. Newman (2009), Time-dependent fiber bundles with local load sharing. II. General Weibull fibers, *Phys. Rev. E* **80**, 6, 066115, DOI: 10.1103/PhysRevE.80.066115.

Pradhan, S., A. Hansen, and B.K. Chakrabarti (2010), Failure processes in elastic fiber bundles, *Rev. Mod. Phys*. **82**, 1, 499-555, DOI: 10.1103/RevModPhys. 82.499.

Pride, S.R., and R. Toussaint (2002), Thermodynamics of fiber bundles, *Physica A* **312**, 1-2, 159-171, DOI: 10.1016/S0378-4371(02)00816-6.

Reasenberg, P.A. (1999), Foreshock occurrence before large earthquakes, *J. Geophys. Res*. **104**, B3, 4755-4768, DOI: 10.1029/1998JB900089.

Savage, M.K., and D.M. dePolo (1993), Foreshock probabilities in the western Great-Basin eastern Sierra Nevada, *Bull. Seismol. Soc. Am*. **83**, 6, 1910-1938.

Scorretti, R., S. Ciliberto, and A. Guarino (2001), Disorder enhances the effects of thermal noise in the fiber bundle model, *Europhys. Lett*. **55**, 5, 626-632, DOI: 10.1209/epl/i2001-00462-x.

Turcotte, D.L. (1997), *Fractals and Chaos in Geology and Geophysics*, 2nd ed., Cambridge University Press, Cambridge, 398 pp.

Turcotte, D.L. (1999), Self-organized criticality, *Rep. Prog. Phys*. **62**, 10, 1377-1429, DOI: 10.1088/0034-4885/62/10/201.

Turcotte, D.L., S.G. Abaimov, R. Shcherbakov, and J.B. Rundle (2007), Nonlinear dynamics of nature hazards. **In:** A.A. Tsonis and J.B. Elsner (eds.), *Nonlinear Dynamics in Geosciences*, Springer, New York, 557-580, DOI: 10.1007/978-0-387-34918-3_30.

Weeks, J., D. Lockner, and J. Byerlee (1978), Change in b-values during movement on cut surfaces in granite, *Bull. Seismol. Soc. Am*. **68**, 2, 333-341.

Weibull, W. (1951), A statistical distribution function of wide applicability, *J. Appl. Mech*. **18**, 293-297.

VERSITA

Dynamical Parameter Analysis of Continuous Seismic Signals of Popocatépetl Volcano (Central Mexico): A Case of Tectonic Earthquakes Influencing Volcanic Activity

Marta TÁRRAGA[1], Servando DE LA CRUZ-REYNA[2],
Ana T. MENDOZA-ROSAS[3], Roberto CARNIEL[2,4],
Alicia MARTÍNEZ-BRINGAS[5], Alicia GARCÍA[6], and Ramon ORTIZ[6]

[1]Institute of Earth Sciences "Jaume Almera", CSIC, Barcelona, Spain

[2]Instituto de Geofísica, Universidad Nacional Autónoma de México,
Ciudad Universitaria, México D.F., México

[3]Posgrado en Ciencias de la Tierra, Instituto de Geofísica, Universidad Nacional
Autónoma de México, Ciudad Universitaria, México D.F., México

[4]Laboratorio di Misure e Trattamento dei Segnali, DICA – Università di Udine, Italy
e-mail: roberto.carniel@uniud.it (corresponding author)

[5]Centro Nacional de Prevención de Desastres (CENAPRED), México

[6]Dep. de Volcanología, Museo Nacional de Ciencias Naturales, CSIC, Madrid, Spain

A b s t r a c t

The continuous background seismic activity contains information on the internal state of a volcanic system. Here, we report the influence of major regional tectonic earthquakes ($M > 5$ in most cases) on such state, reflected as changes in the spectral and dynamical parameters of the volcano continuous seismic data. Although changes do not always occur, analysis of five cases of earthquake-induced variations in the signals recorded at Popocatépetl volcano in central México reveal significant fluctuations following the tectonic earthquakes. External visible volcanic activity, such as small to moderate explosions and ash emis-

sions, were related to those fluctuations. We briefly discuss possible causes of the variations. We conclude that recognition of fluctuations in the dynamical parameters in volcano monitoring seismic signals after tectonic earthquakes, even those located in the far field, hundreds of kilometers away, may provide an additional criterion for eruption forecasting, and for decision making in the definition of volcanic alert levels.

Key words: dynamical parameters, continuous seismic signal, volcanic activity, Popocatépetl volcano, tectonic earthquakes.

1. INTRODUCTION

Popocatépetl (19.02°N, 98.62°W) is an andesitic-dacitic stratovolcano, located about 60 km southeast of México City and about 45 km west of the city of Puebla. With an elevation of 5452 m a.s.l., it is the second highest volcano in the country. It has an elliptical summit crater measuring about 800×600 m. About 23 000 years BP a major eruption destroyed a previous volcanic edifice (Boudal and Robin 1989). Since then Popocatépetl has produced several eruptive episodes of different types, including Plinian phases. The current eruption began on 21 December 1994, after 70 years of quiescence. It has been characterized by a succession of effusive dome growth and explosive destruction episodes, alternating with periods of relative quiescence (De la Cruz-Reyna and Tilling 2008). The seismic monitoring network used for the surveillance of the volcano has produced a large data set that includes continuous base-line signatures of the quiescent periods, the signals produced by the eruptive activity, and the background tectonic seismicity, which is also recorded by the Servicio Sismológico Nacional (SSN; The National Seismic Network of Mexico, http://www.ssn.unam.mx).

The occurrence of a tectonic earthquake sufficiently close to a volcano and/or sufficiently energetic can trigger changes in its internal activity (*i.e.*, Ortiz *et al.* 2003, Manga and Brodsky 2006, and references therein; Walter and Amelung 2007, Walter *et al.* 2009, De la Cruz-Reyna *et al.* 2010) and in some cases even external manifestations such as occurrence of explosions, increased steam or ash emissions, or increased convection in a lava lake (Carniel *et al.* 2003). We present here examples of the influence of tectonic earthquakes located in Mexico on the ongoing activity of Popocatépetl volcano, recorded as fluctuations in its continuous background seismic activity. The analysis has been carried out searching transitions in a number of parameters computed on the basis of the continuous seismic time series. Similar dynamical analyses at several other volcanoes have been reported in the literature (Carniel and Di Cecca 1999, Privitera *et al.* 2003, Tárraga *et al.* 2006, Carniel and Tárraga 2006, Carniel *et al.* 2008). Here, we present several examples of transitions in one or more parameters of the Popocatépetl

continuous seismic signals that may have been induced by the occurrence of tectonic earthquakes. The relation between the tectonic activity and the volcanic response is discussed in De la Cruz-Reyna *et al.* (2010), and it is assumed to be primarily related either to the static stress transfer caused by the earthquake, or to the dynamic transfer related to the transit of seismic waves through the magmatic system.

2. DATA AND METHODS

The data analyzed here were recorded by three short-period seismic stations of the monitoring network for Popocatépetl, operated by CENAPRED (Centro Nacional para la Prevención de Desastres de México – the Mexican National Center for Disaster Prevention, http://www. cenapred.unam.mx). The stations are: Juncos (PPJ), located on the NW slope of the volcano (19.0342°N, 98.6446°W) at 4452 m a.s.l.; Cuervos (PPQ) (19.0009°N, 98.6246°W) on the upper S slope, at 4200 m a.s.l.; and Tetexcaloc (PPT) (18.9745°N, 98.6241°W), located on the lower S slope at 3300 m a.s.l. The continuous seismic signals are sampled at 100 Hz, and transmitted to the CENAPRED monitoring center in Mexico City.

It is important to consider that the entire seismic signal (seismic events, tremor, and seismic noise) contains not only information related to the volcano activity but also additional information, generated by other natural and/or anthropogenic sources. On the basis of this hypothesis, it is necessary to separate and extract the information related to the volcano activity from others. A classical approach to the analysis of seismo-volcanic time series is to look for the seismic events above a reference seismic noise level, which can then be identified and classified in different categories such as volcano-tectonic events, long period events, discrete tremor episodes and explosion quakes (Minakami 1974, Schick 1988, Chouet 2003).

Recently, digital signal processing (DSP) techniques have been considerably developed, leading to the increasing availability of software and even of specific processors. The earliest, and now considered classical, analysis techniques were the spectral analysis (*e.g.*, Van Loan 1992), RSAM (real-time seismic amplitude measurement; Endo and Murray 1991), SSAM (seismic spectral amplitude measurement; Rogers and Stephens 1995), and the spectrogram (*e.g.*, Hellweg 1999). These functions are now normally included in many software packages used for volcano monitoring (*i.e.*, USGS Earthworm System, details at http://folkworm.ceri.memphis.edu/ew-dist).

Besides these techniques, other functions can and should be included in routine seismic noise analyses of volcanic seismic signals. These can be applied directly on the original seismic record (*i.e.*, the minimum spectrum, Vila *et al.* 2006), or sometimes can be applied more efficiently after a pre-

processing that could be simply one of the now classical techniques described above (*i.e.*, RSAM, SSAM). One example is the variogram (Jaquet and Carniel 2001), aimed to recognize the "memory" of the system generating the experimental time series and/or its variations with time. Due to the large data volume to be analyzed, a preprocessing is also necessary to reduce the volume of data and to facilitate the interpretation of the results.

2.1 Spectral analysis

Related to the spectral analysis, one of the techniques is to characterize the system with the most significant spectral parameters in a series of suitably defined time windows, *i.e.*, instead of (re)presenting the full spectrogram, one can reduce it to one or more scalar parameters. In the present work, the time evolution of the frequency content was analyzed by computing three scalar parameters (dominant frequency, average frequency, and spectrum standard deviation), derived from the normalized spectrogram over time windows of 60 s, as proposed by Carniel and Di Cecca (1999). The normalization is carried out in order to look at the relative energy distribution within this frequency range and not at the absolute values. The dominant frequency is the central frequency of the spectrogram bin where the maximum is found in a given time window. The average frequency is computed by weighting the central frequency of each bin by its relative value, so that it represents the baricenter of the spectral distribution. Finally, the spectrum standard deviation measures how disperse the spectrum is in each time window. An hourly average is performed in order to smooth the graphs.

2.2 Autoregressive models

Another method is to represent the signal using a different basis, *i.e.*, carrying out decomposition, and then considering only the most relevant elements, such as the most significant ***autoregressive*** (AR) coefficients (Box *et al.* 1994). Although the volcanic phenomena probably involve nonlinearities, simple linear models like AR can still detect transitions in the time evolution of background seismicity related to significant changes in the volcano activity, as has been shown for instance at Villarrica volcano in Chile (Tárraga *et al.* 2008).

Under the hypothesis that the original data follow a Gaussian distribution, we can represent the signal x_t as a linear combination of its past values with an error term added up. Then, the autoregressive modelling of order p or AR(p) lies on the hypothesis that the time series values have been generated by an equation of the form:

$$x_t = \phi_0 + \phi_1 x_{t-1} + \phi_2 x_{t-2} + \dots + \phi_p x_{t-p} + e_t = \phi_0 + \sum_{i=1}^{p} \phi_i x_{t-i} + e_t \ . \tag{1}$$

The $p+2$ parameters to be estimated are then the $p+1$ autoregressive coefficients $(\phi_0, \phi_1, ..., \phi_p)$ and the variance σ^2 of the residual. In practice, these are estimated using least squares to minimize the quadratic error EC:

$$EC = \sum_{t=p+1}^{n} \left(x_t - \phi_0 - \sum_{i=1}^{p} \phi_i x_{t-i} \right)^2 , \tag{2}$$

where n is the length of the experimental time series.

Therefore, the AR coefficients are

$$\phi = \begin{pmatrix} \phi_0 \\ \phi_1 \\ \vdots \\ \phi_p \end{pmatrix} = (Z^T Z)^{-1} Z^T X , \tag{3}$$

where X and Z are represented by

$$X = \begin{pmatrix} x_{p+1} \\ x_{p+2} \\ \vdots \\ x_n \end{pmatrix} , \qquad Z = \begin{pmatrix} 1 & x_p & x_{p-1} & \cdots & x_1 \\ 1 & x_{p+1} & x_p & \cdots & x_2 \\ \vdots & \vdots & \vdots & \vdots & \vdots \\ 1 & x_{n-1} & x_{n-2} & \cdots & x_{n-p} \end{pmatrix} , \tag{4}$$

and the residual variance is

$$\sigma^2 = \frac{1}{n-p} \sum_{t=p+1}^{n} \left(x_t - \phi_0 - \sum_{i=1}^{p} \phi_i x_{t-i} \right)^2 . \tag{5}$$

The order p of the autoregressive model is chosen as the minimum value for which the residuals are sufficiently decorrelated. In our case we chose the order $p = 15$. Again, the aim is not to do a precise modeling but to look at the time evolution of the coefficients and possible (abrupt) changes in that evolution.

2.3 Dynamical parameters

The next set of parameters derives from the hypothesis that the volcano can be considered as a dynamical system characterized by states that evolve in time. If X is a set of variables that completely describes the system at a given time t_n, the deterministic time evolution can be described by a function F such that $X(t_n + 1) = F[X(t_n)]$. In this way, each variable carries information about the full dynamical history of all the other variables, and can be used to forecast the future evolution of the volcanic system. In practice, as the dimension (*i.e.*, the number of state variables) is generally high, the function F

is nonlinear and random noise cannot be avoided in experimental data, one cannot reasonably expect long-term predictability, *i.e.*, the system will typically show a chaotic behaviour. From the single available variable (in this case the vertical ground velocity) we then reconstruct a pseudo-state space using the time-delay method introduced by Packard *et al.* (1980). Two parameters are needed for the reconstruction: the delay time, τ, that separates each couple of successive coordinates, and the embedding dimension, m, the number of coordinates used in the pseudo-state space (Carniel and Di Cecca 1999). The simplest method to choose the delay time is by using the autocorrelation function:

$$\rho_{XY} = \frac{\sigma_{XY}}{\sigma_X \sigma_Y} \, , \qquad (6)$$

where σ_{XY} represents the covariance, and σ_X and σ_Y the standard deviation of the random variables X and Y; we thus define

$$X = \{x_k\} k = 0, ..., N - \tau \; \left(\text{the original time series}\right)$$

and

$$Y = \{y_{k+\tau}\} \; k = 0, ..., N - \tau \quad \text{and} \quad \tau = 0, ..., t_{\max} \; \left(\text{the delayed time series}\right),$$

where N is the length of the time series.

After computing the correlation between the original time series and the delayed time series for values of τ from 0 to a maximum delay $\tau_{\max}$, the optimal delay time will be the first for which ρ_{XY} is zero, *i.e.*, the first zero of the autocorrelation function. This choice guarantees linear independence of the coordinates.

Another approach to data embedding is the singular value decomposition (SVD; Carniel *et al.* 2003, 2006), whose singular values can then be monitored as a function of time. It is noteworthy that these parameters are often proposed on a mostly empirical basis, although interpretations can follow later. For instance, the information coming from the singular values of SVD has been recently interpreted, using asymptotic properties of the eigenvalues of Toeplitz, as strictly related to the power spectrum of the analyzed time series (Bozzo *et al.* 2010).

The SVD can be described as a four-step procedure. During the first step (***embedding***), the monodimensional time series is transformed into a L-dimensional time series called ***trajectory matrix***. While the time delay for this embedding is chosen equal to 1, the matrix depends on the choice of the window length, which defines the embedding dimension. So, for a time series $\mathbf{x} = \{x_1, x_2, ..., x_n\}$ and an embedding dimension m, the resulting trajectory matrix is

$$\mathbf{X} = \begin{bmatrix} x_1 & x_2 & \cdots & x_m \\ x_2 & x_3 & \cdots & x_{m+1} \\ \vdots & \vdots & \ddots & \vdots \\ x_{n-m+1} & x_{n-m+2} & \cdots & x_n \end{bmatrix} , \tag{7}$$

which is by definition a Hankel matrix, *i.e.*, $X_{i,j} = x_{i+j-1}$.

The embedding dimension must be sufficiently high to capture the global behaviour of the system. Similarly to the case discussed before, a common method to determinate m is by using the first zero of the correlation between the first and the last columns.

In the second step (***decomposition***), this matrix is decomposed as

$$\mathbf{X} = \mathbf{U}\,\mathbf{S}\,\mathbf{V}^T , \tag{8}$$

where $\mathbf{U}$ is a $(n - m + 1) \times (n - m + 1)$ orthogonal matrix, $\mathbf{V}$ is a $m \times m$ orthogonal matrix, and $\mathbf{S}$ is a $(n - m + 1) \times m$ diagonal matrix whose elements are the singular values of $\mathbf{X}$.

This is carried out by computing the covariance matrix

$$\mathbf{C} = \frac{1}{n-m} X^T \mathbf{X} . \tag{9}$$

The spectral decomposition of this matrix is

$$\mathbf{C} = \mathbf{\Phi}\Lambda\mathbf{\Phi}^T , \tag{10}$$

where $\mathbf{\Phi}$ is an orthonormal matrix whose columns are the eigenvectors of $\mathbf{C}$, and $\mathbf{S}$ is a diagonal matrix whose elements σ_i^2 are the eigenvalues of $\mathbf{C}$ in decreasing order. The singular values of $\mathbf{X}$ are given by the square root of the eigenvalues of $\mathbf{C}$. Therefore,

$$S = \begin{bmatrix} \sigma_1 & 0 & \cdots & 0 \\ 0 & \sigma_2 & \cdots & 0 \\ \vdots & \vdots & \ddots & \vdots \\ 0 & 0 & \cdots & \sigma_m \\ 0 & 0 & \cdots & 0 \\ \vdots & \vdots & \ddots & \vdots \\ 0 & 0 & \cdots & 0 \end{bmatrix}, \quad \sigma_1 \geq \sigma_2 \geq \ldots \geq \sigma_m \geq 0 . \tag{11}$$

We then obtain the spectral decomposition of the trajectory matrix as

$$\mathbf{X} = \sum_{i=1}^{m} \sigma_i \mathbf{u}_i \mathbf{v}_i^T , \tag{12}$$

where $\mathbf{u}_i$ and $\mathbf{v}_i$ are the *i*-th columns of the matrices $\mathbf{U}$ and $\mathbf{V}$.

This decomposition can also be expressed in a simpler form as

$$\mathbf{X} = \sum_{i=1}^{m} \mathbf{X} \mathbf{\Phi}_i \mathbf{\Phi}_i^T \, , \tag{13}$$

where $\mathbf{\Phi}_i$ is the i-th column of $\mathbf{\Phi}$.

The n-th eigenvalue represents the variance of the n-th principal component, and the total variance is given by the sum of all eigenvalues. It is then convenient to normalize the eigenvalues so that this sum becomes 1; in this case, each normalized eigenvalue represents the percentage of the variance "explained" by its associated component.

In the optional third (***reconstruction***) and fourth (***de-embedding***) steps, such components are re-aggregated, usually according to some specific optimization criterion. In the present work, however, we limit ourselves to the analysis of the time evolution of the single SVD coefficients, or of the relation between the values of different subsets of them.

3.   RESULTS

We present next five different periods in which earthquakes with magnitudes greater than five were observed at distances less than 600 km from Popocatépetl volcano. In each period, significant changes were observed at the volcano. Those periods are June 1999, July-August 2000, October 2001, and January 2003. It should be emphasized here that the tectonic earthquakes did not always affect the volcano. An example is a $M = 5.9$ earthquake located at only 100 km from the volcano that did not cause any detectable change in the dynamic parameters, nor in the volcanic activity.

3.1 First case: June 1999

On 15 June 1999, 20:42 UTC, a $Mw = 7.0$ earthquake was detected at 144 km SE from the volcano, in the hypocentral location 18.38°N, 97.43°W at 70 km depth (Singh *et al.* 1999, www.ssn.unam.mx). During the next 24 hours, 8 other events were recorded with magnitudes between 3.5 and 4.5, some in the same area of the main shock, and others closer to the volcano (www.ssn.unam.mx). On 16 June, at 15:00 UTC (375 h counted from the beginning of 1 June 1999 as shown in Fig. 1), Popocatépetl showed an increase in the local volcano-tectonic (VT) activity first, and in the ash and gas emission later (CENAPRED daily reports, available at http://www.cenapred.unam.mx/cgi-bin/popo/reportes/consulta.cgi). The VT swarm, shown as shorter bold vertical bars in Fig. 1, included 76 events distributed along 17 hours. Low-intensity exhalations (protracted gas and ash emissions) at the volcano were detected at 397.3 h and two large explosions recorded at 465.2 h and 466.4 h.
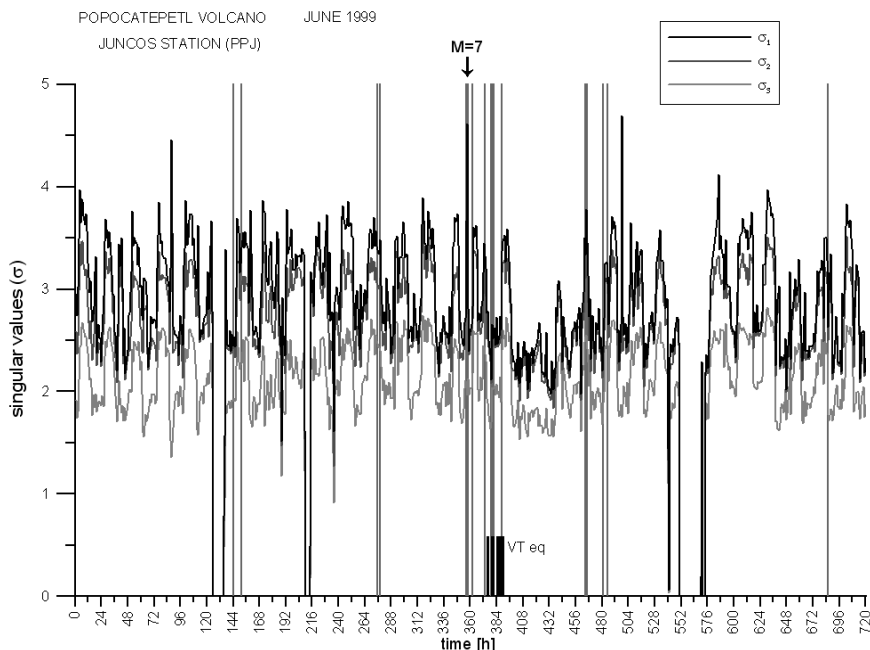
Fig. 1. Evolution of singular value decomposition (SVD) during June 1999, as recorded by the Juncos seismic station. Long vertical lines indicate earthquakes with magnitude greater than 3 and distance less than 200 km (http://www.ssn.unam. mx/). Short vertical bars represent the VT swarms. Time is in hours counted from 1 June at 00:00 UTC.

Continuous seismic data recorded at Juncos (PPJ), Cuervos (PPQ), and Tetexcaloc (PPT) stations were analyzed. Juncos station showed a clear change in most of the parameters after the tectonic earthquake sequence. Figure 1 illustrates the evolution of the first three singular values related to SVD.

In the data recorded by the Tetexcaloc station (not shown), changes associated with the 15 June event are less evident, while a clear transition is seen following two earthquakes with smaller magnitudes, $M = 3.5$ and 3.8, on 7 June 1999, at 00:24 and 07:31 UTC, respectively. The first was located at 30 km from the volcano and 3 km depth, and the second at 150 km from the volcano and 53 km depth, in the same area of the 15 June event.

Analyzing the timing of the transitions in the evolution of the first three SV, and comparing with the evolution of the seismic noise energy SSEM (spectral seismic energy measurement; Tárraga *et al.* 2006) during the same event at Popocatépetl (discussed in De la Cruz-Reyna *et al.* 2010), we observe that significant SV changes do not occur immediately after the $Mw = 7$ earthquake (hour 358), but only at hours 400~408, when the SSEM reveals an hyperbolic acceleration of the seismic energy release rate. The

delay of the SSEM accelerated response was attributed to the retardation of the static stress transfer of the earthquake caused by a viscoleastic shell surrounding the magmatic system and conduit of the volcano (De la Cruz-Reyna *et al.* 2010). The singular values (SV) then return to values comparable to the pre-earthquake state during hours 466~480, when more earthquakes and some explosions at the volcano seem to release the remnant stress perturbation caused by the main earthquake. In this case, we may thus relate the SV changes to the same sources that caused the acceleration of the SSEM, namely a modified stress condition in the marred material holding the magma which develops a progressive sequence of microfailures, until it becomes incapable to keep a pressurized portion of magmatic volatiles and an eruption occurs.

3.2 Second case: August 2000

On 9 August 2000, 11:41 UTC, a $M = 7.0$ earthquake was recorded on the Pacific coast between Guerrero and Michoacan, at 447 km from the volcano and 9 km depth (www.ssn.unam.mx). This event caused significant changes in the activity of Popocatépetl, clearly observed in all parameters and at all stations. During the next 10 hours, 7 aftershocks of $M > 4$ were recorded,
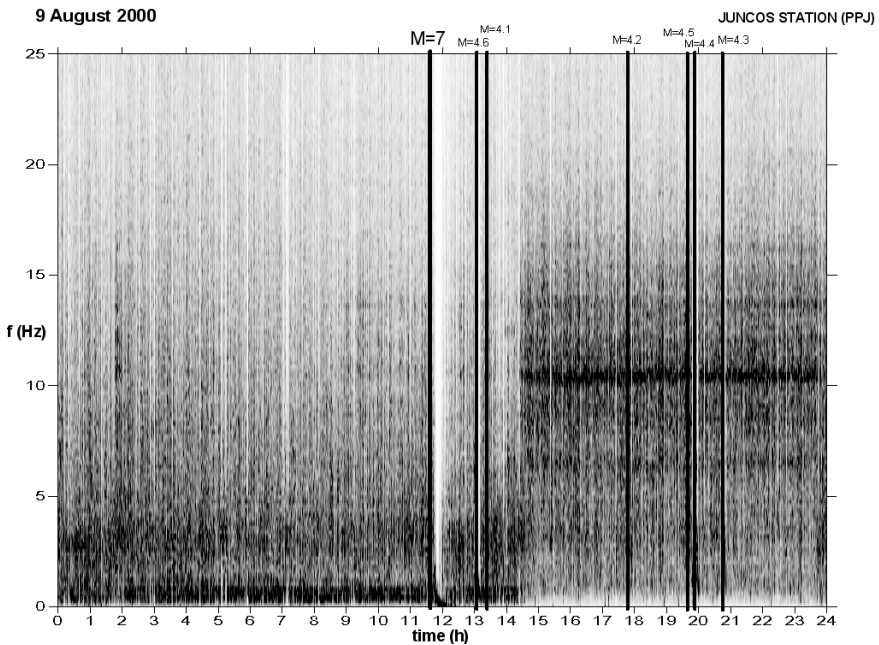
Fig. 2. Spectrogram of 9 August 2000. Long bold vertical lines represent the $M = 7.0$ earthquake and its aftershocks. Time is in hours counted from 9 August at 00:00 UTC.

and on 10 August, 14:14 UTC Popocatépetl erupted with an ash column reaching a height of 3.5 km above the crater (www.cenapred.unam.mx). Figure 2 shows the spectrogram of 9 August, showing a clear change about 2.5 hours after the $M = 7.0$ event.

In this case, the timing of the volcano seismic response shown in the spectrogram is much quicker than in the previous case, suggesting that in this event the spectral response changes had different causes. The epicenter of this $M = 7$ earthquake was located farther away compared with the June 1999 event, reducing the magnitude of the static stress transfer. Therefore, a possible explanation may be an alteration of the spectral content of the seismic signal caused by the pressure increase in the magma bubbles induced by a rectified diffusion during the transit of the main earthquake seismic waves (Ichihara and Nishimura 2009, Chouet *et al.* 2005, Manga and Brodsky 2006, De la Cruz-Reyna *et al.* 2010).

3.3 Third case: October 2001

The significant event was a $M = 6.1$ earthquake recorded on 8 October, 03:39 UTC, at 10 km depth, in Guerrero at 280 km from the volcano (www.ssn.unam.mx). This earthquake was followed by 6 aftershocks of $M > 4$. That earthquake significantly changed the continuous signal of Popocatépetl, as shown by the evolution of the first four SVD singular values displayed in Fig. 3.

The timing in this case is similar as in the August 2000 event, so the causes of the modified state of activity are probably similar.

3.4 Fourth case: January 2003

In January 2003 two significant earthquakes were recorded: the first ($M = 5.3$) at 25 km depth on 10 January, 02:08 UTC, in the Guerrero Pacific coast, at 300 km from the volcano, and the second ($M = 7.6$) at 10 km depth, on 22 January, 02:06 UTC, in the Colima Pacific coast, at 600 km from the volcano. The second was followed by 9 aftershocks with $M > 4$ in the following 4 hours (www.ssn.unam.mx). Changes in volcanic seismic activity caused by these two earthquakes could be observed in all the parameters. This $M = 7.6$ earthquake caused quite evident changes in spite of the greater distance from the volcano. Figure 4 shows the spectrogram for January 2003. This again seems to be a case of a modification of the volcano state by the passage of seismic waves.

3.5 Fifth case: April 2009

An earthquake of $M = 5.7$ was recorded on 27 April 2009, 16:46 UTC, at a depth of 7 km, in the state of Guerrero, at a distance of 349 km SSW from
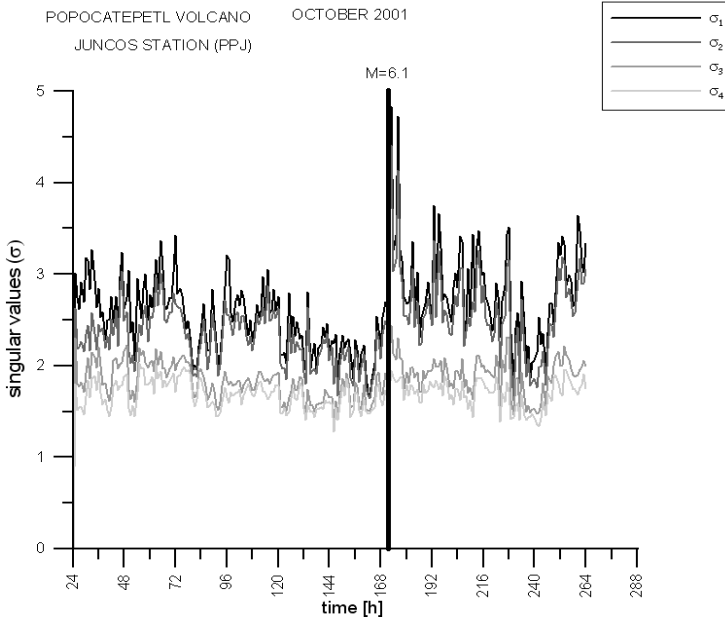
Fig. 3. Evolution of the singular values related to SVD during the period 2-12 October 2001. The bold vertical line marks the $M = 6.1$ earthquake, centered 280 km from the volcano. Time is in hours counted from 2 October at 00:00 UTC.
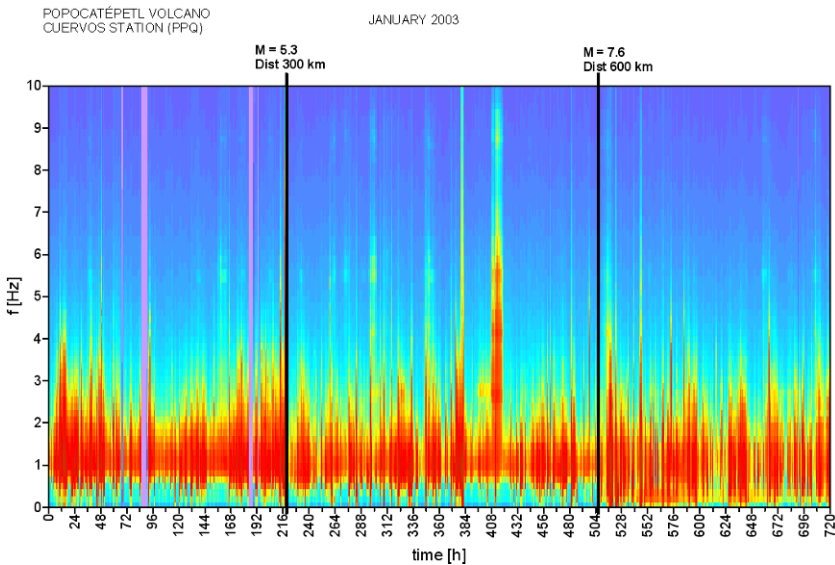

Fig. 4. Spectrogram of January 2003 at Cuervos (PPQ). Bold vertical lines mark the $M = 5.3$ and $M = 7.6$ earthquakes described in the text. Time is in hours counted from 1 January at 00:00 UTC. Colour version of this figure is available in electronic edition only.
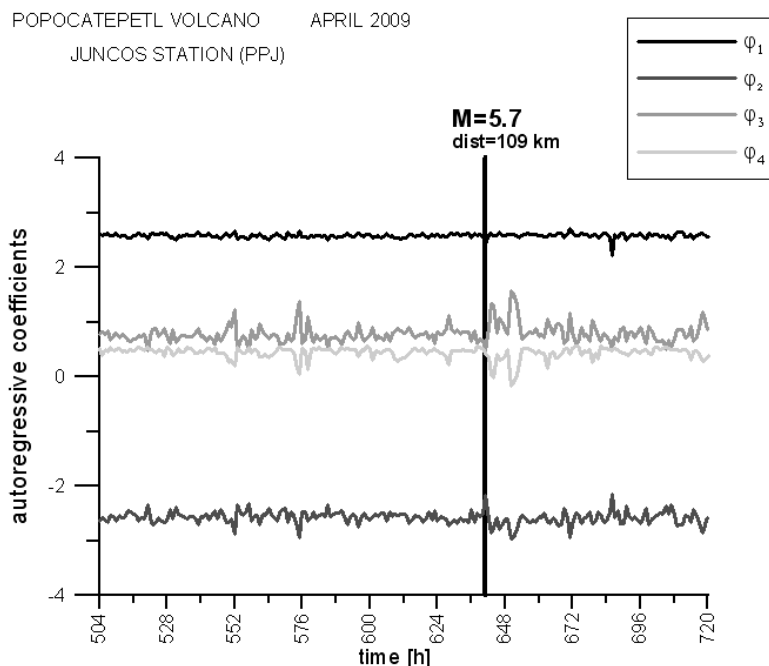
Fig. 5. Autoregressive coefficients for the days 21-30 April 2009 at Juncos (PPJ). Bold vertical line marks the $M = 5.7$ earthquake described in the text. Time is in hours counted from 21 April at 20:00 UTC.

Popocatépetl volcano (www.ssn.unam.mx). The influence of this earthquake on the continuous seismic signal is visible at Cuervos (not shown) and Juncos stations. Figure 5 shows the time evolution of the four first autoregressive coefficients at Juncos station for the last 9 days of April 2009. The influence of the earthquake is mostly visible on the third and fourth AR coefficients. Again, the response of the system is very fast, and the volcano state alteration may be attributed to the transit of high amplitude seismic waves.

3.6 A negative case: July 2000

We consider it important to point out that not all tectonic earthquakes cause changes in the volcano activity, even if their hypocenters are relatively close to the volcano and/or are energetic events. An example is the earthquake occurred on 21 July 2000, 06:13 UTC, at 47 km depth (Fig. 6). Notwithstanding its relative short distance, 109 km from the volcano, and its relatively high magnitude, $M = 5.9$, no effect was observed in the Popocatépetl volcanic seismicity or activity after the event. Figure 6 shows the absence of significant changes in the four first autoregressive coefficients for July 2000.
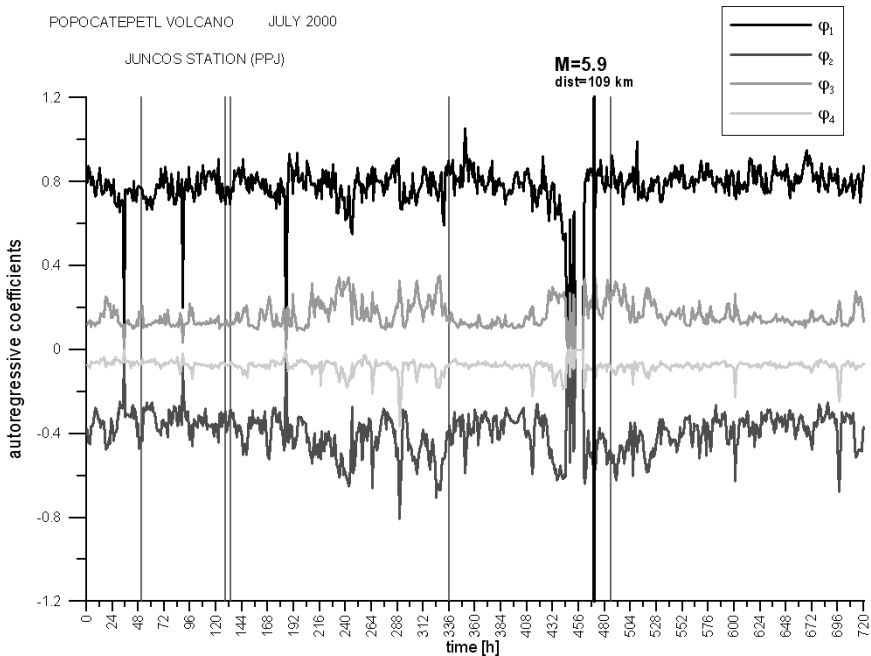
Fig. 6. Autoregressive coefficients, July 2000. Thin vertical lines represent earthquakes with magnitudes greater than 3, located at distances under 200 km from Popocatépetl volcano. The thicker line CENAPRED (the National Center for Disaster Prevention of México; http://www.cenapred.unam.mx) represents the $M = 5.9$ earthquake described in the text (http://www.ssn.unam.mx/). The gap in the data around 450 h was caused by a data-transmission failure. Time is in hours counted from 1 July at 00:00 UTC.

4. CONCLUSIONS

We have described several examples of earthquakes sufficiently energetic ($M > 5$) and/or sufficiently close to the volcano (distance less than 600 km), affecting the volcanic seismicity and the eruptive activity of Popocatépetl. However, we also have observed that other earthquakes do not seem to influence the volcanic activity in any significant way. Furthermore, there are also frequent cases where clear transitions observed in the volcano are unrelated to tectonic earthquakes. Nevertheless, our statistics, although somehow limited, shows that there is usually at least one earthquake per year, with magnitude greater than 5 and distance less than 600 km, out of 2 to 14 earthquakes per year with these characteristics in the period 1999-2009, that affects the behaviour of the volcano, and this we certainly consider significant.

An important question that remains open is why only some earthquakes affect the volcano, while others do not. Possible answers may involve the transfer mechanisms of the stresses released by the earthquakes (De la Cruz-Reyna *et al.* 2010). For a system already in, or approaching, a critical condition such as a chronically restless volcano, the prevailing unstable equilibrium can be disrupted by small perturbations such as those caused by the small stresses transferred by tectonic earthquakes, even if these are located at distances large compared to their rupture lengths. If the volcano is not in a "subcritical" condition (*e.g.*, if the volcanic plumbing system is "open", thereby allowing easy release of pressure) even intermediate magnitude closer earthquakes may not necessarily perturb its internal state. Thus no spectral or dynamical fluctuations are detected in the continuous seismic signals.

Explaining the actual physical changes occurring in a volcanic system that could be linked to the spectral and dynamical parameters fluctuations associated to regional tectonic activity is beyond the scope of this paper. However, some considerations may be discussed regarding the nature of the continuous signal analysis methods described here. All of these methods are based − in different fashions − on the measure of the strength of the autocorrelation of the continuous seismic signal, which in turn is strictly linked to its spectral content. Even the singular value decomposition can be directly related to the classical spectral analysis, as shown by Bozzo *et al.* (2010). In general, the frequencies composing the signal that persist for longer times are strongly emphasized by those autocorrelations, even if the energy contribution of those signals is small. In contrast, transient, high-energy frequencies barely affect the long-term autocorrelations. The persistent frequencies reflect a steady state of a volcano in the same way that the timbre reveals the type of instrument that is playing a note with a given pitch. The source of the continuous signal (a magma body, a hydrothermal system, *etc.*) and the harmonics caused by the geometrical and structural features of the volcanic system generate spectrograms that maintain some of their characteristics for a long time, generating sets of stationary spectral and dynamic parameters. The relevance of the spectral and dynamic parameter analysis presented here is that it permits detection of minute variations in a prone volcanic system caused by the very small changes in the regional stress field produced by the tectonic earthquakes (De la Cruz-Reyna *et al.* 2010) or by the transit of high-amplitude seismic waves (Ichihara and Nishimura 2009). Such variations revealing subtle changes in the internal state of a volcano may remain undetected by other type of analysis.

In any case, the behaviour of Popocatépetl should be monitored with particular attention after an earthquake, because if a significant change is evidenced in the time evolution of the dynamic parameters, the possibility of a triggered eruption cannot be excluded.

Notes

Seismic data used in the study were provided by Servicio Sismológico Nacional (SSN; The National Seismic Network of Mexico), http://www.ssn.unam.mx (last accessed: December 2011.) and Centro Nacional de Prevencion de Desastres, Mexico, (CENAPRED) http://www.cenapred.unam.mx (last accessed: December 2011).

References

Boudal, C., and C. Robin (1989), Volcán Popocatépetl: recent eruptive history, and potential hazards and risks in future eruptions. **In:** J.H. Latter (ed.), *IAVCEI Proc. in Volcanology "Volcanic hazards"*, Springer-Verlag, Berlin, 110-128.

Box, G.E.P., G.M. Jenkins, and G.C. Reinsel (1994), *Time Series Analysis: Forecasting and Control*, 3rd ed., Prentice Hall, Englewood Clifs, NJ.

Bozzo, E., R. Carniel, and D. Fasino (2010), Relationship between singular spectrum analysis and Fourier analysis: Theory and application to the monitoring of volcanic activity, *Comput. Math. Appl.* **60**, 3, 812-820, DOI: 10.1016/j.camwa.2010.05.028.

Carniel, R., and M. Di Cecca (1999), Dynamical tools for the analysis of long term evolution of volcanic tremor at Stromboli, *Ann. Geofis.* **42**, 3, 483-495.

Carniel, R., and M. Tárraga (2006), Can tectonic events change volcanic tremor at Stromboli?, *Geophys. Res. Lett*. **33**, L20321, DOI: 10.1029/2006GL027690.

Carniel, R., M. Di Cecca, and D. Rouland (2003), Ambrym, Vanuatu (July-August 2000): Spectral and dynamical transitions on the hours-to-days timescale, *J. Volcanol. Geoth. Res*. **128**, 1-3, 1-13, DOI: 10.1016/S0377-0273(03) 00243-9.

Carniel, R., F. Barazza, M. Tárraga, and R. Ortiz (2006), On the singular values decoupling in the Singular Spectrum Analysis of volcanic tremor at Stromboli, *Nat. Hazards Earth Syst. Sci.* **6**, 6, 903-909, DOI: 10.5194/nhess-6-903-2006.

Carniel, R., M. Tárraga, F. Barazza, and A. García (2008), Possible interaction between tectonic events and seismic noise at Las Cañadas Volcanic Caldera, Tenerife, Spain, *Bull. Volcanol.* **70**, 9, 1113-1121, DOI: 10.1007/s00445-007-0193-7.

Chouet, B. (2003), Volcano seismology, *Pure Appl. Geophys.* **160**, 3-4, 739-788, DOI: 10.1007/PL00012556.

Chouet, B., P. Dawson, and A. Arciniega-Ceballos (2005), Source mechanism of Vulcanian degassing at Popocatépetl Volcano, Mexico, determined from waveform inversions of very long period signals, *J. Geophys. Res.* **110**, B07301, DOI: 10.1029/2004JB003524.

De la Cruz-Reyna, S., and R.I. Tilling (2008), Scientific and public responses to the ongoing volcanic crisis at Popocatépetl Volcano, Mexico: Importance of an effective hazards-warning system, *J. Volcanol. Geoth. Res.* **170**, 1-2, 121-134, DOI: 10.1016/j.jvolgeores.2007.09.002.

De la Cruz-Reyna, S., I. Yokoyama, A. Martinez-Bringas, and E. Ramos (2008), Precursory seismicity of the 1994 eruption of Popocatépetl Volcano, Central Mexico, *Bull. Volcanol.* **70**, 6, 753-767, DOI: 10.1007/s00445-008-0195-0.

De la Cruz-Reyna, S., M. Tárraga, R. Ortiz, and A. Martinez-Bringas (2010), Tectonic earthquakes triggering volcanic seismicity and eruptions. Case studies at Tungurahua and Popocatépetl volcanoes, *J. Volcanol. Geoth. Res.* **193**, 1-2, 37-48, DOI:10.1016/j.jvolgeores.2010.03.005.

Endo, E.T., and T. Murray (1991), Real-time Seismic Amplitude Measurement (RSAM): A volcano monitoring and prediction tool, *Bull. Volcanol.* **53**, 7, 533-545, DOI: 10.1007/BF00298154.

Hellweg, M. (1999), Seismic signals from Lascar Volcano, *J. South Am. Earth Sci.* **12**, 2, 123-133, DOI: 10.1016/S0895-9811(99)00010-3.

Ichihara, M., and T. Nishimura (2009), Pressure impulses generated by bubbles interacting with ambient perturbation. **In:** R.A. Meyers (ed.), *Encyclopedia of Complexity and Systems Science*, Vol. 7, Springer, New York, 6955-6977.

Jaquet, O., and R. Carniel (2001), Stochastic modelling at Stromboli: a volcano with remarkable memory, *J. Volcanol. Geoth. Res.* **105**, 3, 249-262, DOI: 10.1016/ S0377-0273(00)00254-7.

Manga, M., and E. Brodsky (2006), Seismic triggering of eruptions in the Far Field: Volcanoes and geysers, *Ann. Rev. Earth Planet. Sci.* **34**, 263-291, DOI: 10.1146/annurev.earth.34.031405.125125.

Minakami, T. (1974), Seismology of volcanoes in Japan. **In:** L. Civetta, P. Gasparini, G. Luongo, and A. Rapolla (eds.), *Physical Volcanology*, Elsevier, Amsterdam, 1-27.

Ortiz, R., H. Moreno, A. García, G. Fuentealba, M. Astiz, P. Peña, N. Sánchez, and M. Tárraga (2003), Villarrica volcano (Chile): characteristics of the volcanic tremor and forecasting of small explosions by means of a material

failure method, *J. Volcanol. Geoth. Res.* **128**, 1-3, 247-259, DOI: 10.1016/S0377-0273(03)00258-0.

Packard, N.H., J.P. Crutchfield, J.D. Farmer, and R.S. Shaw (1980), Geometry from a time series, *Phys. Rev. Lett.* **45**, 9, 712-716, DOI: 10.1103/PhysRevLett.45.712.

Privitera, E., T. Sgroi, and S. Gresta (2003), Statistical analysis of intermittent volcanic tremor associated with the September 1989 summit explosive eruptions at Mount Etna, Sicily, *J. Volcanol. Geoth. Res.* **120**, 3-4, 235-247, DOI: 10.1016/S0377-0273(02)00400-6.

Rogers, J.A., and J.A. Stephens (1995), SSAM: Real-time seismic spectral amplitude measurement on a PC and its application to volcano monitoring, *Bull. Seismol. Soc. Am.* **85**, 2, 632-639.

Schick, R. (1988), Volcanic tremor-source mechanisms and correlation with eruptive activity, *Nat. Hazards* **1**, 2, 125-144, DOI: 10.1007/BF00126610.

Singh, S.K., M. Ordaz, J.F. Pacheco, R. Quaas, L. Alcántara, S. Alcocer, C. Gutiérrez, R. Meli, and E. Ovando (1999), A preliminary report on the Tehuacan, Mexico earthquake of June 15, 1999 (Mw = 7.0), *Seismol. Res. Lett.* **70**, 5, 489-504, DOI: 10.1785/gssrl.70.5.489.

Tárraga, M., R. Carniel, R. Ortiz, J.M. Marrero, and A. García (2006), On the predictability of volcano-tectonic events by low frequency seismic noise analysis at Teide–Pico Viejo volcanic complex, Canary Islands, *Nat. Hazards Earth Syst. Sci.* **6**, 3, 365-376, DOI: 10.5194/nhess-6-365-2006.

Tárraga, M., R. Carniel, R. Ortiz, A. García, and H. Moreno (2008), A dynamical analysis of the seismic activity of Villarrica volcano (Chile) during September–October 2000, *Chaos Solitons Fract.* **37**, 5, 1292-1299, DOI: 10.1016/j.chaos.2006.10.062.

Van Loan, C. (1992), *Computational Frameworks for the fast Fourier Transform*, SIAM, Philadelphia.

Vila, J., R. Macià, D. Kumar., R. Ortiz, H. Moreno, and A.M. Correig (2006), Analysis of the unrest of active volcanoes using variations of the base level noise seismic spectrum, *J. Volcanol. Geoth. Res.* **153**, 1-2, 11-20, DOI: 10.1016/j.jvolgeores.2005.10.011.

Walter, T.R., and F. Amelung (2007), Volcanic eruptions following M ≥ 9 megathrust earthquakes: Implications for the Sumatra–Andaman volcanoes, *Geology* **35**, 6, 539-542, DOI: 10.1130/G23429A.1.

Walter, T.R., R. Wang, V. Acocella, M. Neri, H. Grosser, and J. Zschau (2009), Simultaneous magma and gas eruptions at three volcanoes in southern Italy: An earthquake trigger?, *Geology* **37**, 3, 251-254, DOI: 10.1130/G25396A.

VERSITA

Fractal Analysis
of Experimentally Generated Pyroclasts:
A Tool for Volcanic Hazard Assessment

Diego PERUGINI[1,2] and Ulrich KUEPPERS[2]

[1]Department of Earth Sciences, University of Perugia, Perugia, Italy
e-mail: diegop@unipg.it (corresponding author)

[2]Department of Earth and Environmental Sciences,
Ludwig-Maximilians-Universität, Munich, Germany

A b s t r a c t

Rapid decompression experiments on natural volcanic rocks mimic explosive eruptions. Fragment size distributions (FSD) of such experimentally generated pyroclasts are investigated using fractal geometry. The fractal dimension of fragmentation, D, of FSD is measured for samples from Unzen (Japan) and Popocatépetl (Mexico) volcanoes.

Results show that: (i) FSD are fractal and can be quantified by measuring D values; (ii) D increases linearly with potential energy for fragmentation (PEF) and, thus, with increasing applied pressure; (iii) the rate of increase of D with PEF depends on open porosity: the higher the open porosity, the lower the increase of D with PEF; (iv) at comparable open porosity, samples display a similar behavior for any rock composition.

The method proposed here has the potential to become a standard routine to estimate eruptive energy of past and recent eruptions using values of D and open porosity, providing an important step towards volcanic hazard assessment.

Key words: experimental volcanology, rapid decompression experiments, fragment size distributions, fractals, eruptive energy.

1. INTRODUCTION

The introduction of fractal geometry in geosciences (*e.g.*, Turcotte 1992) has caused a growing interest in the use of these techniques to a large number of geological patterns and processes. Any field of research has experienced the application of fractal geometry methods and developed new techniques to quantify geological features (*e.g.*, Sammis *et al.* 1986, Turcotte 1992, Korvin 1992, Barton 1995, Holtz *et al.* 2004, Perugini and Poli 2005, Perugini *et al.* 2006, 2007). The power of fractals in geology is that they have been proven to quantify, often by a single parameter (the fractal dimension, *D*), complex processes that would be otherwise difficult to quantify only by classic geological techniques.

One of the research fields of geosciences where the application of fractal techniques has been very fruitful is the one studying the development of fragmentation processes of Earth materials. In particular, Fragment Size Distributions (FSD) generated by a number of geological processes, such as rock fragmentation (*e.g.*, Matsushita 1985, Turcotte 1986, Sornette *et al.* 1990), fault gauge development (*e.g.*, Sammis *et al.* 1986, Storti *et al.* 2003) and subsidence breccias (Barnett 2004), have been successfully studied by applying fractal statistics. The major result arising from these studies is that fractal dimension, *D*, typically increases as the fragmentation efficiency increases providing a powerful tool to quantify the fragmentation process for different fragmentation mechanisms (*e.g.*, Turcotte 1986).

In recent years, the application of fractal techniques has been proven to be a powerful tool also in the study of volcanic products including the morphology and shape of ash particles (Dellino and Liotino 2002, Maria and Carey 2002, 2007) and FSD resulting from both natural deposits (Taddeucci *et al.* 2004, Pepe *et al.* 2008, Suzuki-Kamata *et al.* 2009, Perugini *et al.* 2011) and experiments (Kueppers *et al.* 2006a, b). These studies provided a deeper understanding of the mechanisms of magma fragmentation during explosive eruptions. They thereby opened new research lines aimed at deriving empirical relationships linking fragmentation efficiency and eruptive energy. A major objective of some of these studies is to furnish new tools for volcanic hazard assessment starting from the analysis of pyroclastic samples (*e.g.*, Kueppers *et al.* 2006b, Suzuki-Kamata *et al.* 2009, Perugini *et al.* 2011).

In this contribution, the fragment size distributions (FSD) of experimentally generated pyroclasts are investigated using fractal geometry techniques. Studied samples derive from Unzen (Japan) and Popocatépetl (Mexico) volcanoes and are sampled from the deposits of pyroclastic density currents and lava flows. We drilled cylinders from these natural products and used them in rapid decompression experiments in the laboratory. The fractal fragmentation theory is applied to FSD obtained under different pressurizations for

samples with different open porosity, and the fractal dimension of fragmentation D of such distributions is measured. The results are discussed in the light of their possible applicability in the study of natural pyroclastic deposits to estimate the eruptive energy of past and recent eruptions and for volcanic hazard assessment.

2. SAMPLE DESCRIPTION AND FRAGMENTATION EXPERIMENTS

Unzen samples derive from the deposits of dense pyroclastic density currents ("block-and-ash flows"), triggered by the gravitational collapse of the active dome during the 1990-1995 eruption. The samples have a dacitic composition and fairly constant phenocryst contents (23-28%, Kueppers *et al.* 2006a). Three sets of samples representing values of open porosity of 7.0, 20.5, and 35.5 vol. % have been chosen. Samples from Popocatépetl have a more heterogeneous origin, with samples from both lava flows (Nealticál eruption, about 2100 years BP) and pyroclastic density currents from a Plinian eruption occurred about 1200 years BP. All samples have andesite composition and a fairly homogeneous phenocryst content of 20% (Alatorre-Ibargüengoitia *et al.* 2011). Three sets of samples with open porosity of 18.0 (lava), 14.0, and 20.0 vol. % (pyroclastic blocks) have been analysed.

Using these six different samples from natural volcanic eruptions, twenty-five rapid decompression experiments were performed in the fragmentation bomb (Alidibirov and Dingwell 1996), modified as described by Spieler *et al.* (2004). This apparatus permits the simulation of the physical conditions during explosive eruptions in terms of temperature (up to 900 °C), gas overpressure (up to 50 MPa), and rate of decompression (up to several GPa/s). It consists of three units (Fig. 1):

- ❑ A low-pressure tank at ambient P and T where the experimentally generated pyroclasts collect (*i.e.*, the atmosphere).
- ❑ A pressurization system with up to three diaphragms, arranged vertically (*i.e.*, a plug, dome or similar).
- ❑ A high-pressure steel autoclave with the sample therein (*i.e.*, the volcano).

This set-up allows for a precise and reproducible pressurization of the sample by argon gas. All experiments were heated externally to 850 °C. The fragmentation process was triggered by a sudden pressure drop due to the opening of diaphragms (Fig. 2) and the propagation of a rarefaction wave into the autoclave that will ultimately hit the sample.

Magmatic fragmentation is driven by gas overpressure in the pore space, generated by volatile oversaturation during magma ascent. As for nature, magma is fragmented during the experiments when the deformation rate (applied via rapidly expanding gas) exceeds the capability of a silicate melt to deform by viscous relaxation (Dingwell 1996). Therefore, our experiments
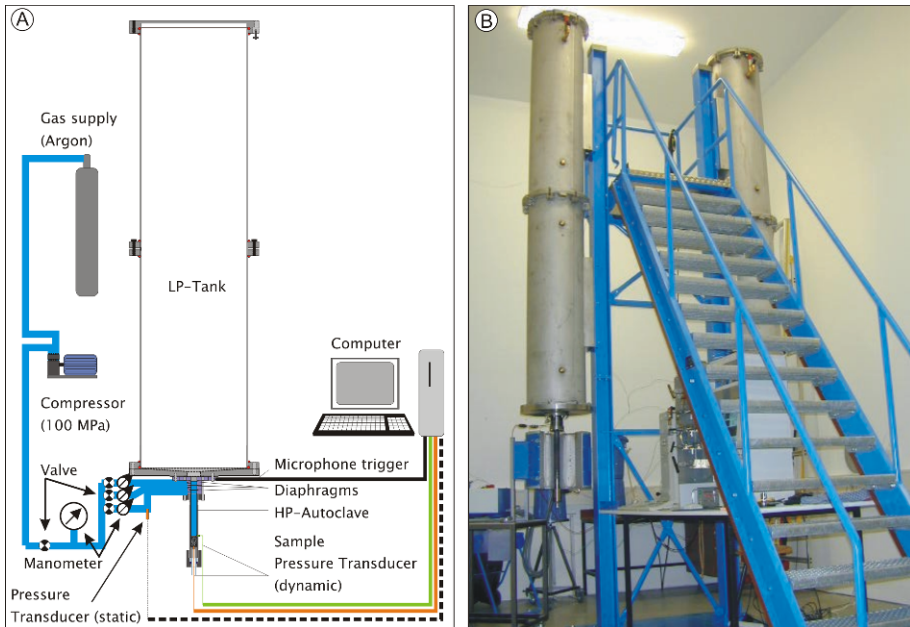
Fig. 1: (A) Schematic drawing and (B) picture of the experimental set-up, the fragmentation bomb. The large tank is at ambient pressure and collects the pyroclasts. A set of three diaphragms maintains the pressure differential to the externally heated, high-pressure autoclave, where the cylindrical sample is placed (after Spieler *et al.* 2004).

are mimicking fragmentation during natural volcanic eruptions as the triggering factor for fragmentation (rapidly expanding gas) and the boundary conditions (at elevated gas overpressure and magmatic temperature) are comparable (Kueppers *et al.* 2006a).

The pyroclasts generated from each decompression experiment have been flushed from the low-pressure tank with distilled water through a 250 µm sieve and thereby separated into a coarse and a fine fraction. Both fractions were dried and weighed. As the experimental set-up is gastight, the sample yield is very high. Sieving was performed at half-Φ steps (Φ = –log$_2$(d), with d equal to particle diameter (in mm); *e.g.*, Cas and Wright 1987 or literature therein). In this study, only the coarse fraction (*i.e.*, greater than 250 µm) has been used. It is important to note that the experimentally generated pyroclast sample does not reflect any transport-related sorting.

The potential energy for fragmentation (PEF) available in any experiment depends on the sample size, the open porosity of the respective sample and the applied pressure:

$$\text{PEF [J]} = V_{\text{Cyl}} \times \theta \times \Delta P \,, \tag{1}$$
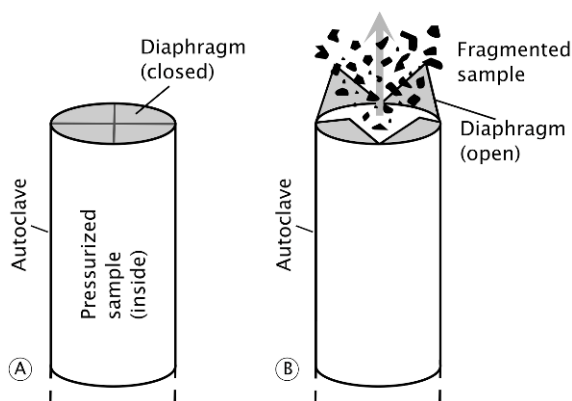
Fig. 2. Schematic drawing of the experimentally driven fragmentation process: (A) A cylindrical rocks sample is placed inside the autoclave, pressurized and heated to the desired temperature; (B) When the pressure applied to the uppermost diaphragm exceeds − on purpose − its stability, this diaphragm fails and opens, causing the immediate opening of the diaphragms below (in the figure only one diaphragm is shown for sake of clarity) and a rarefaction wave propagates into the autoclave and the sample therein, leading to rapid decompression (of the order of GPa/s) and brittle fragmentation.

where V_{Cyl} [m^3], θ, and ΔP [Pa] are the volume of the sample, open porosity fraction and the applied pressure, respectively.

As porosity and also the effectively acting overpressure inside the pore space are subject to strong horizontal and vertical gradients in ascending magmas, the volume of magma affected by an eruption is crucial for the energy calculation. Therefore, we are considering the sample volume also for the calculation of PEF during the experiments. In particular, sample volume was constant for all experiments and equal to 3×10^{-5} m^3. For Unzen samples, open porosity, θ, and applied pressure, ΔP, ranged from 7 to 35.5 vol.% (*i.e.*, $0.07 < \theta < 0.355$) and from 7.5×10^6 to 50×10^6 Pa, respectively, resulting in PEF from about 50 to 270 J. For Popocatépetl, open porosity and applied pressure ranged from 14 to 20 vol.% (*i.e.*, $0.14 < \theta < 0.20$) and from 11×106 to 30×106 Pa, respectively, resulting in PEF from about 55 to 160 J. In all cases, the lower value of applied pressure was depending on sample fragmentation threshold (Spieler *et al.* 2004).

3. FRACTAL ANALYSIS OF EXPERIMENTALLY GENERATED PYROCLASTS: BASIC PRINCIPLES

As reported by Mandelbrot (1982), Korcak in 1938 performed empirical studies on the size distribution of the areas of islands and developed the empirical relationship:

$$N(A > a) \approx a^{-b} , \tag{2}$$

where $N(A > a)$ is the total number of islands having size A greater than a given comparative size, a, and b is a constant equal to $1/2$ for all islands (Korvin 1992). Mandelbrot (1982) studied Korcak's work and found that b actually varied between island regions with b always being greater than $1/2$. In the light of fractal theory, he realized that the size distribution of a population of islands was actually a consequence of fractal fragmentation and that the empirical constant b correlated with the fractal dimension. He therefore suggested that fragmentation could be quantified by measuring the fractal dimension through the equation

$$N(r > R) \approx C \times R^{-D} , \tag{3}$$

where D is the fractal dimension of fragmentation; $N(r > R)$ is the total number of particles with linear dimension r which is greater than a given comparative size, R; and C is a proportionality constant. It is to note that fractal dimension, D, derived from Eq. (1) is not a measure of irregularity, but a measure of the size-number relationship of the particle population or, in other terms, the fragmentation of the population.

The number-based relationship given in Eq. (3) can be utilized in the analysis of fragment size distributions (FSD) of pyroclasts by making assumptions about the unit weight of individual particles, since FSD are typically determined by mass comparison (*i.e.*, mass retained on successive sieve sizes). In particular, Eq. (3) can be used by modeling individual particles as uniform shapes, thereby developing standard uniform densities. By assuming the size of the particle to coincide with sieve screen dimensions, the number of particles per sieve size can be calculated by dividing the total weight material retained on each sieve by the density of an individual particle. Kueppers *et al.* (2006a, b) used this approach in the study of experimentally fragmented samples from Mt. Unzen volcano and they showed that there is a linear relationship between fractal dimension, D, and potential energy of fragmentation (PEF) for samples with different open porosity.

In practical applications, however, the relationship given by Eq. (3) may be not convenient and errors can be introduced in the calculations when considering particle uniformity with respect shape and density. To avoid such potential errors Tyler and Wheatcraft (1992) and Turcotte (1986, 1992) developed a relationship relating mass measurements and sieve diameters. Note that this mass-based approach is directly applicable to data obtained from analyses of pyroclastic deposits, where typically mass fractions, rather than number fractions, are measured. The mass-based form of Eq. (3) can be expressed as

$$\frac{M(r < R)}{M_T} = R^v ,\tag{4}$$

where $M(r < R)$ is the cumulative mass of particles with size r smaller than a comparative size R; M_T is the total mass of particles; R is the sieve size opening; and v is a constant exponent. Equation (4) is a power-law that can be related to the fractal number-based relation by taking incremental values, as reported in Matsushita (1985) and Turcotte (1992). Logarithmic transformation of Eq. (4) results in a linear relationship of $M(r < R)$ and R for a scale-invariant (*i.e.*, fractal) FSD. The exponent v is found by estimating the slope coefficient of the log-log plot. It is possible to derive a direct relationship between the scaling exponent v and the fractal dimension of fragmentation D. Taking the derivatives of Eqs. (3) and (4) with respect to the size R yields, respectively

$$\mathrm{d}N \propto R^{-D-1}\mathrm{d}R ,\tag{5}$$

and

$$\mathrm{d}M \propto R^{-v-1}\mathrm{d}R .\tag{6}$$

The volume of a particle with size r is proportional to its mass m, and, hence, $r^3 \propto m$; it follows that for incremental particle numbers and masses we obtain

$$R^3\mathrm{d}N \propto \mathrm{d}M .\tag{7}$$

As shown by Turcotte (1992), by substituting Eqs. (5) and (6) into (7) we get

$$R^{-D-1} \propto R^{-3}R^{v-1} ,\tag{8}$$

from which it follows that

$$D = 3 - v .\tag{9}$$

Therefore, the fractal dimension of fragmentation, D, can be calculated using the exponent v from the mass-based approach. Equations (4) and (9) are useful in estimating D for pyroclastic deposits since the FSD obtained by particle size analysis can be utilized directly. This approach has been used to analyze FSD of experimentally generated pyroclasts studied in this contribution with the aim to evaluate their possible fractal nature, to estimate the exponent v, and, hence, to compute their fractal dimension of fragmentation, D.

4.   RESULTS AND DISCUSSION

The nature of experimentally generated FSD is displayed in the log-log cumulative distributions plots of Fig. 3, used to quantify the degree of fragmentation by fractal analysis. In this figure, representative samples with
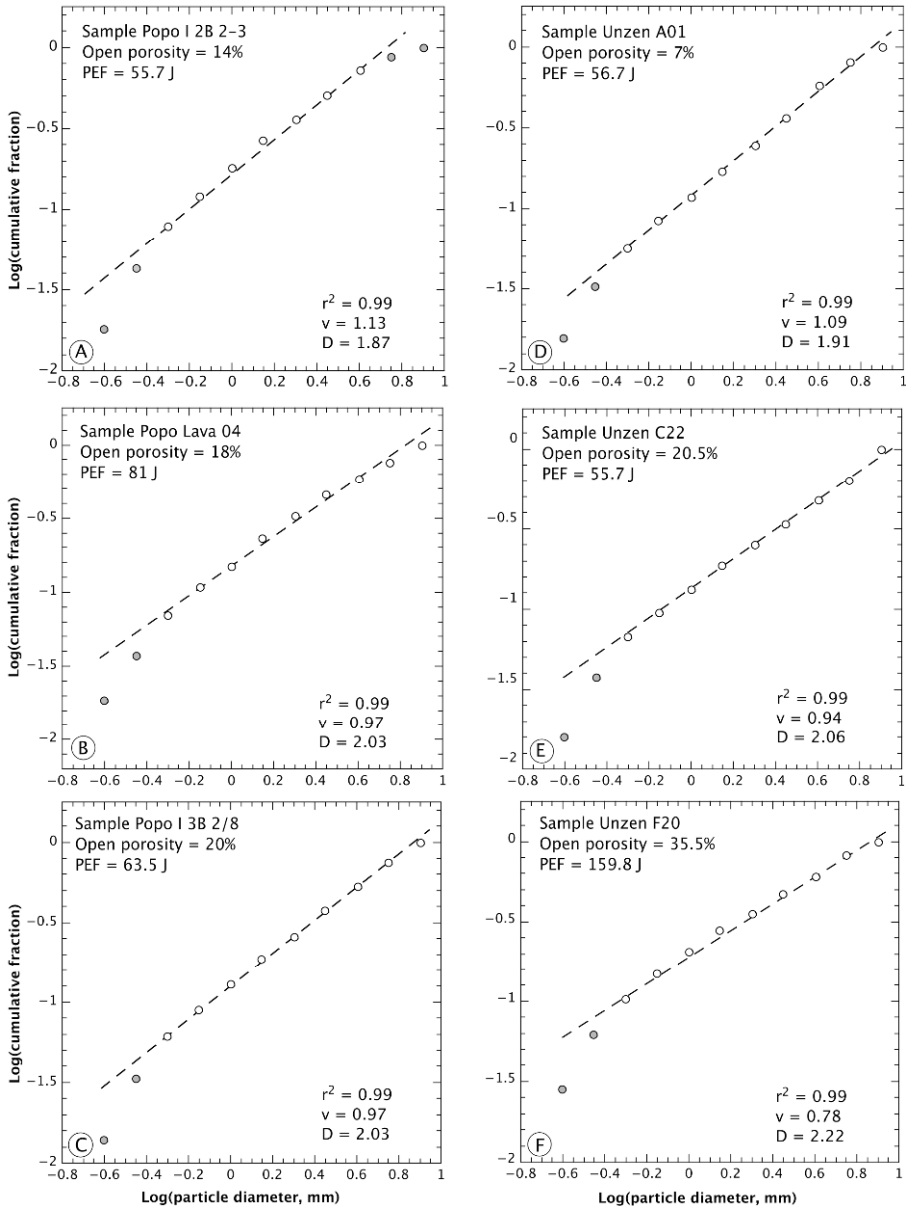
Fig. 3. Log-log plots of fragment size distributions for six representative samples from Popocatépetl (A-C, left) and Unzen (D-F, right) volcanoes with different open porosity and potential energy for fragmentation (PEF). Symbols denote experimental data, dashed lines denote model fits. Grey color data are those not included in the linear fitting. Values of r^2, slope v, and fractal dimension of fragmentation D are also reported in each plot.

different open porosity and potential energy for fragmentation (PEF) from Popocatépetl (left) and Unzen (right) volcanoes are reported. From these graphs it is clear that all FSD display linear trends over a range of length scales, following a fractal distribution. The fractal dimension of fragmentation, D, was estimated for all studied samples from the slope of the linear fitting according to Eqs. (4) and (9). The degree of fragmentation of each sample, hence, was quantified by the value of fractal dimension of fragmentation, D: the larger D, the higher the fragmentation efficiency, *i.e.*, the more fine fragments. Results indicate that for Unzen and Popocatépetl samples D values range from 1.90 to 2.27 and from 1.91 to 2.15, respectively.

The conceptual model used to derive Eqs. (3) and (4) is based on the self-similar fragmentation of an initial solid mass into progressively smaller particles (Matsushita 1985, Turcotte 1986). In particular, starting from a cubic shape of size h, it is fragmented into eight smaller cubes of size $h/2$. These smaller cubes are further fragmented following an iterative procedure to give cubes with size $h/4$, and so forth. In this fragmentation model, the cube has a certain probability, p, to fragment, which is assumed to be constant for all orders of fragmentation. The cube is maximally fragmented into eight smaller cubes if $p = 1.0$ and into one smaller cube if $p = 1/8$. Turcotte (1986) established the following relationship between the fragmentation probability, p, and fractal dimension, D:

$$D = \frac{\log(8p)}{\log(2)},\tag{10}$$

with the possible range of fractal dimension being $0 < D < 3$. A plot of Eq. (10), along with p values calculated using values of D measured on studied samples, is given in Fig. 4. From the graph it is clear that, on average, fractal dimension of fragmentation, D, tends to increase as open porosity increases for both Popocatépetl (Fig. 4A) and Unzen samples (Fig. 4B). This feature appears to be in agreement with recent results of fractal analyses of natural pyroclastic deposits presented by Perugini *et al.* (2011), where a direct relationship has been found between fractal dimension of fragmentation, D, and sample porosity. These authors suggested that, being D correlated with fragmentation probability, p, it can be also interpreted as a proxy for sample "fragility" (*i.e.*, ability to fragment into smaller fragments). The fractal analysis performed on experimentally produced pyroclasts presented in the present work, therefore, appears to corroborate this hypothesis.

Our results also indicate that there is a systematic increase of fractal dimension of fragmentation, D, as the potential energy for fragmentation (PEF) increases. It is worth noting that similar results were obtained by Kueppers *et al.* (2006b) for fractal analysis of grain-size distributions based
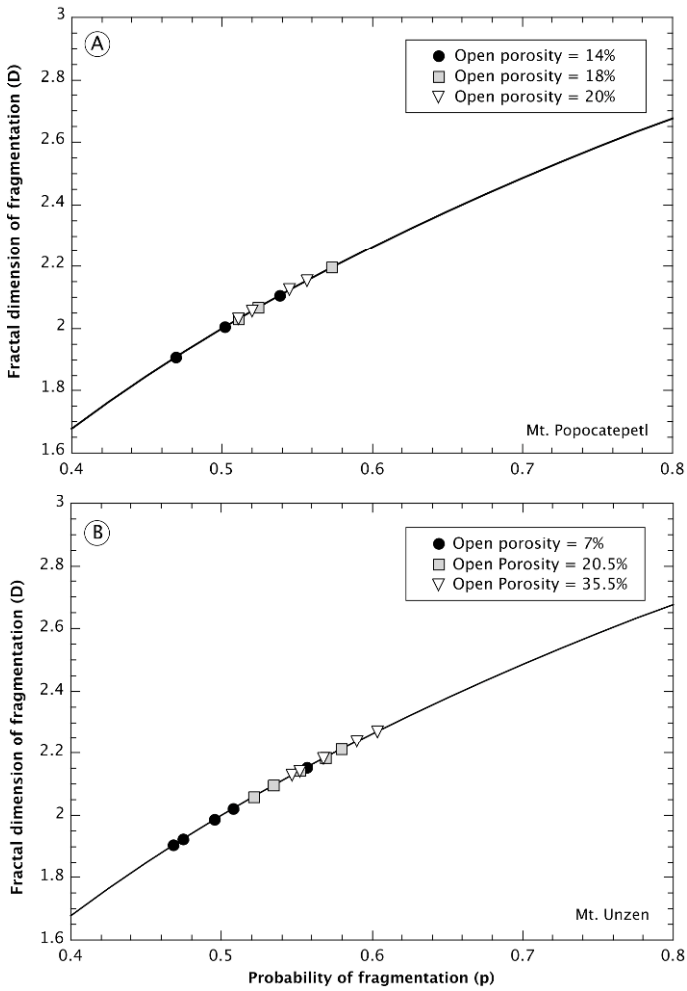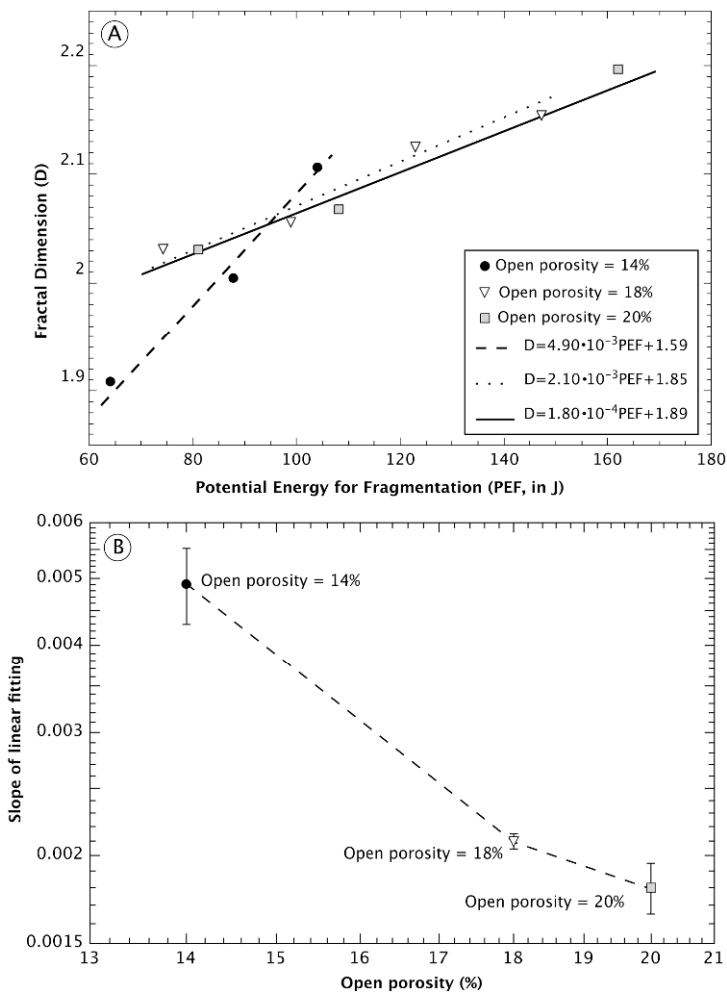
Fig. 4. Fragmentation fractal dimensions, D, and probabilities, p, of fragmentation. The dashed line represents Eq. (10), symbols are calculated with Eq. (10) from experimentally determined fractal dimensions.

on the number of fragments (*i.e.*, by applying Eq. (3)) for Unzen samples. Although absolute values of D necessarily change because the method to measure D in the present work is based on mass comparisons, the structure of data is the same (*i.e.*, linear increase of D with PEF, see below). As grain-size distribution (granulometry) is a generally accepted tool to describe volcanic deposits, we have used the size-dependent mass fractions in this study to estimate the fragmentation efficiency (*i.e.*, D) without recalculating the number of fragments for each class. Figures 5A and 6A show the variation
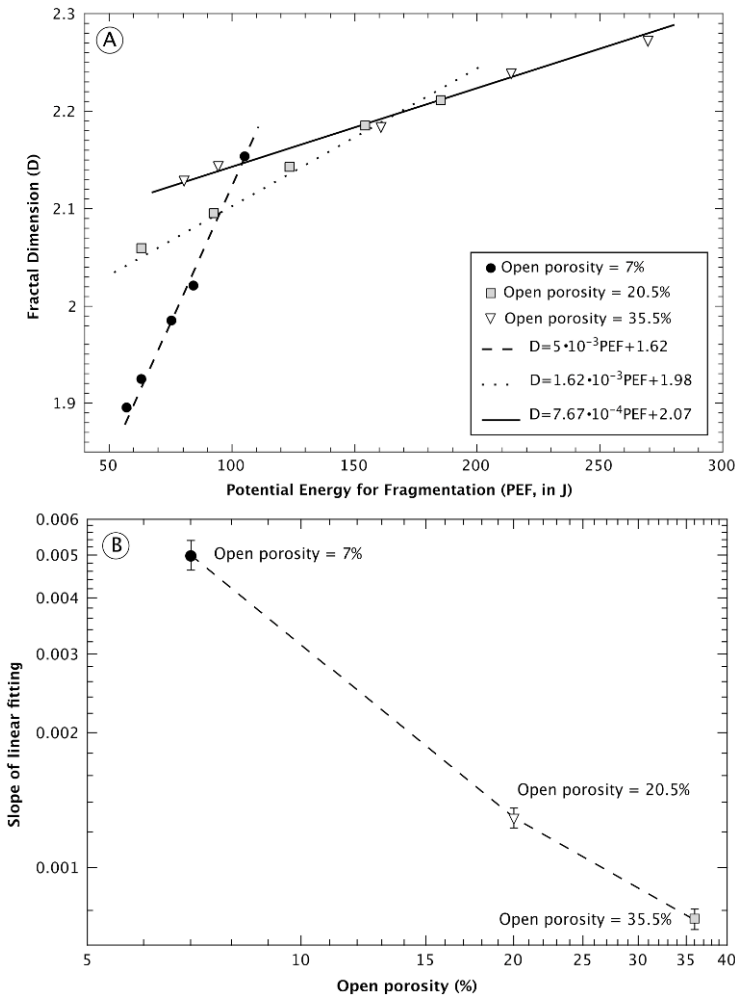
Fig. 5: (A) Linear increase of fractal dimension of fragmentation, *D*, as the potential energy for fragmentation (PEF) increases for samples of Mt. Popocatépetl volcano with different open porosity; (B) Variation of the slope of linear fitting of data presented in (A) plotted against the open porosity of samples.

of *D versus* PEF for experimental samples of Popocatépetl and Unzen, respectively. The graphs show that the increase in the fractal dimension of fragmentation, *D*, is linear (*r* value of linear fitting greater than 0.95) for each sample set but the rate of increase of *D* with PEF is different. Quantitatively this effect is shown in Figs. 5B and 6B in which the variation of the slope of linear fitting of data presented in Figs. 5A and 6A is plotted against the open porosity of samples. It can be seen that there is decrease of slope

Fig. 6: (A) Linear increase of fractal dimension of fragmentation, *D*, as the potential energy for fragmentation (PEF) increases for samples of Mt. Unzen volcano with different open porosity; (B) Variation of the slope of linear fitting of data presented in (A) plotted against the open porosity of samples.

for both sample sets, consistent with the above discussion. Note that the variation slope is significant, *i.e.*, well outside errors estimated with linear regression. The only exceptions are the sample sets at 18 and 20 vol.% of open porosity of Popocatépetl that display quite close values (considering errors) of slopes. The slope similarity of these two sample sets is quite reasonable given that the difference in open porosity is small (*i.e.*, about 2 vol.%). This result also indicates that fragmentation efficiencies may not be easily

discriminated by fractal analysis for differences in open porosity of this order of magnitude. We stress that these two sample sets were collected from entirely different deposit types (lava flow and pyroclastic density current). This may imply that the open porosity of samples is the parameter playing the greatest role in determining fragmentation efficiency, irrespective of the composition of the starting material. Note that this statement is related exclusively to the fragmentation process itself. Without doubt, the chemical composition plays a major role defining the speed and efficiency of any physical process acting during magma ascent. This consideration is corroborated by the comparison of the behaviour of the above two set of samples (Popocatépetl, open porosity equals 18 and 20 vol.%) with the set of samples from Unzen with open porosity of 20.5 vol.%. Indeed, slope values for these three sets of samples are very similar, ranging from 1.62×10^{-3} to 2.10×10^{-3}, arguing again in favour of the hypothesis that fragmentation efficiency does not depend on the starting composition of samples or on specific volcanologic conditions.

On the basis of these results it is possible to derive sets of linear equations relating fractal dimension of fragmentation, D, and potential energy for fragmentation (PEF) for the different sample sets. They are reported in the graphs of Figs. 5A and 6A. Therefore, on the basis of these results we propose that it is possible to estimate the potential energy for fragmentation of natural deposits by measuring values of D and open porosity of samples and using the relationships obtained experimentally for samples with similar open porosity.

5. SUMMARY AND CONCLUSIONS

Fractal analysis of experimentally produced pyroclasts has been carried out for six sets of variously porous samples from Unzen and Popocatépetl volcanoes. Fractal fragmentation theory was applied to mass fragment size distributions and the main results can be summarized as follows:

❑   The fragment size distribution of pyroclasts produced by decompression experiments is consistent with the fractal fragmentation theory in that size distributions are fractals and they can be univocally quantified by measuring a single parameter, *i.e.*, the fractal dimension of fragmentation, D. The fractal nature of fragment size distributions holds for all studied samples, irrespective of potential energy for fragmentation and open porosity. This result corroborates the idea that the fragmentation mechanism during volcanic eruptions can be regarded as a highly non-linear process in which a hierarchical propagation of fractures at different length scales occurs.

❑   Fractal dimension of fragmentation increases linearly with potential energy for fragmentation. This result has been recognized for all six sample

sets irrespective of volcano or deposit type. Such a feature provides new information about the mechanisms acting during decompression-induced fragmentation and, in particular, indicates that a linear increase of fragmentation efficiency (*i.e.*, fractal dimension of fragmentation, *D*) has to be expected at increasing applied pressure.

❑   The velocity of increase of fractal dimension of fragmentation, *D*, with applied pressure (or equivalently potential fragmentation energy, PEF) is different for samples having different open porosity. In particular, the higher the open porosity, the lower the increase of *D* with PEF. This point has important implications because it indicates that it is possible to derive a set of linear equations relating *D* and PEF and allows estimating potential fragmentation energy for natural deposits by measuring *D* and open porosity of samples.

❑   Samples with the same open porosity display a similar behavior irrespective of starting composition and emplacement style (pyroclastic blocks or lava flow samples). This point is very important because it highlights the fact that the method illustrated in this work may become a standard routine to estimate eruptive energy for any volcanic deposit and for any composition of the starting material using values of open porosity and fractal dimension of fragmentation, *D*.

The results presented in this contribution are very encouraging and may represent a further step towards a better understanding of the mechanisms acting for rock fragmentation during explosive volcanic eruptions. Further research needs to be carried out by considering other case studies in order to test the hypotheses presented in this work. In particular, it would be amenable to check for the effect of transport on fragments generated by explosive eruptions to study possible variation in the fragment size distributions due to this secondary process. Our results indicate that it is possible to derive simple equations by which the most important factors influencing volcanic eruption can be estimated. This aspect is particularly important because it constitutes the basis for developing a totally different approach in the study of natural volcanic deposits and, ultimately, may furnish new tools for volcanic hazard assessment. In this respect, results presented in this work may help in evaluating volcanic risk by estimating the explosivity (*e.g.*, pressure in the conduit) from the value of fractal dimension of fragment size distribution for samples collected around volcanic areas. This may give the opportunity to draw iso-*D* or iso-explosivity maps based on fractal statistics (Kueppers *et al.* 2006a, b).

A possible future application of this method may be the on-line estimate of explosivity during volcanic eruptions. By placing sets of sieves with different aperture in strategic positions around an erupting volcano it may be possible to collect masses of pyroclasts with specific grain sizes. Every sieve

set will be equipped with a special inlet device that prevents the destruction due to the impact energy. When the individual sieves are connected to well-calibrated balances, it may be possible to obtain the weight fractions needed to estimate the fractal dimension of fragmentation (*i.e.*, eruptive energy), to estimate in real-time the explosivity of volcanic bursts, and to follow the time-development of an eruption. This idea has to be complemented with existing studies on the influence of transport-related sorting to the grain-size distribution (Taddeucci *et al.* 2004).

References

Alatorre-Ibargüengoitia, M.A., B. Scheu, and D.B. Dingwell (2011), Influence of the fragmentation process on the dynamics of Vulcanian eruptions: An experimental approach, *Earth Planet. Sci. Lett.* **302**, 1-2, 51-59, DOI: 10.1016/j.epsl.2010.11.045.

Alidibirov, M., and D.B. Dingwell (1996), An experimental facility for the investigation of magma fragmentation by rapid decompression, *Bull. Volcanol.* **58**, 5, 411-416, DOI: 10.1007/s004450050149.

Barnett, W. (2004), Subsidence breccias in kimberlite pipes – an application of fractal analysis, *Lithos* **76**, 1-4, 299-316, DOI: 10.1016/j.lithos.2004.03.019.

Barton, C.C. (1995), Fractal analysis of scaling and spatial clustering of fractures. **In:** C.C. Barton, and P.R. La Pointe (eds.), *Fractal in the Earth Sciences*, Plenum Press, NY, 141-178.

Cas, R.A.F., and J.V. Wright (1987), *Volcanic Successions, Modern and Ancient*, Chapman & Hall, London.

Dellino, P., and G. Liotino (2002), The fractal and multifractal dimension of volcanic ash particles contour: a test study on the utility and volcanological relevance, *J. Volcanol. Geotherm. Res.* **113**, 1-2, 1-18, DOI: 10.1016/S0377-0273(01)00247-5.

Dingwell, D.B. (1996), Volcanic dilemma – flow or blow? *Science* **273**, 5278, 1054-1055, DOI: 10.1126/science.273.5278.1054.

Holtz, F., S. Lenne, G. Ventura, F. Vetere, and P. Wolf (2004), Non-linear deformation and break up of enclaves in a rhyolitic magma: A case study from

Lipari Island (Southern Italy), *Geophys. Res. Lett*. **31**, L24611, DOI: 10.1029/2004GL021590.

Korvin, G. (1992), *Fractal Models in the Earth Sciences*, Elsevier, Amsterdam.

Kueppers, U., B. Scheu, O. Spieler, and D.B. Dingwell (2006a), Fragmentation efficiency of explosive volcanic eruptions: A study of experimentally generated pyroclasts, *J. Volcanol. Geotherm. Res*. **153**, 1-2, 125-135, DOI: 10.1016/j.jvolgeores.2005.08.006.

Kueppers, U., D. Perugini, and D.B. Dingwell (2006b), "Explosive energy" during volcanic eruptions from fractal analysis of pyroclasts, *Earth Planet. Sci. Lett*. **248**, 3-4, 800-807, DOI: 10.1016/j.epsl.2006.06.033.

Mandelbrot, B.B. (1982), *The Fractal Geometry of Nature*, Freeman, San Francisco.

Maria, A., and S. Carey (2002), Using fractal analysis to quantitatively characterize the shapes of volcanic particles, *J. Geophys. Res*. **107**, B11, 2283, DOI: 10.1029/2001JB000822.

Maria, A., and S. Carey (2007), Quantitative discrimination of magma fragmentation and pyroclastic transport processes using the fractal spectrum technique, *J. Volcanol. Geotherm. Res*. **161**, 3, 234-246, DOI: 10.1016/j.jvolgeores. 2006.12.006.

Matsushita, M. (1985), Fractal viewpoint of fracture and accretion, *J. Phys. Soc. Japan* **54**, 857-860, DOI: 10.1143/JPSJ.54.857.

Pepe, S., G. Solaro, G.P. Ricciardi, and P. Tizzani (2008), On the fractal dimension of the fallout deposits: A case study of the 79 A.D. Plinian eruption at Mt. Vesuvius, *J. Volcanol. Geotherm. Res*. **177**, 1, 288-299, DOI: 10.1016/ j.jvolgeores.2008.01.023.

Perugini, D., and G. Poli (2005), Viscous fingering during replenishment of felsic magma chambers by continuous inputs of mafic magmas: Field evidence and fluid-mechanics experiments, *Geology* **33**, 1, 5-8, DOI: 10.1130/ G21075.1.

Perugini, D., M. Petrelli, and G. Poli (2006), Diffusive fractionation of trace elements by chaotic mixing of magmas, *Earth Planet. Sci. Lett*. **243**, 3-4, 669-680, DOI: 10.1016/j.epsl.2006.01.026.

Perugini, D., L. Valentini, and G. Poli (2007), Insights into magma chamber processes from the analysis of size distribution of enclaves in lava flows: A case study from Vulcano Island (Southern Italy), *J. Volcanol. Geotherm. Res*. **166**, 3-4, 193-203, DOI: 10.1016/j.jvolgeores.2007.07.017.

Perugini, D., A. Speziali, L. Caricchi, and U. Kueppers (2011), Application of fractal fragmentation theory to natural pyroclastic deposits: insights into volcanic explosivity of the Valentano scoria cone (Italy), *J. Volcanol. Geotherm. Res*. **202**, 200-210, DOI: 10.1016/j.jvolgeores.2011.02.008.

Sammis, C.G., R.H. Osborne, J.L. Anderson, M. Banerdt, and P. White (1986), Self-similar cataclasis in the formation of fault gouge, *Pure Appl. Geophys*. **124**, 1-2, 53-78, DOI: 10.1007/BF00875719.

Sornette, A., P. Davy, and D. Sornette (1990), Growth of fractal fault patterns, *Phys. Rev. Lett*. **65**, 18, 2266-2269, DOI: 10.1103/PhysRevLett.65.2266.

Spieler, O., B. Kennedy, U. Kueppers, D.B. Dingwell, B. Scheu, and J. Taddeucci (2004), The fragmentation threshold of pyroclastic rocks, *Earth Planet. Sci. Lett.* **226**, 1-2, 139-148, DOI: 10.1016/j.epsl.2004.07.016.

Storti, F., A. Billi, and F. Salvini (2003), Particle size distributions in natural carbonate fault rocks: insights for non-self-similar cataclasis, *Earth Planet. Sci. Lett*. **206**, 1-2, 173-186, DOI: 10.1016/S0012-821X(02)01077-4.

Suzuki-Kamata, K., T. Kusano, and K. Yamasaki (2009), Fractal analysis of the fracture strength of lava dome material based on the grain size distribution of block-and-ash flow deposits at Unzen Volcano, Japan, *Sedim. Geol.* **220**, 3-4, 162-168, DOI: 10.1016/j.sedgeo.2009.04.026.

Taddeucci, J., M. Pompilio, and P. Scarlato (2004), Conduit processes during the July-August 2001 explosive activity of Mt. Etna (Italy): inferences from glass chemistry and crystal size distribution of ash particles, *J. Volcanol. Geotherm. Res.* **137**, 1-3, 33-54, DOI: 10.1016/j.jvolgeores.2004.05.011.

Turcotte, D.L. (1986), Fractals and fragmentation, *J. Geophys. Res*. **91**, B2, 1921-1926, DOI: 10.1029/JB091iB02p01921.

Turcotte, D.L. (1992), *Fractals and Chaos in Geology and Geophysics*, Cambridge University Press, Cambridge.

Tyler, S.W., S.W. Wheatcraft (1992), Fractal scaling of soil particle-size distributions: analysis and limitations, *Soil Sci. Soc. Am. J.* **56**, 2, 362-369.

Emulation of Simulated Earthquake Catalogues

Marta GALLUCCI[1,2], Serge GUILLAS[2,3], and Filippos VALLIANATOS[3,4]

[1]Dipartimento di Statistica "G. Parenti", Università di Firenze, Firenze, Italy
e-mail: gallucci@ds.unifi.it (corresponding author)

[2]Department of Statistical Science, University College London, London, UK

[3]Institute for Risk and Disaster Reduction, University College London, London, UK

[4]Technological Educational Institute of Crete,
Laboratory of Geophysics and Seismology, Crete, Greece

A b s t r a c t

In earthquake occurrence studies, the so-called q value can be considered both as one of the parameters describing the distribution of inter-event times and as an index of non-extensivity. Using simulated datasets, we compare four kinds of estimators, based on principle of maximum entropy (POME), method of moments (MOM), maximum likelihood (MLE), and probability weighted moments (PWM) of the parameters (q and τ_0) of the distribution of inter-events times, assumed to be a generalized Pareto distribution (GPD), as defined by Tsallis (1988) in the frame of non-extensive statistical physics. We then propose to use the unbiased version of PWM estimators to compute the q value for the distribution of inter-event times in a realistic earthquake catalogue simulated according to the epidemic type aftershock sequence (ETAS) model. Finally, we use these findings to build a statistical emulator of the q values of ETAS model. We employ treed Gaussian processes to obtain partitions of the parameter space so that the resulting model respects sharp changes in physical behaviour. The emulator is used to understand the joint effects of input parameters on the q value, exploring the relationship between ETAS model formulation and distribution of inter-event times.

Key words: probability weighted moments, q statistics, inter-event times, ETAS model, emulator.

1.   INTRODUCTION

In the context of seismological studies, it is essential to establish the time between subsequent earthquakes, within defined margins of reliability. For this reason, the study of the probability distribution of the so-called inter-event times plays a relevant role. Abe and Suzuki (2003, 2005) suggest that calm times, or periods elapsing between two successive events, follow a Zipf–Mandelbrot type distribution, corresponding to a q-exponential distribution with $q > 1$. Furthermore, recent applications to solid earth physics (in regional or planetary scale), summarized into Tsallis (2009), mainly focused in seismology (Abe and Suzuki 2003, 2005, Telesca 2010a, b) using earthquake catalogues from different seismic zones, fault lengths distribution (Vallianatos *et al.* 2011a, b; Vallianatos and Sammonds 2011) and very recently to natural hazards (Vallianatos 2009), plate tectonics (Vallianatos and Sammonds 2010) and geomagnetic reversals (Vallianatos 2011) supports the applicability of NESP (non-extensive statistical physics) in complex geosystems. More details on q exponential and other q statistics will be presented in the following section. What Abe and Suzuki (2003, 2005) call "q-exponential" function, is indeed the complementary cumulative distribution function (CCDF) of a generalized Pareto distribution with a location parameter of 0, a scale parameters of τ_0, and a shape parameter equal to $(q-1)$. This distribution is already known in seismology, since it has been used to model earthquakes magnitude (Kagan and Shoenberg 2001, Pisarenko *et al.* 2010). The procedure usually applied to estimate the q value refers to the principle of maximum entropy (POME). However, this technique may not be the most adequate in every context: Singh and Guo (1997) suggest using POME estimators when the coefficient of variation of the data is high (CV ≥ 1.5).

The present work is organized as follows: after introducing the main concepts about q statistics (Section 2), we will compare the performance of different estimators (Section 3), based on principle of maximum entropy (POME), probability weighted moments (PWM), method of moments (MOM) and maximum likelihood (MLE), in order to select the most suitable estimator for the computation of the q value. We will be using randomly generated data to compute bias and root-mean-square error (RMSE) for each estimator. Then, we will apply the best estimator to a set of simulated earthquake catalogues obtained according to the ETAS model (Section 4) and we will use the resulting values to build an emulator (Section 5) that will let us draw some conclusions about the relationships between the parameters of the ETAS model and the distribution of inter-events times, summarized by parameters q and τ_0. Conclusive remarks will also include some indications on future work and on possible practical application of this kind of analysis

to real data (Section 6). This work was conducted using the statistical software R and, namely, the following packages: POT, LHS, PtProcess (Harte 2010), nleqslv, tgp (Gramacy 2007).

2. A SUMMARY ON q STATISTICS

We summarize in which way the q value can be interpreted in terms of non-extensive statistical physics. We express the non-extensive Tsallis entropy S_q (Tsallis 1988, 1999, 2009)

$$S_q = k_B \frac{1 - \sum p^q(X)}{q-1},$$

(1)

where k_B is Boltzmann's constant, in terms of the probability distribution $p(X)$, where X could be the scalar moment, M, and the inter-event time, T (*i.e.*, the time interval between two successive events). In the limit $q \to 1$, $S_q \to S_1$ and the approach reduces to the well-known Boltzmann-Gibbs (BG) entropy (Tsallis 2009). However, simple additivity is violated, because for a system composed of two statistically independent systems, A and B, the Tsallis entropy satisfies

$$S_q(A,B) = S_q(A) + S_q(B) + \frac{1-q}{k_B} S_q(A) S_q(B).$$

(2)

The last term on the right hand side of this equation describes the interaction between the two systems and is the origin of non-extensivity. This is the reason why q can be seen as an index of non-extensivity: it accounts for dependency or long-range interaction between microfractures and for $q < 1$, $q = 1$, and $q > 1$, respectively, correspond to super-additivity (super-extensivity), additivity (extensivity), and sub-additivity (sub-extensivity). This is the fundamental principle of non-extensive statistical mechanics. All other quantities, which are concerned with thermodynamics, may be derived from it. As we already mentioned, the distribution $p(X)$ and the parameter q are obtained according to the principle of maximum entropy, which involves the maximization of the entropy under appropriate constraints. This leads to the definition of some auxiliary functions (Tsallis 2009 and references therein), such as the q-exponential:

$$\exp_q(X) = \left[1 + (1-q)X\right]^{1/1-q},$$

(3)

which corresponds to the cumulative distribution function (CCDF) of a generalized (tapered) Pareto distribution (as noted by Shalizi 2007) with a location parameter of 0, a scale parameter of 1 (that is, the variable X has been rescaled dividing its values by the scale parameter τ_0) and a shape parameter equal to $q - 1$.

3.   COMPARISON OF ESTIMATORS

As a first issue, we ask whether there is a better way to estimate the q value, with respect to estimators based on the principle of maximum entropy (POME), comparing the available alternatives in terms of accuracy (measured by the estimator's bias) and efficiency (measured by the root-mean-square error). This will allow us to obtain more reliable results in the computation of the q value from more realistic data samples. Bias and root-mean-square error (RMSE) will be evaluated by means of Monte Carlo experiments where data are randomly drawn from a distribution with known parameters and then are used to estimate parameters themselves. Subsection 3.1 will introduce the alternative estimators, while Subsection 3.2 will present the results of the comparison.

3.1 Estimators under consideration

Principle of maximum entropy (POME): the entropy of a distribution is defined as the expectation of the logarithm of its PDF (probability density function). The estimates of the parameters are obtained maximizing the entropy under linearly independent constraint of the form

$$C_i = \int w_i(x) f(x) dx \ , \tag{4}$$

where $f(x)$ is the PDF and $w_i(x)$ are functions whose averages over $f(x)$ are specified. POME estimators for generalized Pareto distribution were discussed by Singh and Guo (1997) .

   Maximum likelihood estimators (MLE): the likelihood of a distribution with respect to a sample is the joint PDF of the sample, where the real values of the parameters are viewed as unknown; estimates are obtained by maximizing the likelihood, that is, by finding the values of the parameters which make the actual sample more likely to have been obtained.

   Methods of moment (MOM): estimates are obtained by equating as many sample moments as the parameters to be estimated with the corresponding theoretical moments computed as a function of the parameters.

   Probability weighted moments (PWM) were defined by Greenwood *et al.* (1979) as follows:

$$M_{p,r,s} = E\left[X^p \{F(X)\}^r \{1 - F(X)\}^s \right] \ , \tag{5}$$

where $F(X)$ is the cumulative distribution function (CDF). Estimates are obtained considering a selection of these moments. Applications of PWM to generalized Pareto distribution were explored by Hosking and Wallis (1987), in comparison with the two previous estimators. The PWM unbiased estimators (PWMU) are based on the unbiased estimators of $\alpha_s = M_{1,0,s}$, which are given by

$$a_r = n^{-1} \sum_{j=1}^{n} \frac{(n-j)(n-j-1)\ldots(n-j-r)}{(n-1)(n-2)\ldots(n-r)} x_{j:n} \; , \tag{6}$$

where $x_{j:n}$ is the j-th element of the ordered sample. Resulting estimators for the parameters of the generalized Pareto distribution are

$$\hat{a} = \hat{q} - 1 = \frac{a_0}{a_0 - 2a_1} - 2 \quad \text{and} \quad \hat{b} = \hat{\tau}_0 = \frac{2a_0 a_1}{a_0 - 2a_1} \; . \tag{7}$$

3.2 Comparison via Monte Carlo experiments

To compare the aforementioned estimators, two Monte Carlo experiments, as in Singh and Guo (1997), are proposed. We generate $N = 1000$ replications of independent identically distributed samples of size each $n = 100$ or 1000, according to a generalized Pareto distribution (GPD)[1], whose probability density function (PDF) is

$$f(x) = \frac{1}{b}\left(1 + \frac{ax}{b}\right)^{\left(-\frac{1}{a} - 1\right)} \quad \text{if} \quad a \neq 0 \; , \tag{8}$$

$$f(x) = \frac{1}{b} e^{(-x/b)} \quad \text{if} \quad a = 0 \; . \tag{9}$$

where a is the shape parameter (corresponding to $q - 1$) and b is the scale parameter (corresponding to τ_0). Then we apply the proposed estimators and we compute bias and root-mean-square error (RMSE). Real values for the parameters and corresponding coefficients of variation[2] are shown in the Table 1. According to Singh and Guo (1997), the coefficient of variation (CV), which is defined as the ratio between the standard deviation and the mean, is relevant in the selection of the best estimator, since the estimators based on the principle of maximum entropy (POME) should be preferred when CV is greater than 1.5, but in our case CV appears to be often below 1. Table 1 quantifies the biases and the RMSEs of the estimates. On the whole, the comparison of the results is in favor of the unbiased version of PWM (PWMU) estimators which appears to be comparable to competitor estimators in terms of RMSE, but it shows a sensibly lower bias, especially when the sample size, n, is small. Therefore, it is used in the computation of the q value in the simulations in the following section.

---

[1]In Singh and Guo (1997) the parameter a has an opposite sign; this difference affects the expressions of the involved functions but does not change the results.

[2]Note that in the generalized Pareto distribution with location parameter equal to 0 the coefficient of variation does not depend on the scale parameter b.

Table 1

Estimators comparison

	Bias(a)	Bias(b)	RMSE(a)	RMSE(b)
$n = 100$, $a = 0.2$, $b = 5$, CV = 0.77				
MLE	−0.105	0.023	0.633	0.165
PWM	−0.142	0.020	0.595	0.160
PWMU	−0.051	0.005	0.576	0.155
MOM	−0.275	0.058	0.584	0.157
POME	−0.348	0.082	0.641	0.209
$n = 1000$, $a = 0.2$, $b = 5$, CV = 0.77				
MLE	−0.017	0.003	0.193	0.050
PWM	−0.013	0.002	0.186	0.048
PWMU	0.001	−0.002	0.192	0.049
MOM	−0.052	0.012	0.228	0.057
POME	−0.004	−0.004	0.197	0.053
$n = 100$, $a = 0.1$, $b = 0.9$, CV = 0.89				
MLE	−0.266	0.026	1.177	0.158
PWM	−0.217	0.027	1.185	0.159
PWMU	−0.106	0.003	1.169	0.155
MOM	−0.392	0.042	1.106	0.155
POME	−0.677	0.075	0.819	0.150
$n = 1000$, $a = 0.1$, $b = 0.9$, CV = 0.89				
MLE	−0.022	0.002	0.355	0.049
PWM	−0.025	0.003	0.370	0.049
PWMU	0.004	0.002	0.365	0.049
MOM	−0.038	0.005	0.360	0.047
POME	−0.175	0.020	0.459	0.070

4. SIMULATED CATALOGUES AND *q* VALUE ESTIMATES

The simulated earthquake catalogues are generated according to an epidemic type aftershock sequence (ETAS) model (Ogata 1988). The ETAS model is a point process whose full likelihood is given by the marginal distribution of the magnitude multiplied by the conditional distribution of occurrence times, given past history; taking the logarithm, the second part, that is the conditional log-likelihood, can be expressed as

$$\log L = \sum_{i=1}^{n} \lambda(t_i, \theta) - \int_0^T \lambda(t, \theta)\, dt \ , \tag{10}$$

where λ is the conditional intensity function, t_i is the time in which the i-th event occurred and θ is the set of parameters. Among possible formulations for the conditional intensity function, we adopt the following, which combines the Omori Law and the productivity law:

$$\lambda = \mu + A\sum_{t_i < t} e^{\alpha(m_i - m_c)}\left(1 + \frac{t - t_i}{c}\right)^{-p} ,$$ (11)

where m_i is the magnitude of the i-th event and m_c is the cut-off magnitude.

The simulation software (PtProcess) considers the threshold magnitude as an implicit parameter: in fact, all magnitudes are expressed in terms of the difference $m_i - m_c$. In simulation we do not have measurement problems, since all events are observable, and the threshold m_c can be as small as 0; then one may fix another threshold m_0 to select the events for the computation of the inter-event times. Our choice was to consider all available events. Wang *et al.* (2010a) discussed the issue of missing links in simulated catalogues: the problem arises because events above the threshold magnitude m_c can be triggered by events below the threshold itself, and this leads to neglecting the corresponding triggering connections.

In this model, five parameters are involved in the ground intensity function: μ (which represents background seismicity in terms of shocks per day; results remain valid if a different time unit, instead of days, is adopted), A, α, c, and p (which express the aftershocks sequences). The distribution of earthquakes magnitude is assumed exponential (according to the Gutenberg–Richter law) with parameter $\beta = \log(10)$. We select 500 combinations (points) of values for the five parameters of the ETAS model according to a Latin hypercube sampling (LHS) design (McKay *et al.* 1979). The ranges for the parameters are shown in Table 2 and Fig. 1. We selected these ranges after several trials so that they can be short enough that they can be fully explored considering 500 points and wide enough to show some appreciable effect.

For each LHS point, we simulate 10 "replicated" catalogues, each containing 1000 events, we compute the inter-events times and we estimate the parameters q and τ_0 for each catalogue. Replicates are used to obtain more reliable information on the effect of the input parameters: in fact, we obtain different outputs corresponding to the same input values, as the model is stochastic. A single simulation could be affected by the realization of a rare value (so-called "outliers"), but this is compensated by the other catalogues which share the same input values. In this way, even a relatively small number of replicates ($N = 10$) is more effective in order to reduce the uncertainty than a comparable increase in the sample size ($n = 10\,000$) would be, since the usage of replicates reduces the auto-correlation in the simulation (alternative methods are proposed in Naylor *et al.* 2009). Of course, an increase in both the sample size and the number of replicates would improve the results obtained, but it would extend the execution time. The same issue was addressed, in a different context, by Wang *et al.* (2010b). It is difficult

The epidemic type aftershock sequence parameters ranges

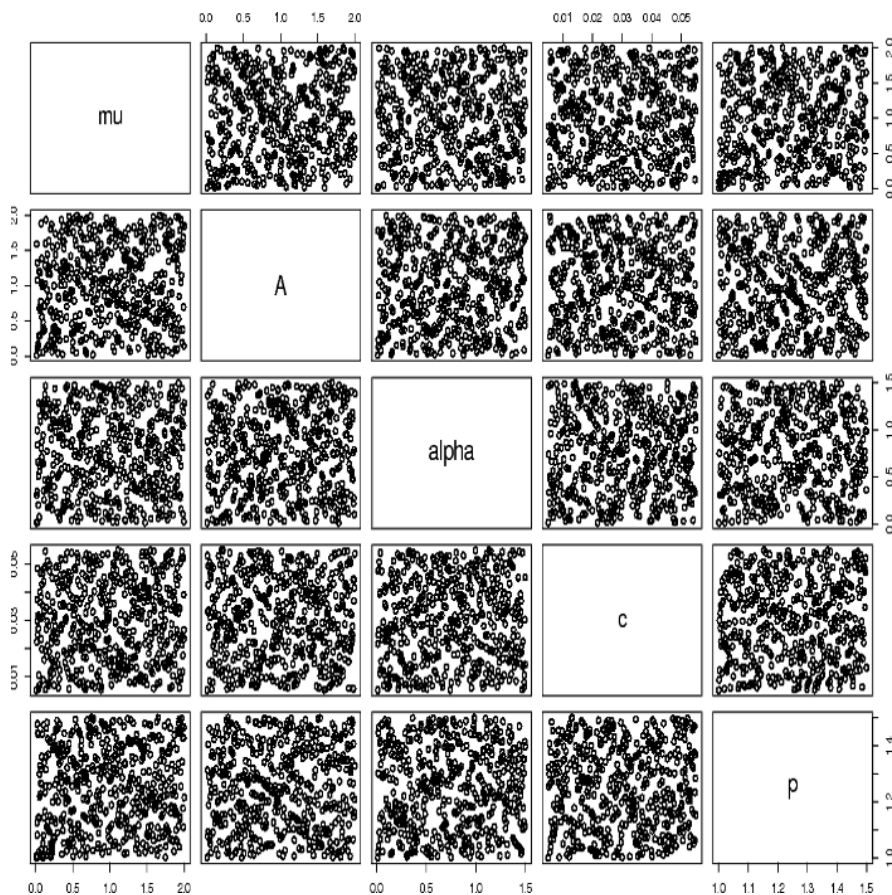| Parameters	Minimum value	Maximum value
μ (shocks/day)	0.014	1.998
A (shocks/Day^{p+1})	0.012	1.998
α	0.012	1.499
C (days)	0.005	0.055
p	1.001	1.499

Fig. 1. The Latin hypercube sampling points projections.

to quantify the improvement provided by our technique: we do not know how large the sample size of a single catalogue should be, in order to have comparable results. However, we have computed that the coefficient of variation of the 10 estimates of the q value, obtained using the PWMU esti-

mators, in each set of replicated catalogues is, on average, 3.5%; so we may consider that using 10 replicates provides a good balance between the reduction of uncertainty and the time of execution. Table 3 shows the ranges of the estimates obtained for the q value and τ_0 using the unbiased version of the probability weighted moments estimators, corresponding to a selection of LHS points. As expected, the variability in the estimates of the q value, due to the changes in the input parameters, is less pronounced with respect to those of the scale parameter τ_0.

Table 3

Parameters estimates (PWMU) ranges for selected LHS points

μ	A	α	c	p	q	τ_0
0.957	1.884	1.399	0.033	1.348	1.350-1.437	0.332-0.438
0.897	1.352	0.031	0.039	1.409	1.088-1.212	0.712-0.891
0.171	1.176	0.454	0.007	1.103	1.025-1.103	4.850-5.660
0.118	0.374	1.308	0.033	1.340	1.051-1.183	6.123-7.514
1.898	1.395	1.381	0.027	1.388	1.145-1.282	0.282-0.348

Touati *et al.* (2009, 2011) studied the relationships between ETAS parameters and mean inter-event time, which is computed as the sample mean of the distances between events. In Figure 2 the relationship between scaled mean inter-event time and the q value is shown, when we adopt the hypothesis of a generalized Pareto distribution for inter-event times and we compute the parameters of the distribution itself. This means that, if the assumption on the form of the distribution is acceptable, we have a description of the
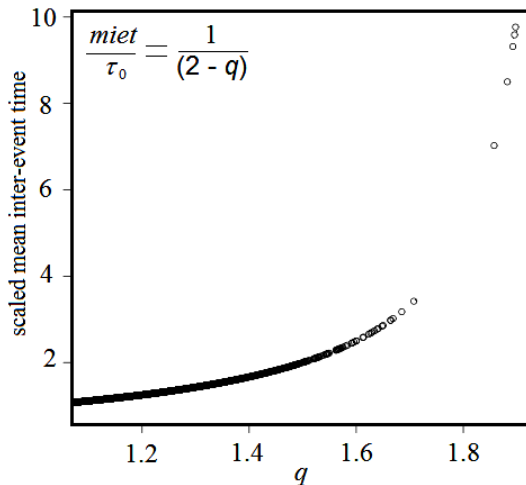
Fig. 2. Relationship between scaled mean inter-event time (*miet*) and q.

phenomenon which is more informative in comparison to an analysis where only the sample mean is considered.

In preliminary studies, we built emulators of mean inter-event times for ETAS models, but the lack of smoothness of the response either required enormous sample sizes or did not yield an emulator with low uncertainties.

Moreover, in our analysis the input values (*i.e.*, ETAS model parameters) are all varying simultaneously, while in the aforementioned studies each parameter effect is analyzed by fixing the values of other parameters, and this gives us the chance to explore possible joint effects.

5. ANALYSIS WITH THE EMULATOR

5.1 Description and functioning of an emulator

When a model is too complex to be explored in direct experimentation, computer simulations, like those performed in the previous section, can substitute the real experiment with virtual ones. But in some cases, simulations are very demanding in terms of computation capability and execution time. Under these circumstances, emulators can give a practical solution. The first references on Design and Analysis of Computer experiments date back to the 1980s (see *e.g.*, Sacks *et al.* 1989). An emulator is a statistical model which gives a simplified (surrogate) representation of a complex simulation model, analyzing the relationships between inputs (parameters) and output (results). The simulator is a function that maps inputs into outputs and the emulator provides an approximation for such a function (O'Hagan 2006), giving the opportunity to identify the effect of each input by means of the sensitivity analysis. Emulators are usually made employing Gaussian processes. These are random functions where, for an untried input x, the output point $f(x)$ has a Gaussian distribution conditional on the set of available outputs. This approach does not assume that the outputs of the computer model are Gaussian, as it constitutes an advanced random interpolation of the model outputs. A Bayesian approach is often applied in parameters fitting as one can include prior expert knowledge to improve the emulator (*e.g.*, Rougier *et al.* 2009). Moreover, to obtain a more flexible model that can accommodate sharp and non-stationary behaviors, the input space can be partitioned so that in each sub-space a different Gaussian process is fitted. In this respect, a possible method is given by treed partitioning (Gramacy and Lee 2008, Gramacy and Taddy 2010), which makes binary splitting for each input variable.

5.2 Results from the emulation

Figures 3a-e show on the left the estimated and emulated projections of q as a function of each individual ETAS parameter (the others vary according to
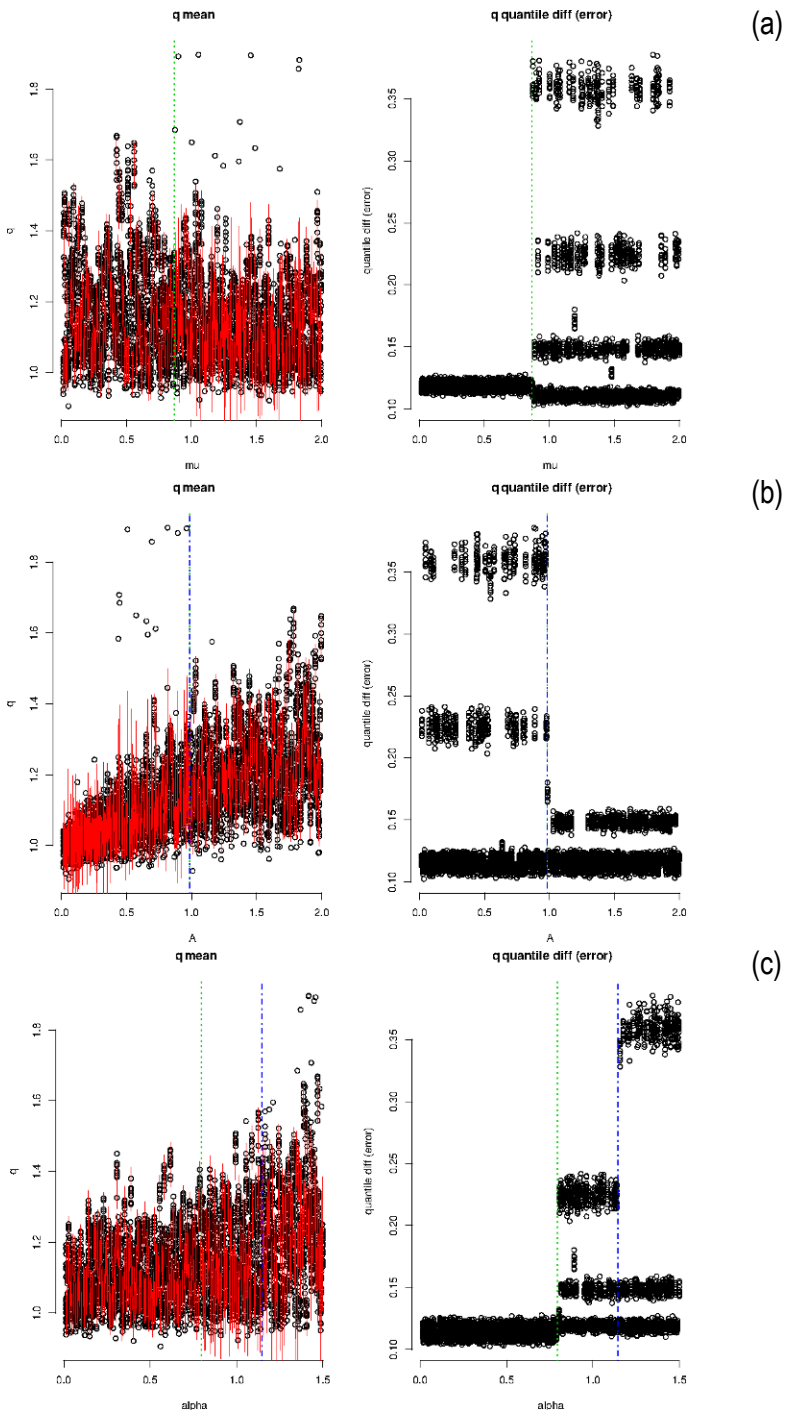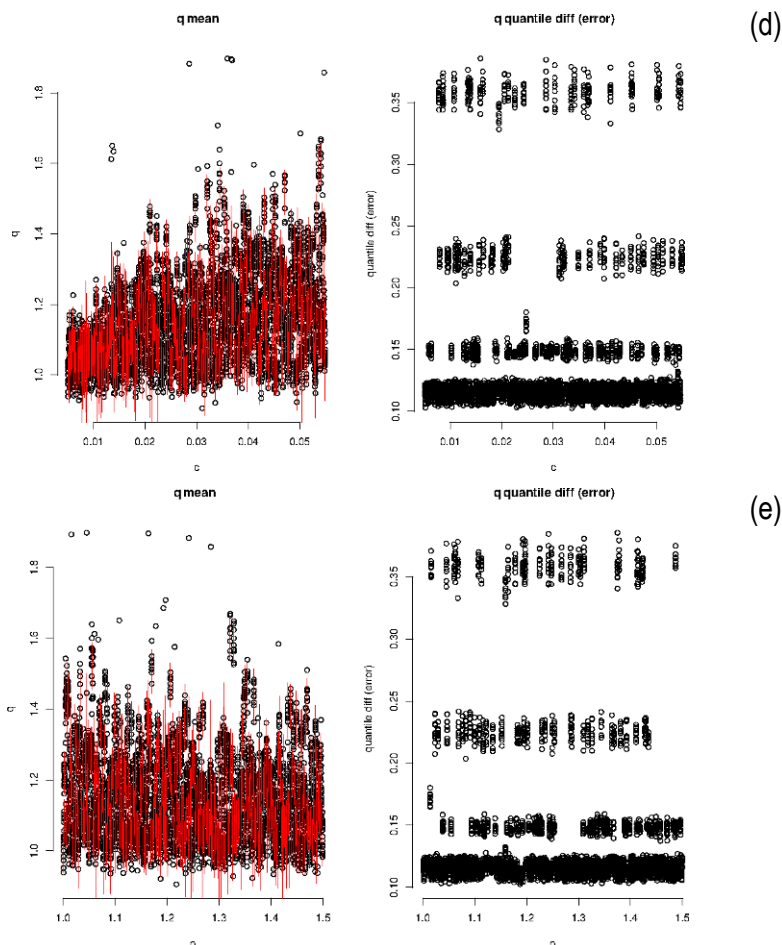
Fig. 3. Continued on next page.

Fig. 3. Effect of each ETAS parameter on the *q* value for: (a) μ, (b) *A*, (c) α, (d) *c*, and (e) *p*. On the left panels, *q* is plotted as a function of the ETAS parameter: circles represent the actual 5000 *q* values (as estimated in the 5000 simulations) while the red lines represent the ranges of the estimates provided by the emulator, that is, the difference between the maximum and the minimum predicted value corresponding to each input point. On the right panels, the error in the estimate of *q* as a function of the ETAS parameter is expressed by the quantile differences (difference between 95% predictive quantiles and 5% predictive quantiles). Vertical dotted lines, where present, show the treed partitioning of the parameter space. Colour version of this figure is available in electronic edition only.

the LHS design, which explains the sharp variation), and on the right a measure of uncertainty in the estimation of this relationship. The error in the estimates (right panel) appears to be differently clustered in parameters
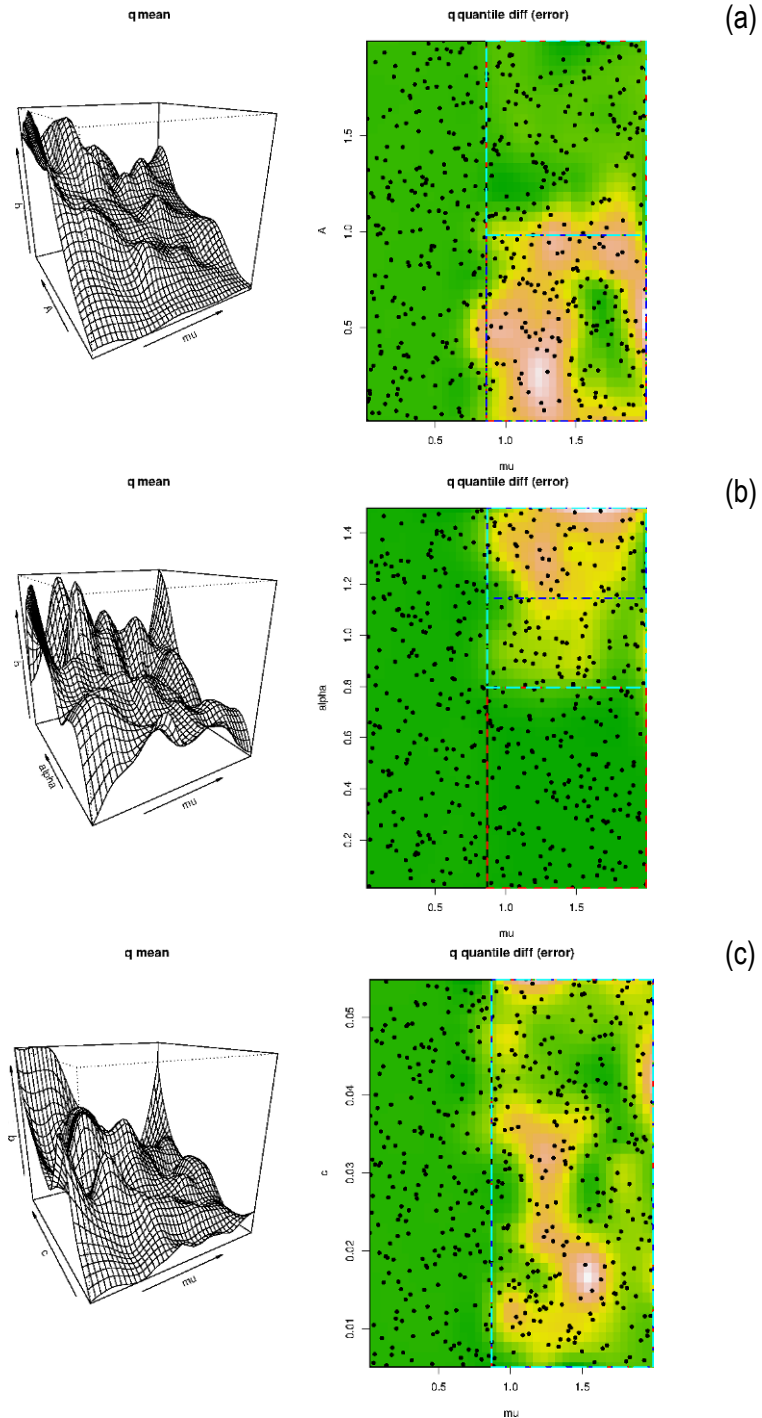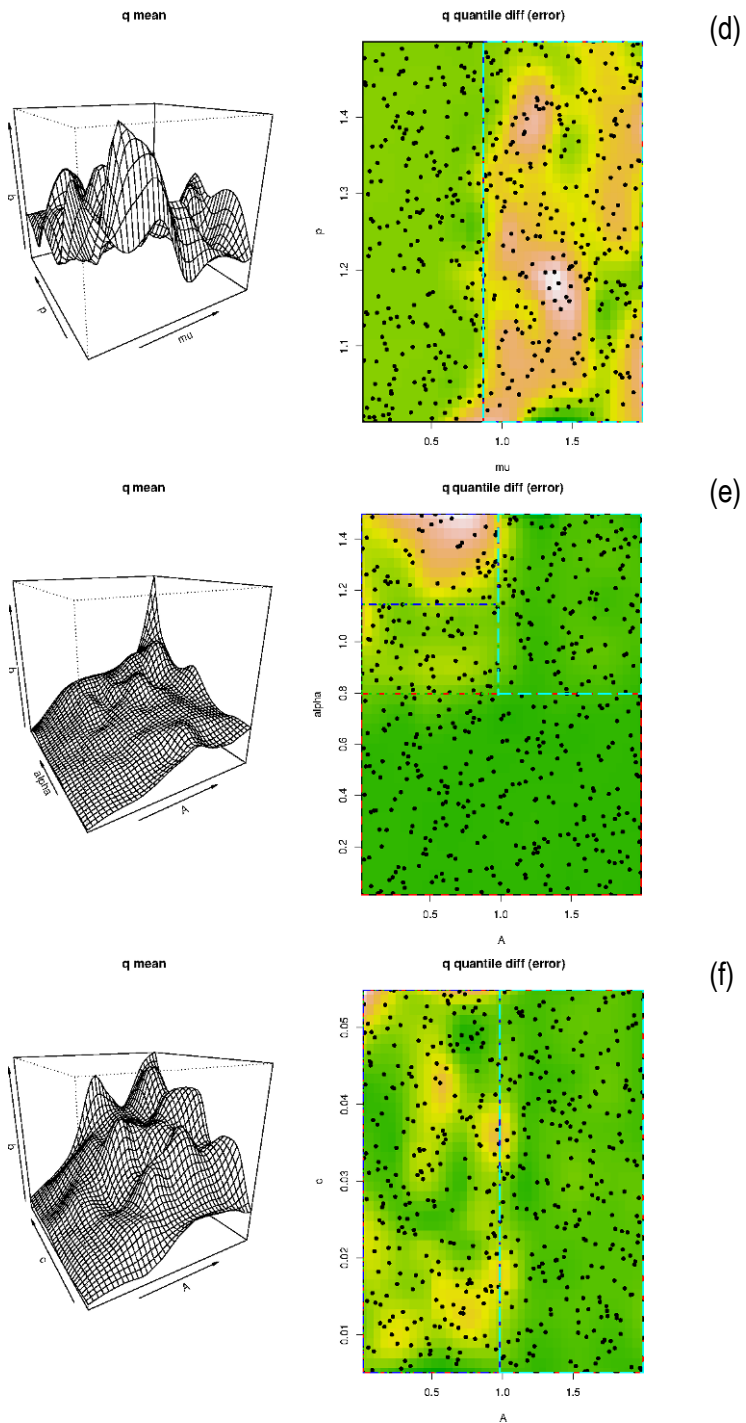
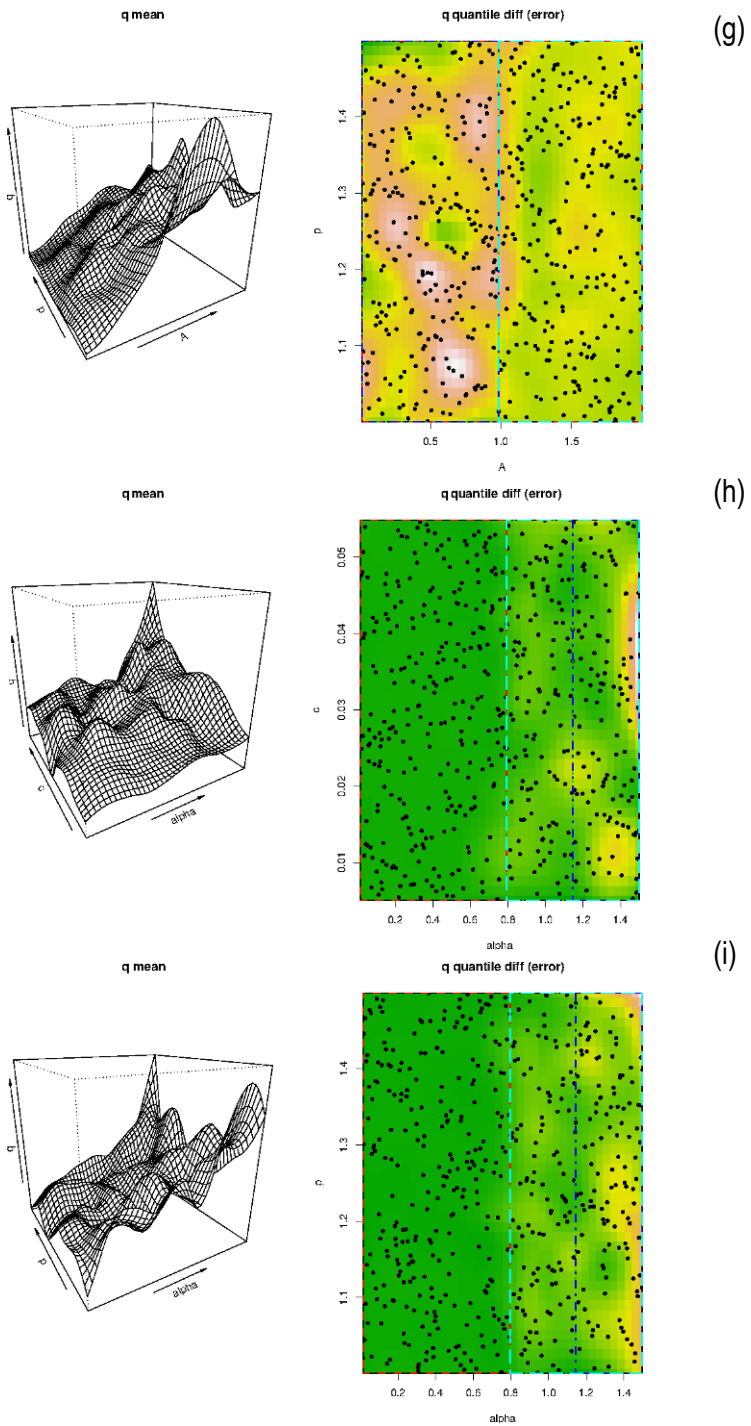Fig. 4. Continued on next page.

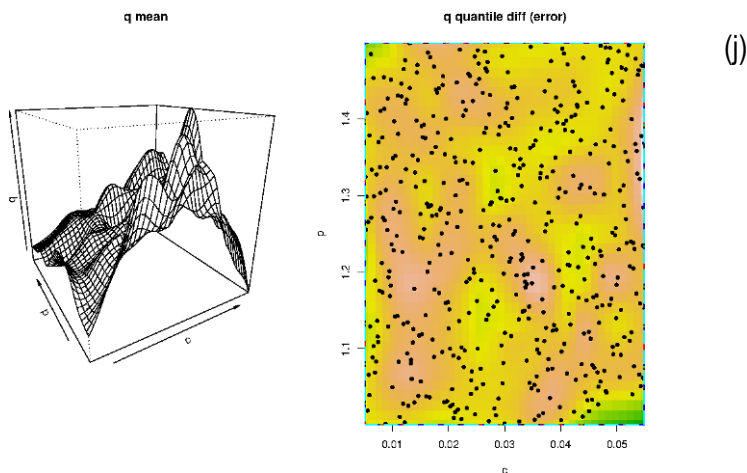Fig. 4. Continued on next page.

Fig. 4. Continued on next page.

Fig. 4. Joint effect of couples of ETAS parameters on the q value for: (a) μ and A, (b) μ and α, (c) μ and c, (d) μ and p, (e) A and α, (f) A and c, (g) A and p, (h) α and c, (i) α and p, and (j) c and p. On the left panels, q is plotted as a function of two ETAS parameters. On the right panels, the error in the estimate of q is shown (green areas present less uncertainty with respect to pink and yellow ones). Vertical and horizontal dotted lines, where present, show the treed partitioning of the parameters space. Colour version of this figure is available in electronic edition only.

subspaces defined by treed partitioning. Parameters A, α and, with more uncertainty, c exhibit a positive effect on q, while the effect of μ and p is not clearly identifiable. This is due to the fact that, as we already mentioned, ETAS parameters are all varying randomly and simultaneously; the emulator will provide a convenient solution since it will let us perform sensitivity analysis.

Similarly, Figs. 4a-j show the projections of q as a function of each couple of ETAS parameters. In Figure 4a (μ and A), the effect of A is prevailing, but a slight decreasing effect of μ on q is detectable. The same behavior is shown in Figs. 4b (μ and α) and 4c (μ and c) but the surfaces appear to be less smoothed, meaning that there is a higher degree of uncertainty. An analogous problem occurs in Fig. 4d (μ and p), where roughness is so pronounced that it is impossible to assess the nature of the joint effect. Finally, in Fig. 4j (c and p), the effect of p seems to be non-monotonic, but this may be due to the high level of uncertainty.

6. CONCLUSIONS

In the analysis of inter-event times, we adopt the hypothesis of a generalized Pareto distribution (GPD) with a location parameter of 0, a scale parameters of τ_0, and a shape parameter equal to $q - 1$. The q value also has a physical

interpretation in terms of non-extensivity. We propose the use of estimators based on unbiased probability weighted moments to compute the parameters of the distribution. We apply this method to catalogues simulated according to the ETAS model. Taking into account the values of parameters of the distribution, with respect to the mean alone, provides more information on the distribution itself. To have a deeper comprehension of the influence of the parameters of the ETAS model on the quantity of interest, we also suggest to let them all vary simultaneously, so that joint effects can be explored. We plan to replicate the analysis with different intervals to verify whether these effects are different over other ranges. In some cases, an extension of the parameter range can be a suitable solution to identify some effects that were not detected in our study; on the other hand, the range cannot be enlarged indefinitely, because, if amplitude is too wide, the effect of one parameter can be so strong that it overwhelms the others.

We considered here the first version of the ETAS model, with no spatial component (Ogata 1988) since at the moment we are interested in exploring the temporal distance among events; we plan to consider the model with a spatial component (Ogata 1998, Ogata and Zhuang 2006) in future work. The use of the emulator let us draw some first conclusions on the relationships between the parameters of the ETAS model and the q value: the effect of μ and p is quite uncertain, so we will need to explore it more accurately performing further sensitivity analysis; the effect of A, α, and c is more detectable and it appears to be positive (an increase in the input variable produces an increase in q). The analysis of joint effects showed a slight negative effect for both μ and p, but further study is required in order to confirm it and also to verify whether the joint effect of couples of input parameters (*e.g.*, c and p) can produce a non-monotonic relationship with q. A possible practical use of this technique is as follows: given a new seismic event, one may update the estimates of ETAS parameters in real time and obtain as a result the updated distribution of inter-event times.

References

Abe, S., and N. Suzuki (2003), Law for the distance between successive earthquakes, *J. Geophys. Res.* **108**, B2, 2113-2116, DOI: 10.1029/2002JB 002220.

Abe, S., and N. Suzuki (2005), Scale-free statistics of time interval between successive earthquakes, *Physica A* **350**, 2-4, 588-596, DOI: 10.1016/j.physa. 2004.10.040.

Gramacy, R.B. (2007), tgp: An R package for Bayesian nonstationary, semiparametric nonlinear regression and design by treed Gaussian process models, *J. Stat. Softw.* **19**, 9, 1-46.

Gramacy, R.B., and H.K.H. Lee (2008), Bayesian treed Gaussian process models with an application to computer modeling, *J. Am. Stat. Assoc.* **103**, 483, 1119-1130, DOI: 10.1198/016214508000000689.

Gramacy, R.B., and M. Taddy (2010), Categorical inputs, sensitivity analysis, optimization and importance tempering with tgp version 2, an R package for treed Gaussian process models, *J. Stat. Softw.* **33**, 6, 1-48.

Greenwood, J.A., J.M. Landwehr, N.C. Matalas, and J.R. Wallis (1979), Probability weighted moments: Definition and relation to parameters of several distributions expressable in inverse form, *Water Resour. Res.* **15**, 5, 1049-1054, DOI: 10.1029/WR015i005p01049.

Harte, D. (2010), PtProcess: An R package for modelling marked point processes indexed by time, *J. Stat. Softw.* **35**, 8, 1-32.

Hosking, J.R.M., and J.R. Wallis (1987), Parameter and quantile estimation for the generalized Pareto distribution, *Technometrics* **29**, 3, 339-349, DOI: 10.2307/1269343.

Kagan, Y.Y., and F. Shoenberg (2001), Estimation of the upper cutoff parameter for the tapered Pareto distribution, *J. Appl. Probab.* **38A**, 158-175, DOI: 10.1239/jap/1085496599.

McKay, M.D., R.J. Beckman, and W.J. Conover (1979), A comparison of three methods for selecting values of input variables in the analysis of output from a computer code, *Technometrics* **21**, 2, 239-245, DOI: 10.2307/1268522.

Naylor, M., I.G. Main, and S. Touati (2009), Quantifying uncertainty in mean earthquake interevent times for a finite sample, *J. Geophys. Res.* **114**, B01316, DOI: 10.1029/2008JB005870.

O'Hagan, A. (2006), Bayesian analysis of computer code outputs: A tutorial, *Reliab. Eng. Syst. Safe.* **91**, 10-11, 1290-1300, DOI: 10.1016/j.ress.2005.11.025.

Ogata, Y. (1988), Statistical models for earthquake occurrences and residual analysis for point processes, *J. Am. Stat. Assoc.* **83**, 401, 9-27, DOI: 10.2307/2288914.

Ogata, Y. (1998), Space-time point-process models for earthquake occurrences, *Ann. Inst. Statist. Math.* **50**, 2, 379-402, DOI: 10.1023/A:1003403601725.

Ogata, Y., and J. Zhuang (2006), Space-time ETAS models and an improved extension, *Tectonophysics* **413**, 1-2, 13-23, DOI: 10.1016/j.tecto.2005.10.016.

Pisarenko, V.F., D. Sornette, and M.V. Rodkin (2010), Distribution of maximum earthquake magnitudes in future time intervals: application to the seismicity of Japan (1923-2007), *Earth Planets Space* **62**, 7, 567-578, DOI: 10.5047/eps.2010.06.003.

Rougier, J., S. Guillas, A. Maute, and A.D. Richmond (2009), Expert knowledge and multivariate emulation: The thermosphere-ionosphere electrodynamics general circulation model (TIE-GCM), *Technometrics* **51**, 4, 414-424, DOI: 10.1198/TECH.2009.07123.

Sacks, J., W.J. Welch, T.J. Mitchell, and H.P. Wynn (1989), Design and analysis of computer experiments, *Stat. Sci.* **4**, 4, 409-423, DOI: 10.1214/ss/1177012413.

Shalizi, C.R. (2007), Maximum likelihood estimation for q-exponential (Tsallis) distributions, *arXiv:math/0701854v2* [math.ST].

Singh, V.P., and H. Guo (1997), Parameter estimation for 2-parameter generalized pareto distribution by POME, *Stoch. Hydrol. Hydraul.* **11**, 3, 211-227, DOI: 10.1007/BF02427916.

Telesca, L. (2010a), Nonextensive analysis of seismic sequences, *Physica A* **389**, 9, 1911-1914, DOI: 10.1016/j.physa.2010.01.012.

Telesca, L. (2010b), A non-extensive approach in investigating the seismicity of L'Aquila area (central Italy), struck by the 6 April 2009 earthquake (M_L = 5.8), *Terra Nova* **22**, 2, 87-93, DOI: 10.1111/j.1365-3121.2009. 00920.x.

Touati, S., M. Naylor, and I.G. Main (2009), Origin and nonuniversality of the earthquake interevent time distribution, *Phys. Rev. Lett.* **102**, 16, 168501, DOI: 10.1103/PhysRevLett.102.168501.

Touati, S., M. Naylor, I.G. Main, and M. Christie (2011), Masking of earthquake triggering behavior by a high background rate and implications for epidemic-type aftershock sequence inversions, *J. Geophys. Res.* **116**, B03304, DOI: 10.1029/2010JB007544.

Tsallis, C. (1988), Possible generalization of Boltzmann–Gibbs statistics, *J. Stat. Phys.* **52**, 1-2, 479-487, DOI: 10.1007/BF01016429.

Tsallis, C. (1999), Nonextensive statistics: theoretical, experimental and computanional evidences and connections, *Braz. J. Phys.* **29**, 1, DOI: 10.1590/S0103-97331999000100002.

Tsallis, C. (2009), *Introduction to Nonextensive Statistical Mechanics: Approaching a Complex World*, Springer, New York, DOI: 10.1007/978-0-387-85359-8.

Vallianatos, F. (2009), A non-extensive approach to risk assessment, *Nat. Hazards Earth Syst. Sci.* **9**, 1, 211-216, DOI: 10.5194/nhess-9-211-2009.

Vallianatos, F. (2011), A non extensive statistical physics approach to the polarity reversals of the geomagnetic field, *Physica A* **390**, 10, 1773-1778, DOI: 10.1016/j.physa.2010.12.040.

Vallianatos, F., and P. Sammonds (2010), Is plate tectonics a case of non-extensive thermodynamics?, *Physica A* **389**, 21, 4989-4993, DOI:10.1016/j.physa. 2010.06.056.

Vallianatos, F., and P. Sammonds (2011), A non-extensive statistics of the fault-population at the Valles Marineris extensional province, Mars, *Tectonophysics* **509**, 1-2, 50-54, DOI: 10.1016/j.tecto.2011.06.001.

Vallianatos, F., E. Kokinou, and P. Sammonds (2011a), Non-extensive statistical physics approach to fault population distribution. A case study from the Southern Hellenic Arc (Central Crete), *Acta Geophys.* **59**, 4, 770-784, DOI: 10.2478/s11600-011-0015-3.

Vallianatos, F., D. Triantis, and P. Sammonds (2011b), Non-extensivity of the iso-thermal depolarization relaxation currents in uniaxial compressed rocks, *Europhys. Lett.* **94**, 6, 68008, DOI: 10.1209/0295-5075/94/68008.

Wang, Q., D.D. Jackson, and J. Zhuang (2010a), Missing links in earthquake clus-tering models, *Geophys. Res. Lett.* **37**, L21307, DOI: 10.1029/2010GL044858.

Wang, Q, F.P. Schoenberg, and D.D. Jackson (2010b), Standard errors of parameter estimates in the ETAS model, *Bull. Seismol. Soc. Am.* **100**, 5A, 1989-2001, DOI: 10.1785/0120100001.

VERSITA

Hierarchy of Non-Extensive Mechanical Processes in Fracturing Sea Ice

Alexandre CHMEL[1], Victor SMIRNOV[2], and Igor SHCHERBAKOV[1]

[1]Fracture Physics Department, Ioffe Physico-Technical Institute, Russian Academy of Sciences, St. Petersburg, Russia
e-mail: chmel@mail.ioffe.ru

[2]Arctic and Antarctic Research Institute, St. Petersburg, Russia

A b s t r a c t

The fracture-induced oscillations in sea ice were detected by seismographs and seismic tiltmeters established on the Arctic ice pack. Field observations were supplemented with a laboratory experiment. The energy distributions in elastic waves generated during: (i) large-scale ice pack fragmentation over area of about 10^5 km^2, (ii) local crack propagation in ice floe, and (iii) laboratory ice crashing were constructed and analyzed using principles of the Tsallis statistics. The energy release regimes at different stages of fracturing were characterized by the parameter of non-extensivity q. In terms of the non-extensive statistical mechanics, $q > 1$ evidences the correlated (non-extensive) dynamics of the process in non-equilibrium system, $q = 1$ responds to the additivity of events occurring in equilibrium system, and $q < 1$ takes place when the energy release is additive and limited by an upper cut-off. All these scenarios were revealed in fracture processes occurring at three hierarchic levels. The variation of the q-value demonstrates high thermodynamic changeability of the fracture process driven by irregular external source. The role of energy conservation in fracturing sea ice is discussed in connection with the observed reversible transitions between extensive and non-extensive modes of fracture.

Key words: sea ice, dynamic fracture, Tsallis statistics.

Un gatto che sogna di specchiarsi fa tre gatti
Giovanni Raboni

1. INTRODUCTION

The Arctic sea ice cover (ASIC) is the open, non-equilibrium, multi-component geophysical system with hierarchic properties (Overland *et al.* 1995, McNutt and Overland 2003) and well-pronounced scaling behavior (Weiss 2003, Chmel *et al.* 2005). Its multi-component structure provides conditions for multi-scale fluctuations in the system's dynamics with forming and maintaining fractal structures. In general, the behavior of each individual component (as well as a limited cluster of components) in open system is unpredictable. However, the space-time trajectory of the whole ensemble of system's elements is determined by the thermodynamic attractor, which manifests itself through power law distributions of principal system's characteristics, such as component size, energy release, and recurrence times between events of energy release/exchange.

As regards the ASIC, the size distribution of ice floes, as well as the geometry of the crack-and-lead pattern exhibit fractal properties (Weiss and Marsan 2004, Chmel *et al.* 2010a); the space and energy scale invariance is supplemented by self-similar recurrence time intervals in trains of fracture events (Chmel *et al.* 2010b).

The sea ice drift is caused, mainly, by the wind forcing and, to a lesser extent, by the ocean currents, tidal action, gravimetric waves, *etc.* (Martin and Drucer 1991, Weiss 2003). Owing to the non-uniform drift speed in different parts of the sea ice cover, there appear significant deformations over vast areas, and the permanent fracture process flows with varying activity. The most significant fracture events, icequakes, are represented by high rate propagation of giant ($\sim 10^2$ km) leads and by formation of "faults" – areas of highly fragmented sea ice, reaching 10^5 km^2. These perturbations are quite similar to those in geostructures both in their spatial scale and in mechanics; however, the mechanical processes in sea ice are much more fluent and statistically reproducible in accessible time intervals due to refreezing of fragmented ice cover.

In this communication we present a statistical analysis of the cracking dynamics in drifting sea ice, which was monitored at the Russian ice research camps "North Pole" established on the ice pack. The project "North Pole" (NP) was launched in 1937. From 1950 to 2011, a total 37 stations worked on the drifting sea ice. These stations carry out the program of complex year-round research in the field of ocean science, ice studies, meteorology, geophysics, and hydrophysics. From 2004, the studies of self-organized

dynamics in the Arctic sea ice cover are performed on a regular basis (Chmel and Smirnov 2008).

We shall consider some statistical characteristics of the fracture process in marine cryosphere at three hierarchic levels represented by: (i) large scale faulting occurred in March 2008 in the working region of the camp NP 35, (ii) localized sea ice cracking in the immediate vicinity of the camp NP 37 in January 2010, and (iii) ice crashing in laboratory experiments.

The icequakes in the ice pack were monitored using seismic devices, seismographs and tiltmeters, capable to detect ice floe oscillations excited during shearing and stick-slip motions and cracking. The laboratory experiments were carried our in order to assess the uniformity of the fracture process in ice at all accessible hierarchic levels.

The obtained results were analyzed and discussed in terms of the non-extensive statistical mechanics (NESM) developed by Tsallis (1988, 2009, 2011) as a generalization of the Boltzmann–Gibbs statistics for cases of the non-exponential energy distribution in non-equilibrium dynamical systems characterized by long-range interrelation between energy release/exchange events. We shall show that the fracturing ice exhibits highly changeable thermodynamic properties under non-regular external forcing.

2. NON-EXTENSIVE CONJECTURE

A vast of experiments and computer simulations carried out in two last decades have demonstrated the scaling character of the fracture process in solids, which manifests itself in fractal pattern of fracture surfaces and invariance of the energy release in fracture events. In the latter case, a term "scaling" is defined through the relation

$$N(\lambda E) = \lambda^{-b} N(E) , \tag{1}$$

where N is the number of events characterized with the energy E, b is the constant, and λ is the scaling factor. This definition corresponds to the power law energy distribution of fracture events, say, breaks of structural links in a loaded solid:

$$N(E > E') \propto E'^{-b} , \tag{2}$$

where $N(E > E')$ is the number of events characterized with the energy E exceeding a threshold value E'. In geophysics, the latter relation is used as an alternative designation of the celebrated Gutenberg–Richter law, $\log N(m > M) \propto -bM$, where N is the number of earthquakes having magnitudes m greater than M.

However, the Gutenberg–Richter law, as well as any other known power law relations between the event number and event size in statistical systems,

is essentially empirical relation, which cannot be derived from the thermo-dynamics of equilibrium systems. The Boltzmann–Gibbs distribution implies the independence of individual events between each other since the effect of each of them on the environment decays exponentially with the distance. This causes the additivity of contributions of individual events to the total process (*i.e.*, extensivity). The function that determines the thermodynamic state of statistical system is the entropy. In classical definition, the entropy is the extensive value because it increases as the system increases in accord-ance with the rule of additivity: if a system can be divided into two inde-pendent parts, *A* and *B*, then for the total entropy, *S*, one has

$$S(A + B) = S(A) + S(B) . \tag{3}$$

Accordingly, the Boltzmann expression for the entropy of closed, equilib-rium system is

$$S = -k \sum_{i=1} p_i \ln p_i , \tag{4}$$

where p_i is the probability of i-th state, and k is the Boltzmann constant.

In open, non-equilibrium systems, the additivity of events might be dis-turbed due to not exponential but power law decay of the interrelations be-tween components. In this case, the correlation radius of each event exceeds the dimension of involved site, and emerging long-range interactions result in non-additive, non-extensive energy distribution in the system's dynamics. The existence of important seismological (Kalimeri *et al.* 2008, Conto-yiannis *et al.* 2010, Telesca 2010a, b), hydrological (Keylock 2005, Chmel and Smirnov 2011), and atmospheric (Shi *et al.* 2005, Ferri *et al.* 2010) phe-nomena characterized by power law relations demonstrates the non-extensive nature of many geophysical processes, which cannot be adequately described in the framework of equilibrium thermodynamics (Genshaft 2009, Vallianatos and Sammonds 2010).

In order to take into account long-range correlations in processes occur-ring in non-equilibrium systems, Tsallis (1988) introduced a concept of non-extensive entropy through a transition from the conventional logarithmic definition for the entropy given by Eq. (4) to the power-law relation, $\ln p \rightarrow (p^{1-q} - 1)(1 - q)$, which led him to the following expression:

$$S_q = k \left(1 - \sum_{i=1} p_i^q \right) \Big/ (q-1) , \tag{5}$$

where q is the parameter that specifies a "degree of non-extensivity". In this case, the expression for the total entropy of two subsystems takes the form

$$S_q (A + B) = S_q (A) + S_q (B) + S_q (A) S_q (B)(1-q)/k . \tag{6}$$

The classical Boltzmann–Gibbs statistics corresponds to the limit $q \rightarrow 1$, because in this case $p_i^{(q-1)} = \exp(q-1) \times \ln p_i \approx 1 + (q-1)\ln p_i$. Then Eq. (5) grades into Eq. (4), and Eq. (6) reduces to Eq. (3). For $q < 1$ the formalism imposes a high-energy cut-off, *i.e.*, $p_i = 0$ whenever the argument of the power function becomes negative, *i.e.*, when all probabilities vanish but one which equals unity. Finally, the value $q > 1$ signalizes the presence of long-range interactions – the distinctive property of open, non-equilibrium systems. It is worthy to note that a temporary transition from the Boltzmann–Gibbs statistics to Tsallis statistics might take place also in a ***closed*** system during a ***limited*** time interval when such a system deviates from the thermodynamic equilibrium state (Milovanov and Zelenyi 2000).

The Tsallis' concept provided a basis for the development of non-extensive statistical mechanics, which considers the processes in both equilibrium and non-equilibrium systems in the framework of a common thermodynamic approach.

3. NON-EXTENSIVE ENERGY DISTRIBUTION

Sotolongo-Costa and Posadas (2004) applied the Tsallis statistics for the analysis of seismic activity. They derived a generalized Gutenberg–Richter relation issuing from a simplified model of the tectonic process as the stick-slip motion of plates controlled (gained or hindered) by the interaction of debris of previous contact breakage with hard asperities. Their key supposition was the proportionality between the energy released and the dimension of rock fragments. This fragment-asperity model was slightly modified by Silva *et al.* (2006) who obtained the following expression for the number of earthquakes with magnitudes, m, larger than a value m' normalized to the total number of events N:

$$\log N(m > m') = \log N + \left(\frac{2-q}{1-q}\right)\log\left[1 - \left(\frac{1-q}{2-q}\right)\left(10^{2m} a^{-2/3}\right)\right], \qquad (7)$$

where a is the volumetric energy density. In terms of the energy released ($m \approx 1/3 \log E$), Eq. (7) takes the form:

$$N(E > E') = N\left[1 - \left(\frac{1-q}{2-q}\right)(E/a)^{2/3}\right]^{\left(\frac{2-q}{1-q}\right)}. \qquad (8)$$

These relations allow one to determine the q-value by fitting the analytical expressions to the plots $N(m > m')$ *versus* m' or $N(E > E')$ *versus* E' constructed on the basis of experimental data. Silva *et al.* (2006) fitted Eq. (7) to the frequency magnitude distributions taken from earthquake catalogues for different seismic regions in Brazil, USA, and Turkey by varying the q and

a values. A good agreement between analytical and registered $N(m > m')/N$ distributions was obtained in all cases. This result was supported by similar calculations performed by Telesca (2010a) and Telesca and Chen (2010) for seismicity in Italy and Taiwan, respectively. Telesca (2010b) reported that the *q*-values corresponding to the best fitting reflect the variation of seismic activity both over area and in time.

4. NON-EXTENSIVE PROCESSES IN FRACTURING SEA ICE

The ASIC is fully open to the exposure from the atmosphere and ocean. The non-uniformity of the external action causes substantial deformations in the ice pack, localized cracking, and cycles of multiple sea ice cover fragmentations over vast areas. The scale of mechanical perturbations depends both on the heterogeneity of the external forcing and on the actual sea ice consolidation: the higher degree of consolidation, the vaster area becomes involved into the common mechanical process.

Fractioning and freezing cause fluctuations in the system's entropy because its total value in the fragmented pack is higher than that in the consolidated sea ice. Therefore, one should consider the fracture processes in sea ice as non-extensive ones (Sotolongo-Costa *et al.* 2000).

The deforming and fracturing of sea ice induce redistribution of internal stresses with generating longitudinal, transverse, flexural, and gravimetric elastic waves in the range 0.1 to 10^3 Hz; some of them propagate over hundreds kilometers. The intensity and frequency of excited oscillations in sea ice give information on their origin and, in particular, on the energy release in icequakes. In the following subsections we shall present the NESM analysis of experimentally determined energy distributions in mechanical processes in sea ice at two scale levels characterized by: (i) large-scale fault formation, and (ii) individual crack propagation. In addition, the ice crashing was studied under laboratory conditions using the high-resolution acoustic emission (AE) technique.

4.1 Faulting

The cracking, shearing, and stick-slip motions in sea ice are similar to those in geostructures. The seismic activity gives rise to wave processes of different nature, which manifest themselves in the electromagnetic emission (EME) (Rabinovich *et al.* 2001, Kapiris *et al.* 2003) and seismic electric signals (SES) (Balasco *et al.* 2002, Varotsos *et al.* 2006). However, in field observations of the cryosphere, the mentioned emission techniques are not much applicable due to their inadequacy to specific physical and mechanical properties of ice. Therefore, some other tools, such as seismographs and tiltmeters, are widely used for analyzing the wave processes in sea ice (Smirnov 1996).
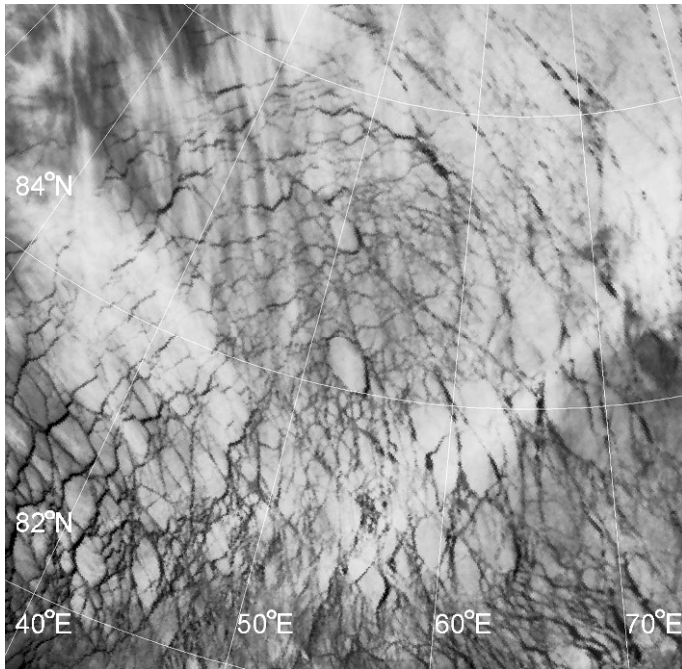
Fig. 1. Satellite image of a fault formed on 5-8 March 2008 in the Polar region in the vicinity of the ice-research camp North Pole 35.

The propagating crack and shearing motions generate in sea ice oscillations in the frequency range 0.1 to 5 Hz (Martin and Drucer 1991, Smirnov 1996). The intensity of ice pack fracturing varies in dependence of the external driving and accumulated inner energy. From time to time, bursts of large scale sea ice cracking cover the area comparable in dimensions with tectonic plates, and a two-dimensional "fault" consisting of highly fragmented sea ice emerges in stressed ice pack.

Figure 1 shows a fault that has formed in the period from 5 to 9 March 2008. The fracture-induced elastic waves emitted from this origin were detected by horizontal seismic tiltmeters established at the research camp NP 35 that drifted at the distance of ~200 km from the fault epicenter.

The accessible frequency range of tiltmeters (10^{-3} to 0.5 Hz) was reduced with a low-frequency cut-off of 0.1 Hz in order to discriminate oscillations caused by swell forcing and gravimetric waves. The range of detectable tilts was 0.1 to 10^3 μrad. A fragment of the series from one of the tiltmeters is depicted in Fig. 2.

There was an interval of low oscillation activity in the pre-faulting period, 2-4 March. Then, two strong bursts of oscillations separated by a short-term
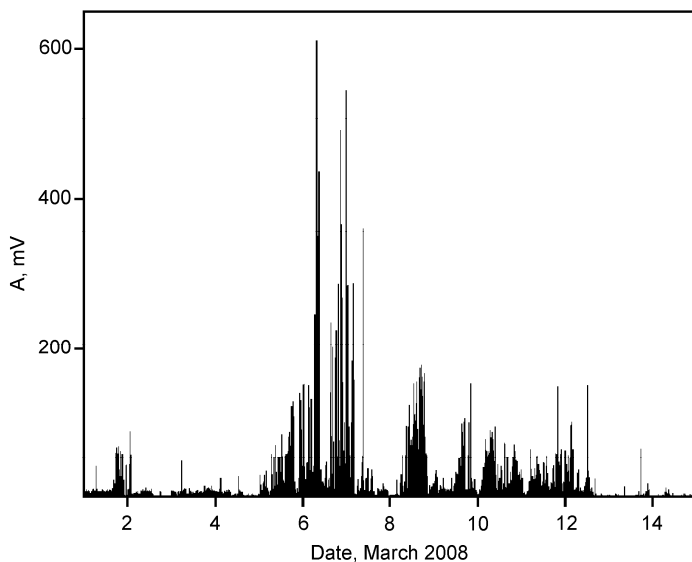
Fig. 2. Amplitudes of tiltmeter's signals excited by elastic waves in sea ice as measured at the camp North Pole 35 from 1 to 15 March 2008.

quiet period were detected on 5-6 and 8 March. In these time intervals the amplitudes of some signals exceeded the background level by more than an order of magnitude. A series of "aftershocks" continued a few days.

The squared signal amplitude, A^2, is proportional to the energy released in stress discharges and, correspondingly, the energy distributions $N(E > E')$ *versus* E' are equivalent to the distributions $N(A^2 > A'^2)$ *versus* A'^2. The intensity/energy distributions in the daily series are depicted in Fig. 3 together with the analytical curves calculated using the best-fitting procedure for parameters q and a in Eq. (8).

The best-fitted q-value decreased from $q \approx 1.2$-1.45 at the pre- and post-faulting periods down to $q = 0.87 \pm 0.04$ on 5 March, and $q = 0.65 \pm 0.11$ on 8 March, respectively. A drop of the q-value to below unity means the prevalence of rare, uncorrelated events, which one could expect in the equilibrium ensemble of flowing ice floes immediately after the fragmentation.

The q-value variation is accompanied with changes in the energy density (Fig. 4). The time-profile of the parameter a reproduces the q-value profile with an opposite trend: the highest values of the parameter a coincide with minima in the q-value profile (and, simultaneously, with periods of the highest fracture activity). A growth of the q-value in the post-faulting period of time is accompanied with a gradual decrease of the energy density. The highest energy densities were during the largest sea ice fragmentations.
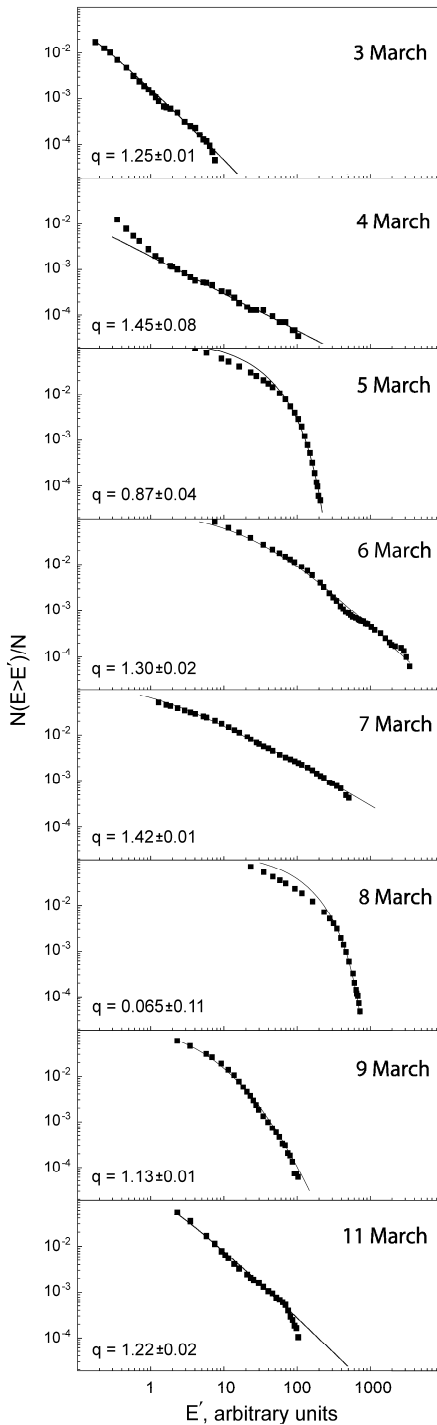
Fig. 3. Daily energy distributions in sea ice oscillations (squares) and fitting with Eq. (8) (curves). The values of $N(E > E')$ are normalized by N because the number of detected events was not the same in different days. The best fitted q-values are given in each panel. More detailed profiles of the parameters q and a are shown in Fig. 4.
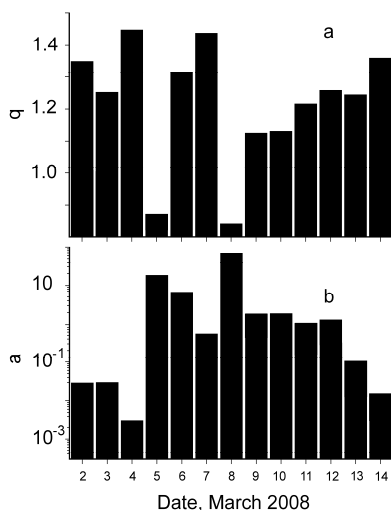
Fig. 4. Variations of the Tsallis parameter, *q*, and the energy density, *a*, as revealed from fitting procedure applied to experimental points shown in Fig. 3.

4.2 Localized cracking

In this experiment, three conjugated seismographs were established on a drifting ice floe in the vicinity of the research camp NP 37. A day-and-night monitoring of the sea ice oscillations continued during three months in 2010. On 18 January 2010, a large-scale crack passed across the ice floe, and two trains of elastic waves were detected by seismographs (Fig. 5) synchronically with the event. A comparison of the signal lags from three spaced seismographs allowed us to measure the speed of passing waves, which was about 2×10^3 m/s. Both trains, separated by a 4-min gap of oscillations, came from the same direction.

The spectral composition of the bursts of oscillations was determined in four 5-min "windows"; one window was selected in the first burst (A), and three other windows (B, C, D) in the second one; time positions of the windows are denoted in Fig. 5 by horizontal bars.

The results of the Fourier analysis of oscillations in selected time windows are depicted in Fig. 6. In interval A, one can see a dominant feature at about 0.24 Hz, which is supplemented with a "comb" of very closely situated higher-frequency peaks, the intensity in which diminishes at about 0.5 Hz. This spectrum can be expected in trains of elastic waves emitted by growing crack; it reflects the irregularity of crack propagation.

The spectra in windows of the second burst are quite different from those in interval A. There are a few wide peaks in the spectra of initial (B) and final (D) portions of the burst, while a discrete spectrum with well-pronounced
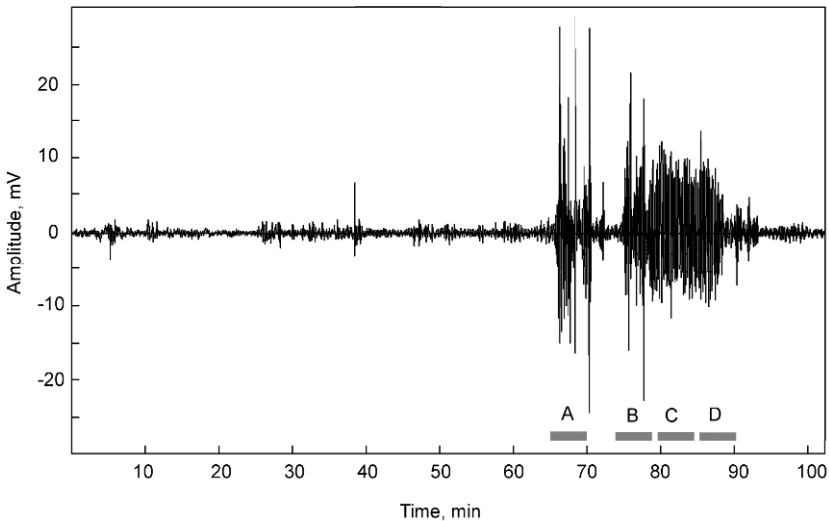
Fig. 5. Time sweep of seismograph signals recorded on 18 January 2010 at ice research station North Pole 37 during the crack propagation. Time windows selected for spectral analysis are denoted by horizontal bars.

frequency gaps between peaks is seen in the middle (C) part. The bursts characterized by the spectra consisting of a few discrete features were detected almost in all daily records during the three-month period of continuous monitoring. We ascribe these bursts to quasi-regular stick-slip motions of neighboring ice floes, which are commonly occurring in drifting sea ice (Smirnov 1996). The spectrum close to continuum (Fig. 6a) was revealed only on the day of large-scale cracking.

So, the monitoring revealed an event of crack propagation followed by the shearing motion of a couple of ice floe pieces.

The intensities (amplitudes squared) of seismograph signals are proportional to the energy release in elementary fracture events, $E \propto A^2$; therefore, the experimental distributions $N(A^2 > A^{2\prime})$ *versus* $A^{2\prime}$ shown in Fig. 7 are equivalent to the energy distributions.

The distributions are not the same in all four windows, this difference reflects a variability of the fracture process. In order to assess its degree of non-extensivity in different time intervals, the parameters q and a in Eq. (8) were fitted to the actual energy distributions. The results of the best-fitting procedure evidence a good agreement between measured and calculated frequency-size dependences under various regimes of fracturing. There are stages specified by $q > 1$, $q \approx 1$, and $q < 1$. The experimental dependences in the first window cannot be adequately described with a single combination of the parameters q and a. The values $q = 1.43$ and $q = 1.07$ in

window A indicate the complexity of fracturing under the given conditions where the well-pronounced non-extensive energy release ($q = 1.43$) is combined with low q-value dynamics typical for near equilibrium process.
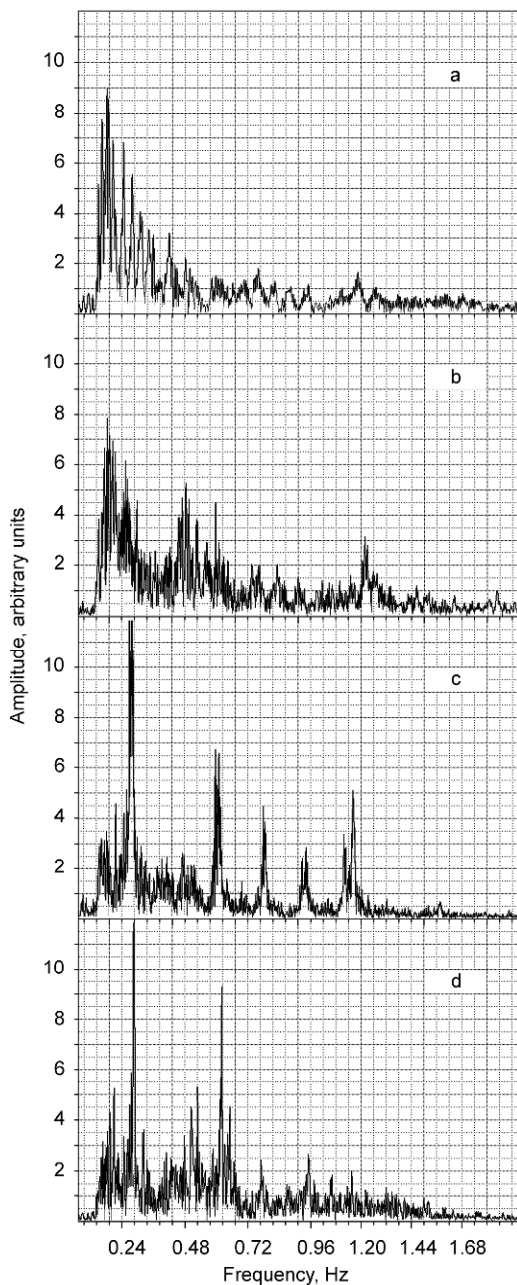

Fig. 6. Spectral composition in bursts of oscillations in time windows: (a) A, (b) B, (c) C, and (d) D shown in Fig. 5.
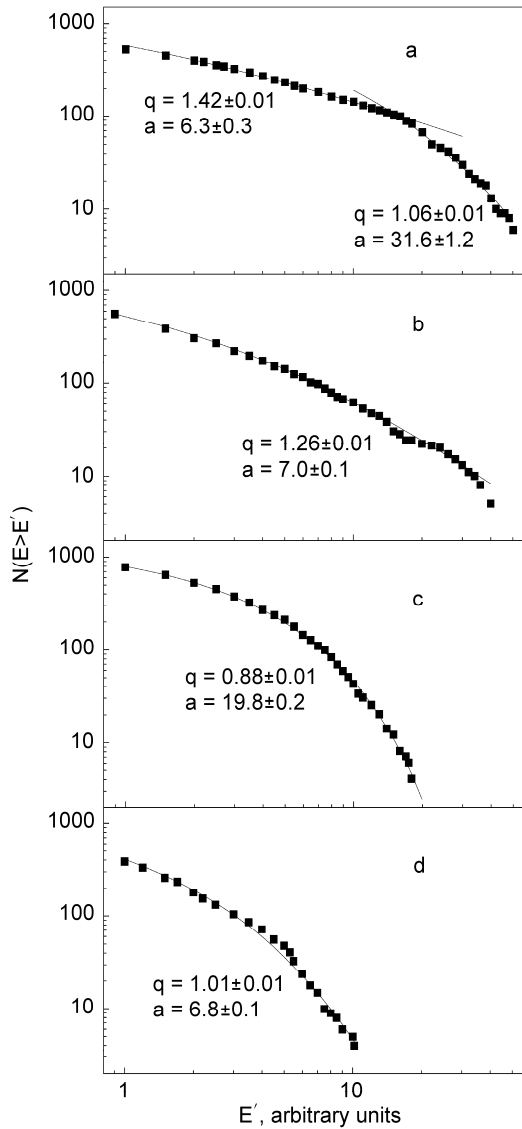
Fig. 7. Experimental (signs) and calculated (lines) dependences $N(E > E')$ *versus* E' in time windows: (a) A, (b) B, (c) C, and (d) D.

The stick-slip motion (second burst) is characterized by lower values of the parameter q. It begins with $q = 1.26$ (window B), and to the end of the motion becomes close to unity. Interestingly, Telesca (2010b) reported a reduced value of the parameter q in tectonic stick-slip process as compared to its value found for interaction between rock fragments with hard formations.

The parameter $q = 0.88$ in window C ("stationary" part of the second burst) responds to the deterministic process with limited energy release. Such periods of regular oscillations in the Arctic ice pack are explained by the parametric energy exchange in clusters of oscillating ice floes (Chmel *et al.* 2007). This is a non-linear but extensive process occurring in dissipative systems. Characteristic frequencies are determined by size, geometry, *etc.* of ice floes. In contrast to non-extensive processes that take place in open systems with a multiplicity of metastable states, the self-organization in dissipative structures is conditioned by certain values ("tuned values") of order parameters. The value $q = 1.01$ in window D means that the dynamic process finishes under almost equilibrium conditions.

4.3 Laboratory modeling

The crack initiation in solids occurs at the microscopic scale level. A commonly used technique for monitoring the micromechanical process is the acoustic emission (AE) method, which is widely used in experiments on the rock fracture. Weiss *et al.* (2001) applied the AE method for studying the ice crashing under compression loading. In this work, we recorded the AE time series during the impact fracture of ice in laboratory.

A fresh water ice sample with dimensions of $20 \times 20 \times 20$ mm was crashed with a falling 3 mm striker, and the excited acoustic emission (AE) signals were detected by a piesoceramic transducer (for description of the experimental setup see Shcherbakov *et al.* 2011, Vettegren *et al.* 2011). A relatively small size of the samples is caused by a necessity to avoid, as much as possible, the signal decay on the path from localized cracking to the transducer established on the sample surface. The signals were processed, converted into the digital form, and stored in PC. The time resolution of the AE signals was 10 ns. Figure 8 shows a recorded 600 µs time series; its beginning is synchronized with the striker impact.

Again, the signal amplitude squared is proportional to the energy released during cracking, as has been proposed by Vallianatos and Triantis (2008). Figure 9 shows the experimental energy distribution $N(>E)$ *versus E* and the distribution function (8) calculated with the best-fitted parameters q and a. One can see a close similarity in the energy release between the fracturing laboratory sample and the crack propagating in sea ice pack (*cf.* Figs. 7a and 9). In both cases, the frequency-size dependences include two well-pronounced portions characterized by the parameter q either greater than unity (flat segment) or less than unity (steep segment).

Similar to the large-scale fracturing, the energy density characterized by the parameter a was approximately 20 times larger at the final part of the dependence (43 against 1.9 at the flat part). Apparently, the high-energy
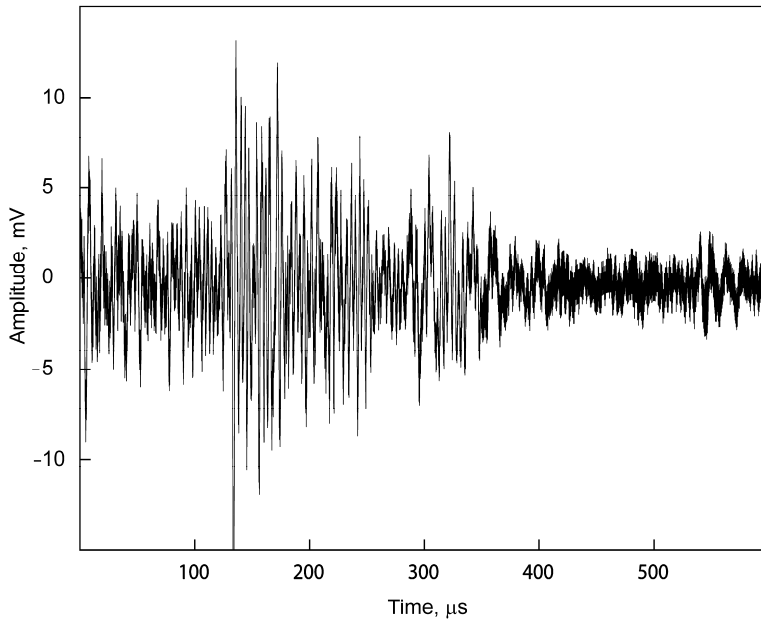
Fig. 8. Time sweep of AE signals recorded during the impact crashing of a fresh water ice sample.
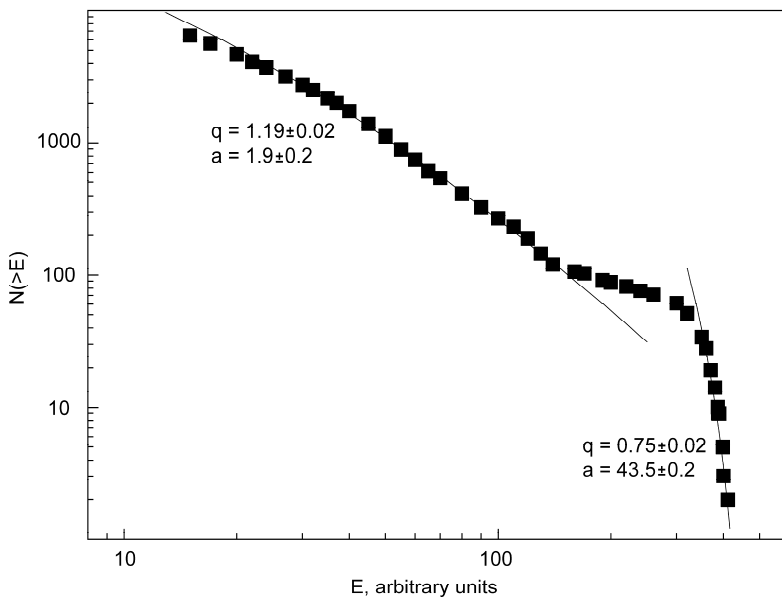

Fig. 9. Experimental (signs) and calculated (lines) dependences $N(>E)$ *versus* E for fracturing ice sample.

(steeper) part of the distribution is associated with the macroscopic crack growth when no correlation between sparse, sample-wide events takes place ($q = 0.75$). The flat portion ($q = 1.19$) reflects the correlated multi-site nucleation of microcracks. Thus, combinations of the non-extensive/expensive modes of fracturing manifest themselves in phenomena which are incomparable both in spatial and temporal scales but have the same physical nature. It is worthy to note that a very similar result was obtained when crushing a Westerly granite sample (Shcherbakov *et al.* 2011). Vallianatos *et al.* (2011) reported the evolution of *q*-values with increasing compression stress applied on rocks.

5. DISCUSSION

The ASIC is the multi-scale, hierarchic, and dynamic geophysical system. Overland *et al.* (1995) suggested the existing of five scale levels in the marine cryosphere. The characteristic linear dimensions of the scale-specific formations and the typical fracture events are shown in Table 1. Characteristic times of recorded events allow one to identify any given hierarchic level. As distinct to the hierarchic architecture of the Earth's crust, which originates from the structural heterogeneity existing at all scale levels (tectonic plates, rocks, minerals), the hierarchic properties of the ASIC are determined by different dominants specific for particular levels: prevailing continental winds, non-uniformity of bottom pack profile, brine pockets, *etc.* In addition, the sea ice dynamics is affected by the dynamics of the ocean.

Table 1

Hierarchic structure for the sea-ice mechanics
(according to Overland *et al.* (1995) with actual updates)

Spatial scale *m*	Features	Fracture events	Characteristic time in this study
10^5	pack ice	faulting	days
10^4	ice floe assemblage	polynya formation	n/a
10^3	ice floe	lead propagation	minutes
10^0-10^2	finger rafted ice	thermal cracks, macrocracks	n/a
10^{-3}-10^{-1}	crystals, brine pockets	microcracks, "wing" cracks	microseconds

In this work we considered the fracture process at three principal levels: fault formation, lead propagation, and microcracking. The energy release distributions in the observed events were analyzed in the framework of a common approach based on the Tsallis statistics. We determined formalistically a degree of non-extensivity/extensivity of the processes through the

parameter q that was introduced by Tsallis (1988) into his definition of entropy. In fact, issuing from the value of this parameter (as it is either greater or less than unity) one could characterize a certain stage of the fracture process as non-equilibrium or equilibrium and, correspondingly, assess the efficiency of correlations in multi-site damaging.

A comparison of the data related to different modes of fracturing reveals both spatial and temporal identity of ice fracture at all accessible scale levels, as regarded from the viewpoint of non-extensive thermodynamics. First of all, the presented energy distributions demonstrate a considerable variability of the degree of equilibrium in the system. Whilst the periods of multi-site fracturing are characterized by small variations of the q-value all time greater than unity, the dynamic fracture takes place at q close to or less than unity (from 0.80 to 1.07 in our experiments). Such transient drops of the parameter q signalize breaks of long-range interactions that are responsible for the correlated dynamics of multiple-site fracture process. The parameter q increases to higher values prior to the strongest bursts of energy release. The non-equilibrium state is a thermodynamic precursor of dynamic fracture.

The value of the parameter q reflects indirectly the conservation properties of the system. Really, the thermodynamic equilibrium of an open system is determined in many instances by its capability for energy conservation. In low-conservative systems, the energy exchange is restricted by neighboring sites, and the non-extensive process should be characterized by low values of the parameter q. On the other hand, there are no interactions between components in fully non-conservative systems, such as flowing fragmented sea ice (Chmel *et al.* 2010a). Recent studies evidenced that the q-value in highly conservative systems, such as tectonic structures, never decreases to unity and varies around the value ~1.5 (Telesca 2010b, c; Vallianatos 2009, Vallianatos and Sammonds 2011). One should expect that the q-value would be a universal constant in a fully conservative system.

A second important similarity between the ice fracturing occurring at different scale levels is a reversed variation of the energy density in relation to the q-value variation. The changes in the value of energy density could cover a few orders of magnitude with reaching the maximum value at the minimum value of the parameter q, that is, during the most important fracture events. This is a clear physical result, which reproduced itself in all our experiments.

Thus, despite a space-time hierarchy of fracturing due to different driving forces and structural particularities existing in the ASIC at different scale levels, the considered thermodynamic characteristics of the process, such as the non-extensivity and energy release, show at all hierarchic levels a uniform behavior, specific for the open, non-equilibrium system with a varying level of conservativity.

In fact, there are no well-defined criteria that could provide an unambiguous partitioning of the system in individual hierarchic levels. A universal estimate could be derived from the correlation radius of interactions that implement the connectedness of the system.

In conventional mechanics, the correlation radius is given by the distance of elasto-dynamic interactions (Bowman *et al.* 1998), which are realized through stationary (structural) links. Permanent sea ice breakage occurring at all scale levels restricts the establishing of the latter ones.

In statistical non-linear mechanics, the correlation radius is determined by dynamic links limited only by the size of the system. The energy exchange in the ice pack is realized through wave processes. The sea ice oscillations that served in this work for detecting the fracture events establish dynamic integrity of the ASIC.

6. CONCLUSIONS

The mechanical processes in drifting sea ice, such as fracturing and contact interactions, exhibit highly variable degree of non-extensivity in the sense of Tsallis statistics. The variations are caused by significant changes in the energy conservation in periods of intensive fracture processes, which disturb the connectedness of sea ice. This variability is a particular feature that distinguishes the thermodynamic of ASIC from that of conservative geostructures, though these geophysical formations are close to each other both in their dimensions and in the nature of mechanical processes.

References

Balasco, M., V. Lapenna, and L. Telesca (2002), $1/f^{\alpha}$ fluctuations in geoelectrical signals observed in a seismic area of Southern Italy, *Tectonophysics* **347**, 4, 253-268, DOI: 10.1016/S0040-1951(02)00062-8.

Bowman, D.D., G. Ouillon, C.G. Sammis, A. Sornette, and D. Sornette (1998), An observational test of the critical earthquake concept, *J. Geophys. Res.* **103**, B10, 24359-24372, DOI: 10.1029/98JB00792.

Chmel, A., and V.N. Smirnov (2008), Self-organized dynamics of the sea ice cover. **In:** K.B. Tewles (ed.), *The Pacific and Arctic Oceans – New Oceanographic Researches*, Nova Science, New York, 131-156.

Chmel, A., and V.N. Smirnov (2011), Correlated energy exchange in drifting sea ice, *Int. J. Oceanography*, DOI: 10.1155/2011/316289.

Chmel, A., V.N. Smirnov, and L.V. Panov (2007), Scaling aspects of the sea-ice-drift dynamics and pack fracture, *Ocean Sci.* **3**, 2, 291-298, DOI: 10.5194/os-3-291-2007.

Chmel, A., V. Smirnov, and O. Golovanov (2010a), Variability of scaling para me-
ters in non-conservative systems: Geophysical aspect, *Physica A*, **389**, 13,
2617-2627, DOI: 10.1016/j.physa.2010.02.055.

Chmel, A., V.N. Smirnov, and I.B. Sheikin (2010b), Variability of scaling time se-
ries in the Arctic sea-ice drift dynamics, *Ocean Sci.* **6**, 1, 211-217, DOI:
10.5194/os-6-211-2010.

Contoyiannis, Y.F., C. Nomicos, J. Kopanas, G. Antonopoulos, L. Contoyianni, and
K. Eftaxias (2010), Critical features in electromagnetic anomalies detected
prior to the L'Aquila earthquake, *Physica A* **389**, 3, 499-508, DOI: 10.1016/
j.physa.2009.09.046.

Ferri, G.L., M.F.Reynoso Savio, and A. Plastino (2010), Tsallis' q-triplet and the
ozone layer, *Physica A* **389**, 9, 1829-1833, DOI: 10.1016/j.physa.2009.
12.020.

Genshaft, Yu.S. (2009), The Earth as an open system: Geological and geophysical
consequences, *Izv. – Phys. Solid Earth* **45**, 8, 624-632, DOI: 10.1134/
S1069351309080023.

Kalimeri, M., C. Papadimitriou, G. Balasis, and K. Eftaxias (2008), Dynamical
complexity detection in pre-seismic emissions using nonadditive Tsallis en-
tropy, *Physica A* **387**, 5-6, 1161-1172, DOI: 10.1016/j.physa.2007. 10.053.

Kapiris, P.G., K.A. Eftaxias, K.D. Nomikos, J. Polygiannakis, E. Dologlou,
G.T. Balasis, N.G. Bogris, A.S. Peratzakis, and V.E. Hadjicontis (2003),
Evolving towards a critical point: A possible electromagnetic way in which
the critical regime is reached as the rupture approaches, *Nonlin. Processes
Geophys.* **10**, 6, 511-524, DOI: 10.5194/npg-10-511-2003.

Keylock, C.J. (2005), Describing the recurrence interval of extreme floods using
nonextensive thermodynamics and Tsallis statistics, *Adv. Water Resour.* **28**,
8, 773-778, DOI: 10.1016/j.advwatres.2005.02.011.

Martin, S., and R. Drucker (1991), Observations of short-period ice floe accelera-
tions during leg II of the Polarbjørn drift, *J. Geophys. Res.* **96**, C6, 10567-
10580, DOI: 10.1029/91JC00785.

McNutt, S.L., and J.E. Overland (2003), Spatial hierarchy in Arctic sea ice dynam-
ics, *Tellus A* **55**, 2, 181-191, DOI: 10.1034/j.1600-0870.2003. 00012.x.

Milovanov, A.V., and L.M. Zelenyi (2000), Functional background of the Tsallis en-
tropy: "coarse-grained" systems and "kappa" distribution functions, *Nonlin.
Processes Geophys.* **7**, 3/4, 211-221, DOI: 10.5194/npg-7-211-2000.

Overland, J.E., B.A. Walter, T.B. Curtin, and P. Turet (1995) Hierarchy and sea ice
mechanics: A case study from the Beaufort Sea, *J. Geophys. Res.* **100**, C3,
4559-4571, DOI: 10.1029/94JC02502.

Rabinovitch, A., V. Frid, and D. Bahat (2001), Gutenberg–Richter-type relation for
laboratory fracture-induced electromagnetic radiation, *Phys. Rev. E* **65**, 1,
011401, DOI:10.1103/PhysRevE.65.011401.

Shcherbakov, I.P., V.S. Kuksenko, and A.E. Chmel (2011), Nonextensive statistical analysis of the data on the high-speed impact fracture of solids, *JEPT Lett.* **94**, 5, 378-381, DOI: 10.1134/S0021364011170152.

Shi, B., B. Vidakovic, G.G. Katul, and J.D. Albertson (2005), Assessing the effects of atmospheric stability on the fine structure of surface layer turbulence using local and global multiscale approaches, *Phys. Fluids* **17**, 5, 055104, DOI: 10.1063/1.1897008.

Silva, R., G.S. França, C.S. Vilar, and J.S. Alcaniz (2006), Nonextensive models for earthquakes, *Phys. Rev. E* **73**, 2, 026102, DOI: 10.1103/PhysRevE.73.026102.

Smirnov, V.N. (1996), *Dynamic Processes in Sea Ice*, Gidrometeoizdat, St. Petersburg (in Russian).

Sotolongo-Costa, O., and A. Posadas (2004), Fragment-asperity interaction model for earthquakes, *Phys. Rev. Lett.* **92**, 4, 048501, DOI: 10.1103/PhysRevLett.92.048501.

Sotolongo-Costa, O., A.H. Rodrigez, and G.J. Rodgers (2000), Tsallis entropy and the transition to scaling in fragmentation, *Entropy* **2**, 4, 172-177, DOI: 10.3390/e2040172.

Telesca, L. (2010a), Nonextensive analysis of seismic sequences, *Physica A* **389**, 9, 1911-1914, DOI: 10.1016/j.physa.2010.01.012.

Telesca, L. (2010b), A non-extensive approach in investigating the seismity of L'Aquila area (central Italy), struck by the 6 April 2009 earthquake, *Terra Nova*, **22**, 2, 87-93, DOI: 10.1111/j.1365-3121.2009.00920.x.

Telesca, L. (2010c), Analysis of Italian seismicity by using a nonextensive approach, *Tectonophysics* **494**, 1-2, 155-162, DOI: 10.1016/j.tecto.2010. 09.012.

Telesca, L., and C.-C. Chen (2010), Nonextensive analysis of crustal seismicity in Taiwan, *Nat. Hazards Earth Syst. Sci.* **10**, 1293-1297, DOI: 10.5194/nhess-10-1293-2010.

Tsallis, C. (1988), Possible generalization of Boltzmann–Gibbs statistics, *J. Stat. Phys.* **52**, 1-2, 479-487, DOI: 10.1007/BF01016429.

Tsallis, C. (2009), *Introduction to Nonextensive Statistical Mechanics. Approaching a Complex World*, Springer, New York, 382 pp.

Tsallis, C. (2011), The nonadditive entropy Sq and its applications in physics and elsewhere: Some remarks, *Entropy* **13**, 10, 1765-1804, DOI: 10.3390/e13101765.

Vallianatos, F. (2009), A non-extensive approach to risk assessment, *Nat. Hazards Earth Syst. Sci.* **9**, 1, 211-216, DOI: 10.5194/nhess-9-211-2009.

Vallianatos, F., and P. Sammonds (2010), Is plate tectonics a case of non-extensive thermodynamics? *Physica A* **389**, 21, 4989-4993, DOI: 10.1016/j.physa. 2010.06.056.

Vallianatos, F., and P. Sammonds (2011), Non-extensive thermodynamics applied to global seismicity before and after the Sumatran mega-earthquake, *Geophys. Res. Abstr.* **13**, EGU2011-10723.

Vallianatos, F., and D. Triantis (2008), Scaling in pressure stimulated currents related with rock fracture, *Physica A* **387**, 19-20, 4940-4946, DOI: 10.1016/j.physa.2008.03.028.

Vallianatos, F., D. Triantis, and P. Sammonds (2011), Non-extensivity of the isothermal depolarization relaxation currents in uniaxial compressed rocks, *Europhys. Lett.* **94**, 6, 68008, DOI: 10.1209/0295-5075/94/68008.

Varotsos, P.A., N.V. Sarlis, E.S. Scordas, H.K. Tanaka, and M.S. Lazaridou (2006), Attempt to distinguish long-range temporal correlations from the statistics of the increments by natural time analysis, *Phys. Rev. E* **74**, 2, 021123, DOI: 10.1103/PhysRevE.74.021123.

Vettegren', V.I., V.S. Kuksenko, and I.P. Shcherbakov (2011), Emission kinetics of light, sound, and radio waves from single-crystalline quartz after impact on its surface, *Tech. Phys.* **56**, 4, 577-580, DOI: 10.1134/S1063784211040311.

Weiss, J. (2003), Scaling of fracture and faulting of ice on Earth, *Surv. Geophys.* **24**, 2, 185-227, DOI: 10.1023/A:1023293117309.

Weiss, J., and D. Marsan (2004) Scale properties of sea ice deformation and fracturing, *C. R. Phys.* **5**, 7, 735-751, DOI: 10.1016/j.crhy.2004.09.005.

Weiss, J., J.-R. Grasso, M.-C. Miguel, A. Vespignani, and S. Zapperi (2001), Complexity in dislocation dynamics: experiments, *Mater. Sci. Eng. A* **309-310**, 360-364, DOI: 10.1016/S0921-5093(00)01633-6.

VERSITA

Simulation and Properties of a Non-Homogeneous Spring-Block Earthquake Model with Asperities

Alejandro MUÑOZ-DIOSDADO[1], Adolfo H. RUDOLF-NAVARRO[2], and Fernando ANGULO-BROWN[2]

[1]Basic Sciences Department,
Unidad Profesional Interdisciplinaria de Biotecnología,
Instituto Politécnico Nacional, Mexico D.F, Mexico
e-mail: amunoz@avantel.net (corresponding author)

[2]Physics Department, Escuela Superior de Física y Matemáticas,
Instituto Politécnico Nacional, Mexico D.F., Mexico

A b s t r a c t

The spring-block model proposed by Olami, Feder and Christensen (OFC) has several properties that are similar to those observed in real seismicity. In this paper we propose a modification of the original model in order to take into account that in a real fault there are several regions with different properties (non-homogeneity). We define regions in the network that is reminiscent of the real seismic fault, with different sizes and elastic parameter values. We obtain the Gutenberg–Richter law for the synthetic earthquake distributions of magnitude and the stair-shaped plots for the cumulative seismicity. Again, as in the OFC-homogeneous case, we obtain the stability for the cumulative seismicity stair-shaped graphs in the long-term situation; this means that the straight line slopes that are superior bounds of the staircases have a behavior akin to the homogeneous case. We show that with this non-homogeneous OFC model it is possible to include the asperity concept to describe high-stress zones in the fault.

Key words: earthquake, faulting, cellular automata, OFC model.

1. INTRODUCTION

The concept of self-organized criticality (SOC) was introduced by Bak *et al*. (1987, 1988) as a general organizing principle governing the behavior of spatially extended dynamical systems with both temporal and spatial degrees of freedom. According to this principle, composite open systems having many interacting elements organize themselves into a stationary critical state with no length or time scales other than those imposed by the finite size of the system. The critical state is characterized by spatial and temporal power laws. In such a state, a smaller event often begins a chain reaction that can lead to a catastrophe. According to Bak *et al*. (1987, 1988), the temporal "finger print" of the SOC state is the presence of $1/f^{\alpha}$ noise and its spatial signature is the emergence of scale invariant (fractal) structure. The scale invariance is a well-known property of a lot of geological structures and phenomena. This statistical self-similar behavior is reflected through several empirical power-laws in geology and geophysics (Turcotte 1997, Ito and Matsuzaki 1990). The earth's crust can be seen as a hierarchical set of shapes and sizes suitable for a fractal description (Barriere and Turcotte 1994). The so-called Gutenberg–Richter (GR) law for the size distribution of earthquakes is a typical power law of seismology (Gutenberg and Richter 1944). In fact, as Bak (1996) has asserted, any theoretical or numerical SOC earthquake model has to reproduce the GR law as a first proof of its seismic consistency.

Since 1989, many authors (Carlson and Langer 1989, Ito and Matsuzaki 1990, Nakanishi 1990, Brown *et al*. 1991, Olami *et al*. 1992, Christensen and Olami 1992, Ceva 1995, Ferguson *et al*. 1999, Muñoz-Diosdado and Angulo-Brown 1999, Angulo-Brown and Muñoz-Diosdado 1999, Caruso *et al*. 2006, Naylor and Main 2008, Bach *et al*. 2008, Main and Naylor 2009, Caruso and Kantz 2011, Yamamoto *et al*. 2010) have reported SOC versions of the Burridge–Knopoff (BK) spring-block model (Burridge and Knopoff 1967) for earthquakes. In this model, the behavior of a real seismic fault is modeled by describing the dynamics of a linear spring-block array using differential equations. Nevertheless, the subsequent BK type models are based on cellular automata. These BK type models have been extended to 2D and 3D versions and they have been very successful in reproducing not only the GR law but several other properties of real seismicity (Muñoz-Diosdado and Angulo-Brown 1999, Angulo-Brown and Muñoz-Diosdado 1999, Hergarten and Neugebauer 2002, Helsmstetter *et al*. 2004, Kotani *et al*. 2008, Kawamura *et al*. 2010). These results have strengthened the idea that the earth's crust is a SOC system. This fact has produced a pessimistic atmosphere around the perspectives of the problem of earthquake prediction (Geller *et al*. 1997, Bak and Tang 1989), because the SOC system is intrinsically unpredictable in the sense that it is not possible to calculate the size and

occurrence time of the next event (Bak 1996). In the present paper, we show several interesting properties of a spring-block SOC model which are concomitant with properties of real seismicity. In particular, we make a comparison between the original model of Olami, Feder and Christensen (Olami *et al.* 1992, Christensen and Olami 1992), which we call the homogeneous OFC model, and a variation of the model introduced by us, as an attempt to take into account the geometry of the seismic fault. The original OFC model is a spatially homogeneous model, but real earthquake faults are spatially non-homogeneous; then, a natural step is to extend the original OFC model to an inhomogeneous one, and there are various ways to do this task, for instance, it is possible to take the model parameters to be random from site to site, or it is possible to take a temporal variation of such parameters (Yamamoto *et al.* 2010). Our proposal is different in that we propose an OFC non-homogeneous model that considers several regions in the fault and that these regions have different elastic properties. We look for the model-properties that are preserved and if there appear new features with this modification. We also make a comparison of the GR law and the stair-shaped plots for cumulative seismicity obtained with the model and the same plots obtained for real seismicity (Rudolf-Navarro *et al.* 2010). We propose that this model can be formulated to include in it the asperity concept, that is to say, a region with high stress surrounded by other region with less stress (Lay and Kanamori 1981, Kanamori 1981, Ruff 1992). Analyzing the results we can obtain valuable insights over the characteristics of the terrain where the seismic faults are located and, if we compare the patterns of real seismicity with the synthetic patterns obtained from the model, we can attempt to explain, at least qualitatively, these patterns.

The paper is organized as follows: In Section 1, we describe the OFC homogeneous model. In Section 2, we present the modification that leads to the OFC non-homogeneous model, which is different from that of Yamamoto *et al.* (2010). In Section 3, we present the results for the non-homogeneous model, and then compare it with the homogeneous model and we further discuss the similarities with real seismicity. In Section 4 we make the proposal that the model can be formulated in terms of the asperity concept. Finally, we make a discussion about the possibilities of this non-homogenous model.

2. THE HOMOGENEOUS MODEL OF OLAMI, FEDER AND CHRISTENSEN

The OFC earthquake model is a version in two dimensions of the spring-block model of Burridge–Knopoff (Burridge and Knopoff 1967). It is the prime example for a supposedly self-organized critical yet nonconservative model. The model consists of equal blocks located on a plate, which is
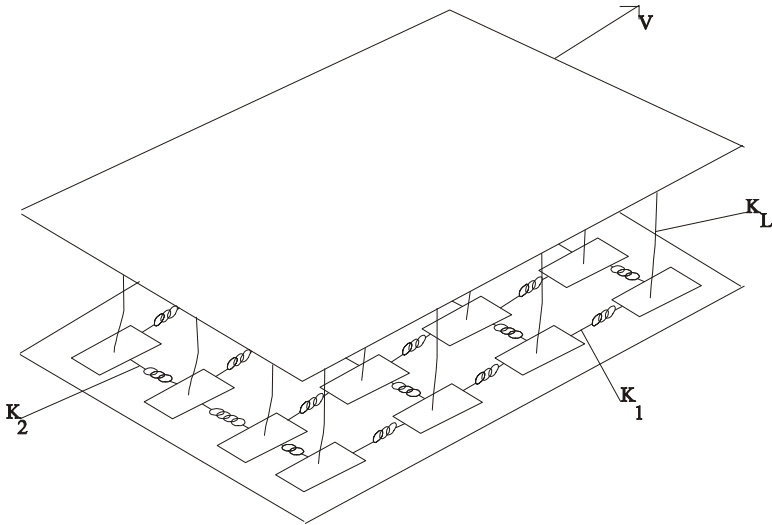
Fig. 1. The geometry of the spring-block model. The force on the blocks increases uniformly as a response to the relative movement of the two plates.

supposed to be in the fault (Fig. 1). Each block is connected to its neighbors by harmonic springs and they are lugged individually by other springs subject to other plate that moves with a constant speed. When the upper plate is moved slowly, it causes the force (or stress) to linearly increase in each block, to the point where the force equals a threshold (the force for the fault breaking); after that, the block slips to a state of residual force. A sliding block transfers force to its nearest neighbors; if these neighbors receive sufficient additional force to cause the slipping, and so on, it can generate a chain reaction or a synthetic earthquake that is stopped once all the blocks are down of the threshold.

In the OFC model, each block is connected to its four nearest neighbors. It should be emphasized that the representation of the faults as objects of two dimensions does not imply that the faults are smooth, as objects without structure. However, a lot of structure is included upon discretizing the fault plane. Olami *et al.* (1992) assumed that the block that is moved will slip to the zero force position. We define an $L \times L$ arrangement of blocks by (i, j), where i and j are integers whose values are between 1 and L and if the displacement of each block from its relaxed position on the lattice is $x_{i,j}$, then the total force exerted by the springs on a given block (i, j) is expressed by (Christensen and Olami 1992)

$$F_{i,j} = k_1 \left[2x_{i,j} - x_{i-1,j} - x_{i+1,j} \right] + \left[2x_{i,j} - x_{i,j-1} - x_{i,j+1} \right] + k_L x_{i,j} , \qquad (1)$$

where K_1, K_2 and K_L are the elastic constants. The force redistribution in the position (i, j) is given by the following relationship

$$F_{i\pm1,j} \rightarrow F_{i\pm1,j} + \delta F_{i\pm1,j} , \quad F_{i,j\pm1} \rightarrow F_{i,j\pm1} + \delta F_{i,j\pm1} , \quad F_{i,j} \rightarrow 0 , \tag{2}$$

where the force increment in the nearest neighbors is given by

$$\delta F_{i\pm1,j} = \frac{k_1}{2k_1 + 2k_2 + k_L} F_{i,j} = \alpha_1 F_{i,j} ,$$

$$\delta F_{i,j\pm1} = \frac{k_2}{2k_1 + 2k_2 + k_L} F_{i,j} = \alpha_2 F_{i,j} , \tag{3}$$

where α_1 and α_2, are the elastic ratios. As can be observed, the force redistribution is not conservative. The model is homogeneous because the same values of α_1 and α_2 are considered in the entire grid. If $\alpha_1 = \alpha_2$ the model is isotropic. Olami *et al.* made the mapping of the spring-block model into a continuous, nonconservative cellular automaton, modeling earthquakes with an algorithm as described in references of Olami *et al.* (1992) and Christensen and Olami (1992).

With open frontier conditions Olami *et al.* obtained a robust SOC behavior for the probability distribution of earthquake sizes, that is to say, that probability distribution is a power law, which, in fact, is in agreement with the GR law, and also establishes that the earthquake occurrence frequency is related to the magnitude *m* by means of the relationship

$$\log_{10} N(M > m) = a - bm ,$$

where *a* and *b* are constants and $N(M > m)$ is the number of earthquakes larger than *m* in a specific time interval. Although the GR relationship is universal, the values of *a* and *b* depend on the region. The constant *a* specifies a regional level of seismicity. Reported values of *b* are approximately between 0.75 and 1.54. Olami *et al.* calculated *b* and concluded that the most approximate values to real seismicity are produced for α values around 0.2. This is reasonable, because if we assume that all the elastic constants are in the same scale ($K_1 \approx K_2 \approx K_L$) then $\alpha \approx 0.20$, see Eq. (3). Olami *et al.* showed also that anisotropy does not seem to be a determinant factor in the modeling of the fault, since a similar behavior to the isotropic case is obtained. It has been proposed that a seismic fault model must be able to produce power laws of the type of the GR law (Bak 1996, Lomnitz-Addler 1993). However, the ability to produce a power law does not mean that the model will be useful, because it also must be able to reproduce other phenomena and lead to features that the seismologists could observe in real faults (Ferguson *et al.* 1999). Fortunately, it has been found that the OFC model has other interesting properties that seem to be related to real seismicity (Muñoz-Diosdado

and Angulo-Brown 1999, Angulo-Brown and Muñoz-Diosdado 1999, Hergarten and Neugebauer 2002, Helsmstetter *et al.* 2004, Kotani *et al.* 2008, Kawamura *et al.* 2010). We calculated the cumulative seismicity, which is obtained by adding the number of blocks that are relaxed in each one of the events, and then we plotted it as a function of time. Such graphics are stair-shaped plots similar to those of real seismicity.

Angulo-Brown and Muñoz-Diosdado (1999) have reported that these stair shaped graphics are a characteristic of the model. They found that the synthetic cumulative seismicity in the long-term situation could be bounded by a straight line, whose slope depends on the system size and cannot be arbitrarily large. For certain values of the elastic parameters of the model, the recurrence times have a log-normal behavior. The best results for the model were found for α values around 0.2, and it coincides with the results reported by Hainzl *et al.* (1999). For this reason, we believe that a more complex model of spring-block simulating a seismic fault must consider values of the elastic parameter α around 0.2. This model can be used as basic model to describe the earthquakes occurrence associated with some seismic fault, because it has several properties that have been observed in real seismicity.

3. THE NON-HOMOGENEOUS MODEL

All the above-mentioned results are only for a homogeneous fault, and a seismic fault has regions with different properties. The present work shows that it is possible to obtain the previous results if it is supposed there are several regions in the fault. The interaction between these regions can be strong or weak. In the first case, if an earthquake begins in a region, it can induce other fractures in other regions; in the second case, the probability that this happen is very small. These regions do not occur in isolation but as parts of a hierarchical structure, often characterized by a fractal dimension with a value between two and three. However, in this work we only work with regions in regular arrays.

Several regions can be modeled putting different α values in each one of the parts in which the grid is divided. In each one there are different elastic properties. As mentioned, in the spring-block model, α represents the values of the elastic properties and better results of the model have been obtained for α around 0.2. So, the α values were such that their average for all the regions would be 0.2 or close to 0.2. We work mainly with the case of two and three parallel regions, the first with the same sizes and the latter with different sizes. As in the homogeneous case, we obtain the probability distribution of earthquake magnitude frequency and with these graphics we obtain the values of the *b* exponent of the GR law. After that, we calculate the cumulative seismicity to investigate if in this case a straight line bounds the stair-

shaped graphics in the long-term situation. The objective is to compare the homogeneous case with the non-homogeneous one and to see which characteristics are conserved or if there are other new properties.

4.   RESULTS AND COMPARISON BETWEEN THE TWO MODELS AND WITH REAL SEISMICITY

In the case of two and three parallel regions we obtained a power-law for the synthetic earthquakes magnitude, that is to say, the GR law. The GR law is obtained even for regions of different size.

Using such graphics we determined the *b* values of the GR law. Logically the values are different from those in the homogeneous case, but furthermore we obtained another important difference. In the homogeneous case, the points of the distribution form a straight line that is extended in several orders of magnitude, before the line is curved downward due to the finite size effect (see Fig. 2). This happens because it is not possible to obtain results for a sufficiently large grid representing the real fault. In the non-homogeneous case, even though we obtained the power-law, it is presented in one or two less magnitude orders than in the homogeneous case. We furthermore obtained the staircase-shaped plots, but the stability towards a constant slope delays more, mainly if the dimension of the matrix that represents the grid is large ($L > 100$) (see Fig. 3). The reason can be that these non-homogeneities delay the system self-organization, that is not as fast as in the homogeneous case (it is the same situation for the frequency magnitude power-law). We must always wait until the system self-organizes, and then we can begin the statistics. At the beginning, the staircases are not stable, but these are stabilized in the long-term situation.

If we wait more time, so that the system is self-organized, then the graphics have the same qualitative form as in the homogeneous case, though the slopes in either case are different. Again, we obtained the stability for the cumulative seismicity stair-shaped graphs in the long-term situation and this means that the straight line slopes that are superior bounds of the staircases have a behavior akin to the homogeneous case.

It has been reported (Angulo-Brown and Muñoz-Diosdado 1999) that the slopes *m* of the straight lines that bound the cumulative seismicity depend on the system-size *L*. We obtained this dependence for a case with two parallel regions with two different α values (0.225 and 0.175) and we found the same behavior in the homogeneous case, that is, the slopes have an absolute maximum. Thus, as shown in Fig. 4, the cumulative synthetic seismicity cannot be arbitrarily large. These results are relevant because of two reasons: first, this model is more realistic than the homogeneous model, but it has the properties that have made it useful and second, the real seismicity has these
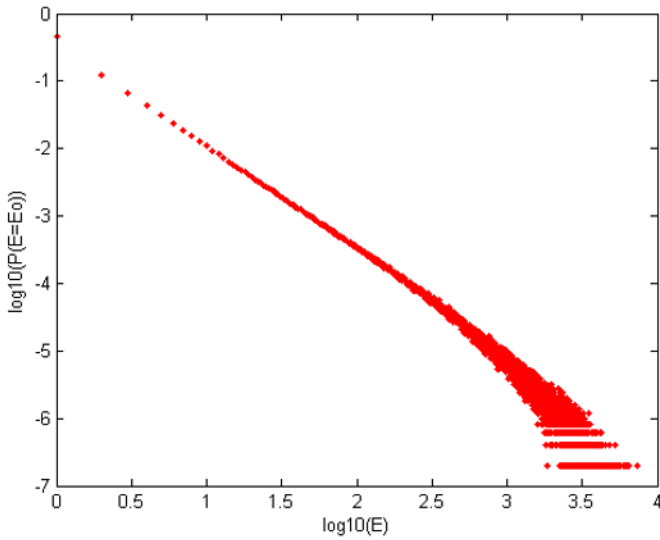
Fig. 2. Distribution of synthetic earthquake magnitude in a 100×100 system with open boundary conditions. The network is divided into two parallel regions with α values of 0.225 and 0.175, respectively; 1 000 000 events.
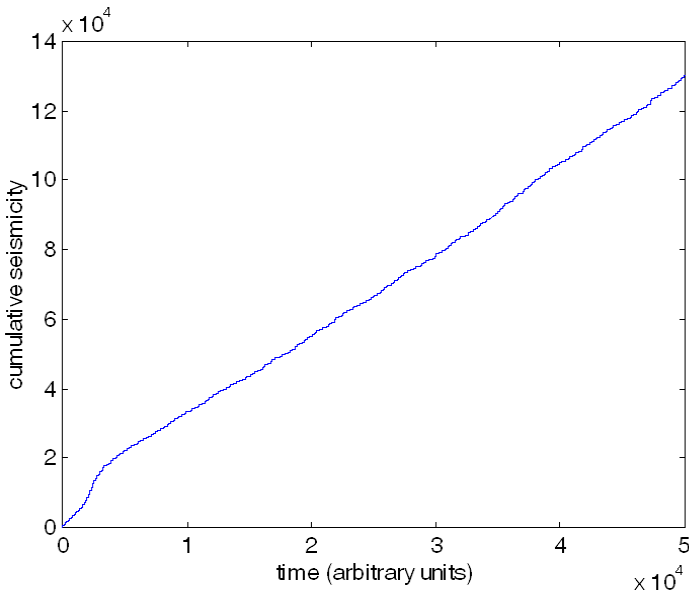

Fig. 3. Cumulative synthetic seismicity for the case with α values of 0.225 and 0.175. The structure of the stair-shaped plots can be seen when we plot less events. Although at the beginning there is no stability, it is reached in the long-term situation, where the fitting with a straight line seems to be excellent.
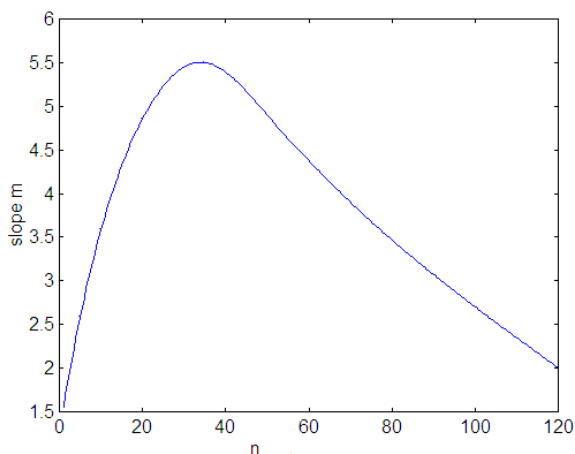
Fig. 4. Dependence of the slopes of the straight line envelopes associated to the stair-shaped curves of cumulative seismicity with system size $N = 100$; there are two parallel regions with α values of 0.225 and 0.175. The curve was smoothed using cubic splines.
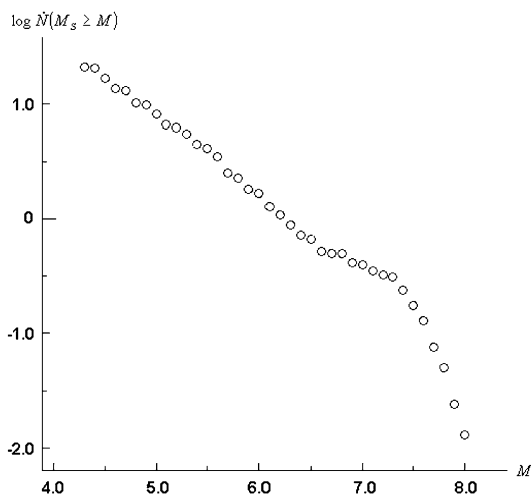

Fig. 5. Gutenberg–Richter law for a region in the Mexican Pacific coast, with $4.2 < m < 8.0$, between 14° and 21°N lat. and 94° and 106°W long., from 1 January 1969 to 30 April 2010, with depths less or equal to 60 km. Note the finite size effect.

characteristics. Actually, we have observed these kinds of plots in the seismological zones of Oaxaca, Guerrero, Michoacán and Jalisco-Colima in Mexico (Rudolf-Navarro *et al.* 2010); all of them have been characterized by one value of the *b* exponent of the GR law. For instance, in Fig. 5, we show

the frequency of earthquakes with M_s (surface wave magnitude) greater or equal to m, for events occurred between 1 January1969 and April 2010, with deep focus less than or equal to 60 km, between 14 and 21 degrees north latitude and 94 and 106 degrees west longitude. The upper points follow a power law for seisms in the interval $4.2 < m < 7.0$ of the form:

$$\log_{10} N(M_S > m) = 4.34 - 0.69\,m\,.$$

In Figure 5 we observe a change in the slope of the power law, which has been explained in two ways: As a finite size effect, which seems to be related with the size of the geographical region that is taken to make the earthquake statistics, or there is a discontinuity in the GR law; it means that we obtain a different behavior for earthquakes of large magnitude (greater than 7.0) than for the rest of the earthquakes (Pacheco *et al.* 1992). Obviously, the last interpretation does not coincide with the model results. Lomnitz-Adler (1993) suggested that if we suppose that there is a fault granularity, then finite size effects could be observed since the real faults have a finite size. Moreover, in Mexican seismological regions we can also obtain the cumulative seismicity for real earthquakes.

As can be seen in the plots as the one shown in Fig. 6 (Colima-Jalisco region) it seems that they can be characterized also by the value of the slope m_f of a long-term straight line. It means that, for real earthquakes, as in the synthetic seismicity, in the long-term behavior the envelope of the stair-shaped plots seems to tend to a straight line, so when a quiescence is produced the plot tends to return to the historical slope of the seismological region. If the quiescence is large, the return has two possible ways: first, with a large earthquake and its aftershocks or second with a swarm (or several ones) of many small earthquakes. When the second process takes place we say that a false alarm was produced. In a plot of this kind, quiescence could be easily recognized, because quiescence is present when a stair step remains almost horizontal during a lot of time. For example, in Fig. 6, the precursory seismic quietude for two earthquakes is shown.

In the model most of the earthquakes have its epicenters in the regions with smaller α, but the earthquakes of greater magnitude are concentrated in the region with greater α values. We can illustrate this in Fig. 7a, which depicts three regions with different α values, the central region with $\alpha = 0.10$ and two lateral regions with $\alpha = 0.245$. The figure shows the epicenters of 10 000 events, the majority of epicenters concentrate in the region with $\alpha = 0.10$, but when we do a cut-off to eliminate the micro-seismicity, we find that the events of great magnitude tend to concentrate in the regions with large α values (Fig. 7b). With the aid of Eq. (3) we can see that the regions with greater α values are more globally stressed regions, because when the relaxation process takes place, almost all the stress is given to the neighbors.
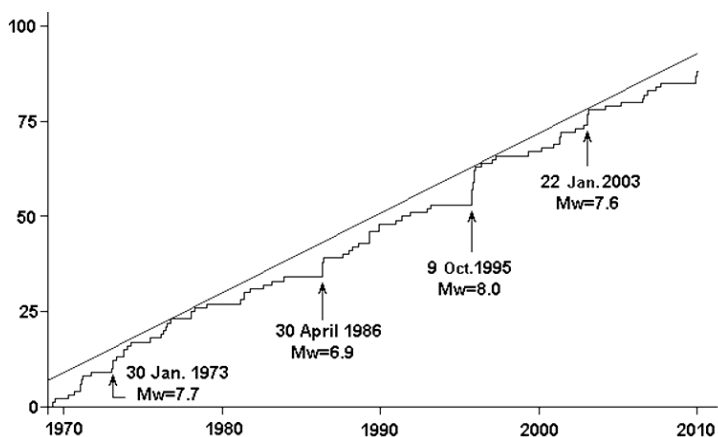
Fig. 6. Number of earthquakes with $Ms \geq 4.3$, for the Colima-Jalisco region in the Mexican Pacific coast, between 17.8° and 19.8°N lat. and 103° and 105.8°W long., from 1 January 1969 to 30 April 2010, with depths less or equal to 60 km. Note the two precursory seismic quietudes.

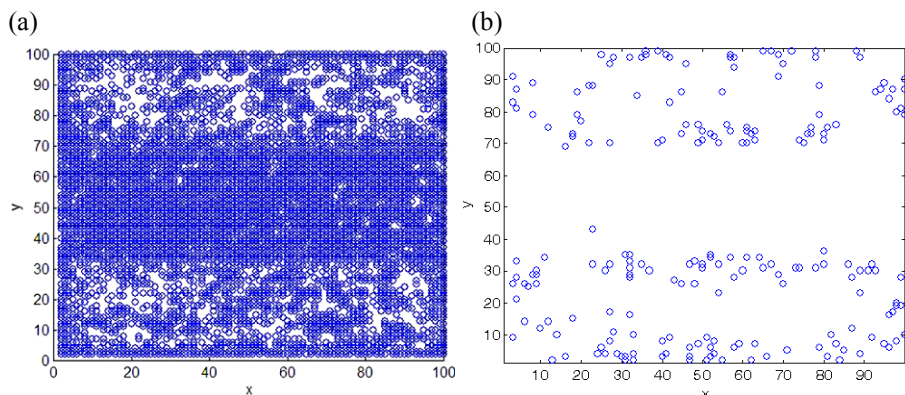(a)   (b)

Fig. 7: (a) The earthquake epicenters for three regions with different α values, the central region with $\alpha = 0.10$ and two lateral regions with $\alpha = 0.245$; most epicenters concentrate in the region with $\alpha = 0.10$, but when we do a cut-off to eliminate the seisms with less magnitude, we find that the events of great magnitude tend to concentrate in the regions with great α values, as we show in panel (b). The latter is obtained when we take away the events less than 1/16 of the event with maximum magnitude.

In contrast, the regions with smaller α values are regions less globally stressed because only a little fraction of stress is given to the neighbors, that is to say, these regions do not store a lot of energy. Most of the energy is stored in the regions with greater α values, so it is in these regions where the earthquakes of greater magnitude are going to occur. These results motivated

us to see if there was possible to incorporate the asperity concept in our model, and later, if this model was able to describe at least qualitatively a pattern of real seismicity in some seismic region.

5. THE ASPERITY CONCEPT AND THE NON-HOMOGENEOUS MODEL

The asperity concept was first proposed by Byerlee (1970) and further developed by Scholz and Engelder (1976), who suggested that the two sides of a fault are held together by surfaces of high strength called asperities. The stress on the asperities is higher than the average stress on the entire fault plane. We are not going to describe the origin of the stress concentrations, but the fact is that there should be a random distribution of stress concentrations on various regions on the contact zone in a seismic fault. When a slip occurs in an asperity it is accompanied by an increase of stress on stronger asperities. A consequence of this is that when a stronger asperity breaks, an earthquake of great magnitude occurs and the aftershocks occur around the broken surface. Asperity size and stress distribution govern the degree of loading of adjacent asperities when a large asperity fails. Lay and Kanamori (1981) proposed that asperities can be seen as if the fault zone were subdivided into sub-faults of somewhat independent behavior. These sub faults could interact themselves but it would be stress barriers between sub faults, like ridges, submarine canyons, or changes in the strike of the trench that vary the asperities interaction along the fault. Taking as a basis the paragraph at the end of last section, we can define a region (or regions) in the grid that represents the seismic fault; if we assign to it an α value larger than the surrounding zone then we have a region into the grid that could be considered as an asperity. We can define several regions with different sizes and α values (it means different properties of the terrain). As a result we have encountered from the model that the synthetic earthquakes with great magnitude occurs just on the zones with greater α values and sizes. When a synthetic seism is produced, then in certain part of this zone a relaxation occurs, which implies that the next seisms will not occur in the same region, but it is possible that they occur near the region, out of the frontier, because there are sites in this part that were left for the relaxation process very close to the threshold. Thus, if there are aftershocks there is a high probability that they occur just outside the modeled asperity.

If we have a high stressed asperity close to other asperity of the same kind and an earthquake is produced in one of them, then it is also possible that an event in one of them can trigger an event in the other. For example, taking as basis the results reported by Suárez et al. (1990), we defined two asperities with $\alpha = 0.245$ immersed in the network that represents the rest of the fault, $\alpha = 0.13$, but taking into account the geometry of the region.
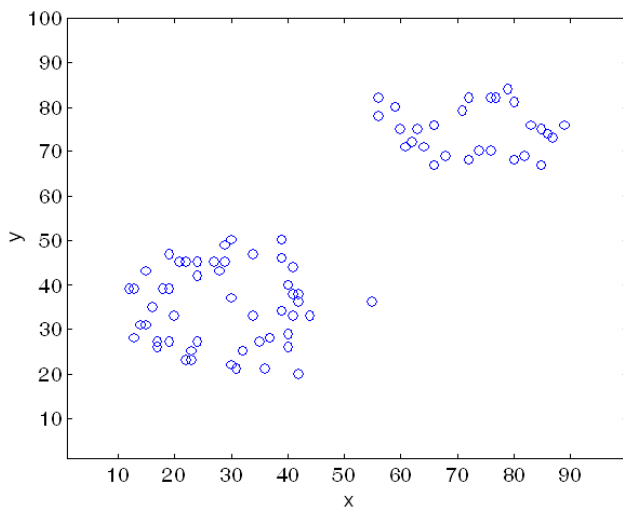
Fig. 8. The earthquake epicenters in a region with two asperities with $\alpha = 0.245$ immersed in the network that represents the rest of the fault, with $\alpha = 0.13$, without micro-seismicity. Taking into account the geometry of the region, we have obtained a seismicity pattern similar to the one observed in the Guerrero, Mexico gap.

As a result we have obtained a seismicity pattern similar to the one observed by Suárez *et al.* (1990) in the Guerrero gap (Fig. 8). They found that the seismicity is concentrated in two parallel regions and between them there is another region with almost no seismicity. We have reproduced qualitatively this pattern and suggested the presence of two great asperities that surround the quiet zone. The type of asperities that we can model should be of the type described by Lay and Kanamori (1981), that observed four fundamental categories of the behavior of stress distribution on the fault plane: (a) The Chile-type regular occurrence of great ruptures of more than 500 km; (b) the Aleutian-type variation in rupture extent with occasional ruptures up to 500 km long, an temporal clustering of large events; (c) the Kurile-type repeated failure over a limited zone of 100-300 km in isolated events and (d) the Marianas-type absence of large earthquakes. It seems that in Mexican seismological zones we have an intermediate case between (b) and (c), that is, there are asperities of several sizes.

6. DISCUSSION

We think that the model is useful to describe the asperities if we imagine than asperities are immersed in the fault, but in a seismological region there are several faults. We have to consider that if most of the large earthquakes occur in preexisting faults, then the long time scale associated with the after-shock sequence, compared with the duration of an individual event, indicates
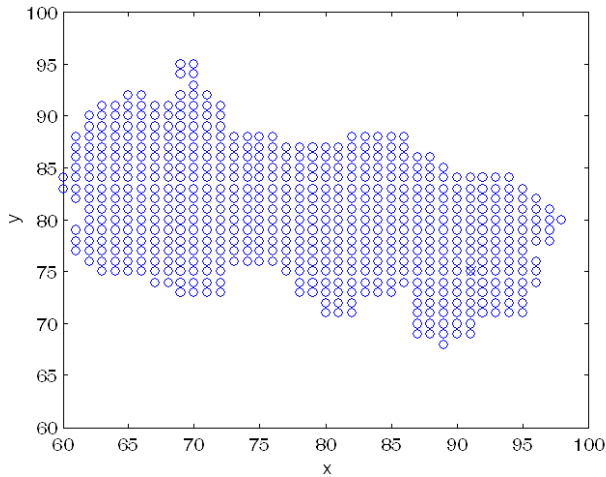
Fig. 9. The propagation of the fracture in a synthetic earthquake, in the case described in Fig. 7a. Although the epicenter is near the central zone, the fracture does not propagate to the central zone; it is confined within the zone with greater α value.

that the coupling between individual faults that make up the network is weak (Lomnitz-Addler 1993). So, the model can be applied to a fault with several sub-regions, and the whole process described is valid when an event occurs.

However, if we want to apply the model as if the different parts of the network were faults, then we must suppose that there are regions that are not faults that separate them. Depending on the properties of these regions we can take them as barriers in the sense proposed by Lay and Kanamori (1981), or we can take them not as barriers, but as zones where the terrain properties are different, in such a way that they do not permit that the fracture could be propagated. For instance, in the situation described for three parallel zones where the intermediate zone has an α value of 0.13 and the others have an α value of 0.235, the earthquakes of great magnitude occur in the lateral regions, the central region has only a micro seismicity, but the most important thing is that if an earthquake of great magnitude occurs in the lateral zones it almost never reaches the central region. It means that the fracture cannot propagate towards this zone (Fig. 9). Although the epicenter was near the central zone, the fracture will not propagate to the central zone, and it will be confined within the zone with a large α value.

It is necessary to stress that there is certain non-homogeneity introduced in the model by the boundary conditions that have been used. Actually, as the boundary conditions are open, the blocks that are at the edge of the network have a different behavior from the other blocks. This is because the frontier blocks only have three or two neighbors. This fact produces a behav-

ior qualitatively similar to the one reported by Corbi *et al*. (2011) for subduction faults. Most of the global seismic energy is released by the slip between the subducting and the overriding plates. Corbi *et al*. reported that the interplate contact is seismogenic only in a specific depth interval, globally comprised between 11 ± 4 and 51 ± 9 km. The cumulative seismic moment is not homogeneously distributed along the seismogenic zone. It shows an approximately Gaussian distribution with a peak around 20-30 km of depth. This is physically reasonable, because the interplate is confined between the surface and the mantle, *i.e*., large earthquakes have no bounds in rupture length, but their down-dip width is limited by thickness of the region capable of generating earthquakes (Pacheco *et al*. 1992).

If we take a grid of 100×100 blocks in the homogeneous OFC model, locate all the synthetic earthquake epicenters, and take bands of width equal to 5 (20 bands). We summed the magnitudes of all the earthquakes that occurred in each of the bands, and obtained that the distribution is not homogeneous. In Figure 10, we have plotted the cumulative rupture surface from the fourth to the sixteenth band. As shown in Fig. 9, a synthetic earthquake magnitude can be quantified by counting the relaxed blocks, and these blocks represent the rupture surface for this earthquake. When we plot the cumulative rupture surface for each strip we get what is shown in Fig. 10, *i.e*., a non homogeneous distribution with a peak situated more or less at the center. We only plotted from the fourth to the sixteenth bands to make the graph more similar to the graphic of Corbi *et al*. (2011)
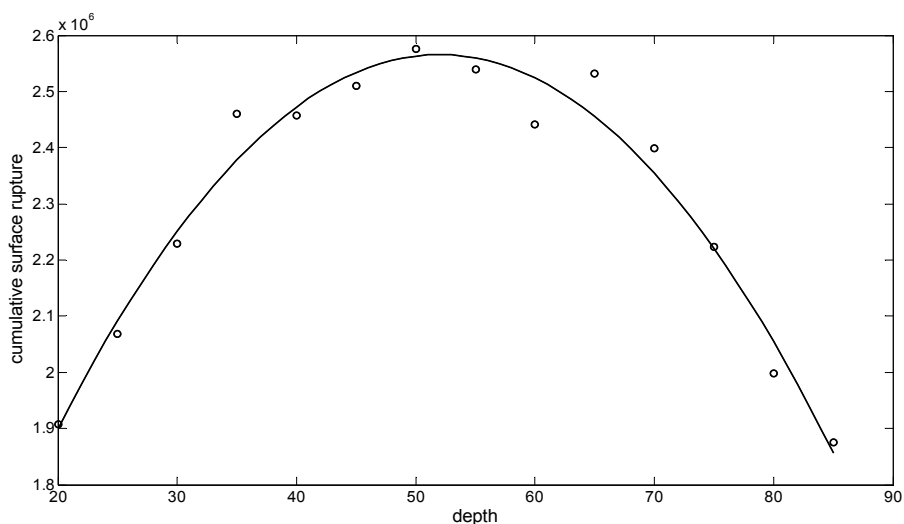

Fig. 10. Cumulative rupture surface from the fourth to the sixteenth band, for a grid of 100×100 blocks in the homogeneous OFC model.

7. CONCLUSIONS

We have shown that if we make subdivisions into the network that represents the seismic fault, with different sizes and values of the elastic parameters, then we still obtain the GR law and the stair shaped plots similar to real seismicity, but the self-organizing process delays more than in the homogenous OFC model, so the stability for the stair-shaped plots also delays. We have found that the slope of the straight line that bounds the stair-shaped plots depends on the lattice linear size N, similar to the homogeneous case, and always with a global maximum slope. The results are similar to the ones obtained with real data, so we think we are in the correct way to have in the future a more appropriate model for a seismic fault based on a spring-block model. This is supported by the fact that the asperity concept can be included into the model through simple α distributions.

References

Angulo-Brown, F., and A. Muñoz-Diosdado (1999), Further seismic properties of a spring-block earthquake model, *Geophys. J. Int.* **139**, 2, 410-418, DOI: 10.1046/j.1365-246x.1999.00946.x.

Bach, M., F. Wissel, and B. Drossel (2008), Olami–Feder–Christensen model with quenched disorder, *Phys. Rev. E* **77**, 067101, DOI: 10.1103/PhysRevE.77.067101.

Bak, P. (1996), *How Nature Works*, Springer, New York.

Bak, P., and C. Tang (1989), Earthquakes as a self-organized critical phenomenon, *J. Geophys. Res.* **94**, B11, 15635-15637, DOI: 10.1029/JB094iB11p15635.

Bak, P., C. Tang, and K. Weisenfeld (1987), Self organized criticality: An explanation of 1/f noise, *Phys. Rev. Lett.* **59**, 381-384, DOI: 10.1103/PhysRevLett.59.381.

Bak, P., C. Tang, and K. Weisenfeld (1988), Self-organized criticality, *Phys. Rev. A* **38**, 1, 364-374, DOI: 10.1103/PhysRevA.38.364.

Barriere, B., and D.L. Turcotte (1994), Seismicity and self-organized criticality, *Phys. Rev. E* **49**, 2, 1151-1160, DOI: 10.1103/PhysRevE.49.1151.

Brown, S.R., C.H. Scholz, and J.B. Rundle (1991), A simplified spring block model of earthquakes, *Geophys. Res. Lett.* **18**, 215-218, DOI: 10.1029/91GL00210.

Burridge, R., and L. Knopoff (1967), Model and theoretical seismicity, *Bull. Seismol. Soc. Am.* **57**, 341-371.

Byerlee, J. D. (1970), Static and kinetic friction under high stress, *Int. J. Rock Mech. Min. Sci.* **7**, 577-582, DOI: 10.1016/0148-9062(70)90018-5.

Carlson, J.M., and J.S. Langer (1989), Mechanical model of an earthquake fault, *Phys. Rev. A* **40**, 6470-6484, DOI: 10.1103/PhysRevA.40.6470.

Caruso, F., and H. Kantz (2011), Prediction of extreme events in the OFC model on a small world network, *Eur. Phys. J. B* **79**, 7-11, DOI: 10.1140/epjb/e2010-10635-5.

Caruso, F., V. Latora, A. Pluchino, A. Rapisarda, and B. Tadic (2006), Olami–Feder–Christensen model in different networks, *Eur. Phys. J. B* **50**, 243-247, DOI: 10.1140/epjb/e2006-00110-5.

Ceva, H. (1995), Influence of defects in a coupled map lattice modeling earthquakes, *Phys. Rev. E* **52**, 1, 154-158, DOI: 10.1103/PhysRevE.52.154.

Christensen, K., and Z. Olami (1992), Scaling, phase transitions, and nonuniversality in a self organized critical cellular automaton model, *Phys. Rev. A* **46**, 1829-1838, DOI: 10.1103/PhysRevA.46.1829.

Corbi, F., F. Funiciello, C. Facenna, G. Ranalli, and A. Heuret (2011), Seismic variability of subduction thrust faults: Insigths from laboratory models, *J. Geophys. Res.* **116**, B06304, DOI: 10.1029/2010JB007993.

Ferguson, C.D., W. Klein, and J.B. Rundle (1999), Long-range earthquake fault models, *Comput. Phys*. **12**, 34-40.

Geller, R.J., D.D. Jackson, Y. Kagan, and F. Mulargia (1997), Earthquakes cannot be predicted, *Science* **275**, 1616-1617, DOI: 10.1126/science.275.5306.1616.

Gutenberg, B., and C.F. Richter (1944), Frequency of earthquakes in California, *Bull. Seismol. Soc. Am*. **34**, 185-188.

Hainzl, S., G. Zöller, and J. Kurths (1999), Similar power laws for foreshock and aftershock sequences in a spring-block model for earthquakes, *J. Geophys. Res.* **104**, B4, 7243-7253, DOI: 10.1029/1998JB900122.

Helmstetter, A., S. Hergarten, and D. Sornette (2004). Properties of foreshocks and aftershocks of the nonconservative self-organized Olami-Feder-Christensen model, *Phys. Rev. E* **70**, 046120, DOI: 10.1103/PhysRevE.70.046120.

Hergarten, S., and H.J. Neugebauer (2002), Foreshocks and aftershocks in the Olami–Feder–Christensen model, *Phys. Rev. Lett.* **88**, 23, 238501, DOI: 10.1103/PhysRevLett.88.238501.

Ito, K., and M. Matsuzaki (1990), Earthquakes as a self organized critical phenomena*, J. Geophys. Res*. **95**, B5, 6853-6860, DOI: 10.1029/JB095iB05p06853.

Kanamori, H. (1981), The nature of seismicity patterns before large earthquakes. **In**: D.W. Simpson, and P.G. Richard (eds.), *Earthquake Prediction, an International Review*, American Geophysical Union, Washington D.C., 1-19.

Kawamura, H., T. Yamamoto, T. Kotani, and H. Yoshino (2010), Asperity characteristics of the Olami–Feder–Christensen model of earthquakes, *Phys. Rev. E* **81**, 0311119, DOI: 10.1103/PhysRevE.81.031119.

Kotani, T., H. Yoshino, and H. Kawamura (2008), Periodicity and criticality in the Olami–Feder–Christensen model of earthquakes, *Phys. Rev. E* **77**, R010102, DOI: 10.1103/PhysRevE.77.010102.

Lay, T., and H. Kanamori (1981), An asperity model of large earthquake sequences. **In**: D.W. Simpson, and P.G. Richard (eds.), *Earthquake Prediction, an*

International Review, American Geophysical Union, Washington D.C., 579-592.

Lomnitz-Addler, J. (1993), Automaton models of seismic fracture: Constraints imposed by the magnitude-frequency relation, *J. Geophys. Res*. **98**, B10, 17745-17756, DOI: 10.1029/93JB01390.

Main, I.G., and M. Naylor (2009), Entropy production and self-organized (sub)criticality in earthquake dynamics, *Philos. Trans. Roy. Soc. A* **368**, 131-144, DOI: 10.1098/rsta.2009.0206.

Muñoz-Diosdado, A., and F. Angulo-Brown (1999), Patterns of synthetic seismicity and recurrence times in a spring-block earthquake model, *Rev. Mex. Fís*. **45**, 4, 393-400.

Nakanishi, H. (1990), Cellular automaton model of earthquakes with deterministic dynamics, *Phys. Rev. A* **41**, 7086-7089, DOI: 10.1103/PhysRevA.41.7086.

Naylor, M., and I.G. Main (2008), Cell scale self-organization in the OFC model for earthquake dynamics, *Eur. Phys. J. B* **64**, 139-146, DOI: 10.1140/epjb/e2008-00279-5.

Olami, Z., H.J.S. Feder, and K. Christensen (1992), Self organized criticality in a continuous, nonconservative cellular automaton model, *Phys. Rev. Lett*. **68**, 1244-1247, DOI: 10.1103/PhysRevLett.68.1244.

Pacheco, J.F., C.H. Scholz, and L.R. Sykes (1992), Changes in frequency size relationship from small to large earthquakes, *Nature* **355**, 71-73, DOI: 10.1038/355071a0.

Rudolf-Navarro, A.H., A. Muñoz-Diosdado, and F. Angulo-Brown (2010), Seismic quiescence patterns as possible precursors of great earthquakes in Mexico, *Int. J. Phys. Sci*. **5**, 6, 651-670.

Ruff, L.R. (1992), Asperity distributions and large earthquake occurrence in subduction zones, *Tectonophysics* **211**, 61-83, DOI: 10.1016/0040-1951(92)90051-7.

Scholz, C.H., and J.T. Engelder (1976), The role of asperity indentation and ploughing in rock friction, I. Asperity creep and stick slip, *Int. J. Rock Mech. Min. Sci*. **13**, 149-154, DOI: 10.1016/0148-9062(76)90819-6.

Suárez, G., T. Monfret, G. Wittlinger, and C. David (1990), Geometry of subduction and depth of the seismogenic zone in the Guerrero gap, Mexico, *Nature* **345**, 336-338, DOI: 10.1038/345336a0.

Turcotte, D.L. (1997), *Fractals and Chaos in Geology and Geophysics*, Cambridge University Press, Cambridge.

Yamamoto, T., H. Yoshino, and H. Kawamura (2010), Simulation study of the inhomogeneous Olami–Feder–Christensen model of earthquakes, *Eur. Phys. J. B* **77**, 559-564, DOI: 10.1140/epjb/e2010-10503-4.

A Non-Extensive Statistical Physics View to the Spatiotemporal Properties of the June 1995, Aigion Earthquake (M6.2) Aftershock Sequence (West Corinth Rift, Greece)

Filippos VALLIANATOS[1,2], Giorgos MICHAS[1], Giorgos PAPADAKIS[1], and Peter SAMMONDS[1]

[1]Earth Sciences Department, University College London, London, United Kingdom
e-mail: georgios.michas.10@ucl.ac.uk (corresponding author)

[2]Technological Educational Institute of Crete,
Laboratory of Geophysics and Seismology, Crete, Greece

A b s t r a c t

In the present study, the spatiotemporal properties of the Aigion earthquake (15 June 1995) aftershock sequence are being studied using the concept of non-extensive statistical physics (NESP). The cumulative distribution functions of the inter-event times and the inter-event distances are being estimated for the data set which is assumed to be complete and the analysis yielded the thermodynamic q parameter to be $q_T = 1.58$ and $q_r = 0.53$ for the two distributions, respectively. The results fit rather well to the inter-event distances and times distributions, implying the complexity of the spatiotemporal properties of seismicity and the usefulness of NESP in investigating such phenomena. The temporal structure is also being discussed using the complementary to NESP approach of superstatistics, which is based on a superposition of ordinary local equilibrium statistical mechanics. The result indicates that very low degrees of freedom describe the temporal evolution of the Aigion earthquake aftershock seismicity.

Key words: aftershock sequences, complexity, non-extensive statistical physics, Aigion earthquake, Gulf of Corinth rift.

1. INTRODUCTION

On 15 June 1995 at 00:15 GMT, a strong earthquake, of magnitude 6.2 (Bernard *et al.* 1997), occurred at the western part of the Gulf of Corinth (Greece). The earthquake was located at 38.37°N, 22.15°E, at about 12 km to the NNE of the city of Aigion, where 26 people were killed and many buildings suffered severe damages. The Gulf of Corinth region has long now been recognized as one of the most seismotectonically active areas in Europe (Ambraseys and Jackson 1990), with an important continental N-S extension of about 13 mm/yr, and 6 mm/yr at the west and east part, respectively (Clarke *et al.* 1997).

The evolution of such tectonically active regions is expressed through seismicity and is characterized by complex phenomenology. However, some simple empirical relationships are valid, such as the Omori law (Omori 1894) that describes the temporal distribution of aftershocks, $n(t) = K/(t + c)^p$, and the Gutenberg–Richter law (Gutenberg and Richter 1944) for the relationship between the frequency and magnitude of earthquakes, $\log N(M) = a - bM$, exhibiting the scale-free nature of seismicity. Non-extensive statistical physics (NESP) (Tsallis 1988, 2009), which is a generalization of Boltzmann–Gibbs statistical physics, seems a suitable framework for studying complex systems exhibiting scale-free nature. Using this concept, Abe and Suzuki (2003, 2005) investigated the spatial and temporal properties of the seismicity in California and Japan and more recently Darooneh and Dadashinia (2008) in Iran. In these studies, the inter-event times and distances distributions between successive earthquakes are nicely fitted by a *q*-exponential distribution.

The question whether earthquake aftershocks are described by non-extensive statistical physics, even at the phenomenological level (*i.e.*, without specifying any underlying model), represents a challenge. This is the problem we address here. Our aim is not to develop a precise model, but rather to present a simple argument of physical plausibility.

Recent applications to solid earth physics (in regional or planetary scale) summarized by Tsallis (2009), mainly focused in seismology (Telesca 2010a, b; 2011) using earthquake catalogs from different seismic zones, fault lengths distribution (Vallianatos *et al.* 2011a, Vallianatos and Sammonds 2011) and very recently to natural hazards (Vallianatos 2009), plate tectonics (Vallianatos and Sammonds 2010), rock physics (Vallianatos *et al.* 2011b), and geomagnetic reversals (Vallianatos 2011).

In the present study, we use the concept of non-extensive statistical physics (NESP) (Tsallis 1988, 2009) to analyze the temporal and spatial properties of the Aigion earthquake aftershock sequence. The temporal occurrence of the aftershock sequence is also being discussed using the complementary

to NESP approach of superstatistics, which is based on a superposition of ordinary local equilibrium statistical mechanics, using a suitable intensive parameter β that fluctuates on a relatively large temporal scale.

2. NON EXTENSIVE STATISTICAL PHYSICS

A monument of contemporary physics is Boltzmann–Gibbs statistical mechanics which is a link between the mechanical microscopic laws and classical thermodynamics. Since Boltzmann, many entropic forms have been introduced and in 1988 (Tsallis 1988, 2009) a more general form was proposed, known as non-extensive statistical mechanics:

$$S_q = k_B \frac{1 - \sum_{i=1}^{W} p_i^q}{q-1}, \quad q \in R, \tag{1}$$

where k_B is Boltzmann's constant, p_i^q is a set of probabilities, and W is the total number of microscopic configurations. For the particular case where $q = 1$ then $S_1 = S_{BG}$, we obtain the Boltzmann–Gibbs (BG) entropy:

$$S_{BG} = -k_B \sum_{i=1}^{W} p_i \ln p_i. \tag{2}$$

Although Tsallis entropy shares a lot of common properties with the Boltzmann–Gibbs entropy, S_{BG} is additive, whereas S_q ($q \neq 1$) is nonadditive.

For any two probabilistically independent systems, A and B, the Tsallis entropy satisfies:

$$\frac{S_q(A+B)}{k} = \frac{S_q(A)}{k} + \frac{S_q(B)}{k} + (1-q)\frac{S_q(A)}{k}\frac{S_q(B)}{k}. \tag{3}$$

The origin of non-extensivity comes from the last term on the right-hand side of this equation. We can see that $q < 1$, $q = 1$, and $q > 1$, correspond to superadditivity, additivity, and subadditivity, respectively. This is the fundamental principle for non-extensive statistical mechanics.

If X is a physical parameter that describes the system, then the probability distribution of X is obtained by the maximization of the entropy under appropriate constraints (Tsallis *et al.* 1998, Lyra and Tsallis 1998, Tsallis 1999) with the Lagrange multipliers method. Applying the normalization constraint $\int_0^\infty p(X)\,\mathrm{d}X = 1$ and introducing a generalized expectation value X_q defined as

$$X_q = \langle X \rangle_q = \int_0^\infty X P_q(X)\,\mathrm{d}X,$$

where

$$P_q(X) = \frac{p^q(X)}{\int\limits_0^\infty p^q(X)\,\mathrm{d}X}$$

is the escort probability (Tsallis 2009), we optimize the non-extensive entropy requiring $\vartheta S_q^* = 0$ for the functional

$$S_q^* = S_q - a\int\limits_0^\infty p(X)\,\mathrm{d}X - \beta^* X_q \ ,$$

where α and β^* represent the Lagrange multipliers. Thus we obtain the physical probability:

$$p(X) = \frac{\left[1-(1-q)BX\right]^{1/1-q}}{Z_q} = \frac{\exp_q(-BX)}{Z_q} \ , \tag{4}$$

where the q-exponential function is defined as

$$e_q(x) = \left[1+(1-q)x\right]^{1/(1-q)} \quad \text{for} \quad 1+(1-q)x \geq 0 \ ,$$

and

$$e_q(x) = 0 \quad \text{for} \quad 1+(1-q)x < 0 \ . \tag{5}$$

Z_q is the q partition function

$$Z_q = \int\limits_0^\infty \exp_q(-BX)\,\mathrm{d}X \ ,$$

where

$$B = \frac{\beta^*}{C_q + (1-q)\beta^* X_q} \quad \text{and} \quad C_q = \int\limits_0^\infty P_q(X)\,\mathrm{d}X \ .$$

The obtained probability function will be used in order to calculate the cumulative distribution function and to compare the theoretical formulation with the distribution of inter-event times and distances.

3. AIGION AFTERSHOCK SEQUENCE ANALYSIS

Suppose that the inter-event time T is the time between two successive earthquakes defined as $T = T(i+1) - T(i)$ and the inter-event distance r is the three-dimensional Euclidean distance between the successive earthquakes defined as $r = \|r(i+1) - r(i)\|$. The concept of NESP previously described, is in this section applied to the inter-event times and distances distributions of the Aigion earthquake aftershock sequence.

The data set analyzed in this study is taken from the catalogs of the Geodynamic Institute of the National Observatory of Athens (http://www.gein.
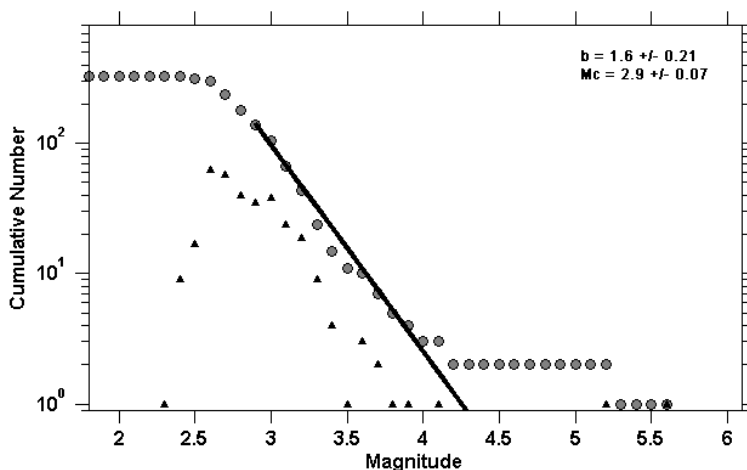
Fig. 1. The cumulative (circles) and non-cumulative (triangles) distribution function on logarithmic scale for the magnitude range of the Aigion aftershock sequence. The maximum likelihood fit of the Gutemberg–Richter law gives a *b* value of 1.6 ± 0.21. The magnitude of completeness, *Mc*, according to EMR method is 2.9 ± 0.07, M_L.

noa.gr/). We used the aftershocks detected at the first 17 days after the main shock. The aftershocks selected from the catalog define an active zone of about 60 km E-W and 40 km N-S. The application of the Gutenberg–Richter law according to the maximum likelihood technique (Aki 1965) gives a *b* value of 1.6 ± 0.21 (Fig. 1). The magnitude of completeness, *Mc*, of our data set, according to the entire-magnitude-range (EMR) method (Woessner and Wiemer 2005), is 2.9, M_L (Fig. 1). The uncertainty of *Mc* can be estimated using the bootstrap method (*e.g.*, Chernick 1999, Woessner and Wiemer 2005) and in our case is for *Mc* 2.9 ± 0.07. We have also applied the modified Omori law $n(t) = K/(t + c)^p$ (*e.g.*, Utsu *et al.* 1995) to our data set for the events equal or greater than the threshold magnitude of 3, according to our previous calculation of *Mc*. The maximum likelihood estimation (Ogata 1983) gives a *p* value of 1.7 and implies the fast decay rate of the aftershock sequence, with the energy being released mainly during the main shock and the first big aftershock of magnitude 5.2, M_L.

An important point to non-extensive analysis is that the quantity to be compared with the observed distribution is the associated escort distribution (Tsallis 2009, Abe and Suzuki 2003, 2005). Following the latter approach, the cumulative distribution function is given by the expression

$$P(> X) = \int_0^\infty P_q(X)\,\mathrm{d}X \ ,$$

where

$$P_q(X) = \frac{p^q(X)}{\int_0^\infty p^q(X)\,\mathrm{d}X} \quad,$$

and combining with the probability function $p(X)$ given in Eq. (4) we obtain $P(>X) = \exp_q(-BX)$. The latter implies that after the estimation of the appropriate q that describes the observed distributions $P(>T)$ and $P(>r)$, the q-logarithmic functions $\ln_q(P(>T))$ and $\ln_q(P(>r))$ expressed as

$$\ln_q(x) = \frac{1}{1-q}\left(x^{1-q} - 1\right) ,$$

are linear with T and r, respectively (Vallianatos 2011 and references therein).

Following the latter approach, the analysis of the inter-event distances distribution indicates a value of $q_r = 0.53$ for the data set with magnitudes equal or greater than the threshold magnitude $Mc = 3$. The semi-q-log plot of the cumulative distribution for the inter-event distances with $q_r = 0.53$ is presented in Fig. 2. The straight line is the q-logarithmic function given by the model described earlier.

The same analysis for the inter-event times distribution gives a value of $q_T = 1.58$ for the dataset with magnitudes equal or greater of the threshold magnitude $Mc = 3$. The semi-q-log plot of the cumulative distribution of the inter-event times with $q_T = 1.58$ is presented in Fig. 3. The q-logarithmic
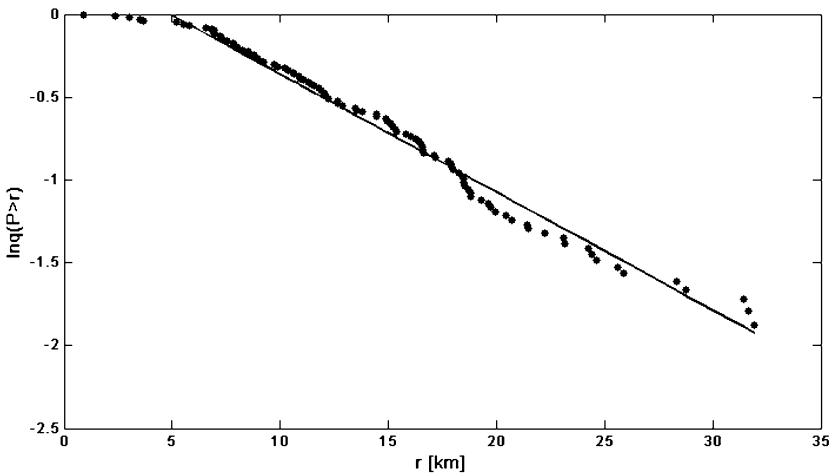

Fig. 2. The semi-q-log plot of the cumulative distribution of the inter-event distances for the dataset with magnitudes equal or greater than the threshold magnitude $Mc = 3$. The straight line represents the q-logarithmic function. The value of q_r for the best fit regression is $q_r = 0.53$ with a correlation coefficient $\rho = -0.9896$.
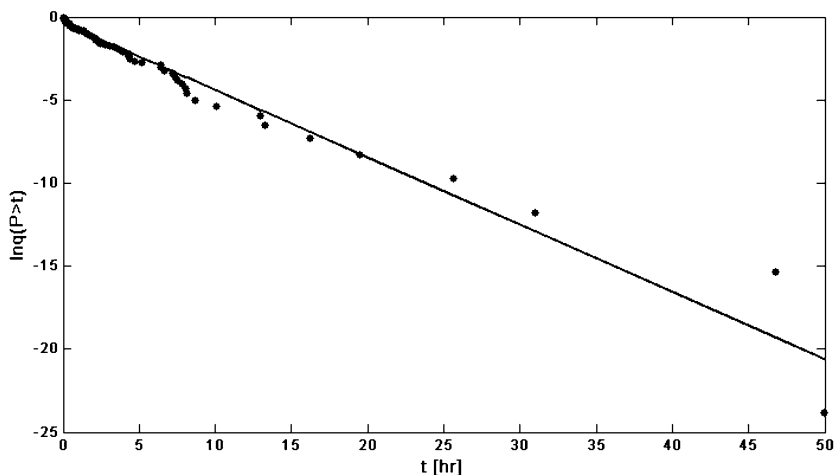
Fig. 3. The semi-*q*-log plot of the cumulative distribution for the inter-event times for the data set with magnitudes equal or greater than the threshold magnitude of 3. The straight line represents the *q*-logarithmic function. The value of q_T for the best fit regression is $q_T = 1.58$ with a correlation coefficient $\rho = -0.9836$.

function is symbolized with the straight line. In both cases the model describes well the observed distributions of *T* and *r* for the data set which is assumed to exhibit magnitude completeness.

We have also checked the sensitivity of the computed *q* value to the data set used each time. For this purpose we have randomly removed several times the 10% of the data set used to perform the non-extensive analysis described earlier. Indeed, the q_T value exhibits sensitiveness to the data set used each time, with results taking values from 1.44 to 1.63.

4.   A SUPERSTATISTICAL VIEW
TO THE AIGION AFTERSHOCK SEQUENCE

Considering a class of generalized statistics, which are called "superstatistics", we have a complementary approach to understand the dynamical reason of non-extensive statistical mechanics (Beck and Cohen 2003, Beck 2009). Tsallis statistics is a special case of these superstatistics. There is an intensive parameter *β* of the complex system that fluctuates on a relatively large spatio-temporal scale. Theoretical developments of the superstatistics concept includes many complex systems, such as the atmospheric turbulence, the cosmic ray statistics and hydroclimatic fluctuations (Beck 2009).

Recently a superstatistical model has been applied to the recurrence of the geomagnetic reversals (Vallianatos 2011). In order to have a superstatistical approach to Aigion inter-event times we follow the latter approach, assuming a simple model where the local distribution is given by that of

a Poisson process $p(T\,|\,\beta) = \beta e^{-\beta T}$ (Beck 2009). The expression $p(T\,|\,\beta)$ denotes the conditional probability density to observe the inter-event time T when the parameter β has a certain given value. This exponential model becomes superstatistical by making the parameter β a fluctuating random variable as well. If β is distributed with probability density $f(\beta)$ and fluctuates on a large time scale, then we can obtain the marginal distributions of inter-event times as:

$$p(T) = \int_0^\infty f(\beta)\,p(T\,|\,\beta)\,\mathrm{d}\beta = \int_0^\infty f(\beta)\,\beta e^{-\beta T}\,\mathrm{d}\beta \;. \tag{7}$$

Constructing a simple model for the distribution of $f(\beta)$, there may be n different Gaussian random variables X_i, $i = 1, \ldots, n$, that influence the dynamics of the positive random variable β in an additive way (Beck 2009). We can also assume a simple model that $\beta = \sum_{i=1}^n X_i^2$, where $\langle X_i \rangle = 0$ and $\langle X_i^2 \rangle \neq 0$. In this case, the probability density of β is given by a χ^2 – distribution with n degrees of freedom:

$$f(\beta) = \frac{1}{\Gamma(n/2)}\left(\frac{n}{2\beta_0}\right)^{n/2} \beta^{\frac{n}{2}-1}\exp\left(-\frac{n\beta}{2\beta_0}\right)\;.$$

The average of β is given by $\langle\beta\rangle = n\langle X_i^2\rangle = \int_0^\infty \beta f(\beta)\,\mathrm{d}\beta = \beta_0$ and the variance by $\langle\beta\rangle^2 - \beta_0^2 = (2/n)\beta_0^2$. The integral (7) is easily evaluated (Beck 2009) and one obtains $p(T) \approx C\left(1 + B(q-1)T\right)^{1/(1-q)}$, which is exactly the result obtained in the frame of non-extensive statistical physics, where $q = 1 + 2/(n+2)$ and $B = 2\beta_0/(2-q)$.

From the latter we can calculate the degrees of freedom that are influencing the value of β by $n = \left(2/(q-1)\right) - 2$. Using the q_T value of the inter-event times calculated earlier from our q-statistics fit and taking into consideration the fluctuation of q_T due to its sensitiveness to the data set used each time, we can see that very low degrees of freedom describe the temporal evolution of the Aigion earthquake aftershock seismicity.

5.   CONCLUSIONS

In the present study, the spatiotemporal properties of the Aigion earthquake aftershock sequence have been investigated using the concept of non-extensive statistical physics. The b value of the Gutenberg–Richter law is estimated as 1.6 ± 0.21, while the maximum likelihood estimation of the p value of the modified Omori law gave a value of $p = 1.7$, implying the fast

decay rate of the aftershock sequence, with the energy being released mainly during the main shock and the first big aftershock. The threshold magnitude above which the catalog is assumed to be complete has been estimated according to the EMR method, taking also in account its uncertainty, as 3, M_L. The NESP approach to the inter-event times distribution of the Aigion aftershock sequence leads to a non-extensive thermodynamic parameter $q_T = 1.58$ for the dataset equal or greater than the threshold magnitude. For the same data set, the NESP approach to the inter-event distances distribution gave a q value of $q_r = 0.53$. The model used fits rather well to the observed distributions, implying the complexity of the spatiotemporal properties of seismicity and the usefulness of NESP in investigating such phenomena, exhibiting scale-free nature and long-range memory effects.

We have also checked the sensitiveness of the calculated q value to the data set by randomly removing each time the 10% of the data. The q_T value exhibited dependence to the data set used each time with fluctuating values, pointing that the completeness of the catalog that we use to evaluate the non-extensive thermodynamic parameter can affect the final results. Another interesting feature is that the sum of q_T and q_r is approximately equal to 2, indicating non-extensive statistical physics duality, as has been also pointed out by Abe and Suzuki (2003) and Darooneh and Dadashinia (2008).

Finally, we used the complementary to NESP approach of superstatistics, which is based on a superposition of ordinary local equilibrium statistical mechanics, using a suitable intensive parameter β that fluctuates as χ^2 distribution on a relatively large temporal scale. The superstatistical approach leads us to the conclusion that very low degrees of freedom describe the temporal evolution of the Aigion earthquake aftershock sequence.

References

Abe, S., and N. Suzuki (2003), Law for the distance between successive earthquakes, *J. Geophys. Res.* **108**, B2, 2113, DOI: 10.1029/2002JB002220.

Abe, S., and N. Suzuki (2005), Scale-free statistics of time interval between successive earthquakes, *Physica A* **350**, 2-4, 588-596, DOI: 10.1016/j.physa.2004.10.040.

Aki, K. (1965), Maximum likelihood estimate of b in the formula log N = a – bM and its confidence limits, *Bull. Earthq. Res. Inst. Tokyo Univ*. **43**, 2, 237-239.

Ambraseys, N.N., and J.A. Jackson (1990), Seismicity and associated strain of central Greece between 1890 and 1988, *Geophys. J. Int*. **101**, 3, 663-708, DOI: 10.1111/j.1365-246X.1990.tb05577.x.

Beck, C. (2009), Recent developments in superstatistics, *Brazilian J. Physics* **39**, 2A, 357-363, DOI: 10.1590/S0103-97332009000400003.

Beck, C., and E.G.D. Cohen (2003), Superstatistics, *Physica A* **322**, 267-275, DOI: 10.1016/S0378-4371(03)00019-0.

Bernard, P., P. Briole, B. Meyer, H. Lyon-Caen, J.-M. Gomez, C. Tiberi, C. Berge, R. Cattin, D. Hatzfeld, C. Lachet, B. Lebrun, A. Deschamps, F. Courboulex, C. Larroque, A. Rigo, D. Massonnet, P. Papadimitriou, J. Kassaras, D. Diagourtas, K. Makropoulos, G. Veis, E. Papazisi, C. Mitsakaki, V. Karakostas, E. Papadimitriou, D. Papanastassiou, M. Chouliaras, and G. Stavrakakis (1997), The $M_s = 6.2$, June 15, 1995 Aigion earthquake (Greece): evidence for low angle normal faulting in the Corinth rift, *J. Seismol*. **1**, 2, 131-150, DOI: 10.1023/A:1009795618839.

Chernick, M.R. (1999), *Bootstrap Methods: A Practitioner's Guide*,Wiley Series in Probability and Statistics, W.A. Shewhart (ed.), Wiley and Sons Inc., New York, 288 pp.

Clarke, P.J., R.R. Davies, P.C. England, B.E. Parsons, H. Billiris, D. Paradissis, G. Veis, P.H. Denys, P.A. Cross, V. Ashkenazi, and R. Bingley (1997), Geodetic estimate of seismic hazard in the Gulf of Korinthos, *Geophys. Res. Lett*. **24**, 11, 1303-1306, DOI: 10.1029/97GL01042.

Darooneh, A.H., and C. Dadashinia (2008), Analysis of the spatial and temporal distributions between successive earthquakes: Nonextensive statistical mechanics viewpoint, *Physica A* **387**, 14, 3647-3654, DOI: 10.1016/j.physa.2008.02.050.

Gutenberg, B., and C.F. Richter (1944), Frequency of earthquakes in California, *Bull. Seismol. Soc. Am*. **34**, 4, 185-188.

Lyra, M.L., and C. Tsallis (1998), Nonextensivity and multifractality in low-dimensional dissipative systems, *Phys. Rev. Lett*. **80**, 1, 53-56, DOI: 10.1103/PhysRevLett.80.53.

Ogata, Y. (1983), Estimation of the parameters in the modified Omori formula for aftershock frequencies by the maximum likelihood procedure, *J. Phys. Earth* **31**, 2, 115-124, DOI: 10.4294/jpe1952.31.115.

Omori, F. (1894), On the aftershocks of earthquakes, *J. Coll. Sci. Imp. Univ. Tokyo* **7**, 111-200.

Telesca, L. (2010a), A non-extensive approach in investigating the seismicity of L'Aquila area (central Italy), struck by the 6 April 2009 earthquake ($M_L = 5.8$), *Terra Nova* **22**, 2, 87-93, DOI: 10.1111/j.1365-3121.2009.00920.x.

Telesca, L. (2010b), Analysis of Italian seismicity by using a nonextensive approach, *Tectonophysics* **494**, 155-162, DOI: 10.1016/j.tecto.2010.09.012.

Telesca, L. (2011), Tsallis-based nonextensive analysis of the Southern California seismicity, *Entropy* **13**, 7, 1267-1280, DOI: 10.3390/e13071267.

Tsallis, C. (1988), Possible generalization of Boltzmann–Gibbs statistics, *J. Stat. Phys*. **52**, 1-2, 479-487, DOI: 10.1007/BF01016429.

Tsallis, C. (1999), Nonextensive statistics: theoretical, experimental and computational evidences and connections, *Braz. J. Phys*. **29**, 1, 1-35, DOI: 10.1590/S0103-97331999000100002.

Tsallis, C. (2009), *Introduction to Nonextensive Statistical Mechanics: Approaching a Complex World*, Springer, New York, DOI: 10.1007/978-0-387-85359-8.

Tsallis, C., R.S. Mendes, and A.R. Plastino (1998), The role of constraints within generalized nonextensive statistics, *Physica A* **261**, 3-4, 534-554, DOI: 10.1016/S0378-4371(98)00437-3.

Utsu, T., Y. Ogata, and R.S. Matsura (1995), The centenary of the Omori formula for a decay law of aftershock activity, *J. Phys. Earth* **43**, 1, 1-33, DOI: 10.4294/jpe1952.43.1.

Vallianatos, F. (2009), A non-extensive approach to risk assessment, *Nat. Hazards Earth Syst. Sci.* **9**, 1, 211-216, DOI: 10.5194/nhess-9-211-2009.

Vallianatos, F. (2011), A non-extensive statistical physics approach to the polarity reversals of the geomagnetic field, *Physica A* **390**, 10, 1773-1778, DOI: 10.1016/j.physa.2010.12.040.

Vallianatos, F., and P. Sammonds (2010), Is plate tectonics a case of non-extensive thermodynamics?, *Physica A* **389**, 21, 4989-4993, DOI: 10.1016/j.physa.2010.06.056.

Vallianatos, F., and P. Sammonds (2011), A non-extensive statistics of the fault-population at the Valles Marineris extensional province, Mars, *Tectonophysics* **509**, 1-2, 50-54, DOI: 10.1016/j.tecto.2011.06.001.

Vallianatos, F., E. Kokinou, and P. Sammonds (2011a), Non-extensive statistical physics approach to fault population distribution. A case study from the Southern Hellenic Arc (Central Crete), *Acta Geophys*. **59**, 4, 770-784, DOI: 10.2478/s11600-011-0015-3.

Vallianatos, F., D. Triantis, and P. Sammonds (2011b), Non-extensivity of the isothermal depolarization relaxation currents in uniaxial compressed rocks, *EPL* **94**, 6, 68008, DOI: 10.1209/0295-5075/94/68008.

Woessner, J., and S. Wiemer (2005), Assessing the quality of earthquake catalogues: Estimating the magnitude of completeness and its uncertainty, *Bull. Seismol. Soc. Am*. **95**, 2, 684-698, DOI: 10.1785/0120040007.

Ergodicity Examined
by the Thirumalai–Mountain Metric
for Taiwanese Seismicity

Hsien-Chi LI and Chien-Chih CHEN

Department of Earth Sciences and Institute of Geophysics,
National Central University, Jhongli, Taiwan
e-mail: chencc@earth.ncu.edu.tw (corresponding author)

A b s t r a c t

Ergodicity is a behavior generally limited to equilibrium states and is here defined as the equivalence of ensemble and temporal averages. In recent years, effective ergodicity is identified in simulated earthquakes generated by numerical fault models and in real seismicity of natural fault networks by using the Thirumalai–Mountain metric. Although the effective ergodicity is already reported for Taiwanese seismicity, an immediate doubt is the unrealistic gridded sizes for discretizing the seismic data. In this study, we re-examined the effective ergodicity in Taiwanese seismicity by using reasonable gridded sizes which corresponded with the location errors in the real earthquake catalogue. Initial time and magnitude cut-off were examined for the validity of ergodic behavior. We found that several subsets extracted from Taiwanese seismicity possessed effectively ergodic intervals and all terminations of these ergodic intervals temporally coincided with the occurrences of large earthquakes ($M_L < 6.5$). We thus confirm the ergodicity in the crustal seismicity by using the Thirumalai–Mountain metric.

Key-words: ergodicity, Thirumalai–Mountain metric, seismicity, Taiwan.

1. INTRODUCTION

Ergodicity is a behavior generally limited to equilibrium states in physical systems. Although the definition of ergodicity varies with the contents studied, we here define the ergodicity as the equivalence of ensemble and temporal averages. A necessary condition of ergodicity is thus the statistical stationarity for a physical system. Practically, if the actual measurement time is finite but long enough, most of the accessible phase space for the system will be equally likely sampled; thus, the system is **effectively ergodic**. The Thirumalai–Mountain (TM) metric, which is usually used in material science, is originally developed to examine the time scale to obtain ergodicity in numerical models of liquids, supercooled liquids, glasses and so forth (Thirumalai *et al.* 1989). The TM metric, $\Omega_e(t)$, which is related to the time-averaged energy of individual sites, is used to measure the effective ergodicity by calculating the difference between the temporal average of a specific quantity at each site and its ensemble average over the entire system. Once the system is identified as effectively ergodic over an interval, the spatial statistics of the system maintain stationarity. Furthermore, a dynamical scaling law of $\Omega_e(t)$ then furthermore characterizes the behavior of effective ergodicity.

In recent years, earthquake fault networks are viewed as a subset of natural nonlinear, driven threshold systems (Scholz 1990, Rundle and Klein 1995, Fisher *et al.* 1997). Other examples of such systems include neural networks (Hertz *et al.* 1991, Herz and Hopfield 1995), depinning transitions in charge-density waves and superconductors (Fisher 1985), magnetized domains in ferromagnets (Urbach *et al.* 1995), sand-piles (Bak *et al.* 1987), and foams (Gopal and Durian 1995). For seismic fault networks, effective ergodicity is first identified while the TM metric is applied to analyze the simulated seismicity generated by numerical fault models with nonlinear parameters (Ferguson *et al.* 1999, Klein *et al.* 1997). In the scenario developed from the analyses of fault models, small to moderate earthquakes are treated as fluctuations of a system in thermal equilibrium. On the other hand, occurrence of large earthquakes drives the system out of existing equilibrium state and results in the destruction of ergodicity (Chen *et al.* 2008, Lee *et al.* 2008). The effective ergodicity in natural seismic catalogues has already been reported in several regions with different tectonics, such as California, eastern Canada, Spain, and Taiwan (Tiampo *et al.* 2003, 2007, 2010). All of the fault systems display punctuated ergodic behaviors in several intervals while various combinations of magnitude cut-off and spatial gridding are used in Tiampo *et al.* (2003, 2007, 2010).

Although the effective ergodicity has already been reported for Taiwanese seismicity by Tiampo *et al.* (2010), an immediate doubt is the unrealistic

application of gridded size for discretizing the seismic data. For example, the side length of two-dimensional planar box is 0.02° and the depth discretization of three-dimensional rectangular box is even as small as 0.25 km in Tiampo *et al.* (2010). Obviously, these length scales are unrealistically small considering the location quality in real earthquake catalogue like Taiwanese Central Weather Bureau Seismometer Network (TCWBSN). We wonder if unrealistic small discretization could induce an artificial ergodicity as identified in the early study due to the noises of earthquake location.

In Tiampo *et al.* (2010), the data used is 1973-2009 and the authors are forced to apply too small gridding box to search for possible effective ergodicity. However, we find that once the earlier data is excluded, effective ergodicity exists using various, statistical reasonable, grid sizes. The influence about catalogue quality is never evaluated in detail in previous researches about effective ergodicity of natural catalogues. Our research shows crucial influence of heterogeneity in the CWBSN catalogue on effective ergodicity evaluated by TM metric. In this paper we adopt statistically reasonable gridded sizes, all of which corresponded to the tolerance of seismic location quality, instead of unrealistic applications in previous research to search for possible effectively ergodic behaviors in the Taiwanese seismicity. Initial time and magnitude cut-off are chosen to define various subsets of the TCWBSN catalogue. Each subset of earthquake data is divided spatiotemporally and then utilized to calculate the TM metric. We examine whether effective ergodicity exists in these subsets by evaluating their TM metrics. We find that several subsets of TCWBSN catalogue possess effectively ergodic intervals indeed. Furthermore, all terminations of identified ergodic intervals are temporally related to the occurrences of large earthquake. The existence of effective ergodicity in Taiwanese seismicity reveals the possibility of applying forecasting algorithms based on statistical stationary of seismicity (*e.g.*, Chen *et al.* 2005, 2006). For example, correct seismic anomalies evaluated by pattern informatics (PI) crucially depend on stationary spatial variance of long-term average seismic rate (Rundle *et al.* 2002, Tiampo *et al.* 2002). The determination of effective ergodicity can provide crucial parameters to decompose seismic data into many segments having statistical stationarity.

2. SEISMICITY DATA

The primary seismicity dataset for Taiwan and nearby islands used in this study is the earthquake catalogue released from the Central Weather Bureau, Taiwan. The seismic history of instrumental observation was initiated in 1896, when the Japanese government set up the first seismometer in Taipei. By 1941 there were a total of fourteen seismometers installed on the Taiwan

Island. This seismic observation network was then furthermore upgraded to the electromagnetic instruments by the Taiwanese Central Weather Bureau (CWB). At the same time, the coverage of seismic network was also improved by establishing more observation stations. A seismology group (the predecessor of the Institute of Earth Sciences) based on the Academia Sinica, Taipei, Taiwan, began to set up the first modern telemetered monitoring network in 1972. That telemetered seismic network with twenty five stations significantly improved the location precision of hypocenters and the detection ability for small earthquakes. Teleseismic network of the Institute of Earth Sciences, Academia Sinica, was eventually combined with the original CWB seismic network (CWBSN) in 1991 as a new real-time digital observation network. In 1993, the CWBSN instruments were upgraded to the continuous recording mode, instead of the triggered recording mode. Arrival times of P and S waves are then manually picked for determining epicenter location and Richter local magnitude (M_L). Therefore, available modern record of Taiwanese seismicity can be traced back from 1973. We use the dataset of modern Taiwanese seismic catalogue from 1973 through 2009 in this study.

We introduced several important characteristics of Taiwanese seismicity in Fig. 1. Figure 1a shows the distribution of cumulative ratio of earthquake number above various depth thresholds. The seismic data was selected to locate between 119° to 123° longitude, and 21° to 26° latitude, and no magnitude threshold was used. The seismic data was separated into three intervals, 1973-1983, 1984-1990, and 1991-2009, by referring to important improvements of seismometer network. Total numbers of earthquake in each interval are 46 187, 44 421, and 350 036, respectively. The x value indicates depth threshold, D_c, and continuously changes from 100 km underground to ground surface (0 km) in application. Cumulative number of earthquakes was the number of earthquakes whose focal depths locate in the depth range from ground surface to D_c [km]. The y axis indicates the ratio of cumulative earthquake number and was obtained by dividing cumulative numbers of earthquakes by the total earthquake number in the corresponding interval. Black, gray, and light gray curves indicate the seismic data of 1973-1983, 1984-1990, and 1991-2009, respectively. The distribution curves of 1973-1983 and 1984-1990 show that 80 percent of earthquakes occurred above 30 km, and 90 percent of earthquakes occurred above 40 km. The curve of 1991-2009 shows that 80 percent of earthquakes occurred above 20 km, and 90 percent of earthquakes occurred above 30 km. There are merely 10 percent of earthquakes in the range of 40-100 km. Figure 1a reveals that most earthquakes in Taiwan occurred in a very thin depth range from ground surface to 30 km underground. This characteristic motivated us to use 30 km as a proper depth threshold.
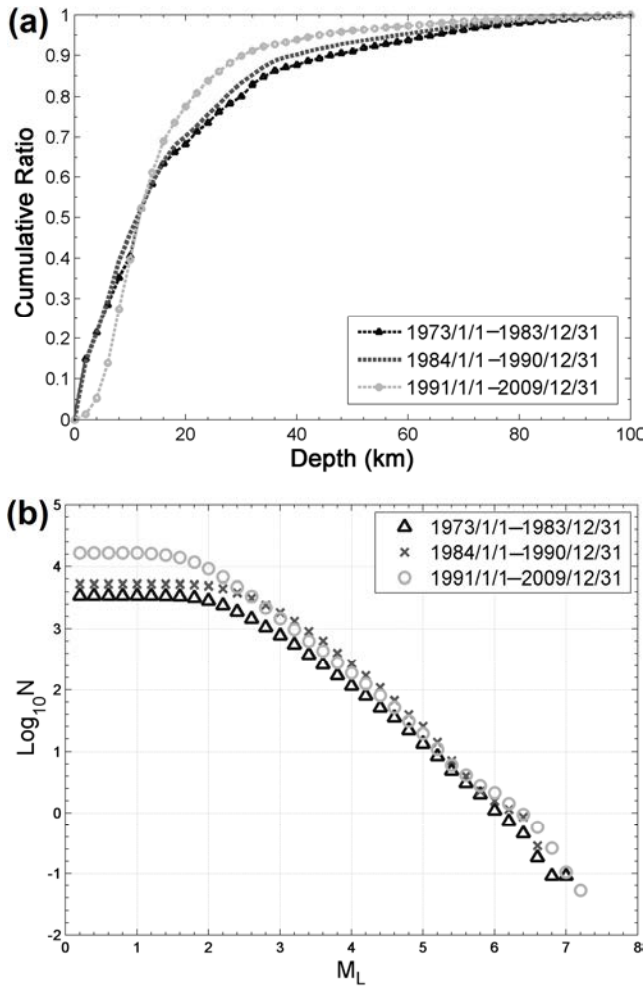
Fig. 1: (a) Distribution of cumulative ratio of earthquake number above successive depth thresholds in Taiwan. Black, gray, and light gray curves indicate the seismic data of 1973-1983, 1984-1990, and 1991-2009. (b) Gutenberg–Richter frequency distributions of seismic data in Fig. 1a. The x value indicates magnitude which continuously changed from 8.0 to 1.0. Yearly seismic rate for a specific cut-off magnitude is defined as the total number of earthquakes ($\geqq M$) divided by the number of years in an interval and expressed on logarithmic scale.

The Gutenberg–Richter frequency distributions for seismic data above 30 km in focal depth are displayed in Fig. 1b. The seismic data are separated into three intervals in the same way as in Fig. 1a. According to the definition of the Gutenberg–Richter (GR) law (Gutenberg and Richter 1954), the x value indicates magnitude and continuously changes from 8.0 to 1.0 in our

application. Yearly seismic rate of a specific magnitude in an interval was defined by dividing the total number of earthquakes with magnitudes equal to or greater than this magnitude by number of years. For a specific magnitude, the corresponding y value was obtained by expressing yearly seismic rate on a logarithmic scale. Based on the curves in Fig. 1b, there are yearly 90, 205, and 162 earthquakes whose magnitudes are equal to or greater than 3.0 in 1973-1983, 1984-1990, and 1991-2009. Unlike linear patterns of other two curves at magnitude 2.5 to 3.8, there is an interesting bulge of the curve for 1984-1990. Referring to corresponding seismic data, we found that only the seismicity in 1986 was much higher than in other years of the period 1984-1990. Thus we suggest that this bulge of GR law curve was caused by the aftershocks due to four large earthquakes in 1986. On the other hand, there is also a bulge of GR law curve in 1991-2009 at a magnitude greater than 5.0. We found that only the seismicity of magnitude greater than 4.0 in 1999 was several times the intensity of other years in the 1991-2009 period and thus contributed to this bulge with the enormous aftershocks created by the 1999 Chichi earthquake.

Wu *et al.* (2008) analyzed the spatial distribution of completeness magnitude for the CWBSN catalogue using the data from 1994 to 9 October 2003 and 35 km as the depth threshold. They show that the completeness magnitude is 2.2 for on-land events and even reaches 1.2 in several metropolises. On the other hand, the completeness magnitude ranges from 2.5 to 3.0 for offshore events. Also, Mignan *et al.* (2011) used the data from 1994 to March 2010 shallower than 35 km and concluded that the completeness magnitude is 2.0 for most of the Taiwan Island region and is 2.4 for the coast region. In Telesca *et al.* (2009), the completeness magnitude is determined to be 2.0 by using data from 1990 to 2007 and 30 km as depth threshold. In Tsai *et al.* (2011), the CWBSN catalogue can be divided into six time-periods with different stable M_c according to the fluctuations of completeness magnitude, which are: (i) 1973-1978 ($M_c = 2.7$), (ii) 1978-1986 ($M_c = 2.8$), (iii) 1986-1994 ($M_c = 3.2$), (iv) 1994-2002 ($M_c = 2.3$), (v) 2002-2008 ($M_c = 2.2$), and (vi) 2008-2010 ($M_c = 2.1$). We also applied the freely available tool ZMAP (Wiemer 2001) to analyze the completeness magnitude corresponding to each interval in Fig. 1a. Using the maximum curvature method (MAXC; Wiemer and Wyss 2000) and the entire-magnitude-range method (EMR; Ogata and Katsura 1993), the completeness magnitudes are 2.1, 2.6, 2.0, and 2.4, 2.7, 2.1 for the intervals of 1973-1983, 1984-1990, and 1991-2009, respectively. The values of completeness magnitude for the shallower seismicity after 1994 are quite consistent in those studies addressed above and our analysis. Furthermore, the larger completeness magnitude for 1984-1990 corresponds with the pattern of frequency-magnitude curve observed in Fig. 1a.

3. THIRUMALAI–MOUNTAIN FLUCTUATION METRIC

For a seismic fault network, the parameter $E_i(t')$ is a quantity which is the energy or a proxy of the energy of an individual site at time t'. For each individual box i in a system, let

$$\varepsilon_i(t) = \frac{1}{t}\int_0^t E_i(t')\,dt' \tag{1}$$

be the time average of E_i over an interval. If there are N boxes in the seismic fault network, the ensemble average is obtained by averaging the temporal average rates, evaluated in the same interval, over all boxes,

$$\overline{\varepsilon}(t) = \frac{1}{N}\sum_{i=1}^{N}\varepsilon_i(t). \tag{2}$$

To evaluate the difference between the temporal mean and the ensemble mean, a TM metric is introduced as

$$\Omega_e(t) = \frac{1}{N}\sum_{i=1}^{N}\left[\varepsilon_i(t) - \overline{\varepsilon}(t)\right]^2. \tag{3}$$

In fact, this measure is the spatial variance of the temporal averages. If the system is ergodic on the time scale τ_{obs}, the measure $\Omega_e(t)$ should vanish as t approaches τ_{obs} due to the rapid and uniform sampling of all allowed phase space. On the other hand, when ergodicity is broken, the measure $\Omega_e(t)$ should approach a nonzero constant as t approaches τ_{obs}.

   Thirumalai *et al*. (1989) deduced a dynamical scaling law to describe the finite-time properties of ergodicity from their numerical simulations of liquid model. The scaling law reveals that, for an effectively ergodic system, the reciprocal of the spatial variance grows linearly with time, just like the following equation:

$$\frac{\Omega_e(0)}{\Omega_e(t)} = \frac{t}{D_e}. \tag{4}$$

The denominator, $\Omega_e(0)$, in Eq. (4) is the TM measure at initial time t which equals zero. The constant parameter D_e is related to the exploration rate of the phase space and can be used to estimate the time required to make a system attain ergodicity. This scaling behavior is suggested to relate to the central limit theorem, where the variance becomes a constant controlled by the large sample size N and is divided by the increasing time t.

   In applying the TM metric to analyze real seismic catalogue, the number of earthquake is adopted as a proxy for seismic energy release (Tiampo *et al*. 2007). The research region ranged from 21° to 26° latitude and from 119° to

123° longitude. Several factors, such as moving time step of t in Eq. (1), dimensionality and size of dividing box, and cut-off magnitude, were tested to define possible effective-ergodic intervals in the CWB catalogue at which the statistical distribution of long term average seismic rates remained stationary. Referring to Fig. 1a, we used the seismic data whose focal depths were above 30 km in order to focus on the behavior of seismicity in shallower depths. Furthermore, we adapted both two- and three-dimensional boxes to divide the same seismic data set in space to reveal the depth effect of the CWB catalogue in TM metric calculation. For each inverse TM metric figure, the values of inverse TM metric at every time step were divided by the value of the first time step in each analysis, for example: 1-30 January 1973 while the unit time step is 30 days, to produce the normalized values. Besides several factors addressed above, we also noticed possible influence induced by the combination of the seismic networks and by the upgrade of seismometers on quality of earthquake location.

4. RESULTS OF NORMALIZED INVERSE TM METRIC

4.1 Cut-off magnitude of 2.5

Referring to the Gutenberg–Richter frequency distributions in Fig. 1b, the completeness of CWBSN catalogue can extend to magnitude 2.5. Thus we used 2.5 as a magnitude cut-off to compose earthquake data set. Figure 2 shows the results of normalized inverse TM metric using 30 days as unit time step. Based on the record of seismic location quality, the average of standard error of focal location in epicenter and depth is 1.84 and 2.79 km, respectively, during 1973-2009. For the earlier data, during 1973-1986, the average of standard error of focal location in epicenter and depth increases to 3.27 and 5.82 km, respectively. Thus we applied a reasonable two-dimensional square dividing box which was 0.1° in side length to easily overcome the error of epicenter location.

Figure 2a shows the result of normalized inverse TM metric, the data of which began in January 1973. Two thicker arrows in Fig. 2a, respectively, indicate the time points of two major evolutions of CWBSN, *i.e.*, upgrade to electromagnetic instruments since 1984 and the combination of IES and original CWB networks in 1991. The bars extending vertically from the time axis of Fig. 2a indicate the big earthquakes which are greater than or equal to 6.0 in magnitude from 1973 to 2009. The value of normalized inverse TM metric is very large and fluctuates apparently while the parameter t is moving from 1973 to June 1978, drops dramatically in 1978 and then gradually decreases in 1979 to 1986. Finally, the normalized inverse TM metric value remains stable around 0.25 after 1987.
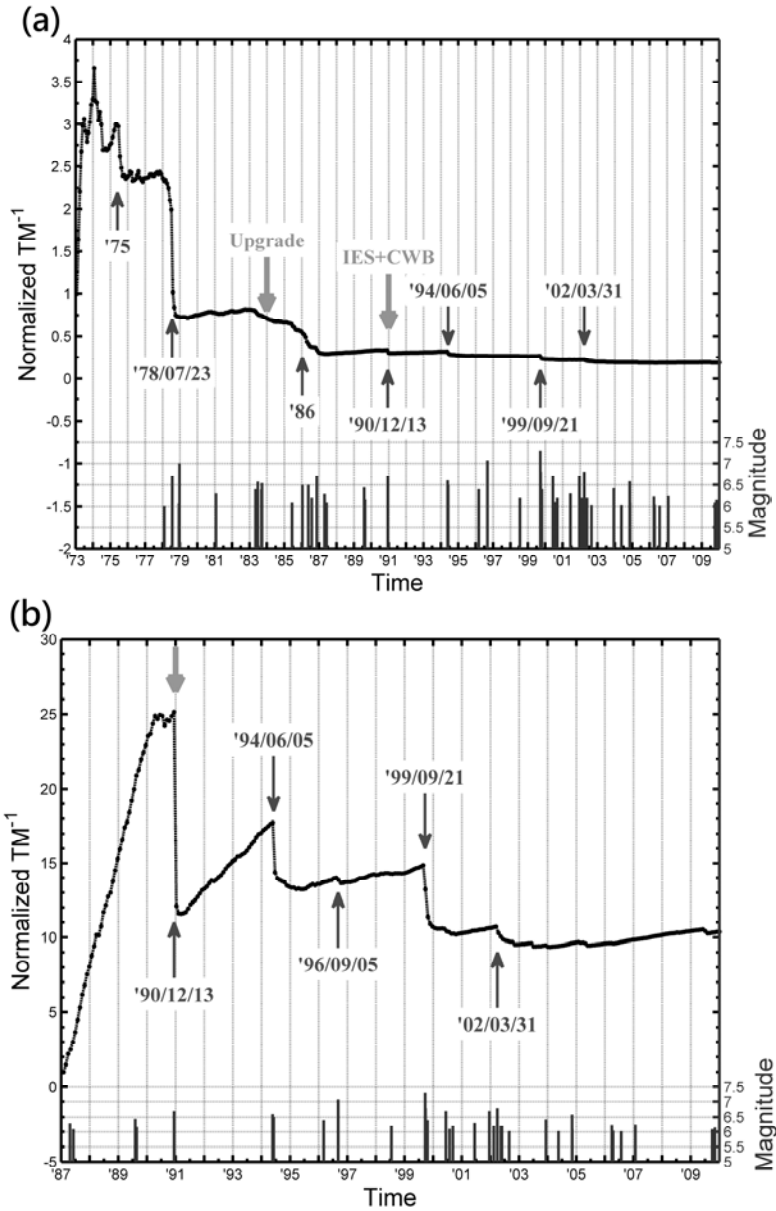
Fig. 2. Normalized inverse TM metric for Taiwan, two-dimensional box size equal to $0.1° \times 0.1°$, $M \geqq 2.5$, and $D_c = 30$ km. Vertical bar indicates the occurrence time of $M \geqq 6.0$ earthquakes. Thicker arrow indicates the time point of major evolutions of CWBSN. Upgrade: upgrade to electromagnetic instruments, IES+CWB: combination of IES network and original CWB network. Study period is (a) 1973-2009; (b) 1987-2009.

    Although the pattern of normalized inverse TM metric curve in Fig. 2a is far from the required linear pattern of effective ergodicity, we identified apparent influence of large earthquakes on three large drops of normalized TM metric. In 1975, there was a series of earthquakes whose magnitude ranged from 5 to 6. On 23 July 1978, there was a big earthquake of 6.7 magnitude. In 1986, there were four big earthquakes whose magnitudes ranged from 6.2 to 6.7. Besides these large drops, we also identified four smaller drops of normalized inverse TM metric in December 1990, June 1994, September 1999, and March 2002. All of the smaller drops are correlated with the occurrences of large earthquake, including the 1999 Chichi earthquake and the 2002 Hualian earthquake.

    Considering the quite different patterns of normalized inverse TM metric between 1973 to 1986 and 1987 to 2009 in Fig. 2a, we adopted 1987 as another beginning to remove an influence due to heterogeneity of earlier data in CWB catalogue and Fig. 2b shows the result. The thick arrow indicates the time point of combination of IES and original CWB networks since 1991. We identified three large drops of normalized inverse TM metric in December 1990, June 1994, and September 1999. All of them are temporally correlated with the occurrences of a big earthquake whose magnitude is greater than 6.5.

    We also identified three intervals as candidates for an effectively ergodic interval, *i.e.*, January 1987 to April 1990, June 1991 to April 1994, and November 1996 to August 1999. The linear regression models for each interval are obtained by least-square fitting and the slopes of each regression model are 0.627, 0.158, and 0.029, respectively.

4.2 Cut-off magnitude of 3.0

We tested another data set whose cut-off magnitude was 3.0. Based on the record of data quality from 1973 to 2009, the average of standard error of focal location in epicenter and depth was, respectively, 1.81 and 2.4 km. For the earlier data from 1973 to 1986, poorer location quality raised the average of standard error of focal location in the epicenter and depth to 4.43 and 7.83 km, respectively. Thus, we still applied two-dimensional square dividing boxes, whose side length was 0.1° to overcome the error of epicenter location.

    The pattern of normalized inverse TM metric in Fig. 3a is very similar to the curve in Fig. 2a. Two large drops in 1975 and 1978 are the same as those in Fig. 2a, but the drops in 1986 become steeper. Figure 3b-c shows the normalized inverse TM metric results using seismic data since 1987. Based on the record of data quality in 1987 to 2009, the average standard error of focal location in epicenter and depth was 1.2 and 1.45 km, respectively. We used two-dimensional square gridding box whose side length was 0.1° in

Fig. 3b and three-dimensional gridding box whose size was 0.1° × 0.1° × 3 km in Fig. 3c.

The patterns of normalized inverse TM metric in Fig. 3b-c are quite different from that in Fig. 3a. Both inverse TM metric curves in Fig. 3b-c show several linearly increasing patterns which are terminated by drops. We
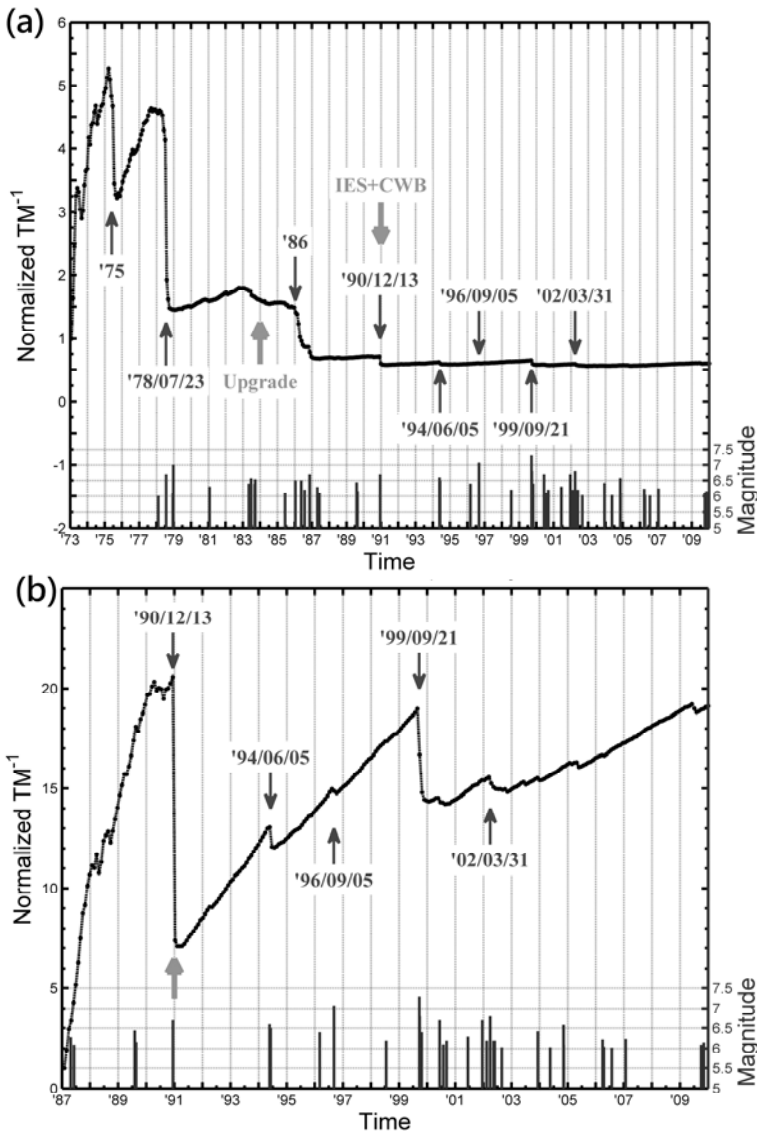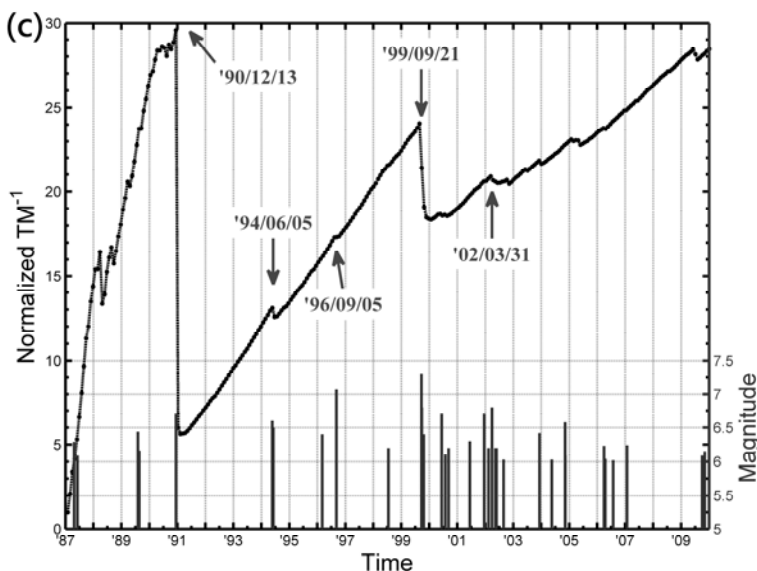
Fig. 3. Continued on next page.

Fig. 3. Normalized inverse TM metric for Taiwan, $M \geqq 3.0$, and $D_c = 30$ km. Box size is $0.1° \times 0.1°$ in (a) and (b); $0.1° \times 0.1° \times 3$ km in (c). Study period is 1973-2009 in (a); 1987-2009 in (b) and (c).

identified four big drops in December 1990, June 1994, September 1996, and September 1999, and three possible effectively ergodic intervals between the drops in Fig. 3b. All drops are closely correlated to the occurrences of big earthquake whose magnitude exceeds or equals 6.5. We also identified two possible effectively ergodic intervals, from September 2000 to February 2002 and from June 2005 to June 2009.

Furthermore, we found that the magnitude of normalized inverse TM metric drops in June 1994 and September 1996 in Fig. 3b are larger than those in Fig. 3c. The values of inverse TM metric which change in June 1994 and September 1996 in Fig. 3b are –1 and –0.2, being –0.55 and 0.2 in Fig. 3c. This disappearance of drop in September 1996 in Fig. 3c was caused by the enormous increase of the number of three-dimensional dividing boxes. The significantly increasing number of dividing boxes strongly reduced the influences of seismic data at a next time step and maintained the statistical distribution of long-term average seismic rate stable.

Similar to Section 4.1, we obtained linear regression models of each possible effectively ergodic interval by least-square fitting. Five candidates of effectively ergodic intervals are: June 1991 to May 1994, August 1994 to August 1996, November 1996 to August 1999, September 2000 to February 2002, and June 2005 to June 2009. The corresponding slopes are 0.154,

0.117, 0.119, 0.078, and 0.066 in Fig. 3b, and 0.199, 0.181, 0.191, 0.131, and 0.118 in Fig. 3c.

4.3 Cut-off magnitudes of 4.0 and 5.0

Figure 4a-b shows the results of normalized inverse TM metric using seismic data which exceed or equal 4.0 in magnitude. In both cases we discretized
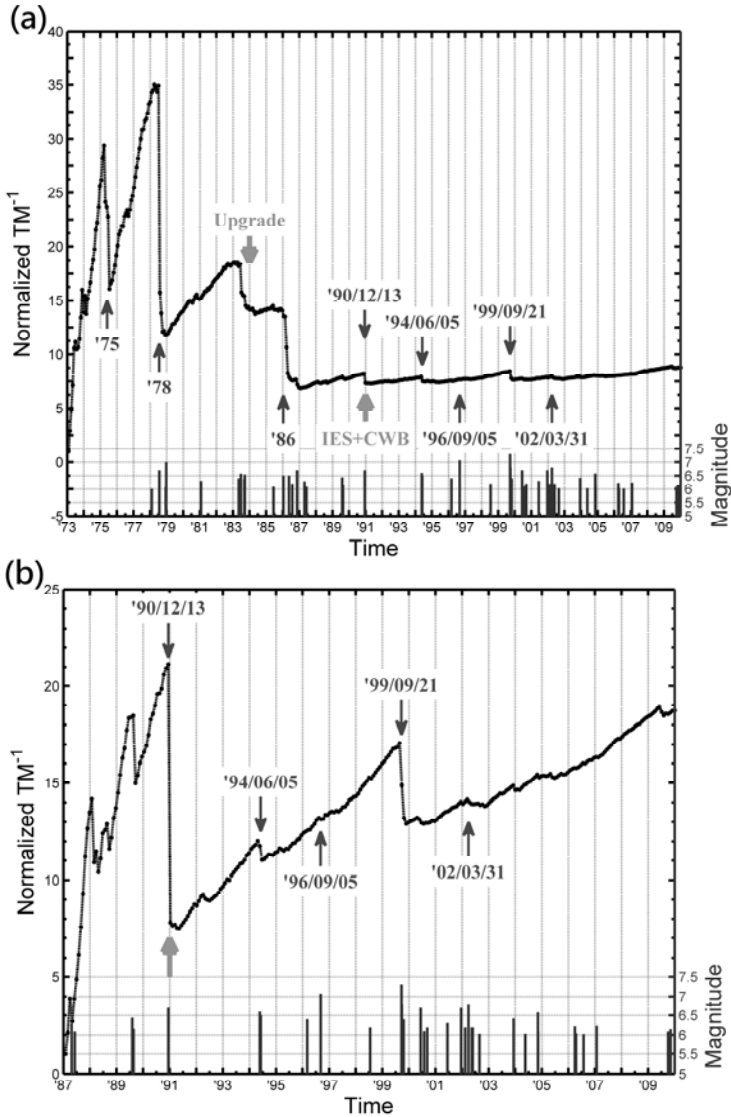

Fig. 4. Continued on next page.
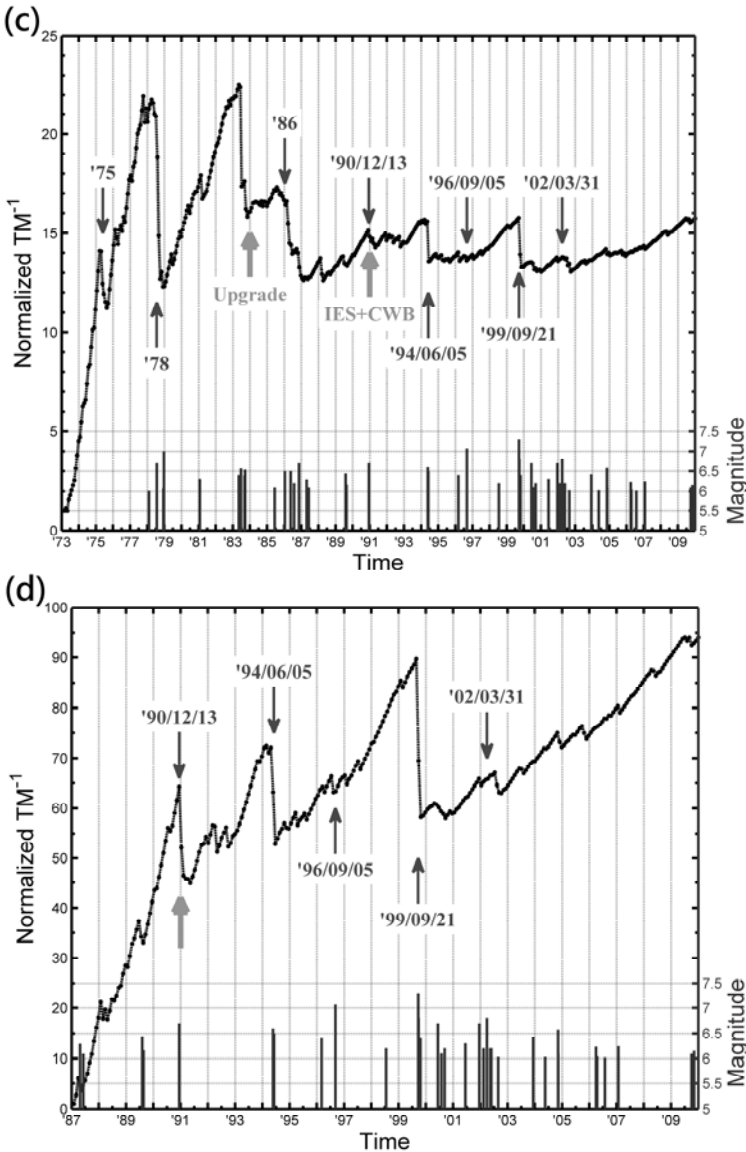
Fig. 4. Normalized inverse TM metric for Taiwan, two dimensional box size is equal 0.1° × 0.1°, D_c = 30 km. $M \geqq 4.0$ for (a) and (b); $M \geqq 5.0$ for (c) and (d). Study period is 1973-2009 for (a) and (c); 1987-2009 for (b) and (d).

the data set by using thirty days as the unit time step and two-dimensional square dividing box whose side length was 0.1°. The only difference between Fig. 4a and b is the initial time of seismic data set. The data initi-

ated, respectively, from January 1973 in Fig. 4a and from January 1987 in Fig. 4b. Similar to Figs. 2a and 3a, the normalized inverse TM metric curve fluctuates strongly before 1987 in Fig. 4a. The pattern of normalized inverse TM metric in Fig. 4b is similar to Fig. 3b-c. We observed new drops of inverse TM metric in April 1992 to June 1992, which did not exist in the analyses using smaller magnitude cut-off. Comparing to the seismic catalogue, there is a series of shallow earthquakes whose magnitude ranged from 5.0 to 5.6. We also observed that the inverse TM metric in September 1996 formed a bulge instead of a drop. We suggested that the application of 4.0 as a magnitude cut-off eliminated the influence of smaller aftershocks which were generated by the Lanyu earthquake on 5 September 1996.

We identify two candidates of effectively ergodic interval, June 1991 to April 1992 and August 1992 to April 1994, from Fig. 4b. Another interval, from July 1994 to August 1999, in which the inverse normalized TM metric fluctuates stronger, is also tested. The slopes are 0.159, 0.143, and 0.095, respectively.

Figure 4c-d shows the results of normalized inverse TM metric using 5.0 as magnitude cut-off. The initial time of seismic data is January 1973 in Fig. 4c and January 1987 in Fig. 4d. The impact of using earlier seismic data, before 1987, is still obvious in Fig. 4c. Comparing to Figs. 3b-c and 4b, the magnitudes of inverse normalized TM metric do not raise very rapidly in 1973 to 1986. On the other hand, the inverse TM metric curve in January 1991 to May 1994 and June 1994 to August 1999 fluctuates more apparently than in Figs. 3b-c, and 4b. We suggest that the earthquakes whose magnitude is greater than 5.0 are too few to construct a stable statistical distribution of long-term average seismic rate. The statistical distribution of long term average seismic rate is easily affected by the number of earthquake at a following time step.

5. DISCUSSION

The evolution of detecting ability and coverage of CWBSN must have caused the statistical properties of seismicity to be different in varying time points. For example, an evaluation of homogeneity in the CWBSN catalogue shows significant rate increases until pre-1980 and the rate anomalies corresponding to large earthquake sequences (Habermann 1987, Tiampo *et al*. 2010). Figure 1 specifically illustrates different statistical properties of seismicity due to the evolutions of CWBSN. In Figures 2a, 3a, and 4a, we identified apparent influences of using earlier data, before 1987, in the calculation of inverse TM metric. Conversely, obvious linearly increasing patterns of inverse normalized TM metric curves exist in the analyses disregarding the earlier data. However, even in Figs. 3b-c, and 4b, the abrupt raise and relatively larger fluctuations of inverse TM curve in 1987 to 1990

still implied the influences of heterogeneity in seismic data. In further tests, not shown in this paper, which used January 1991 as the initial time, there is no such large fluctuation of inverse TM metric in the beginning interval. We suggested that this change is due to more stable detecting ability of CWBSN since 1991. These tests about heterogeneity of catalogue reveal the necessity of carefully considering possible bias of long term seismic rate while earlier seismic data is involved.
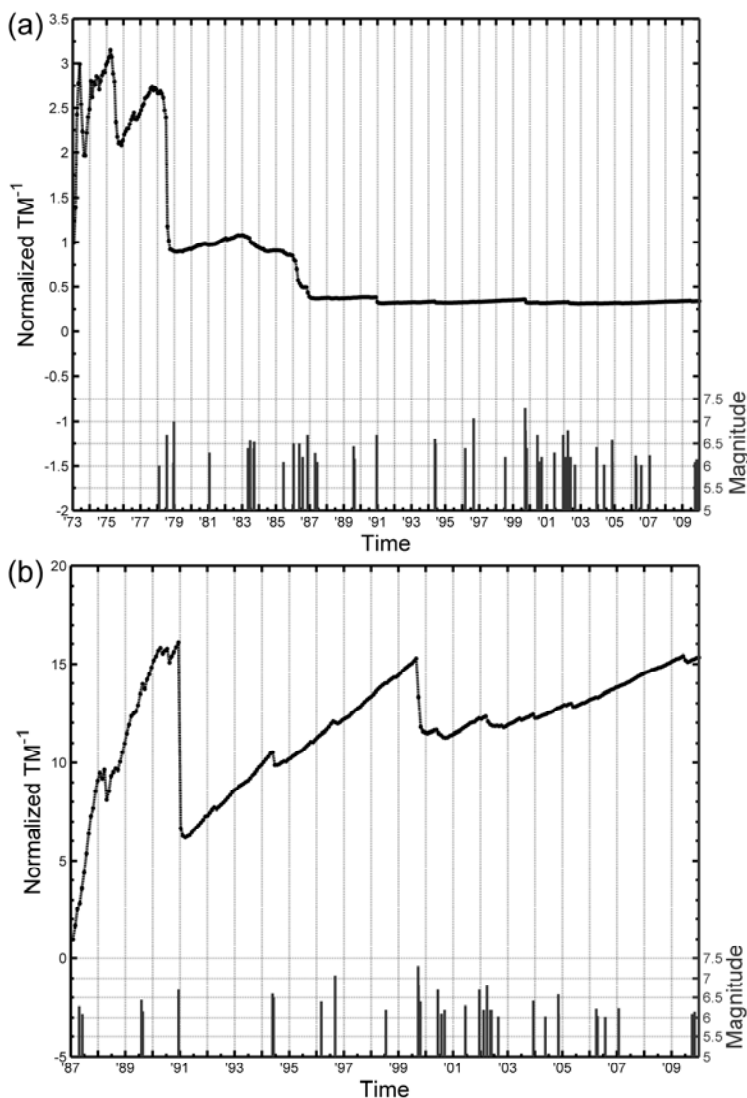
Fig. 5. Continued on next page.
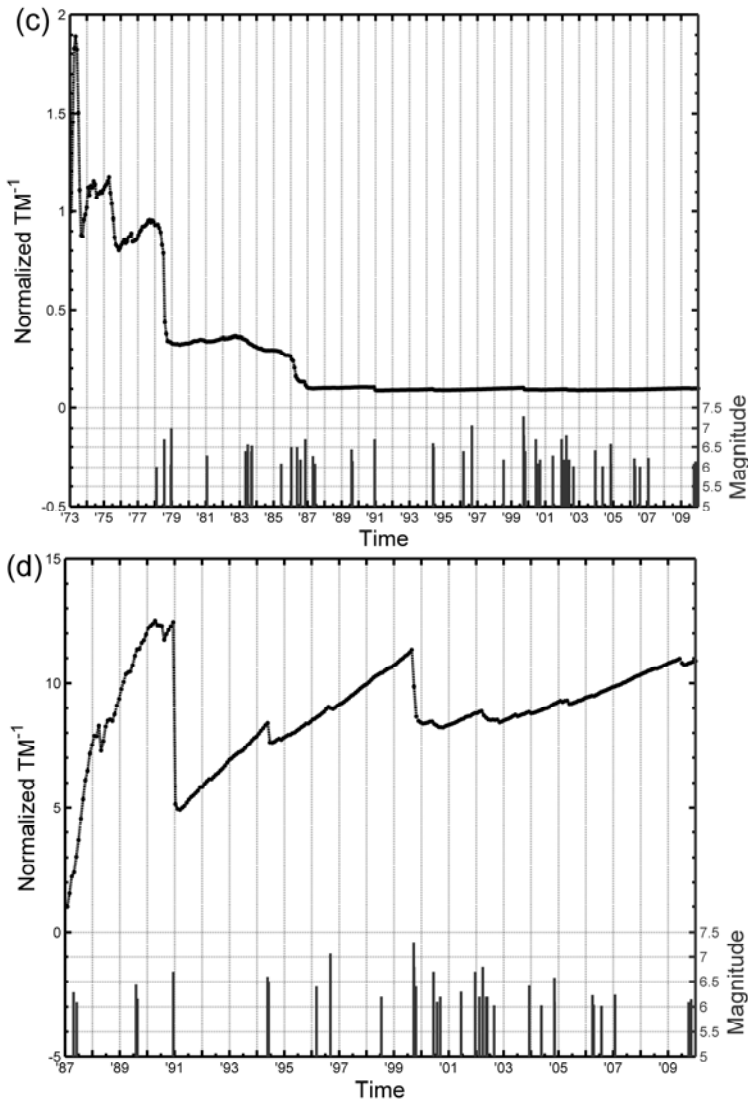
Fig. 5. Normalized inverse TM metric for Taiwan, $M \gtrsim 3.0$, and $D_c = 30$ km. Box size is $0.2° \times 0.2°$ in (a) and (b); $0.1° \times 0.5°$ in (c) and (d). Study period is 1973-2009 in (a) and (c) as a comparison to Fig. 3a; 1987-2009 in (b) and (d) as a comparison to Fig. 3b.

Through the results in Figs. 2b, 3b and d, and 4b, we identified several intervals in which the inverse normalized TM metric curves had linearly increasing patterns. According to the somewhat obscure dynamical law

addressed in the method section, the Taiwanese fault network might be regarded as being effectively ergodic in these intervals. However, more quantitative analyses are necessary for finding further details of the candidates of effective ergodicity. First, are these linearly increasing patterns originated from the nature of Taiwanese seismicity or merely obtained occasionally due to application of a specific gridding box? Second, if these effectively ergodic intervals exist in nature, is there any common characteristic among them?

We tested the possible influence of gridding box size by using larger grid to discretize the data sets used in Fig. 3a-b, and illustrated the inverse TM metric results in Fig. 5. The side length of two-dimensional square gridding box is 0.2° in Fig. 5a-b, and 0.5° in Fig. 5c-d. The initial time is January 1973 in Fig. 5a and c, the same as in Fig. 3a, and January 1987 in Fig. 5b, d, the same as in Fig. 3b. An immediate observation is that the curve patterns are highly similar among the results using the same data set. These results show that the size of gridding box does not alter the behavior of inverse TM metric curve obviously. The linearly increasing patterns of inverse TM metric curve observed in Fig. 3b still exist in Fig. 5c-d. Thus we conclude that the existence of possible effective ergodicity crucially depends on the inherent properties, *e.g*., heterogeneity, of data set used. The linearly increasing patterns of inverse TM metric curve in Fig. 3b exist naturally; they are not an artificial effect using a specific gridding box.

In order to further understand properties of natural local seismicity, we implemented the stochastic test by using the same parameters, *i.e*., the number of time steps, the number of earthquakes, and number of gridding boxes, of Fig. 3b to generate 500 artificial random seismic catalogues. An artificial catalogue was generated by using the same total number of earthquakes, assigning occurrence times from a uniform probability distribution from 1987 to 2009, and then distributing the earthquakes in each time step with uniform probability over the research region. Randomizing the catalogue in this way destroyed any inherent space-time structure, *e.g*., the main shock-aftershock sequences, earthquake clusters, and induced earthquakes, which possibly existed in the original CWBSN catalogue. We performed the time series of inverse normalized TM metric for each artificial catalogue and calculated its correlation coefficient (Hoel 1966) with the result in Fig. 3b. We also generated another set of random catalogues by using the parameters of Fig. 3c and calculated their correlation coefficients with the result in Fig. 3c. Figure 6a, c shows the correlation coefficients relative to Fig. 3b-c, respectively. Figure 6b and d illustrates three inverse TM metric curves of random catalogues which correspond to the top three correlation coefficient values in Fig. 6a and c, respectively. The most immediate characteristic is that these curves merely have small fluctuations, instead of large drops observed in

Fig. 3b or c. In Figures 2b, 3b-c, and 4b, we observe that several candidates of effectively ergodic intervals are terminated by big drops. We suggest that the participation of enormous number of aftershocks temporally clustered in successive unit time steps obviously changed the stable distribution of long-term average seismic rate evaluated from previous seismicity. This iterative process of formation and sudden termination of effective ergodicity is similar to the researches using other natural catalogues such as of California, Spain, and eastern Canada (Tiampo *et al*. 2007).
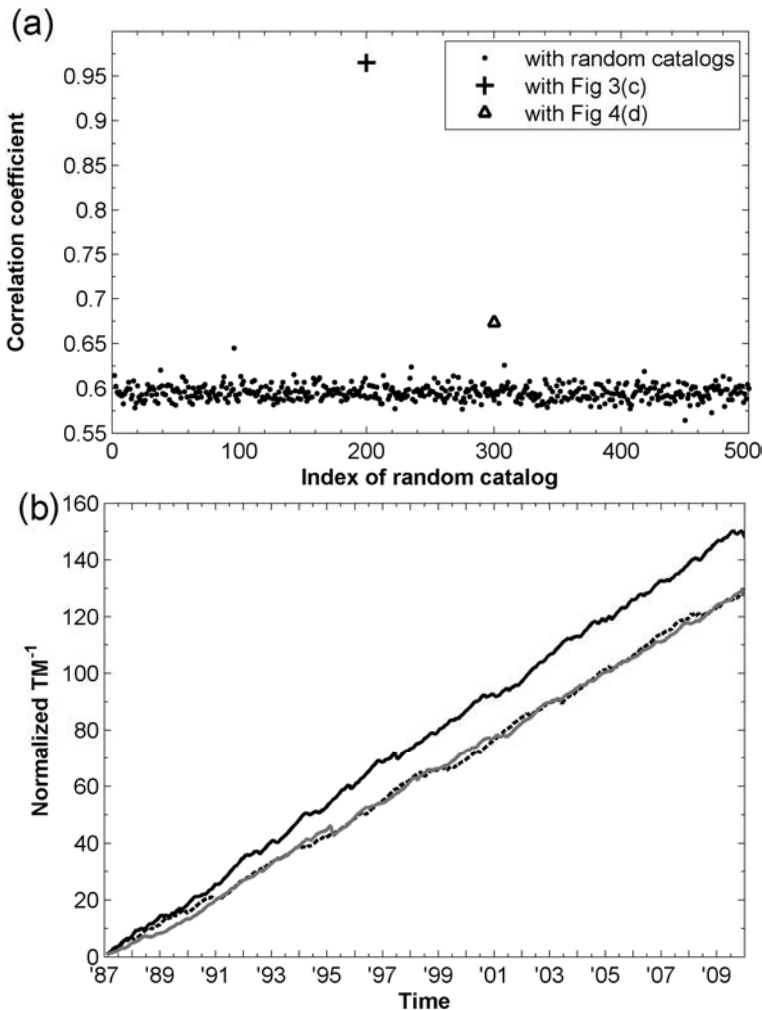

Fig. 6. Continued on next page.
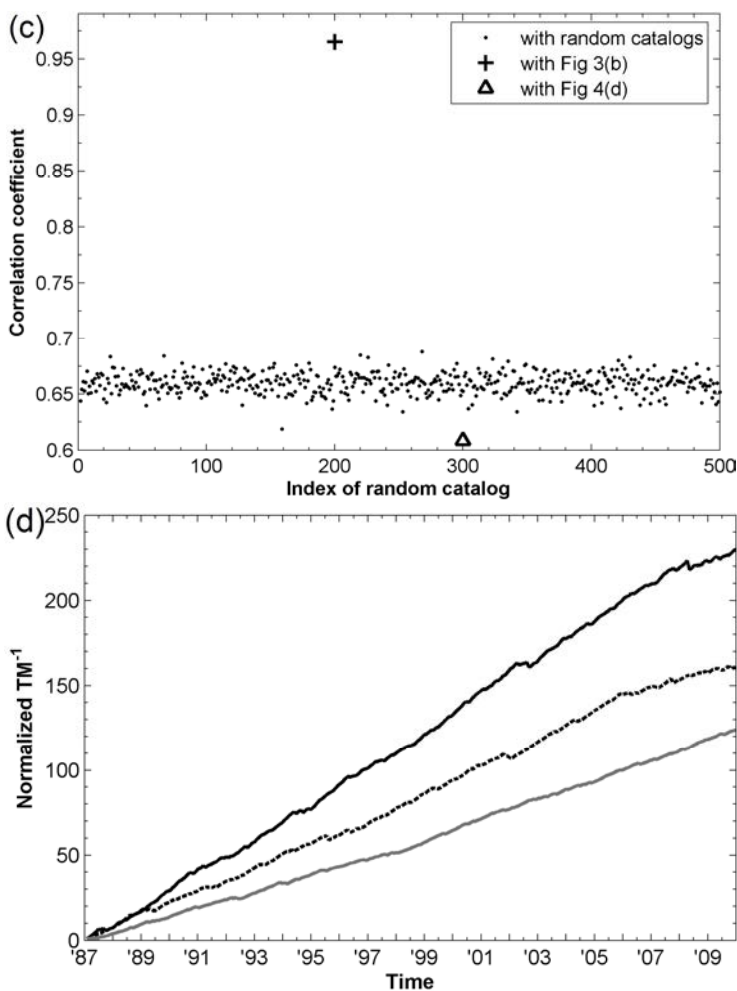
Fig. 6. Correlation coefficients of normalized inverse TM metric curves. Panel (a): cross refers to Fig. 3b and c, open triangle to Figs. 3b and 4d, and black dots to Fig. 3b and random catalogues. Panel (c): cross refers to Fig. 3c and b, open triangle to Figs 3c and 4d, and black dots to Fig. 3c and random catalogues. For (a) and (c), top three normalized inverse TM metric curves which have the highest correlation coefficients are shown in (b) and (d), respectively.

To illustrate the availability of correlation coefficient in distinguishing different patterns of inverse TM metric curves, we calculated the correlation coefficients for each pair of Figs. 3b-c and 4d. With visual inspection, the patterns of inverse TM metric curve are similar between Fig. 3b and c, but are quite different in 1987 to 1991 between Figs. 3b and 4d, and between

Figs. 3c and 4d. The cross in Fig. 6a and c indicates the value of correlation coefficient, amounting to 0.965, between Fig. 3b and c. The open triangles in Fig. 6a and c respectively, indicate the values of correlation coefficient between Figs. 3b and 4d, and between Figs. 3c and 4d. The value is 0.674 in Fig. 6a and 0.609 in Fig. 6c. With the interpretation developed by Dawson and Trapp (2004), values of correlation coefficient from 0.5 to 0.75 or from –0.5 to –0.75 indicate moderate to good correlation, and values from 0.75 to 1 or from –0.75 to –1 point to very good to excellent correlation between the variables. These apparent differences support the application of correlation coefficient as a simple but efficient statistical quantity to evaluate the similarity between patterns of inverse TM metric curve. The correlation coefficients ranged from 0.564 to 0.645 for each pair of Fig. 3b and random catalogues, and from 0.619 to 0.688 for the case of Fig. 3c. In both cases, the relatively lower values of correlation coefficient indicate that the patterns of inverse TM metric for random catalogues are quite different from Fig. 3b or c. The slopes of linear regression model for the curves in Fig. 6b are 0.541, 0.463, and 0.467, being 0.861, 0.605, and 0.446 for the curves in Fig. 6d. All slopes are much larger than those fitted by any candidate of effectively ergodic interval in Fig. 3b-c. Through the tests of correlation coefficient and fitted slope for randomized catalogues, we exclude the possibility that the big drops observed in Fig. 3b-c are generated occasionally due to parametric selection.

The Shapiro–Wilk test (Shapiro and Wilk 1965, Royston 1995) is applied to the candidates of effectively ergodic intervals in Figs. 3b-c, 4b, and the random catalogues in Fig. 6a, c to test if linear regression models are proper to simulate the behaviors of inverse TM metric in each case. The Shapiro–Wilk test is a widely used algorithm to test the null hypothesis that a sample came from a population with normal distribution. The Shapiro–Wilk test has better performance than the Kolmogorov–Smirnov (KS) test for testing for normality (Kvam and Vidakovic 2007). In our application, a sample is composed by the residuals of inverse normalized TM metric between simulated values obtained from linear regression model and values calculated from original data. According to the fundamental assumption of simple linear regression, the fitted regression model is adequate to describe the behaviors of a system once the residuals displays normal distribution (Cohen *et al.* 2003). We used two-side test and 0.05 as the significance level in our tests. In 500 random catalogues used in Fig. 6a, there are 439 catalogues the p values of which locate in the interval 0 to 0.05 (reject null hypothesis). In the random catalogues used in Fig. 6c, there are 446 catalogues the p value of which is under the predefined significance level. Briefly speaking, for over 90% of random catalogues in this analysis, the linear model is not suitable to describe the behaviors of inverse TM metric. The

p values of candidates of effectively ergodic interval are listed in Tables 1-4. Only the interval from July 1994 to August 1999, in Fig. 4b, has a relatively low *p* value comparing to other candidates, *i.e.*, 0.102. This low *p* value seems to correspond to stronger fluctuation of inverse normalized TM metric in the interval. On the other hand, most *p* values listed in Tables 1-4 are greater than the predefined significance level and support the adequacy of describing the behavior of normalized inverse TM metric curve by fitted linear regression model. Thus, we conclude that the statistical behaviors of long-term average seismicity can be regarded as effectively ergodic in several data sets selected from the CWBSN catalogue.

   The identifications of effectively ergodic intervals in the CWBSN cata-logue supports the researches in other natural seismic catalogues, such as of California, Spain, and eastern Canada. These analyses concluded that natural fault network displayed at least some of the dynamics of driven mean-field system, as observed in the numerical simulations of interacting slider block model and coupled map lattices. Ergodicity is a necessary condition to effec-tively use linear principal component analysis. The identified temporal and

Table 1

Slope of linear regression model and *p* value of Shapiro–Wilk test for Fig. 2b

Interval	1987/1-1990/4	1991/6-1994/5	1996/11-1999/8
Slope	0.627	0.158	0.029
p value	0.766	0.907	0.799

Table 2

Slope of linear regression model and *p* value of Shapiro–Wilk test for Fig. 3b

Interval	1991/6-1994/5	1994/8-1996/8	1996/11-1999/8	2000/9-2002/2	2005/6-2009/6
Slope	0.154	0.117	0.119	0.078	0.066
p value	0.916	0.886	0.690	0.912	0.866

Table 3

Slope of linear regression model and *p* value of Shapiro–Wilk test for Fig. 3c

Interval	1991/6-1994/5	1994/8-1996/8	1996/11-1999/8	2000/9-2002/2	2005/6-2009/6
Slope	0.199	0.181	0.190	0.131	0.118
p value	0.673	0.963	0.441	0.889	0.939

Table 4

Slope of linear regression model and *p* value of Shapiro–Wilk test for Fig. 4a

Interval	1991/6-1992/4	1992/8-1994/4	1994/7-1999/8
Slope	0.160	0.143	0.095
p value	0.756	0.607	0.102

spatial parameters which corresponded to effective ergodicity are critical for employing such linear approximation methods based on long term statistic quantity.

References

Bak, P., C. Tang, and K. Weisenfield (1987), Self-organized criticality: An explanation of the $1/f$ noise, *Phys. Rev. Lett.* **59**, 4, 381-384, DOI: 10.1103/PhysRevLett.59.381.

Chen, C.-C., J.B. Rundle, J.R. Holliday, K.Z. Nanjo, D.L. Turcotte, S.C. Li, and K.F. Tiampo (2005), The 1999 Chi-Chi, Taiwan, earthquake as a typical example of seismic activation and quiescence, *Geophys. Res. Lett.* **32**, L22315, DOI: 10.1029/2005GL023991.

Chen, C.-C., J.B. Rundle, H.C. Li, J.R. Holliday, K.Z. Nanjo, D.L. Turcotte, and K.F. Tiampo (2006), From tornadoes to earthquakes: Forecast verification for binary events applied to the 1999 Chi-Chi, Taiwan, earthquake, *Terr. Atmos. Ocean. Sci.* **17**, 503-516.

Chen, C.-C., Y.-T. Lee, and L.-Y. Chiao (2008), Intermittent criticality in the long-range connective sandpile (LRCS) model, *Phys. Lett. A* **372**, 24, 4340-4343, DOI: 10.1016/j.physleta.2008.04.043.

Cohen, J., P. Cohen, S.G. West, and L.S. Aiken (2003), *Applied Multiple Regression Correlation Analysis for the Behavioral Sciences,* Lawrence Erlbaum Associates Inc., New Jersey.

Dawson, B., and R.G. Trapp (2004), *Basic and Clinical Biostatistics*, 4th ed., Lange Medical Books, McGraw-Hill, New York.

Ferguson, C.D., W. Klein, and J.B. Rundle (1999), Spinodals, scaling and ergodicity in a model of an earthquake fault with long-range stress transfer, *Phys. Rev. E* **60**, 1359-1373, DOI: 10.1103/PhysRevE.60.1359.

Fisher, D.S. (1985), Sliding charge-density waves as a dynamic critical phenomenon, *Phys. Rev. B* **31**, 3, 1396-1427, DOI: 10.1103/PhysRevB.31.1396.

Fisher, D.S., K. Dahmen, S. Ramanathan, and Y. Ben-Zion (1997), Statistics of earthquakes in simple models of heterogeneous faults, *Phys. Rev. Lett.* **78**, 25, 4885-4888, DOI: 10.1103/PhysRevLett.78.4885.

Gopal, A.D., and D.J. Durian (1995), Nonlinear bubble dynamics in a slowly driven foam, *Phys. Rev. Lett.* **75**, 2610-2613, DOI: 10.1103/PhysRevLett.75.2610.

Gutenberg, B., and C.F. Richter (1954), *Seismicity of the Earth and Associated Phenomena*, 2nd ed., Princeton University Press, New Jersey.

Habermann, R.E. (1987), Man-made changes of seismicity rates, *Bull. Seismol. Soc. Am.* **77**, 141-159.

Hertz, J., A. Korgh, and R.G. Palmer (1991), *Introduction to the Theory of Neural Computation*, Addison Wesley, Reading, MA.

Herz, A.V.M., and J.J. Hopfield (1995), Earthquake cycles and neural reverberations: Collective oscillations in systems with pulse-coupled threshold elements, *Phys. Rev. Lett.* **75**, 1222-1225, DOI: 10.1103/PhysRevLett.75.1222.

Hoel, P.G. (1966), *Introduction to Mathematical Statistics*, Wiley Series in Probability and Statistics, John Wiley & Sons, New York.

Klein, W., J.B. Rundle, and C.D. Ferguson (1997), Scaling and nucleation in models of earthquake faults, *Phys. Rev. Lett.* **78**, 19, 3793-3796, DOI: 10.1103/ PhysRevLett.78.3793.

Kvam, P.H., and B. Vidakovic (2007), *Nonparametric Statistics with Applications to Science and Engineering*, John Wiley & Sons, New Jersey.

Lee, Y.-T., C.-C. Chen, Y.-F. Chang, and L.-Y. Chiao (2008), Precursory phenomena associated with large avalanches in long-range connective sandpile (LRCS) model, *Physica A* **387**, 21, 5263-5270, DOI: 10.1016/j.physa. 2008.05.004.

Mignan, A., M.J. Werner, S. Wiemer, C.-C. Chen, and Y.-M. Wu (2011), Bayesian estimation of the spatially varying completeness magnitude of earthquake catalogs, *Bull. Seismol. Soc. Am.* **101**, 3, 1371-1385, DOI: 10.1785/ 0120100223.

Ogata, Y., and K. Katsura (1993), Analysis of temporal and spatial heterogeneity of magnitude frequency distribution inferred from earthquake catalogues, *Geophys. J. Int.* **113**, 727-738, DOI: 10.1111/j.1365-246X.1993.tb04663.x.

Royston, P. (1995), A remark on algorithm AS 181: the W-test for normality, *J. Roy. Stat. Soc., Ser. C* **44**, 4, 547-551.

Rundle, J.B., and W. Klein (1995), New ideas about the physics of earthquakes, *Rev. Geophys.* **33**, S1, 283-286, DOI: 10.1029/95RG00106.

Rundle, J.B., K.F. Tiampo, W. Klein, and J.S. Sá Martins (2002), Self-organization in leaky threshold systems: The influence of near-mean field dynamics and its implications for earthquakes, neurobiology, and forecasting, *Proc. Nat. Acad. Sci. USA* **99**, Suppl. 1, 2514-2521, DOI: 10.1073/pnas.012581899.

Scholz, C.H. (1990), The *Mechanics of Earthquakes and Faulting*, Cambridge University Press, Cambridge, UK.

Shapiro, S.S., and M.B. Wilk (1965), An analysis of variance test for normality (complete samples), *Biometrika* **52**, 3-4, 591-611.

Telesca, L., C.-C. Chen, and Y.-T. Lee (2009), Scaling behaviour in temporal fluctuations of crustal seismicity in Taiwan, *Nat. Hazards Earth Syst. Sci.* **9**, 2067-2071, DOI: 10.5194/nhess-9-2067-2009.

Thirumalai, D., R.D. Mountain, and T.R. Kirkpatrick (1989), Ergodic behavior in supercooled liquids and in glasses, *Phys. Rev. A* **39**, 7, 3563-3574, DOI: 10.1103/PhysRevA.39.3563.

Tiampo, K.F., J.B. Rundle, S. McGinnis, S.J. Gross, and W. Klein (2002), Mean-field threshold systems and phase dynamics: An application to earthquake fault systems, *Europhys. Lett.* **60**, 3, 481-487, DOI: 10.1209/epl/i2002-00289-y.

Tiampo, K.F., J.B. Rundle, W. Klein, J.S. Sá Martins, and C.D. Ferguson (2003), Ergodic dynamics in a natural threshold system, *Phys. Rev. Lett.* **91**, 238501, DOI: 10.1103/PhysRevLett.91.238501.

Tiampo, K.F., J.B. Rundle, W. Klein, J. Holliday, J.S. Sá Martins, and C.D. Ferguson (2007), Ergodicity in natural earthquake fault networks, *Phys. Rev. E* **75**, DOI: 10.1103/PhysRevE.75.066107.

Tiampo, K.F., W. Klein, H.-C. Li, A. Mignan, Y. Toya, S.Z.L. Kohen-Kadosh, J.B. Rundle, and C.-C. Chen (2010), Ergodicity and earthquake catalogs: Forecast testing and resulting implications, *Pure Appl. Geophys.* **167**, 6-7, 763-782, DOI: 10.1007/s00024-010-0076-2.

Tsai, C.-Y., G. Ouillon, and D. Sornette (2011), New empirical tests of the multifractal Omori law for Taiwan, *arXiv:1109.5017v1*.

Urbach, J.S., R.C. Madison, and J.T. Markert (1995), Interface depinning, self-organized criticality, and the Barkhausen effect, *Phys. Rev. Lett.* **75**, 2, 276-279, DOI: 10.1103/PhysRevLett.75.276.

Wiemer, S. (2001), A software package to analyze seismicity: ZMAP, *Seismol. Res. Lett.* **72**, 3, 373-382, DOI: 10.1785/gssrl.72.3.373.

Wiemer, S., and M. Wyss (2000), Minimum magnitude of completeness in earthquake catalogs: Examples from Alaska, the Western United States, and Japan, *Bull. Seismol. Soc. Am.* **90**, 4, 859-869, DOI: 10.1785/0119990114.

Wu, Y.-M., C.-C. Chen, L. Zhao, and C.-H. Chang (2008), Seismicity characteristics before the 2003 Chengkung, Taiwan, earthquake, *Tectonophysics* **457**, 177-182, DOI: /10.1016/j.tecto.2008.06.007.

Testing Fractal Coefficients Sensitivity on Real and Simulated Earthquake Data

Dragomir GOSPODINOV, Alexander MARINOV,
and Elisaveta MAREKOVA

Plovdiv University "Paisiy Hilendarski", Plovdiv, Bulgaria
e-mails: drago@uni-plovdiv.bg (corresponding author),
amarinov@uni-plovdiv.bg, eligeo@uni-plovdiv.bg

A b s t r a c t

We examined the behavior of different fractal dimensions when applied to study features of earthquake spatial distribution on different types of data. We first examined simulated spatial fields of points of different clustering level, following the so called Soneira–Peebles model. The model was chosen because it displays some similarity to the real clustering structure of earthquakes occurring on hierarchically ordered faults. The analysis of the capacity, clustering and correlation dimensions revealed that their behavior did not completely correlate with the clustering level of the simulated data sets. We also studied temporal variations of the fractal coefficients, characterizing the spatial distribution of the 1999 İzmit–Düzce aftershock sequence. The calculated coefficient values demonstrated analogous behavior like for the simulated data. They exposed different variability in time, but for all of them a systematic fluctuation was observed before the occurrence of the Düzce earthquake. Our analysis revealed that although fractal coefficients could be applied to measure earthquake clustering, they should be used with caution, trying to figure out the best coefficient for a certain data set.

Key words: fractals, Monte Carlo simulation, İzmit earthquake, correlation integral, capacity dimension.

1. INTRODUCTION

The analysis of earthquake spatial distribution can provide information for different aspects of the seismic process. Firstly, it throws light on the seismotectonic settings of a region and helps to develop new tectonic hypotheses (Makropoulos and Burton 1984). Also, earthquake spatial models represent an essential input in seismic hazard analysis (Todorovska *et al.* 1995).

While conventional analysis of earthquake spatial distribution has been the purpose of many studies (Kagan and Knopoff 1980, Kagan 1981a, b; 2007, Ben-Zion and Sammis 2003, Karakostas and Papadimitriou 2010), it is a comparatively new approach to examine hypocenter or epicenter distributions as fractal objects. In fact, even a brief inspection of seismological datasets manifests that earthquake occurrences reveal scale-invariant or fractal features in the time, spatial and energy domain (Kagan 1981a, b; Mandelbrot 1982, Telesca *et al.* 2004). Strong events occur rarely in a region, leading to poor statistics and it is important to know whether self-similarity of the seismic process is observed at different scales, because there are numerous data for weaker shocks.

When considering fractal features of seismicity, we may start from Mandelbrot (1977, 1982), who developed the concepts of fractal geometry and fractal dimension, and applied them to the description of many natural features, including fault and earthquake distribution. Two possible models may result in fractal features of earthquake distributions. The first model assumes that spatial fractality is a consequence of faults' fractal distribution, because each earthquake is characteristic of the fault on which it occurs. The second one assumes that each fault has a fractal distribution of earthquakes. Observations strongly support the first hypothesis. Generally, a simple definition for a fractal is a "shape made of parts similar to the whole in some way" (Feder 1989). This pure form of self-similarity, however, is rarely observed in nature and therefore a statistical form of self-similarity is defined. In other words, if an object (curve, surface or point field) is examined at any scale, it will resemble the whole in a statistical sense. This is the way fractality is being considered in seismology, too.

The analysis of seismic events spatial distribution by evaluating their fractal coefficients provides some important advantages. One of them is the simple way to quantify scale-invariant distributions of complex objects or phenomena by a small number of parameters. Also, it is becoming evident that the applicability of fractal distributions to seismological problems could have a more fundamental basis, helping to understand the properties of the underlying geological processes, for which chaotic behavior could turn to be an essential feature. Fractal analysis, however, is associated with certain problems arising from the fact that there is no clarity about the genesis of

seismicity fractal properties. It is considered that the concept of self-organized criticality (SOC) is relevant for explaining the processes underlying fractal properties of earthquakes. Seismic events are part of the crust relaxation mechanism. The crust is submitted to inhomogeneous increasing stresses accumulating at seismic faults. The SOC concept then suggests that earthquakes in turn organize the crust both at the spatial and temporal levels (Sornette and Sornette 1989).

Except for these quite general ideas, however, there is no detailed theory to explain the processes leading to fractal features of earthquake epicenter distribution, which hinders the interpretation of the coefficients values. Kagan (2007) reveals that practically any value for the correlation dimension can be obtained if there are many errors and inhomogeneities in observational data. What is more, there is a number of different fractal coefficients which measure various clustering patterns, and it is difficult to choose the right unless one knows the generating mechanism of the earthquake clusters. Delsanto *et al.* (2003) identify eight different effective fractal dimensions and Lasocki and De Luca (1998) find out that some fractal coefficients display different behavior to one and the same data set.

The aforementioned results motivated us to conduct this study with the purpose to analyze the fractal coefficients sensitivity on different sets of simulated and real earthquake spatial data. The main purpose is to verify if different coefficients exhibit similar behavior, firstly, on simulated data, whose properties are known to us, and secondly, on real earthquake data. The simulated data sets were generated by the realization of the Soneira and Peebles hierarchical model (Soneira and Peebles 1978), applied widely to study galaxy distributions. The model seems appropriate for modeling the spatial distribution of earthquakes, because its internal hierarchical structure is similar to the hypocenter clustering structure where earthquakes occur on a hierarchical system of faults. Real data covers the aftershock sequence epicenters after the strong $M_w = 7.4$ İzmit earthquake in western Turkey, occurred on 17 August 1999, on the North Anatolian fault.

2. FRACTAL COEFFICIENTS FOR SPATIAL ANALYSIS

Among the different coefficients being used to examine the fractal features of earthquake spatial distribution, we chose the box-counting method, the number-radius method and the correlation dimension approach, which are among the most widely used techniques to perform fractal analysis.

The box-counting method provides an estimate of the ***box-counting dimension***, also called ***capacity dimension***, defined as follows: For any $r > 0$, let $N(r)$ be the minimum number of *n*-dimensional boxes (cubes, squares) of side-length *r* needed to cover the object (the point field). If there is a number

D_c so that $N(r) \sim 1/r^{D_c}$ as $r \to 0$, then it is said that the box-counting dimension of the field is D_c. It has to be noted that the box-counting dimension is D_c if and only if there is some positive constant k so that

$$\lim_{r \to 0} \frac{N(r)}{1/r^{D_c}} = k \ . \tag{1}$$

Since both sides of the equation above are positive, it will still hold if we take the logarithm of both sides to obtain

$$\lim_{r \to 0} \left(\ln N(r) + D_c \ln r \right) = \ln k \tag{2}$$

and solving for D_c

$$D_c = \lim_{r \to 0} \frac{\ln k - \ln N(r)}{\ln r} = -\lim_{r \to 0} \frac{\ln N(r)}{\ln r} \ . \tag{3}$$

Note that the $\ln k$ term drops out, because it is constant while the denominator becomes infinite as $r \to 0$. Also, since $0 < r < 1$, ln is negative, so D_c is positive as one would expect. If the point field has a statistical fractal character, the $\log N(r)$ *versus* $\log (1/r)$ relation can be approximated with the straight line in a certain range of r. The slope of the line defines the estimate of the capacity dimension value (Turcotte 1997).

The number-radius method is used to evaluate the cluster dimension D_b. This method refers to a specific point known as the counting center and gives the law of distribution of the occupied points around this point. If by (x_i, y_i) we denote the position of epicenter i, then the counting center is located in the center of mass of the epicenter distribution, defined by the pair of expected values of the random variables X and Y. A circle is drawn around this point, and the radius r is gradually increased. At each step, the total number of occupied points $N(\varepsilon)$ inside the circle is counted. The slope of linear approximation of the $\log N(r)$ *versus* $\log (r)$ relation produces the estimate of cluster dimension (Xie 1993).

Another approach to perform fractal analysis of a points' field is to use total counts of point pairs as they depend on their distance. The so-called correlation dimension estimate D_2 may be defined through the two point correlation integral $C(r)$, presented by

$$C(r) = \frac{1}{N^2} \sum_{i \neq j} H(r - L) \ . \tag{4}$$

Here N is the total number of points, $L = \left\| \bar{x}_i - \bar{x}_j \right\|$ is the distance between locations of i and j points, and $H(z)$ is the Heviside function, which equals

1.0 when $z \geq 0$ and 0.0 when $z < 0$. For a set of points which demonstrates scale-invariance, $C(r)$ must follow a power law

$$\lim_{r \to 0} C(r) \propto r^{D_2} .$$ (5)

Then the simplest estimate of D_2 is a straight line in a loglog plot $C(r)$ *versus* r (Grassberger and Procaccia 1983).

$$D_2 = \lim_{r \to 0} \frac{\log C(r)}{\log r} ,$$ (6)

which reveals that D_2 is estimated by the slope of the straight line relating both variables.

All of the above dimensions have their advantages and disadvantages. By definition, the number-radius method measures clustering, referring to a specific point and thus it seems suitable for the analysis of the main shock-aftershocks data sets. The box-counting method is a purely metric concept, appropriate for geometric characterization and it may be applied for systems of great complexity. The algorithm treats all cubes needed to cover an object or distribution with no difference. This is a minus of the method, because it implies to construct and check the emptiness of all boxes at each resolution. But in the box-counting method the problem of homogeneity, which is essential for the correlation dimension estimate, can be avoided (Murdzek 2007). Another advantage of the box-counting method is that it uses a single set of measured coordinates in calculus, since it takes into account only whether or not an epicenter is contained by a given box. For the correlation integral there is a contribution of two sets of measured coordinates, and from this point of view, the correlation function means additional errors.

3. DATA SIMULATION AND ANALYSIS

The three fractal coefficients, defined above, were applied in the present paper to analyze fractal features of simulated and real data. We first analyzed the dependence of the defined fractal coefficients on different sets of simulated data. When selecting a simulation procedure it must be considered that earthquakes can be regarded as realizations of a random process. Usually the term process first brings to mind a time series, but it can be generalized to any suitable parameter space. If the space is a spatial volume it can be referred to as a spatial random field. Different algorithms can be applied to simulate such a field – the Poisson process, the Segment Cox process and the Matern process (Pons-Bordería *et al.* 2003), *etc*. For our simulation we chose the so-called Soneira–Peebles model (Soneira and Peebles 1978), which is widely used for galaxy distribution analysis. The choice was made because

this is one of the few analytic self-similar models for which the two-point correlation function can be analytically evaluated. Also, the simulation algorithm is such that it follows some features of real hierarchical patterns of earthquake clustering, like the one depicted by the epidemic type aftershock sequence (ETAS) model for earthquake occurrence (Ogata 1998). The Soneira–Peebles model is a fractal-like point distribution involving hierarchically embedded levels of ever larger point density. The model is controlled through three parameters, η, L, and λ. A realization of this model is generated following the next steps:

  1. A level-0 sphere of radius R is generated as a starting point.

  2. η level-1 spheres are placed in this sphere with radius $R = R/\lambda$ and $\lambda > 1$. The new spheres are placed at a random position inside the level-0 circle, such that their centers fall inside the original level-0 sphere.

  3. Then one places η level-2 spheres of radius R/λ^2 within each of these η level-1 spheres.

  4. The process is repeated until a total of η^L level-L spheres of radius R/λ^L are generated. A point is placed at the center of each of these level-L spheres.

If this recursive process is repeated indefinitely, a homogeneous fractal is obtained. In any stage of the construction, each sphere is similar to whichever of the others and looks like the whole set under the appropriate magnification. The truncated set of points at level L is a fractal set. If an object of size R is formed by $\eta^{D_{th}}$ similar objects of size R/λ, the similarity dimension is D_{th} and it depends on the parameters η and λ in the following way (Paredes *et al.* 1995):

$$D_{th} = \frac{\log \eta}{\log \lambda} . \tag{7}$$

For the Soneira–Peebles model, the two point correlation function can be theoretically evaluated (Paredes *et al.* 1995) and in a 3D space it is presented by $\xi(r) \propto r^{-\gamma}$, where

$$\gamma = 3 - \left(\frac{\log \eta}{\log \lambda} \right) \quad \text{for} \quad \frac{R}{\lambda^{L-1}} \leq r \leq R . \tag{8}$$

In our case we considered a 2D space, utilizing circles instead of spheres and obtained η^L points after each simulation, which represented epicenters.

For a plane, Eq. (8) turns to $\gamma = 2 - D_c$. We chose $\eta = 2$ and $L = 13$ to produce the simulations and by changing λ from 2 to 1.41 we generated data sets with fractal dimensions D_{th} from 1.0 to 2.0 (see Table 1 and Fig. 1).

For each value of λ we generated a number of 30 data sets and calculated the corresponding coefficients values. In Figure 1 we have demonstrated

a) $D_{th} = 1.0$ b) $D_{th} = 1.1$ c) $D_{th} = 1.2$

d) $D_{th} = 1.3$ e) $D_{th} = 1.4$ f) $D_{th} = 1.5$

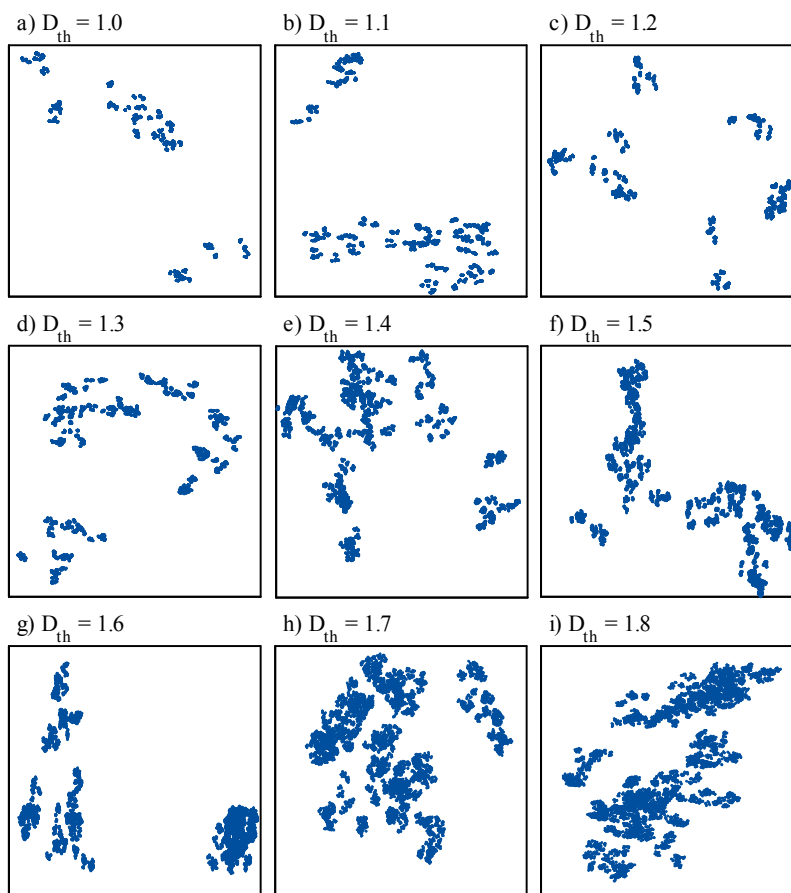g) $D_{th} = 1.6$ h) $D_{th} = 1.7$ i) $D_{th} = 1.8$

Fig. 1. Examples of data sets simulated after the Soneira–Peebles model for different values of the similarity dimension D_{th} (see Eq. (7)) in the range 1.0-1.8. Each data set contains 8192 points. One can see that decreased clustering level is related to bigger values of D_{th}.

Table 1

Values of λ and corresponding fractal coefficients values (see Eq. (7)):
D_{th} – values calculated after Eq. (7), D_c – capacity dimension,
D_b – cluster dimension, D_2 – correlation dimension

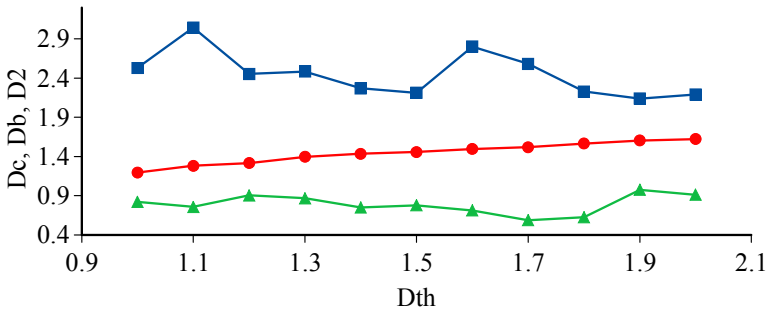| λ	2.00	1.88	1.78	1.70	1.64	1.59	1.54	1.50	1.47	1.44	1.41
D_{th}	1.00	1.10	1.20	1.30	1.40	1.50	1.60	1.70	1.80	1.90	2.00
D_c	1.19	1.28	1.31	1.39	1.43	1.45	1.49	1.51	1.56	1.60	1.62
D_b	2.52	3.04	2.45	2.48	2.27	2.21	2.80	2.58	2.22	2.14	2.19
D_2	0.82	0.76	0.90	0.87	0.75	0.77	0.71	0.59	0.62	0.97	0.91

Fig. 2. Values of the fractal coefficients D_c (circles), D_b (squares), D_2 (triangles), calculated for simulated data sets. Simulation was performed after the Soneira–Peebles model for different values of the similarity dimension D_{th} (see Eq. (7)) in the range 1.0-2.0. Different coefficients do not perform similarly on the diverse simulated data.

examples of data sets for different values of D_{th} in the range 1.0-1.8. Each data set contains 8192 points. One can see that decreased clustering level is related to bigger values of D_{th}.

After that, the average coefficients values were estimated for the 30 data sets generated for each value of λ, and these average values are presented in Table 1 and Fig. 2.

Generally, one would expect that the different coefficients (D_c, D_b, and D_2), being measures of clustering, would strongly correlate with the similarity dimension D_{th} used in the simulation procedure. However, as can be seen in Fig. 2, the coefficients reveal diverse sensitivity to the various simulated data sets. All three dimensions cover different value ranges (lines in Fig. 2 do not cross each other). In fact, only the capacity dimension (circles in Fig. 2) exhibited systematic increase with the increase of D_{th} (positive correlation, $r = 0.97$), but the range in which it changes is smaller than the one of D_{th}. The other two coefficients, the clustering dimension and the correlation dimension, could not correctly identify the direction in which clustering level changed. The correlation coefficient stayed nearly constant (triangles in Fig. 2) and the number-radius dimension even revealed a little decrease with the increase of D_{th} (squares in Fig. 2).

In a similar study, Lasocki and De Luca (1998) obtained results on simulated data, which reveal that the three fractal dimensions demonstrated different sensitivity, too, as in our study, but there the D_b coefficient turned to be most sensitive, while D_c did not change its behavior with various sets of data. Most probably, their results are due to the different simulation procedure which they used, leading to dissimilar type of data clustering.

4.   REAL DATA ANALYSIS

The 1999 İzmit earthquake was one of the strongest earthquakes to occur in northwestern Turkey during the past 100 years. It took place on 17 August 1999 on the North Anatolian Fault (NAF) with magnitude $M_w = 7.4$. The shock caused more than 18 000 casualties and enormous economic losses for Turkey. The epicenter was located near İzmit, Turkey (40.75°N, 29.86°E) and the shock generated a rupture extended over 150 km. The NAF is one of the most seismically active regions of the world and the tectonic processes along this zone accommodate the westward motion of Turkey relative to Eurasia by right-lateral shear (Daniel *et al.* 2006). The fault experienced a number of $M > 7.0$ events during the 20th century. On 12 November 1999, three months after the first strong event, a $M_w = 7.2$ earthquake took place eastward, in the vicinity of Düzce, Turkey (40.76°N, 31.16°E). Both strong events were followed by numerous series of aftershocks. This sequence is being extensively studied by many researchers as it is expected that the next strong earthquake on the NAF could occur to the west of the İzmit event source zone, in the Marmara Sea region (Hubert-Ferrari *et al.* 2000). Special attention is paid to the spatio-temporal distribution of seismicity before the strong event and during the aftershock sequence. Öncel *et al.* (1995) examined the temporal variations of the seismicity fractal properties in the western part of the NAF, while Öncel and Wilson (2007) analyzed the fractal dimensions anomalous variations of the seismicity preceding the 1999 İzmit event.

The importance to increase knowledge on the seismicity of this region motivated us to analyze the fractal features of the İzmit-Düzce aftershocks. Their spatial distribution is relevant to seismic hazard in the region and an advantage is that good quality spatial data is compiled for the sequence, which is necessary for fractal analysis.

The aftershock catalog was compiled by data from the National Earthquake Monitoring Center (NEMC) of Turkey and by personal communication with Dr. Dogan Kalafat from Kandilli Observatory and Earthquake Research Institute in Turkey. We executed initial analysis of the data by ZMAP6.0 (Wiemer 2001) and determined a lower magnitude cut-off of $M_w = 3.0$, above which the catalog should be complete. A number of $N = 1427$ events above this limit entered the catalog for the period between the main 17 August shock until the end of December 2000 (see Fig. 3a). Their epicenter spatial distribution was analyzed for three magnitude ranges and the fractal coefficients values are presented in Table 2. As can be seen, the three fractal coefficients exhibit different behavior to the increase of the magnitude lower cut-off. The capacity dimension D_c decreases with the increase of the cut-off, which can be regarded as a proof of stronger clustering. This can
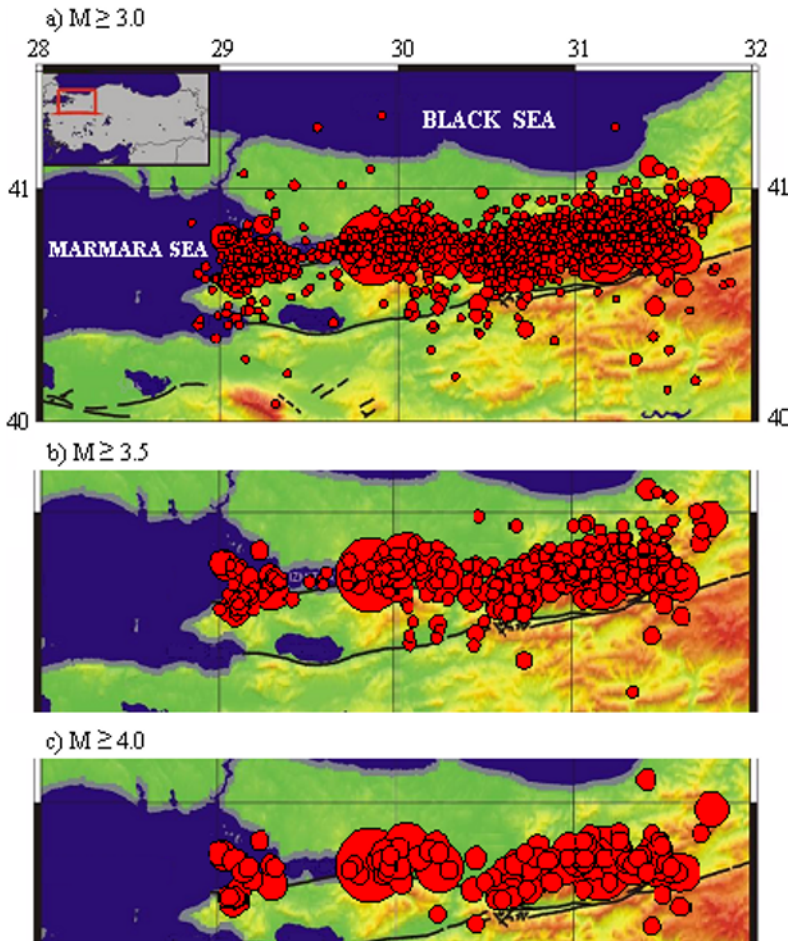
Fig. 3. Epicenter maps of the İzmit–Düzce aftershock sequence for three lower magnitude cut-offs: (a) $M_w \geq 3.0$, (b) $M_w \geq 3.5$, and (c) $M_w \geq 4.0$. It can be seen that stronger aftershocks are more clustered to the main shocks fault. Colour version of this figure is available in electronic edition only.

Table 2

Fractal coefficients for three different magnitude cut-offs
of the İzmit–Düzce aftershock sequence

Fractal coefficient	$M_w \geq 3.0$	$M_w \geq 3.5$	$M_w \geq 4.0$
D_c	1.56	1.42	1.32
D_b	1.14	1.17	1.07
D_2	0.74	0.83	0.83

be traced by visual inspection of Fig. 3, on which we have plotted the epicenters for the three different magnitude ranges. These results can be interpreted as a verification that locations of stronger events in an aftershock sequence are less scattered and closer to the main earthquake rupture.

The changes of the cluster dimension D_b are not so significant but the coefficient value for the biggest magnitude cut-off is again smaller (Table 2). It is the opposite for the correlation dimension D_2, where we observe a small increase of the estimated value. On the whole, as for the simulated data, the different coefficients do not reveal correlated behavior, the box-counting dimension D_c being most sensitive to the different data sets.

We also traced how the coefficients changed in time by analyzing subsequent subsamples of the aftershock data. The results are presented in Fig. 4, where the dashed vertical line marks the occurrence of the second strong shock near Düzce. One can again find discrepancies between changes of the different coefficients and it is interesting to follow the coefficients variations in time. Although there are dissimilarities, all coefficients reveal a general decrease before the Düzce earthquake. Its occurrence is marked by abrupt changes in all three coefficients. The capacity dimension D_c quickly gets less, which could be an indication that the sequence after the Düzce earth-

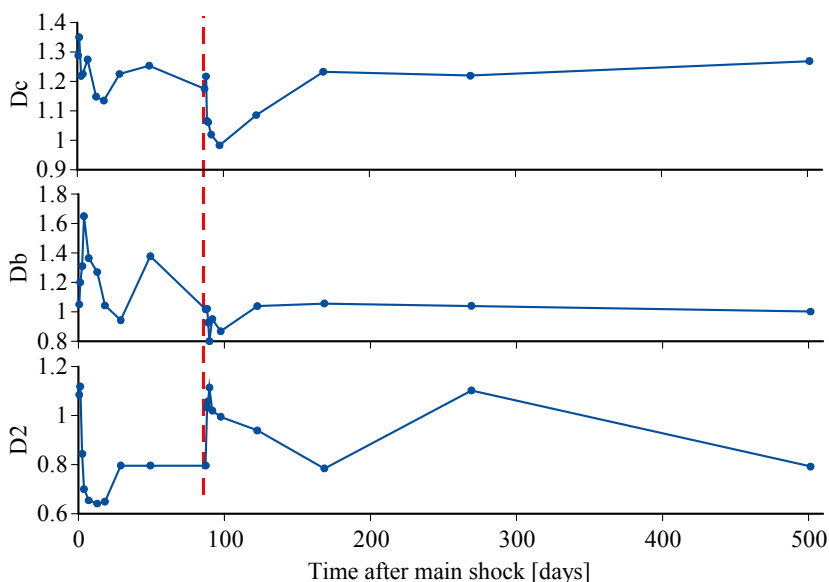

Fig. 4. Values of the fractal coefficients D_c, D_b, and D_2, calculated for subsequent subsamples of the İzmit-Düzce aftershock sequence. The time period ranges from the İzmit earthquake occurrence up to the end of December 2000. Dashed vertical line points the befall of the Düzce strong event, which is followed by abrupt changes in all three coefficients.

quake starts with the events that are highly clustered in space. A similar behavior can be observed for the cluster dimension D_b but the changes here are not so clear. On the opposite, the Düzce earthquake is followed by a significant increase in the value of the correlation dimension D_2. The fact that all three fractal dimensions decrease before the Düzce earthquake, can be considered as precursory behavior, but in this paper we consider it only in a retrospective manner. The abrupt change of the fractal coefficients, marked by the Düzce earthquake, reveals that it is an event strong enough to cause significant stress field variations, leading to an alteration in the type of clustering. An important question here is whether the Düzce earthquake can be considered as the strongest aftershock of the İzmit strong event or it is a second main shock, causing its own aftershock activity (Seeber *et al.* 2000). The results, revealed in Fig. 4, strongly support the second alternative. Not only we have a drop of the coefficients values before the Düzce event, but the value ranges before and after the shock for all three dimensions are different and do not overlap for a period of 30 to 50 days. We suppose this comes to support that the Düzce earthquake should be taken as a separate main shock, occurring on a different fault segment and causing a different aftershock clustering pattern.

5. CONCLUSIONS

The results from the fractal analysis of simulated data, using the three most widely applied fractal dimensions, D_c, D_b, and D_2, leads to the conclusion that not all fractal coefficients can capture the specified changes in the level of clustering. While one could expect that the different coefficients would correlate with the similarity dimension D_{th}, which controls data clustering, it turned out that only the capacity dimension D_c was sensitive to changes in the similarity dimension and best captured the alteration in clustering level. The other two dimensions, the cluster dimension D_b and the correlation dimension D_2, hardly reacted to clustering variations and the ranges of their values were quite different from the one of D_c. From these results we can deduce that fractal analysis should be performed, if data allows it, after selecting the most appropriate fractal coefficient for a certain dataset (see Lasocki and De Luca 1998, for similar results). The very values of the fractal coefficients should be considered with caution, following their changes as more informative of the clustering level variations. On the whole, this first part of our experiment to follow clustering variations by different fractal dimensions was only partially successful.

The second part of our experiment was to analyze the temporal evolution of İzmit aftershocks spatial distribution by following the fractal dimensions changes in time. We estimated the same fractal coefficients. On the one hand, the coefficients showed different sensitivity to real data, as was the

case for simulated data. In the real data case, however, all three coefficients revealed a general decrease before the Düzce earthquake, which at least shows that the clustering pattern is different from the hierarchical Soneira–Peebles model. In fact, this behavior could be considered as precursory, but only in a retrospective way, because in a real time case fractal dimension decrease alone is not enough to define a precursor. The occurrence of the Düzce earthquake leads to a change in all three dimensions. The capacity co-efficient is most sensitive and it is worth focusing our attention on the different value ranges it has before and after this event. One could speculate on this result as an indication that the İzmit and Düzce strong events caused different types of aftershock clustering after them.

The results from our study, both for simulated and for real data, revealed that fractal dimensions, being uniparameter characteristics of point distribution geometry, are difficult for geotectonic interpretation, but they are suitable to follow temporal changes of the clustering level. These results can also be used to discriminate between the occurrence of a new main seismic event in a region and the continuation of a previous strong earthquake sequence.

R e f e r e n c e s

Ben-Zion, Y., and C.G. Sammis (2003), Characterization of fault zones, *Pure Appl. Geophys.* **160**, 3-4, 677-715, DOI: 10.1007/PL00012554.

Daniel, G., D. Marsan, and M. Bouchon (2006), Perturbation of the İzmit earthquake aftershock decaying activity following the 1999 M_w 7.2 Düzce, Turkey, earthquake, *J. Geophys. Res.* **111**, B05310, DOI: 10.1029/2005JB003978.

Delsanto, P.P., D. Iordache, and Ş. Puşcă (2003), Study of the correlations between different effective fractal dimensions used for fracture parameters descriptions. **In:** *Proc. First South-East European Symp. Interdisciplinary Approaches in Fractal Analysis, 7-10 May 2003, Bucharest, Romania.*

Feder, J. (1989), Fractals, *Physics Today* **42**, 9, 90, DOI: 10.1063/1.2811154.

Grassberger, P., and I. Procaccia (1983), Characterization of strange attractors, *Phys. Rev. Lett.* **50**, 5, 346-349, DOI: 10.1103/PhysRevLett.50.346.

Hubert-Ferrari, A., A. Barka, E. Jacques, S.S. Nalbant, B. Meyer, R. Armijo, P. Tapponnier, and G.C.P. King (2000), Seismic hazard in the Marmara Sea

region following the 17 August 1999 İzmit earthquake, *Nature* **404**, 269-273, DOI: 10.1038/35005054.

Kagan, Y.Y. (1981a), Spatial distribution of earthquakes: the three-point moment function, *Geophys. J. Roy. Astron. Soc.* **67**, 3, 697-717, DOI: 10.1111/j.1365-246X.1981.tb06948.x.

Kagan, Y.Y. (1981b), Spatial distribution of earthquakes: the four-point moment function, *Geophys. J. Roy. Astron. Soc.* **67**, 3, 719-733, DOI: 10.1111/j.1365-246X.1981.tb06949.x.

Kagan, Y.Y. (2007), Earthquake spatial distribution: the correlation dimension, *Geophys. J. Int.* **168**, 1175-1194, DOI: 10.1111/j.1365-246X.2006.03251.x.

Kagan, Y.Y., and L. Knopoff (1980), Spatial distribution of earthquakes: the two-point correlation function, *Geophys. J. Roy. Astron. Soc.* **62**, 2, 303-320, DOI: 10.1111/j.1365-246X.1980.tb04857.

Karakostas, V.G., and E.E. Papadimitriou (2010), Fault complexity associated with the 14 August 2003 Mw6.2 Lefkada, Greece, aftershock sequence, *Acta Geophys.* **58**, 5, 838-854, DOI: 10.2478/s11600-010-0009-6.

Lasocki, S., and L. De Luca (1998), Monte Carlo studies of relations between fractal dimensions in monofractal data sets, *Pure Appl. Geophys.* **152**, 2, 213-220, DOI: 10.1007/s000240050151.

Makropoulos, K.C., and P.W. Burton (1984), Greek tectonics and seismicity, *Tectonophysics* **106**, 3-4, 275-304, DOI: 10.1016/0040-1951(84)90181-1.

Mandelbrot, B. (1977), *Fractals: Form, Chance and Dimension*, Freeman and Co., San Francisco.

Mandelbrot, B. (1982), *The Fractal Geometry of Nature*, Freeman and Co., New York.

Murdzek, R. (2007), The box-counting method in the large scale structure of the universe, *Rom. J. Phys.* **52**, 1-2, 149-154.

Ogata, Y. (1998), Space-time point-process models for earthquake occurrences, *Ann. Inst. Statist. Math.* **50**, 2, 379-402, DOI: 10.1023/A:1003403601725.

Öncel, A.O., and T. Wilson (2007), Anomalous seismicity preceding the 1999 İzmit event, NW Turkey, *Geophys. J. Int.* **169**, 1, 259-270, DOI: 10.1111/j.1365-246X.2006.03298.x.

Öncel, A.O., Ö. Alptekin, and I. Main (1995), Temporal variations of the fractal properties of seismicity in the western part of the north Anatolian fault zone: possible artefacts due to improvements in station coverage, *Nonlin. Processes Geophys.* **2**, 3/4, 147-157, DOI: 10.5194/npg-2-147-1995.

Paredes, S., B.J.T. Jones, and V.J. Martínez (1995), The clustering of galaxy clusters: synthetic distributions and the correlation function amplitude, *Mon. Not. R. Astron. Soc.* **276**, 1116-1130.

Pons-Bordería, M.J., V. Martínez, B. López-Martí, and S. Paredes (2003), Correlations at large scale. **In:** E.D. Feigelson and G. Jogesh Babu (eds.), *Statistical Challenges in Astronomy*, Springer-Verlag, New York, 475-476.

Seeber, L., J.G. Armbruster, N. Ozer, M. Aktar, S. Baris, D. Okaya, Y. Ben-Zion, and N. Field (2000), The 1999 earthquake sequence along the North Anatolian transform fault at the juncture between the two main ruptures. **In:** A. Barka, O. Kozaci, S. Akyuz, and E. Altunel (eds.), *The 1999 İzmit and Düzce Earthquakes: Preliminary Results*, Istanbul Technical University, Istanbul.

Soneira, R.M., and P.J.E. Peebles (1978), A computer model universe – Simulation of the nature of the galaxy distribution in the Lick catalog, *Astron. J.* **83**, 845-857, DOI: 10.1086/112268.

Sornette, A., and D. Sornette (1989), Self-organized criticality and earthquakes, *Europhys. Lett.* **9**, 3, 197-202, DOI: 10.1209/0295-5075/9/3/002.

Telesca, L., V. Lapenna, and M. Macchiato (2004), Mono- and multi-fractal investigation of scaling properties in temporal patterns of seismic sequences, *Chaos Solitons Fract.* **19**, 1, 1-15, DOI: 10.1016/S0960-0779(03)00188-7.

Todorovska, M.I., I.D. Gupta, V.K. Gupta, V.W. Lee, and M.D. Trifunac (1995), Selected topics in probabilistic seismic hazard analysis, Report No. CE 95-08, Dept. of Civil Eng., University of Southern California, Los Angeles, U.S.A.

Turcotte, D.L. (1997), *Fractals and Chaos in Geology and Geophysics*, 2nd ed., Cambridge University Press, Cambridge.

Wiemer, S. (2001), A software package to analyze seismicity: ZMAP, *Seismol. Res. Lett.* **72**, 3, 373-382, DOI: 10.1785/gssrl.72.3.373.

Xie, H. (1993), *Fractals in Rock Mechanics*, Balkema Publishers, Rotterdam.

Scaling Features of Ambient Noise at Different Levels of Local Seismic Activity: A Case Study for the Oni Seismic Station

Teimuraz MATCHARASHVILI[1,2], Tamaz CHELIDZE[1],
Zurab JAVAKHISHVILI[2], Nato JORJIASHVILI[2], and Natalia ZHUKOVA[1]

[1]M. Nodia Institute of Geophysics, Tbilisi, Georgia
e-mail: Matcharashvili@gtu.ge (corresponding author)
[2]Ilia State University, Tbilisi, Georgia

A b s t r a c t

Investigation of dynamical features of ambient seismic noise is one of the important scientific and practical research challenges. We investigated scaling features of the ambient noises at the Oni seismic station, Georgia, using detrended fluctuation analysis method. Data from this seismic station, located in the epicentral zone of Oni $M6.0$, 2009, earthquake, were selected to include time periods with different levels of local seismic activity.

It was shown that the investigated ambient noise is persistent long-range correlated at calm seismic conditions in the absence of earthquakes. Fluctuation features of the analyzed ambient noises were affected by local earthquakes, while remote seismic activity caused just slight quantitative changes. Processes related to the preparation of a strong local earthquake may cause quantifiable changes in fluctuation features of ambient noises. Fluctuation features of seismic noise for periods of increased local seismic activity cease to be long-range correlated and appear to become a complicated mixture of random and correlated behaviours.

Key words: ambient noise, earthquake, dynamics, scaling.

1. INTRODUCTION

Earthquakes (EQs) are regarded as one of the most dramatic phenomena occurring in nature, causing enormous human and economic loses. A multitude of underground events and fluctuations of the Earth's surface occur annually as a result of complex spatio-temporal phenomena related to the convective motion in the mantle, provoking relative motion of the faults bordering the tectonic plates. This leads to fast emission of energy propagating over long distances in the form of elastic seismic waves (Kanamori and Brodsky 2001). Thousands of seismic waves are worldwide detected by seismographs in the form of vibrations of the Earth's surface and have been collected in seismic data bases.

At the same time, seismic waves are not the only cause for the Earth surface vibrations. Many other factors, ranging from atmospheric pressure variation and ocean waves to human activity, always contribute to the vibrations of the Earth ground (Webb 1998, Yulmetyev *et al.* 2001, SESAME 2004, Correig *et al*. 2007). These vibrations − microseisms or microtremors − representing superposition of waves of different origin are often collectively named the ambient noises.

Because of their diverse origin and complicated spatio-temporal features, the Earth surface vibrations or ambient noise, represent random-like high-dimensional dynamical processes (Yulmetyev *et al.* 2001, 2003, Padhy 2004, Correig *et al*. 2007, Lyubushin 2010, Sobolev *et al.* 2010). Such complicated processes are normally characterized by uniform spectral features and dynamical structure, which are extremely difficult to be quantified.

On the other hand, the seismic signals contributing to the ambient noise are regarded as having more regular dynamical structure comparing to random noise (Padhy 2004, Tabar *et al*. 2006, Manshour *et al*. 2009). This looks quite logical in the light of, as has been established in the last decades, the presence of nonrandom, though high-dimensional dynamical structure in the seismic process – the source of seismic signals (see *e.g.*, Goltz 1997, Lapenna *et al*. 1998, Rundle *et al*. 2000, Matcharashvili *et al*. 2000, Chelidze and Matcharashvili 2007, Matcharashvili and Chelidze 2010). Physically, the presence of nonrandom dynamical structure in the earthquake (EQ) generation processes, and seismic waves accordingly, is related to the processes accompanying stress accumulation and the breakdown of a disordered solid together with concomitant stick-slip movement. Generally speaking, these complex processes, involving cascades of transitions (changes) in wide spatial, temporal and energetic scales are, or can be, in principle detectable. Some of these transitions − precursory changes − preceding or accompanying breakdown and stick-slip movement in disordered solid rocks, have already been observed both at the laboratory and geophysical scales (Kapiris

et al. 2003, Telesca and Lapenna 2006, Karamanos *et al*. 2006, Chelidze *et al*. 2006, Tabar *et al*. 2006, Manshour *et al*. 2009). It is also understandable that, because of the complexity of seismic process, such changes might be of different forms, related to variations in mechanical, chemical, hydrological, electromagnetic, and other processes in the seismic source or peculiarities of wave propagation in rocks, *e.g.*, acoustic or electromagnetic emissions (Karamanos *et al*. 2006, Tabar *et al*. 2006).

At the same time, it should be stressed here that opinions about the researches on the marker changes which may have earthquake predictive value are still controversial. It is not clear what changes, in which characteristics, and to what degree, can be regarded as precursors, or what may be the length of the spatial and time scales over which different precursory anomalous changes may occur and accumulate. At present, there are many pro and contra arguments in these precursory-related discussions. There are also contradictions between supporters of precursory phenomena. Some authors assume that precursory patterns develop at short spatial distances, within few days to weeks before the main shock from the impending large earthquakes, while others claim that precursory anomalies may occur up to decades before it at distances much longer than the length of the main shock rupture (Scholz 1990, Keilis-Borok and Soloviev 2003, Tabar *et al.* 2006).

Notwithstanding all these difficulties, changes in the dynamical features of ambient surface noise, caused by processes related to the earthquake preparation, are by many authors assumed to be quantifiable and are regarded among possible precursors (Padhy 2004, Tabar *et al.* 2006, Sobolev and Lyubushin 2006, Manshour *et al*. 2009, 2010). Moreover, in the context of possible dynamical changes it was suggested that as the final failure in the disordered media is approached, the underlying complexity manifests itself in specific linkages between space and time features. This in turn may lead to producing detectable (precursory) patterns on many scales and the emergence of fractal structures in different accompanying process (Karamanos *et al*. 2006).

In general, the present level of dynamical data analysis enables these changes in dynamical structure of the Earth surface vibrations to be assessed qualitatively and quantitatively. Indeed, in the last years, a lot of interdisciplinary research works have been devoted to the complexity of seismic noises, analysis of their fractal, power law, long memory and many other statistical and dynamical features in order to detect and describe the spatial, temporal and energetic scaling properties of the processes related to earthquake preparation (Yulmetyev *et al*. 2001, Padhy 2004, Tabar *et al*. 2006, Correig *et al*. 2007, Caserta *et al*. 2007).

In the present research, we focus on the fluctuation features of the ambient seismic noise time series using similar concepts. The main goal of this

research was to carry out comparative analysis of scaling features of ambient noise time series in the time periods of increased as well as relatively low local seismic activity on the example of seismic data recorded at Oni seismic station in Georgia. The advantage of specified location was that the Oni station is situated close to the last strongest Caucasian earthquake of $M6.0$, which occurred in September 2009.

The targeted problem on fluctuation features of local seismic noise is of general interest and has a great scientific significance, being related to the recognition of changes in apparently similar signals with different physical origins. The recognition of changes caused by an arrival of seismic signals in the background random noise is of prime importance from scientific and practical points of views. Such analyses of seismic data are often the subject of vivid interests for different purposes, including earthquake forecasting, and numerous methods of data analysis are used (Yulmetyev *et al.* 2001, 2003, Caserta *et al.* 2007).

2. THE DATA USED AND METHODS OF ANALYSIS

The data used in this study are digital seismograms recorded by broad-band permanent station located in Great Caucasus mountains near the town Oni (42.5905°N, 43.4525°E), Georgia (Fig. 1). We investigated all three components of vibrations of the Earth's surface, but mainly focused on time
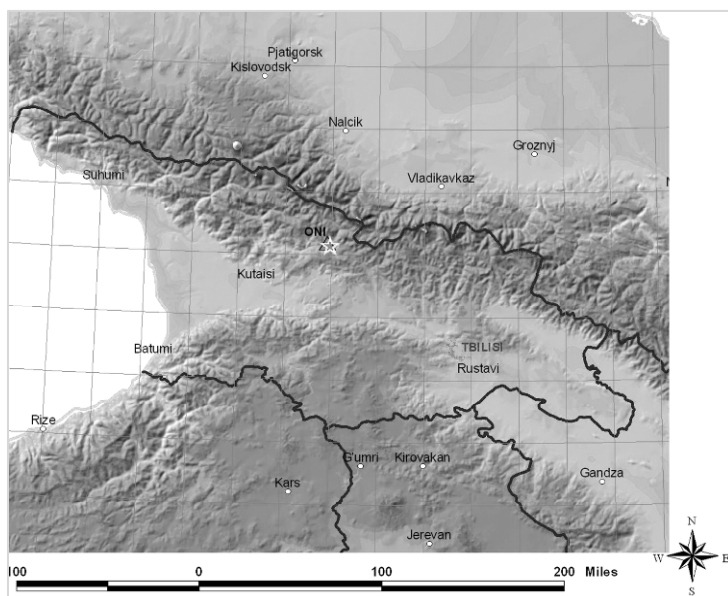

Fig. 1. Map of location of Oni seismic station. By the star, the epicenter of Racha $M6.0$ earthquake is shown.
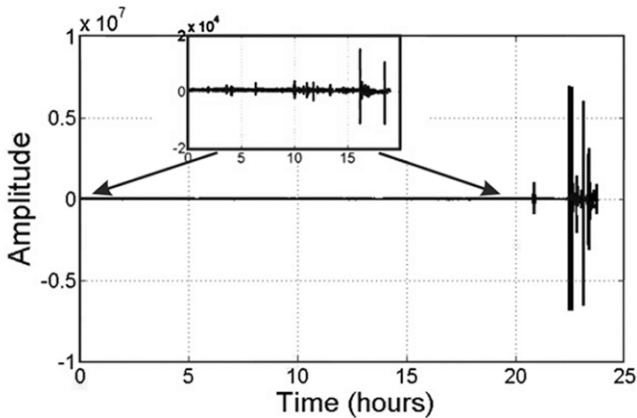
Fig. 2. The ambient noise data record including waveforms of the M6.0 Racha earthquake.

series of the Earth's vertical velocity, V_z (see a typical four-day recording in Fig. 2). The data were recorded at a sampling frequency of 100 Hz with a dynamic range over 140 dB. The station has a flat velocity response from 0.01 to 100 Hz frequency band. The seismograms are corrected for instrument response before the analysis, so as to get the ground velocity. The seismic station Oni is part of seismic network operated by the Ilia State University, Seismic Monitoring Centre of Georgia.

In order to compare scaling characteristics of ambient noise data sets at different levels of local seismic activity, we selected datasets for different time periods. Namely, the four-day recordings preceding the Racha M6.0 earthquake (22:41:35 UTC on 7 September 2009; 42.5727°N, 43.4825°E), the epicenter of which was located at a distance of 4 km from the Oni station, have been investigated at first.

In these recordings, waveforms arriving from two remote earthquakes are visible. Namely, the M4.9 EQ occurred in Afghanistan (09:01:53 UTC on 7 September 2009; 36.45°N, 70.73°E) and the M6.2 EQ occurred in Indonesia (16:12:22 UTC on 7 September 2009; 10.20°N, 110.63°E). Besides, two foreshocks of the Racha earthquake occurred during this four-day period: M1.6 (14:06:35 UTC on 3 September 2009; 42.5414°N, 43.5282°E) and M2.1 (14:17:31 UTC on 3 September 2009; 42.5508°N, 43.528°E). Seismic waveforms from all these events are involved in the analyzed time series. So, ambient fluctuations at Oni station in the considered case were affected by strong and weaker local, as well as by remote seismic activities. The next series of analysis were accomplished on seismic record data sets for the time period in March 2011, when no local seismic activity was detected. At the end of this period, arrivals of waveforms from Japan M9.0

earthquake (05:46:24 UTC on 11 March 2011; 38.322°N, 142.369°E) were recorded by the Oni station. Additionally, seismic records were considered from 23:59 UTC on 21 January 2009 to 19:00 UTC on 22 January 2009, when no local and remote seismic activity was detected by broad-band Oni station. In addition, we selected the period from 18:00 UTC on 20 January 2011 to 16:00 UTC on 21 January 2011. This period can also be regard as locally calm because no seismic activity was detected by broad-band Oni station and epicenter of Vani (Georgia) M5.3 earthquake, located about 100 km from the station (09:17:49 UTC; 41.9458°N, 42.6935°E), occurred 33 h before this time period. Other period considered was from 00:00 to 18:59 UTC on 30 October 2010, when a slight local seismic activity was detected (series of M0.7-M1.6 events occurred in 10 km area around the Oni station) and also waveforms that arrived from M5.2 earthquake, which occurred in Japan (19:06:19 UTC on 30 October 2010; 34.38°N, 141.33°E).

In general, complex systems time series, like ambient noise, exhibit fluctuations on a wide range of time scales, which is often accompanied by the broad amplitude and frequencies distributions. Such fluctuations usually follow scaling laws, which allow characterization of the data and the generating complex system by fractal (or multifractal) scaling exponents. The know- ledge of these scaling exponents is very important because they provide unique information on systems' behavior and may serve as characteristic fingerprints for comparison with other systems and models.

In this research, in order to quantify scaling features of ambient noise, detrended fluctuation analysis (DFA) method has been used (Peng *et al.* 1993a, b; 1995). We selected DFA in order to quantify long-range time-correlations in the investigated ambient noise data sets. Usually DFA is conceived as a method for detrending local variability in a sequence of events, which provides insight into long-term variation features in the complex data sets. This scaling analysis technique provides a simple quantitative parameter (DFA scaling exponent) representing the correlation properties of a time series. As already mentioned, the very important practical advantage of DFA over many other scaling techniques is that it enables the detection of long-range correlations embedded in the time series. Moreover, DFA helps to avoid the spurious detection of apparent long-range correlations that are an artifact of non-stationarity.

In practice, the DFA method consists of three steps (Peng *et al.* 1993a, b). First, the initial time series $x(k)$ (of length N) is integrated and "profile" $Y(i)$ is determined. After this, the resulting series $Y(i)$ is divided into boxes of size n. In each box of length n, local trend, $Y_n(i)$, is calculated. Next, the line points are subtracted from the integrated series $Y(i)$ in each box. The root mean square fluctuation of the integrated and detrended series is calculated as

$$F(n) = \sqrt{\frac{1}{N} \sum_{i=1}^{N} \left[Y(i) - Y_n(i) \right]^2} \; .$$

This process is repeated for different scales (box sizes) to obtain a power law behavior between $F(n)$ and n. When the signal follows the scaling law, a power law behavior for the function $F(n)$ is observed:

$$F(n) \sim n^{\alpha} \; .$$

The scaling exponent α gives information about the long-range power law correlation properties of the signal (Peng *et al.* 1993a, b; 1995, Ivanov *et al.* 2002, Rodriguez *et al.* 2007). Specifically, the scaling exponent $\alpha = 0.5$ corresponds to white noise (noncorrelated signal); when $\alpha < 0.5$, the correlation in the signal is anti-persistent; if $\alpha > 0.5$, the correlation in the signal is persistent. The value $\alpha = 1$ means uniform power law behavior of $1/f$ noise. The value $\alpha = 1.5$, indicating uncorrelated behavior, represents a random-walk type process of Brownian motion. The value $\alpha > 1.5$ corresponds to persistent long-range correlations that may be related to both stochastic and deterministic correlations, and $\alpha < 1.5$ corresponds to anticorrelated behavior.

It may often happen that the correlations of recorded data do not follow the same scaling law for all considered n time scales. In such cases, the function $F(n)$ displays different power-law behaviors and in the double logarithmic plots of the DFA fluctuation function, one or more crossovers between different scaling regimes are observed. These crossover (time) scales separate regimes with different scaling exponents (Peng *et al.* 1995, Ivanov *et al.* 2002, Kantelhardt *et al.* 2002). In practice, the crossover region is defined by the values of n where the function $F(n)$ changes its behavior.

Quantification of the fractal properties through calculation of scaling exponent by the above methods is often used to describe features of complex systems behavior. In the frame of this research, we calculated DFA scaling exponent for consecutive non-overlapping sliding windows of different length. By this method, it was established that the time window of 2 min duration is the most appropriate one, enabling to cover the scaling region of fluctuation curve, indicating at the same time the presence of periodic trends at larger time scales.

3. RESULTS AND DISCUSSION

In Figure 3, an example of a power spectrum of seismic noise data recorded at the Oni station is presented. It is similar to the power spectrums for data sets from other broad-band seismic stations worldwide, with a typical
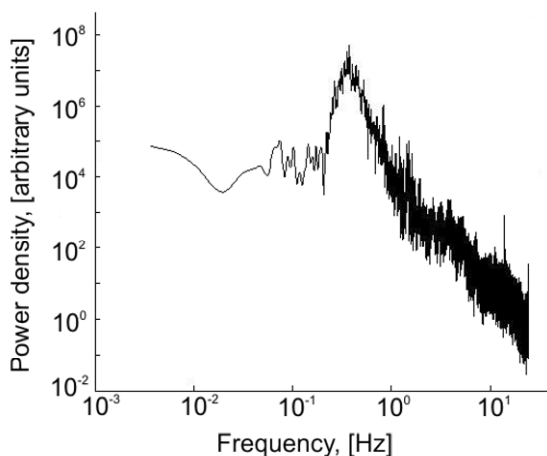
Fig. 3. Typical power spectrum of seismic noise recorded at the Oni station.

location of the largest spectral peak, sometimes regarded as an observational invariant for such data (Correig *et al.* 2007, Ryabov *et al.* 2003).

As already mentioned, we selected data sets recorded at Oni seismic station because it is located very close (4 km) to the epicenter of strong $M6.0$ earthquake that occurred on 7 September 2009 (22:41:35 UTC; 42.5727°N, 43.4825°E). Besides, two foreshocks of the $M6.0$ main shock also occurred within 10-km distance from the Oni station. An analysis of such good-quality data sets from a rural place with low anthropic influences, recorded almost in the centre of the critical zone of a strong earthquake, looked very interesting from the point of view of detecting changes in the ambient noise fluctuation features, which can possibly be related to the local earthquake preparation process.

The total length of the ambient noise data series used in our research, recorded for time periods of different duration (1 to 4 days), were in the range from about 10 to 35 million. We started from the investigation of correlation characteristics of ambient noise data sets by the DFA, a method enabling to avoid effects of nonstationarities in data sets. As already mentioned, DFA is often successfully used for data sets of different origin in different fields, including geophysics and seismology (*e.g.*, Peng *et al.* 1993a, b; 1995, Telesca *et al.* 2005, 2008, Bunde *et al.* 2002, *etc.*). It was most attractive for the purpose of our research that the DFA method enables identifying different states of the dynamical system according to its different scaling behaviors (Peng *et al.* 1995, Hu *et al.* 2001). Thus, it may help to find out whether quantifiable changes in local Earth surface vibrations have occurred prior to the strong earthquake, which can be regarded as related to local seismic activity.
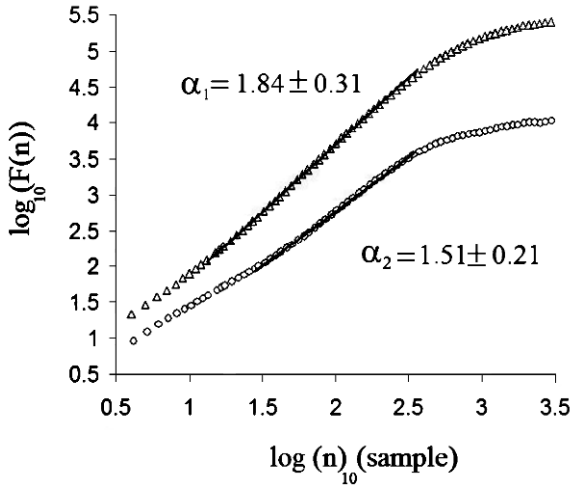
Fig. 4. Averaged DFA fluctuation curves obtained for Z-components of seismic noise records at the Oni station. The lower curve corresponds to the period covering 72 h before and 20 h after the 2009 Racha M6.0 EQ, including foreshocks, as well as the arrival of waveforms from remote events and aftershocks. The upper curve corresponds to periods of 48 h before the arrival of waveforms from remote Japan M9.0 EQ and 10 h after. Curves are shifted along the y axis for clarity.

In Figure 4, DFA plot of averaged $\log F(n)$ *versus* $\log n$ relation calculated for ambient noise data recorded at the Oni station is presented. Calculations have been carried out for consecutive 12 000 sample data length non-overlapping (2 min) windows of ambient seismic noise of the Z-component records. The lower curve corresponds to time period of increased local seismic activity around the Oni station and includes seismic waveforms from foreshock, main shock, and aftershocks of the Racha M6.0 earthquake as well as wavetrains from remote Afghanistan M4.9 and Indonesia M6.2 earthquakes (see the methods section). The upper curve corresponds to time period of low local seismic activity and includes wavetrains from devastating M9.0 earthquake that occurred in Japan in March 2011. According to Fig. 4, averaged $F(n)$ *versus* n relation, for both time series considered, looks generally similar, though slopes of scaling linear parts of curves are different. Also, it is noticeable that the linear scaling part of fluctuation curves, indicating the power law $F(n)$ *versus* n relation, is longer for data sets recorded at a seismically quiet period around the Oni station in March 2011 comparing to fluctuation curve of seismic noise in September 2009, when the M6.0 earthquake occurred. We also see in Fig. 4 the crossover points separating regimes of ambient noise vibrations with different scaling characteristics. Crossover points' locations are not coinciding for these data sets because of

the above-mentioned different lengths of fluctuation function scaling regions. At low frequencies, the crossover time scales are about 3 s in both cases. In the high frequency range, the crossover time scale is 0.3 s for the period when the 2009 Oni M6.0 earthquake occurred. At the same time, for three-day long data set recorded in March 2011, a crossover at higher frequencies is hardly identifiable and seems to be at about 0.1 s.

Next, in order not to be restricted by the results of averaged slopes and to better compare scaling properties of complicated ambient noise data sets for certain time periods, we performed additional distributional analysis of DFA scaling exponents. Specifically, for each 2 min windows, a scaling region of $\log F(n)$ *versus* n relation was identified and the slope was calculated. In Figure 5, histograms of these scaling exponents obtained for consecutive windows of the above-mentioned ambient noise data recorded in September 2009 (involving signal from the Racha M6.0 earthquake as well as its fore-shocks and aftershocks) and in March 2011 (involving wavetrains from the Japan M9.0 earthquake) are presented. On the left side of Fig. 5, histograms of scaling exponents calculated for the same time series after shuffling procedure are presented. We see that more than 95% of scaling exponent values for both shuffled data sets are concentrated close to 0.5, corresponding to white noise (the significance of difference between the scaling exponents for original and shuffled data sets was quantified by the method described in
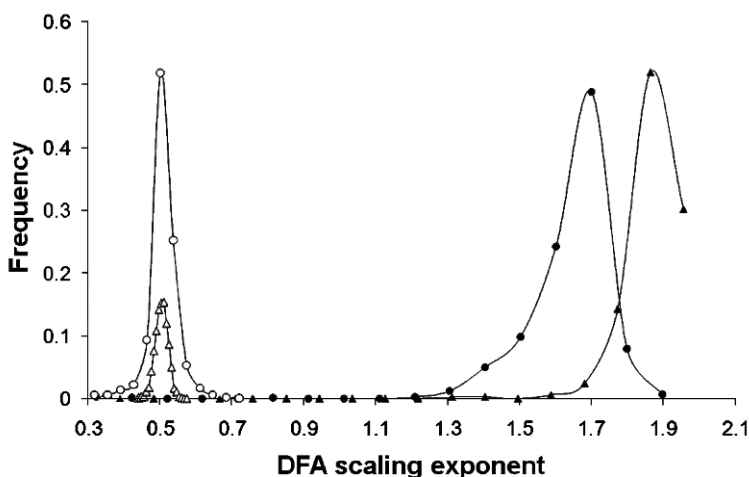
Fig. 5. The histograms of the scaling exponents calculated for consecutive windows of 12 000 sample of seismic noise Z-components data sets recorded at the Oni station. Dark circles correspond to 2836 windows involving the periods prior to the Racha M6.0 EQ, dark triangles correspond to 2100 windows in March 2011 involving the period before arrival of seismic waves from the Japan M9.0 EQ, open circles and triangles correspond to shuffled data sets.

Theiler *et al.* (1992). Contrary to this, original time series, by their DFA scaling exponents, are always much different from the white noise behavior (histograms on the right side of Fig. 5). These histograms indicate important differences in the fluctuation properties of the Earth surface vibration for the two time periods considered.

Results presented in Fig. 5 show that ambient seismic noise at increased local seismic activity comprises a multitude of processes of diverse dynamics, from uniform power law behavior of $1/f$ type ($\alpha = 1$) to long-range correlations; the latter one may be of stochastic fractional Brownian-motion type or even of deterministic nature ($\alpha > 1.5$). We see that at least 25% of DFA scaling exponent values calculated for time period before and after the strong local Racha earthquake occurrence indicate closeness to Brownian-motion type processes ($\alpha = 1.5$) and not less than 15% show anticorrelated behavior (dark circles in Fig. 5). At the same time, data recorded at a locally quiet period, before and after the arrival of seismic waves from the remote Japan M9.0 earthquake, always reveal a significant shift to the larger scaling exponents (up to $\alpha = 1.91$) indicating persistent long range correlation. It is worth to point out that in the last case the Brownian-motion type behavior was never observed and more than 98% of calculated DFA scaling exponents exceeded the value of 1.5.

These different kinds of fluctuation characteristics, with respect to scaling behavior, demonstrate different stochastic structures in ambient noise data sets at different levels of local seismic activity.

We point out again that all the results presented above were obtained for data sets which included waves of different local as well as remote origin. In order to see how the fluctuation features of ambient noise Z-component data may be influenced by the different seismic waveforms, we undertook an analysis for the time windows when wavetrains of certain origin were detected at the Oni station. Specifically, we focused on time windows under the following conditions: (i) neither local earthquakes occurrence nor arrival of wavetrains from remote earthquakes have been registered, (ii) only arrivals of waveforms from remote earthquakes were detected, (iii) strong local M6.0 earthquake occurred, and (iv) its aftershocks occurred.

Results of this analysis are presented in Fig. 6. In the lowest curve, results of calculations for the period prior to the Racha M6.0 earthquake are shown. Specifically, about 1700 windows of 12 000 data (2 min each), were selected so as to make the shape of fluctuation curves typical to the ones observed when no arrival of seismic waves have been detected at the Oni station. The fluctuation curve, averaged for all these time windows, shows clear crossovers at long and short time scales. Between these crossovers, we observe a linear scaling region. The presence of such a scaling part in this curve means that the ambient noise for considered periods revealed power
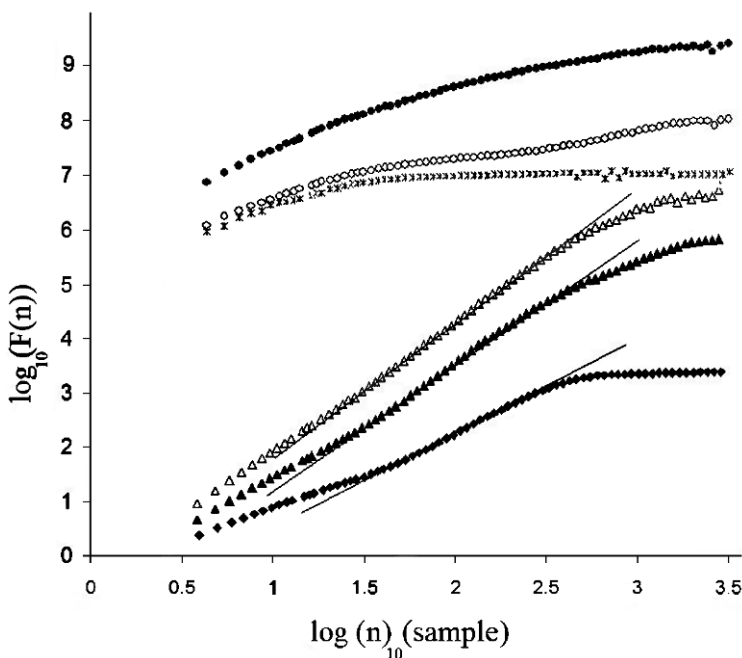
Fig. 6. Averaged DFA fluctuation curves obtained for the *Z*-component of seismic noise data at the Oni station calculated for consecutive non-overlapping 2-min windows. Diamonds − before the Oni *M*6.0 EQ for time windows with no local earthquakes and without arrival of remote waveforms; white and black triangles − for windows when the arrival of waveforms from remote earthquakes was detected; asterisks − for window when foreshocks of the Oni *M*6.0 event occurred; dark circles − for a window when the Oni *M*6.0 EQ occurred, and open circles when its aftershocks occurred. Curves are shifted along the *y* axis for clarity.

law behavior in the frequency range of about 0.3-3 Hz. For lower frequencies (longer time scales) we see breakdown of the power law scaling behavior, which can be observed in the systems when different quasi-periodic trends dominate (Hu *et al*. 2001, Alvarez-Ramirez *et al*. 2005). For small scales, at frequencies above 3-4 Hz, the linear relation is questionable, especially taking into consideration that for small scales of *n* the deviations from the scaling law are intrinsic to the usual DFA method (Peng *et al*. 1993a).

The next two curves in the upward direction in Fig. 6 correspond to time periods when seismic signals from remote events have arrived at Oni station prior to local *M*6.0 earthquake. We see that the arrival of wavetrains from remote events, *M*4.9 that occurred in Afghanistan and *M*6.2 in Indonesia (see the methods section for details), do not essentially change general fluctuation features of ambient noise around the Oni station. Indeed, as shown in Fig. 6,

the general shape of averaged DFA fluctuation curves of ambient seismic noise data, for the time windows when arrivals of wavetrains from the above-mentioned remote earthquakes have been detected, is similar to that for calm windows (the lowest curve in Fig. 6). At the same time, the frequency range and slope of scaling linear part seems to be larger in this case comparing to windows when no clear seismic waves were detected at the Oni station. Besides, the linear scaling region of fluctuation curve is longer and crossover points at small scales are not so clear for time periods of remote wavetrains arrival, but still detectable.

It is noticeable from Fig. 6 that a strong local seismic activity essentially alters the character of scaling features of ambient noise fluctuation. Indeed, fluctuation curves of seismic noise data for the time windows when the Oni M6.0 earthquake, as well as its foreshocks and aftershocks, occurred do not reveal credible scaling behavior. This means that contrary to remote seismic activity, the arrival of seismic waves from local earthquakes completely destroyed the fluctuation feature of ambient noise. This is quite logical taking into consideration the amount of strain energy released by an earthquake, which many times exceeds the energy sources of other components of seismic noise.

Thus we see in Figs. 4 and 6 (lower curves) that the shape of averaged fluctuation curves for the whole ambient noise data sets and for windows when no local or remote earthquakes have been detected are similar. In both cases, we observe crossovers and clear scaling regions. This can be understood as an indication that for the purpose of general consideration the use of whole data sets of ambient noise time series, without identification of the type of arrived signal, may be applicable.

At the same time, as it was already mentioned, the arrival of seismic waves, especially from a strong local event, can essentially affect fluctuation features of ambient noises (see Fig. 6). Apparently, both qualitative as well as quantitative changes in the earth surface vibrations occur for the certain time periods of seismic wave arrivals, which is revealed in changes of the shape as well as of the scaling features of fluctuation curves.

Therefore, in order to consider the dynamics of ambient noises and to be focused on the changes which can possibly be related to the local earthquake preparation, we intentionally eliminated from data sets those sections in which the arrival of remote or local seismic waveforms has been detected. Such compiled time series of ambient noise data, consisting of recordings at time periods when no arrival of seismic wavetrains at the Oni station was detected, have been considered prior to the Oni M6.0 earthquake occurrence in September 2009, as well as in March 2011, when wavetrains from Japan M9.0 earthquake arrived at the Oni station.
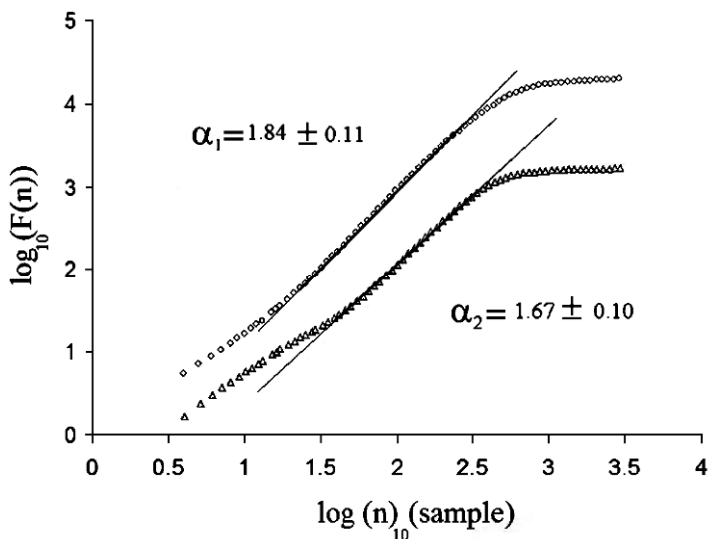
Fig. 7. Averaged DFA fluctuation curves of *Z*-components of seismic noise records at the Oni station when no local or remote seismic activity was observed. The lower curve corresponds to the period prior to the Racha *M*6.0 EQ (2009). The upper curve corresponds to the period before the arrival of waveforms from remote Japan *M*9.0 EQ. Curves are shifted along the *y* axis for clarity.

Results of analysis are shown in Fig. 7. We see two crossovers in $\log F(n)$ *versus* $\log n$ relation curves of both time series. Between these crossovers, time scales fluctuations of ambient noise always reveal long range correlations ($\alpha > 1.5$) for both data sets. Similar to the results for the whole data sets, results in Fig. 7 indicate different dynamical structures with respect to scaling behavior in the considered ambient noise data for seismically quiet and active time periods around the Oni station. Thus, the observed differences cannot be affected by the arrival of seismic wavetrains from local or remote earthquakes.

In addition to the above analysis of averaged fluctuation curves calculated for time periods when no local earthquakes and arrival of wavetrains from remote events were detected, we also calculated individual scaling exponents for consecutive 2-min time windows of locally quiet time periods. Results of calculation, presented in Fig. 8, show that the distribution range of scaling exponents is here somewhat narrower though in general similar to what we see for the whole data sets in Fig. 5. Differences mainly concern the lower and upper limits of scaling exponents' distribution range. It is interesting that the majority of encountered values of scaling exponents calculated for "calm" windows of seismically active and locally quiet periods become

closer in this case, comparing to what was found for the whole data sets. Anyway, we see from Fig. 8 that distribution functions of scaling exponents' values, for increased local seismic activity and for quiet periods, are still well distinguishable. By these results, ambient noises in calm seismic conditions indicate persistent correlated process ($\alpha > 1.5$), while at increased local seismic activity we observe the mixture of processes involving correlated, anticorrelated and uncorrelated behaviors ($1.2 < \alpha < 1.8$).

Thus, as we see in Fig. 8, the distribution of features of scaling exponents for the considered groups is different. Indeed, according to the Kolmogorov–Smirnov test, indicating the goodness of fit, the value of p for Gaussian distribution is 0.75 for ambient noise data prior to the Oni M6.0 earthquake and 0.9 for period before the arrival of wavetrains from the Japan M9.0 earthquake. This also provides an additional argument in favor of the opinion that the dynamics of seismic noises in the considered periods is different.
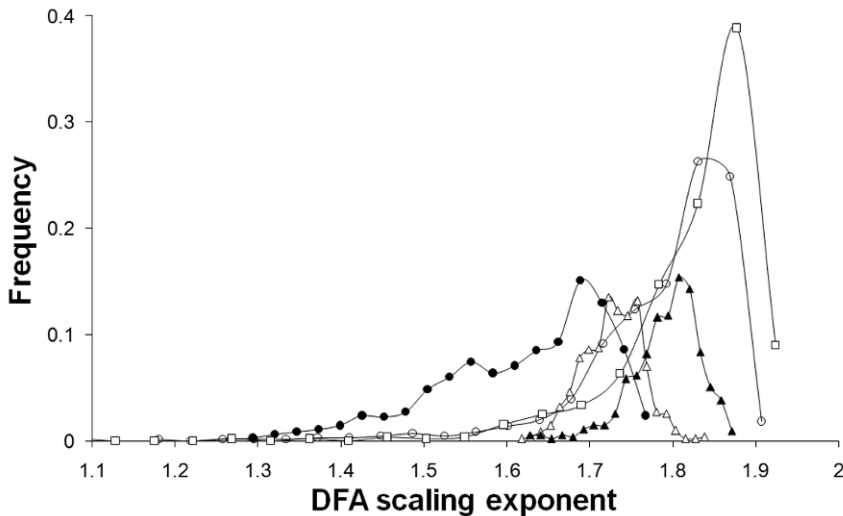

Fig. 8. The histograms of scaling exponents calculated for consecutive 12 000 sample data length windows of Z-components of seismic noise time series recorded at the Oni station for the periods regarded as seismically calm. Dark circles − time windows before the 2009 Racha M6.0 EQ, when no local activity or arrival of remote wavetrains were detected; dark triangles − time windows when before and after the arrival of wavetrains from the 2011 Japan M9.0 EQ no seismic activity was detected; open squares – period from 23:59 to 19:00 UTC on 22 January 2009, when no local activity or arrival of remote waves was detected; open circles – locally calm period from 00:00 UTC on 20 to 21 January 2011; open triangles – moderate seismic activity around the Oni station, period from 00:00 to 19:00 UTC on 30 October 2010.

It is of special importance to underline that this difference is not caused by the influence of seismic component of ambient noise (*i.e.*, by waves from local or remote earthquakes). Indeed, the result was practically the same when we selected quiet time windows only (when arrivals of seismic waves from local or remote earthquakes have not been detected at the Oni station).

Then, in order to exclude inaccuracies because of possible specificities of analyzed time periods, we tested our results for three additional periods. For this, we aimed to select one to several days long periods with local seismic activity as low as possible, and an additional period with moderate local seismic activity. Specifically, from the data sets of ambient noises recorded at Oni seismic station, a 20-hour period, from 00:00 to 19:00 UTC on 30 October 2010, was selected. As it was mentioned in the section on data and methods, the seismic activity around Oni station in this period slightly increased and, moreover, at the end of the selected time interval, arrivals of seismic waves from $M5.2$ earthquake that occurred in Japan were detected. The next time period was selected from 23:59 to 19:00 UTC on 21 January 2009. During this period and immediately before and after it, neither an increase of local seismic activity nor an arrival of seismic waves from remote earthquakes has been detected. A locally calm period was from 00:00 on 20 to 21 January 2011, 33 hours after the Vani (Georgia) $M5.3$ earthquake, whose epicenter was located about 100 km from the Oni station and thus the station was outside of critical zone ever detected for strong Caucasian earthquakes.

For these time periods, calculations of DFA scaling exponents, similar to those described above, have been carried out. In Figure 8, results of these calculations are presented in the form of histograms of DFA linear part scaling exponents. It can be seen that for time periods which can be regarded as locally quiet, because no seismic waveforms have been detected at Oni station, *e.g.*, in January 2009 and 2011 or March of 2011, the scaling exponent distribution looks similar to the one before the arrival of waves from Japan $M9.0$ earthquake, *i.e.*, for the time period which was locally quiet too. In these cases, the calculated values of ambient noise scaling exponents exceeded the value $\alpha = 1.5$, typical for a random walk, which indicates more persistent correlated behavior. On the other hand, from Fig. 8 it follows that for the period of slightly increased local seismic activity in October 2010, the distribution of scaling exponents resembles the pattern observed in the period when the strong $M6.0$ Racha earthquake occurred. In this case, the scaling exponents' values calculated for ambient noise remain characteristic for correlated process, though they are shifted to the left, closer to $\alpha = 1.5$.

Next, though we have used DFA for ambient noises data, we additionally investigated increments' time series of original time series in order to further exclude a possible influence of different kinds of trends.
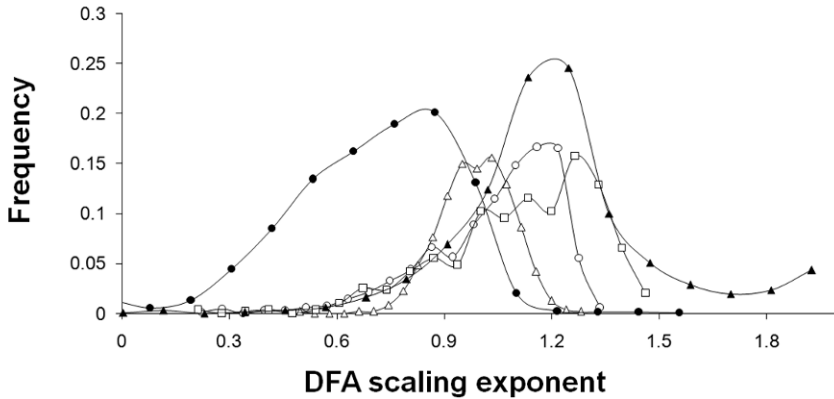
Fig. 9. The histograms of scaling exponents calculated for increment time series of noise *Z*-components data sets recorded at the Oni station. Calculation have been carried out for consecutive 12 000 sample data length windows of increment data sets for the periods regarded as seismically calm. Description of symbols as in Fig. 8.

In Figure 9 we see that scaling exponents of differenced data (increments' time series) are shifted to the left comparing to the results in Fig. 8. It is quite logical that the differentiation of ambient noise time series decreases their scaling exponent (in the histogram we see a decrease by about one). Most importantly, the distribution functions of scaling exponents of increments of ambient noise data are still different for time periods of increased and decreased local seismic activity around the Oni station (dark circles and triangles in Fig. 9). Moreover, disposition to the each other of the scaling exponents distribution curves, calculated for data recorded at other calm and/or activated seismic conditions, is similar to that presented in Fig. 8. This points out that the obtained results concerning features of distribution of scaling exponents at different local seismic conditions are not influenced by different possible trends.

Next, knowing that the ambient noises may be caused by a diversity of different, often unrelated and continuous sources of diverse origins from spatially distributed local and remote sources (SESAME 2004), we carried out an analysis in different frequency ranges, similar to the above analysis. We started from frequency interval of 0.04-4 Hz to cover the whole microseism activity range (Webb 1998). Specifically, we filtered original data to analyze scaling features of ambient noises for the following frequency contents: (i) below a frequency of 0.04 Hz, (ii) in the frequency range of 0.04 to 4 Hz, and (iii) above 4 Hz. By this, we aimed to clear up which frequency band of ambient noise is responsible for the changes observed in fluctuation scaling features.
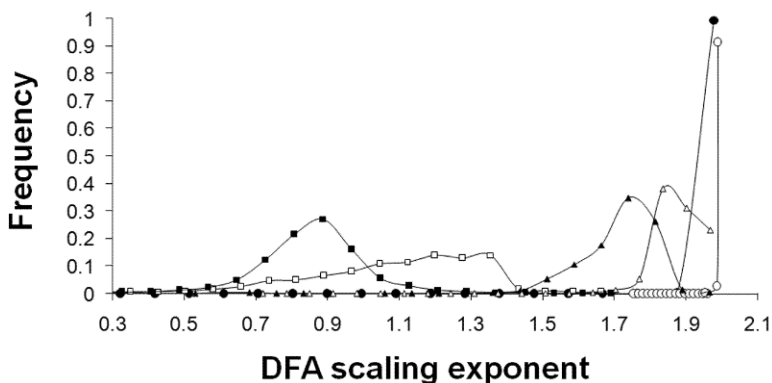
Fig. 10. The histograms of scaling exponents calculated for different frequency bands of ambient noise data sets. Prior to the Oni *M*6.0 (black symbols), before arrival of waveforms from the Japan *M*9.0 EQ (white symbols). For the frequencies: below 0.04 Hz (squares), in the range of 0.04-4 Hz (triangles), and above 4 Hz (circles).

We see in Fig. 10 that the high frequency range, above 4 Hz, which is regarded as caused by local and cultural noises (Webb 1998, SESAME 2004), does not reveal changes during the considered periods in September 2009 and March 2011. This is quite logical because the location of station or industrial or ambient conditions in the small town of Oni have not changed. In the low frequency range, below 0.04 Hz, where the influence of infragravity oceanic waves is predominant, we see clear difference between ambient noise scaling exponent distributions. It is very difficult to comment now but still worth to mention that before and after the Oni 6.0 earthquake that occurred in September 2009, low frequency ambient noises showed predominantly persistent behavior; the calculated DFA scaling exponent values (about 70%) are in 0.7-0.9 range. In the locally quiet period of March 2011 broad diversity of behaviours, from random to Brownian motion, was observed ($0.5 < \alpha < 1.5$). Most important for the purpose of the present paper is that such a difference is opposite to what we observe in original data as well as in filtered data in the 0.04-4 Hz frequency range. From these results we can conclude that differences found between fluctuation features of ambient noises at activated and calm local seismicity conditions, apparently cannot be caused by high or low frequency components and should be related to microseisms' constituents.

Results of similar analysis for calm time intervals selected from the above-mentioned periods in September 2009 and March 2011 provide additional arguments for such a conclusion. Indeed, in Fig. 11 we see that the distribution of scaling exponents for high and low frequency ranges are akin
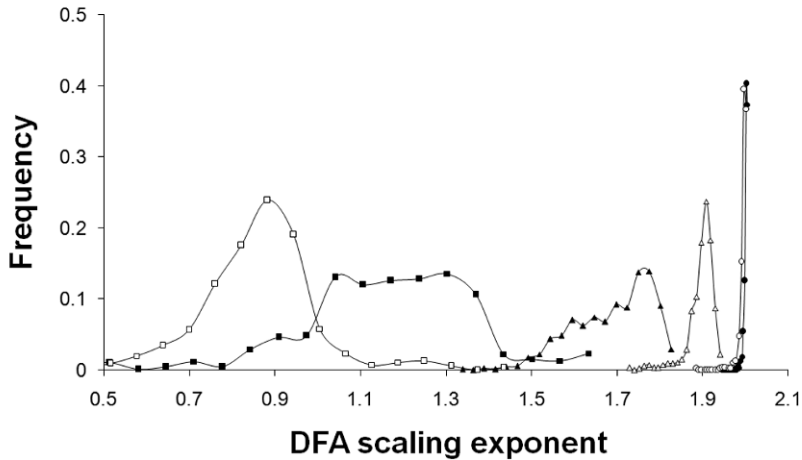
Fig. 11. The histograms of scaling exponents calculated for different frequency bands of ambient noise data sets compiled for calm periods, when no local earthquakes or arrival of waveforms from remote seismic activity were detected at the Oni station. Prior to the Oni M6.0 EQ (black symbols), before arrival of waveforms from the Japan M9.0 EQ (white symbols). For frequencies below 0.04 Hz (squares), in the range of 0.04-4 Hz (triangles), and above 4 Hz (circles).

to those shown in Fig. 10 for the whole time series. At the same time, in microseisms' frequency range of 0.04-4 Hz, the difference between distribution features of ambient noises scaling exponents in time period before the Oni M6.0 earthquake are clearly different from those in locally quiet period in March 2009, prior and after the arrival of wavetrains from the Japan M9.0 earthquake.

Afterwords, we decided to focus on the fluctuation features in the frequency bands directly contributing to the observed linear scaling parts of $\log F(n)$ *versus* $\log n$ curves of the considered ambient noise data. Specifically, from the analysis of fluctuation curves in Figs. 4 and 7 it follows that, in average, the scaling holds for time scales between crossovers at about 0.3 and 3 s (upper curves) and 0.2 and 3 s (lower curves). Therefore, we have filtered our data to analyze ambient noise scaling features in the frequency range of 0.3-3.8 Hz for the period when strong local earthquakes occurred in September 2009 and in the frequency range of 0.3-5 Hz for the period when wavetrains from the remote Japan earthquake arrived in March 2011. The results of analysis are presented in Fig. 12. As it follows from a comparison of this figure and previous ones (Figs. 10 and 11), the shift of high frequency threshold (from 4 to 3.8 Hz for activated and from 4 to 5 Hz for calm seismic conditions) of the considered ambient noise data has almost no effect on the distribution of scaling exponent values. The ambient noise

still looks like a persistent process for the period of activated local seismicity (white squares) and indicates wide distribution features for calm seismic conditions. Contrary to this, slight change in low frequency threshold, from 0.04 to 0.3 Hz, in the considered ambient noise data led to the noticeable change in observed fluctuation features (compare black and white circles in Figs. 10 and 12). It is worth mentioning that at calm conditions of local seismicity, the scaling exponents' values range is wider than for period of active seismicity. The most important fact is that neither low nor high frequency components of considered ambient noises do show any scaling features which could have masked differences observed in targeted frequency intervals, of 0.3-3.8 Hz for the time period when strong local earthquakes occurred in September 2009 and in the range of 0.3-5 Hz for the time period when wavetrains from the remote Japan earthquake arrived at Oni station in March 2011. Thus, it can be suggested that the observed differences in dynamics of ambient noises revealed through the differences in the fluctuation scaling exponents are related to processes directly contributing to local earthquake preparation.

As it was said above, prior to the strong local Oni M6.0 earthquake the values of DFA scaling exponents are distributed in a wide range, indicating coincidence of different dynamical behaviors with a slight dominance of long-range persistent correlations in ambient noises.

The origin of the shift from mostly persistent long-range correlated pattern in calm periods to the mixture of different fluctuation patterns, including antipersistent correlated and uncorrelated behavior at increased
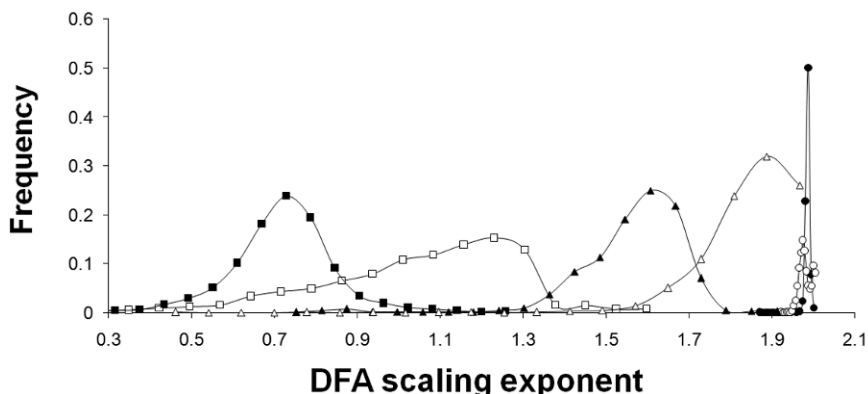

Fig. 12. The histograms of the scaling exponents calculated for different frequency bands of ambient noise data sets. Time period in September 2009: below 0.3 Hz (black squares), 0.3-3.8 Hz (black triangles), and above 3.8 Hz (black circles). Time period in March 2011: below 0.3 Hz (white squares), 0.3-5 Hz (white triangles), and above 5 Hz (white circles).

local seismic activity, remains mostly unclear, though it may be speculated that it is related to the distortion of dynamical structure of the background Earth surface vibration pattern under the influence of earthquake preparation processes.

The findings that fractal dimensions of ambient noise and seismic signals may be different, and that the probability density function (PDF) of ambient noise may undergo a transition from Gaussian to long-tailed non-Gaussian distribution prior to moderate and large earthquakes (Padhy 2004, Tabar *et al.* 2006, Manshour *et al.* 2009, 2010) are, from general point of view, in agreement with our results.

4. CONCLUSIONS

On the example of seismic noise data sets recorded at the Oni seismic station we have shown that, generally speaking, the ambient noise data sets are, for a wide time scale, characterized by long range persistent correlations.

Fluctuation properties of ambient noise are significantly affected by an influence of seismic waves from both local and remote earthquakes. At the same time, wavetrains from remote events cause quantitative changes in ambient noise data scaling properties, while seismic waves from local earthquakes lead to their complete qualitative distortions.

The analysis carried out on data sets from the epicentral zone of Oni *M*6.0 earthquake supports the opinion that scaling properties of ambient noise prior to strong local earthquakes may be quantifiable. The increased seismic activity can be accompanied by a distortion of persistent long-range correlations and an appearance of mixture of dynamical constituents with diverse persistent, antipersistent, and random behaviors.

R e f e r e n c e s

Alvarez-Ramirez, J., G. Espinosa-Paredes, and A. Vazquez (2005), Detrended fluctuation analysis of the neutronic power from a nuclear reactor, *Physica A* **351**, 2-4, 227-240, DOI: 10.1016/j.physa.2004.08.087.

Bunde, A., J. Kropp, and H.J. Schellnhuber (eds.) (2002), *The Science of Disasters: Climate Disruptions, Heart Attacks, and Market Crashes*, Springer, Berlin.

Caserta, A., G. Consolini, and P. De Michelis (2007), Statistical features of the seismic noise-field, *Stud. Geophys. Geod.* **51**, 2, 255-266, DOI: 10.1007/s11200-007-0013-8.

Chelidze, T., and T. Matcharashvili (2007), Complexity of seismic process; measuring and applications – A review, *Tectonophysics* **431**, 1-4, 49-60, DOI: 10.1016/j.tecto.2006.05.029.

Chelidze, T., O. Lursmanashvili, T. Matcharashvili, and M. Devidze (2006), Triggering and synchronization of stick slip: Waiting times and frequency-energy distribution, *Tectonophysics* **424**, 3-4, 139-155, DOI: 10.1016/j.tecto.2006.03.031.

Correig, A.M., M. Urquizu, J. Vila, and R. Macià (2007), Microseism activity and equilibrium fluctuations. **In**: A. Tsonis and J. Elsner (eds.), *Nonlinear Dynamics in Geosciences*, Springer, Berlin, 69-85, DOI: 10.1007/978-0-387-34918-3_5.

Goltz, C. (1997), Fractal and chaotic properties of earthquakes, *Lect. Notes Earth Sci*. **77**, 3-164, DOI: 10.1007/BFb0028315.

Hu, K., P.Ch. Ivanov, Z. Chen, P. Carpena, and H.E. Stanley (2001), Effect of trends on detrended fluctuation analysis, *Phys. Rev. E* **64**, 1, 011114, DOI: 10.1103/PhysRevE.64.011114.

Ivanov, P.Ch., A.L. Goldberger, and H.E. Stanley (2002), Fractal and multifractal approaches in physiology. **In**: A. Bunde, J. Kropp, and H.J. Schellnhuber (eds.), *The Science of Disasters: Climate Disruptions, Heart Attacks, and Market Crashes*, Springer-Verlag, Berlin, 219-257.

Kanamori, H., and E.E. Brodsky (2001), The physics of earthquakes, *Phys. Today* **54**, 6, 34-40, DOI: 10.1063/1.1387590.

Kantelhardt, J.W., S.A. Zschiegner, E. Koscielny-Bunde, S. Havlin, A. Bunde, and H.E. Stanley (2002), Multifractal detrended fluctuation analysis of nonstationary time series, *Physica A* **316**, 1-4, 87-114, DOI: 10.1016/ S0378-4371(02)01383-3.

Kapiris, P.G., K.A. Eftaxias, K.D. Nomikos, J. Polygiannakis, E. Dologlou, G.T. Balasis, N.G. Bogris, A.S. Peratzakis, and V.E. Hadjicontis (2003), Evolving towards a critical point: A possible electromagnetic way in which the critical regime is reached as the rupture approaches, *Nonlin. Processes Geophys.* **10**, 6, 511-524, DOI: 10.5194/npg-10-511-2003.

Karamanos, K., D. Dakopoulos, K. Aloupis, A. Peratzakis, L. Athanasopoulou, S. Nikolopoulos, P. Kapiris, and K. Eftaxias (2006), Preseismic electromagnetic signals in terms of complexity, *Phys. Rev. E* **74**, 1, 016104, DOI: 10.1103/PhysRevE.74.016104.

Keilis-Borok, V.I., and A.A. Soloviev (eds.) (2003), *Nonlinear Dynamics of the Lithosphere and Earthquake Prediction*, Springer-Verlag, Berlin.

Lapenna, V., M. Macchiato, and L. Telesca (1998), *$1/f^\beta$* Fluctuations and self-similarity in earthquake dynamics: observational evidences in southern Italy, *Phys. Earth Planet. Inter*. **106**, 1-2, 115-127, DOI: 10.1016/S0031-9201(97)00080-0.

Lyubushin, A. (2010), Multifractal parameters of low-frequency microseisms. **In:** V. de Rubeis, Z. Czechowski, and R. Teisseyre (eds.), *Synchronization and Triggering: from Fracture to Earthquake Processess*, GeoPlanet: Earth and Planetary Sciences, Vol. 1, Springer-Verlag, Berlin, 253-272, DOI: 10.1007/978-3-642-12300-9_15.

Manshour, P., S. Saberi, M. Sahimi, J. Peinke, A.F. Pacheco, and M.R.R. Tabar (2009),Turbulencelike behavior of seismic time series, *Phys. Rev. Lett.* **102**, 1, 014101, DOI: 10.1103/PhysRevLett.102.014101.

Manshour, P., F. Ghasemi, T. Matsumoto, J. Gómez, M. Sahimi, J. Peinke, A.F. Pacheco, and M.R.R. Tabar (2010), Anomalous fluctuations of vertical velocity of Earth and their possible implications for earthquakes, *Phys. Rev. E* **82**, 3, 036105, DOI: 10.1103/PhysRevE.82.036105.

Matcharashvili, T., and T. Chelidze (2010), Nonlinear dynamics as a tool for revealing synchronization and ordering in geophysical time series: Application to caucasus seismicity. **In:** V. de Rubeis, Z. Czechowski, and R. Teisseyre (eds.), *Synchronization and Triggering: from Fracture to Earthquake Processess*, GeoPlanet: Earth and Planetary Sciences, Vol. 1, Springer, Berlin, 3-21, DOI: 10.1007/978-3-642-12300-9_1.

Matcharashvili, T., T. Chelidze, and Z. Javakhishvili (2000), Nonlinear analysis of magnitude and interevent time interval sequences for earthquakes of Caucasian region, *Nonlin. Processes Geophys.* **7**, 1/2, 9-20, DOI: 10.5194/npg-7-9-2000.

Padhy, S. (2004), Rescaled range fractal analysis of a seismogram for identification of signals from an earthquake, *Curr. Sci.* **87**, 5, 637-641.

Peng, C.-K., S.V. Buldyrev, A.L. Goldberger, S. Havlin, M. Simons, and H.E. Stanley (1993a), Finite-size effects on long-range correlations: Implications for analyzing DNA sequences, *Phys. Rev. E* **47**, 5, 3730-3733, DOI: 10.1103/PhysRevE.47.3730.

Peng, C.-K., J. Mietus, J. Hausdorff, S. Havlin, H.E. Stanley, and A.L. Goldberger (1993b), Long-range anticorrelations and non-Gaussian behavior of the heartbeat, *Phys. Rev. Lett.* **70**, 9, 1343-1346, DOI: 10.1103/PhysRevLett. 70.1343.

Peng, C.-K., S. Havlin, H.E. Stanley, and A.L. Goldberger (1995), Quantification of scaling exponents and crossover phenomena in nonstationary heartbeat time series, *Chaos* **5**, 1, 82-87, DOI: 10.1063/1.166141.

Rodriguez, E., J.C. Echeverria, and J. Alvarez-Ramirez (2007), Detrended fluctuation analysis of heart intrabeat dynamics, *Physica A* **384**, 2, 429-438, DOI: 10.1016/j.physa.2007.05.022.

Rundle, J.B., D.L. Turcotte, and W. Klein (eds.) (2000), *GeoComplexity and the Physics of Earthquakes*, AGU Monograph 120, American Geophysical Union, Washington, DC, 284 pp.

Ryabov, V.B., A.M. Correig, M. Urquizú, and A.A. Zaikin (2003), Microseism oscillations: from deterministic to noise-driven models, *Chaos Soliton. Fract.* **16**, 2, 195-210, DOI: 10.1016/S0960-0779(02)00165-0.

Scholz, C.H. (1990), *The Mechanics of Earthquakes and Faulting*, Cambridge University Press, Cambridge.

SESAME (2004), Guidelines for the implementation of the H/V spectral ratio technique on ambient vibrations. Measurements, processing and interpretation,

WP12 European Commission – Research General Directorate, Project No. EVG1-CT-2000-0026 SESAME, report D23.

Sobolev, G.A., and A.A. Lyubushin (2006), Microseismic impulses as earthquake precursors, *Izv. – Phys. Solid Earth* **42**, 9, 721-733, DOI: 10.1134/ S1069351306090023.

Sobolev, G.A., A.A. Lyubushin, and N.A. Zakrzhevskaya (2010), Synchronizations of microseismic oscillations as the indicators of the instability of a seismically active region. **In:** V. de Rubeis, Z. Czechowski, and R. Teisseyre (eds.), *Synchronization and Triggering: from Fracture to Earthquake Processess*, GeoPlanet: Earth and Planetary Sciences, Vol. 1, Springer, Berlin, 243-252, DOI: 10.1007/978-3-642-12300-9_14.

Tabar, M.R.R., M. Sahimi, F. Ghasemi, K. Kaviani, M. Allamehzadeh, J. Peinke, M. Mokhtari, M. Vesaghi, M.D. Niry, A. Bahraminasab, S. Tabatabai, S. Fayazbakhsh, and M. Akbari (2006), Short-term prediction of medium- and large-size earthquakes based on Markov and extended self-similarity analysis of seismic data, *Lect. Notes Phys.* **705**, 281-301, DOI: 10.1007/3-540-35375-5_11.

Telesca, L., and V. Lapenna (2006), Measuring multifractality in seismic sequences, *Tectonophysics* **423**, 1-4, 115-123, DOI: 10.1016/j.tecto.2006.03.023.

Telesca, L., V. Lapenna, and M. Macchiato (2005), Multifractal fluctuations in seismic interspike series, *Physica A* **354**, 629-640, DOI: 10.1016/j.physa. 2005.02.053.

Telesca, L., M. Lovallo, V. Lapenna, and M. Macchiato (2008), Space-magnitude dependent scaling behaviour in seismic interevent series revealed by detrended fluctuation analysis, *Physica A* **387**, 14, 3655-3659, DOI: 10.1016/ j.physa.2008.02.035.

Theiler, J., S. Eubank, A. Longtin, B. Galdrikian, and J.D. Farmer (1992), Testing for nonlinearity in time series: the method of surrogate data, *Physica D* **58**, 1-4, 77-94, DOI: 10.1016/0167-2789(92)90102-S.

Webb, S.C. (1998), Broadband seismology and noise under the ocean, *Rev. Geophys*. **36**, 1, 105-142, DOI: 10.1029/97RG02287.

Yulmetyev, R., F. Gafarov, P. Hänggi, R. Nigmatullin, and S. Kayumov (2001), Possibility between earthquake and explosion seismogram differentiation by discrete stochastic non-Markov processes and local Hurst exponent analysis, *Phys. Rev. E* **64**, 6, 066132, DOI: 10.1103/PhysRevE.64.066132.

Yulmetyev, R., P. Hänggi, F. Gafarov, and D.G. Yulmetyeva (2003), Non-stationary time correlation in discrete complex systems: Applications in cardiology and seismology, *Nonlin. Phen. Compl. Systems* **6**, 3, 791-799.

Non-Extensivity Analysis of Seismicity
within Four Subduction Regions in Mexico

Sharon M. VALVERDE-ESPARZA[2], Alejandro RAMÍREZ-ROJAS[1],
E. Leticia FLORES-MÁRQUEZ[2], and Luciano TELESCA[3]

[1]Departamento de Ciencias Básicas, Universidad Autónoma Metropolitana,
Azcapotzalco, México D.F., México; e-mail: arr@correo.azc.uam.mx

[2]Instituto de Geofísica, Universidad Nacional Autónoma de México,
México D.F., México

[3]Institute of Methodologies for Environmental Analysis,
National Research Council, Tito Scalo, Potenza, Italy

A b s t r a c t

The non-extensivity approach based on the Tsallis entropy has been
applied to seismicity that occurred from 1988 to 2010 along the Mexican
South Pacific coast. We analyzed four different regions, characterized by
different subduction patterns. Our results indicate a possible correlation
between the non-extensive parameters and the seismicity pattern associ-
ated with the inclination angle of each subduction region.

Key words: non-extensivity, subduction, Tsallis entropy, Mexico.

1. INTRODUCTION

The log-linear relationship between the cumulative number of earthquakes
with magnitude $m > M_{th}$ and the threshold magnitude M_{th} is the well known
Gutenberg–Richter (GR) law (Gutenberg and Richter 1944), which
represents an empirical relationship, also deduced in the context of the self-
organizing criticality (Bak *et al.* 1988). Only few attempts were proposed to
relate the GR law with general physical principles (Varotsos *et al.* 2006,
Wesnousky 1999, King 1983, Kagan and Knopoff 1981). Sotolongo-Costa
and Posadas (2004) (SCP) proposed a model for earthquake generation

---

mechanism, considering the role played by the fragments between the fault planes, of diverse size, originated by the local breakage of the tectonic plates (Hasumi 2009), from which the faults are generated; the interaction between such fragments and the asperities of the fault planes leads to an earthquake triggering mechanism. The non-extensive model, developed starting from Tsallis' entropy (Tsallis 1988), is able to describe shock fragmentation processes, as it occurs in the fragment-asperity interaction. Since the fragment-asperity interaction phenomenon, considered as one of the triggering mechanisms of earthquakes, leads to the existence of long-range interactions, in which the entropy is nonadditive, the non-extensive approach based on the Tsallis entropy seems more adequate. The SCP model was revisited by Silva *et al.* (2006), where a different relationship between earthquake energy and fragment size, in full agreement with the standard theory of seismic moment (Lay and Wallace 1995), has led to a magnitude distribution different from that deduced in the SCP model, providing an equally excellent fit to several seismic distributions worldwide. This model was applied to regional seismicities as well as to specific seismic zones (Telesca 2010, Telesca and Chen 2010, Silva *et al.* 2006, Sarlis *et al.* 2010, Darooneh and Mehri 2010, De Santis *et al.* 2011).

Other works have been focused on theoretical and experimental studies of the relative displacements between fault planes and the interaction with their fragments, based, *e.g.*, on cellular automata, spring-block model, and interaction between surfaces (Burridge and Knopoff 1967, Turcotte 1997, Olami *et al.* 1992, Carlson and Langer 1989, Vargas *et al.* 2008).

The tectonic plate processes are the principal cause for the fragmentation of the Earth's crust, and therefore the fragmentation dynamics is the origin of earthquakes. The seismicity in Mexico and Central America region is characterized by active seismic belt along the Middle America Trench that has been studied by a large number of authors (Ohtake *et al.* 1981, Singh *et al.* 1983, Pardo and Suarez 1995, Kostoglodov and Ponce 1994, Iglesias *et al.* 2004, Ramírez-Herrera *et al.* 2011). The items analyzed from the seismo-logical point of view are the rupture zone, the type and magnitude of earth-quakes, the epicenter location, and the pattern of seismicity changes expected to precede the main shock (Ohtake *et al.* 1981). Data provided by different catalogues, and their corresponding corrections, have been analyzed (Zuñiga and Wiemer 1999).

In this work, we study the seismic activity observed in four seismically active zones in the Mexican South Pacific coast (Jalisco, Michoacan, Guer-rero, and Oaxaca) by using the non-extensive approach, in order to charac-terize the subduction zone in terms of non-extensivity parameter q. A subduction zone has the geometry and geodynamics associated with tec-tonic factors, so that it is possible that the local seismicity could be correlat-

ed with the subduction features. In this sense, it is important to characterize the seismicity produced in a subduction zone in terms of q values because we could get information about the stability of the region.

2. ASPERITY-FRAGMENTATION INTERACTION MODEL

Non-extensive systems, which are characterized by long-range spatial correlations, violate of the Boltzmann–Gibbs (BG) statistics (Sotolongo-Costa and Posadas 2002, 2004). The classical Boltzmann–Gibbs entropy has an additive property and includes just short-length interactions, so that the total entropy will depend on the size of the object. Tsallis (1988) generalized the BG statistics, defining an entropy characterized by a parameter q, quantifying the non-extensivity of the system; for $q = 1$ the extensive BG statistics is recovered. In Tsallis' non-extensive formulation of entropy, interactions of any length scale are allowed; thus, the process of shock fragmentation, especially when high energies are involved, leads to the emergence of long-range interactions between all parts of the object being fragmented. The non-extensive approach seems, therefore, well suited for investigating the complex mechanism of relative displacement of fault plates, which is the main cause of earthquakes.

The model of earthquake generation that we will use hereafter is that proposed by Silva *et al.* (2006), in which the relative position of fragments filling the gap between two rough faults can hinder their relative motion. The stress increases until a displacement of one of the asperities, due to the displacement of the hindering fragment, or even its breakage in the point of contact with the fragment, leads to a relative displacement of the fault planes of the order of the size ρ of the hindering fragment, with the subsequent release of energy ε (Sotolongo-Costa and Posadas 2004), which is supposed to relate with the volume of the fragment, $\varepsilon \sim \rho^3$, in agreement with the scaling relationship between seismic moment and the product of the fault rupture area with the average displacement of the fault (Lay and Wallace 1995). The maximum entropy principle for the Tsallis entropy (Tsallis 1988) is

$$S_q = k \frac{1 - \int p_\sigma^q(\sigma)\,\mathrm{d}\sigma}{q - 1} \, , \tag{1}$$

where $p_\sigma(\sigma)$ is the probability of finding a fragment of surface σ, q is a real number, k is the Boltzmann constant; this entropy becomes the Boltzmann entropy when $q \to 1$. Let us set $k = 1$ for the sake of simplicity.

In order to determine $p_\sigma(\sigma)$, the maximization of Tsallis' entropy is made under the two constraints:

(i) the normalization of $p_\sigma(\sigma)$,

$$\int_0^\infty p_\sigma(\sigma)\mathrm{d}\sigma = 1 , \tag{2}$$

(ii) the condition about the q-expectation value (Abe 2003)

$$\sigma_q = \langle\sigma\rangle_q = \frac{\displaystyle\int_0^\infty \sigma p_\sigma^q(\sigma)\mathrm{d}\sigma}{\displaystyle\int_0^\infty p_\sigma^q(\sigma)\mathrm{d}\sigma} . \tag{3}$$

For $q \to 1$, the last condition becomes the definition of mean value. Using the technique of Lagrange multipliers, the following functional is maximized:

$$f_q(p,\lambda_0,\lambda_1) = S_q + \lambda_0\int_0^\infty p_\sigma(\sigma)\mathrm{d}\sigma - \lambda_1\sigma_q , \tag{4}$$

where λ_0 and λ_1 are the Lagrange multipliers. Imposing that

$$\frac{\partial f_q}{\partial p_q} = 0 \tag{5}$$

after some algebra, the area distribution for fragments of the fault planes is obtained (Silva *et al.* 2006):

$$p_\sigma(\sigma) = \left[1 - \frac{(1-q)}{(2-q)}(\sigma - \sigma_q)\right]^{\frac{1}{1-q}} . \tag{6}$$

Assuming the energy scale $\varepsilon \sim \rho^3$, the proportionality between the released energy ε and ρ^3 becomes

$$\sigma - \sigma_q = \left(\frac{\varepsilon}{a}\right)^{2/3} , \tag{7}$$

where σ scales with ρ^2, and a (the proportionality constant between ε and ρ^3) is proportional to volumetric energy density. The energy distribution function (EDF) of the earthquakes is, then

$$p_\varepsilon(\varepsilon) = \frac{C_1\varepsilon^{-\frac{1}{3}}}{\left[1 + C_2\varepsilon^{2/3}\right]^{1/(q-1)}} \tag{8}$$

with $C_1 = \dfrac{2}{3a^{2/3}}$ and $C_2 = -\dfrac{(1-q)}{(2-q)a^{2/3}}$.

On the basis of the relationship between m and ε (Silva *et al.* 2006) the cumulative magnitude distribution function is obtained as follows:

$$\frac{N_{>M}}{N} = \left[1 - \left(\frac{1-q}{2-q}\right)\frac{10^{2M}}{a^{2/3}}\right]^{\frac{2-q}{1-q}} , \qquad (9)$$

which represents the number of events with magnitude $m > M$ normalized to the total number of events N.

And then

$$\log\left(\frac{N_{>M}}{N}\right) = \left(\frac{2-q}{1-q}\right)\log\left[1 - \left(\frac{1-q}{2-q}\right)\frac{10^{2M}}{a^{2/3}}\right] , \qquad (10)$$

where the q values are within the interval $1 < q < 2$, and $a \in (10^{-3},\ 10^{11})$. The above expression represents a non-extensive modification of the Gutenberg–Richter law.

The q value is a quantitative measure of the length scale of the spatial interactions: $q \approx 1$ indicates short-ranged spatial correlations; as q increases, the physical state becomes much more unstable. High values of q mean that the fault planes are not in equilibrium and more earthquakes can be expected (Sotolongo-Costa and Posadas 2002).

3. TECTONIC AND SEISMOLOGICAL SETTINGS

The Mexican subduction region was described by Pardo and Suarez (1995), Iglesias *et al.* (2004), and Singh *et al.* (1983), reporting a complete study that takes into account the geometry of the subducted Rivera and Cocos plates beneath the North American lithosphere (Fig. 1). The subduction in southern Mexico might be approximated as a subhorizontal slab bounded at the edge by the steep subduction geometry of the Cocos plate beneath the Caribbean plate to the east and of the Rivera plate beneath North America to the west. The dip of the interplate contact geometry is constant to a depth of 30 km, and lateral changes in the dip of the subducted plate are only observed once it is decoupled from the overriding plate. On the basis of seismicity, the focal mechanisms and the geometry of the downgoing slab, southern Mexico may be segmented into four regions: (i) the Jalisco region to the west, where the Rivera plate subducts at a steep angle that resembles the geometry of the Cocos plate beneath the Caribbean plate in Central America; (ii) the Michoacan region, where the dip angle of the Cocos plate decreases gradually toward the southeast; (iii) the Guerrero–Oaxaca region bounded approximately
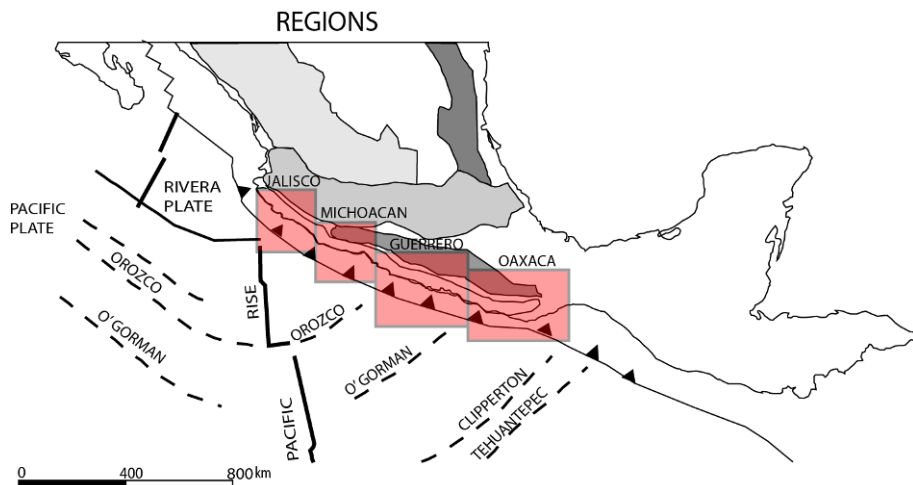
Fig. 1. Four studied regions described by Singh *et al.* (1983) and Pardo and Suarez (1995); main tectonic features are also shown.

by the onshore projection of the Orozco and O'Gorman fracture zones, where the subducted slab is almost subhorizonatal and underplates the upper continental plate for about 250 km; and (iv) the southern Oaxaca and Chiapas region in southeastern Mexico, where the dip of the subduction gradually increases to a steeper subduction of Central America. These drastic changes in dip do not appear to take place on tear faults, suggesting that smooth contortions accommodate for these changes in geometry.

The four sections previously described (Fig. 1) were assumed to have differences in subduction mechanism and then the seismic events in each one are analyzed independently, in terms of non-extensivity approach.

We analyzed the corrected Mexican seismic catalogue (Casiano Jiménez Cruz, personal communication) provided by the National Seismic Service (http://www.ssn.unam.mx). The investigated period spans from 1 January 1988 to 31 December 2010. The minimum magnitude is 2.2. The seismicity recorded within each of the four regions is shown in Fig. 2; it can be observed that Guerrero region displays the major number of earthquakes and Michoacan is the region with the lowest activity. In all regions, earthquakes with magnitudes $M_w > 7$ have occurred. According to the historical information (Ramírez-Herrera *et al.* 2011), in Jalisco region, only three earthquakes with $M_w > 7.5$ occurred within the last century which possibly indicates, in average, a recurrence interval of 77 years for 7.5 magnitude earthquakes, as estimated by Singh *et al.* (1985). The Guerrero seismic gap stands out as a region of the highest seismic potential because major seismic
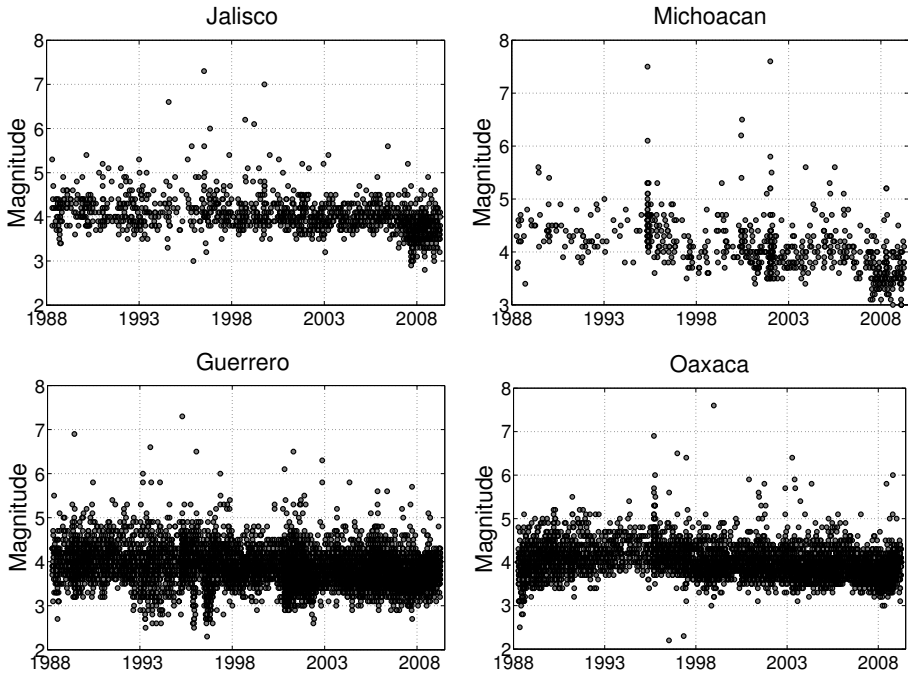
Fig. 2. Seismicity recorded from 1 January 1988 to 31 December 2010. Corrected seismic catalogue (Casiano Jiménez Cruz, personal communication) was provided by the National Seismic Service (http://www.ssn.unam.mx).

events have occurred in this area in the beginning of the last century. Almost the whole Guerrero coast is currently considered the most likely to experience a large, severe earthquake or several smaller seismic events eventually (Anderson *et al.* 1999, Song *et al.* 2009). In particular, the South-East Guerrero subduction zone has accumulated a large amount of strain during the last 50 years or so. The slow slip events or "silent earthquakes" that have recently been observed to occur within the Guerrero gap region (Larson *et al.* 2004) do not preclude this area from having a large subduction thrust event.

4. DATA ANALYSIS

We calculated the normalized cumulative number of earthquake (NCMD) with magnitude $m > M_{th}$ along with the fitting with Eq. (10) for each of the four regions under study (Fig. 3). The fitting was performed with an iterative nonlinear least square algorithm proposed by Levenberg and Marquardt (LM; Levenberg 1944, Marquardt 1963, Moré 1978). The nature of this method is such that we need to initialize it with q_0 and a_0 as initial conditions;
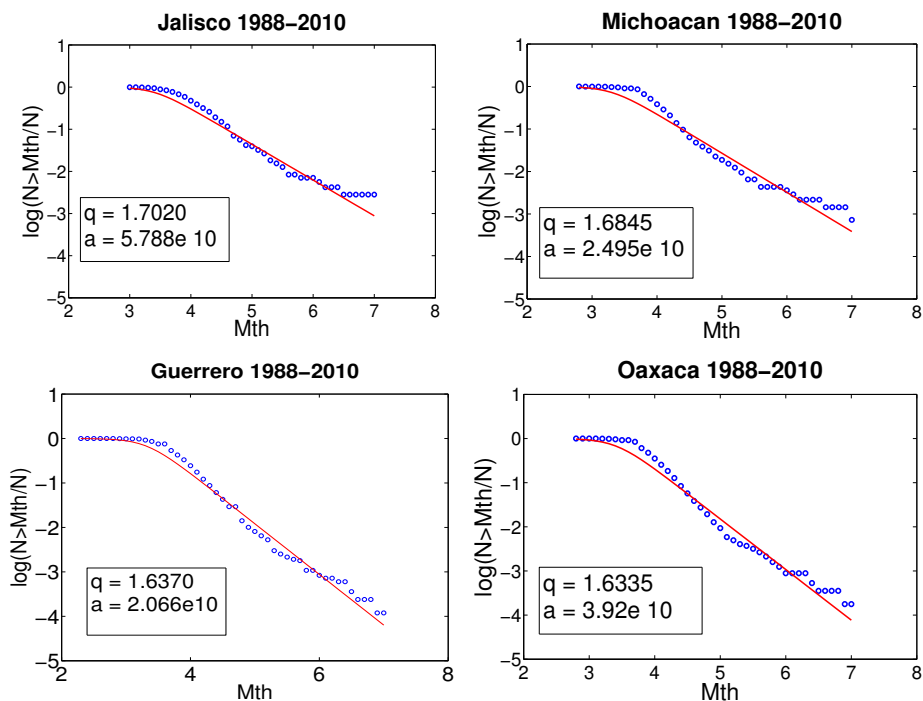
Fig. 3. Normalized cumulative number of earthquake with magnitude $m > M_{th}$ and fitting obtained with LM-algorithm for the seismicity monitored in each seismic region. The circles correspond to NCMD and lines are the fitting.

the final q and a values are obtained when the error attains a minimum or the fixed error is reached. The error is given by the square-2 norm of the residual, which is the difference between the original data and the values evaluated by the nonlinear fitting function. Since the initial values q_0 and a_0 giving the minimum estimation error e are not known *a priori*, this error e was calculated varying the initial values of a_0 and q_0. Figure 4 shows the numerical runs to compute the minimum error. The value of e is stable for $a_0 \geq 10^{10}$; for this range the obtained values of q are also stable, with q around 1.7. The minimum error was obtained for $q_0 = 1.698$ and $a_0 = 10^{10}$; then, these initial values were used to find the best fitting parameters; the q and a values calculated for each sub-catalogue are summarized in Table 1. Given a magnitude threshold ($M > 5.5$) of main shocks, we employ the declustering algorithm used by Telesca and Chen (2010) that specifies the two linking parameters in time and space scales: 3 days and 5 km. By using those parameters, we had removed the aftershock events generated from the main shocks with $M > 4.5$. The declustering algorithm removed less than 5 events
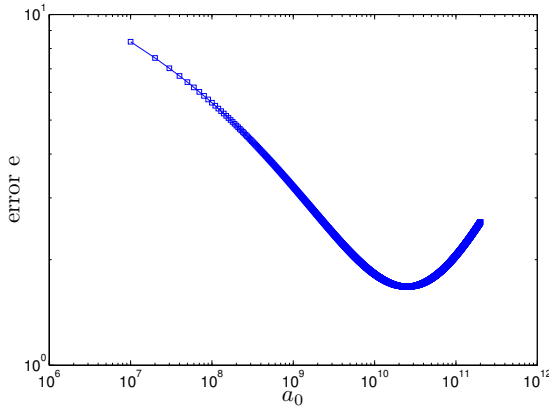
Fig. 4. Numerical runs to compute the minimum error in the adopted values q_0 and a_0.

Table 1

The q and a values obtained for each region

Region	q	a
Jalisco	1.7020	5.788×10^{10}
Michoacan	1.6845	2.495×10^{10}
Guerrero	1.6370	2.066×10^{10}
Oaxaca	1.6635	3.920×10^{10}

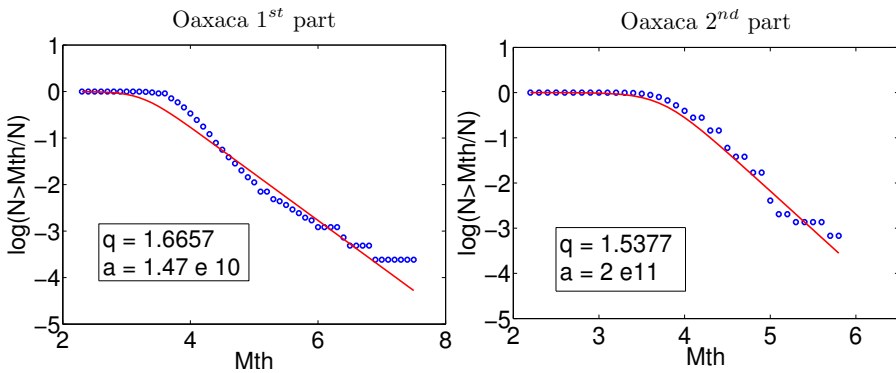Fig. 5. New fitting considering two sections in the Oaxaca region.

in each region for each main shock and the NCMD is basically the same as that shown without declustering. Then we can conclude that the proposed model is robust even with the presence of aftershocks.

The analysis of the NCMD yields q values between 1.6 and 1.7 for all the studied regions, the greatest value being at Jalisco; in that case it was not

possible to asseverate differences in their geodynamic process. We also observe that it is not possible to fit a unique curve for the whole range of magnitudes in the Oaxaca region. We can observe in Fig. 3 that around magnitudes 4.5 and 5, the behavior of the NCMD values changes, showing different slope for the fitting: particularly, the Oaxaca region shows a clear crossover. It is important to point out that this region also comprises the EQs occurred in Tehuantepec region that has a different subduction process. Then we analyzed independently the EQs for each region, observing a better fit for each one, as shown in Fig. 5.

5. CONCLUDING REMARKS

An analysis of the 1988-2010 Mexican South Pacific seismicity was performed by means of the non-extensive approach. We analyzed four regions: Jalisco, Michoacan, Guerrero, and Oaxaca, which are characterized by different tectonic regimes. The q values obtained are in agreement with those reported in the literature. It is remarkable to observe that the highest q value is obtained in Jalisco zone, with $q = 1.702$, while Oaxaca (second part) region has the lowest value, $q = 1.5377$. These results suggest that the subduction zone is more unstable in the northwestern (Jalisco) than in the southeastern part. From Fig. 2, it can be observed that stronger main shocks ($M_w > 7.5$) have occurred in the Jalisco–Michoacan region. The proposed models show different slopes for the fitting in Oaxaca region; this fact suggests that it may be expedient to analyze this region by considering narrow areas in the whole subduction region under study.

References

Abe, S. (2003), Geometry of escort distributions, *Phys. Rev. E* **68**, 3, 031101, DOI: 10.1103/PhysRevE.68.031101.

Anderson, R.S., A.L. Densmore, and M.A. Ellis (1999), The generation and degradation of marine terraces, *Basin Res.* **11**, 1, 7-19, DOI: 10.1046/j.1365-2117.1999.00085.x.

Bak, P., C. Tang, and K. Wiesenfeld (1988), Self-organized criticality, *Phys. Rev. A* **38**, 1, 364-374, DOI: 10.1103/PhysRevA.38.364.

Burridge, R., and L. Knopoff (1967), Model and theoretical seismicity, *Bull. Seismol. Soc. Am*. **57**, 3, 341-371.

Carlson, J.M., and J.S. Langer (1989), Mechanical model of an earthquake fault, *Phys. Rev. A* **40**, 11, 6470-6484, DOI: 10.1103/PhysRevA.40.6470.

Darooneh, A.H., and A. Mehri (2010), A nonextensive modification of the Gutenberg–Richter law: q-stretched exponential form, *Physica A* **389**, 3, 509-514, DOI: 10.1016/j.physa.2009.10.006.

De Santis, A., G. Cianchini, P. Favali, L. Beranzoli, and E. Boschi (2011), The Gutenberg–Richter law and entropy of earthquakes: two case studies in Central Italy, *Bull. Seismol. Soc. Am*. **101**, 3, 1386-1395, DOI: 10.1785/0120090390.

Gutenberg, B., and C.F. Richter (1944), Frequency of earthquakes in California, *Bull. Seismol. Soc. Am*. **34**, 4, 185-188.

Hasumi, T. (2009), Hypocenter interval statistics between successive earthquakes in the two-dimensional Burridge–Knopoff model, *Physica A* **388**, 4, 477-482, DOI: 10.1016/j.physa.2008.10.017.

Iglesias, A., S.K. Singh, A.R. Lowry, M. Santoyo, V. Kostoglodov, K.M. Larson and S.I. Franco-Sánchez (2004), The silent earthquake of 2002 in the Guerrero seismic gap, Mexico (M_w = 7.6): Inversion of slip on the plate interface and some implications, *Geof. Int*. **43**, 309-317.

Kagan, Y.Y., and L. Knopoff (1981), Stochastic synthesis of earthquake catalogs, *J. Geophys. Res*. **86**, B4, 2853-2862, DOI: 10.1029/JB086iB04p02853.

King, G. (1983), The accommodation of large strains in the upper lithosphere of the earth and other solids by self-similar fault systems: the geometrical origin of b-value, *Pure Appl. Geophys*. **121**, 5-6, 761-815, DOI: 10.1007/BF02590182.

Kostoglodov, V., and L. Ponce (1994), Relationship between subduction and seismicity in the Mexican part of the Middle America trench, *J. Geophys. Res*. **99**, B1, 729-742, DOI: 10.1029/93JB01556.

Larson, K.M., A.R. Lowry, V. Kostoglodov, W. Hutton, O. Sánchez, K. Hudnut and G. Suarez (2004), Crustal deformation measurements in Guerrero, Mexico, *J. Geophys. Res*. **109**, B4, 1-19, DOI: 10.1029/2003JB002843.

Lay, T., and T.C. Wallace (1995), *Modern Global Seismology*, Academic Press, New York.

Levenberg, K. (1944), A method for the solution of certain non-linear problems in least squares, *Quart. Appl. Math*. **2**, 164-168.

Marquardt, D.W. (1963), An algorithm for least-squares estimation of nonlinear parameters, *SIAM J. Appl. Math*. **11**, 2, 431-441, DOI: 10.1137/0111030.

Moré, J.J. (1978), The Levenberg–Marquardt algorithm: Implementation and theory, *Lect. Notes Math.* **630/1978**, DOI: 10.1007/BFb0067700.

Ohtake, M., T. Matumoto, and G.V. Latham (1981), Evaluation of the forecast of the 1978 Oaxaca, Southern Mexico earthquake based on a precursory seismic quiescence. **In:** D.W. Simpson and P.G. Richards (eds.), *Earthquake Prediction*, Maurice Ewing Series, AGU, United States, 53-62.

Olami, Z., H.J.S. Feder, and K. Christensen (1992), Self-organized criticality in a continuous, nonconservative cellular automaton modeling earthquakes, *Phys. Rev. Lett.* **68**, 8, 1244-1247, DOI: 10.1103/PhysRevLett.68.1244.

Pardo, M., and G. Suarez (1995), Shape of the subducted Rivera and Cocos plates in southern Mexico: Seismic and tectonic implications, *J. Geophys. Res*. **100**, B7, 12357-12373, DOI: 10.1029/95JB00919.

Ramírez-Herrera, M.T., V. Kostoglodov, and J. Urrutia-Fucugauchi (2011), Overview of recent coastal tectonic deformation in the Mexican subduction zone, *Pure Appl. Geophys*. **168**, 8-9, 1415-1433, DOI: 10.1007/s00024-010-0205-y.

Sarlis, N.V., E.S. Skordas, and P.A. Varotsos (2010), Nonextensivity and natural time: The case of seismicity, *Phys. Rev. E* **82**, 2, 021110, DOI: 10.1103/PhysRevE.82.021110.

Silva, R., G.S. França, C.S. Vilar, and J.S. Alcaniz (2006), Nonextensive models for eartquakes, *Phys. Rev. E* **73**, 026102, DOI: 10.1103/PhysRevE.73.026102.

Singh, S.K., M. Rodriguez, and L. Esteva (1983), Statistics of small earthquakes and frequency of occurrence of large earthquakes along the Mexican subduction zone, *Bull. Seismol. Soc. Am*. **73**, 6A, 1779-1796.

Singh, S.K., L. Ponce, and S.P. Nishenko (1985), The great Jalisco, Mexico, earthquakes of 1932: Subduction of the Rivera plate, *Bull. Seismol. Soc. Am*. **75**, 5, 1301-1313.

Song, T.-R.A., D.V. Helmberger, M.R. Brudzinski, R.W. Clayton, P. Davis, X. Pérez-Campos, and S.K. Singh (2009), Subducting slab ultra-slow velocity layer coincident with silent earthquakes in southern Mexico, *Science* **324**, 5926, 502-506, DOI: 10.1126/science.1167595.

Sotolongo-Costa, O., and A. Posadas (2002), Tsallis entropy: A non-extensive frequency-magnitude distribution of earthquakes, arXiv:cond-mat/0211160v1 [cond-mat.soft].

Sotolongo-Costa, O., and A. Posadas (2004), Fragment-asperity interaction model for earthquakes, *Phys. Rev. Lett*. **92**, 4, 048501, DOI: 10.1103/PhysRevLett.92.048501.

Telesca, L. (2010), Nonextensive analysis of seismic sequences, *Physica A* **389**, 9, 1911-1914, DOI: 10.1016/j.physa.2010.01.012.

Telesca, L., and C.-C. Chen (2010), Nonextensive analysis of crustal seismicity in Taiwan, *Nat. Hazards Earth Syst. Sci*. **10**, 1293-1297, DOI: 10.5194/nhess-10-1293-2010.

Tsallis, C. (1988), Possible generalization of Boltzmann–Gibbs statistics, *J. Stat. Phys*. **52**, 1-2, 479-487, DOI: 10.1007/BF01016429.

Turcotte, D.L. (1997), *Fractals and Chaos in Geology and Geophysics*, 2nd ed., Cambridge University Press, Cambridge.

Vargas, C.A., E. Basurto, L. Guzmán-Vargas, and F. Angulo-Brown (2008), Sliding size distribution in a simple spring-block system with asperities, *Physica A* **387**, 13, 3137-3144, DOI: 10.1016/j.physa.2008.01.108.

Varotsos, P.A., N.V. Sarlis, E.S. Skordas, H.K. Tanaka, and M.S. Lazaridou (2006), Entropy of seismic electric signals: Analysis in natural time under time reversal, *Phys. Rev. E* **73**, 3, 031114, DOI: 10.1103/PhysRevE.73.031114.

Wesnousky, S.G. (1999), Crustal deformation processes and the stability of the Gutenberg–Richter relationship, *Bull. Seismol. Soc. Am*. **89**, 4, 1131-1137.

Zúñiga, F.R., and S. Wiemer (1999), Seismic patterns: are they always related to natural causes?, *Pure Appl. Geophys*. **155**, 2-4, 713-726, DOI: 10.1007/s000240050285.

Ito Equations out of Domino Cellular Automaton with Efficiency Parameters

Zbigniew CZECHOWSKI and Mariusz BIAŁECKI

Institute of Geophysics, Polish Academy of Sciences, Warszawa, Poland
e-mails: zczech@igf.edu.pl, bialecki@igf.edu.pl

Abstract

Ito equations are derived for simple stochastic cellular automaton with parameters describing efficiencies for avalanche triggering and cell occupation. Analytical results are compared with the numerical one obtained from the histogram method. Good agreement for various parameters supports the wide applicability of the Ito equation as a macroscopic model of some cellular automata and complex natural phenomena which manifest random energy release. Also, the paper is an example of effectiveness of histogram procedure as an adequate method of nonlinear modeling of time series.

Key words: stochastic processes, cellular automata, avalanches, discrete solvable models, time series.

1. INTRODUCTION

The Ito equation describes evolution of a stochastic diffusion Markov process (of order 1). Its parameters can be nonlinear functions of the process. Therefore, the Ito equation is a good candidate for a nonlinear model of phenomenon which manifests non-regular, random behaviour. Quite often, observed variables have macroscopic character, and hence the Ito equation can be considered as a macroscopic model of the complex system, in which microscopic collective interactions have been averaged to an adequate form of terms in the equation.

Various complex geophysical, biological, economical and other processes, in spite of apparent random appearance, can lead to some regular behaviours

---

or patterns. Registered time series are investigated by different, less or more sophisticated methods, which help to find these dependencies. Some interesting regularities may consist of new macroscopic laws of complex systems.

Time series analysis is a well developed branch of science. In the linear case, well known procedures were elaborated (ARMA, *etc.*). Autoregressive models can be generalized by introducing nonlinearity. One important class consists of threshold autoregressive models (TAR, SETAR, Markov switching model) (Tong and Lim 1980, Tong 1983, 1990) which are piecewise linear AR models (for a comprehensive review, see Tong 2011). The primary objective of the models is the general drift of the time series. Nonlinear models which are focused on the conditional variance are autoregressive models with conditional heteroscedasticity (ARCH) and GARCH (Engle 1982, Bollerslev 1986, Cryer and Chan 2008). The most natural generalization of linear ARMA models is the bilinear model BL (Granger and Andersen 1978), in which products of previous values of noise with previous values of time series are included. It was shown that GARCH models (for a square function of the investigated random value) and some BL models have linear ARMA representation (see, *e.g.*, Fan and Yao 2005). Summarizing, TAR models introduce nonlinearity in the drift but GARCH in the diffusion term. The Ito equation introduces a nonlinearity in drift and diffusion terms at the same time and offers a wide class of distributions (from Gaussian up to long tail). Therefore, using the Ito equation may provide some progress in the field of effective methods of constructing nonlinear models from time series data.

First attempts of determination of the Ito equation were proposed by Haken and Borland (Haken 1988, Borland and Haken 1992a, b; 1993, Borland 1999). Their procedure (SEQUIN) uses the knowledge of some moments of the joint distribution function, which form constraints for the Maximum Information Principle. The SEQUIN method works sufficiently well for the case of a weak noise. However, it was shown (Rozmarynowska 2009) that the procedure fails in the case of strong multiplicative noise, when long-tail distributions appear.

A purely numerical procedure of construction of the Ito equation from time series data was proposed by Siegert *et al.* (1998). This direct procedure, based on the histogram of the joint distribution function, always produces an output (*i.e.*, clouds of points). It gives some approximation of terms in the Ito equation. It is effective for strong noise too, but fitting proper functions to scattered clouds of points is a difficult task. Moreover, it should be underlined that this method may be fallacious when the time series cannot be approximated by a diffusion Markov process. It is possible to determine the Markov order of a given time series (Racca *et al.* 2007) but there is no method to verify if it is a diffusion process or not. The only verification we may perform is a comparison of the input time series with that generated by the reconstructed Ito equation.

An adequacy of approximation of a natural phenomena by nonlinear models is of great importance. To touch the topic in the context of the Ito equation we propose what follows. First, we replace the natural phenomenon by the domino cellular automaton, which can be fully monitored. Due to a complete knowledge of the three level hierarchy of the model, relations between the macroscopic (the Ito equation, moment equations) and the microscopic (rules of the automaton) description are clear and understandable. Then, we construct the Ito equation in two independent ways. The standard histogram method is compared with results derived analytically. Derivation of the Ito equation out of a cellular automaton is a crucial step in this approach. To this aim, a special stochastic cellular automaton with avalanches was introduced (Białecki and Czechowski 2010b, Czechowski and Białecki 2010). The defining rules of the domino automaton were chosen to satisfy two opposite requirements: complex behavior and relatively simple mathematical structure. Introducing efficiency parameters in the domino automaton leads to a big diversity of states, which covers wide range of avalanche sizes. The goal of this paper is an analytical derivation of the Ito equations for a domino cellular automaton with efficiency parameters and a comparison with results of the histogram method.

In Section 2 we shortly introduce the domino cellular automaton with the efficiency parameters and present equations describing its behaviour in equilibrium state. Properties of the automaton for various efficiency parameters are analysed. In Section 3 we consider fluctuations around the equilibrium and propose suitable approximation formulas. In Section 4 the Ito equation is derived. The comparison of histogram procedure results and analytical formulas are presented. We conclude with short remarks in Section 5.

2. DOMINO CELLULAR AUTOMATON WITH EFFICIENCY PARAMETERS

We present shortly the rules governing the automaton and some relations derived in Białecki and Czechowski (2010a, b). Consider 1-dimensional grid of cells. There are only two states of a cell: empty or occupied (by a single ball). The evolution rules are as follows. In a time step a single new ball is added to a randomly chosen cell of the system.

- If the new ball hits an empty cell, it becomes occupied with probability ν, or the ball rebounds from the grid with probability $(1 - \nu)$.

- If the new ball hits an occupied cell, it rebounds with probability $(1 - \mu)$, or with probability μ it knocks out balls from the cell and other adjacent occupied cells from the whole cluster (they become empty – an avalanche is triggered).
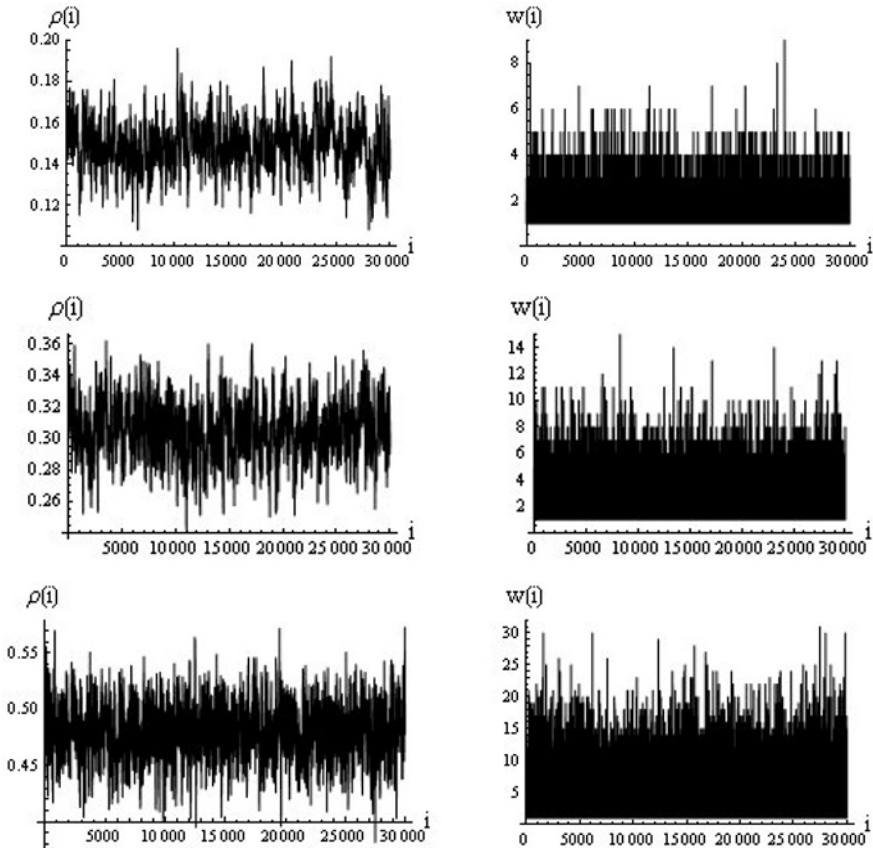
Fig. 1.   Simulation results of the domino cellular automaton at the statistically stationary state: left – time series for density $\rho(i)$, right – time series for avalanche sizes $w(i)$. Three examples for different cases: $\eta = 4$ (upper diagrams), $\eta = 1$ (middle) and $\eta = 0.25$ (lower). Grid size $N = 1000$.

An important macroscopic variable which describes the state of the automaton is the density ρ, *i.e.*, the rate of number of occupied cells to the grid size. We monitor two time series generated by the cellular automaton: the avalanche sizes $w(i)$ and the density $\rho(i)$ computed after each avalanche. Figure 1 presents three examples of such time series for three chosen values of the ratio $\eta = \mu/\nu = 4, 1$, and 0.25. In simulations we use grid size $N = 1000$. An increase of the average density, the average avalanche size and the range of fluctuations of ρ with decreasing μ/ν is evident.

A state of the automaton can be characterized by the cluster size distribution n_i, *i.e.*, by numbers of clusters of size i (normalized by the size of the grid).

The following relations, which are exact in the stationary state, were derived (Białecki and Czechowski 2010a, b):

$$n_1 = \frac{1}{\eta + 2}(1 - \rho - 2n + n_1^0) \tag{1}$$

$$n_2 = \frac{2}{2\eta + 2}\left(1 - \frac{n_1^0}{n}\right)n_1 \tag{2}$$

$$n_i = \frac{1}{\eta i + 2}\left(2n_{i-1}\left(1 - \frac{n_1^0}{n}\right) + n_1^0 \sum_{k=1}^{i-2} \frac{n_k n_{i-1-k}}{n^2}\right) \quad \text{for} \quad i \geq 3. \tag{3}$$

Here η is the rate μ/ν, n is the number of all clusters, $n = \sum_{i \geq 1} n_i$, and ρ is the density of occupied cells, $\rho = \sum_{i \geq 1} i n_i$. The n_1^0 is the number of single empty cells and is given by the formula $n_1^0 = 2n/(3 + \frac{2\eta\rho}{n})$.

The following simple balance equations for moments of n_i were also derived (Białecki and Czechowski 2010a, b):

$$2m_0 + (1 + \eta)m_1 = 1, \tag{4}$$

$$m_1 + \eta m_2 = 1, \tag{5}$$

where $m_0 = n$, $m_1 = \rho$, and $m_2 = \sum_{i \geq 1} n_i i^2$. The average cluster size $<i>$, the average avalanche size $<w>$ and the average square deviation from the average cluster size $<T>$ (*i.e.*, the analogue of temperature) are expressed by these moments:

$$<i> = \frac{m_1}{m_0} = \frac{2\rho}{1 - (1 + \eta)\rho} \tag{6}$$

$$<w> = \frac{m_2}{m_1} = \frac{1 - \rho}{\eta\rho} \tag{7}$$

$$<T> = \sum_{i \geq 1} n_i(i - <i>)^2 = \rho(<w> - <i>). \tag{8}$$

The stationary value of the density ρ_s can be found by numerical solution of implicit algebraic equation

$$\rho = \sum_{i \geq 1} i n_i, \tag{9}$$

where n_i are given by Eqs. (1)-(3).

Figure 2 shows dependencies of stationary variables ρ_s, n, $<i>$, $<w>$, and $<T>$ on the ratio η. As it was expected, they decrease with increasing η, because greater probability μ (relevant to ν) of triggering the avalanche reduces the number of occupied cells on the grid. Only the total number of clusters n has a maximum for η around $1/4$. Table 1 displays a comparison of values of ρ_s and $<w>$ calculated from equations with respective values taken from simulation.
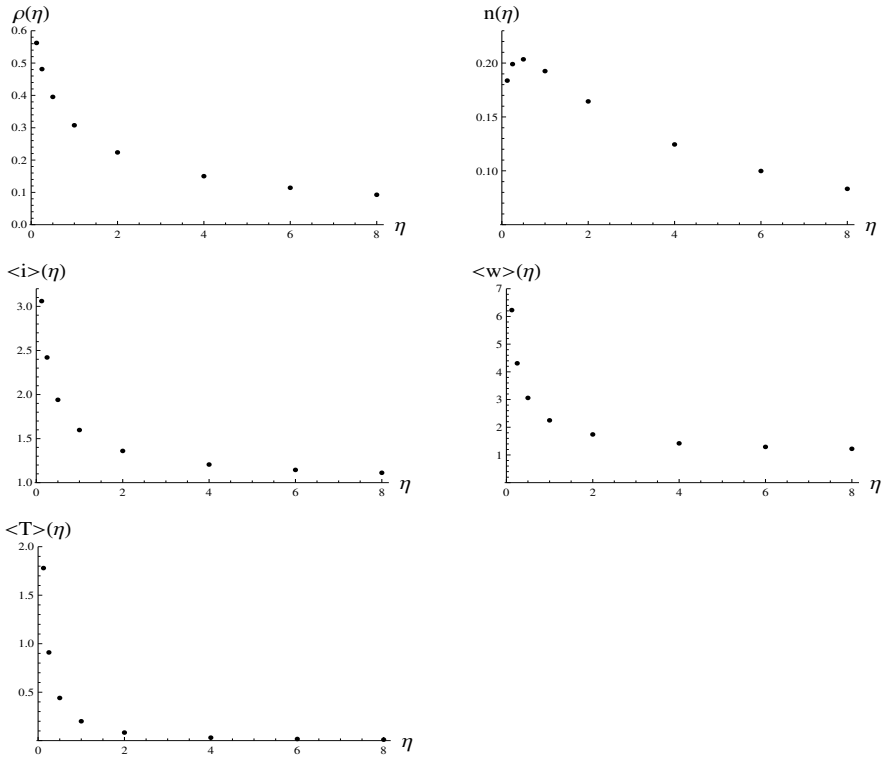
Fig. 2. Dependences of stationary variables: ρ_s, n, $<i>$, $<w>$, and $<T>$ on the ratio of efficiency parameters $\eta = \mu/\nu$.

Table 1

Comparison of values of stationary density ρ_s
and average avalanche size $<w>$ calculated from equations
with those obtained from simulations (grid size $N = 1000$)

	ρ_s		$<w>$	
	analytical	simulation	analytical	simulation
$\eta = 4$	0.1501	0.1498	1.4147	1.4159
$\eta = 1$	0.3075	0.3068	2.2520	2.2421
$\eta = 1/4$	0.4815	0.4801	4.3074	4.3382

3. FORMULAS FOR FLUCTUATIONS
AROUND THE STATIONARY STATE

For deviations from the stationary state ρ_s, formulas from Section 2 are not valid. Therefore, we use the approximation introduced in our parallel paper

(Czechowski and Białecki 2012). It was based on the assumption that the following geometric-like form for $n_i(\rho)$ is maintained:

$$n_1(\rho) = (1-\rho)^2 a_1(\rho) = (1-\rho)^2 a_1\rho, \tag{10}$$

$$n_k(\rho) = n_{k-1}(\rho)a_k(\rho) \quad \text{for} \quad 4 \geq k \geq 2, \tag{11}$$

$$n_k(\rho) = n_{k-1}(\rho)(a_5(\rho))^{k-4} \quad \text{for} \quad k \geq 5, \tag{12}$$

where $a_k(\rho)$, $k = 1, \ldots, 5$, are linear functions of ρ (in particular, $a_1(\rho) = a_1\rho$). The forms of formulas (10)-(12) extend the 1D percolation geometric cluster size distribution, $n_k = \rho^k(1-\rho)^2$. Numerical simulations of the domino automaton confirm the validity of this approximation.

Linear functions $a_k(\rho)$, $k = 2, \ldots, 5$, are found from the Taylor expansion of the ratios:

$$n_k(\rho)/n_{k-1}(\rho) \tag{13}$$

around ρ_s to the order 1. Using the procedure presented in Czechowski and Białecki (2012), numerical formulas for $a_k(\rho)$, $k = 1, \ldots, 5$, for chosen values of the parameter η were found and they are presented in Table 2. As a check for these expressions, we plot the first moment of $n_k(\rho)$ (which should be equal to the density ρ) as a function of ρ for chosen parameters η. Figure 3 shows satisfactory fit in the full range of variability of ρ for all three values of η.

Table 2

Numerical values of functions a_k for Eqs. (10)-(12)

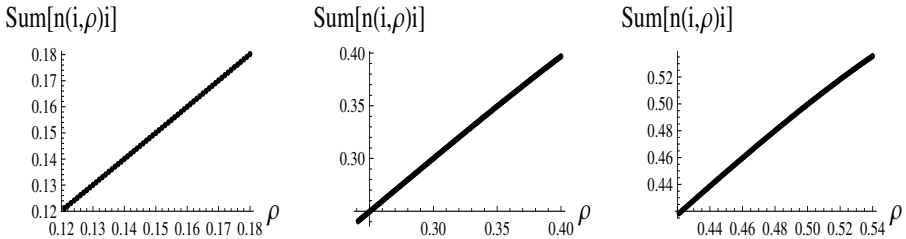|	$\eta = 4$	$\eta = 1$	$\eta = 0.25$
$a_1(\rho)$	0.9528ρ	0.8365ρ	0.7348ρ
$a_2(\rho)$	$0.6449\rho + 0.0715$	$0.7032\rho + 0.1223$	$0.5669\rho + 0.1470$
$a_3(\rho)$	$2.4095\rho - 0.1846$	$1.4316\rho - 0.0484$	$1.3742\rho - 0.0546$
$a_4(\rho)$	$0.5163\rho + 0.0989$	$0.5651\rho + 0.2273$	$0.4908\rho + 0.3761$
$a_5(\rho)$	$0.5139\rho + 0.0994$	$0.5569\rho + 0.2328$	$0.4772\rho + 0.4054$

Fig. 3. Sum $\sum_{i \geq 1} i n_i$ computed by using Eqs. (10)-(12) *versus* ρ for three cases: $\eta = 4$ (left graph), $\eta = 1$ (middle), $\eta = 0.25$ (right).

4. DERIVATION OF THE ITO EQUATION

First of all, we should decide which one of the time series, the density $\rho(i)$ or the avalanche size $w(i)$, may be treated as a realization of the Markov diffusion process. Because the avalanche time series is more complex and not Markovian of order 1, we use the time series for density. An easy check ensures that automaton rules provide the required 1st order Markov property for $\rho(i)$. We emphasize that the following convention is assumed: the state of the grid (and the size of the avalanche) is monitored after each avalanche only. In this way we avoid less interesting stairs-like increase of $\rho(i)$ in periods between avalanches.

In order to derive the Ito equation

$$d\rho = a(\rho)\mathrm{d}t + \sqrt{b(\rho)}\mathrm{d}W(t), \tag{14}$$

we need the transition probability function $P(\rho+\Delta\rho, t+\Delta t \,|\, \rho, t)$ (see Risken 1996). Functions $a(\rho)$ and $b(\rho)$ are known to be the drift and diffusion coefficients, respectively, and $W(t)$ is the Wiener process. Following Czechowski and Białecki (2010) and our parallel paper (Czechowski and Białecki 2012, in which the case $\eta = 1$ was considered), the probability of effective gain $EG(k)$ (an increase of $\rho(i)$ by k occupied cells) and effective loss $EL(k)$ are given by the formulas:

$$EG(k) \equiv P\left(\rho_i + \frac{k}{N}, i+1|\rho_i, i\right) = \sum_{s=k+1} (\nu(1-\rho))^s \mu\rho w_{s-k}(\rho) \ \ \text{for } k \geq 0, \tag{15}$$

$$EL(k) \equiv P\left(\rho_i - \frac{k}{N}, i+1|\rho_i, i\right) = \sum_{s=k} (\nu(1-\rho))^{s-k} \mu\rho w_s(\rho) \ \ \text{for } k \geq 1, \tag{16}$$

where $w_s = \frac{n_s s}{\rho}$ is the probability that the occupied cell is a part of the cluster of size s (which also corresponds to the probability of avalanche of size s) and N is the grid size.

Balls rebounded off the grid do not trigger avalanches; they set the relative efficiency for triggering an avalanche with respect to the efficiency of occupation of an empty cell. Hence, for time series analysis, one can consider only active (not rebounded) balls introducing appropriate corrective coefficient. Thus, in expressions (15) and (16) parameters μ and ν should be replaced by effective parameters:

$$\mu_e = \frac{\mu}{\mu\rho + \nu(1-\rho)} = \frac{\eta}{\eta\rho + 1 - \rho}, \tag{17}$$

$$\nu_e = \frac{\nu}{\mu\rho + \nu(1-\rho)} = \frac{1}{\eta\rho + 1 - \rho}. \tag{18}$$

As a result, probabilities $EG(k)$ and $EL(k)$ satisfy the normalization condition.

The drift and diffusion forces in the Ito equation correspond (see Risken 1996) to the first and the second moment of the transition probability:

$$a(\rho) \propto \sum_{k \geq 1} k \left(EG(k) - EL(k) \right), \tag{19}$$

$$b(\rho) \propto \sum_{k \geq 1} k^2 \left(EG(k) + EL(k) \right). \tag{20}$$

Tedious transformations on sums (see Appendix in Czechowski and Białecki, 2012) lead to expressions for $a(\rho)$ and $b(\rho)$ in terms of the first, second and third moment of $n_k(\rho)$:

$$a(\rho) \propto \frac{\nu_e(1-\rho)}{1 - \nu_e(1-\rho)} - \frac{1}{\rho} \sum_{k \geq 1} k^2 n_k, \tag{21}$$

$$b(\rho) \propto \frac{\nu_e(1-\rho)(1 + \nu_e(1-\rho))}{(1 - \nu_e(1-\rho))^2}$$
$$- \frac{2\nu_e(1-\rho)}{\rho(1 - \nu_e(1-\rho))} \sum_{k \geq 1} k^2 n_k + \frac{1}{\rho} \sum_{k \geq 1} k^3 n_k. \tag{22}$$

Note that the dependence on ν_e is not essential. The above formulas can be also expressed in terms of μ_e; in fact, they depend on η and ρ only. The second and the third moments themselves can be calculated using approximate Eqs. (10)-(12) from Section 3.

5.   CONCLUSIONS

Introduction of efficiency parameters μ and ν essentially enriched the automaton. By changing the ratio $\eta = \mu/\nu$, the domino cellular automaton can attain a wide range of values for important variables: ρ_s, n, $<i>$, $<w>$ and $<T>$ (see Fig. 2), which characterize a macroscopic behaviour. The time evolution of the model can be described by the Ito equation; therefore, we derive analytically a satisfactory approximation of Ito terms $a(\rho)$ and $b(\rho)$ as functions of the ratio $\eta = \mu/\nu$. For three chosen values of η, analytical and simulation results were compared. Figure 4 shows a good fit for these three cases. Thus, we have a simple, fully elaborated model which can manifest a wide range of behaviours.

Moreover, we show that the histogram method of reconstruction of Ito equation from time series works well in the case of domino cellular automaton. The automaton plays a role of a complex system, in which energy is slowly accumulated and rapidly released in avalanches. Therefore, it is possible that
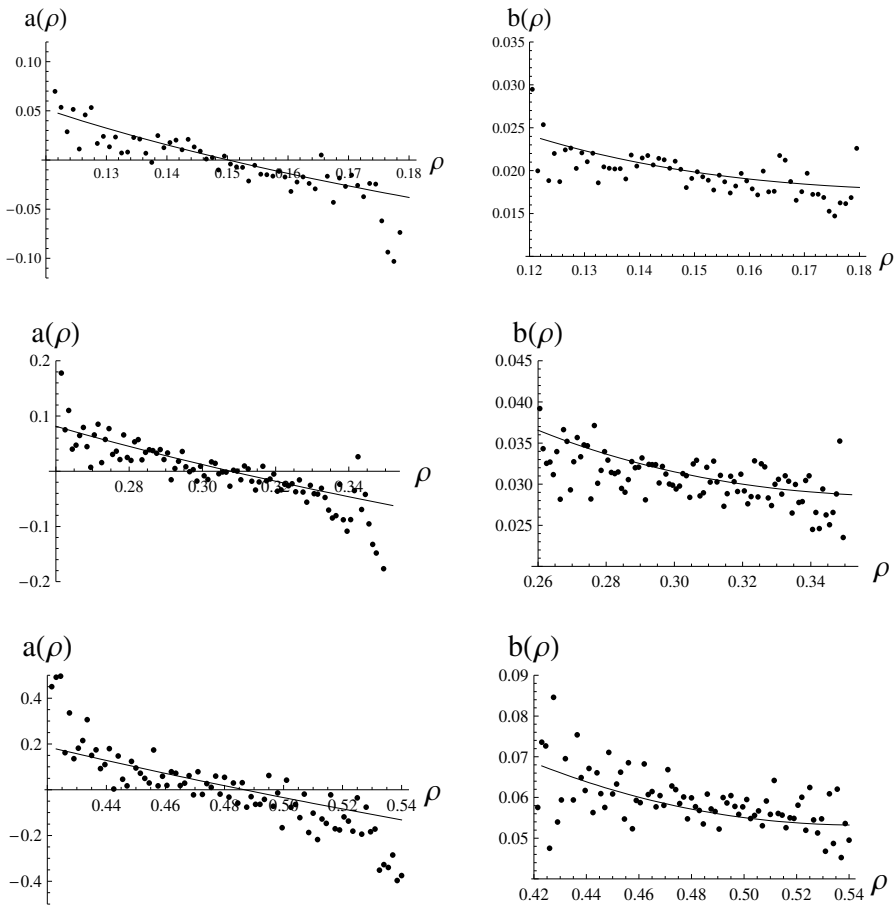
Fig. 4.   Illustration of functions $a(\rho)$ and $b(\rho)$ in Ito equations for three values of parameters: $\eta = 4$ (upper diagrams), $\eta = 1$ (middle), $\eta = 0.25$ (lower). Dots represent values reconstructed by the histogram procedure from time series generated by the domino cellular automaton (see Fig. 1), lines – calculated from Eqs. (21) and (22) using approximation (10)-(12) and parameters presented in Table 2.

the histogram procedure can offer an adequate method of nonlinear modeling of similar natural phenomena basing on the time series data. The method fills a gap between linear stochastic models (ARMA, *etc.*) and nonlinear deterministic models (Takens method, see Takens 1981) because it is both stochastic and nonlinear.

R e f e r e n c e s

Białecki, M., and Z. Czechowski (2010a), Analytic approach to stochastic cellular automata: exponential and inverse power distributions out of Random Domino Automaton, *arXiv:1009.4609* [nlin.CG].

Białecki, M., and Z. Czechowski (2010b), On a simple stochastic cellular automaton with avalanches: simulation and analytical results. **In**: V. de Rubeis, Z. Czechowski, and R. Teisseyre (eds.), *Synchronization and Triggering: from Fracture to Earthquake Processess*, GeoPlanet: Earth and Planetary Sciences, Vol. 1, Springer, Berlin, 63-75, DOI: 10.1007/978-3-642-12300-9-5.

Bollerslev, T. (1986), Generalized autoregressive conditional heteroskedasticity, *J. Econometrics* **31**, 307-327.

Borland, L. (1999), Simultaneous modelling of nonlinear deterministic and stochastic dynamics, *Physica D* **90**, 2-3, 175-190, DOI: 10.1016/S0167-2789(96)00143-1.

Borland, L., and H. Haken (1992a), Unbiased determination of forces causing observed processes. The case of additive and weak multiplicative noise, *Z. Phys. B* **88**, 95-103, DOI: 10.1007/BF01573843.

Borland, L., and H. Haken (1992b), Unbiased estimate of forces from measured correlation functions, including the case of strong multiplicative noise, *Ann. Physik* **504**, 6, 452-459, DOI: 10.1002/andp.19925040607.

Borland, L., and H. Haken (1993), On the constraints necessary for macroscopic prediction of time-dependent stochastic processes, *Rep. Math. Phys.* **33**, 1-2, 35-42, DOI: 10.1016/0034-4877(93)90038-G.

Cryer, J.D., and K.S. Chan (2008), *Time Series Analysis: With Applications in R*, Springer, New York.

Czechowski, Z., and M. Białecki (2010), Ito equations as macroscopic stochastic models of geophysical phenomena – construction of the models on the basis of time series. **In**: V. de Rubeis, Z. Czechowski, and R. Teisseyre (eds.), *Synchronization and Triggering: from Fracture to Earthquake Processess*, GeoPlanet: Earth and Planetary Sciences, Vol. 1, Springer, Berlin, 77-96, DOI: 10.1007/978-3-642-12300-9-6.

Czechowski, Z., and M. Białecki (2012), Three-level description of the domino cellular automaton, *J. Phys. A: Math. Theor.* **45**, 155101, DOI:10.1088/1751-8113/45/15/155101.

Engle, R. (1982), Autoregressive conditional heteroscedasticity with estimates of variance of United Kingdom inflation, *Econometrica* **50**, 4, 987-1008.

Fan, J., and Q. Yao (2005), *Nonlinear Time Series: Nonparametric and Parametric Methods*, Springer, New York.

Granger, C.W.J., and A.P. Andersen (1978), *Introduction to Bilinear Time Series Models*, Vandenhoeck and Puprecht, Gottingen.

Haken, H. (1988), *Information and Self-Organization: A Macroscopic Approach to Complex Systems*, Springer, Berlin.

Racca, E., F. Laio, D. Poggi, and L. Ridolfi (2007), Test to determine the Markov order of time series, *Phys. Rev. E* **75**, 1, 011126, DOI: 10.1103/PhysRevE.75.011126.

Risken, H. (1996), *The Fokker–Planck Equation*, Springer, Berlin.

Rozmarynowska, A. (2009), On the reconstruction of Ito models on the base of time series with long-tail distributions, *Acta Geophys.* **57**, 2, 311-329, DOI: 10.2478/s11600-008-0074-2.

Siegert, S., R. Friedrich, and J. Peinke (1998), Analysis of data sets of stochastic systems, *Phys. Lett. A* **243**, 5-6, 275-280, DOI: 10.1016/S0375-9601(98)00283-7.

Takens, F. (1981), Detecting strange attractors in turbulence. **In**: D.A. Rand and L.S. Young (eds.), *Dynamical Systems and Turbulence*, Lecture Notes in Mathematics Vol. 898, Springer, New York.

Tong, H. (1983), *Threshold Models in Nonlinear Time Series Analysis*, Lecture Notes in Statistics, Springer, New York.

Tong, H. (1990), *Nonlinear Time Series Analysis: A Dynamical Systems Approach*, Oxford University Press, Oxford.

Tong, H. (2011), Threshold models in time series analysis   30 years on (with discussions by P. Whittle, M. Rosenblatt, B.E. Hansen, P. Brockwell, N.I. Samia and F. Battaglia), *Statistics and Its Interface* **4**, 107-136.

Tong, H., and K.S. Lim (1980), Threshold autoregression, limit cycles and cyclical data, *J. Roy. Statist. Soc. B* **42**, 3, 245-292.

Testing a Scaling Law
for the Earthquake Recurrence Time Distributions

Elisaveta MAREKOVA

Plovdiv University "Paisiy Hilendarski", Plovdiv, Bulgaria
e-mail: eligeo@uni-plovdiv.bg

A b s t r a c t

The earthquake recurrence time distribution in a given space-time window is being studied, using earthquake catalogues from different seismic regions (Southern California, Canada, and Central Asia). The quality of the available catalogues, taking into account the completeness of the magnitude, is examined. Based on the analysis of the catalogues, it was determined that the probability densities of the earthquake recurrence times can be described by a universal gamma distribution, in which the time is normalized with the mean rate of occurrence. The results show a deviation from the gamma distribution at the short interevent times, suggesting the existence of clustering. This holds from worldwide to local scales and for quite different tectonic environments.

Key words: recurrence times, scaling law, universality, power law, earthquake catalogues.

1. INTRODUCTION

Seismicity and earthquake triggering are highly complex phenomena in the spatial, temporal, and energy domains. The dynamics of these phenomena is not fully understood, because there is no complete knowledge of the physical processes occurring in the Earth's lithosphere.

The statistical properties of seismicity have been a subject of intensive interest for many years; *e.g.*, one can mention Omori law (for the aftershocks, which defines the decrease in the number of earthquakes following

the main shock with time), and the Gutenberg–Richter law (for the events with particular magnitude) (Gutenberg and Richter 1965, Reasenberg and Jones 1989, Kagan 1994, Utsu *et al*. 1995, Turcotte 1997, Utsu 2002, Knopoff 1997).

In order to understand the long-term variation in the earthquake occurrences, earthquake prediction, and seismic risk estimates, it is necessary to study either the frequency or the probability distribution of interoccurrence times of the earthquakes. For a long time, the earthquakes occurrence has been considered to be independent. Hence, the temporal variation of earthquakes has to be considered only due to random processes. Mathematically, such processes in which the events occur continuously and independently of one another are described by Poisson processes. However, the existence of nests, swarms, and clusters in the spatial and temporal distributions of earthquakes obviously shows the existence and the importance of non-Poisson processes for earthquake occurrences.

Nowadays, the attention paid to the statistics of the interoccurrence times (also called waiting time, interevent time, *etc*.) between the consecutive earthquakes is continuously growing (Bak *et al*. 2002, Corral 2003, 2004a, b; Davidsen and Goltz 2004). There are different distributions proposed, as for instance exponential (Poisson), Log-normal, that of Weibull, gamma, *etc*. (Gardner and Knopoff 1974, Udias and Rice 1975, Wang and Kuo 1998, Ellsworth *et al*. 1999). Aside from that, there is an opinion that the strong events, alongside some faults, show the tendency of periodic or semi-periodic repetition (Schwartz and Coppersmith 1984, Utsu 1984, Kagan and Jackson 1995, Sieh 1996, Kagan 1997, Stein 2002, Murray and Segall 2002).

On the other hand, as for the aftershock series obeying Omori law, it seems obvious that the interevent time distribution follows a power law. However, there is a difference between the power constant derived from Omori equation and that from interevent time distribution (Utsu *et al*. 1995, Utsu 2002).

Corral (2004a, b), having analyzed different catalogues, found out that the density distribution of the observed time intervals could be described by gamma distribution. The equation, after the simplification of Hainzl *et al*. (2006), is as follows:

$$f(\theta) = C\,\theta^{\gamma-1}\exp\left(-\frac{\theta}{\beta}\right), \tag{1}$$

where the constants are: $C = 0.5 \pm 0.1$, $\gamma = 0.67 \pm 0.005$, $\beta = 1.58 \pm 0.15$, and θ is a normalized time interval, which is a product of time interval, Δt, and the seismic activity, R, *i.e.*, $\theta = R\Delta t$. It plays the role of a dimensionless recurrence time.

It has been established that the distribution for stationary seismicity is universal, so it holds for both worldwide and local scales, as well as for all magnitude intervals. In this case, however, the regions (or periods) should be chosen so that the aftershock activity is not dominant.

The results obtained for stationary rate periods have been summarized as non-stationary periods (Corral 2006) and Omori sequences (Shcherbakov *et al*. 2005, Bottiglieri *et al*. 2010). On the other hand, recent studies have questioned the universality of the interevent time distribution (Davidsen and Goltz 2004, Molchan 2005, Hainzl *et al*. 2006, Saichev and Sornette 2006, 2007; Sornette *et al*. 2008, Touati *et al*. 2009).

The universality has been also doubted based on the theoretical investigations (Saichev and Sornette 2006, 2007; Sornette *et al*. 2008).

Following Bak *et al*. (2002), the present study addressed the problem of universality of the scaling law by considering seismicity as a phenomenon on its own. This study concentrates on the temporal properties of seismicity. First, the events will be examined either without separation into different types (foreshocks, mainshocks, and aftershocks), or will divide the crust into zones with different tectonic properties, but will place all events and regions on the same footing. Subsequently, two different methods for declustering will be applied and their effect on the gamma scaling law will be investigated.

2. DESCRIPTION OF THE DATA AND THE DECLUSTERING PROCEDURES

The seismic zones selected for the present study are described in Table 1. The catalogues are available on the Internet:

- ❑ http://seismo.nrcan.gc.ca/stnsdata/nedb/bull_e.php for Cascadia, Offshore region, Charleviox and Lower St. Lawrence;
- ❑ http://neic.usgs.gov/neis/epic/epic.html for Morgan Hill, Imperial Valley, Calaveras fault, West Quebec;
- ❑ http://www.wdcb.rssi.ru for Garm;
- ❑ http://zeus.wdcb.ru/wdcb/sep/toktogul/resru.html for Toktogul Region.

Rectangular spatial windows were used and their coordinates are indicated in Table 1. The same table shows the periods studied for each catalogue, as well as the number of the events, including the present study.

The choice of the seismoactive zones was predetermined by the available information and by the different geotectonic environments where these zones are situated.

In addition to the zones and events described in Table 1, the following catalogues were also used in the current research:

Parameters of zones used in this study

No.	Region	Time period	Space window	~ area [km]	M_C	N
1	Charlevoix, Canada	1977-1993	47.2-48°N 69.6-70.5°W	70×90	1.7	260
2	Imperial Valley, California	1932-1974	32.5-33.25°N 115-115.75°W	70×85	3.5	168
3	Calaveras fault, California	1947-1974	36.92-37.4°N 121.42-121.75°W	30×50	2.5	354
4	West Quebec, Canada	1927-1992	44-47.5°N 72.0-77.5°W	430×390	2.4	445
5	Morgan Hill, California	1944-1974	37.1-37.4°N 121.5-121.8°W	26×30	2.0	329
6	Lower St. Lawrence, Canada	1982-1992	46-50.2°N 65-69°W	300×465	2.0	522
7	Garm, Asia	1962-1979	38.5-39.5°N 70-71.6°E	140×110	2.8	1416
8	Cascadia, Canada	1964-1999	47.8-52°N 121-131°W	715×465	3.9	159
9	Offshore region, Canada	1960-1991	48-52°N 127.5-133°W	395×610	3.0	1062
10	Toktogul, Asia	1965-1991	39.23-43.47°N 69.23-76.98°E	650×470	1.7	229
11	NEIC catalogue	1972-2008	global		6.0	3964
12	SHLK catalogue	1983-2002	31-34°N 114-122°W		2.5	13 095
13	NCDEC catalogue	1983-2008	32.5-43°N 113-123°W		3.0	10 243

Explanations: N is the number of events, M_C is the completeness magnitude.

❑ Catalogues from Corral's papers:
   • http://www.neic.cr.usgs.gov/neis/epic/epic_global.html – NEIC-PDE catalogue (National Earthquake Information Center, Preliminary Determination of Epicenters; Corral 2005a);
   • http://www.data.scec.org/ftp/catalogs/SHLK – the Southern California catalogue of Shearer *et al.* (Corral 2009, Shearer *et al.* 2005).

❑ Catalogue from Hainzl *et al*. paper:

    • http://www.ncedc.org/anss – ANSS catalogue (Advanced National Seismic System; Hainzl *et al*. 2006).

The catalogues chosen for investigation cover the time after 1900. This selection aims to make the catalogues more complete and homogeneous. Before dealing with the frequency distribution of the interevent times, the catalogues data were checked for the magnitude of completeness, M_C (the threshold value M_C is the minimum magnitude for which the catalogue is considered complete for the spatial and temporal windows studied). For each one, only events with magnitude M above M_C were considered. The freely available software Zmap, written by Wiemer (2001), was used for this purpose.

It is supposed that the universal law is restricted to stationary seismicity (homogeneity in time, where statistical properties of the process are independent of the time window). It should be kept in mind that the aftershock sequences in general are not stationary. In order to insure the process stationarity, linear ranges of the cumulative curve of the events (with $M \geq M_C$) were selected, *i.e.*, periods of time for which no aftershock sequence dominates in the spatial region were considered. All these stationary periods were studied together. It is to be noted that by removing such time periods, "holes" appear in the catalogue data, *e.g.*, there appear relatively long time intervals in which "no events are observed". Since these "holes" are artificial, they are not considered in the interevent time distributions. Table 1 includes only the values after the final data treatment of the catalogues.

The earthquakes' appearance, in time and space, is a complex process, which is considered as a combination of independent (main) and dependent (secondary) events. It is supposed that the main events are mainly caused by secular tectonic movements. The secondary earthquakes correspond to shocks triggered by the static and dynamic stress changes, seismically activated fluid flows, afterslips, *etc*. In this regard, they are controlled by mechanical processes, which are partially controlled by previous earthquakes.

To study the randomness of a series of main events it is necessary first to identify the aftershocks (secondary shocks) and to remove them from the catalogues. The process itself is called declustering. There are different algorithms of the aftershock removal from the seismic catalogues. They are based on different characteristics of the aftershock process. One such class is the so-called „space-time windows" (Gardner and Knopoff 1974, Christoskov and Lazarov 1981, Prozorov and Dziewonski 1982). Another possibility is to apply the so-called "method of the moments" of second or higher order. It appears to be suitable for aftershock removal (Reasenberg 1985).

Table 2

Zones used in this study

No.	Region	M_C	Time period	N_{Zmap}	Time period	$N_{Knopoff}$
1	Charlevoix, Canada	3.0	1910-1993	97	1907-1993	77
2	Imperial Valley, California	3.5	1932-1975	122	1915-1975	66
3	Calaveras fault, California	3.0	1941-1975	151	1941-1975	97
4	West Quebec, Canada	3.0	1903-1995	217	1905-1995	159
5	Morgan Hill, California	3.0	1941-1974	66	1941-1974	57
6	Lower St. Lawrence, Canada	3.0	1941-1992	145	1941-1992	98
7	Garm, Asia	3.0	1962-1989	678	1962-1989	156
8	Cascadia, Canada	3.9	1964-1999	149	1964-1999	69
9	Offshore region, Canada	3.0	1960-1991	788	1961-1991	155
10	Toktogul, Asia	3.3	1965-1991	229	1929-1991	192

Explanations: M_C is the chosen magnitude threshold, N is the number of remaning events after the declustering by Reasenberg method (programm Zmap, N_{Zmap}) and by Knoppoff method ($N_{Knopoff}$).

The next step in the present investigation was to perform the declustering to the initial catalogues for the zones listed in Table 1. The time intervals, and the number of the earthquakes, after declustering, are listed in Table 2.

It is a well-known fact that there is no best solution for the declustering. In the present study, the preliminary removal of the aftershock events was made according to the "Reasenberg's spatial-time window", included in the Zmap program (Wiemer 2001), as well as by "Knopoff window". The comparison of the results of both algorithms gives the information about the influence of the declustering process on the derived final interevent time distribution.

3. RESULTS AND DISCUSSION

The events in the catalogues were thought as a point process in time. All the events were ordered in time, from $i = 1$ to N, and were characterized only according to their occurrence time, t_i. From the data, one defines the interevent time, Δt ($\Delta t_i \equiv t_i - t_{i-1}$), as the time interval between consecutive events. First, one may say that Δt ranges from seconds to more than 100 days.

One could work with the logarithm of Δt but a more direct possibility is to define the bins over which the probability density is calculated as c^n, with $c > 1$ and n labeling consecutive bins. This ensures an appropriate bin size for each time scale ($c = 2.5$ s is adopted).

The number of pairs of consecutive events separated by time whose value lies in a given bin, and divided by the total number of pairs of events and by the size of the bin to attain the estimation of the probability density $D(\Delta t)$ over that bin, were then counted.

Using a procedure similar to that of Corral (2004a, b; 2005a, b, c), we have determined that a universal scaling law describes the probability density $D(\Delta t)$ of the recurrence time. In this way, $D(\Delta t)$ scales with the rate of seismic activity R in the area as

$$D(\Delta t) = R f(R \Delta t) , \tag{2}$$

where the functional form of $f(x)$ is independent of the geographic zone and the magnitude threshold; R is defined as the mean number of earthquakes per unit time, $R = N/T$ ($T =$ catalogue time span). R is considered to be independent of time (stationary seismic activity is discussed). Note that multiplying Δt by R gives dimensionless time ($\theta = R\Delta t$).

The best fit is obtained from a (truncated) gamma distribution (Corral 2005a, b, c) in the form:

$$f(\theta) = a (b\theta)^{\gamma-1} \exp(-b\theta) , \tag{3}$$

where a, b, and γ are the parameters which were varied.

All the catalogues were evaluated separately and the obtained frequency distributions of time intervals were fitted with a single curve. Noteworthy, the different distributions look similar in shape, although the ranges are different. During the fitting, some scattering of the parameters of the fitting curve was observed. The shape parameter γ lies in the interval from 0.63 to 0.88, parameter a from 0.15 to 0.80, and b from 0.27 to 0.61.

Figure 1 shows the distributions of the interevent times as a function of the rescaled recurrence time bins, *i.e.*, $D(\theta)/R$ *versus* θ. In this case, all the distributions merge into a single curve $f(x)$. The good quality of the data indicates the validity of a "scaling law" of the type (3). Figure1 contains the data labeled with No. 1 through 10, as described in Table 1.

Figure 2 represents the same data as in Fig. 1, but the data of the additional catalogues, cited by Corral (2005a) and Hainzl *et al.* (2006), are added (Nos. 11-13, Table 1).

The data shown in Figs. 1 and 2 were approximated according to Eq. (3). The fit of the rescaled distributions by the gamma function is good for
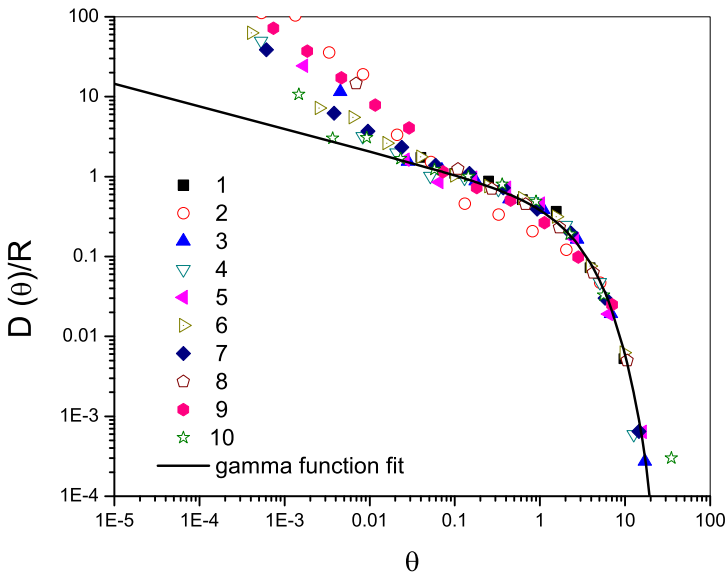
Fig. 1. Probability densities of dimensionless recurrence times from local catalogues listed in Table 1. The continuous line is a gamma fit. Colour version of this figure is available in electronic edition only.
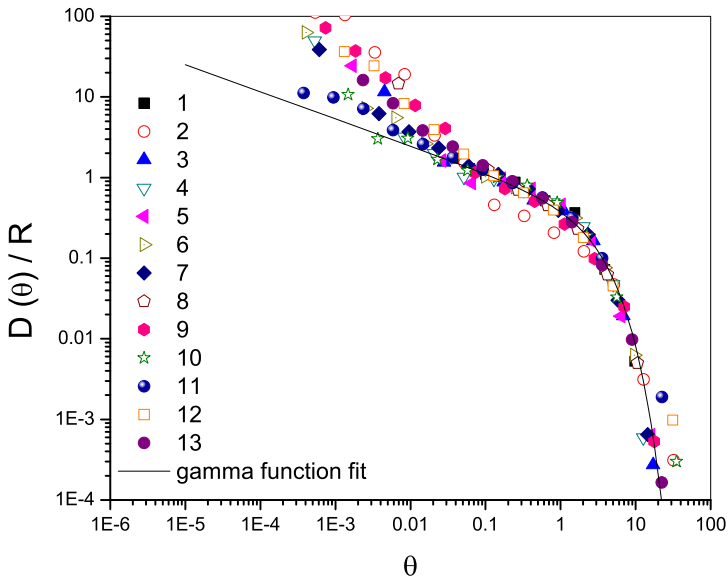

Fig. 2. Probability densities of dimensionless recurrence times from local catalogues, as listed in Table 1, and the additional catalogues, as mentioned in the text: 11 – NEIC, 12 – NCDEC, 13 – SHLK. The continuous line is a gamma fit. Colour version of this figure is available in electronic edition only.

intermediate and large values of the recurrence time, with $\theta > 0.05$. The parameters of the fitting procedure are as follows:

❑ For data Nos. 1-10 from Table 1 (Fig. 1)

$$a = 0.43 \pm 0.10; \quad b = 0.39 \pm 0.12; \quad \gamma = 0.718 \pm 0.046;$$

❑ For all data from Table 1 (Fig. 2)

$$a = 0.36 \pm 0.09; \quad b = 0.34 \pm 0.11; \quad \gamma = 0.664 \pm 0.042.$$

In the present paper, the Chi-square, χ^2, test was used to determine the goodness of fit between theoretical gamma scaling function and experimental data for interevent time distributions. The Chi-square test indicates that the hypothesis about the compatibility between the observed data from Table 1 (with Nos. 1-10 and all data) and expected values from gamma distributions is not rejected at the 5% significance level.

Our values of γ coincide with the values obtained by Corral (2004a, b; 2005a, b, c). The data of all investigated catalogues obey the scaling law for recurrence-time distributions for stationary seismicity. This law is equivalent to the invariance of seismicity under renormalization-group-like transformations, for which the role of correlations between recurrence times and magnitudes is essential (Corral 2005c). Hence, the universality of the gamma law is confirmed.

For some regions there is a clear tendency for the distribution to exceed the value given by the scaling function; there is an excess of short interevent times.

It should be clear that considering stationary seismicity has nothing to do with declustering (the removal of aftershocks from data). We simply consider periods of time for which no aftershock sequence dominates, but many smaller sequences may be hidden in the data, intertwined in such a way to give rise to an overall stationary seismic rate. In particular, deviations from universality at small Δt have been related to the interplay between correlated earthquakes following a gamma distribution, and uncorrelated events following a pure exponential decay.

Seismicity declustering, the process to separate the seismicity catalogue into mainshocks and fore- and aftershocks, is widely used in seismology, in particular for seismic hazard assessment or in earthquake prediction models. There exists a variety of declustering algorithms that have been proposed over the years. Up to now, most users have applied either the algorithm of Gardner and Knopoff (1974) or Reasenberg (1985).

The aftershock sequence is considered to be a clear and apparent relation between a strong earthquake and the accompanying weaker quakes. Right after the strong one, a number of secondary quakes happen in relatively short intervals of time. Having all that in mind, we may observe a great number of short time intervals between the following earthquakes of the aftershock

sequence. The removal of the secondary events from the catalogues decreases the short time intervals which will influence the distribution of the latter. Besides, it would not surprisingly reduce the deviation between the real data and the fitting line in Eq. (3)

After the declustering, the initial catalogues for the zones Nos. 1-10 from Table 1, investigation for interevent time distribution for the earthquakes listed in Table 2 was performed again.

The separate fitting of the data with function (3) once again shows certain scattering of the values of parameters a, b, and γ. The interval of deviation of parameter γ is wider after the declustering according to "Knopoff window" method.

The corresponding rescaled recurrence-time probability densities after the declustering are shown in Fig. 3 (Reasenberg's method) and Fig. 4 ("Knopoff window"), together with the scaling function (3) used in the previous case. The collapse of the data onto a single curve is again an indication of the validity of a scaling law, and the fact that this curve is well fitted by the same scaling law is a sign of "universality". The fit of the rescaled distributions by the gamma scaling function is again good for intermediate and large values of the recurrence time (for $\theta > 0.05$).

There is a significant deviation in the values of the shape parameter γ
   ❑ for Reasenberg's method, $\gamma = 0.763 \pm 0.062$;
   ❑ for "Knopoff window", $\gamma = 1.059 \pm 0.088$.

The Chi-square, χ^2, test was used again to determine the goodness of fit between gamma scaling function and data after declustering. The experimental results are consistent with the theoretical results at the 5% significance level.

When Reasenberg method (Reasenberg 1985) is applied, a small number of short recurrence times is marked. Nevertheless, the real data in Fig. 3 is deviated from the gamma function in this time intervals, the scaling law remains. This could be considered, on the one hand, as the presence of secondary events, which were not successfully removed. On the other hand, the points under discussion could be approximated with a power-law that is much flatter. This could be an indication for smaller clustering degree. Nevertheless, it is remarkable that this kind of clustering is different from the clustering of aftershock sequences, as in this case we are dealing with a stationary process.

In the case of "Knopoff window" declustering method, the parameter values $\gamma \approx 1$, cause a change into the scaling law (3) to an exponential function. This is typical for the interevent time distribution, when the appearance could be described by means of Poisson distribution. Usually such events are defined as independent (main) shocks.
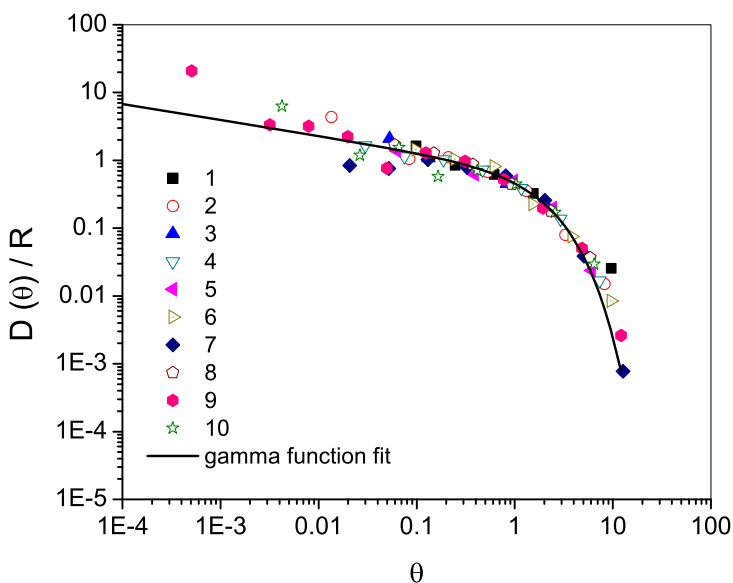
Fig. 3. Probability densities of dimensionless recurrence times from the zones listed in Table 1. Data after Reasenberg declustering procedure (Zmap). The continuous line is a gamma fit. Colour version of this figure is available in electronic edition only.
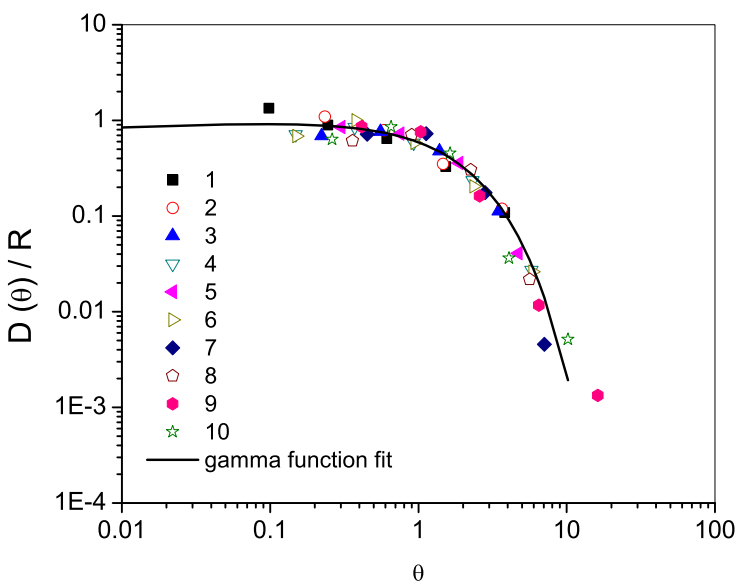

Fig. 4. Probability densities of dimensionless recurrence times from the zones listed in Table 1. Data after declustering based on the "Knopoff window". The continuous line is a gamma fit. Colour version of this figure is available in electronic edition only.

A well-known fact is that using "Knopoff window" for aftershocks separation leads to the removal of 60-70% of events from the catalogue. This way, some "holes" in the remaining catalogue appear. One can speculate that possibly some weaker earthquakes, near the stronger one, could be considered dependent and will be wrongly removed from the catalogue. As a consequence, as one can see from the present study, events in the short time intervals are missing.

4.   CONCLUSIONS

In the present survey, data from catalogues are included from some relatively small seismic zones, differentiated by seismic zones in the relevant countries. The main purpose is to verify the statement that a universal law exists for the time intervals distribution between sequence earthquakes. The survey has been conducted for the local catalogues first and then conducted together with the data from the catalogues for which such surveys and publications have already been made.

The results confirm the universality of the law. The data collapse occurs under a simple rescaling of the data from different regions or time periods and they can be described by a single gamma scaling law. The fit of the rescaled distributions by the gamma function is good for intermediate and large values of the recurrence time (about $\theta > 0.05$). The deviations are considerable for small values of θ. In this case the statistics is low (few events in the small bins being considered; that is why, when fitting, these intervals are partly united). For certain regions there is a clear tendency for the distribution to exceed the values given by the scaling function. The accuracy of the gamma fit is guaranteed as the seismic activity is stationary in large range of recurrence times; on the contrary, short times are usually not free of disturbances of the stationariness, due to the triggering of small aftershock sequences, which destroy the universal scaling behavior.

Some authors argued that the times between consecutive earthquakes depend on the selection of the coordinates of the region under study and the range of magnitudes selected. The conclusion is also that the size of the chosen zones and the cut-off magnitude threshold do not affect the results.

The application of declustering procedures keeps the character of the density distribution of the waiting times. When the "Knopoff window" was applied, the small interevent times diminish and the distribution becomes exponential. Applying Reasenberg method, a small number of short times remains. This could be thought to be an indication of different sort of clustering between the earthquakes.

However, because of the non-unique nature of seismicity declustering, we did not make an absolute judgment on the quality of seismicity decluster-

ing. Even though a great progress has been made in the last decade, there are still many open questions, *i.e.*, starting with the physical triggering of earthquakes (aftershocks), effects of uncertainties in the catalogue on the results of declustering, or the effect of censored data (selection in time, space and magnitude range) on the outcome.

The surveys about the distribution of the time intervals between the earthquakes from declustered sequence might be useful for comparing the numerous qualities of declustering procedures. On the other hand, this might be used to develop methodics of identifying the clusterisation in the seismic sequence of another type, a different one from the aftershocks.

References

Bak, P., K. Christensen, L. Danon, and T. Scanlon (2002), Unified scaling law for earthquakes, *Phys. Rev. Lett.* **88**, 17, 178501, DOI: 10.1103/PhysRevLet. 88.178501.

Bottiglieri, M., L. de Arcangelis, C. Godano, and E. Lippiello (2010), Multiple-time scaling and universal behavior of the earthquake interevent time distribution, *Phys. Rev. Lett.* **104**, 15, 158501, DOI: 10.1103/PhysRevLett. 104. 158501.

Christoskov, L., and R. Lazarov (1981), A method for estimating the seismological catalogues representativeness and its application to the central part of the Balkan region, *Bulg. Geophys. J.* **8**, 3, 66-76 (in Bulgarian).

Corral, A. (2003), Local distributions and rate fluctuations in a unified scaling law for earthquakes, *Phys. Rev. E* **68**, 3, 035102(R), DOI: 10.1103/PhysRevE. 68.035102.

Corral, A. (2004a), Long-term clustering, scaling, and universality in the temporal occurrence of earthquakes*, Phys. Rev. Lett.* **92**, 10, 108501, DOI: 10.1103/ PhysRevLett.92.108501.

Corral, A. (2004b), Universal local versus unified global scaling laws in the statistics of seismicity, *Physica A* **340**, 590-597, DOI: 10.1016/j.physa.2004.05.010.

Corral, A. (2005a), Mixing of rescaled data and Bayesian inference for earthquake recurrence times, *Nonlin. Processes Geophys.* **12**, 1, 89-100, DOI: 10.5194/npg-12-89-2005.

Corral, A. (2005b), Time-decreasing hazard and increasing time until the next earthquake, *Phys. Rev. E* **71**, 1, 017101, DOI: 10.1103/PhysRevE.71. 017101.

Corral, A. (2005c), Renormalization-group transformations and correlations of seismicity, *Phys. Rev. Lett.* **95**, 2, 028501; DOI: 10.1103/PhysRevLett.95. 028501.

Corral, A. (2006), Statistical features of earthquake temporal occurrence, *Lect. Notes Phys.* **705**, 191-221, DOI: 10.1007/3-540-35375-5_8.

Corral, A. (2009), Statistical tests for scaling in the inter-event times of earthquakes in California, *Int. J. Mod. Phys. B* **23**, 28-29, 5570-5582, DOI: 10.1142/S0217979209063869.

Davidsen, J., and C. Goltz (2004), Are seismic waiting time distributions universal?, *Geophys. Res. Lett.* **31**, L21612, DOI: 10.1029/2004GL020892.

Ellsworth, W.L., M.V. Matthews, R.M. Nadeau, S.P. Nishenko, P.A. Reasenberg, and R.W. Simpson (1999), A physically-based earthquake recurrence model for estimation of long-term earthquake probabilities, U.S. Geological Survey Open-File Report 99-522.

Gardner, J.K., and L. Knopoff (1974), Is the sequence of earthquakes in Southern California, with aftershocks removed, Poissonian?, *Bull. Seimol. Soc. Am.* **64**, 5, 1363-1367.

Gutenberg, B., and C.F. Richter (1965), *Seismicity of the Earth*, Hafner Pub., New York.

Hainzl, S., F. Scherbaum, and C. Beauval (2006), Estimating background activity based on interevent-time distribution, *Bull. Seismol. Soc. Am.* **96**, 1, 313-320, DOI: 10.1785/0120050053.

Kagan, Y.Y. (1994), Observational evidence for earthquakes as a nonlinear dynamic process, *Physica D* **77**, 1-3, 160-192, DOI: 10.1016/0167-2789(94)90132-5.

Kagan, Y.Y. (1997), Statistical aspects of Parkfield earthquake sequence and Parkfield prediction experiment, *Tectonophysics* **270**, 3-4, 207-219, DOI: 10.1016/S0040-1951(96)00210-7.

Kagan, Y.Y., and D.D. Jackson (1995), New seismic gap hypothesis: Five years after, *J. Geophys. Res.* **100**, B3, 3943-3959, DOI: 10.1029/94JB03014.

Knopoff, L. (1997), Scale invariance of earthquakes. **In:** B. Dubrulle, F. Graner, and D. Sornette (eds.), *Scale Invariance and Beyond*, Springer-Verlag, Berlin, 159-172.

Molchan, G. (2005), Interevent time distribution in seismicity: A theoretical approach, *Pure Appl. Geophys.* **162**, 6-7, 1135-1150, DOI: 10.1007/s00024-004-2664-5.

Murray, J., and P. Segall (2002), Testing time-predictable earthquake recurrence by direct measurement of strain accumulation and release, *Nature* **419**, 287-291, DOI: 10.1038/nature00984.

Prozorov, A.G., and A.M. Dziewonski (1982), A method of studying variations in the clustering property of earthquakes: Application to the analysis of global seismicity, *J. Geophys. Res.* **87**, B4, 2829-2839, DOI: 10.1029/JB087iB04p02829.

Reasenberg, P. (1985), Second-order moment of Central California seismicity, 1969-1982, *J. Geophys. Res.* **90**, B7, 5479-5495, DOI: 10.1029/JB090iB07p05479.

Reasenberg, P.A., and L.M. Jones (1989), Earthquake hazard after a mainshock in California, *Science* **243**, 4895, 1173-1176, DOI: 10.1126/science.243.4895. 1173.

Saichev, A., and D. Sornette (2006), "Universal" distribution of interearthquake times explained, *Phys. Rev. Lett.* **97**, 7, 078501, DOI: 10.1103/PhysRevLett. 97.078501.

Saichev, A., and D. Sornette (2007), Theory of earthquake recurrence times, *J. Geophys. Res.* **112**, B04313, DOI: 10.1029/2006JB004536.

Schwartz, D.P., and K.J. Coppersmith (1984), Fault behavior and characteristic earthquakes: Examples from the Wasatch and San Andreas fault zones, *J. Geophys. Res.* **89**, B7, 5681-5698, DOI: 10.1029/JB089iB07p05681.

Shcherbakov, R., G. Yakovlev, D.L. Turcotte, and J.B. Rundle (2005), Model for the distribution of aftershock interoccurrence times, *Phys. Rev. Lett.* **95**, 21, 218501, DOI: 10.1103/PhysRevLett.95.218501.

Shearer, P., E. Hauksson, and G. Lin (2005), Southern California hypocenter relocation with waveform cross-correlation, Part 2: Results using source-specific station terms and cluster analysis, *Bull. Seismol. Soc. Am.* **95**, 3, 904-915, DOI: 10.1785/0120040168.

Sieh, K. (1996), The repetition of large-earthquake ruptures, *Proc. Natl. Acad. Sci. USA* **93**, 9, 3764-3771, DOI: 10.1073/pnas.93.9.3764.

Sornette, D., S. Utkin, and A. Saichev (2008), Solution of the nonlinear theory and tests of earthquake recurrence times, *Phys. Rev. E* **77**, 6, 066109, DOI: 10.1103/PhysRevE.77.066109.

Stein, R.S. (2002), Parkfield's unfulfilled promise, *Nature* **419**, 257-258, DOI: 10.1038/419257a.

Touati, S., M. Naylor, and I.G. Main (2009), Origin and nonuniversality of the earthquake interevent time distribution, *Phys. Rev. Lett.* **102**, 16, 168501, DOI: 10.1103/PhysRevLett.102.168501.

Turcotte, D.L. (1997), *Fractals and Chaos in Geology and Geophysics*, 2nd ed., Cambridge University Press, Cambridge, 398 pp.

Udias, A., and J. Rice (1975), Statistical analysis of microearthquake activity near San Andreas geophysical observatory, Hollister, California, *Bull. Seismol. Soc. Am.* **65**, 4, 809-827.

Utsu, T. (1984), Estimation of parameters for recurrence models of earthquakes, *Bull. Earthq. Res. Inst. Univ. Tokyo* **59**, 53-66.

Utsu, T. (2002), Statistical features of seismicity. **In:** W.H.K. Lee, H. Kanamori, P.C. Jennings, and C. Kisslinger (eds.), *International Handbook of Earthquake and Engineering Seismology*, *Part A*, Elsevier, New York, 719-732, DOI: 10.1016/S0074-6142(02)80246-7.

Utsu, T., Y. Ogata, and R.S. Matsu'ura (1995), The centenary of the Omori formula for a decay law of aftershock activity, *J. Phys. Earth* **43**, 1, 1-33, DOI: 10.4294/jpe1952.43.1.

Wang, J.-H., and C.-H. Kuo (1998), On the frequency distribution of interoccurrence times of earthquakes, *J. Seismol.* **2**, 4, 351-358, DOI: 10.1023/A: 1009774819512.

Wiemer, S. (2001), A software package to analyze seismicity: ZMAP, *Seismol. Res. Lett.* **72**, 3, 373-382, DOI: 10.1785/gssrl.72.3.373.

VERSITA

Cross-Correlation Earthquake Precursors in the Hydrogeochemical and Geoacoustic Signals for the Kamchatka Peninsula

Gennadiy V. RYABININ[1], Valeriy A. GAVRILOV[2],
Yuriy S. POLYAKOV[3], and Serge F. TIMASHEV[4,5]

[1]Kamchatka Branch, Geophysical Survey of Russian Academy of Sciences,
Petropavlovsk-Kamchatsky, Russia; e-mail: gena@emsd.iks.ru

[2]Institute of Volcanology and Seismology,
Far Eastern Branch of the Russian Academy of Sciences,
Petropavlovsk-Kamchatsky, Russia; e-mail: vgavr@kscnet.ru

[3]USPolyResearch, Ashland, PA, USA
e-mail: ypolyakov@uspolyresearch.com (corresponding author)

[4]Institute of Laser and Information Technologies, Russian Academy of Sciences,
Troitsk, Moscow Region, Russia; e-mail: serget@mail.ru

[5]Karpov Institute of Physical Chemistry, Moscow, Russia

A b s t r a c t

We propose a new type of earthquake precursor based on the analysis of correlation dynamics between geophysical signals of different nature. The precursor is found using a two-parameter cross-correlation function introduced within the framework of flicker-noise spectroscopy, a general statistical physics approach to the analysis of time series. We consider an example of cross-correlation analysis for water salinity time series, an integral characteristic of the chemical composition of groundwater, and geoacoustic emissions recorded at the G-1 borehole on the Kamchatka peninsula in the time frame from 2001 to 2003, which is characterized by a sequence of three groups of significant seismic events. We found that cross-correlation precursors took place 27, 31, and 35 days ahead of the strongest earthquakes for each group of seismic

events, respectively. At the same time, precursory anomalies in the signals themselves were observed only in the geoacoustic emissions for one group of earthquakes.

Key words: earthquake precursor, flicker-noise spectroscopy, cross-correlation analysis, hydrogeochemical time series, geoacoustic time series.

1. INTRODUCTION

Earthquake prediction within a time frame of several months to less than an hour before the catastrophic event, which is often referred in literature as "short-term" prediction, has been a subject of extensive research studies and controversial debates, both in academia and mass media, in the past two decades (Geller 1997, Geller *et al.* 1997, Wyss *et al.* 1997, Uyeda *et al.* 2009, Cicerone *et al.* 2009). One of the key areas in this field is the study of earthquake precursors, physical phenomena that reportedly precede at least some earthquakes. The precursory signals are usually grouped into electromagnetic, hydrological/hydrochemical, gasgeochemical, geodetic, and seismic (Geller 1997, Hartmann and Levy 2005, Uyeda *et al.* 2009, Cicerone *et al.* 2009, Ryabinin *et al.* 2011).

Despite the large number of earthquake precursors reported in literature, most of which are summarized by Hartmann and Levy (2005), Cicerone *et al.* (2009), an International Commission on Earthquake Forecasting for Civil Protection concluded on 2 October 2009, "the search for precursors that are diagnostic of an impending earthquake has not yet produced a successful short-term prediction scheme" (ICEFCP 2009). The reports of the International Association of Seismology and Physics of the Earth's Interior contain similar findings (Wyss and Booth 1997). The lack of confidence can be attributed to several reasons. First, some fundamental aspects of many non-seismic signals, for example, lithosphere-atmosphere-ionosphere coupling and propagation of high-frequency electromagnetic signals in the conductive earth, are unresolved, and many of the proposed physical models are questionable (Uyeda *et al.* 2009). Second, the experimental data on precursory signals are often limited to few earthquakes and few measurement sites and they frequently contain gaps and different types of noise (Hartmann and Levy 2005, Cicerone *et al.* 2009, Uyeda *et al.* 2009). Third, different techniques of identifying the anomalies are used for different signals or even in different studies for the same signal. In some cases, the anomalous changes are determined by analyzing the signals themselves (Hartmann and Levy 2005, Uyeda *et al.* 2009, Cicerone *et al.* 2009), while in other cases they are identified by studying the derived statistics or functions, such as Fisher

information or scaling parameters (Telesca *et al.* 2009a, b). Moreover, seasonal changes and instrumentation or other background noise often need to be filtered out prior to the identification of precursors.

In view of the above, we believe that earthquake precursor research can be advanced by employing a phenomenological approach to the analysis of signals of different types in the same local geographic region. We assume that a large earthquake may be preceded by a reconfiguration of a geophysical system on different time and space scales, which manifests itself in qualitative changes of various signals within relatively short time intervals. In our previous study (Ryabinin *et al.* 2011), we used a nonstationarity factor introduced within the framework of flicker-noise spectroscopy (FNS), a statistical physics approach to the analysis of time series (Timashev and Polyakov 2007, Timashev 2007, Timashev *et al.* 2010), to determine the time moments of abrupt rearrangements in the seismic zone of the Kamchatka peninsula. We analyzed together the nonstationarity factors for chlorine-ion concentration of groundwater and geoacoustic emissions in a deep borehole within that seismic zone in the time frame around a large earthquake on 8 October 2001. Our analysis showed that nonstationarity-factor peak values (potential precursors) take place in the interval from 70 to 50 days before the earthquake for the hydrogeochemical data, and at 29 and 6 days in advance for the geoacoustic data.

In this paper, we suggest a new type of earthquake precursor based on cross-correlation analysis of the dynamics for two different types of signals: hydrogeochemical and geoacoustic. The idea of examining qualitative changes in the cross-correlations for signals of different types stands on the systematic analysis of common earthquake precursors presented by Cicerone *et al.* (2009). Most of the known models suggest that earthquake precursory anomalies are driven by rapid deformations and strain changes within the earth in the rock near or in the fault zone at the region of eventual earthquake rupture. It was shown that the rapid deformations just prior to fracture combined with changes in the groundwater and gas flow in the earth caused by the variation of porosity and permeability in the rock volume, which in its turn is effected by micro-fractures, can generate all of the earthquake precursors studied by Cicerone *et al.* (2009). In other words, cross-correlation precursors rely on a common mechanism of "preparatory" changes attributed to a system reconfiguration preceding a large earthquake. It should be pointed out that the analysis of cross-correlations may uncover hidden qualitative changes which cannot be determined from the analysis of specific signals by themselves because of seasonal changes and instrumentation and other background noise.

We would like to note that the precursory role of synchronization effects in geophysical signals of different nature was previously studied by Lyubu-

shin *et al.* (1997) and Lyubushin (1998, 2000, 2007). Based on the assumption that a large earthquake is preceded by a substantial increase in the synchronization between various geophysical processes, the author developed mathematical methods to build an aggregate signal that provides maximum information on the most general variations common to all analyzed processes. This assumption came from the catastrophe theory stating that the spatial radius of fluctuations increases and the collective component in the behavior of different parts of a complex system rises when the underlying complex system approaches a catastrophe or a phase transition. The aggregate signal used for detecting precursory anomalies is obtained using covariance matrices for multidimensional vectors and Fourier or wavelet transformations (Lyubushin 2007). In contrast to this method, the cross-correlation precursor suggested in this paper is focused on local dynamic correlations for a pair of signals, with zero or non-zero time shift between each other. The method proposed in this paper does not automatically assume that maximum cross-correlations correspond to a precursor, but looks for significant changes in the cross-correlation function, which are believed to be associated with system reconfiguration.

The paper is structured as follows. In Section 2, we provide the fundamentals of FNS and present the cross-correlation function. Section 3 describes the experimental setup. Section 4 discusses the cross-correlation analysis of hydrogeochemical and geoacoustic data for the Kamchatka peninsula in the time frame from 2001 to 2003. Section 5 presents the conclusions.

2. FLICKER-NOISE SPECTROSCOPY (FNS) CROSS-CORRELATION FUNCTION

Here, we will only deal with the basic FNS relations needed to understand the cross-correlation function. FNS is described in more detail elsewhere (Timashev 2006, 2007, Timashev and Polyakov 2007, 2008, Timashev *et al.* 2010).

2.1 Principles of flicker-noise spectroscopy

In FNS, all introduced parameters for signal $V(t)$, where t is time, are related to the autocorrelation function

$$\psi(\tau) = \left\langle V(t)\, V(t+\tau) \right\rangle_{T-\tau} , \qquad (1)$$

where τ is the time lag parameter ($0 \leq \tau \leq T_M$) and T_M is the upper bound for τ ($T_M \leq T/2$). This function characterizes the correlation in the values of dynamic variable V at higher, $t + \tau$, and lower, t, values of the argument.

The angular brackets in Eq. (1) stand for the averaging over time interval $[0, T - \tau]$

$$\left\langle (...) \right\rangle_{T-\tau} = \frac{1}{T-\tau} \int_0^{T-\tau} (...) \, dt \;. \tag{2}$$

As the length of the averaging interval should be less than the overall length of the time series, T, and be equal to $T - |\tau|$, we consider, for simplicity, only nonnegative values of τ. The averaging over interval $[0, T - \tau]$ implies that all the characteristics that can be extracted by analyzing functions $\psi(\tau)$ should be regarded as average values on this interval. To extract the information contained in $\psi(\tau)$ ($\left\langle V(t) \right\rangle = 0$ is assumed), the following transforms, or "projections", of this function are analyzed: cosine transforms ("power spectrum" estimates) $S(f)$, where f is the frequency,

$$S(f) = 2 \int_0^{T_M} \left\langle V(t) \, V(t + t_1) \right\rangle_{T-\tau} \cos(2\pi f t_1) \, dt_1 \;, \tag{3}$$

and its difference moments (Kolmogorov transient structure functions) of the second order $\Phi^{(2)}(\tau)$

$$\Phi^{(2)}(\tau) = \left\langle \left[V(t) - V(t + \tau) \right]^2 \right\rangle_{T-\tau} \;. \tag{4}$$

Here, we use the quotes for power spectrum because according to the Wiener–Khinchin theorem the cosine (Fourier) transform of autocorrelation function is equal to the power spectral density only for wide-sense stationary signals at infinite integration limits.

The information contents of $S(f)$ and $\Phi^{(2)}(\tau)$ are generally different, and the parameters for both functions are needed to solve parameterization problems. By considering the intermittent character of signals under study, interpolation expressions for the stochastic components $S_s(f)$ and $\Phi_s^{(2)}(\tau)$ of $S(f)$ and $\Phi^{(2)}(\tau)$, respectively, were derived using the theory of generalized functions by Timashev (2006). It was shown that structural functions $\Phi_s^{(2)}(\tau)$ are formed only by jump-like (random-walk) irregularities corresponding to a dissipative process of anomalous diffusion, and functions $S_s(f)$, which characterize the "energy side" of the process, are formed by spike-like (inertial) and jump-like irregularities. It should be noted that τ in Eqs. (1)-(4) is considered as a macroscopic parameter exceeding the sampling period by at least one order of magnitude. This constraint is required to derive the expressions and separate out contributions of dissipative jump-like and inertial (non-dissipative) spike-like components.

2.2 Cross-correlation function

Flicker-noise spectroscopy cross-correlation expressions allow one to analyze cause-and-effect relations in different signals measured simultaneously. The information about the dynamics of correlation links in variables $V_i(t)$ and $V_j(t)$, where indices i and j denote two different signals, can be extracted by analyzing the dynamics of various correlators. Here, we will limit our attention to the simplest two-point cross-correlation expression characterizing the links between $V_i(t)$ and $V_j(t)$ (Timashev 2006, 2007, Timashev and Polyakov 2007):

$$q_{ij}(\tau,\theta_{ij}) = \left\langle \left[\frac{V_i(t) - V_i(t+\tau)}{\sqrt{\Phi_i^{(2)}(\tau)}} \right] \left[\frac{V_j(t+\theta_{ij}) - V_j(t+\theta_{ij}+\tau)}{\sqrt{\Phi_j^{(2)}(\tau)}} \right] \right\rangle_{T-\tau-|\theta_{ij}|} , \qquad (5)$$

where τ is the "lag" time corresponding to different time scales; θ_{ij} is the "time shift" parameter. Higher values of τ correspond to coarser (low-resolution) analysis of cross-correlations.

In discrete form, Eq. (5) is written as

$$q_{ijd}(n_\tau, n_\theta) = \frac{\sum\limits_{k=U[-n_\theta]|n_\theta|+1}^{N-n_\tau-U[n_\theta]|n_\theta|} \left[V_{id}(k) - V_{id}(k+n_\tau) \right] \left[V_{jd}(k+n_\theta) - V_{jd}(k+n_\theta+n_\tau) \right]}{\sqrt{\sum\limits_{k=U[-n_\theta]|n_\theta|+1}^{N-n_\tau-U[n_\theta]|n_\theta|} \left[V_{id}(k) - V_{id}(k+n_\tau) \right]^2}}$$

$$\times \frac{1}{\sqrt{\sum\limits_{k=U[-n_\theta]|n_\theta|+1+n_\theta}^{N-n_\tau-U[n_\theta]|n_\theta|+n_\theta} \left[V_{jd}(k) - V_{jd}(k+n_\tau) \right]^2}} , \qquad (6)$$

where

$$n_\tau = \lfloor \tau / \Delta t \rfloor, \qquad n_\theta = \lfloor \theta_{ij} / \Delta t \rfloor, \qquad U[x] = \begin{cases} 1, & x \geq 0 \\ 0, & x < 0 \end{cases} .$$

Here, subscript d is used to denote the discrete form and Δt is the sampling period.

The dependence of cross-correlation $q_{ij}(\tau, \theta_{ij})$ on θ_{ij} generally describes the cause-and-effect relation, *i.e.*, the characteristic time of information transfer between points (or events) i and j. For instance, it may describe the "flow direction" between signals $V_i(t)$ and $V_j(t)$. When $\theta_{ij} > 0$, event j follows event i or, alternatively, the flow moves from point i to point j; when $\theta_{ij} < 0$, it is the opposite. When the distance between points i and j is fixed, the value

of θ_{ij} can be used to estimate the rate of information transfer between these two points. The dependence of the value and magnitude of cross-correlation $q_{ij}(\tau, \theta_{ij})$ on τ and θ_{ij} can be used to analyze the flow dynamics with signals $V_i(t)$ and $V_j(t)$ changing in phase ($q_{ij} > 0$) and in antiphase ($\theta_{ij} < 0$). In some cases, both signals may be affected by a common external factor manifesting itself after different time lags.

The magnitude and behavior of the two-parameter expression (5) may significantly depend on the value of selected averaging interval T and upper-bound values of τ and θ_{ij}, which we will refer to as τ_{max} and θ_{max}. From the statistical reliability point of view, we set the constraint $\tau_{max} + \left| \theta_{max} \right| \leq T/2$.

For conciseness, from now on we will refer to q_{ij} as q and θ_{ij} as θ.

3. DATA

The data were recorded in the south-eastern part of the Kamchatka peninsula located at the Russian Far East. The eastern part of the peninsula is one of the most seismically active regions in the world. The area of highest seismicity localized in the depth range between 0 and 40 km represents a narrow stripe with a length of approximately 200 km along the east coast of Kamchatka, which is bounded by a deep-sea trench on the east (Fedotov 1985).

Specialized measurements of groundwater characteristics were started in 1977 to find and study possible hydrogeochemical precursors of Kamchatka earthquakes. Currently, the observation network includes four stations in the vicinity of Petropavlovsk-Kamchatsky (Fig. 1). The Pinachevo station includes five water reservoirs: four warm springs and one borehole GK-1 with a depth of 1261 m. The Moroznaya station has a single borehole No. 1 with a depth of 600 m. The Khlebozavod station also includes a single borehole G-1 with a depth of 2540 m, which is located in Petropavlovsk-Kamchatsky. The Verkhnyaya Paratunka station comprises four boreholes (GK-5, GK-44, GK-15, and GK-17) with depths in the range from 650 to 1208 m.

The system of hydrogeochemical observations includes the measurement of atmospheric pressure and air temperature, measurement of water discharge and temperature of boreholes and springs, collection of water and gas samples for their further laboratory analyses. For water samples, the following parameters are determined: pH, ion concentrations of chlorine (Cl^-), bicarbonate (HCO_3^-), sulfate (SO_4^{2-}), sodium (Na^+), potassium (K^+), calcium (Ca^{2+}), and magnesium (Mg^{2+}); concentrations of boric (H_3BO_3) and silicone (H_4SiO_4) acids. For the samples of gases dissolved in water, the following concentrations are determined: methane (CH_4), nitrogen (N_2), oxygen (O_2), carbon dioxide (CO_2), helium (He), hydrogen (H_2), hydrocarbon gases: ethane (C_2H_6), ethylene (C_2H_4), propane (C_3H_8), propylene (C_3H_6), butane
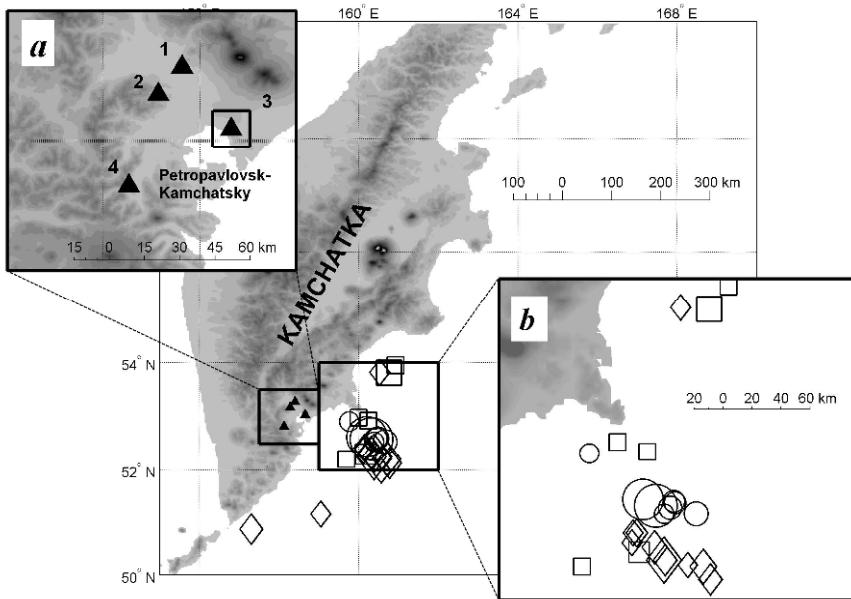
Fig. 1. Schematic of the measurement area, observation points, and epicenters of largest earthquakes ($M \geq 5.0$, $H \leq 50$ km, $D \leq 350$ km) from 2001 to 2003, where M is the earthquake magnitude, H depth, and D is the distance from the epicenter to the Khlebozavod station. Frame (a) shows an enlarged view of the positions of hydrogeological stations: 1 – Pinachevo, 2 – Moroznaya, 3 – Khlebozavod, 4 – Verknyaya Paratunka. Frame (b) shows an enlarged view of the area including most of the earthquakes. Circles, squares, and diamonds denote earthquakes in 2001, 2002, and 2003, respectively. The earthquakes were selected using the catalog of U.S. Geological Survey: http://earthquake.usgs.gov/earthquakes/eqarchives/epic/.

(C_4H_{10}n), and isobutane (C_4H_{10}i). The data are recorded at nonuniform sampling intervals with one dominant sampling frequency. For the Pinachevo, Moroznaya, and Khlebozavod stations, this average sampling frequency is one measurement per 3 days; for the Verknyaya Paratunka station, one measurement per 6 days. Multiple studies of the hydrogeochemical data and corresponding seismic activity for the Kamchatka peninsula reported anomalous changes in the chemical and/or gas composition of groundwater prior to several large earthquakes (Kopylova *et al.* 1994, Bella *et al.* 1998, Biagi *et al.* 2000, 2006, Khatkevich and Ryabinin 2006).

Geoacoustic emissions (GAE) in the frequency range from 25 to 1400 Hz (with transmission coefficient of 0.7 or above relative to the maximum value) have also been recorded in the deep G-1 borehole of the Khlebozavod station under the supervision of V.A. Gavrilov since August 2000. The data analyzed in this paper were obtained by a three-component

geophone MAG-3S with magnetoelastic crystal ferromagnetic sensors, designed and developed in the Institute of Physics of the Earth, Russian Academy of Sciences (Belyakov 2000). The vertical channel sensitivity of the geophone is $0.15 \, \mathrm{V \, s^3 m^{-1}}$. The sensitivity of horizontal channels is $0.60 \, \mathrm{V \, s^3 m^{-1}}$. The output signal of such a sensor is proportional to the third derivative of ground displacement, *i.e.*, jerk, and the gain slope is 60 dB per decade of frequency change. This configuration makes it possible to compensate for the increase in the damping of geoacoustic emissions with frequency in a real geophysical medium. The geophone was set up at the depth of 1035 m, which is enough to reduce anthropogenic noise levels by more than two orders of magnitude (Gavrilov *et al.* 2008). The geophone body was fixed inside the borehole casing by a spring. The sensor output signals are separated by third-octave band pass filters into four frequency bands with central frequencies 30, 160, 560, and 1200 Hz, which is followed by the measurement of mean square values of signals from each filter. The resultant
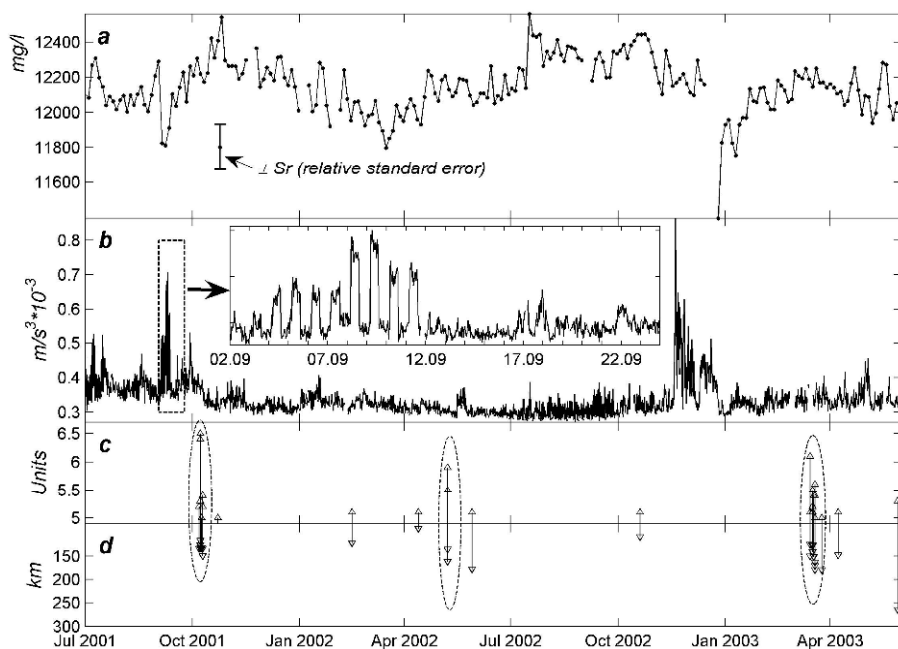

Fig. 2. Experimental data: (a) Variation of water salinity at G-1 borehole (Klebozavod station); vertical lines with horizontal ticks denote doubled value of relative standard error ($\pm S_r$); (b) Time series of GEA variation at G-1 borehole. Frame (b) also shows an enlarged view of a GAE segment illustrating the degradation of diurnal cycle; (c) and (d) Time sequences of earthquakes expressed in terms of magnitudes and epicenter distances. Dashed lines in panels (c) and (d) denote three groups of strongest seismic events in 2001, 2002, and 2003, respectively.

signals are then digitally processed: the values of signals are averaged for one-minute intervals and the data are recorded. More detailed description of geoacoustic emission observations and experimental setup for the G-1 borehole is presented elsewhere (Gavrilov *et al.* 2008, 2011).

Table 1

Largest earthquakes ($M \geq 5.0$, $H \leq 50$ km, $D \leq 350$ km)
from 30 June 2001 to 1 June 2003 according to the catalog of U.S. Geological Survey
(http://earthquake.usgs.gov/earthquakes/eqarchives/epic/)

Date	Latitude	Longitude	D [km]	M		H [km]
7 Oct. 2001	52.62	160.47	33	5.2	*Mw*HRV	134
8 Oct. 2001	52.58	160.44	33	5.3	*Mw*HRV	133
8 Oct. 2001	52.59	160.32	48	6.5	*Mw*HRV	126
8 Oct. 2001	52.63	160.21	33	6.4	*Mw*HRV	117
9 Oct. 2001	52.54	160.39	33	5.0	*mb*GS	133
10 Oct. 2001	52.54	160.66	33	5.4	*Mw*HRV	149
10 Oct. 2001	52.61	160.48	33	5.2	*Mw*HRV	134
23 Oct. 2001	52.92	159.76	42	5.0	*mb*GS	76
15 Feb. 2002	52.21	159.70	33	5.1	*Mw*HRV	122
13 Apr. 2002	52.99	160.00	41	5.1	*Mw*HRV	91
8 May 2002	52.30	160.18	44	5.5	*Mw*HRV	136
8 May 2002	53.81	160.77	39	5.9	*Mw*HRV	161
29 May 2002	53.95	160.93	43	5.1	*Mw*HRV	178
20 Oct. 2002	52.93	160.25	46	5.1	*Mw*HRV	109
15 Mar. 2003	52.25	160.39	30	6.1	*Mw*GS	150
15 Mar. 2003	52.42	160.13	33	5.1	*Ms*GS	125
17 Mar. 2003	52.36	160.12	33	5.1	*Mw*HRV	128
17 Mar. 2003	52.42	160.16	33	5.2	*Mw*HRV	126
17 Mar. 2003	52.33	160.31	33	5.5	*mb*GS	141
18 Mar. 2003	52.25	160.40	33	5.4	*Mw*HRV	151
19 Mar. 2003	52.13	160.78	33	5.4	*Mw*HRV	179
19 Mar. 2003	52.22	160.59	33	5.0	*mb*GS	163
19 Mar. 2003	52.21	160.72	33	5.6	*Mw*HRV	171
25 Mar. 2003	51.99	160.57	33	5.0	*Mw*HRV	179
8 Apr. 2003	53.82	160.53	33	5.1	*Mw*HRV	148
29 May 2003	50.88	157.30	49	5.3	*Mw*HRV	264

Explanations: H – depth, D – distance from the epicenter to the Khlebozavod station. The earthquake magnitude M is listed using different scales: *Mw* – moment magnitude, *Ms* – surface wave magnitude, and *mb* – body wave magnitude, HRV – Harvard University, GS – U.S. Geological Survey.

The objects of this study are GEA time series for central frequency 160 Hz and water salinity times series, both recorded at the G-1 borehole from 30 June 2001 to 1 June 2003 (Fig. 2). The most significant earthquakes (with magnitudes over 5 units) in this time range are listed in Table 1. The water salinity time series is an integral characteristic of the chemical composition of groundwater calculated as a sum of concentrations for basic hydrogeochemical parameters (HCO_3^-, Cl^-, Ca^{2+}, SO_4^{2-}, Na^+, K^+, Mg^{2+}). The sum is dominated by the contributions from Cl^--ion (multi-year-averaged value is 6600 mg/l) and Na^+-ion (4200 mg/l). This time frame was selected due to the following three reasons. First, there were no large gaps in the GEA measurements during this period. Second, this time frame includes several large earthquakes ($M > 5$) with epicenters located relatively close to the Khlebozavod station (distances in the range from 100 to 200 km). Third, the individual time series, especially for water salinity, do not contain apparent anomalies (precursors) clearly related to earthquakes during this period. These earthquakes were clustered in time into three groups (Fig. 2c, d).

4. RESULTS AND DISCUSSION

Hydrogeochemical and geoacoustic observations are two independent methods for monitoring seismotectonic processes that are used to continuously collect changes in various parameters. The goal of observations is to identify and study effects intrinsically related to the preparation and occurrence of strong earthquakes. The independence of these two types of observations implies that the information on the preparation of a strong earthquake may look differently in the statistical structure of their experimental data. It was previously shown that the most reliable precursor of a strong earthquake on the Kamchatka peninsula is a significant and usually reversible drop or rise of the average concentration of materials dissolved in water (Khatkevich and Ryabinin 2006). The description and analysis of similar hydrogeochemical anomalies as well as irreversible ones, recorded at the G-1 borehole, can be found in the study by Biagi *et al.* (2004). The results of multi-year geoacoustic observations show that in seismically quiescent periods the GAE variation at the G-1 borehole for central frequencies 30 and 160 Hz contains a clear daily component with a maximum at night time ("diurnal cycle"). A suppression (degradation) of the diurnal cycle was suggested as a precursor of strong earthquakes (Gavrilov *et al.* 2008), which is illustrated in Fig. 2b. In this paper, we demonstrate that precursor-related information may be derived from the cross-correlation analysis of hydrogeochemical and geoacoustic data by the FNS method.

The combined analysis of hydrogeochemical and geoacoustic data was complicated by the fact that the sampling periods for hydrogeochemical and

geoacoustic data were much different: 3 days and 1 minute, respectively. The experimental data could be reduced to the same sampling frequency either by decreasing the frequency for geoacoustic data or increasing it for the water salinity time series. We used a trade-off solution by changing the sampling frequency of both time series to $(6\,\text{h})^{-1}$. This sampling frequency was selected because it is the highest frequency that does not erase information about the diurnal cycle. At the same time, the artificial step-up in the sampling frequency of water salinity data to $(6\,\text{h})^{-1}$ does not distort the information at frequencies $(3\,\text{days})^{-1}$ and below. The complete preprocessing procedure included the removal of single-point spikes and resampling of both time series to uniform sampling frequency $(6\,\text{h})^{-1}$. The thinning of GAE data from sampling frequency $(1\,\text{min})^{-1}$ to $(6\,\text{h})^{-1}$ was performed using the following approach. A low-pass filter with a cut-off frequency equal to the new Nyquist frequency $(12\,\text{h})^{-1}$ was applied to the GAE data to eliminate the false frequency components. The final GAE time series with the sampling frequency of $(6\,\text{h})^{-1}$ was formed by taking every 360th point from the filtered series. The increase of the sampling rate for water salinity time series from $(3\,\text{days})^{-1}$ to $(6\,\text{h})^{-1}$ was achieved using linear interpolations.

To analyze the mutual dynamics of time series, we used the cross-correlation function (5). The graphical representation of $q(\tau,\theta)$ is a 3D surface, which often has a relatively complex shape. The analysis of cross-correlation evolution in time is performed by calculating $q(\tau,\theta)$ within a sliding window T. A time sequence of such 3D surfaces with a shifted sliding window is used to build frames for a video file in the avi format.

The analysis of 3D cross-correlation plots for the water salinity and geoacoustic time series allowed us to detect a peculiarity in the structure of correlations prior to the group of earthquakes in October 2001. This peculiarity represents a significant negative correlation between the time series at time lags τ more than 5 days and time shifts $\theta \approx 0$ days. We observed the same effect prior to the group of earthquakes in March 2003 and saw its less-pronounced instance prior to the group of events in May 2002. Figure 3 illustrates examples of 3D surfaces of cross-correlation $q(\tau,\theta)$ calculated for different time intervals of length $T = 30$ days. 3D plots numbered II, IV, and VI (Fig. 3d) correspond to the intervals preceding the seismic events of 2001, 2002, and 2003. These plots illustrate the peculiarity, *i.e.*, the onset of a major negative correlation with a value of approximately 0.7. The time spans between the right boundaries of intervals II, IV, VI and time moments of strongest earthquakes in 2001, 2002, and 2003 are 27, 31, and 35 days, respectively. It should be pointed out that the data resampling procedure could not significantly distort the observed effect of major negative correlation because its manifestation only at $\tau > 5$ days implies the low contribu-
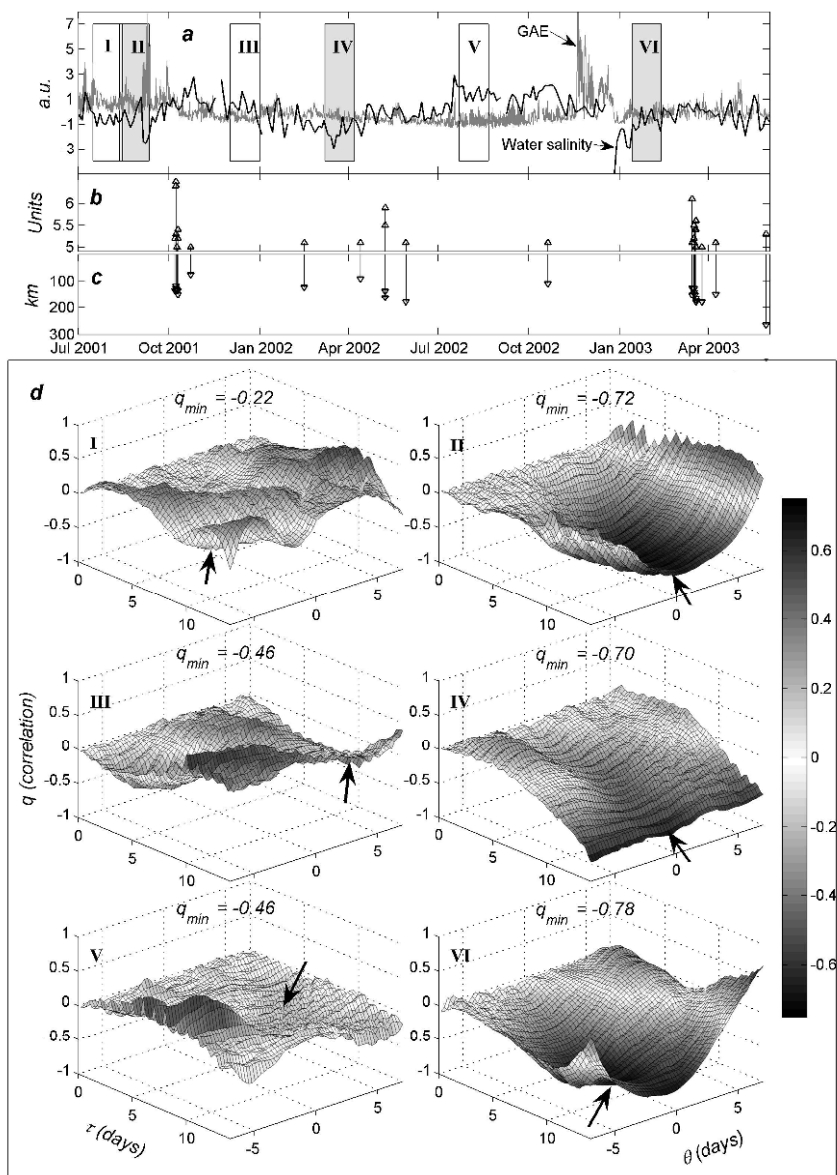
Fig. 3. Results of FNS cross-correlation analysis: (a) GEA and water salinity time series for G-1 borehole; (b) and (c) Time sequences of earthquakes expressed in terms of magnitudes and epicenter distances. Rectangles in plot (a) denote intervals (T = 30 days) used in evaluating the 3D surfaces of cross-correlation $q(\tau, \theta)$ (τ_{max} = 14 days, θ_{max} = ±7 days), which are presented in plots (d). Roman numerals in plots (a) and (d) refer to respective time intervals. Arrows near 3D surfaces denote the positions of correlation minima q_{min}, with values of the latter listed above each plot.

tion of high-frequency components ($f_d = 1$ min^{-1}) in GAE signals. Moreover, the functional form of cross-correlation function (5), which is based on differences of the dynamic variables, is determined by the low-frequency components of the signals (Timashev 2006, Timashev and Polyakov 2007). Let us also note that the absolute value q_{min} of cross-correlation (5) at $\tau > 5$ varied only by 10% when the sampling rate of the GAE signal was gradually reduced in the range from $(30$ min$)^{-1}$ to $(6$ h$)^{-1}$. It is clear that the further reduction of sampling frequency to values of about $(10$ days$)^{-1}$ causes the major negative cross-correlations to disappear.

The 3D plots of cross-correlation $q(\tau, \theta)$ labeled I, III, and V are shown for comparison and illustrate the cross-correlations for time intervals much further away from the groups of seismic events. All six 3D plots also suggest that the behavior of cross-correlations varies at different intervals. This variability is observed not only in extreme values of cross-correlation $q(\tau, \theta)$, but also in the shape of 3D surfaces. It can be seen that the structure of 3D surfaces on intervals II, IV, and VI, characterized by maximum negative correlations of at least 0.7, has similar features representing a smooth decline of cross-correlation with an increase in time lag τ and time shift θ being close to zero. These features in the structure and magnitude of the cross-correlations between water salinity and geoacoustic time series, which were observed in the time frame from 2001 to 2003, allow us to consider them as precursors of seismic events. It should be pointed out that this is a new type of precursor incorporating both the quantitative measure of cross-correlation and its qualitative features described by the structure of 3D surface for cross-correlation $q(\tau, \theta)$.

It should be noted that on certain intervals of length $T = 30$ days in the time frame from 2001 to 2003 the structure of 3D surfaces contained high values of negative correlation $q_{min} < -0.7$ between water salinity and geoacoustic emissions, even though those intervals cannot be associated with significant seismic events. Such examples are illustrated in Fig. 4, which shows that the extreme vales of q_{min} took place at values of θ far from zero. Moreover, the shape of 3D surfaces in Fig. 4 was dramatically different as compared to the monotonous decline of $q(\tau, \theta)$ at $\theta \approx 0$ on intervals II, IV, and VI of Fig. 3. Therefore, the cross-correlation structures plotted in Fig. 4 could not be considered as precursors of strong earthquakes, despite the high values of negative correlation on specific segments of the 3D structures.

High values of negative correlation at practically zero values of time shift imply that the changes in water salinity and GAE level happen almost simultaneously, but in opposite directions. To clarify this statement, let us consider in detail the cross-correlation dynamics around the 8 October 2001 earthquake (Fig. 5). It can be seen that the 3D plots of cross-correlation
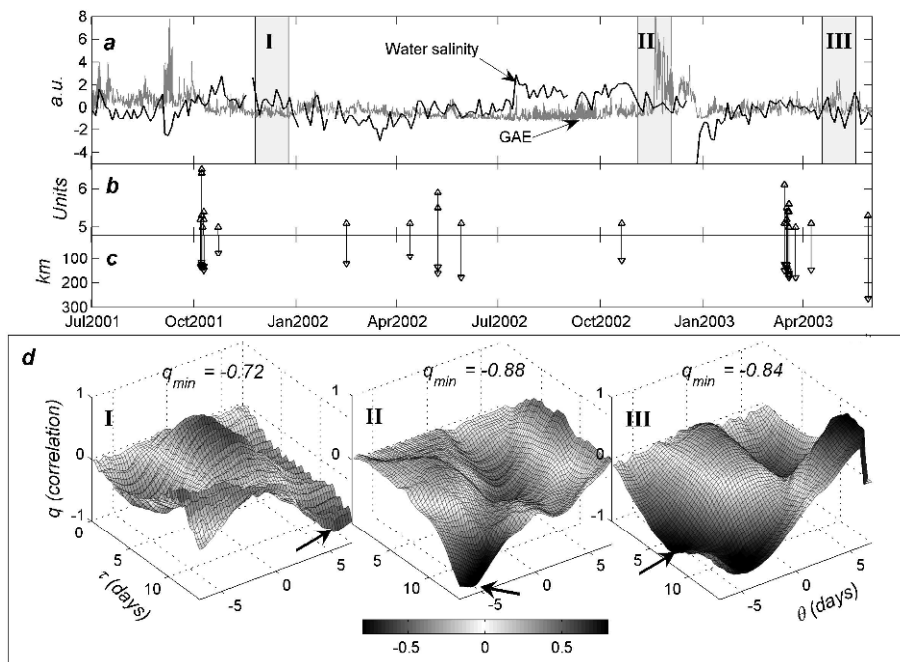
Fig. 4. Results of FNS cross-correlation analysis for non-precursory intervals with high absolute values of correlation minima q_{min}. Nomenclature same as in Fig. 3.

$q(\tau, \theta)$ for two different time intervals vary substantially. In the first case, the cross-correlation is relatively simple and has one clear correlation minimum (Fig. 5c). In the second case, the structure is more complex and contains several local maxima and minima (Fig. 5d). These plots suggest that cross-correlation on the first interval is dominated by simultaneous increase in the GAE level and decline in the water salinity. It can also be seen that the rise in the GAE level can be attributed to the increase in the amplitudes of daily variations (diurnal cycle). On the second interval, which is characterized by a lack of the GAE diurnal cycle, the negative correlations are not significant.

The above results demonstrate that the dynamics of cross-correlations between water salinity and GAE time series contains precursors for all three groups of seismic events in the time frame from 2001 to 2003. The geo-acoustic signals generated by a seismically active medium are usually attributed to simultaneous processes of formation/expansion of micro-fractures and their collapse/contraction due to stretching and compression associated with structural reconfiguration of the medium. This also changes the conditions for transport processes in groundwater containing various dissolved inorganic and organic components as well as a variety gases, both
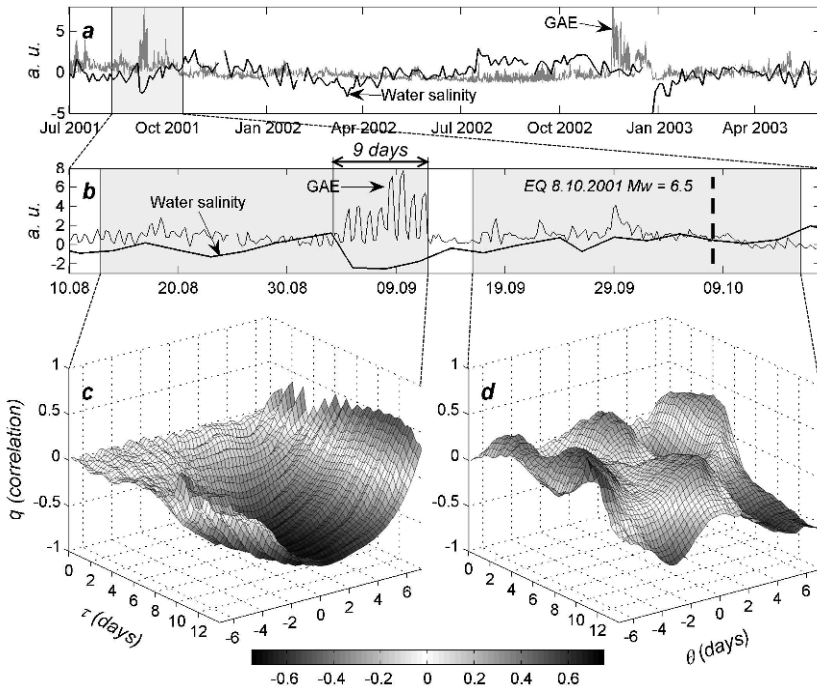
Fig. 5. Plots illustrating the variation of cross-correlation in the time frame around October 2001 (first group of earthquakes): (a) GEA and water salinity time series for G-1 borehole; (b) enlarged segment of time series. Time along the abscissa axis in plot (b) is presented in dd.mm format. Vertical dashed line corresponds to the time of earthquake on 8 October 2001. Shaded rectangular areas in plot (b) highlight the intervals of length $T = 30$ days used in evaluating the 3D surfaces of cross-correlation $q(\tau, \theta)$ ($\tau_{max} = 14$ days, $\theta_{max} = \pm 7$ days), which are plotted in (c) and (d). The horizontal arrow denotes the interval of abrupt increase in GAE (9 days in total) and simultaneous decrease in water salinity.

in dissolved and microbubble forms. We suggest that the interrelation between fracture expansion (contraction) and increase (decrease) of water permeability in the medium, accompanied by increased (decreased) transport of hydrated ions due to "sieving" and electrokinetic effects (Timashev 1991, Zeman and Zydney 1996, Cicerone et al. 2009), may produce the negative correlations shown in Figs. 3d and 5c.

5. CONCLUSIONS

This study shows that new precursory information can be extracted from the analysis of the dynamics of cross-correlations between geophysical signals, even when there are no apparent anomalies in the signals themselves. This

conclusion is illustrated through the combined analysis of the dynamics for water salinity and geoacoustic emissions in the time frame from 2001 to 2003 at one of the boreholes in a seismically active region of the south-eastern part of the Kamchatka peninsula. The individual dynamics of measured times series did not contain characteristic anomalies pointing to possible strong earthquakes, except for the precursor of the October 2001 group of earthquakes in the dynamics of geoacoustic emissions. At the same time, the cross-correlations between water salinity and geoacoustic emissions demonstrated clear precursors prior to all three groups of significant seismic events in this time frame. This result is in agreement with known physical views on the transport of endogenous fluids in rock volumes during the formation of an earthquake source in a seismically active medium, accompanied with fracturing and related geoacoustic phenomena. The new earthquake precursor type suggested in this paper may also be used for the cross-correlation analysis of other known geophysical signals with precursory properties: electromagnetic, hydrological, gasgeochemical, geodetic, and seismic.

References

Bella, F., P.F. Biagi, M. Caputo, E. Cozzi, G. Della Monica, A. Ermini, E.I. Gordeev, Y.M. Khatkevich, G. Martinelli, W. Plastino, R. Scandone, V. Sgrigna, and D. Zilpimiani (1998), Hydrogeochemical anomalies in Kamchatka (Russia), *Phys. Chem. Earth* **23**, 9-10, 921-925, DOI: 10.1016/S0079-1946(98)00120-7.

Belyakov, A.S. (2000), Magnetoelastic acoustic geophones for geophysical research and earthquake prediction, *Seismicheskie Pribory* **33**, 27-45 (in Russian).

Biagi, P.F., A. Ermini, E. Cozzi, Y.M. Khatkevich, and E.I. Gordeev (2000), Hydrogeochemical precursors in Kamchatka (Russia) related to the strongest earthquakes in 1988-1997, *Nat. Hazards* **21**, 2-3, 263-276, DOI: 10.1023/A:1008178104003.

Biagi, P.F., L. Castellana, R. Piccolo, A. Minafra, G. Maggipinto, A. Ermini, V. Capozzi, G. Perna, Y.M. Khatkevich, and E.I. Gordeev (2004), Disturbances in groundwater chemical parameters related to seismic and volcanic activity in Kamchatka (Russia), *Nat. Hazards Earth Syst. Sci.* **4**, 4, 535-539, DOI: 10.5194/nhess-4-535-2004.

Biagi, P.F., L. Castellana, A. Minafra, G. Maggipinto, T. Maggipinto, A. Ermini, O. Molchanov, Y.M. Khatkevich, and E.I. Gordeev (2006), Groundwater chemical anomalies connected with the Kamchatka earthquake (M = 7.1) on March 1992, *Nat. Hazards Earth Syst. Sci*. **6**, 5, 853-859, DOI: 10.5194/nhess-6-853-2006.

Cicerone, R.D., J.E. Ebel, and J. Britton (2009), A systematic compilation of earthquake precursors, *Tectonophysics* **476**, 3-4, 371-396, DOI: 10.1016/j.tecto.2009.06.008.

Fedotov, S.A., A.A. Gusev, G.V. Chernysheva, and L.S. Shumilina (1985), Seismic focal zone of Kamchatka: Geometry, earthquake source distribution, and relation to volcanism, *Vulc. Seismol*. **4**, 91-107 (in Russian).

Gavrilov, V., L. Bogomolov, Y. Morozova, and A. Storcheus (2008), Variations in geoacoustic emissions in a deep borehole and its correlation with seismicity, *Ann. Geophys*. **51**, 5-6, 737-753, DOI: 10.4401/ag-3013.

Gavrilov, V.A., L.M. Bogomolov, and A.S. Zakupin (2011), Comparison of the geoacoustic measurements in boreholes with the data of laboratory and in-situ experiments on electromagnetic excitation of rocks, *Izv. Phys. Solid Earth* **47**, 11, 1009-1019, DOI: 10.1134/S1069351311100041.

Geller, R.J. (1997), Earthquake prediction: a critical review, *Geophys. J. Int*. **131**, 3, 425-450, DOI: 10.1111/j.1365-246X.1997.tb06588.x.

Geller, R.J., D.D. Jackson, Y.Y. Kagan, and F. Mulargia (1997), Earthquakes cannot be predicted, *Science* **275**, 5306, 1616-1617, DOI: 10.1126/science.275.5306.1616.

Hartmann, J., and J.K. Levy (2005), Hydrogeological and gasgeochemical earthquake precursors – A review for application, *Nat. Hazards* **34**, 3, 279-304, DOI: 10.1007/s11069-004-2072-2.

ICEFCP (2009), Operational earthquake forecasting: State of knowledge and guidelines for utilization, http://www.iaspei.org/downloads/Ex_Sum_v5_THJ9_A4format.pdf.

Khatkevich, Y., and G. Ryabinin (2006), Geochemical and ground-water studies in Kamchatka in the search for earthquakes precursors, *Vulc. Seismol.* **4**, 34-42 (in Russian).

Kopylova, G., V. Sugrobov, and Y. Khatkevich (1994), Variations in the regime of springs and hydrogeological boreholes in the Petropavlovsk polygon (Kamchatka) related to earthquakes, *Vulc. Seismol.* **2**, 53-70 (in Russian).

Lyubushin, A.A., Jr. (1998), An aggregated signal of low-frequency geophysical monitoring systems, *Izv. Phys. Solid Earth* **34**, 3, 238-243.

Lyubushin, A.A., Jr. (2000), Wavelet-aggregated signal and synchronous peaked fluctuations in problems of geophysical monitoring and earthquake prediction, *Izv. Phys. Solid Earth* **36**, 3, 204-213.

Lyubushin, A.A. (2007), *Analiz Dannykh Sistem Geofizicheskogo i Ekologicheskogo Monitoringa* (Analysis of Data Acquired by Geophysical and Ecological Monitoring Systems), Nauka, Moscow (in Russian).

Lyubushin, A.A., Jr., G.N. Kopylova, and Yu.M. Khatkevich (1997), Analysis of the spectral matrices of hydrogeological observations at the Petropavlovsk geodynamic research site, Kamchatka, and their comparison with the seismic regime, *Izv. Phys. Solid Earth* **33**, 6, 497-507.

Ryabinin, G.V., Yu.S. Polyakov, V.A. Gavrilov, and S.F. Timashev (2011), Identification of earthquake precursors in the hydrogeochemical and geoacoustic data for the Kamchatka peninsula by flicker-noise spectroscopy, *Nat. Hazards Earth Syst. Sci*. **11**, 2, 541-548, DOI: 10.5194/nhess-11-541-2011.

Telesca, L., M. Lovallo, A. Ramirez-Rojas, and F. Angulo-Brown (2009a), A nonlinear strategy to reveal seismic precursory signatures in earthquake-related self-potential signals, *Physica A* **388**, 10, 2036-2040, DOI: 10.1016/j.physa.2009.01.035.

Telesca, L., M. Lovallo, A. Ramirez-Rojas, and F. Angulo-Brown (2009b), Scaling instability in self-potential earthquake-related signals, *Physica A* **388**, 7, 1181-1186, DOI: 10.1016/j.physa.2008.12.029.

Timashev, S.F. (1991), *Physical Chemistry of Membrane Processes*, Ellis Horwood, Chichester.

Timashev, S.F. (2006), Flicker noise spectroscopy and its application: Information hidden in chaotic signals (review), *Russ. J. Electrochem*. **42**, 5, 424-466, DOI: 10.1134/S102319350605003X.

Timashev, S.F. (2007), *Fliker-Shumovaya Spektroskopiya: Informatsiya v khaoticheskikh signalakh* (Flicker-Noise Spectroscopy: Information in Chaotic Signals), Fizmatlit, Moscow (in Russian).

Timashev, S.F., and Y.S. Polyakov (2007), Review of flicker noise spectroscopy in electrochemistry, *Fluct. Noise Lett.* **7**, 2, R15-R47, DOI: 10.1142/S0219477507003829.

Timashev, S.F., and Y.S. Polyakov (2008), Analysis of discrete signals with stochastic components using flicker noise spectroscopy, *Int. J. Bifurcat. Chaos* **18**, 9, 2793-2797, DOI: 10.1142/S0218127408022020.

Timashev, S.F., Y.S. Polyakov, P.I. Misurkin, and S.G. Lakeev (2010), Anomalous diffusion as a stochastic component in the dynamics of complex processes, *Phys. Rev. E* **81**, 4, 041128, DOI: 10.1103/PhysRevE.81.041128.

Wyss, M., and D.C. Booth (1997), The IASPEI procedure for the evaluation of earthquake precursors, *Geophys. J. Int*. **131**, 3, 423-424, DOI: 10.1111/j.1365-246X.1997.tb06587.x.

Wyss, M., R.L. Aceves, S.K. Park, R.J. Geller, D.D. Jackson, Y.Y. Kagan, and F. Mulargia (1997), Cannot earthquakes be predicted?, *Science* **278**, 5337, 487-490, DOI: 10.1126/science.278.5337.487.

Uyeda, S., T. Nagao, and M. Kamogawa (2009), Short-term earthquake prediction: Current status of seismo-electromagnetics, *Tectonophysics* **470**, 3-4, 205-213, DOI: 10.1016/j.tecto.2008.07.019.

Zeman, L.J., and A.L. Zydney (1996), *Microfiltration and Ultrafiltration: Principles and Applications*, Marcel Dekker, New York.

VERSITA

Experimental Evidence of a Non-Extensive Statistical Physics Behavior of Electromagnetic Signals Emitted from Rocks Under Stress up to Fracture. Preliminary Results

Filippos VALLIANATOS[1], Andriano NARDI[2], Roberto CARLUCCIO[2], and Massimo CHIAPPINI[2]

[1]Technological Educational Institution of Crete,
Laboratory of Geophysics and Seismology, Chania, Crete, Greece
e-mail: fvallian@chania.teicrete.gr

[2]Istituto Nazionale di Geofisica e Vulcanologia, Roma, Italy

A b s t r a c t

The application of mechanical stress on a rock sample can induce electromagnetic emissions. Such emissions can be detected experimentally and in principle could be used as precursors of the upcoming failure.

Using experimental observations of stress-induced electromagnetic emissions (SIEME), we apply the concepts of non-extensive statistical physics (NESP) to the time intervals between consecutive SIEME. The application of NESP is appropriate to systems such as fracture-induced effects, where non-linearity, long-range interactions and scaling are important. We find that the SIEME energy release distribution and the inter-event time distribution reflect a sub-extensive system with thermodynamic q-values of the order of $q_E = 1.67$ and $q_\tau \approx 1.7$, respectively.

Key words: electromagnetic emissions, non-extensive statistical physics, rocks.

1. INTRODUCTION

The phenomena of electromagnetic emissions (EME) that are met when a material is about to fail due to mechanical reasons are most interesting, especially when the material under study belongs to the class of brittle geomaterials, since such phenomena are promising candidates of earthquake precursors (Hayakawa and Fujinawa 1994, Hayakawa 1999, Hayakawa and Molchanov 2002). During the development of the deformation, when a geomaterial is subject to externally applied stress, various mechanisms contribute to the generation of electric and electromagnetic emission. These mechanisms are related to the crack generation and propagation processes (Vallianatos and Tzanis 1998, 1999a, b; 2003, Tzanis and Vallianatos 2001, 2002, Enomoto and Hashimoto 1990, O'Keefe and Thiel 1995, Takeuchi and Nagahama 2001, Frid *et al.* 2003, 2009 and references therein).

This concept is documented and efforts are focused on two main paths. Theoretical works have been introduced in order to model the underlying physical mechanisms that can generate transient electric and EM signals (Vallianatos and Tzanis 1999a, Slifkin 1993, Varotsos 2005), while several experimental works have concurrently been performed to investigate in detail the characteristics of such electric and EM emissions (Yoshida *et al.* 1997, Stavrakas *et al.* 2003, 2004, Anastasiadis *et al.* 2004, Vallianatos *et al.* 2004).

Recently, a series of laboratory experiments (Nardi 2001, 2005, Nardi and Caputo 2006, 2009, Nardi *et al.* 2007) have confirmed that the application of uniaxial stress is accompanied by the production of electromagnetic emissions termed as stress-induced ones (SIEME). Specifically, SIEME along with pressure stimulated currents (PSC) (Vallianatos *et al.* 2004 and references therein) and acoustic emission (AE) (Benson *et al.* 2007, 2008) are generically associated to microcrack propagation preceding a macroscopic failure (Vallianatos and Tzanis 1999a, Hayakawa and Molchanov 2002).

Fracture in heterogeneous materials such as rocks along with stress-induced effects as electromagnetic signals, stimulated currents and acoustic emissions are complex processes involving a wide range of time and length scales. These effects are governed by the non-linear and non-equilibrium processes of nucleation, growth and coalescence of microcracks.

Recently, the statistical properties of both fracture and stress induced effects have attracted a wide interest in the statistical physics community (Herrmann and Roux 1990, Chakrabarti and Benguigui 1997), since they can be seen as the outcome of the irreversible dynamics of a long-range interacting, disordered system described by scale-invariant laws (Vallianatos *et al.* 2011a, b).

Laboratory observed SIEME exhibit some remarkable similarities with acoustic emissions and large-scale seismological events and earthquake physics, such as power law and frequency-magnitude distributions (Vallianatos and Tzanis 2003, Vallianatos and Triantis 2008, Frid *et al.* 2011). The main motivation of our work is to investigate the statistical physics of stress-induced electromagnetic emissions in heterogeneous rock materials under uniaxial deformation, analyzing the temporal evolution of energy release of SIEME from micro-fractures that occurs before the final fracture.

Since the disorder and long-range interactions are two of the key components of microfracture's induced electromagnetic emissions, we use a current generalization of Boltzmann–Gibbs (BG) statistical physics due to Tsallis, referred to as non-extensive statistical physics (NESP) (see Tsallis 2001, 2009 and references therein), to explore the distribution of SIEME energy release and the inter-event times. The advantage of considering the Tsallis distribution is that, based on the principle of entropy, it can be related to statistical mechanics and reduces to the traditional BG statistical physics as a special case. Fracture related phenomena presents fractality, long range interaction and memory effects (Vallianatos *et al.* 2011a, b). It is precisely such phenomena that constitute the scope of non-extensive statistical mechanics (Tsallis 2009). We note that recent applications to solid earth physics (in regional or planetary scale) summarized in Tsallis (2009), mainly focused in seismology (Abe and Suzuki 2003, 2005, Telesca 2010a, b), using earthquake catalogues from different seismic zones, fault lengths distribution (Vallianatos *et al.* 2011a, Vallianatos and Sammonds 2011) and very recently to natural hazards (Vallianatos 2009), plate tectonics (Vallianatos and Sammonds 2010) and geomagnetic reversals (Vallianatos 2011) support the applicability of NESP in complex geosystems.

The question whether fracture is described by non-extensive statistical physics, even at the phenomenological level (*i.e.*, without specifying any underlying model), represents a challenge. This is the problem we address here. Our aim is not to develop a precise model, but rather to present a simple argument of physical plausibility.

2. STRESS-INDUCED ELECTROMAGNETIC EMISSIONS IN ROCKS UNDER UNIAXIAL COMPRESSION

Rock samples with diverse lithologies and dimensions (some with dimensions of $8 \times 8 \times 10$ cm, and some of $10 \times 10 \times 10$ cm) have been subject to nearly-linearly increasing uniaxial compression, until they fractured. The experiments originally presented by Nardi (2001, 2005) have been made on samples surrounded by air or fresh or salty water, with boundary conditions free of confining pressure, at a temperature of about $20\,°C$. The load used was a hydraulic Hamsler 500t. During the compression, impulsive SIEME
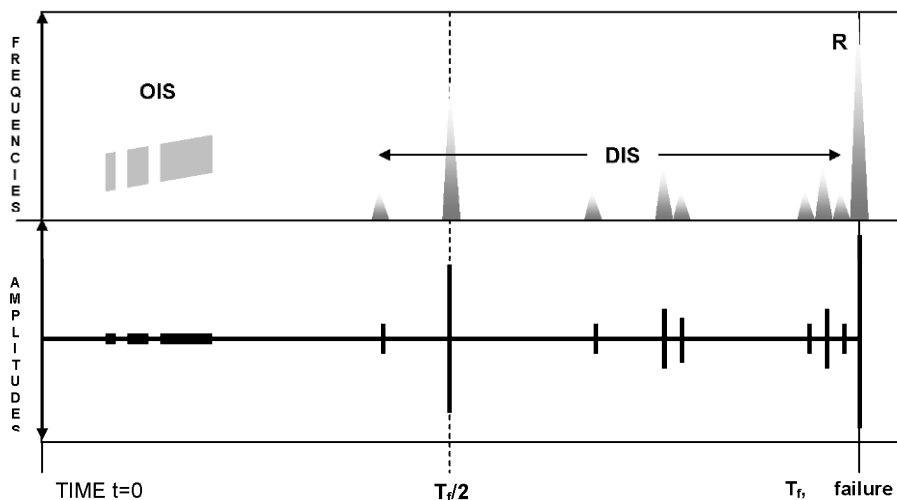
Fig. 1. Time chart of DIS and OIS signal appearing in both amplitude and frequency domains.

were observed (see Fig. 1), occurring with two different modes: orderly impulsive sequences (OIS) and disorderly impulsive sequences (DIS) (Nardi and Caputo 2006, 2009).

The orderly sequences are characterised by high frequency micro-impulses, which follow one another at regular intervals. Assuming as unity the time T_f necessary to bring the sample to fracture with linearly increasing stress, the DIS occurs after half of the time T_f. Comparing the SIEME with the acoustic ones, Nardi and Caputo (2009) noted that each SIEME corresponds to an acoustic emission associated to micro-fractures (see Fig. 2). Near the fracturing time, the clusters are more numerous and produce a maximum density and intensity, with a peak at the time of the fracture. All different lithologies examined (massive limestone, clay sandstone, metamorphic rocks and also concrete) showed SIEME. During these experiments (Nardi 2005), the electromagnetic emission by rock samples was measured from different lithologies, including limestone, lava, granite, metamorphic rock, and even concrete (see Nardi and Caputo 2009).

To detect the electric part of the EM field, an active antenna that operates on the VLF band (0.8-12 kHz) was used. It was positioned at a fixed distance of 20 cm from the samples centre, protected by a plastic shield from rock debris. A detailed analysis of experimental apparatus is given by Nardi (2005). A typical SIEME is presented in Fig. 2: from a qualitative point of view, all measured signals are short pulses or pulse clusters that on a larger timescale define the observed complex time behaviour.
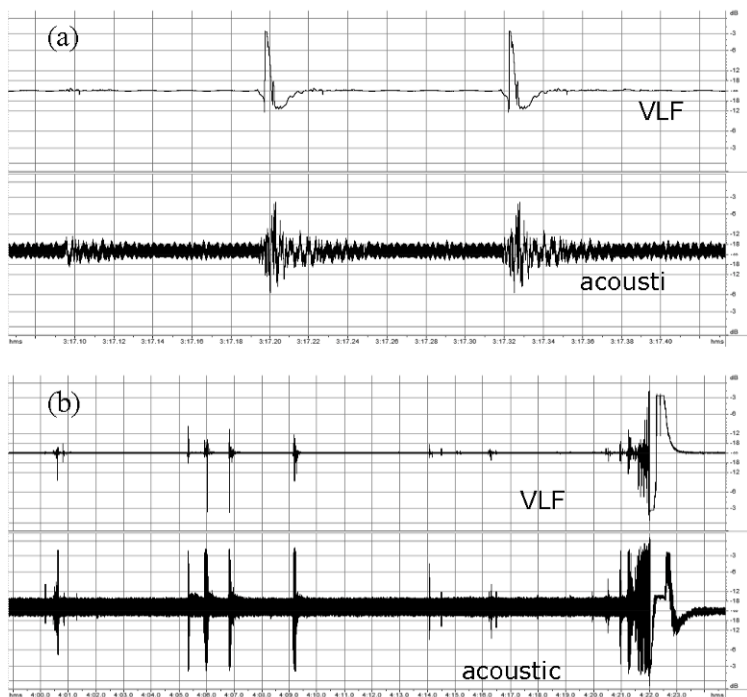
Fig. 2. Typical DIS pattern of signals observed during the stressing of the rock. SIEME pulses (top of (a) and (b) panels) are always associated with acoustic emissions (AE) (at the bottom of (a) and (b) panels). Panel (a) presents a view of SIEME and the associated AE, while (b) presents the whole sequence of SIEME signals as compared with the corresponding AE.

3.   NON-EXTENSIVE STATISTICAL PHYSICS FORMULATION

We proceed now to recapitulate the non-extensive statistical physics formulation, which will be used for the analysis of AE. We express the non-extensive Tsallis entropy S_q (Tsallis 1988, 1999, 2001, 2009),

$$S_q = k_B \frac{1 - \sum p^q(X)}{q - 1} ,$$

where k_B is Boltzmann's constant, in terms of the probability distribution $p(X)$ of a fundamental SIEME parameter, X, that could be the energy released, E, or the inter-event time, T (*i.e.*, the time interval between two successive SIEME). The index q is the degree of non-extensivity. In the limit $q \rightarrow 1$, $S_q \rightarrow S_1$ and the approach reduces to the well-known Boltzmann–Gibbs (BG) entropy, with which the Tsallis entropy shares many common

properties (Tsallis 2009). However, the simple additivity is violated, because for a system composed of two statistically independent systems, A and B, the Tsallis entropy satisfies:

$$S_q(A,B) = S_q(A) + S_q(B) + \frac{1-q}{k_B} S_q(A) S_q(B) \ .$$

The last term on the right-hand side of this equation describes the interaction between the two systems and is the origin of non-extensivity. So the index q indicates the degree of non-extensivity. It accounts for dependency or long-range interaction between microfractures and for $q < 1$, $q = 1$, and $q > 1$, respectively, corresponds to super-additivity (super-extensivity), additivity (extensivity), and sub-additivity (sub-extensivity). This is the fundamental principle of non-extensive statistical mechanics. All other quantities, which are concerned with thermodynamics, may be derived from it.

The probability distribution $p(X)$ of the SIEME parameter X (*i.e.*, the energy released or the inter-event time T) is obtained by maximizing the non-extensive entropy under appropriate constraints with the Lagrange multipliers method. Herein we use the normalization condition and a generalized expectation value definition as appropriate parameters to optimize the non-extensive entropy

$$\int_0^\infty p(X)\mathrm{d}X = 1 \qquad \text{and} \qquad X_q = \langle X \rangle_q = \int_0^\infty X P_q(X)\mathrm{d}X \ ,$$

where

$$P_q(X) = \frac{p^q(X)}{\int_0^\infty p^q(X)\mathrm{d}X} \ .$$

We note that X_q denotes the generalized expectation value (q-expectation value) and $P_q(X)$ is the escort probability (Tsallis 2009). Now we write the following auxiliary function to use the Lagrange multipliers method (Abe and Suzuki 2005)

$$S_q^* = S_q - \alpha \int_0^{x_{\max}} p(X)\mathrm{d}X - \beta X_q \ ,$$

where α and β represent Lagrange multipliers. Letting $\delta S_q^* = 0$, we obtain the physical probability:

$$p(X) = \frac{\left[1-(1-q)\beta_q X\right]^{\frac{1}{1-q}}}{Z_q} = \frac{\exp_q\left(-\beta_q X\right)}{Z_q} \ ,$$

where the *q*-exponential function is defined as

$$\exp_q(X) = \left[1 + (1-q)X\right]^{1/(1-q)} ,$$

when $1 + (1-q)X \geq 0$ and $\exp_q(X) = 0$ in all the other cases, and

$$Z_q = \int_0^{x_{max}} \exp_q(-\beta_q X)\,dX ,$$

the *q*-partition function, where

$$\beta_q = \frac{\beta}{c_q + (1-q)\beta X_q} \qquad \text{and} \qquad c_q = \int_0^{x_{max}} p^q(X)\,dX .$$

In the limit $q \to 1$, the *q*-exponential function leads to the ordinary exponential. If $q > 1$, Eq. (1) has a long power law tail. In contrast, for $0 < q < 1$ a cut-off appears (Abe and Suzuki 2005).

4. SCALING LAWS IN STRESS-INDUCED ELECTROMAGNETIC EMISSIONS

In the following, we focus on two quantities that characterize each SIEME event: (i) the square of SIEME adjusted amplitude A_{eme}^2, which expresses a normalized energy quantity, *i.e.*, $e = E / E_{\max} = A_{\text{eme}}^2 / A_{\text{eme-max}}^2$, where $A_{\text{eme-max}}^2$ is the maximum value of the observed SIEME, and (ii) the time of occurrence of each observed SIEME (Vallianatos and Triantis 2008). A fundamental observation in seismology is the Gutenberg–Richter law which indicates scale invariance in seismic phenomena. In the present experiments, the main source of SIEME is the opening of charged dislocations (Vallianatos *et al.* 2004, Frid *et al.* 2009). It is therefore inferred that a power-law behavior may be fundamental, owing to the SIEME being generated by a massive fracturing process, when spontaneously activated microcracks tend to coalesce, leading to rock failure. Figure 3a presents time chart examples of the SIEME. Figure 3b shows the associated normalized cumulative distribution function (CDF) $P(>e) = N(>e)/N_0$ *versus* e, where $N(>e)$ is the number of SIEME close to fracture having e_i larger than e and N_0 is the total number of observed SIEME. The CDF is rather similar to the Gutenberg–Richter law, supporting a power-law like decrease, which characterizes the global frequency-magnitude relation of earthquakes and AE (Vallianatos and Triantis 2008 and references therein).

We now proceed to analyze the waiting times between SIEME events, in time series obtained from different rock fracture experiments. To this effect, the SIEME series is transformed to a point process where events occur at
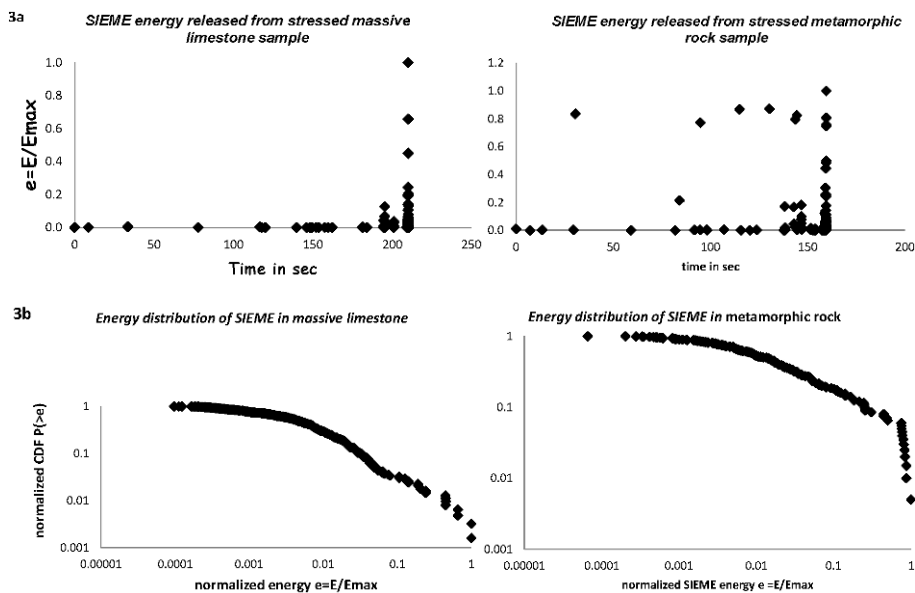
Fig. 3: (a) Examples of SIEME energy released as we approach failure, (b) Normalized cumulative distribution function (CDF) $P(>e)$, of $e = E/E_{max}$.

times t_i with $1 \leq i \leq N$, and therefore, the time between successive events can be obtained by $T_i = t_{i+1} - t_i$. Figure 4 shows the log-log plot of CDF of the normalized SIEME waiting times $\chi = T/T_{max}$ where T_{max} is the maximum observed waiting time.

Analyzing the normalized energy released e, we lead to a q index for the normalized energy release, $q_e = 1.67$ and regarding the SIEME inter-event times we conclude that q_T is of the order of 1.7, where the shape of CDF depends on the quality of sample. This is consistent with previous calculations of q for earthquakes, tectonic effects and other natural hazards, as well (Telesca 2010a, b; Vallianatos 2009).

We proceed now to study the observed distribution which were interpreted in the frame of NESP, following an analogy with the spring-block, Burridge–Knopoff (BK) model (Burridge and Knopoff 1967) which has been widely used in seismology (see Rundle *et al.* 2000 and references therein). Here we attempted to qualitatively work out how the interoccurrence time statistics is influenced by the variation of the major physical quantities, such as stiffness and frictional parameters of material that control the evolution of cracks.

We apply the 2D spring-block model, with analogy to that presented in Hasumi (2007). The model is composed of blocks, two plates, two different
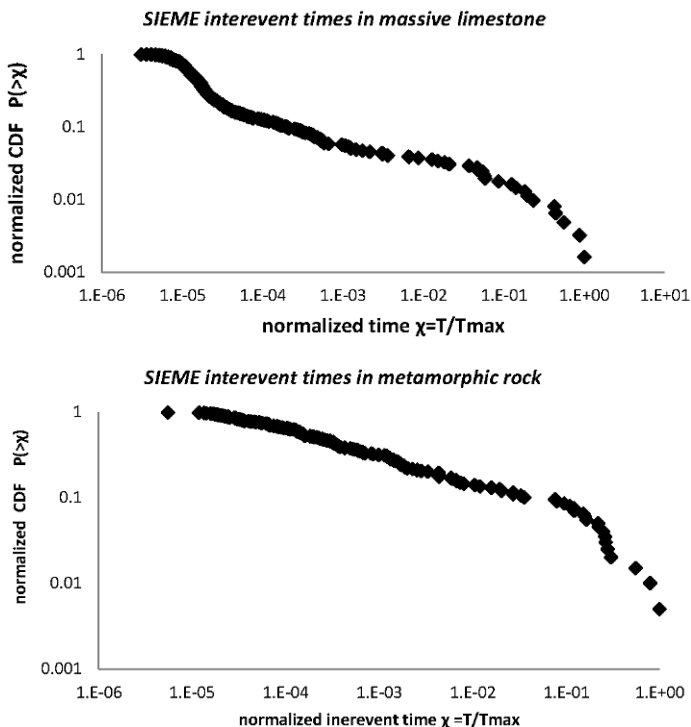
Fig. 4. The normalized cumulative distribution function CDF $P(>\chi)$, of the normalized SIEME waiting times $\chi = T/T_{max}$.

kinds of coil springs, k_x and k_y, and a leaf spring, k_p, corresponding, respectively, to segments of a cracks, boundary loaded plates, a compression and a shear stress. The fundamental idea of the model is that EME are caused by the motion of the existing charged microcracks (Vallianatos *et al.* 2004). Such a motion creates acoustic emissions due to the opening of cracks (Benson *et al.* 2007 and references therein) and an associated stress induced electromagnetic emission (SIEME) as a result of charge's motion (Tzanis and Vallianatos 2002). We assume that the slip direction of blocks is restricted only to the y direction. The equation of motion at site i, j can be written as

$$M \frac{d^2 Y_{i,j}}{dt^2} = k_x \left(Y_{i+1,j} + Y_{i-1,j} - 2Y_{i,j} \right) + k_y \left(Y_{i,j-1} + Y_{i,j+1} - 2Y_{i,j} \right) - k_p Y_{i,j} - F\left(V + \frac{dY_{i,j}}{dt} \right),$$

$$(1)$$

where M and $Y_{i,j}$ are, respectively, mass and displacement of the block and F is a dynamical force between the block and the bottom plate.

Now we rewrite Eq. (1) into a dimensionless form. The dimensionless dynamical friction force Φ is obtained as $(\dot{Y}/V_1) = F(\dot{Y})/F_0$, where F_0 and V_1 are the maximum friction force and the characteristic velocity, respectively. A dimensionless time τ and displacement $U_{i,j}$ are defined by

$$\tau = \omega_p t = t\left(\sqrt{\frac{k_p}{M}}\right), \qquad U_{i,j} = \frac{Y_{i,j}}{D_0} = \frac{Y_{i,j}}{F_0/k_p} \; .$$

Then the dimensionless form is

$$M\frac{\mathrm{d}^2 U_{i,j}}{\mathrm{d}t^2} = l_x^2\left(U_{i+1,j} + U_{i-1,j} - 2U_{i,j}\right) + l_y^2\left(U_{i,j-1} + U_{i,j+1} - 2U_{i,j}\right)$$

$$- U_{i,j} - \Phi\left[2a\left(v + \frac{\mathrm{d}U_{i,j}}{\mathrm{d}\tau}\right)\right], \tag{2}$$

where

$$l_x^2 = \frac{k_x}{k_p}, \qquad l_y^2 = \frac{k_y}{k_p}, \qquad v = \frac{V}{D_0\omega_p} = \frac{V}{\hat{V}}, \qquad 2a = \frac{D_0\omega_p}{V_1} = \frac{\hat{V}}{V_1},$$

and $\hat{V}$ is the crack velocity (Frid *et al.* 2006). We choose the friction force as the velocity-weakening constitutive law which states that as the slipping velocity increases, the dynamical friction force decreases. This constitutive law was observed in the accurate rock fracture experiment (Yoshida *et al.* 1997). We express this with the dimensionless dynamical friction force Φ given by (Carlson *et al.* 1991)

$$\Phi(U) = \begin{pmatrix} (-\infty, 1], & \dot{U} = 0 \\ \dfrac{(1-\sigma)}{\left\{1 + 2a\left[\dfrac{U}{(1-\sigma)}\right]\right\}}, & \dot{U} > 0 \end{pmatrix} . \tag{3}$$

The latter is related with an ideal friction function involving cracks motion. The model is governed by five parameters, l_x, l_y, α, σ, and v, where l_x and l_y are dimensionless stiffness parameters in the x and y directions, respectively, α expresses the decrement of the dynamical friction force with increasing slipping velocity. Parameter σ is a stress gap between the normalized maximum friction force and dynamical friction force $\Phi(0)$, the v is a dimensionless loading velocity. Parameters l_x and l_y are related to Lame's constants, as (Yamashita 1976)

$$l_x^2 = \left(\frac{\Delta x}{\Delta y}\right)^2 \qquad \text{and} \qquad l_y^2 = \frac{5\lambda + 6\mu}{\lambda + 2\mu}\left(\frac{\Delta z}{\Delta y}\right)^2,$$
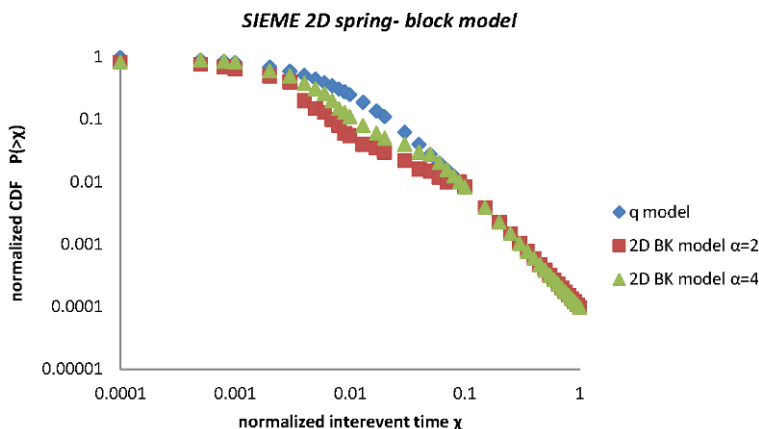
Fig. 5. Example of the normalized cumulative distribution function CDF $P(>\chi)$ of the SIEME normalized inter-event time $\chi = T/T_{\max}$, simulated within a 2D spring-block model, along with that expected in the frame of non-extensive statistical physics. Colour version of this figure is available in electronic edition only.

where Δx, Δy, and Δz are infinitesimal lengths in the x, y, and z directions, respectively. According to the experiments, α is positive and of the order of 1 (Yoshida *et al.* 1997). Since no other event takes place during an ongoing event, we can treat v as being equal to zero, in agreement with Hasumi (2007). In the present work, we select $\Delta x = \Delta y = \Delta z$ along with the assumption that $\lambda = \mu$. We solved Eqs. (2) and (3) by the fourth-order Runge–Kutta method under a free boundary condition. We use a 10^4 order of simulated evolutions and the interoccurrence time statistics are studied by changing the parameter α.

In this model, a SIEME event appears when a slip of blocks is created. The inter-event time is the time interval between successive events. In Figure 5 we show the normalized cumulative distribution function of the normalized inter-event time $\chi = T/T_{\max}$, for $\alpha = 2$ and $\alpha = 3$. For comparison, the normalized CDF for $q = 1.7$, expected in the frame of non-extensive statistics formulation, is given in Fig. 5, indicating that as the friction parameter a increases then the CDF $P(>\chi)$ approaches the expected one in the frame of non extensive approach.

5.   CONCLUDING REMARKS

Stress induced electromagnetic emissions (SIEME) studies in the laboratory can give us an insight into the fracture network evolution processes that take place in such situations and provide us with an opportunity to develop laws suitable for testing at larger scales.

In the present work analyzing rock's SIEME energy release and its temporal distribution, during a laboratory test, the NESP properties of the process were verified. The latter could be useful in understanding earthquake mechanisms and may contribute to solving the problem of earthquake prediction.

To summarize, we have shown that SIEME obey a frequency-size law similar to the well known Gutenberg–Richter law. Taking into account the expression of generalized entropy suggested in the frame of non-extensive statistical mechanics, we conclude that the SIEME data are described by a q-statistics probability density function. We have shown that the energy release distribution and the inter-event time distribution of SIEME, are expressed by the non-extensive statistical mechanics of a sub-extensive process with q-values $q_e = 1.67$ and q_τ of the order of 1.7, respectively, supporting the idea of the presence of long-range effects.

Furthermore, a 2D spring-block model was used to simulate the expected waiting time distribution and to examine its compatibility with NESP. The first results indicate that the waiting time distribution is crucially controlled by the frictional properties of the material.

References

Abe, S., and N. Suzuki (2003), Law for the distance between successive earthquakes, *J. Geophys. Res.* **108**, B2, 2113, DOI: 10.1029/2002JB002220.

Abe, S., and N. Suzuki (2005), Scale-free statistics of time interval between successive earthquakes, *Physica A* **350**, 2-4, 588-596, DOI: 10.1016/j.physa.2004.10.040.

Anastasiadis, C., D. Triantis, I. Stavrakas, F. Vallianatos (2004), Pressure Stimulated Currents (PSC) in marble samples, *Ann. Geophys.* **47**, 1, 21-28.

Benson, P.M., B.D. Thompson, P.G. Meredith, S. Vinciguerra, and R.P. Young (2007), Imaging slow failure in triaxially deformed Etna basalt using 3D acoustic-emission location and X-ray computed tomography, *Geophys. Res. Lett.* **34**, 3, L03303, DOI: 10.1029/2006GL028721.

Benson, P.M., S. Vinciguerra, P.G. Meredith, and R.P. Young (2008), Laboratory simulation of volcano seismicity, *Science* **322**, 5899, 249-252, DOI: 10.1126/science.1161927.

Burridge, R., and L. Knopoff (1967), Model and theoretical seismicity, *Bull. Seismol. Soc. Am.* **57**, 3, 341-371.

Carlson, J.M., J.S. Langer, B.E. Shaw, and C. Tang (1991), Intrinsic properties of a Burridge–Knopoff model of an earthquake fault, *Phys. Rev. A* **44**, 2, 884-897, DOI: 10.1103/PhysRevA.44.884.

Chakrabarti, B.K., and L.G. Benguigui (1997), *Statistical Physics of Fracture and Breakdown in Disordered Systems*, Oxford University Press, Oxford, 161 pp.

Enomoto, Y., and H. Hashimoto (1990), Emission of charged particles from indentation fracture of rocks, *Nature* **346**, 641-643, DOI: 10.1038/346641a0.

Frid, V., A. Rabinovitch, and D. Bahat (2003), Fracture induced electromagnetic radiation, *J. Phys. D: Appl. Phys.* **36**, 13, 1620-1628, DOI: 10.1088/0022-3727/36/13/330.

Frid, V., A. Rabinovitch, and D. Bahat (2006), Crack velocity measurement by induced electromagnetic radiation, *Phys. Lett. A* **356**, 2, 160-163, DOI: 10.1016/j.physleta.2006.03.024.

Frid, V., J. Goldbaum, A. Rabinovitch, and D. Bahat (2009), Electric polarization induced by mechanical loading of Solnhofen limestone, *Phil. Mag. Lett.* **89**, 7, 453-463, DOI: 10.1080/09500830903022636.

Frid, V., J. Goldbaum, A. Rabinovitch, and D. Bahat (2011), Time-dependent Benioff strain release diagrams, *Phil. Mag.* **91**, 12, 1693-1704, DOI: 10.1080/14786435.2010.544684.

Hasumi, T. (2007), Interoccurrence time statistics in the two-dimensional Burridge–Knopoff earthquake model, *Phys. Rev. E* **76**, 2, 026117, DOI: 10.1103/PhysRevE.76.026117.

Hayakawa, M. (ed.) (1999), *Electromagnetic Phenomena Related to Earthquake Prediction*, TERRAPUB, Tokyo.

Hayakawa, M., and Y. Fujinawa (eds.) (1994), *Electromagnetic Phenomena Related to Earthquake Prediction*, TERRAPUB, Tokyo.

Hayakawa, M., and O.A. Molchanov (eds.) (2002), *Seismo Electromagnetics: Lithosphere-Atmosphere-Ionosphere Coupling*, TERRAPUB, Tokyo, 478 pp.

Herrmann, H.J., and S. Roux (1990), *Statistical Models for the Fracture of Disordered Media*, North-Holland, Amsterdam.

Nardi, A. (2001), Emissioni elettromagnetiche in rocce sottoposte a sollecitazione meccanica. Un possibile precursore sismico?, Master thesis, University of Rome "La Sapienza" (in Italian).

Nardi, A., (2005), Emissioni elettromagnetiche naturali come precursori di fenomeni sismici, Ph.D. thesis, University of Rome "La Sapienza" (in Italian).

Nardi, A., and M. Caputo (2006), A perspective electric earthquake precursor observed in the Apennines, *Boll. Geofis. Teor. Appl.* **47**, 1-2, 3-12.

Nardi, A., and M. Caputo (2009), Monitoring the mechanical stress of rocks through the electromagnetic emission produced by fracturing, *Int. J. Rock Mech. Min. Sci.* **46**, 5, 940-945, DOI: 10.1016/j.ijrmms.2009.01.005.

Nardi, A., M. Caputo, and C. Chiarabba (2007), Possible electromagnetic earthquake precursors in two years of ELF-VLF monitoring in the atmosphere, *Boll. Geofis. Teor. Appl.* **48**, 2, 205-212.

O'Keefe, S.G., and D.V. Thiel (1995), A mechanism for the production of electromagnetic radiation during fracture of brittle materials, *Phys. Earth Planet. In.* **89**, 1-2, 127-135, DOI: 10.1016/0031-9201(94)02994-M.

Rundle, J.B., D.L. Turcotte, and W. Klein (eds.) (2000), *Geocomplexity and the Physics of Earthquakes*, American Geophysical Union, Washington, 284 pp.

Slifkin, L. (1993), Seismic electric signals from displacement of charged dislocations, *Tectonophysics* **224**, 1-3, 149-152, DOI: 10.1016/0040-1951(93) 90066-S.

Stavrakas, I., C. Anastasiadis, D. Triantis, and F. Vallianatos (2003), Piezo stimulated currents in marble samples: Precursory and concurrent-with-failure signals, *Nat. Hazards Earth Syst. Sci.* **3**, 3/4, 243-247, DOI: 10.5194/nhess-3-243-20.

Stavrakas, I., D. Triantis, Z. Agioutantis, S. Maurigiannakis, V. Saltas, F. Vallianatos, and M. Clarke (2004), Pressure stimulated currents in rocks and their correlation with mechanical properties, *Nat. Hazards Earth Syst. Sci.* **4**, 563-567, DOI: 10.5194/nhess-4-563-2004.

Takeuchi, A., and H. Nagahama (2001), Voltage changes induced by stick-slip of granites, *Geophys. Res. Lett.* **28**, 17, 3365-3368, DOI: 10.1029/2001GL 012981.

Telesca, L. (2010a), Nonextensive analysis of seismic sequences, *Physica A* **389**, 9, 1911-1914, DOI: 10.1016/j.physa.2010.01.012.

Telesca, L. (2010b), A non-extensive approach in investigating the seismicity of L'Aquila area (central Italy), struck by the 6 April 2009 earthquake (M_L = 5.8), *Terra Nova* **22**, 2, 87-93, DOI: 10.1111/j.1365-3121.2009.00920.x.

Tsallis, C. (1988), Possible generalization of Boltzmann–Gibbs statistics, *J. Stat. Phys.* **52**, 1-2, 479-487, DOI: 10.1007/BF01016429.

Tsallis, C. (1999), Nonextensive statistics: theoretical, experimental and computational evidences and connections, *Braz. J. Phys.* **29**, 1, 1-35, DOI: 10.1590/ S0103-97331999000100002.

Tsallis, C. (2009), *Introduction to Nonextensive Statistical Mechanics: Approaching a Complex World*, Springer, New York, DOI: 10.1007/978-0-387-85359-8.

Tsallis, C. (2001), Nonextensive statistical mechanics and thermodynamics: Historical background and present status. **In:** S. Abe and Y. Okamoto (eds.), *Nonextensive Statistical Mechanics and Its Applications*, Springer, Berlin, 3-98.

Tzanis, A., and F. Vallianatos (2001), A critical review of ULF electric earthquake precursors, *Ann. Geofis.* **44**, 2, 429-460.

Tzanis, A., and F. Vallianatos (2002), A physical model of Electric Earthquake Precursors due to crack propagation and the motion of charged edge dislocations. **In:** M. Hayakawa and O.A. Molchanov (eds.), *Seismo Electromagnetics: Lithosphere-Atmosphere-Ionosphere Coupling*, TERRAPUB, Tokyo,117-130.

Vallianatos, F. (2009), A non-extensive approach to risk assessment, *Nat. Hazards Earth Syst. Sci.* **9**, 1, 211-216, DOI: 10.5194/nhess-9-211-2009.

Vallianatos, F. (2011), A non-extensive statistical physics approach to the polarity reversals of the geomagnetic field, *Physica A* **390**, 10, 1773-1778, DOI: 10.1016/j.physa.2010.12.040.

Vallianatos, F., and P. Sammonds (2010), Is plate tectonics a case of non-extensive thermodynamics?, *Physica A* **389**, 21, 4989-4993, DOI: 10.1016/j.physa.2010.06.056.

Vallianatos, F., and P. Sammonds (2011), A non-extensive statistics of the fault-population at the Valles Marineris extensional province, Mars, *Tectonophysics* **509**, 1-2, 50-54, DOI: 10.1016/j.tecto.2011.06.001.

Vallianatos, F., and D. Triantis (2008), Scaling in Pressure Stimulated Currents related with rock fracture, *Physica A* **387**, 19-20, 4940-4946, DOI: 10.1016/j.physa.2008.03.028.

Vallianatos, F., and A. Tzanis (1998), Electric current generation associated with the deformation rate of a solid: Preseismic and coseismic signals, *Phys. Chem. Earth* **23**, 9-10, 933-939, DOI: 10.1016/S0079-1946(98)00122-0.

Vallianatos, F., and A. Tzanis (1999a), A model for the generation of precursory electric and magnetic fields associated with the deformation rate of the earthquake focus. **In:** M. Hayakawa (ed.), *Atmospheric and Ionospheric electromagnetic phenomena associated with Earthquakes*, TERRAPUB, Tokyo, 287-305.

Vallianatos, F., and A. Tzanis (1999b), On possible scaling laws between electric earthquake precursors (EEP) and earthquake magnitude, *Geophys. Res. Lett.*, **26**, 13, 2013-2016, DOI: 10.1029/1999GL900406.

Vallianatos, F., and A. Tzanis (2003), On the nature, scaling and spectral properties of pre-seismic ULF signals, *Nat. Hazards Earth Syst. Sci.* **3**, 3/4, 237-242, DOI: 10.5194/nhess-3-237-2003.

Vallianatos, F., D. Triantis, A. Tzanis, C. Anastasiadis, and I. Stavrakas (2004), Electric earthquake precursors: from laboratory results to field observations, *Phys. Chem. Earth* **29**, 4-9, 339-351, DOI: 10.1016/j.pce.2003.12.003.

Vallianatos, F., E. Kokinou, and P. Sammonds (2011a), Non-extensive statistical physics approach to fault population distribution. A case study from the Southern Hellenic Arc (Central Crete), *Acta Geophys.* **59**, 4, 770-784, DOI: 10.2478/s11600-011-0015-3.

Vallianatos, F., D. Triantis, and P. Sammonds (2011b), Non-extensivity of the isothermal depolarization relaxation currents in uniaxial compressed rocks, *EPL* **94**, 6, 68008, DOI: 10.1209/0295-5075/94/68008.

Varotsos, P. (2005), *The Physics of Seismic Electric Signals*, TERRAPUB, Tokyo.

Yamashita, T. (1976), On the dynamical process of fault motion in the presence of friction and inhomogeneous initial stress. Part I. Rupture propagation, *J. Phys. Earth* **24**, 4, 417-444, DOI: 10.4294/jpe1952.24.417.

Yoshida, S., M. Uyeshima, and M. Nakatani (1997), Electric potential changes associated with slip failure of granite: Preseismic and coseismic signals, *J. Geophys. Res.* **102**, B7, 14883-14897, DOI: 10.1029/97JB00729.

Parameters of Higuchi's Method to Characterize Primary Waves in Some Seismograms from the Mexican Subduction Zone

Gonzalo GÁLVEZ-COYT[1], Alejandro MUÑOZ-DIOSDADO[1],
José A. PERALTA[2], José A. BALDERAS-LÓPEZ[1],
and Fernando ANGULO-BROWN[2]

[1]Basic Sciences Department,
Unidad Profesional Interdisciplinaria de Biotecnología,
Instituto Politécnico Nacional, México D.F., Mexico
e-mail: amunoz@avantel.net (corresponding author)

[2]Physics Department, Escuela Superior de Física y Matemáticas,
Instituto Politécnico Nacional, México D.F., Mexico

A b s t r a c t

Higuchi's method is a procedure that, if applied appropriately, can determine in a reliable way the fractal dimension *D* of time series; this fractal dimension permits to characterize the degree of correlation of the series. However, when analyzing some time series with Higuchi's method, there are oscillations at the right-hand side of the graph, which can cause a mistaken determination of the fractal dimension. In this work, an appropriate explanation is given to this type of behaviour. Using the seismogram as a time series and the properties of the *P* and *S* waves, it is possible to use the properties of Higuchi's method to previously detect the arrival of the earthquake shacking stage, some seconds in advance, approximately 30-35 s in the case of Mexico City. Thus, we propose the Higuchi's method to characterize and detect the *P* waves in order to estimate the strength of the forthcoming *S* waves.

Key words: Higuchi's method, time series, seismograms, earthquake early warning.

1. INTRODUCTION

Over the past three decades, the problem of the so-called earthquake early warning (EEW) has been faced by many researchers (Allen *et al.* 2009a, b; Alcik *et al.* 2009, Böse *et al.* 2009, Hsiao *et al.* 2009, Zollo *et al.* 2009). In Mexico, a seismic alert system (SAS) has been implemented from 1961 (Espinosa-Aranda *et al.* 1995), consisting of seismic stations along the coast near the Middle American trench, which is the border between the Cocos and the American Tectonic Plates. The instruments of these stations trigger on earthquakes and transmit the warning about 320 km to Mexico City. Recently, two special issues of *Seismological Research Letters* (vol. 80, 2009) and *Geophysical Research Letters* (vol. 36, 2009), were devoted to the EEW problem.

As it is well known, the registration of seismic activity is carried out on seismograms, in which we can distinguish up to four wave types: *P*, *S*, Love and Rayleigh waves (Lay and Wallace 1995). The *P* waves are the first to get anywhere and they come mixed with background noise, followed by more destructive waves. The first approach to EEW is to detect strong ground motion and then transmit a warning. Using the *P* wave to determine whether an earthquake will produce dangerous shaking in populated areas provides additional warning. Several methods have been proposed for using the *P* wave to assess earthquake hazard. Many of them estimate the magnitude of the earthquake, by measuring, for instance, the predominant period of the first few seconds of the *P* wave (Nakamura 1988, Allen and Kanamori 2003), other methods use the amplitude of the *P* wave to estimate earthquake hazard (Wu and Kanamori 2005, 2008, Zollo *et al.* 2006). Other methods use mathematical techniques as multiscale wavelet analysis in order to attain an automatic detection of the *P*-wave arrival (Zhang *et al.* 2003, Simons *et al.* 2006).

Some complex systems, such as the seismic zones, generate time series showing the combination of fractal and periodic components. Two decades ago, the so-called Higuchi's method (Higuchi 1988, 1990) to calculate the fractal dimension of complex time series has been used to investigate correlations and non-linear dynamic properties embedded in nonstationary time series. For example, this method has been used to analyze electroseismic time series (Guzmán-Vargas *et al.* 2009, Ramírez-Rojas *et al.* 2007) and simulated heat release fluctuations in a spark ignition heat engine (Curto-Risso *et al.* 2010). Recently, Higuchi's method has been used to detect periodic components mixed with fractal signals (Peralta *et al.* 2006, Muñoz-Diosdado *et al.* 2008, 2009, 2010).

In the present work, we apply a windowing Higuchi's method to a set of seismograms corresponding to some events linked to the Mexican sub-

duction zone along the Pacific Coast in order to study some relevant properties of the *P* waves, which may be possibly used in improving an EEW instrument based in the analysis of *P* waves, nowadays tested at the National Polytechnic Institute of Mexico.

The paper is organized as follows: in Section 2, we briefly describe the Higuchi's method; in Section 3, we present the Higuchi's analysis of periodic time series; in Section 4, we apply the Higuchi's analysis to time series of white noise with periodic components, and in Section 5, we apply the windowing Higuchi's method to the detection of periodic components in seismograms. Finally, we present some concluding remarks.

2. HIGUCHI'S METHOD

A time series can be expressed by $x(i)$, $i = 1, \ldots, N$, where each datum is taken at equally spaced time intervals, with a uniform time denoted by δ. Usually, $\delta = 1$ is assumed, because in principle this parameter does not alter the data analysis. The following describes how to apply the Higuchi's method (Higuchi 1988, 1990) to a time series:

❑ From the time series $x(i)$ the new series $x_k^m(i)$ are obtained

$$x_k^m, \ x(m), \ x(m+k), \ x(m+2k), \ x(m+3k), \ \ldots, \ x\left(m+\left[\frac{N-m}{k}\right]k\right),$$
$$(m = 1, 2, 3, \ldots, k), \quad (1)$$

where k and m are integer numbers, m represents the initial time, k the interval width, and [ ] denotes the integer part.

❑ The length of the series $x_k^m(i)$ is defined as

$$L_m(k) = \left\{ \left(\sum_{i=1}^{\left[\frac{N-m}{k}\right]} \left| x(m+ik) - x(m+(i-1)k) \right| \right) \frac{N-1}{\left[\frac{N-m}{k}\right]k} \right\} \Big/ k \ . \quad (2)$$

The term $(N-1)/[(N-m)/k]k$ represents the normalization factor for the length of the subset.

❑ The length of the series $L(k)$ for $x(i)$ is obtained by averaging all the subseries lengths $L_m(k)$ that have been obtained for a given k value.

❑ If $L(k) \propto k^{-D}$, that is, if it behaves as a power law, we find that the exponent D is the fractal dimension of the series.

Applying the above relation implies the proper choice of a maximum value of k for which the relationship $L(k) \propto k^{-D}$ is approximately linear.

3. HIGUCHI'S ANALYSIS OF WHITE NOISE TIME SERIES WITH PERIODIC COMPONENTS

Suppose we have the sum of a white noise time series with mean zero and variance with another series obtained from the sampling of a sine signal; we choose the sampling frequency so that the two series have the same data number. Figure 1a shows the corresponding graph y_r *versus* t. Performing the respective Higuchi's analysis to the series y_r at a value of $k_{max} = 1000$, we obtain the result shown in Fig. 1b; practically, the fractal dimension is $D = 2$, which indicates that the part belonging to the white noise dominates over the sine signal ($D = 1$). On the other hand, oscillations which are due to the sine component can be seen on the right side of the graph.

The location of the first minimum in the oscillatory part of Higuchi's analysis is related to the sampling frequency and the angular frequency of the sine signal. To show this, consider that for a sampling frequency f_m, and a time τ, the series will have $N_\tau = \tau f_m$ data. On the other hand, if the wave is periodic of the form $y = \sin(\omega_0 t)$, the period is $T = 2\pi/\omega_0$, so N_τ can be calculated from the relationship

$$N_\tau = (2\pi/\omega_0) f_m = \frac{2\pi}{20}(1000) = 314.1593 .$$ (3)

Applying logarithm to the previous result, we obtain the value of 2.4971, that is fairly close to 2.5040, as obtained directly from the graph shown in
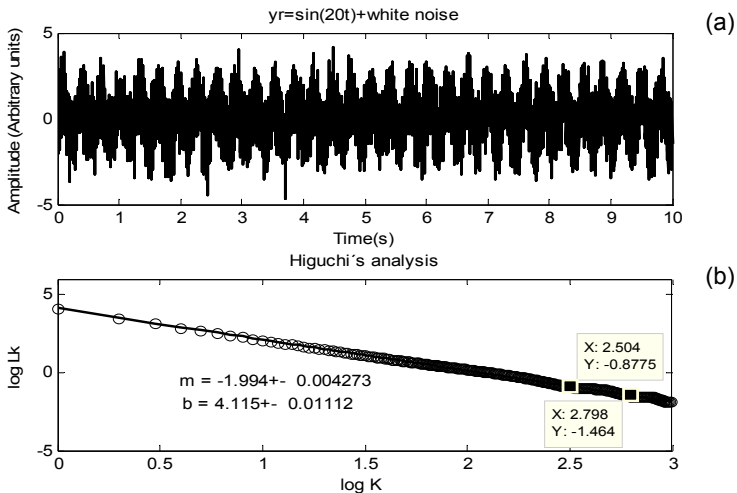

Fig. 1: (a) Graph of a time series $y_r = y_w + y_s$ (white noise + $\sin(20 t)$); y_w is a white noise time series with 10 000 data, and y_s is other time series obtained from the sampling of the sine signal, $\sin(20 t)$, at a frequency $f_m = 1000$ data/s for 10 s, *i.e.*, this second time series also has $N = 10 000$ data; and (b) Higuchi's analysis for y_r ($D = 1.9945 \pm 0.0043$) and detection of the first and second minima of oscillations.

Fig. 1. The following minimum can also be calculated considering the double of data, this is, $N_\tau = 2(314.1593) = 628.3186$, where $\log(628.3186) = 2.7982$, which is also obtained from the graph of Fig. 1b.

Now considering a triple amplitude $(y_s = 3\sin(20\,t))$, we have $y_r = 3\sin(20\,t) +$ white noise. In Figure 2a we show the corresponding graph, in which the sine component is better distinguished. The respective Higuchi's analysis is shown in Fig. 2b; the oscillations appear again in the graph, but now they are more evident than in Fig. 1b. By comparing the respective slopes we can see now that the fractal dimension presents a decrease from 1.9945 to 1.9797, due to the presence of more pronounced peaks. The oscillations are also more evident. The location of the first and second minimum is exactly the same as in the last case, which reaffirms the fact that its appearance depends only on the angular frequency of the sine component of the signal. We can also see a significant increase in the respective errors in the calculation of the slope and the y-intersect due to the presence of the undulations in the Higuchi's analysis.

The explanation for the appearance of these undulations on the graph of Higuchi's analysis can be understood by looking at the definition of subsets $x_k^m(i)$ when k is very close or equal to the number of data for the period of the function $k \approx N_T$, the sub-series for each value of m will consist of values very similar to each other, *i.e.*, they have the form: $x_0 + \varepsilon_0$, $x_1 + \varepsilon_1$, $x_2 + \varepsilon_2$, $x_3 + \varepsilon_3$, ..., $x_n + \varepsilon_n$, where $\varepsilon_0, \varepsilon_1, \varepsilon_2, \varepsilon_3, ..., \varepsilon_n$ are very small values.

In the case of the equality, that is, $k = N_T$, virtually $\varepsilon_0 = \varepsilon_1 = \varepsilon_2 = \varepsilon_3 = ... = \varepsilon_n = 0$, so the subsets are nearly constant. By using these sub-series in the
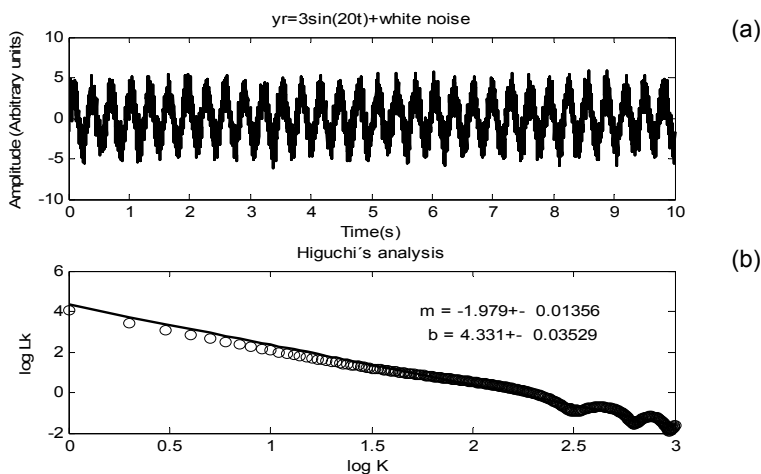

Fig. 2: (a) Graph of a time series $y_r = y_w + y_s$ (white noise $+ 3\sin(20\,t)$), and (b) Higuchi's analysis for y_r ($D = 1.9797 \pm 0.0136$).

calculation of the length $L_m(k)$ by the Higuchi's method, first, we have to evaluate the expression

$$\sum_{i=1}^{\left[\frac{N-m}{k}\right]} \left| x(m+ik) - x(m+(i-1)k) \right| = \sum_{i=1}^{\left[\frac{N-m}{k}\right]} \left| x_0 + \varepsilon_i - (x_0 + \varepsilon_{i-1}) \right| = \sum_{i=1}^{\left[\frac{N-m}{k}\right]} \left| \varepsilon_i - \varepsilon_{i-1} \right| \approx \varepsilon_{mT} ,$$

(4)

where ε_{mT} is very small. Substituting this into the definition of the length of the curve we have

$$L_m(k) = \frac{N-1}{\left[\frac{N-m}{k}\right]k^2} \varepsilon_{mT} \cong L_{m\varepsilon} ,$$

(5)

If ε_{mT} is small, then $L_{m\varepsilon}$ will also be small. Moreover, the length $L(k)$ is the average of all lengths $L_m(k)$ that can be built from the original time series $x(i)$. Although each of the sub-series may have different length $L_m(k)$, in the case of periodic time series the values are very similar and, therefore, $L(k)$ will also be very small, so $L(k) \approx L_\varepsilon \approx 0$.

Furthermore, to determine D of the power law $L(k) \propto k^{-D}$, the logarithm is applied on both sides of the above equation,

$$\log(L(k)) = A - D \log(k) .$$

(6)

On the left part, $L_{m\varepsilon}$ will be small when $k \approx N_T$ and therefore in the strictly periodic case

$$\log(L_{m\varepsilon}) \approx -\infty .$$

(7)

Thus, the explanation of oscillations shown in Higuchi's analysis is due to the periodic behavior of the time series.

Although it is possible to determine some frequencies contained in a time series with this idea, in the following section we will show an application to the analysis of seismograms by using the fact that the earthquake frequencies modify the value of Higuchi's fractal dimension D and its respective b parameter (the y-intercept).

4. SIMPLE MODEL FOR A SEISMOGRAM

A seismogram may be approximately visualized as a signal consisting of the following components: first, a background white noise of small amplitude; second, a mixture with the white noise and a set of sinusoidal signals with a slightly larger amplitude; third, a composition of signals of slightly larger amplitude compared to the previous, of white noise and sinusoidal signals (these last two parts correspond to the arrival of the P waves); fourth, again a combination of damped sinusoidal signals with white noise, but with initial
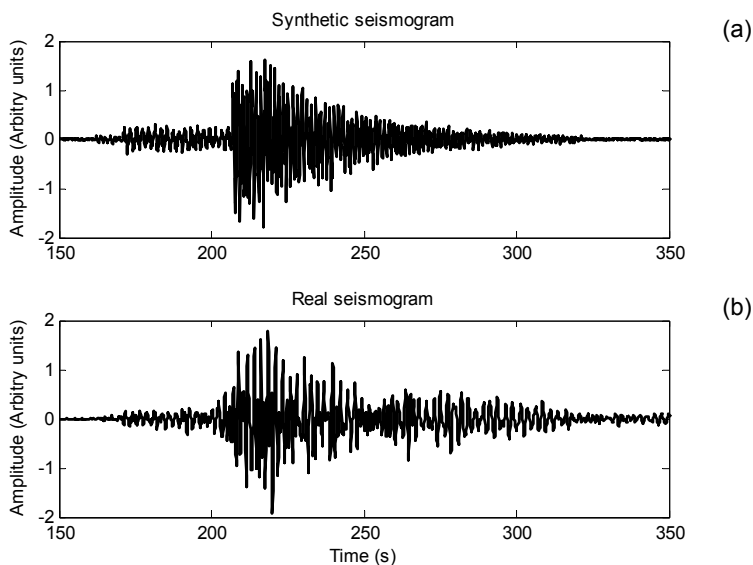
Fig. 3: (a) Synthetic seismogram, and (b) seismogram for an event of considerable magnitude occurred on 17 August 2006 in Michoacán, Mexico, $M_s = 4.6$.

amplitude much higher than the precedent. Finally, the signal returns to the initial condition of background white noise. This model is partially based on the assumption that other authors have made that the seismogram can be divided into locally stationary segments (Sleeman and van Eck 1999, Zhang *et al.* 2003). The graph of one synthetic seismogram is shown in Fig. 3a and a real one in Fig. 3b; this $M_s = 4.6$ seism occurred on 17 August 2006, in Michoacán, Mexico (18.71, 102.47), about 300 km from the seismograph.

It is clear that the synthetic seismogram proposed here does not reproduce all the characteristics observed in a real earthquake; however, it presents the main stages. Perhaps a more complicated combination of waves would give a much better result, but for the purpose of this paper, this model is sufficient.

5. THE WINDOWING HIGUCHI'S METHOD APPLIED TO SEISMOGRAMS

As mentioned in the previous sections, the presence of periodic signals is reflected in the graph of Higuchi's analysis, so the basic idea is to properly identify the moment in which the oscillations indicating the presence of *P* or *S* waves appear. To carry out the series monitoring, we use the windowing method, which consists of segmenting the signal in equal parts, long enough for the method to be applicable.
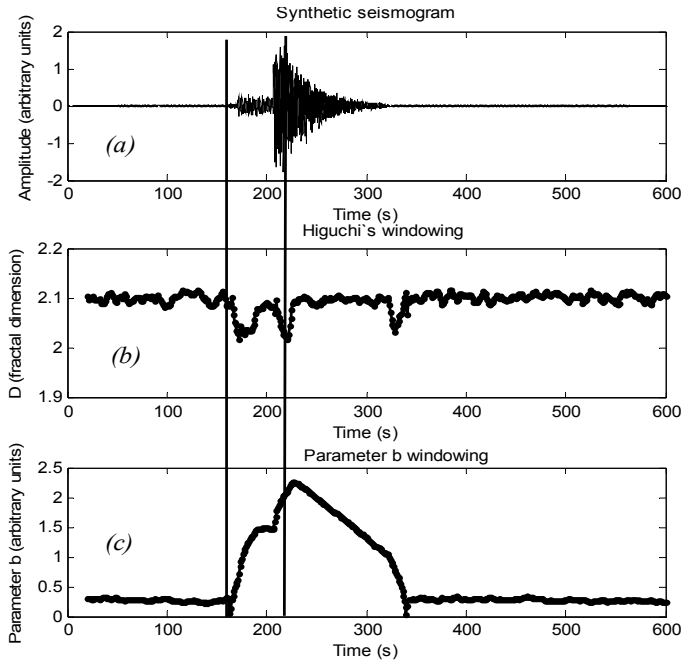
Fig. 4: (a) Synthetic seismogram, (b) windowing for the fractal dimension, and (c) windowing for the parameter *b*.

Windows' width of 20 s (200 data) and a displacement of 1 s (10 data) were used to apply the windowing Higuchi's method to a synthetic seismogram. Each window provides the fractal dimension value *D* and their respective *y*-intercept or parameter *b*. Figure 4b shows the windowing for the fractal dimension, and Fig. 4c the windowing of parameter *b*. The region of interest is indicated in the figure by parallel lines. Prior to this region, the windowing displays values that oscillate around a mean value for both indicators, but immediately when it comes to the region in which the oscillations begin, a quite notable change from its prior average values can be seen. It is precisely this variation that can be used as a seismic estimator. In Figure 5 we show an approaching to the indicated region; here it is possible to observe in more detail what is happening. If a threshold for each parameter value is set, as the lines shown in the respective figures, it would be a time of 40 s before the arrival of the *S* waves, in the synthetic seismogram.

The previous analysis was performed to a synthetic seismogram, then we carried out the analysis of one real earthquake occurred on 17 August 2006, in Michoacán, Mexico. For this analysis we used the same parameters as in the case of the synthetic seismogram; the real seismogram was sampled at a frequency of 10 data/s. Figure 6a shows the graph of the actual earth-
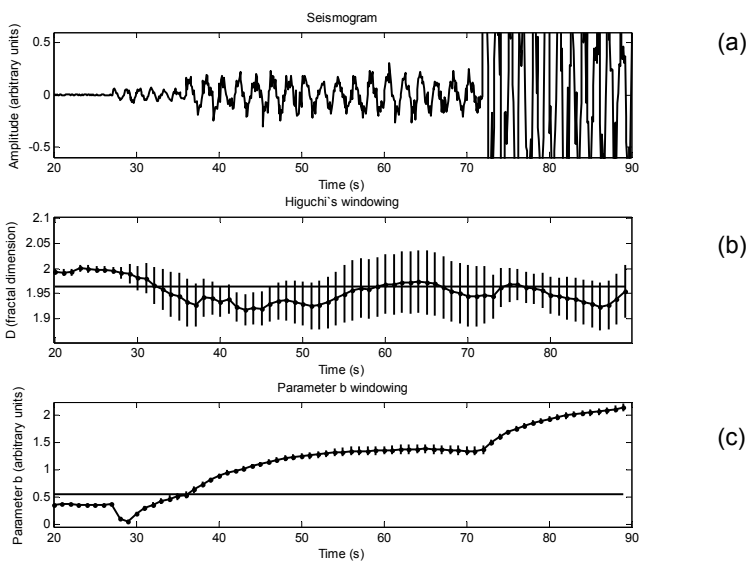
Fig. 5: (a) Approaching to the region of interest in the synthetic seismogram, (b) and (c) windowing of the fractal dimension *D*, and the parameter *b* with their corresponding error bars, respectively.
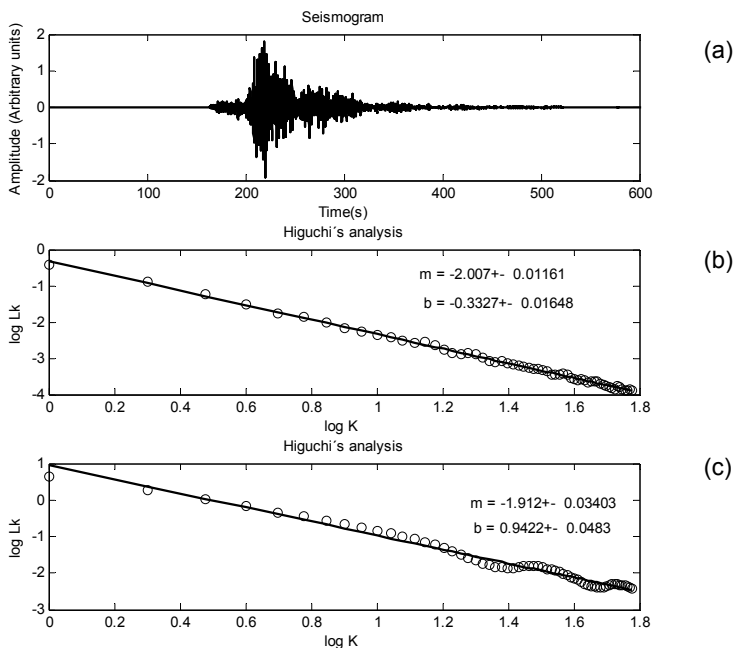

Fig. 6: (a) Seismogram for an event occurred on 17 August 2006, in Michoacán, Mexico, $M_s = 4.6$; (b) Higuchi's analysis for a window corresponding to 100-120 s; and (c) Higuchi's analysis for a window corresponding to 160-180 s.

quake, Fig. 6b shows the Higuchi's analysis of the region between 110-120 s; the graph presents very slight variations. However, it is almost linear and the value of the fractal dimension corresponds to white noise. On the other hand, the Higuchi's analysis from the region comprised of 160-180 s is shown in Fig. 6c, where the oscillations in the graph clearly appear, indicating the presence of periodic components due to the P waves. The complete Higuchi's windowing of the real seismogram for the fractal dimension D and the b parameter is seen in Fig. 7b-c, respectively. An approaching to the region where the earthquake begins is shown in Fig. 8; the behavior observed is very similar to that described by the synthetic seismogram, $i.e.$, the fractal dimension and the b parameter change significantly.

From the previous values we can choose a value as a threshold to activate an alarm; the case of Fig. 7b-c is indicated by vertical lines, which correspond to a time $t = 173$ s. On the other hand, if the main event begins at $t = 206$ s, we will have a time of $\Delta t = 33$ s to activate a seismic alarm.

The analysis described above for the real seismogram was applied to a set of 35 seismograms of earthquakes of different magnitudes. Some of the analyses performed are shown in Fig. 9.
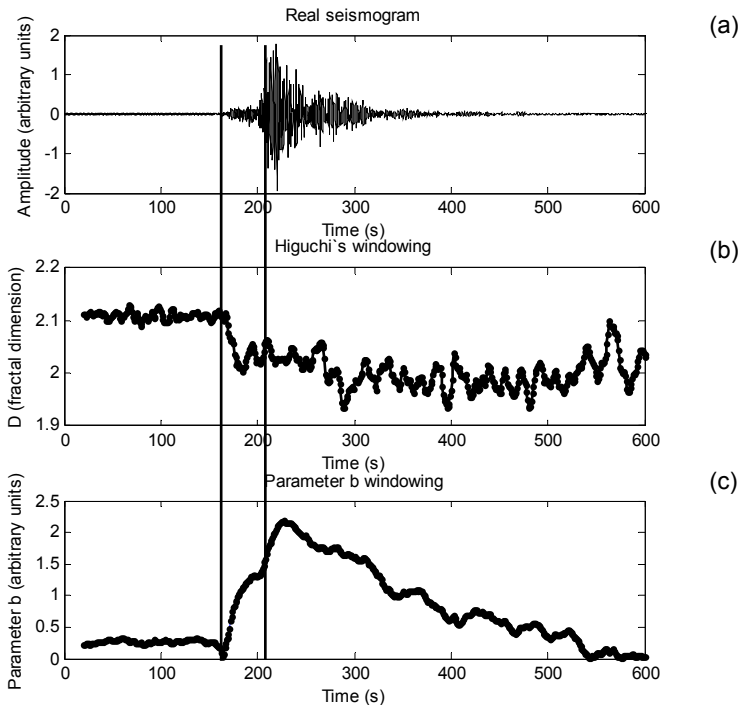

Fig. 7: (a) Seismogram sectioned into three parts of interest, (b) windowing Higuchi's method for the fractal dimension D, and (c) the b parameter.
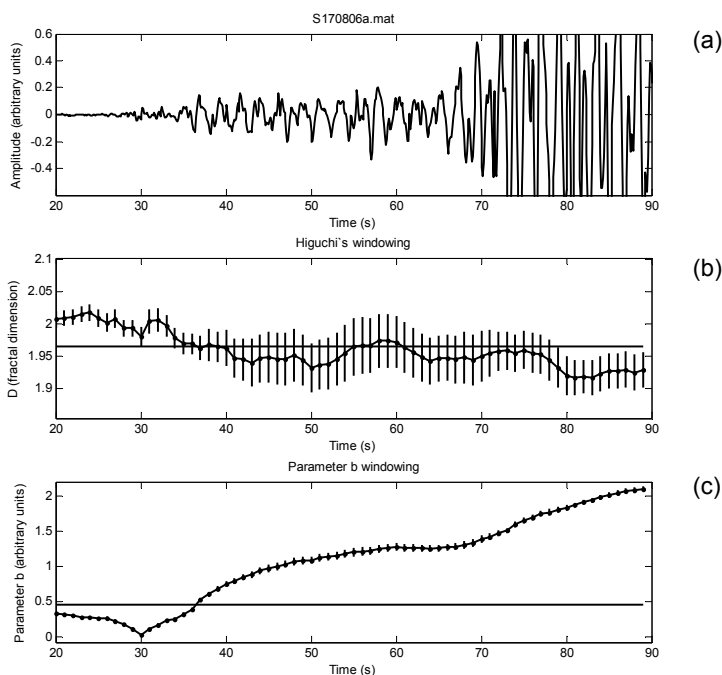
Fig. 8: (a) Detail of the region of interest in the seismogram, (b) windowing Higuchi's method fractal dimension D, and (c) windowing parameter b. Error bars are depicted over curves in (b) and (c).

To perform a comparison between all analyzed seismograms we begin the analysis approximately at the same time. In Figure 10a we observe the totality of the windowing made to the set of seismograms for the fractal dimension, hence it is possible to choose a threshold value, which is also shown in the same graph. In order to have a better view of the previous graph, the set of seismograms was divided into three cases depending on their maximum *S*-waves amplitudes A_s: small, medium, and large earthquakes. It is well known that A_s determines the magnitude scale M_s, and that *P*-wave amplitude, A_p, determines the m_b scale (Gutenberg and Richter 1956). The average of each set is shown in Fig. 10b, it is notorious that there is a relationship between the magnitude of the earthquake and the speed with which its respective fractal dimension decreases.

The comparison of all windowings made for parameter b is shown in Fig. 11a. As in Figure 10a, it is possible to select a threshold value that includes all cases (as shown in the same figure). The corresponding Fig. 11b shows the averages made for parameter b for each set; there is a clear separation between large, medium-sized and small earthquakes.
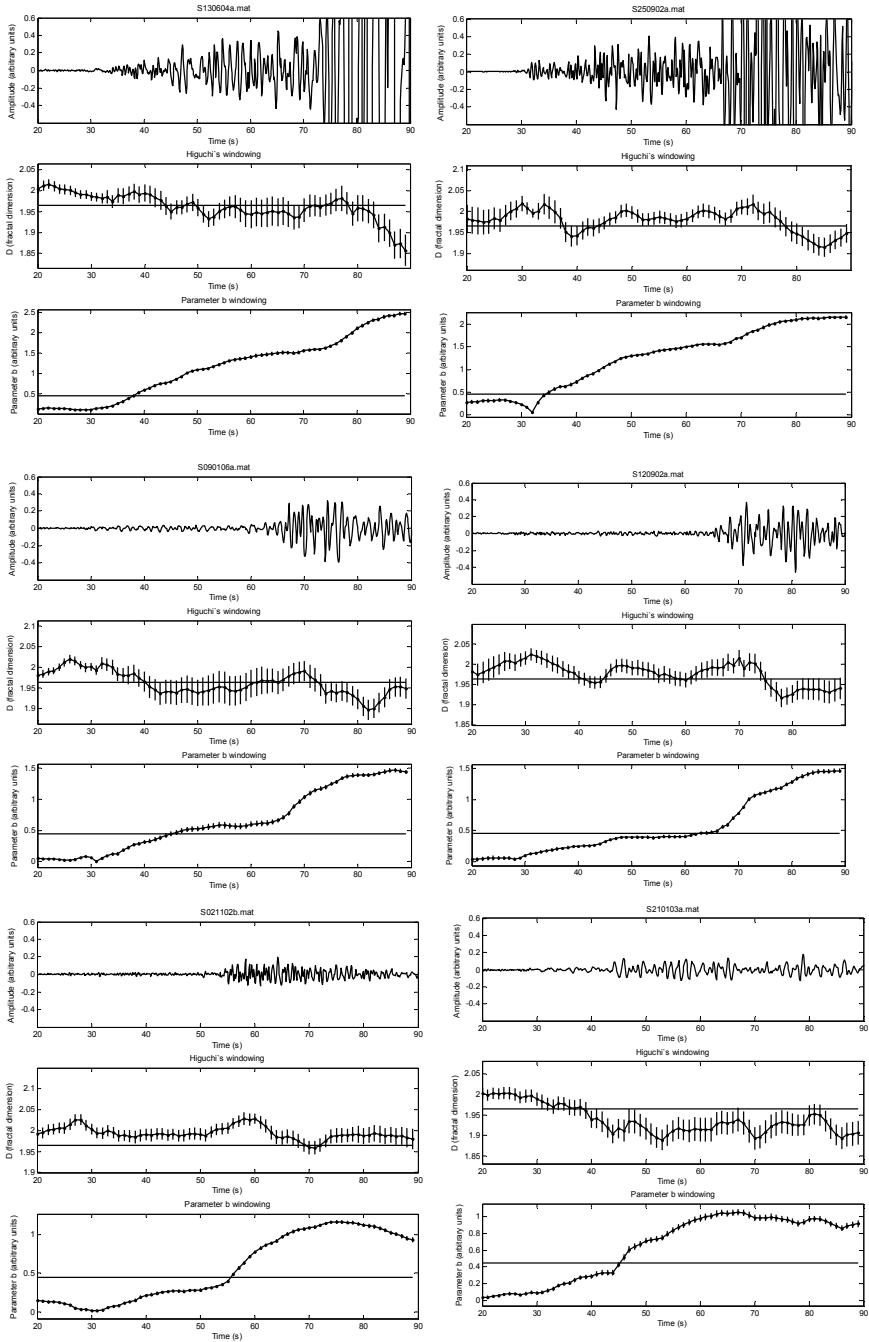
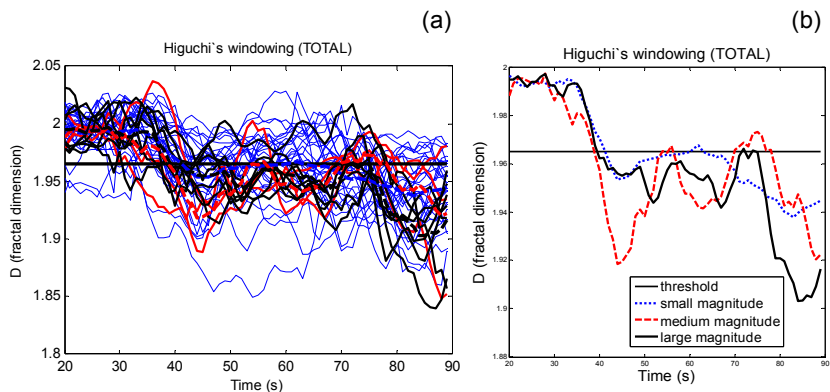Fig. 9. Details of the windowing for a set of six seismograms.

Fig. 10: (a) All the windowings for the fractal dimension for the set of 35 seismograms, and (b) average of windowing of the fractal dimension for small, medium, and large earthquakes. Colour version of this figure is available in electronic edition only.
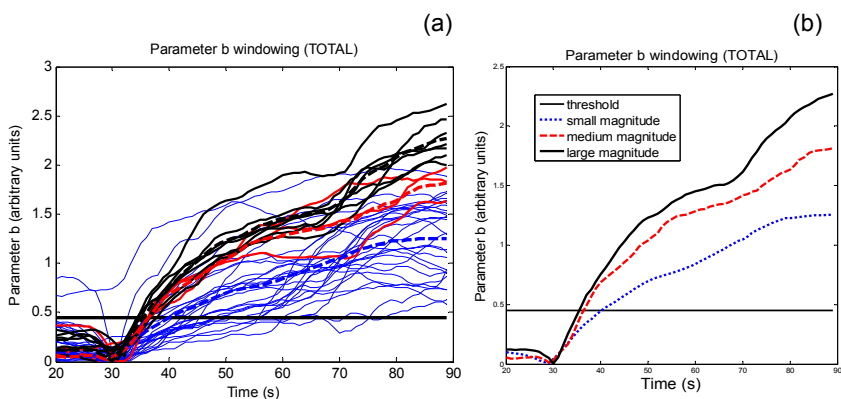
Fig. 11: (a) All the windowings for the parameter *b* for the set of 35 seismograms, and (b) average of windowing of the parameter *b* for small, medium, and large earthquakes. Colour version of this figure is available in electronic edition only.

The windowing Higuchi's method can be adapted to continuous monitoring of seismograms along with other existing methods in order to detect earthquakes of more significant magnitude, in places distant enough from the source, so that the alarm can be raised with sufficient time to take preventive action. For example, for the sampling frequency of the seismogram data used, it takes an average of 8 s for detecting the presence of primary and secondary waves. On the other hand, if the earthquake comes from the seismic zones that affect Mexico City, *i.e.*, the coasts of Guerrero, Oaxaca or Michoacán, near the Middle American tectonic trench, there would be a time of at least 30 s to raise an alarm.

Fig. 12. Windowing of the maximum magnitude of a seismogram and separation in magnitudes previous to the maximum magnitude. Colour version of this figure is available in electronic edition only.

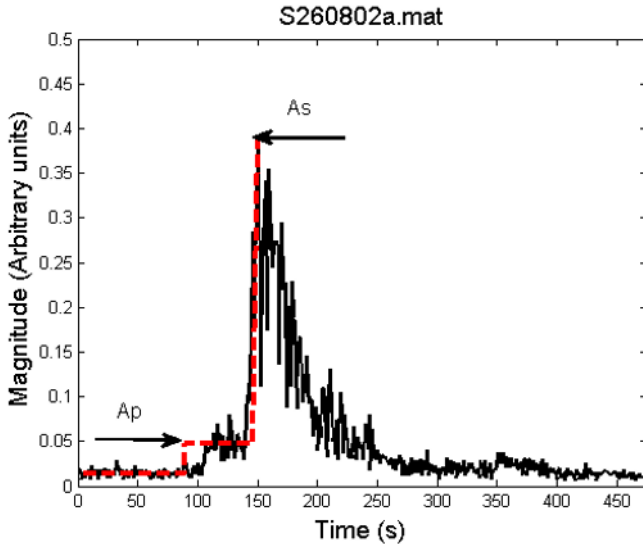According to the last results, the alarm will be activated when the magnitude of the primary waves is larger than the background noise, but does not give any indication of the possible future magnitude of the earthquake. Therefore, it would be good to have a criterion to discriminate between great magnitude earthquakes and low magnitude earthquakes that can activate the alarm unnecessarily. Below is a first attempt towards discrimination of small and large earthquakes. The basic idea is to show the relationship of the amplitude of the P wave and the amplitude of the S wave.

Figure 12 shows the absolute value of one seismogram (continuous line) and the segmented line shows the average magnitude before, during and after the P waves. The first horizontal part corresponds to the magnitude of background noise (about 0.02, practically zero), the following horizontal part of the step represents the average magnitude of wavelength P and the maximum value of the graph represents the magnitude of the S wave.

The previous analysis was performed for a set of 35 seismograms of different magnitudes to calculate their corresponding A_p and A_s. The graph corresponding to the comparison of the magnitude of the P wave and the respective maximum magnitude of the wave is shown in Fig. 13. The majority of the events are of small magnitude, and fall within the rectangle limited on the X-axis by 0.3 and on the Y-axis by 3, which corresponds to small earthquake magnitude (of 3.5 or less). The graph also shows that there is
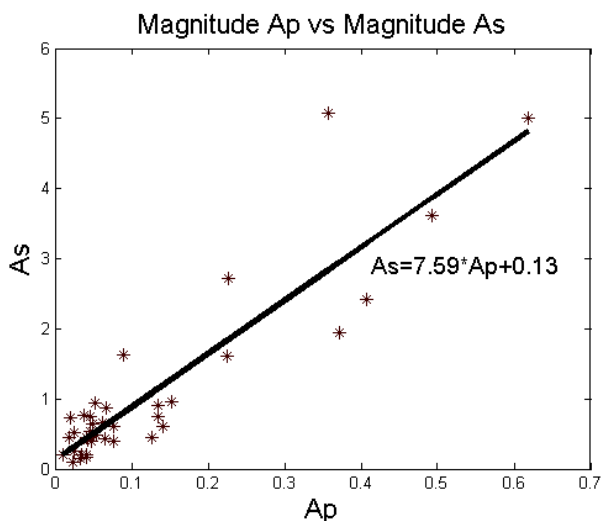
Fig. 13. Graph of the maximum magnitude of an earthquake and the magnitude of the *P* wave; although the relationship is not strictly linear there is a positive correlation that can be used to discriminate small earthquakes from large ones.

a correlation between A_p and A_s. The continuous graph is the least squares fitting. The relationship at least shows that there is a strong relationship between the magnitude of the *P* wave with the subsequent magnitude of the *S* wave. This fact can be used as a criterion to discriminate a small earthquake from a big one.

6. CONCLUSIONS

The proposed model for a synthetic seismogram composed simply by white noise and sine waves, reproduces quite well the properties of a seismogram of a real earthquake (only for the purposes of this paper).

The oscillatory behavior in the graph of the Higuchi's method has been observed in real time series such as heart interbeat, series of air pollutants, seismograms, *etc*. This feature is explained with no doubt by the presence of one or more periodic components in the time series.

Higuchi's method can be applied to the detection of periodic components of high or low frequency and amplitude changes in time series. It is also possible to use it to detect the occurrence of sudden fluctuations in signals when they are continuously monitored.

The windowing Higuchi's method was applied to the seismogram time series of some considerable magnitude earthquakes and actually it was able

to detect the presence of *P* waves in the respective graphical display, which correspond to the expected frequencies in the seismogram.

The parameter *b* of the Higuchi's analysis turns out to be a better estimator of the presence of *P* waves that the fractal dimension.

Mexico City is a vulnerable area to earthquakes generated on the coasts of Guerrero, Oaxaca or Michoacán, and because of its distance, we would have at least 30 s to raise an alarm. This approach can be complementary to other methods of *P*-wave detection which work as seismic alarms (Zhang *et al.* 2003, Hsiao *et al.* 2009).

References

Alcik, H., O. Ozel, N. Apaydin, and M. Erdik (2009), A study on warning algorithms for Istanbul earthquake early warning system, *Geophys. Res. Lett.* **36**, L00B05, DOI: 10.1029/2008GL036659.

Allen, R.M., and H. Kanamori (2003), The potential for earthquake early warning in southern California, *Science* **300**, 5620, 786-789, DOI: 10.1126/science.1080912.

Allen, R.M., P. Gasparini, O. Kamigaichi, and M. Böse (2009a), The status of earthquake early warning around the world: An introductory overview, *Seismol. Res. Lett.* **80**, 5, 682-693, DOI: 10.1785/gssrl.80.5.682.

Allen, R.M., H. Brown, M. Hellweg, O. Khainovski, P. Lombard, and D. Neuhauser (2009b), Real-time earthquake detection and hazard assessment by ElarmS across California, *Geophys. Res. Lett.* **36**, L00B08, DOI: 10.1029/2008GL036766.

Böse, M., E. Hauksson, K. Solanki, H. Kanamori, and T.H. Heaton (2009), Real-time testing of the on-site warning algorithm in southern California and its performance during the July 29, 2008 Mw 5.4 Chino Hills earthquake, *Geophys. Res. Lett.* **36**, 3, L00B03, DOI: 10.1029/2008GL036366.

Curto-Risso, P.L., A. Medina, A. Calvo-Hernández, L. Guzmán-Vargas, and F. Angulo-Brown (2010), Monofractal and multifractal analysis of simulated heat release fluctuations in a spark ignition heat engine, *Physica A* **389**, 24, 5662-5670, DOI: 10.1016/j.physa.2010.08.024.

Espinosa-Aranda, J.M., A. Jiménez, G. Ibarrola, F. Alcantar, A. Aguilar, M. Inostroza, and S. Maldonado (1995), Mexico City Seismic Alert System, *Seismol. Res. Lett.* **66**, 6, 42-53, DOI: 10.1785/gssrl.66.6.42.

Gutenberg, B., and C.F. Richter (1956), Earthquake magnitude, intensity, energy, and acceleration, *Bull. Seismol. Soc. Am.* **46**, 2, 105-145.

Guzmán-Vargas, L., A. Ramírez-Rojas, R. Hernández-Pérez, and F. Angulo-Brown (2009), Correlations and variability in electrical signals related to earthquake activity, *Physica A* **388**, 19, 4218-4228, DOI: 10.1016/j.physa.2009.06.019.

Higuchi, T. (1988), Approach to an irregular time series on the basis of the fractal theory, *Physica D* **31**, 2, 277-283, DOI: 10.1016/0167-2789(88)90081-4.

Higuchi, T. (1990), Relationship between the fractal dimension and the power law index for a time series: A numerical investigation, *Physica D* **46**, 2, 254-264, DOI: 10.1016/0167-2789(90)90039-R.

Hsiao, N.-C., Y.-M. Wu, T.-C. Shin, L. Zhao, and T.-L. Teng (2009), Development of earthquake early warning system in Taiwan, *Geophys. Res. Lett.* **36**, L00B02, DOI: 10.1029/2008GL036596.

Lay, T., and T.C. Wallace (1995), *Modern Global Seismology*, Academic Press, San Diego.

Muñoz-Diosdado, A., H. Reyes-Cruz, D. Bueno-Hernández, G. Gálvez-Coyt, and J. Arellanes-González (2008), New results in magnitude and sign correlations in heartbeat fluctuations for healthy persons and congestive heart failure (CHF) patients, *AIP Conf. Proc.* **1032**, 255-258, DOI: 10.1063/1.2979284.

Muñoz-Diosdado, A., G. Gálvez-Coyt, B.M. Pérez-Uribe, and J. Arellanes-González (2009), Analysis of RR intervals time series of congestive heart failure patients with Higuchi's fractal dimension. **In:** *Proc. IEEE EMBS Ann. Int. Conf., 3-6 September 2009*, 3453-3456.

Muñoz-Diosdado, A., G. Gálvez-Coyt, and B.M. Pérez-Uribe (2010), Oscillations in the evaluation of fractal dimension of RR intervals time series. **In:** *Proc. IEEE EMBS Ann. Int. Conf., 31 August – 4 September 2010*, 4570-4573.

Nakamura, Y. (1988), On the urgent earthquake detection and alarm system (UrEDAS). **In:** *Proc. 9th World Conf. Earthquake Engineering, 2-9 August 1988, Tokyo–Kyoto*, Vol. 7, 673-678.

Peralta, J.A., A. Muñoz-Diosdado, P. Reyes-López, R. Delgado-Lezama, G. Gálvez-Coyt, and J.L. Del Río-Correa (2006), Criteria based on the index of physical work by unitary distance and multifractal analysis of the slow movement of the forefinger to determinate neurological lesion, *AIP Conf. Proc.* **854**, 218-220, DOI: 10.1063/1.2356453.

Ramírez-Rojas, A., E.L. Flores-Márquez, L. Guzmán-Vargas, J. Márquez-Cruz, C.G. Pavía-Miller, and F. Angulo-Brown (2007), A comparison of ground geoelectrical activity between three regions of different level of seismicity, *Nat. Hazards Earth Syst. Sci.* **7**, 5, 591-598, DOI: 10.5194/nhess-7-591-2007.

Simons, F.J., B.D.E. Dando, and R.M. Allen (2006), Automatic detection and rapid determination of earthquake magnitude by wavelet multiscale analysis of

the primary arrival, *Earth Planet. Sci. Lett.* **250**, 1-2, 214-223, DOI: 10.1016/j.epsl.2006.07.039.

Sleeman, R., and T. van Eck (1999), Robust automatic P-phase picking: an on-line implementation in the analysis of broadband seismogram recordings, *Phys. Earth Planet. Inter.* **113**, 1-4, 265-275, DOI: 10.1016/S0031-9201(99) 00007-2.

Wu, Y.-M., and H. Kanamori (2005), Rapid assessment of damage potential of earthquakes in Taiwan from the beginning of *P* waves, *Bull. Seismol. Soc. Am.* **95**, 3, 1181-1185, DOI: 10.1785/0120040193.

Wu, Y.-M., and H. Kanamori (2008), Development of an earthquake early warning system using real-time strong motion signals, *Sensors* **8**, 1-9, DOI: 10.3390/ s8010001.

Zhang, H., C. Thurber, and C. Rowe (2003), Automatic P-wave arrival detection and picking with multiscale wavelet analysis for single-component recordings, *Bull. Seismol. Soc. Am.* **93**, 5, 1904-1912, DOI: 10.1785/0120020241.

Zollo, A., M. Lancieri, and S. Nielsen (2006), Earthquake magnitude estimation from peak amplitudes of very early seismic signals on strong motion records, *Geophys. Res. Lett.* **33**, L23312, DOI: 10.1029/2006GL027795.

Zollo, A., G. Iannaccone, M. Lancieri, L. Cantore, V. Convertito, A. Emolo, G. Festa, F. Gallovič, M. Vassallo, C. Martino, C. Satriano, and P. Gasparini (2009), Earthquake early warning system in southern Italy: Methodologies and performance evaluation, *Geophys. Res. Lett.* **36**, L00B07, DOI: 10.1029/2008GL036689.

VERSITA

Fractal Characteristics of the ULF Emissions Along a Meridian Profile, Based on the 210 MM Stations Data

Anton VARLAMOV[1], Natalia SMIRNOVA[1],
Masashi HAYAKAWA[2], and Kiyohumi YUMOTO[3]

[1]Institute of Physics, St. Petersburg University, St. Petersburg, Russia
e-mail: nsmir@geo.phys.spbu.ru (corresponding author)

[2]University of Electro-Communications, Chofu, Tokyo, Japan
e-mail: hayakawa@whistler.ee.uec.ac.jp

[3]Kyushu University, Department of Earth and Planetary Sciences,
Hakozaki, Fukuoka, Japan; e-mail: yumoto@geo.kyushu-u.ac.jp

A b s t r a c t

Fractal analysis of magnetic records (1 Hz sampling rate) of 5 stations (Guam, Moshiri, Paratunka, Magadan, and Chokurdakh) located along the 210 magnetic meridian (210 MM) has been performed using the Higuchi method. The period of 22 months (October 1992 to July 1994) that embodies the date of the strong Guam earthquake of 8 August 1993 has been considered. A comparison of the ULF emissions scaling parameters (spectral exponents β and fractal dimensions D) obtained at different latitudes has been made. Dependence of β and D on the Kp index of geomagnetic activity has been analyzed for each of the 24 local time intervals. It is revealed that D decreases (β increases) with increasing geomagnetic activity at all stations, but the rates of decrease (increase) are different at different stations and in different time intervals. It is shown that the evening, night and early morning hours are preferable to study magnetospheric effects, whereas the noon hours are the most suitable for the analysis of lithospheric effects. A possibility of using the data of the 210 MM stations as reference materials for the Guam seismically active area is discussed.

Key words: ULF emissions, fractal analysis, 210 MM, SOC dynamics.

1. INTRODUCTION

Extraction of earthquake precursory signatures from the geophysical time series obtained in seismically active regions is one of the important scientific tasks. A large number of data, including electromagnetic ones, have been used for this purpose (see *e.g.*, Proceedings related to International Workshops on Seismo-Electromagnetics: Hayakawa 1999 (IWSE1997), Hayakawa and Molchanov 2002 (IWSE2000), Hayakawa 2005 (IWSE2005), and references therein). Contemporary methods of statistical mechanics, probability theory, and other mathematical approaches have been developed in search for the natural hazard precursory signatures of different origins. Among such methods, a fractal analysis seems to be especially promising (see *e.g.*, Hayakawa *et al*. 1999, Vallianatos and Tzanis 1999, Telesca *et al*. 2004, Gotoh *et al*. 2004, Vallianatos *et al*. 2002, 2004, Ida and Hayakawa 2006). In a series of papers by Smirnova and Hayakawa, specific dynamics of fractal characteristics of ULF emissions registered at the Guam observatory has been reported in relation to the strong (*M*8) Guam earthquake of 8 August 1993 (Hayakawa *et al*. 1999, 2000, Smirnova *et al*. 2001, 2004, Smirnova and Hayakawa 2007). Namely, the spectral exponents β of the ULF emissions decrease and the corresponding fractal dimensions D increase when approaching the date of the Guam earthquake. It is also revealed that those scaling parameters of the ULF time series are influenced by geomagnetic activity. Hence, we see that the local seismo-electromagnetic phenomena are screened by magnetospheric effects, which are of more global character. To distinguish between these effects, the data from reference stations are necessary in addition to the Guam data. Here we consider coordinated magnetic records (1 Hz sampling rate) of the 5 stations located approximately at the Guam geomagnetic meridian (210 MM stations). The purpose of our investigation is to compare the fractal properties of ULF emissions along this meridian profile and an attempt to answer the question which station could be used as a Guam reference point in our seismic-electromagnetic research.

2. EXPERIMENTAL DATA

Magnetic records (components ΔH, ΔD, and ΔZ) which have been used for our analysis were obtained at the 210 MM stations by means of ring-core-type fluxgate magnetometers with a sampling rate of 1 s. The detailed description of the 210 MM project can be found in Yumoto *et al*. (1992). The chain of the five stations chosen for our analysis includes Chokurdakh (CHD), Magadan (MGD), Paratunka (PTK), Moshiri (MSR), and Guam (GUA). This profile covers a wide range of latitudes, from the equatorial area to the auroral zone (see the map in Fig. 1 and the stations coordinates in Table 1).
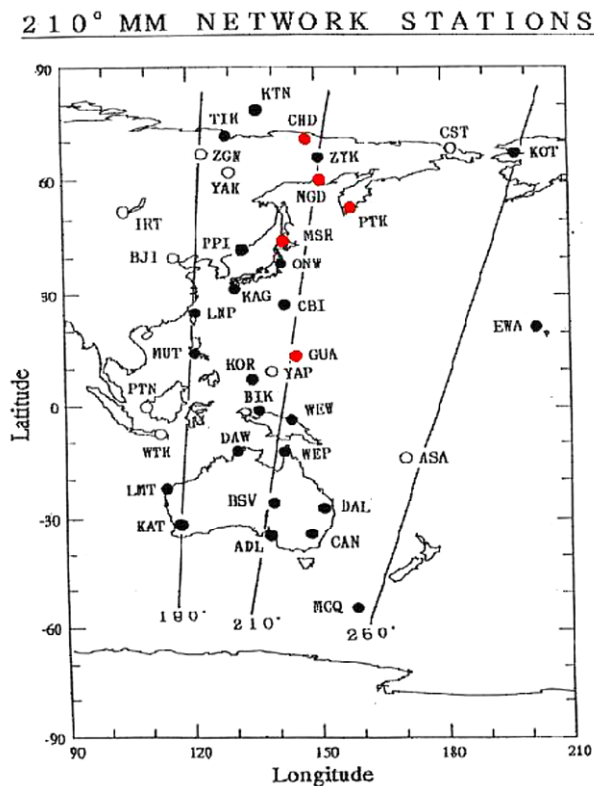
Fig. 1. Map showing the locations of the 210 MM stations in geographic coordinates (5 stations under question are pointed out by the red color).

Table 1

The list of the 210 MM stations used for our analysis

Abbreviation	Geographic coordinates		Geomagnetic coordinates	
GUA	13.58° N	144.87° E	5.61° N	215.55° E
MSR	44.37° N	142.87° E	37.28° N	213.55° E
PTK	52.94° N	158.25° E	46.17° N	226.02° E
MGD	59.97° N	150.86° E	53.49° N	218.75° E
CHD	70.62° N	147.89° E	64.66° N	212.14° E

The analyzed period covers 22 months, from October 1992 to July 1994. This period is chosen to embody the date of the strong $M8$ Guam earthquake (EQ) of 8 August 1993: depth about 60 km, $\Phi = 12.98°N$, $\Lambda = 144.80°E$ as shown in Fig. 2.

It should be noted that, in the period from October 1992 to 8 August 1993, there were no EQs with magnitude $M > 5$ near the Guam island. The
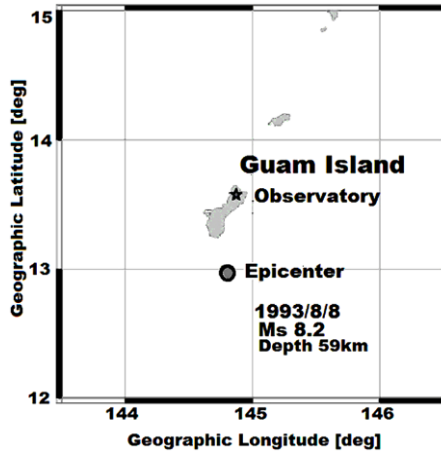
Fig. 2. Epicenter of the Guam earthquake of 8 August 1993 in relation to the location of the ULF observing Guam station.
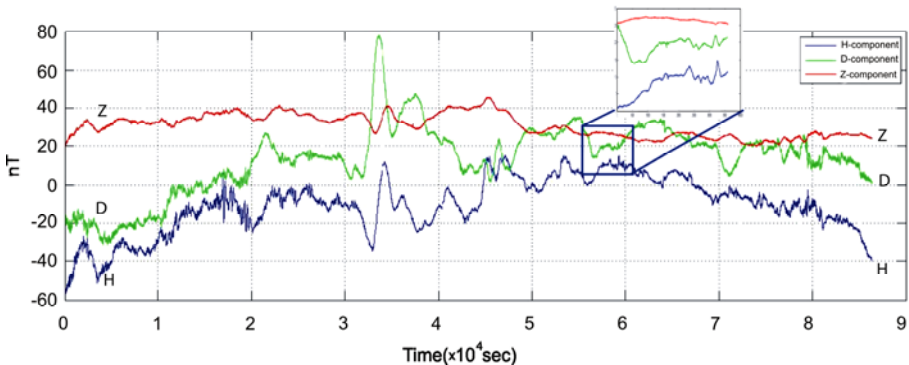
Fig. 3. An example of a typical 210 MM magnetic record (Paratunka, 15/10/92).

strong $M8$ EQ of 8 August 1993 occurred suddenly at 08:34 UT without any foreshocks. There were a lot of aftershocks related to this EQ (In the same date, there were 17 aftershocks of $M > 4.5$). After this strong EQ, seismic activity around Guam continued to be rather high up to the end of the analyzed period, *i.e.*, July 1994 (more than 25 EQs with $M > 5$).

A typical daily magnetic record obtained at the 210 MM profile is presented in Fig. 3; it is an example of the Paratunka station data.

In this study we have analyzed separately the magnetic data in each of the 24 daily 1-hour intervals. As an inset to Fig. 3, one can see the enlarged 1-hour record (ULF emissions) for 16-17 UT. So, each analyzed time series, which represents ULF fluctuations of the Earth's magnetic field (ULF emis-

sions) in 1-hour interval, contains 3600 points. We apply fractal methods to those ULF data to analyze their scaling (fractal) characteristics and study their dynamics in each spatial location in relation to geomagnetic activity and in relation to the strong Guam earthquake of 8 August 1993.

3. FRACTAL APPROACH

Now it is recognized that the extended dissipative dynamical systems evolve naturally to the state of self-organized criticality, SOC (see Bak *et al*. 1987, 1988, Bak 1997). The SOC state is characterized by very high sensitivity of the system to any external perturbations and a fairly broad energy spectrum of dissipation events. The Earth's magnetosphere and lithosphere were shown to exhibit this type of complex SOC behavior (see *e.g*., Chang *et al.* 2003, Sornette and Sornette 1989, Jensen 1998, Hergarten 2002). The fingerprint of the SOC state is fractal organization (power-law distributions) of the output parameters in both space and time domains (scale-invariant structures and fractal noise or $1/f$ fluctuations). Hence we can use fractal methods for analysis of spatiotemporal scaling characteristics of the magnetospheric and lithospheric emissions.

Three methods of fractal analysis have been considered: (i) PSD (Power spectral density) method (Feder 1988, Turcotte 1997); (ii) Burlaga–Klein method (Burlaga and Klein 1986); (iii) Higuchi method (Higuchi 1988, 1990).

A time series can be considered as fractal in the chosen frequency range, if its PSD, $S(f)$, follows the power law at those frequencies: $S(f) \sim f^{\beta}$. The spectral exponent β, and the corresponding fractal dimension D, characterize the rate of irregularity of the time series. β and D are connected via the Berry equation (Berry 1979): $D = (5 - \beta)/2$. In the case of ULF emission analysis, a more advanced fractal approach appears to be the Higuchi method (see Smirnova *et al*. 2001), because it provides more stable values of fractal dimensions. The method is based on estimation of the length of a fractal curve $X(N)$. We consider each set of the 1-hour ULF data with sampling rate of 1 s ($N = 3600$) as a time sequence $X(1)$, $X(2)$, ..., $X(N)$. From a given time series, k new time series are constructed, defined as follows:

$$X_m^k = \left\{ X(m), X(m+k), X(m+2k), ..., X\left(m + \left[\frac{N-m}{k} \right] k \right) \right\} \qquad (m = 1, 2, ..., k) \quad .$$

Then we estimate the length of the curves, which represents the new time series for each k:

$$L_m(k) = \left(\left[\sum_{i=1}^{\left[\frac{N-m}{k} \right]} \left| X(m+ik) - X\left[m + (i-1)\, k \right] \right| \right] \frac{N-1}{\left[\frac{N-m}{k} \right] k} \right) \frac{1}{k} \quad .$$
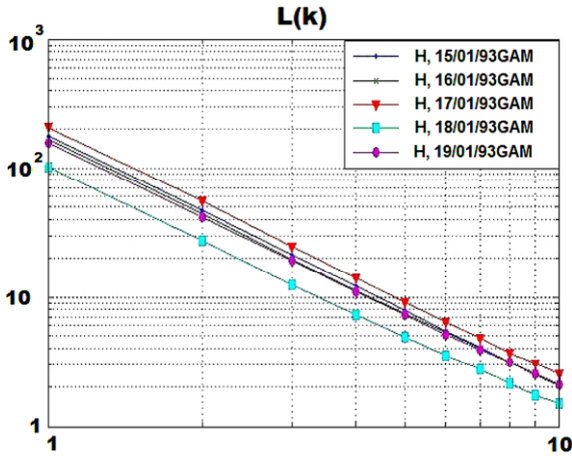
Fig. 4. Examples of the calculation of the ULF emissions fractal dimension using the Higuchi method. Guam, H component, 15-19 January 1993, 11-12 UT interval.

Then the total length of the curve, which represents the original ULF emission time series, is defined as follows:

$$\langle L(k)\rangle = \frac{\sum_{m=1}^{k} L_m(k)}{k}.$$

And finally, we plot $\langle L(k)\rangle$ *versus* k ($k = 1, 2, \ldots, 10$) in the log-log form. If $\langle L(k)\rangle \propto k^{-D}$ and scales linearly in log-log presentation, then we can consider this time series as fractal and we estimate fractal dimension from the slope of curve as seen in Fig. 4.

Using such a procedure, we have calculated fractal dimensions D of the ULF emissions time series for each of the 5 chosen 210 MM stations during the whole investigated period from October 1992 to July 1994. The calculations have been fulfilled in each of the 24 hourly intervals for horizontal (H, D) and vertical (Z) components of the magnetic field. Based on the D values, the corresponding spectral exponents of the ULF emissions have been calculated using the Berry equation: $\beta = 5 - 2 D$. The dynamics of D and β has been analyzed depending on local time, geomagnetic activity, and the observation point location.

4. OBSERVATIONAL RESULTS

We have revealed that variations of the ULF emissions fractal characteristics manifest stochastic character, depending on dates, local time, and geomagnetic activity. So we have made averaging of D and β over different temporal intervals to extract deterministic part in such a stochastic behavior. The

results obtained are presented below in the form of temporal variations of the ULF emissions fractal dimensions along meridian profile, and the dependence of D and β on Kp index of geomagnetic activity.

4.1 Dynamics of the ULF emissions fractal dimensions

For each of the magnetic components (H, D, Z) registered at 5 stations along the 210 MM profile (see Table 1), we have obtained as many as 24 sets of the plots representing dynamics of the ULF emissions fractal dimensions in each of the 24 hourly intervals. Two examples of such dynamics for an interval of 11-12 UT for the auroral Chokurdakh station and the near-equatorial Guam station are shown in Figs. 5 and 6, respectively.
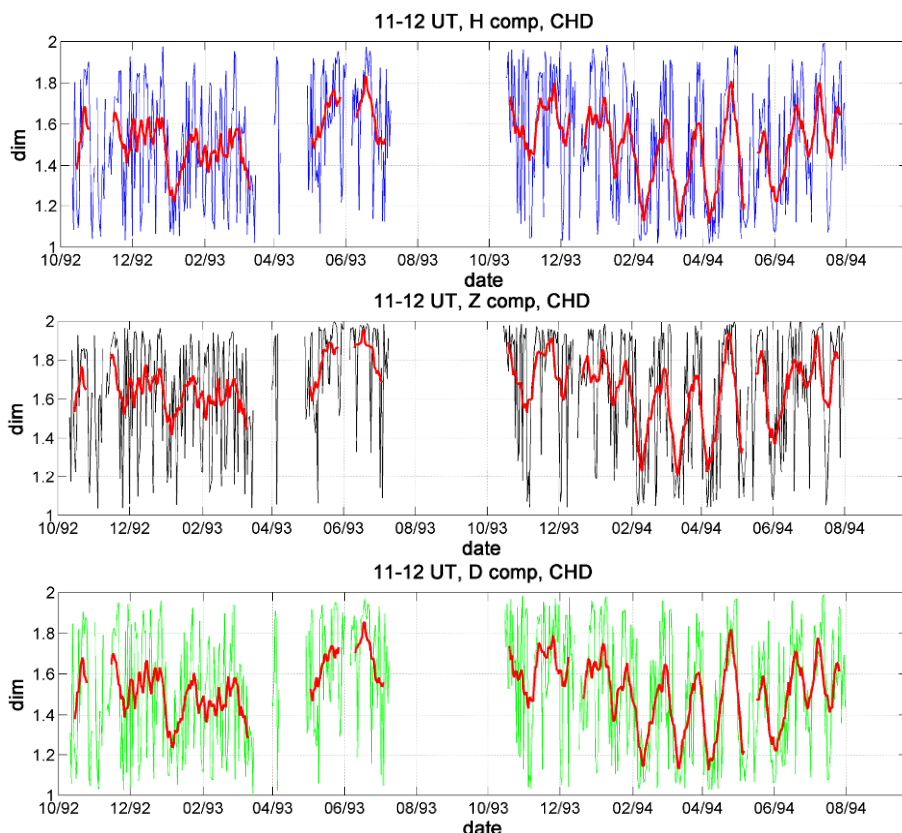
Fig. 5. Dynamics of the ULF emissions fractal dimensions D calculated through the period from October 1992 to July 1994 for the interval of 11-12 UT at the auroral Chokurdakh station (components H, D, and Z). The thin (blue, green, and black) curves represent the $D_{11\text{-}12UT}$ values for the corresponding day; the thick red curves relate to the ±5 day running averages.
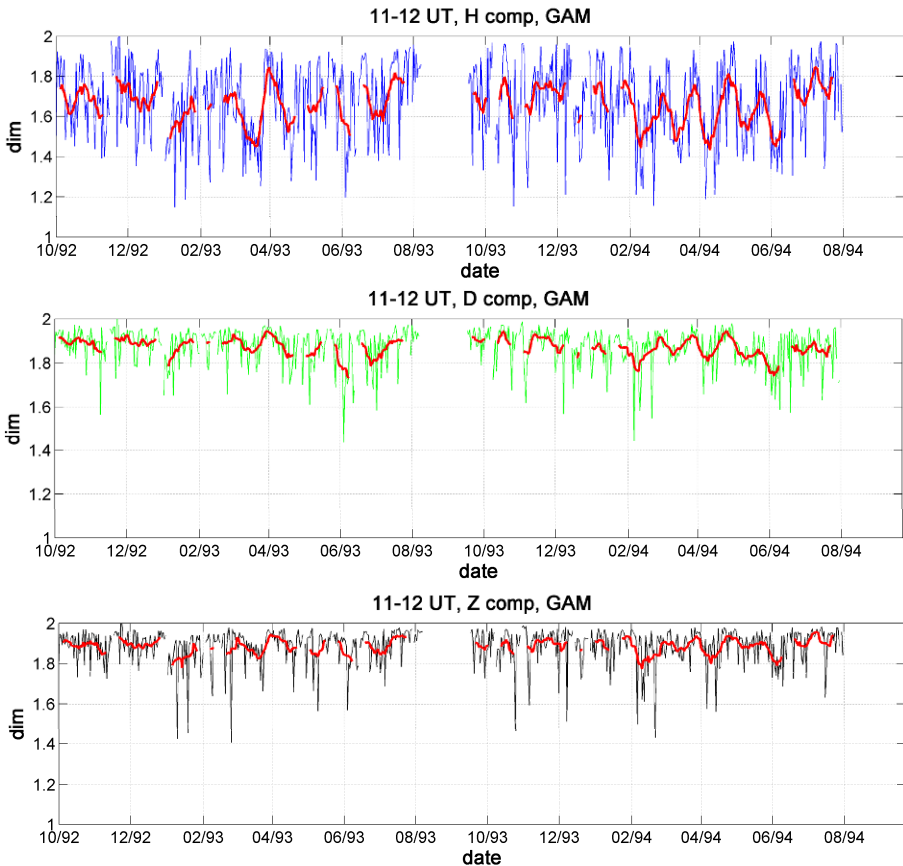
Fig. 6. The same dynamics as in Fig. 5, but for the Guam station.

From Figs. 5 and 6, one can see the following peculiarities:

❏ Daily fluctuations of *D* exhibit chaotic dynamics. It is difficult to understand whether such fluctuations are random or represent a deterministic chaos. Those fluctuations may contain the influence of the magnetospheric, ionospheric, lithospheric processes as well as effects of the man-made origin. It should be stated that such a chaotic dynamics is typical for all of 24 hourly intervals at each of the 5 chosen stations.

❏ Averaging over ±5 days (running average values of *D*) exhibits some features of deterministic behavior. Namely, the distinct modulation of *D* with a period of approximately 27 days is outlined, which corresponds to the rotation of the Sun around its axis. So it is definitely a magnetospheric (non-lithospheric) effect, which is confirmed by looking at the corresponding variations of *Kp* index, as seen in Fig. 7.

❑   Going to the longer-term variations of *D*, one can find the effect revealed earlier in the reference papers by Hayakawa *et al.* (1999) and Smirnova *et al.* (2001), that is, a gradual increase of the ULF emission fractal dimensions before the Guam earthquake of 8 August 1993. One can see this tendency in the upper part of Fig. 6 from the dynamics of *D* for the H component 2-3 months before the EQ. A rough long-term approximation of the *D* dynamics at Guam for the H component is presented in Fig. 8. This may be an earthquake precursory effect. According to our analysis, this effect is rather pronounced at the Guam location (mainly in the H component), and it nearly disappears in the data at Moshiri, Paratunka, and Magadan. As concerns Chokurdakh, a lot of gaps in the data at that station do not allow us to trace such a tendency.

❑   The modulation by the 27-day period is the most pronounced in the auroral zone (Chokurdakh), where it is manifested in the H, D, and Z components (see Fig. 5). At the other stations which are situated inside the plasmasphere, the modulation is observed in the H and D components, and never in Z component. As to the Guam station, which is situated in the region of equatorial electrojet, such a modulation is seen also in Z component (see Fig. 6).
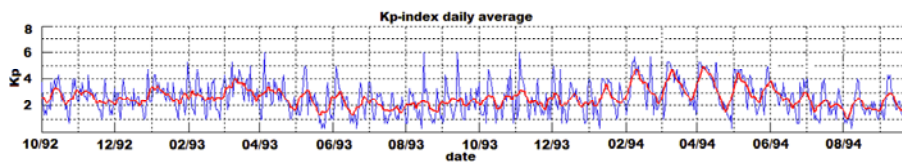
Fig. 7. Variations of the daily averaged *Kp* index during the analyzed period from October 1992 to July 1994 (the thin blue curve). The thick red curve corresponds to the ±5 day running average values.
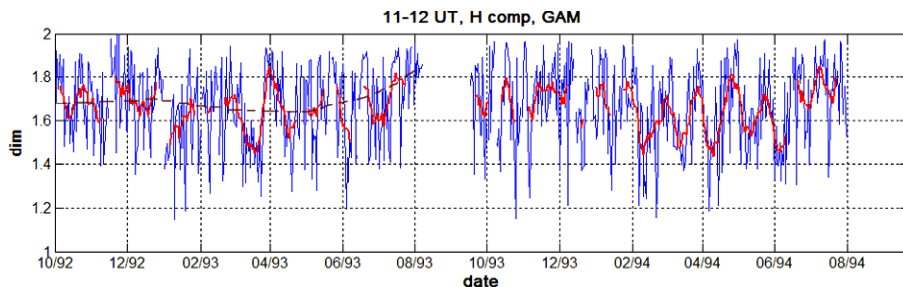
Fig. 8. The long-term approximation (dashed line) of the *D* dynamics at Guam for the H component. It is seen that the ULF emissions fractal dimensions increase starting approximately 2-3 months before the Guam EQ of 8 August 1993.

❑   The range of variations of D (in the H component) at the auroral Chokurdakh station and the equatorial Guam station is wider in comparison with that obtained at the inside-the-plasmasphere Magadan, Paratunka, and Moshiri stations.

4.2 Correlation of the ULF emission fractal dimensions with geomagnetic activity

From Figures 5-7, one can see rather synchronous variations in the curves representing the ±5 day running average values of the ULF emission fractal dimensions D and the Kp index of geomagnetic activity. That means a possible dependence of D from Kp. So the detailed correlation analysis has been fulfilled to examine such dependence.

Some results of the study of correlations between fractal dimensions of ULF emission time series and the Kp index of geomagnetic activity are presented in Fig. 9.
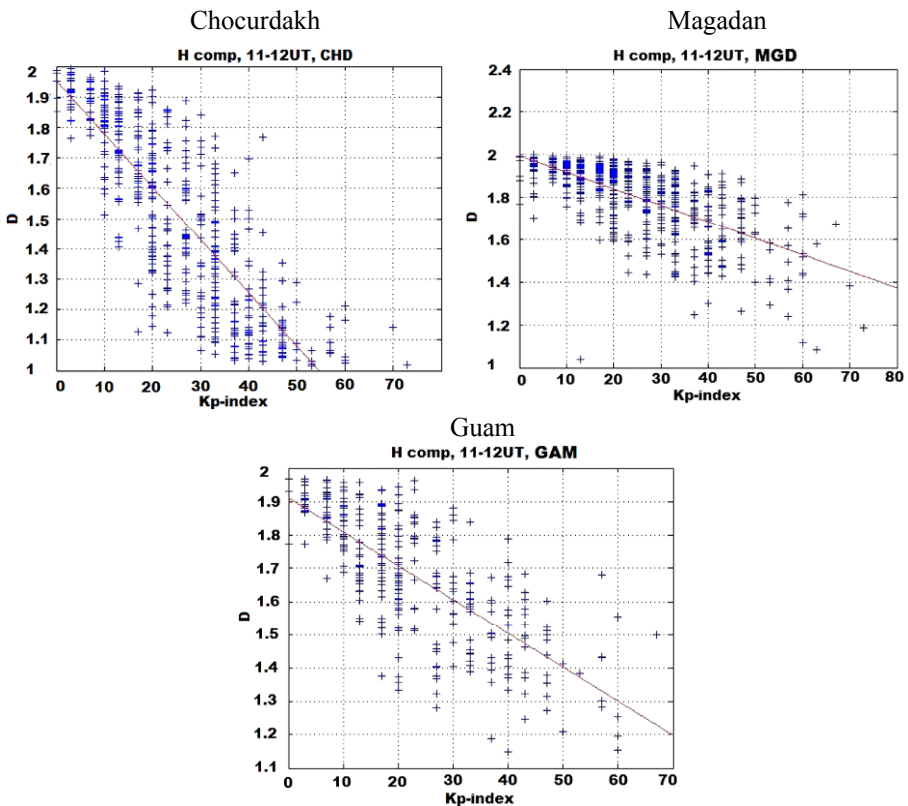
Fig. 9. Examples of plots representing fractal dimensions of the ULF time series (H component, 11-12 UT) *versus* Kp index for 3 locations: Chocurdakh (auroral zone), Magadan (middle latitudes), Guam (equatorial region).

We have obtained that fractal dimensions D of the ULF emissions time series decrease (and the corresponding spectral exponents β of the ULF emissions increase) with increasing magnetic activity. Such an effect is observed at all stations along 210 MM and in all sectors of LT. But the rates of the decrease of D (increase of β) are different at the different stations and in different time intervals. The dependence of D on Kp is most pronounced in the auroral zone (Chocurdakh), and it is rather smooth at the middle latitudes (Magadan and Paratunka). Near the equator (Guam) it becomes again sharper (see Fig. 9 for a comparison).

We have revealed also the daily variation of the correlation coefficients between D and Kp. This variation is more regular in the middle latitudes (Magadan, Paratunka, Moshiri) with a pronounced maximum near 15 UT (01 LT) and minimum around 4 UT (14 LT). As to the auroral zone (Chokurdakh) and equatorial region (Guam) the maximum is not so pronounced there, and it is scattered in the time interval of 10-20 UT (20-06 LT). But the minimum is also around 4 UT, which corresponds to LT around the noon (14 LT). So, we may conclude that the evening, night and early morning hours are preferable to study magnetospheric effects, whereas the noon hours are most suitable for the analysis of lithospheric effects.

5. DISCUSSION

We have obtained rather pronounced dynamics of the ULF emission fractal dimension D along 210 MM profile, which reflects the global magnetospheric effects as well as some local processes at each of the 5 stations. One can see magnetospheric effects from the thick red lines (±5 days running average values of D) in Figs. 5-6 as a modulation in D with the same period close to 27 days. That is a characteristic period of the Sun rotation, and it is clearly seen from the corresponding modulation of the Kp index of geomagnetic activity in Fig. 8. In the horizontal components H and D, this effect is pronounced at all the stations, but in the vertical component Z it is more visible near the projection of characteristic electrojet locations: auroral electrojet − Chokurdakh station, and equatorial electrojet – Guam station. At the stations situated inside the plasmasphere, which are Magadan, Paratunka and Moshiri, the modulation of the 27-days period has practically disappeared in the Z component. So, in order to exclude magnetospheric effects from the horizontal components of the Guam station, all the other stations of 210 MM are appropriate. But to exclude magnetospheric effects from the vertical component of the Guam station, the Chokurdakh station belonging to auroral zone is more recommendable, if there is no other reference station situated near equatorial electrojet projection. As to the preferable local hours for analyzing lithospheric effects, the noon hours (near 4 UT or 14 LT) are

the most suitable, since the influence of geomagnrtic activity on fractal properties of ULF emissions is depressed near the noon hours.

6. CONCLUSIONS

The following conclusions have been drawn from the present analysis.

❑   Our analysis shows that the results of fractal analysis of the data from 210 MM chain of stations may give support to the results of the Guam station data analysis when we attempt to distinguish between magnetospheric and lithospheric effects.

❑   Since magnetospheric effects are of global character, they give the correlated part in the results obtained at all the stations. Lithospheric effects could be of individual and local character at each of the stations. So we have to manage how to remove the correlated part from the raw 210 MM results. Now we are working in this direction.

❑   We understand that our results are of preliminary character, and they need to be checked and confirmed on the other independent materials. Nevertheless, we may conclude that the peculiarities revealed can be used as control factors in the forthcoming investigations of the earthquake precursory signatures based on the analysis of scaling (fractal) characteristics of ULF emissions. In a statistical sense, the dynamics of ULF emissions fractal characteristics at the Guam station is more similar to that obtained at the auroral Chokurdakh station. So this station is more preferable for using it as a reference station to exclude magnetospheric effects while doing seismo-electromagnetic research.

References

Bak, P. (1997), *How Nature Works*, Oxford University Press, Oxford, 210 pp.

Bak, P., C. Tang, and K. Wiesenfeld (1987), Self-organized criticality: An explanation of 1/*f* noise, *Phys. Rev. Lett.* **59**, 4, 381-384, DOI: 10.1103/PhysRevLett. 59.381.

Bak, P., C. Tang, and K. Wiesenfeld (1988), Self-organized criticality, *Phys. Rev. A* **38**, 1, 364-374, DOI: 10.1103/PhysRevA.38.364.

Berry, M.V. (1979), Diffractals, *J. Phys. A* **12**, 6, 781, DOI: 10.1088/0305-4470/12/6/008.

Burlaga, L.F., and L.W. Klein (1986), Fractal structure of the interplanetary magnetic field, *J. Geophys. Res*. **91**, A1, 347-350, DOI: 10.1029/JA091iA01p00347.

Chang, T., S.W.Y. Tam, C.C. Wu, and G. Consolini (2003), Complexity, forced and/or self-organized criticality, and topological phase transitions in space plasmas, *Space Sci. Rev.* **107**, 1-2, 425-445, DOI: 10.1023/A:1025502023494.

Feder, J. (1988), *Fractals*, Plenum Press, New York, 283 pp.

Gotoh, K., M. Hayakawa, N.A. Smirnova, and K. Hattori (2004), Fractal analysis of seismogenic ULF emissions, *Phys. Chem. Earth* **29**, 4-9, 419-424, DOI: 10.1016/j.pce.2003.11.013.

Hayakawa, M. (ed.) (1999), *Atmospheric and Ionospheric Electromagnetic Phenomena Associated with Earthquakes*, *Proc. Int. Workshop on Seismo-Electromagnetics of NASDA (IWSE1997), 2-5 March 1997, Chofu Tokyo*, TERRAPUB, Tokyo.

Hayakawa, M. (ed.) (2005), *Programme and Extended Abstracts of International Workshop on Seismo-Electromagnetics (IWSE2005), 15-17 March 2005, Chofu Tokyo.*

Hayakawa, M., and O.A. Molchanov (eds.) (2002), *Seismo Electromagnetics: Lithosphere-Atmosphere-Ionosphere Coupling*, *Proc. Int. Workshop on Seismo-Electromagnetics of NASDA (IWSO2000), 19-22 September 2000, Chofu Tokyo*, TERRAPUB, Tokyo, 478 pp.

Hayakawa, M., T. Ito, and N. Smirnova (1999), Fractal analysis of ULF geomagnetic data associated with the Guam earthquake on August 8, 1993, *Geophys. Res. Lett.* **26**, 18, 2797-2800, DOI: 10.1029/1999GL005367.

Hayakawa, M., Yu. Kopytenko, N. Smirnova, V. Troyan, and T. Peterson (2000), Monitoring ULF magnetic disturbances and schemes for recognizing earthquake precursors, *Phys. Chem. Earth A* **25**, 3, 263-269, DOI: 10.1016/S1464-1895(00)00042-9.

Hergarten, S. (2002), *Self-Organized Criticality in Earth Systems*, Springer-Verlag, Berlin Heidelberg, 272 pp.

Higuchi, T. (1988), Approach to an irregular time series on the basis of the fractal theory, *Physica D* **31**, 2, 277-283, DOI: 10.1016/0167-2789(88)90081-4.

Higuchi, T. (1990), Relationship between the fractal dimension and the power law index for a time series: A numerical investigation, *Physica D* **46**, 2, 254-264, DOI: 10.1016/0167-2789(90)90039-R.

Ida, Y., and M. Hayakawa (2006), Fractal analysis for the ULF data during the 1993 Guam earthquake to study prefracture criticality, *Nonlin. Processes Geophys*. **13**, 4, 409-412, DOI: 10.5194/npg-13-409-2006.

Jensen, H.J. (1998), *Self-Organized Criticality: Emergent Complex Behavior in Physical and Biological Systems*, Cambridge Lecture Notes in Physics, Vol. 10, Cambridge University Press, Cambridge, 153 pp.

Smirnova, N.A., and M. Hayakawa (2007), Fractal characteristics of the ground-observed ULF emissions in relation to geomagnetic and seismic activities, *J. Atmos. Sol.-Terr. Phys.* **69**, 15, 1833-1841, DOI: 10.1016/j.jastp.2007.08. 001.

Smirnova, N., M. Hayakawa, K. Gotoh, and D. Volobuev (2001), Scaling characteristics of the ULF geomagnetic fields at the Guam seismoactive area and their dynamics in relation to the earthquake, *Nat. Hazards Earth Syst. Sci.* **1**, 3, 119-126, DOI: 10.5194/nhess-1-119-2001.

Smirnova, N., M. Hayakawa, and K. Gotoh (2004), Precursory behavior of fractal characteristics of the ULF electromagnetic fields in seismic active zones before strong earthquakes, *Phys. Chem. Earth* **29**, 4-9, 445-451, DOI: 10.1016/j.pce.2003.11.016.

Sornette, A., and D. Sornette (1989), Self-organized criticality and earthquakes, *Europhys. Lett.* **9**, 3, 197-202, DOI: 10.1209/0295-5075/9/3/002.

Telesca, L., V. Lapenna, F. Vallianatos, J. Makris, and V. Saltas (2004), Multifractal features in short-term time dynamics of ULF geomagnetic field measured in Crete, Greece, *Chaos Soliton. Fract.* **21**, 2, 273-282, DOI: 10.1016/ j.chaos.2003.10.020.

Turcotte, D.L. (1997), *Fractals and Chaos in Geology and Geophysics*, 2nd ed., Cambridge University Press, Cambridge, 398 pp.

Vallianatos, F., and A. Tzanis (1999b), On possible scaling laws between electric earthquake precursors (EEP) and earthquake magnitude, *Geophys. Res. Lett.*, **26**, 13, 2013-2016, DOI: 10.1029/1999GL900406.

Vallianatos, F., V. Lapenna, V. Troyan, N. Smirnova, Yu. Kopytenko, V. Korepanov, and T. Matiashvili (2002), Study of the ULF electromagnetic phenomena related to earthquakes: Strategy of the SUPRE project. **In:** M. Hayakawa and O. Molchanov (eds.), *Seismo Electromagnetics: Lithosphere-Atmosphere-Ionosphere Coupling, Proc. Int. Workshop on Seismo-Electromagnetics of NASDA 2000*, TERRAPUB, Tokyo, 437-442.

Vallianatos, F., J. Makris, V. Saltas, L. Telesca, and V. Lapenna (2004), Monofractal and multifractal analysis in short-term time dynamics of ULF geomagnetic field measured in Crete, Greece, *Bull. Geol. Soc. Greece* **36**, 3, 1298-1307, http://openarchives.gr/visit/105510.

Yumoto, K., Y. Tanaka, T. Oguti, K. Shiokawa, Y. Yoshimura, A. Isono, B.J. Fraser, F.W. Menk, J.W. Lynn, M. Seto, and the 210 MM Magnetic Observation Group (1992), Globally coordinated magnetic observations along 210° magnetic meridian during STEP period: 1. Preliminary results of low-latitude Pc 3's, *J. Geomag. Geoelectr.* **44**, 4, 261-276, DOI: 10.5636/jgg.44. 261.

Evaluation of the Feasibility of Recovering the Magma Chamber's Parameters by 3D Bayesian Statistical Inversion of Synthetic MT Data

Viacheslav V. SPICHAK

Geoelectromagnetic Research Centre IPE RAS, Troitsk, Moscow Region, Russia
e-mail: v.spichak@mail.ru

A b s t r a c t

Feasibility of recovering the magma chamber's parameters by 3D Bayesian statistical inversion of magnetotelluric data is estimated for the simplified conductivity model of the Vesuvios volcano. The results indicate that in the lack of prior information and data, the most efficient approach may consist in successive estimation of the geometry and the depth of the anomaly followed by estimation of the electric conductivity distribution in it. The horizontal boundaries of the target could be outlined by the high gradients of the impedance determinant phase pseudosections determined by the upward analytical continuation of the anomalous electromagnetic fields from the relief surface to the artificial reference plane located above the summit of the volcano. The vertical boundaries and the target extension as well as the electric conductivity could be estimated successively by means of 3D Bayesian statistical inversion of the collected magnetotelluric data carried out in the domain delimited by the estimated horizontal boundaries.

Key words: magma chamber, magnetotelluric, 3D inversion, prior information and data "trade-off".

1. INTRODUCTION

Magnetotelluric (MT) sounding of volcanoes is an important tool for studying their structure, for the spatial mapping, assessment of the depth of the magma chamber, and the determination of its physical properties related to

electric conductivity. The internal structure of volcanoes was studied by MT sounding in Fitterman *et al.* (1988), Jackson and Keller (1972), Mogi and Nakama (1990), Mauriello *et al.* (1997), Di Majo *et al.* (1998), Spichak (1999, 2001, 2007), Manzella *et al.* (2000, 2004), and Spichak *et al.* (2004, 2007). In particular, Newman *et al.* (1985) explored the possibility of detecting the magma chamber depending on the background one-dimensional layering; Moroz *et al.* (1988) evaluated the MT field anomalies caused by the volcano cone, and Park and Torres-Verdin (1988) and Spichak (2001, 2002) developed the approaches to the MT data interpretation in the volcanic environments.

At the same time, efforts to construct two-dimensional (2D) and even three-dimensional (3D) models of volcanoes, which are often based on a limited number of MT sites sparsely distributed on the relief volcanic slopes, often yield inadequate results that nevertheless find a "reasonable" interpretation. In this connection, it seems critically important to estimate the resolving power of MT data with respect to assessment of the magma chamber geometrical parameters as well as the electric conductivity distribution depending on the available prior information.

Despite some progress in a full-range 3D inversion of MT data (see the review paper by Siripunvaraporn (2012) and references therein) the most suitable tool for such a research seems to be the Bayesian statistical inference, also known as the Markov Chain Monte Carlo (MCMC) method (Tarantola and Valette 1982, Tarantola 1987, Backus 1988, Press 1989, Besag *et al.* 1995, *etc.*). This approach not only results in the solution of the inverse problem, but also provides probabilistic posterior uncertainty estimations, which depend on the data and the prior information represented in probabilistic terms. If applied to the study of implications of the prior knowledge or the hypotheses about the magma chamber's parameters, this approach can help to understand the implicit limitations of MT sounding of a local target under the conditions of uncertainty (Spichak *et al.* 1999a, b). The present paper is the first attempt to obtain posterior estimates for the parameters of the magma chamber as functions of the available prior information for a simplified electric conductivity model of the Vesuvius volcano.

2. THE 3D MT IMAGING

As it was shown in Spichak (2002), the efficient way of magnetotelluric data interpretation under conditions of uncertainty about the parameters of the target and the hosting medium consists in successive application of fast imaging and full-range inversion. At the first stage, a preliminary image of the studied area is obtained using pseudo-sections of the electromagnetic fields or their transforms, which provide the best focusing of the target

parameters. At the second stage, a Bayesian statistical inversion is carried out aimed at refinement of the model parameters taking into account the prior information that comes from other methods or prior estimates formulated in probabilistic terms.

2.1 Electric conductivity model and synthetic MT data

A simplified 3D electric conductivity model of the Vesuvius volcano (Fig. 1) was built basing on the findings of Di Maio *et al.* (1998). According to prior information that comes from electromagnetic and other geophysical methods, the Vesuvius magma chamber has a diameter of about 3 km, its upper edge is located approximately at a depth of 5 km (4 km according to De Natale *et al.* (2006)), while its floor does not exceed 9 km; the background, σ_b, and magma chamber, σ_t, electric conductivities could be considered equal to 0.0001 and 0.03 S/m, respectively. The height of the volcanic cone is 1.3 km and the crater has a diameter of 0.2 km.

In order to simplify the numerical modeling and the subsequent inversion of MT data, it was assumed that both the magma chamber and the area where the solution of the inverse problem was searched for are symmetric with respect to two vertical planes crossing the center of the crater (Fig. 1 shows a vertical cross-section along one of the planes). The synthetic MT data for this model were calculated at six periods, $T = 0.01, 0.1, 1.0, 10.0,$
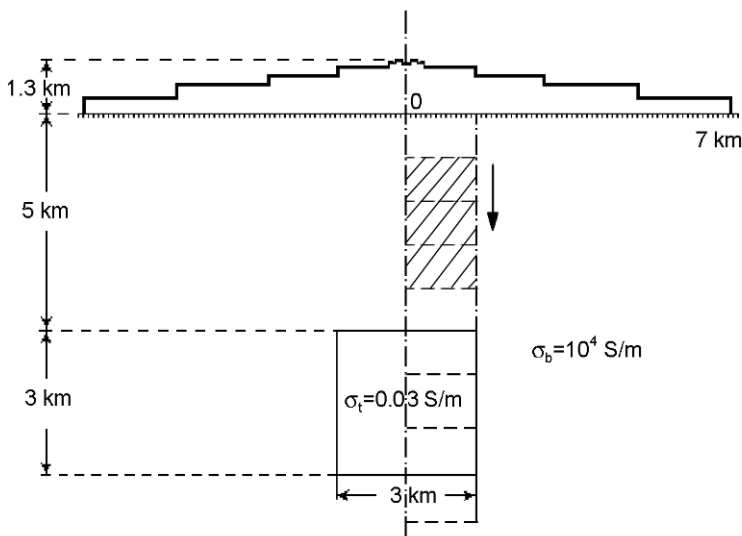

Fig. 1. The 2D cross-section of the simplified electrical conductivity model of the Vesuvius volcano. The dashed line delimits the search area composed of uniform blocks as large as 1.5×1.0 km. The search area "moving" along the vertical axis is hatched.

100.0, and 1000.0 s, using the balance technique (Spichak and Zhdanov 2007). Then, a number of the MT field transformations were calculated and analysed at the earth's surface and at different levels in the atmosphere.

2.2 Imaging volcanic structure

The behavior of the synthetic field components and their transforms, including impedances, apparent resistivities, *etc.*, were analyzed in order to select those which allow the best imaging of the volcanic interior. The results of numerical experiments indicate that, albeit the true conductivity values of the complex volcanic environments are poorly determined, the conductivity gradients could be detected based on the isosurfaces of the real and imaginary parts of the electric field and the impedance phases mapped to the system of coordinates (X, Y, $\text{Log}_{10}T$; here X and Y are the horizontal coordinates); see Spichak 2001.

The technique for 3D imaging of the volcanic interior using the MT data collected at the relief surface was suggested in Spichak (1999, 2001). It is based on the upward analytical continuation of the data to artificial "reference" plane, positioned in the atmosphere above the top level of the relief surface, using integral transformation of the Stratton–Chu type:

$$\mathbf{E}^a(\mathbf{r}) = \iint_S \left\{ \left(\mathbf{n} \times \mathbf{E}^a\right)\nabla G + \left[\mathbf{n} \times \mathbf{E}^a\right] \times \nabla G + \mathrm{i}\omega\mu_0 \left[\mathbf{n} \times \mathbf{H}^a\right] G \right\} \mathrm{d}s',$$

$$\mathbf{H}^a(\mathbf{r}) = \iint_S \left\{ \left(\mathbf{n} \times \mathbf{H}^a\right)\nabla G + \left[\mathbf{n} \times \mathbf{H}^a\right] \times \nabla G \right\} \mathrm{d}s', \tag{1}$$

where $\mathbf{E}^a$ and $\mathbf{H}^a$ are the anomalous electric and magnetic fields, respectively, determined at the reference plane, μ_0 is the magnetic permeability of the vacuum, ω is frequency, $G = 1/(4\pi|\mathbf{r} - \mathbf{r}'|)$ is Green's function of free space, S is the surface of measurements, $\mathbf{r}'$ is the radius-vector of the points belonging to this surface, and $\mathbf{n}$ is a unit vector normal to the surface S and pointing outwards.

The analytical continuation of anomalous MT field from the Earth's surface to the atmosphere could be proved to be unique and the corresponding numerical calculations are straightforward and stable. So, the continued data may be used for the interpretation providing the best focused images of the relief volcanic environment.

Another important item concerns the appropriate height of the reference plane. At lower heights, the pseudo-sections become distorted mostly by the nearest parts of the topography and by the noise (natural and artificial), whereas at greater heights, details of the geoelectric structure may be lost. In each case the choice of the best height for a given structure requires preliminary research. In the present study it was found that the compromise between

increasing the resolution of the subsurface structure and decreasing the distortions caused by the relief surface (in particular, by the crater of the volcano) is supported by placing the artificial plane 100 m above the summit.

Similarly to the MT imaging of the Hawaiian volcano (Spichak 1999, 2001, 2007), it was found that 3D isosurfaces and 2D pseudo-sections of the transforms based on the real and imaginary parts of the electric field and the impedance determinant phase are most suitable for imaging the interior of the Vesuvius volcano's model.
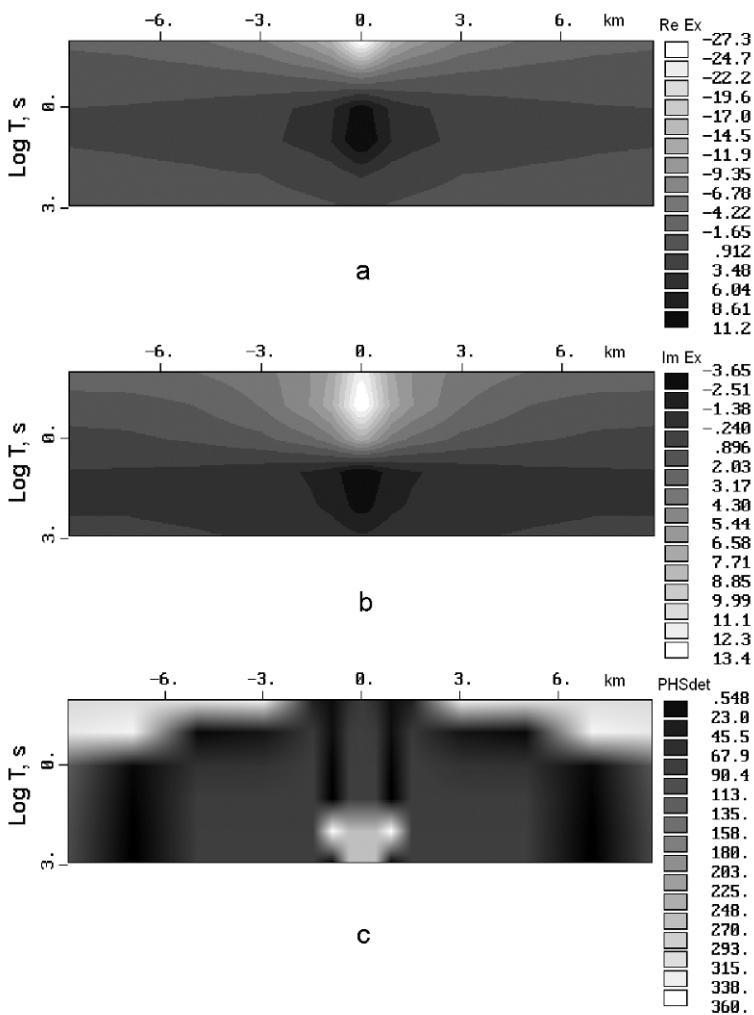
Fig. 2. Electric field and impedance determinant phase pseudo-sections along the central profile: (a) *Re Ex*, (b) Im *Ex*, (c) φ_{det}.
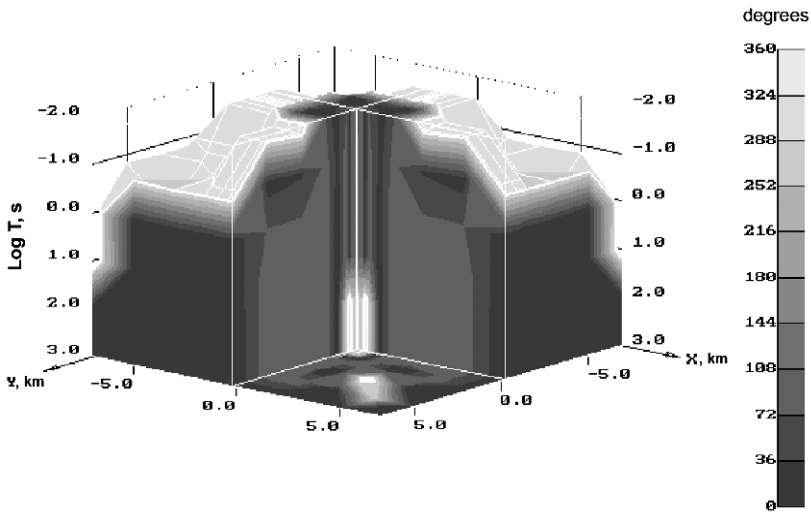
Fig. 3. The 3D volcano image based on the impedance determinant phase.

Both components of the electric field enable estimation of the lateral boundaries of the magma chamber (Fig. 2a, b). However, the best focused image was obtained from the impedance determinant phase (Fig. 2c). It enables 3D imaging of the volcano (Fig. 3) including the relief of its surface and the lateral boundaries of the magma chamber. However, the vertical boundaries of the magma chamber are determined only qualitatively due to absence of appropriate geometrical scale. In order to study the possibility of detection of the remaining geometrical parameters of the magma chamber as well as its electric conductivity, a Bayesian statistical inversion was used.

3. ALGORITHM OF THE BAYESIAN STATISTICAL INVERSION

Despite some progress in deterministic 3D inversion of MT data (see review paper by Siripunvaraporn (2012) and references therein), the inversion of real data evidently requires foregoing study of the items, mentioned above. Bayesian statistical formalism, proposed for the inversion of geophysical data in Tarantola and Valette (1982) and Backus (1988) is a convenient tool for estimating the model parameters and appropriate uncertainties depending on the data and prior information used in the inversion. It is described briefly below following Spichak *et al*. (1999a).

The electric conductivity model can be divided into two kinds of regions: those with known (or fixed) conductivity values and those with unknown values to be determined by inverting the MT measurements at the surface, subject to constrains imposed by prior information. Each of the latter regions can be considered, in turn, as to be composed of homogeneous domains

(cells). Let K be the total number of domains P_k $(k = 1, ..., K)$ in the region(s) of search, whose conductivities $\sigma = (\sigma_k, k = 1, ..., K)$ are to be determined.

Let $y_{i,j}$ be the values of a known function of the electric and magnetic field $h[E(M_i, \omega_j, \sigma), H(M_i, \omega_j, \sigma)]$ measured at given sites M_i $(i = 1, ..., I)$ on the surface for a number of frequencies ω_j $(j = 1, ..., J)$. For each site M_i and each frequency ω_j we can write:

$$y_{ij} = h\big[E(M_i, \omega_j, \sigma), H(M_i, \omega_j, \sigma)\big] + w_{ij} , \tag{2}$$

where $(w_{i,j}; i = 1, ..., I; j = 1, ..., J)$ is a noise function, considered to be a realization of an indenpendent random variable with the probability density function (PDF) $p_{i,j}$ and a zero mean value.

Usually we are searching for the conductivity distribution in the region(s) of interest taking into account the geophysical experience, or by forming some simplifying hypotheses concerning the conductivity distribution in the regions considered (homogeneity, one- or two-dimensionality, thin sheet type, *etc*.). In the context of the Bayesian approach, these prior knowledge and hypotheses are easily incorporated into the process of inversion in terms of a probability law q, named prior PDF, on the set of possible values of the conductivities. To determine the support of q is a primary objective. Numerical computations make it necessary to define the support of q as a finite set. Furthermore, for the sake of simplicity it is supposed that the number of possible conductivities consists of L different values $c_1, ..., c_L$ for each homogeneous domain. The support of q is then the set A of the L^K possible elements (refered to below as images of the conductivity) $a = (a_k; k = 1, ..., K)$, where a_k belongs to $c_1, ..., c_L$. It is evident that the greater the L, the more precise might be the result of the inversion, but the longer the computation. We determine the same set of L possible conductivities (palette) for each domain, but, of course, it is possible to narrow the range of prior conductivities in some domain by making the appropriate prior probabilities equal to zero. If no prior information is available for each homogeneous domain, it is possible to vary the prior palette of conductivities between reasonable minima and maxima with uniform PDF.

From the Bayesian point of view (Press 1989), both observations and the model parameters (conductivities) are considered to be random variables. The aim of the Bayesian analysis is to compute the posterior PDF of the conductivities, *i.e.*, the conditional probabilities of the conductivities given the data and noise level. Standard computation of conditional probabilities results in the posterior law for any image a of conductivities and any data y:

$$P(\sigma = a / Y = y) \; = \; \frac{f(y/a)q(a)}{\sum\limits_{b \in A} f(y/b)q(b)} \; , \tag{3}$$

where $q(a)$ is the prior probability of the image a and $f(y/a)$ is a conditional probability of the variable $(y_{i,j}; \; i = 1, ..., I; \; j = 1, ..., J)$ given the values of the conductivities. It is a function of $a = (a_k; k = 1, \ldots, K)$ through E and H and could be calculated directly using the following formula:

$$f(y/a) \; = \; \prod_{i=1}^{I} \prod_{j=1}^{J} p_{i,j} \left\{ y_{i,j} - h\left[E(M_i, \omega_j, a), H(M_i, \omega_j, a) \right] \right\} \; , \tag{4}$$

where $p_{i,j}$ is the probability density of the noise $w_{i,j}$.

If the probability densities $p_{i,j}$ are Gaussian with zero mean and covariances $(\xi_{i,j})^2$, the above formula can be re-written as

$$f(y/a) \; = \; Z \exp\left(-\sum_{i,j} \frac{\left\{ y_{i,j} - h\left[E(M_i, \omega_j, a), H(M_i, \omega_j, a) \right] \right\}^2}{2(\xi_{i,j})^2} \right) , \tag{5}$$

where Z is a normalizing constant. We will assume in this paper the latter case, but it is important to note that this method could be formulated also without this assumption.

If $A(k, c_l)$ is a set of images that have the conductivity c_l in the domain P_k, the k-th marginal posterior probability po_k is

$$po_k(c_l) \; = \; P\left(\sigma \in A(k,c_l) / Y \right) \; = \; \frac{\sum\limits_{a \in A(k,c_l)} f(y/a)q(a)}{\sum\limits_{b \in A} f(y/b)q(b)} \; . \tag{6}$$

We can take as estimator of the conductivity in the domain P_k either the mean value or the value, corresponding to the maximum probability of the k-th marginal posterior probability. However, in the above formula there is a hidden difficulty: the computation of the denominator requires to calculate $f(y/b)q(b)$ for all possible images b of the conductivity, *i.e.*, L^K times, which is evidently unrealistic.

In order to overcome this difficulty a stochastic algorithm named a „Gibbs sampler" (see the review paper by Besag *et al.* (1995) and references therein) is used, which permits to reduce greatly the computation time. The procedure of the inversion consists of two cycles: in the outer one a regular scanning of all K homogeneous domains in the regions of search is done, whereas in inner one a solution of the forward problem for L prior values of the conductivity is carried out.

Let $(\sigma_k^{(n)}, k = 1,..., K)$ be the conductivities in the homogeneous domains in the regions of search after n iterations of the outer cycle. If the domain $P_{k(n)}$ is scanned at iteration $n + 1 [k(n) = n + 1 (\mathrm{mod}\, K)]$, the image of the conductivities is updated by changing only the conductivity of the domain $P_{k(n)}$, the new value being chosen by a random selection with the following probability:

$$P\left(\sigma_{k(n)}^{(n+1)} = c_l\right) = \frac{f\left\{y / a\left[\sigma^{(n)}, k(n), c_l\right] q\left[a(\sigma^{(n)}, k(n), c_l\right]\right\}}{\sum\limits_{l=1}^{L} f\left\{y / a\left[\sigma^{(n)}, k(n), c_l\right]\right\} q\left\{a\left[\sigma^{(n)}, k(n), c_k\right]\right\}} , \qquad (7)$$

where $a(\sigma, k, c_l)$ denotes the image equal to σ in all domains other than P_k and equal to c_l in the domain P_k. The computation $P(\sigma_{k(n)}^{(n+1)} = c_l)$ requires to calculate $f\{y / a[\sigma^{(n)}, k(n), c_l]\}\, q\{a[\sigma^{(n)}, k(n), c_l]\}$ L times. Thus, the total number of forwad modelings per one iteration of the outer cycle could be reduced from L^K to $L \times K$.

The sequence of images $(\sigma^{(n)}, n \geq 0)$ forms a random process, which is a Markov chain over the finite space of all possible images. The conditional probability, calculated in the k-th domain at the n-th iteration, is

$$po_k^n(c_l) = \frac{f\left[y / a(\sigma^{(k+nK)}, k, c_l)\right] q\left[a(\sigma^{(k+nK)}, k, c_l)\right]}{\sum\limits_{l=1}^{L} f\left[y / a(\sigma^{(k+nK)}, k, c_l)\right] q\left[a(\sigma^{(k+nK)}, k, c_l)\right]} . \qquad (8)$$

It may be shown that the posterior PDF is an invariant for this Markov chain and that for each domain in the region of search the sequence of the mean conditional probabilities converges towards the corresponding marginal probability:

$$po_k(c_l) = \lim_{N \to \infty} \frac{1}{N+1} \sum_{n=0}^{N} po_k^n(c_l) . \qquad (9)$$

This enables estimating the mean posterior conductivities in each homogeneous domain of the region of search:

$$\sigma_k = \sum_{l=1}^{L} c_l\, po_k(c_l), \quad k = 1,..., K . \qquad (10)$$

Thus, the solution of the inverse problem is reduced to the search for the posterior conductivity distribution by means of successive solutions of the forward problem for the prior values of the conductivities preset in the

homogeneous domains. The inversion of synthetic MT data in the following section is carried out using the INVMT3D code tested earlier by Spichak *et al.* (1999a).

4.   ESTIMATION OF THE TARGET DEPTH AND VERTICAL SIZE

In order to analyze the possibility of estimating the location of vertical boundaries of the magma chamber by means of the Bayesian statistical inversion it was supposed that the electric conductivity varies in the vertical direction only and this variation is described by a stepwise function of depth. Each of the nine uniform blocks within the search area has a thickness of 1 km. The ambiguity in the prior knowledge about the electric conductivity of these blocks was ensured by the equal probability (= 0.5) of each block to have either the background conductivity $\sigma_b = 0.0001$ S/m or the target conductivity $\sigma_t = 0.03$ S/m. In other words, the average prior conductivity of each block was equal to 0.015 S/m, and the variance was 0.0149 S/m (or 99.3% of the average value).

In order to decrease the CPU time, the symmetry of both the model and the search area was taken into account, so the latter was restricted by the planes $x = 0$, $x = 1.5$ km, $y = 0$, $y = 1.5$ km, $z = 0$, and $z = 9$ km. In each case, the inversion of synthetic MT data was carried out until the normalized difference of the electric conductivity in all cells of the search area for two successive iterations of the outer loop was reduced to 1%.

Table 1 presents the posterior probabilities and corresponding values of the conductivity and their variance in all blocks of the search area. It is clearly seen from the Table 1 that the ceiling of the anomaly, which is located at a depth of 5 km in the model, is determined rather well: in the five shallowest layers (from the surface to a depth of 5 km), the posterior probabilities of the background conductivity (0.0001 S/m) are much higher than the corresponding values for the target conductivity (0.03 S/m).

The floor of the anomaly, which is located at a depth of 8 km in the model, is also recognized: the posterior probability of the background conductivity in the lowermost layer (0.55) exceeds the corresponding value for the target conductivity (0.45).

Within the anomalous zone ($5 < z < 8$ km), the conductive inclusion is distinctly identified only in the uppermost layer, whereas in the two lower layers the posterior probabilities of the two values of conductivity are practically similar and equal to the corresponding prior ones. In other words, the initial data and the above prior information turned out to be sufficient for the determination of the vertical boundaries and extension of the magma chamber; however, its conductivity distribution could not be estimated simultaneously.

Table 1

Average posterior conductivities of blocks
when the domain of search is larger than the target boundaries

Number of the block	Coordinates in Z axis [km]	p_b	p_t	Average posterior conductivity [S/m]	Posterior variance [S/m]
1	$0 < z < 1.0$	1.00	0.00	1×10^{-4}	0.0
2	$1.0 < z < 2.0$	1.00	0.00	1×10^{-4}	0.0
3	$2.0 < z < 3.0$	1.00	0.00	1×10^{-4}	0.614×10^{-5}
4	$3.0 < z < 4.0$	0.98	0.02	0.76×10^{-3}	0.440×10^{-2}
5	$4.0 < z < 5.0$	0.72	0.28	0.86×10^{-2}	0.135×10^{-1}
6	$5.0 < z < 6.0$	0.33	0.66	0.20×10^{-1}	0.141×10^{-1}
7	$6.0 < z < 7.0$	0.50	0.50	0.15×10^{-1}	0.141×10^{-1}
8	$7.0 < z < 8.0$	0.51	0.49	0.15×10^{-1}	0.149×10^{-1}
9	$8.0 < z < 9.0$	0.55	0.45	0.14×10^{-1}	0.149×10^{-1}

Explanations: p_b and p_t – average posterior probabilities of the background and target conductivities σ_b and σ_t, accordingly.

5. ESTIMATION OF THE TARGET CONDUCTIVITY

5.1 The effect of the guess on the magma chamber conductivity distribution

Let us now assume that the location and the dimensions of the magma chamber are foreknown. Suppose for definiteness that it is *a priori* known that the electric conductivity in the magma chamber can vary within broad limits, from $\sigma_b = 0.0001$ S/m (electric conductivity of the background geological cross-section) to 0.1 S/m, taking any of the logarithmically spaced values 0.0001, 0.0003, 0.001, 0.003, 0.01, 0.03, and 0.1 S/m with equal probabilities ($p_i = 0.1428$; $i = 1, ..., 7$), average prior conductivity of 0.206×10^{-1} S/m, and variance 0.339×10^{-1} S/m. Thus, the search area was defined so as to coincide with the true position of the target and was divided vertically into three uniform blocks, each having a thickness of 1 km.

The distribution of electric conductivity in the search area with *a priori* known horizontal and vertical dimensions of the target was estimated using 3D inversion of synthetic MT data. Table 2 presents the results of the inversion for the three different blocks after 130 iterations. As seen in Table 2, in the central block of the search area, the average posterior conductivity (0.23×10^{-1} S/m) is close to the true value (0.3×10^{-1} S/m), while in the upper block it is twice as high (0.602×10^{-1} S/m) and in the lower block it is three times less (0.967×10^{-2} S/m). Hence, the used data and the prior information turn out to be insufficient for adequate estimation of the electric conductivity in the entire search area.

Average posterior conductivities of blocks
when the domain of search is restricted by the target boundaries

N	p_1	p_2	p_3	p_4	p_5	p_6	p_7	Average posterior conductivity [S/m]	Posterior variance [S/m]
1	0.04	0.05	0.07	0.09	0.09	0.11	0.56	0.60×10^{-1}	0.453×10^{-1}
2	0.10	0.14	0.16	0.15	0.14	0.15	0.17	0.23×10^{-1}	0.358×10^{-1}
3	0.29	0.24	0.17	0.10	0.07	0.05	0.07	0.98×10^{-1}	0.255×10^{-1}

Explanations: N is the number of the block inside the target; $p_1, ..., p_7$ are the average posterior probabilities for the electrical conductivity of a given block to be equal to one of the prior palette.

At the same time, with the additional prior assumption of the uniformity of the search area (in other words, if the magma chamber is supposed to be a single uniform block, which is just the case with the considered model) the posterior conductivity in it coincided with the true values (the average posterior conductivity was equal to 0.3×10^{-1} S/m and the variance was 0.359×10^{-2} S/m).

5.2 The effect of the accuracy of prior guess about the depth of the magma chamber

The influence of the accuracy of the prior information about the anomaly depth on the posterior value of electric conductivity in the search area was estimated. Here, it was assumed that the horizontal boundaries and the vertical extension of the anomaly are known in advance. During the experiments, the vertical boundaries of the search area (hatched area in the Fig. 1) were moved vertically so that its upper edge each time was located at a different depth from the surface.

The results of the experiments are presented in Table 3, and the dependency of the normalized average posterior anomalous conductivity on the prior estimate of its depth is plotted in Fig. 4. As seen from the graph, the stronger the depth of the upper edge of the anomalous domain is underestimated, the lower the posterior values of the conductivity are. In particular, if the guessed depth varies from 0.0 to 2.0 km, the conductivity of the anomalous domain resulted from 3D inversion is less than 10% of its true value.

On the other hand, constraining the prior depth to be greater than a true depth to the ceiling of the anomalous domain even by an amount as small as 1 km (6 km instead of 5 km), results in a doubling of the electric conductivity. Hence, a 20% error in the estimation of the depth of the search area can lead to a 200% error in the determination of electric conductivity in it.

Average posterior conductivity of the blocks
as a function of the guessed depth D to the upper edge of the target

D [km]	p_1	p_2	p_3	p_4	p_5	p_6	p_7	Average posterior conductivity [S/m]	Posterior variance [S/m]
0.	1.000	0.0	0	0	0	0	0	0.100×10^{-3}	0.602×10^{-7}
1.0	0.962	0.038	0	0	0	0	0	0.108×10^{-3}	0.384×10^{-4}
2.0	0.009	0.446	0.544	0.001	0	0	0	0.682×10^{-3}	0.363×10^{-3}
3.0	0	0	0.172	0.647	0.180	0.001	0	0.394×10^{-2}	0.303×10^{-2}
4.0	0	0	0	0.013	0.378	0.609	0	0.221×10^{-1}	0.991×10^{-2}
5.0 (true)	0	0	0	0	0.008	0.990	0.002	0.300×10^{-1}	0.359×10^{-2}
6.0	0.037	0.087	0.051	0.003	0.008	0.201	0.613	0.675×10^{-1}	0.419×10^{-1}

Explanations: $p_1, ..., p_7$ are the average posterior probabilities for the electrical con-
ductivity of a given block to be equal to one of the prior palette.
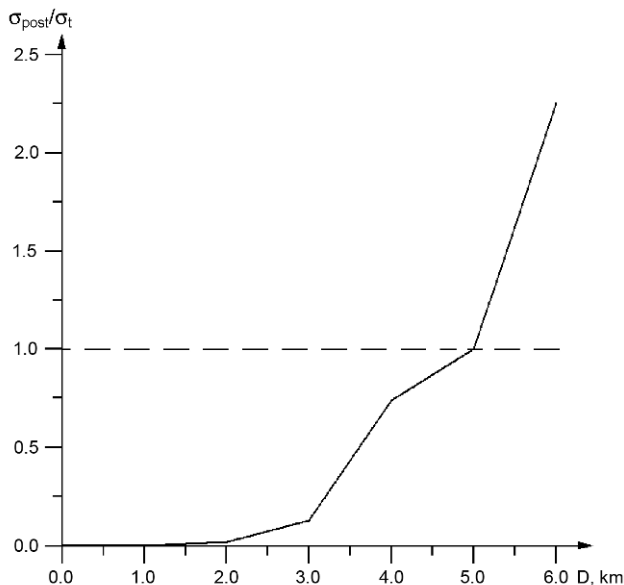

Fig. 4. The normalized average posterior electric conductivity of the target σ_t as
a function of the prior estimation of its depth D.

6.   CONCLUSIONS

In the case both the data and prior information are lacking, the estimation of
the limited number of the target macro-parameters (see *e.g.*, Spichak and
Popova 2000) is often a more efficient way of the inverse problem solution

than regular searching for the conductivity distribution in the lower half-space. In particular, the 3D imaging and inversion of synthetic MT data in a simplified conductivity model of the Vesuvius volcano showed that the simultaneous estimation of the geometry, depth and distribution of electric conductivity within the magma chamber does not lead to reliable assessment of these parameters.

On the other hand, each of these parameters can be quite reliably estimated provided that the others are known *a priori*. So, when searching for a few model parameters based on the inversion of a limited data volume (this concerns both the numbers of MT sites and periods) one could benefit taking into account the "trade-off" between the data and prior information studied in advance for the considered class of models. In particular, the results obtained in this study indicate:

❑   there is an equivalence domain formed by the following relations between the prior estimate of the depth of the anomalous zone and the distribution of the electric conductivity in the search area − the stronger the prior underestimation of the depth, the lower the posterior conductivity within the anomalous zone;

❑   with the additional prior assumption of the uniformity of the search area (in other words, if the magma chamber is supposed to be a single uniform block, which is just the case with the considered model), its posterior conductivity can be recovered precisely.

It is worth noting in this connection that these findings could be also useful for deterministic inversion using the regularization technique, when the regularization factor is adjusted depending of the trade-off chosen. Meanwhile, the interpretation of the real MT data in each case requires foregoing modeling aimed at finding the optimal ratio.

Meanwhile, the above results indicate that in case of insufficient prior information about the sought parameters and the lack of data, the model macro-parameters could be estimated in the mode of "step-by-step" inversions:

❑   the horizontal boundaries of the magma chamber are best outlined by high gradients of the impedance determinant phase and could be estimated from, at least, two orthogonal pseudo-sections determined at the artificial plane located above the summit of the volcano (according to the algorithm proposed by Spichak 2001);

❑   the vertical boundaries and the depth of the magma chamber as well as its electric conductivity could be estimated by means of 3D Bayesian inversion carried out in the domain, delimited by the horizontal boundaries estimated at the first stage.

The above inferences could be useful for assessing the parameters of not only the magma chamber but of any other local target buried in the Earth's crust; however, in order to develop the scientifically substantiated interpretation methodology, farther studies using both synthetic and real MT data are required.

References

Backus, G.E. (1988), Bayesian inference in geomagnetism, *Geophys. J.* **92**, 1, 125-142, DOI: 10.1111/j.1365-246X.1988.tb01127.x.

Besag, J., P. Green, D. Higdon, and K. Mengersen (1995), Bayesian computation and stochastic systems, *Statist. Sci.* **10**, 1, 3-66, DOI: 10.1214/ss/1177010123.

De Natale, G., C. Troise, F. Pingue, G. Mastrolorenzo, and L. Pappalardo (2006), The Somma-Vesuvius volcano (Southern Italy): Structure, dynamics and hazard evaluation, *Earth-Sci. Rev.* **74**, 1-2, 73-111, DOI: 10.1016/j.earscirev.2005.08.001.

Di Maio, R., P. Mauriello, D. Patella, Z. Petrillo, S. Piscitelli, and A. Siniscalchi (1998), Electric and electromagnetic outline of the Mount Somma-Vesuvius structural setting, *J. Volcanol. Geoth. Res.* **82**, 1-4, 219-238, DOI: 10.1016/S0377-0273(97)00066-8.

Fitterman, D.V., W.D. Stanley, and R.J. Bisdorf (1988), Electrical structure of Newberry Volcano, Oregon, *J. Geophys. Res.* **93**, B9, 10119-10134, DOI: 10.1029/JB093iB09p10119.

Jackson, D.B., and G.V. Keller (1972), An electromagnetic sounding survey of the summit of Kilauea Volcano, Hawaii, *J. Geophys. Res.* **77**, 26, 4957-4965, DOI: 10.1029/JB077i026p04957.

Manzella, A., G. Volpi, and A. Zaja (2000), New magnetotelluric soundings in the Mt. Somma-Vesuvius volcanic complex: preliminary results, *Ann. Geofis.* **43**, 2, 259-270.

Manzella, A., G. Volpi, A. Zaja, and M. Meju (2004), Combined TEM-MT investigation of shallow-depth resistivity structure of Mt Somma-Vesuvius, *J. Volcanol. Geoth. Res.* **131**, 1-2, 19-32, DOI: 10.1016/S0377-0273(03)00313-5.

Mauriello, P., D. Patella, Z. Petrillo, and A. Siniscalchi (1997), Mount Etna structural exploration by magnetotellurics, *Acta Volcanol.* **9**, 1/2, 141-146.

Mogi, T., and K. Nakama (1990), Three-dimensional geoelectrical structure of geothermal system in Kuju volcano and its interpretation, *Geoth. Res. Council Trans.* **14**, part II, 1513-1515.

Moroz, Y.F., V.I. Kobzova, I.P. Moroz, and A.F. Senchina (1988), Analogue modeling of MT-fields of volcano, *Vulkanol. Seismol.* **3**, 98-104 (in Russian).

Newman, G.A., P.E. Wannamaker, and G.W. Hohmann (1985), On the detectability of crustal magma chambers using the magnetotelluric method, *Geophysics* **50**, 7, 1136-1143, DOI: 10.1190/1.1441987.

Park, S.K., and C. Torres-Verdin (1988), A systematic approach to the interpretation of magnetotelluric data in volcanic environments with applications to the quest for magma in Long Valley, California, *J. Geophys. Res.* **93**, B11, 13265-13283, DOI: 10.1029/JB093iB11p13265.

Press, S.J. (1989), *Bayesian Statistics: Principles, Models and Applications*, John Wiley and Sons, New York.

Siripunvaraporn, W. (2012), Three-dimensional magnetotelluric inversion: An introductory guide for developers and users, *Surv. Geophys.* **33**, 1, 5-27, DOI: 10.1007/s10712-011-9122-6.

Spichak, V.V. (1999), Imaging of volcanic interior using MT data. **In:** M. Oristaglio and B. Spies (eds.), *3D Electromagnetics*, Geophys. Devel. Ser. 7, Soc. Explor. Geophys. Publ., Tulsa, 418-425.

Spichak, V.V. (2001), Three-dimensional interpretation of MT data in volcanic environments (computer simulation), *Ann. Geofis.* **44**, 2, 273-286.

Spichak, V.V. (2002), Advanced three-dimensional interpretation technologies applied to the MT data in the Minamikayabe thermal area (Hokkaido, Japan), **In:** *Proc. EAGE 64th Conference and Exhibition, 27-30 May 2002, Florence, Italy*, 243-246.

Spichak, V.V. (2007), Modeling of magnetotelluric fields in 3-D media. **In:** V.V. Spichak (ed.), *Electromagnetic Sounding of the Earth's Interior*, Elsevier, Amsterdam, 313-350, DOI: 10.1016/S0076-6895(06)40012-3.

Spichak, V.V., and I. Popova (2000), Artificial neural network inversion of magnetotelluric data in terms of three-dimensional earth macroparameters, *Geophys. J. Int.* **142**, 1, 15-26, DOI: 10.1046/j.1365-246x.2000.00065.x.

Spichak, V.V., and M.S. Zhdanov (2007), 3-D EM forward modeling using balance technique. **In:** V.V. Spichak (ed.), *Electromagnetic Sounding of the Earth's Interior*, Elsevier, Amsterdam, 105-142, DOI: 10.1016/S0076-6895(06)40005-6.

Spichak, V.V., M. Menvielle, and M. Roussignol (1999a), Three-dimensional inversion of MT fields using Bayesian statistics. **In:** M. Oristaglio and B. Spies (eds.), *3D Electromagnetics*, Geophys. Devel. Ser. 7, Soc. Explor. Geophys. Publ., Tulsa, 406-417.

Spichak, V.V., M. Menvielle, and M. Roussignol (1999b), Estimation of the effects of quality and volume of a priori information and data on 3-D inversion of magnetotelluric fields, *Izv. – Phys. Solid Earth* **35**, 4, 260-270.

Spichak, V.V., Y. Yamaya, and T. Mogi (2004), ANN modeling of 3D conductivity structure of the Komagatake volcano (Hokkaido, Japan) by MT data. **In:** *Proc. IV Int. Symp. MEEMSV 2004, La Londe Les Maures, France*, 121-122.

Spichak, V.V., V.P. Borisova, E.B. Fainberg, A.A. Khalezov, and A.G. Goidina (2007), Electromagnetic 3D tomography of the Elbrus volcanic center according to magnetotelluric and satellite data, *J. Volcanol. Seismol.* **1**, 1, 53-66, DOI: 10.1134/S0742046307010046.

Tarantola, A. (1987), *Inverse Problem Theory*, Elsevier, New York, 613 pp.

Tarantola, A., and B. Valette (1982), Inverse problems = quest for information, *J. Geophys*. **50**, 159-170.

Optimizing Statistical Classification Accuracy of Satellite Remotely Sensed Imagery for Supporting Fast Flood Hydrological Analysis

Dimitrios D. ALEXAKIS[1], Athos AGAPIOU[1],
Diofantos G. HADJIMITSIS[1], and Adrianos RETALIS[2]

[1]Department of Civil Engineering and Geomatics, Remote Sensing Lab.,
Faculty of Engineering and Technology, Cyprus University of Technology,
Limassol, Cyprus; e-mails: dimitrios.alexakis@cut.ac.cy (corresponding author),
athos.agapiou@cut.ac.cy, d.hadjimitsis@cut.ac.cy

[2]National Observatory of Athens, Institute for Environmental Research
and Sustainable Development, Athens, Greece; e-mail: adrianr@meteo.noa.gr

A b s t r a c t

The aim of this study is to improve classification results of multi-spectral satellite imagery for supporting flood risk assessment analysis in a catchment area in Cyprus. For this purpose, precipitation and ground spectroradiometric data have been collected and analyzed with innovative statistical analysis methods. Samples of regolith and construction material were *in situ* collected and examined in the spectroscopy laboratory for their spectral response under consecutive different conditions of humidity. Moreover, reflectance values were extracted from the same targets using Landsat TM/ETM+ images, for drought and humid time periods, using archived meteorological data. The comparison of the results showed that spectral responses for all the specimens were less correlated in cases of substantial humidity, both in laboratory and satellite images. These results were validated with the application of different classification algorithms (ISODATA, maximum likelihood, object based, maximum entropy) to satellite images acquired during time period when precipitation phenomena had been recorded.

Key words: classification, statistics, spectroradiometer, remote sensing, floods.

1. INTRODUCTION

One of the important tools for detection and quantification of land-cover changes across catchment areas is the classification of multispectral satellite imagery. Such results are very important for hydrological analysis and flood scenarios. Flash floods represent one of the most destructive natural hazards that exist in the Mediterranean region (Moussa and Bocquillon 2009, Hadjimitsis 2007). Indeed, flooding is characterized as one of the most common natural disasters leading to life and economic losses. Ecosystems and floods are closely related and any changes in the ecosystems, such as urbanization across the catchment's area, may trigger off a sequence of flood occurrence causes (Hadjimitsis 2010). Land cover changes may be used to describe dynamics of urban settlements and vegetation patterns as an important indicator of urban ecological environments (Du *et al.* 2010). Indeed, during the last years remotely-sensed data (*i.e.*, satellite or aerial imagery) have been widely used in order to define land use and land use changes such as urban growth (Brown *et al.* 2000, Weng 2002, Karl and Maurer 2010).

In such studies, classification is a common procedure in order to retrieve valuable information regarding land use from multispectral images data. Several techniques have been reported to improve classification results in terms of land use discrimination and accuracy of resulting classes (Eiumnoh and Shrestha 2000). However, the multispectral images acquired from different satellite sensors suffer from serious problems and errors, such as radiometric distortions, areas with low illumination, physical changes of the environment, *etc*. Radiation from the Earth's surface undergoes significant interaction with the atmosphere before it reaches the satellite sensor. The correction of deficiencies and the removal of flaws present in the raw data are defined as pre-processing and are carried out prior to any use of the data. Pre-processing refers to those operations that are preliminary to the main analysis. In the context of digital analysis of remotely sensed data, pre-processing is generally characterized by two types of data correction: (1) radiometric pre-processing which addresses conversion of digital numbers to radiance at the sensor, and (2) geometric correction which addresses errors in the relative positions of pixels, mainly due to the sensor viewing geometry and terrain variations. Radiometric corrections are distinguished between calibrations, de-striping approaches, atmospheric corrections and removal of data errors or flaws (Hadjimitsis and Clayton 2007). Solar radiation must travel through the Earth's atmosphere before it reaches the Earth. As the electromagnetic radiation is reflected by the Earth, it passes again through the atmosphere before it is detected by the satellite sensor. This propagation of electromagnetic radiation through the atmosphere is affected by two essential processes: scattering and absorption. Indeed, the use of radiative

transfer equation is essential for quantifying the atmospheric effects to the satellite signal.

Moreover, in many occasions the imagery spatial resolution is not high enough. These limitations make the analysis of remote sensing images more complex and difficult (Shankar *et al.* 2011). For several authors (Congalton 1991, Congalton and Green 1999) the quality of Land Use/Land Cover (LULC) maps is determined mainly either by the accuracy of the classification approach or from the definition of training samples, since an incorrect definition of training areas may downgrade classification results (Foody 2002).

However, during the last years many studies have proved that the accuracy of classification of remote sensing imagery does not increase by improving the applied algorithms. This is due to the fact that classification is mainly dependent on the physical and chemical parameters of the ground objects (Zhang and Zhu 2011) although in many cases the performance of each algorithm strongly depends on the background approach. Thus, exploration of new statistical methods is essential, for example by developing image-understanding techniques characterized by diagnostic expert systems (Gamanya *et al.* 2007) or with fusion of spectral information with spatial and temporal contextual information (Melgani and Serpico 2002). In order to understand the processes involved, multi-temporal and multi-scale aspects of their dynamics, arising from both natural and human induced factors, have to be further explored. The temporal dynamics of both precipitation and surface characteristics, which also vary spatially, have significant influences on soil spectral response (*e.g.*, surface runoff, crusting, and evapotranspiration). Therefore, studies testing the potential of satellite remote sensing techniques to handle such kind of issues could be of outmost importance to fill the current knowledge (Liberti *et al.* 2009).

Serious problems in the effective discrimination between certain geologic formations and urban areas might be occurred due to the influence of different topsoil characteristics on surface colors (texture, soil moisture, *etc.*) (Liberti *et al*. 2009). Such problems were recorded for freely available Landsat TM/ETM+ (USGS database) within the area of Yialias watershed basin in Cyprus, related to the high correlation of the spectral signatures between the marl/chalk outcrops and the urban fabric. As a result, the spectral behavior of natural soils and regolith remains a major constraint which strongly affects the performance and the accuracy of different satellite classification algorithms. This fact offered a motivation for researchers to integrate the spatial and spectral patterns in order to modify the accuracy and the reliability of the classification in a process similar to the human brain (Blumberg and Zhu 2007). In addition, conventional pixel based classifiers, such as maximum likelihood, minimum distance and ISODATA (Iterative Self

Organizing Data Analysis Technique) solve the specific problem by merging images from different sources. This process results in the serious "Pepper-salt" effect in the final classification product which can be outreached with the use of object-based algorithm. In object-based classification the already segmented image is used in conjunction with the spectral, context and texture information in order to produce the final LULC map. Principally, segmentation is the process of grouping image elements according to homogeneity (De Kok *et al.* 2000). In this way the landscape is composed of multiple irregular shape objects that are larger than individual pixels and are homogeneous. Segment-based classification approaches are often rule-based or knowledge-based methods relying on classification rules developed by the experts (Matikainen and Karila 2011).

In addition, in various remote sensing applications there is a need for a classification of one specific land type without considering the other classes. Such problems are also quite common in analytical biology, evolution epidemiology and ecological niche modeling. Thus, Philips *et al.* (2004) proposed the application of maximum entropy algorithm/technique in order to model species geographic distribution based only on real training data (Philips *et al.* 2006, Peterson and Shaw 2003). However, this approach can also contribute to one-class satellite remote sensing classification process, as previous studies have proved (Li and Guo 2010).

This paper describes the results obtained by integrating remote sensing techniques such as classification analysis, and contemporary statistical analysis like maximum entropy for detecting urbanization activities in a catchment area in Cyprus. The final results will be incorporated in an integrated flood risk management model. This study aims to test different material samples in the Yialias region in order to: (a) examine their spectral behavior under different precipitation rates, and (b) introduce an alternative methodology to optimize the classification results derived from single satellite
imagery with the combined use of satellite, spectroradiometric and precipitation data. At the end, different classification algorithms and statistical analysis are used to verify and optimize the final results. Thus, object-based classification and maximum entropy algorithms are simultaneously used; however, the main aim of the study is the verification of the hypothesis that the multispectral classification accuracy is improved if the land surface humidity is high. This hypothesis was tested against Landsat derived reflectance values and validated with *in situ* reflectance observations with the use of high spectral resolution spectroradiometers. In this way this study aspires to highlight the potential of medium resolution satellite images such as those of Landsat TM/ETM+ for LULC studies under certain circumstances in the broader Eastern Mediterranean region.

2. STUDY AREA AND DATA

2.1 Study area

Located in the central part of the island of Cyprus, the Yialias basin extends to an area of 110 km^2 (Fig. 1). Specifically, the basin is situated between longitudes 33°11′24.28″ and 33°26′31.52″ and latitudes 34°54′36.74″ and
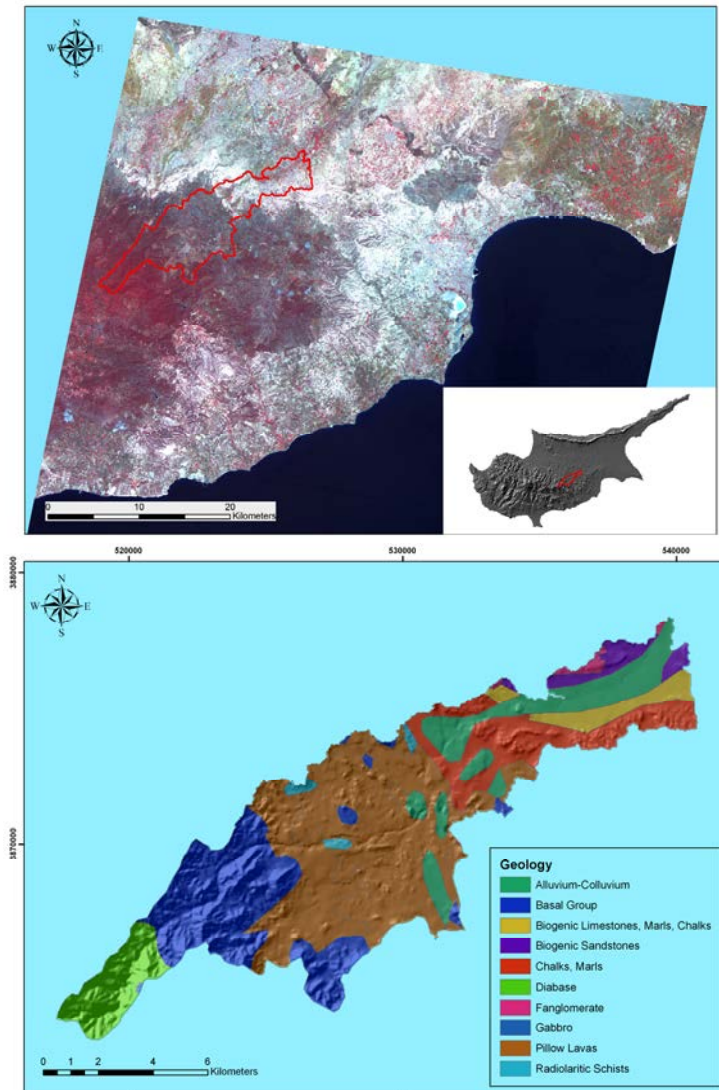

Fig. 1. The study area (top). Geological map of the study area (bottom). Colour version of this figure is available in electronic edition only.

35°2′52.16″. The island of Cyprus is located in the northeasternmost corner of the Mediterranean Sea and, therefore, has a typical Eastern Mediterranean climate: the combined temperature-rainfall regime is characterized by cool-to-mild wet winters and warm-to-hot dry summers (Michaelides *et al.* 2009). Concerning the geological regime of the area following the general cessation of volcanic activity, is one of chalk and marl sedimentation accompanied by advance and retreat of the sea. The marl-chalk sequence in the area is mainly of white colour which means that it contains >98% calcium carbonate. However, more greyish chalk formations are also present in the area due to increased marl composition. Figure 1 shows the generalised geological map of the watershed basin where the chalk/marl formation covers the 10% of the study area (12 km^2). This essentially calcareous sedimentation continued from the Upper Cretaceous to the Pliocene.

The Yialas basin is characterized as a high-risk area since many fast floods have occurred in the last years with extreme destructive results. Local authorities with the assistance of research institutions are involved in the SatFlood project (funded from the Cyprus Research Promotion Foundation) in order to detect land use changes in the last decades and to perform extensive hydraulic and hydrological analysis for this basin. The results will provide invaluable information to the authorities concerning catchment's flood vulnerability in order to take all the necessary actions for minimizing destructive effects from natural disaster phenomena such as floods in the near future.

2.2 Ground samples

According to some preliminary classification results (Alexakis *et al.* 2011), spectral mixing between urban areas and specific geological formations were observed (Fig. 2). Thus, samples of regolith and construction material were collected and tested for their spectral response under different conditions of humidity with the use of spectroradiometer in the premises of the Remote Sensing and Geomatics Laboratory of Cyprus University of Technology.

In most cases, chalk is characterized as pure (>95% carbonate), highly porous (>40%), and low permeable (Hjuler and Fabricius 2009). Chalk is considered to be a special type of granular material because the structure reflects its organic origin (Risnes *et al.* 2005). Concerning their composition, chalks are mainly built up of whole and fragmentary parts of calcite skeletons produced by planktonik algae, known as coccolithophorids (Risnes *et al.* 2003). A characteristic of outcrop chalk is that its strength depends strongly on the type of fluid in the pores. It is a general observation that water-saturated chalk is mechanically weaker than the dry chalk. This phenomenon is referred to as the water-weakening effect (Risnes *et al.* 2005).
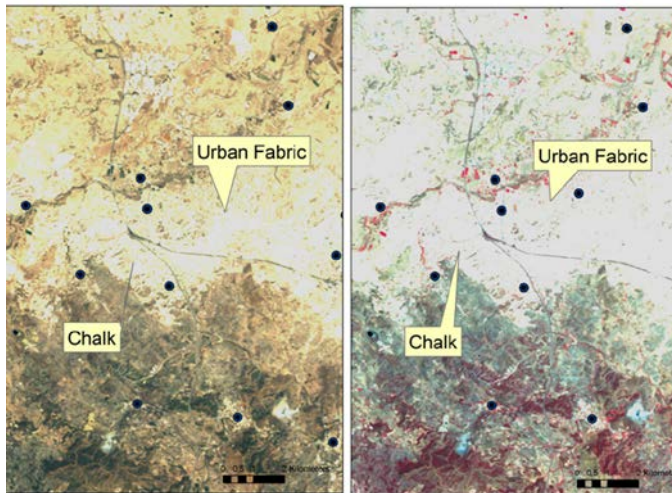
Fig. 2. The RGB (left) and NIR-R-G (right) composites of the Landsat image at the area of interest (Yialas basin). Arrows indicate the spectral similarity of urban fabric areas and specific formations (chalk) at satellite images where no precipitation has been observed. Colour version of this figure is available in electronic edition only.

In order to avoid confusion with "soil", the term "regolith" was used to define unconsolidated marl-chalk surface material resting above consolidated bedrock (Shafique *et al.* 2011). According to Eggleton (2011), as regolith can be defined the entire unconsolidated or secondarily recemented cover that overlies coherent bedrock, that has been formed by weathering, erosion, transport, and/or deposition of older material.

2.3 Satellite and precipitation data

Further on, to the regolith samples multiple Landsat TM/ETM+ images were used, covering the same area, acquired either during humid or drought period and analyzed in order to be compared with the laboratory results. For the purpose of the study the following tools and data were incorporated:

❑ Four Landsat TM/ETM+ multispectral images of medium resolution (30×30 m^2 pixel size). These data were acquired for free from GLOVIS website (Global Visualisation Viewer, URL: http://glovis.usgs.gov/) and cover the time period 2000-2009 (Fig. 2).

❑ Precipitation data obtained from the Meteorological Service of Cyprus (Pera-Chorio Meteorological Station). All these data were compared with the satellite imagery data. The selected downloaded images were acquired a day after the record of substantial scaling amount of precipitation from the Pera-Chorio Metereological Station, as indicated in Table 1.

❑ Data derived from spectroradiometric field campaigns. For this reason, the GER 1500 spectroradiometer was used. This instrument can record electromagnetic radiation from 350 up to 1050 nm. It includes 512 different channels and each channel covers a range of about 1.5 nm. The field of view (FOV) of the instrument was set to 4°. The accuracy provided from the manufacturer of radiometric measurements was: 400 nm ± 5%, 700 nm ± 4%, and 1000 nm ± 5%.

Table 1

Acquisition dates of satellite images and corresponding precipitation statistics

No.	Date of acquisition	Precipitation [mm]	Precipitation [mm] 1 day before	Precipitation [mm] 2 days before
1	2 June 2005	27.3	0	0
2	19 May 2000	8.6	0	0
3	16 October 2002	3	1.2	4
4	23 July 2009	0	0	0

3. MEASUREMENTS

3.1 Laboratory spectroradiometric lab measurements

For the purpose of this study, five different targets from the Yialias watershed basin were selected and their corresponding samples were collected. These were three samples (by the name A, B, and C with different percentage of chalk content, collected from three different places of the catchment area) of marl-chalk outcrops from three different areas within the watershed (the B sample was a little more whitish than the others), a sample of tile, and a sample of construction material (roof house). The first three samples represent regolith and the other two urban fabric materials. However, all these five samples have low hydro-permeability and different levels of porosity. During the field campaign for the collection of the samples (Fig. 3 left), the areas of *in situ* collection were recorded with Global Positioning System (GPS) and their correspondent coordinates were overlaid as digital point layer on georeferenced Landsat TM/ETM+ images in a GIS environment. At the next stage, all the samples were used in order to extract their spectral signatures in the premises of the Laboratory of Remote Sensing and Geomatics of Cyprus University of Technology (CUT) (Fig. 3 right).

For that purpose, ten measurements were carried out consecutively for each sample and a final mean measurement, corresponding to Landsat TM/ETM+ bands, was extracted from each of them. In detail, the hyperspectral − narrow bands − signatures acquired using the spectroradiometer were recalculated as broadbands of the selected multispectral

Fig. 3. Collection of soil data (left). Spectroradiometric measurements of samples at the premises of the Remote Sensing and Geomatics Laboratory of CUT (right). Colour version of this figure is available in electronic edition only.

satellite (Landsat TM/ETM+). The relative spectral response (RSR) filters of the Landsat sensor were used for this purpose. The RSR filters describe the relative sensitivity of the satellite sensor to radiance at various parts of the electromagnetic spectrum (Wu *et al.* 2010). The RSR values range from 0 to 1 and have no units since they are relative to the peak response (Fig. 4). Therefore, the broadband reflectance from the spectroradiometer was calculated based on the wavelength of the Landsat sensor and the RSR filter, as described by the equation:

$$R_{\text{band}} = \frac{\sum (R_i \times \text{RSR}_i)}{\sum \text{RSR}_i} \, , \tag{1}$$

where R_{band} is the reflectance at a range of wavelength (*e.g.*, Band 1), R_i the reflectance at a specific wavelength (*e.g.*, $i = 450$ nm), and RSR_i is the relative response value at the specific wavelength.

Moreover, in order to search for the different spectral response of each sample under different moisture conditions, all samples were sank with water in a step-by-step process and measured for the rate of their humidity with the use of a soil moisture meter. The specific hand-held instrument used in this study could measure moisture values from 0 to 50% within an accuracy of 0.1%. The probe of the instrument was inserted into the soil sample and the moisture value was recorded. The regolith samples under investigation were divided in four different categories according to their level of humidity: 0% (dry sample), 25, 50, and >50%. Concerning tile and roof specimens, the results were divided to "dry" or "humid" categories due to the difficulty with measuring the scaling levels of humidity in those kinds of
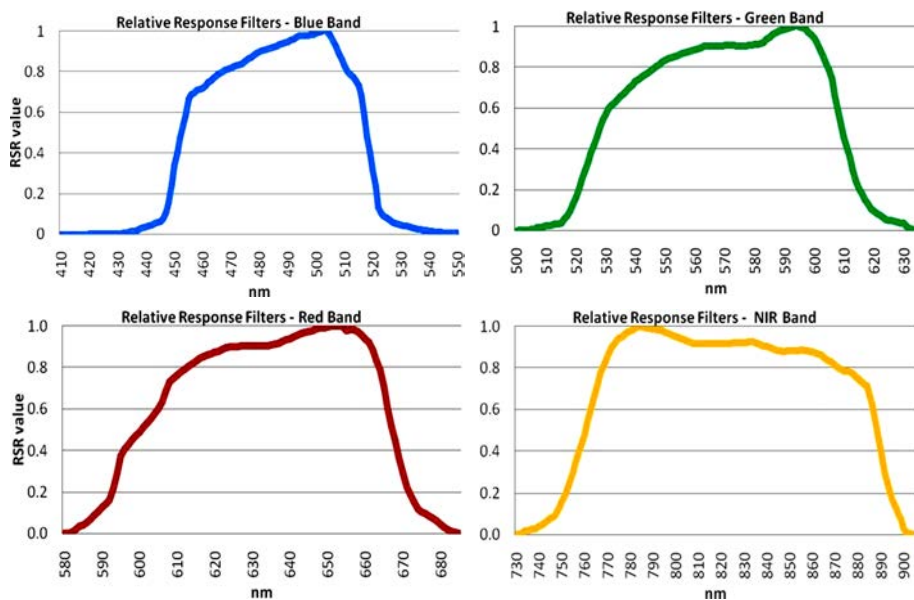
Fig. 4. The RSR filters for Bands 1-4 (B-G-R-NIR). Data provided from the Committee on Earth Observation Satellite (CEOS, http://calvalportal.ceos.org/). Colour version of this figure is available in electronic edition only.
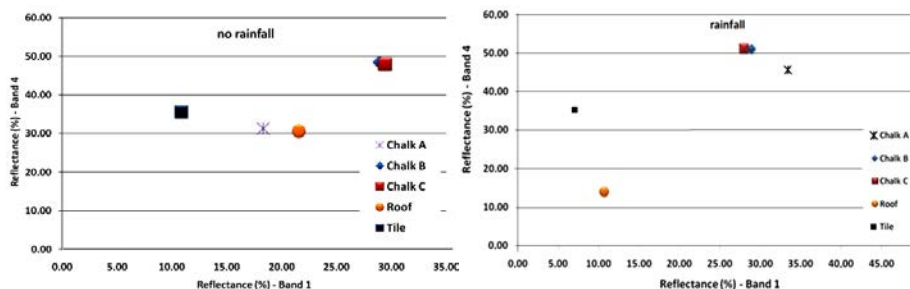
Fig. 5. Scatter-plots of the different targets examined in this study for Bands 1-4 (left) and Bands 3-4 of Landsat (right).

materials. Figure 5 indicates the correlation between Bands 1 and 4 for all the samples and for different levels of humidity.

Based on the results of the scatter-plots it was proved that in the case of dry samples there is a strong spectral confusion between the chalk A response and the urban fabric (roof and tile) materials. The "moisture" scatter plot (humidity >50%) highlights the different spectral response between artificial materials (roof and tile) and natural materials (chalks A, B, and C).

In this plot, the spectral difference between different samples is increased and two major clusters are created. This was accomplished due to the increase of chalk A spectral response and the substantial decrease of tile and house roof (constructed by clay and cement consecutively) spectral response. Figure 6 indicates in diagram forms the spectral response of the three chalk samples. As it was proved concerning the chalk sample A, its reflectance was increased as the humidity level arose. However, concerning the other two chalk samples, their spectral response remained generally steady.

Euclidean distances play a central role in a multivariate statistical analyses for continuous data as principal component analyses, discriminant analyses or multidimensional scaling (McLachlan 1992, Mortier *et al.* 2006). Thus, the Euclidean distance between the measurements acquired from all the different targets in the spectral range of the first four spectral bands of Landsat TM/ETM+ VNIR was calculated and presented in Table 2.

The results highlighted once again the different spectral response of materials under different humidity levels. Specifically, reflectance values of the

Fig. 6: (a, b, c) Diagrams of the spectral response of chalk samples (A, B, and C) for different bands (1, 2, 3, and 4) and different levels of humidity (0, 25, 50, and >50%); (d) Spectral signatures profile from spectroradiometer laboratory with 50% humidity. Colour version of this figure is available in electronic edition only.
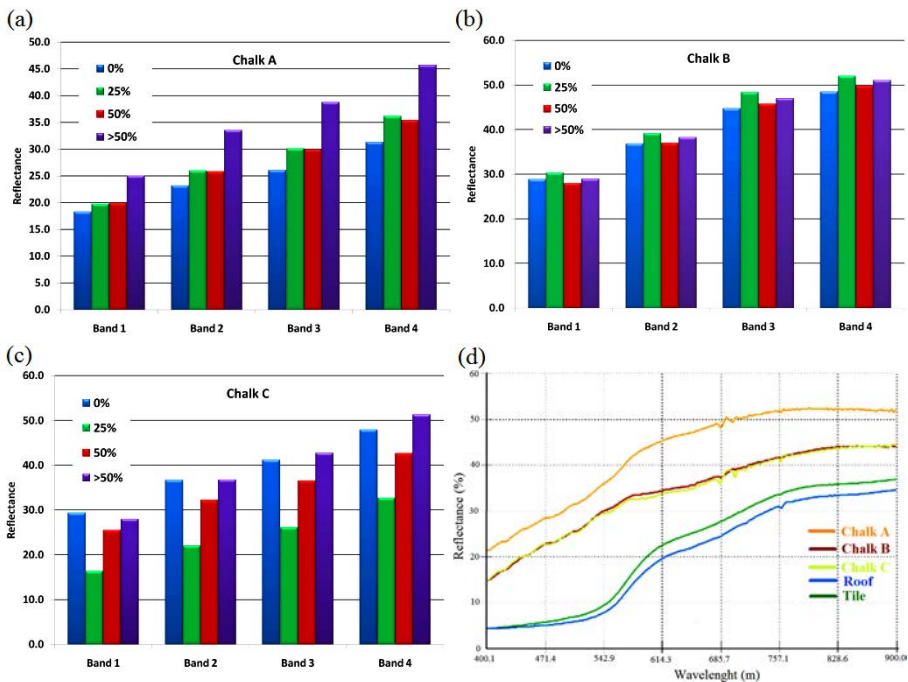
Table 2

Euclidean distance measurements for different targets (VNIR)

Band 1

	Chalk A	Chalk B	Chalk C	Roof	Tile		Chalk A	Chalk B	Chalk C	Roof	Tile
			0% Humidity						25% Humidity		
Chalk A		30.1	29.6	3.2	7.5	Chalk A		15.8	3.5	25.5	29
Chalk B			0.6	26.9	37.6	Chalk B			19.3	41.3	44.9
Chalk C				26.4	37.1	Chalk C				22.0	25.5
Roof					10.7	Roof					3.6
Tile						Tile					

Band 2

	Chalk A	Chalk B	Chalk C	Roof	Tile		Chalk A	Chalk B	Chalk C	Roof	Tile
Chalk A		18.7	15.1	3.4	0.4	Chalk A		13.2	3.9	13.3	12.2
Chalk B			3.6	15.3	18.3	Chalk B			17.1	26.5	25.4
Chalk C				11.7	14.7	Chalk C				9.4	8.3
Roof					3.0	Roof					1.1
Tile						Tile					

Band 3

	Chalk A	Chalk B	Chalk C	Roof	Tile		Chalk A	Chalk B	Chalk C	Roof	Tile
Chalk A		18.7	15.1	3.4	0.4	Chalk A		18.2	3.9	16.6	4.3
Chalk B			3.6	15.3	18.3	Chalk B			22.2	34.8	22.6
Chalk C				11.7	14.7	Chalk C				12.6	0.4
Roof					3.0	Roof					12.2
Tile						Tile					

Band 4

	Chalk A	Chalk B	Chalk C	Roof	Tile		Chalk A	Chalk B	Chalk C	Roof	Tile
Chalk A		17.2	16.6	0.7	4.3	Chalk A		15.8	3.5	22.1	0.7
Chalk B			0.6	17.9	12.9	Chalk B			19.3	37.9	16.6
Chalk C				17.3	12.3	Chalk C				18.6	2.8
Roof					5.0	Roof					21.4
Tile						Tile					

chalk samples (A and C) tend to be separated from those of urban samples (tile and roof) as humidity increases. This is obvious for all spectral bands with some minor exceptions (*e.g*., distance between chalk C and tile in Bands 3 and 4). The general view from Table 3 is that the spectral separability between the chalk samples and urban samples increases with growing humidity, and therefore classification techniques should have better results in images acquired after rainfall phenomena.

3.2 Satellite imagery data

3.2.1 *Application of pre-processing techniques*

Based on the laboratory experiments, the authors investigated the potential of optimizing classification of satellite images. Multispectral satellite imagery such as Landsat TM/ETM+ is considered to be a precious source of

multi-temporal data for diachronic analysis of different surface processes, such as landform changes and land degradation mechanisms at regional scale (Takagi *et al.* 2007). For the purposes of the study, four Landsat TM/ETM+ satellite images were acquired and analysed. As it was mentioned in Section 2.3, there was an assessment of the correlation between the acquisition dates of the satellite images with the precipitation data obtained from the Meteorological Service of Cyprus so as to ensure the strong correlation of imagery acquisition dates with specific dates when higher or lower precipitation phenomena had been recorded in the area.

Initially, the geometric corrections concerning satellite imagery were carried out using standard techniques with ground control points and a second order polynomial fit. For this purpose, topographical maps were used to track the position of ground control points in conjunction with the digital shoreline of Cyprus extracted from a detailed 25 m pixel size Digital elevation model (DEM). At a next step, the authors proceeded to the conversion of DN values to radiance and finally to reflectance values. The DN values of Landsat image were converted to radiance through the equation:

$$L_{rad} = DN \times G_{rescale} + B_{rescale}, \tag{2}$$

where $G_{rescale}$ and $B_{rescale}$ are band specific rescaling factors.

Moreover, for the images of both sensors, the at-satellite radiance values were converted to at-satellite reflectance values by using the general equation:

$$P_\lambda = \left(\frac{\pi L_\lambda d^2}{ESUN_\lambda \cos\theta_s} \right), \tag{3}$$

where P_λ is the unitless planetary reflectance, L_λ the spectral radiance at the sensor's aperture, d^2 the earth-sun distance in astronomical units, $ESUN_\lambda$ the mean solar exoatmospheric irradiances, and θ_s is the solar zenith angle in degrees. At the end, the darkest pixel atmospheric correction method was applied to every satellite image (Hadjimitsis *et al.* 2004a, b; Agapiou *et al.* 2011). For the application of the darkest pixel atmospheric correction, the following assumptions are taken: the atmospheric transmittance is ignored between the ground and the sensor, and the atmospheric transmittance is ignored between the top of the atmosphere and the ground. Indeed, the atmospheric transmittance is assumed to be 1. Such an assumption can be done in the visible bands, however in the near-infrared the effects of the water vapour is an important factor that must be considered and determined since any omission of water vapour thickness can lead to not-effective removal of atmospheric effects in the NIR region (Hadjimitsis *et al.* 2004a, b). The authors used the method developed by Hadjimitsis and Clayton (2008)

in which the relative humidity (RH) % values have been acquired from the nearby meteorological stations and the water vapour thickness was determined using the graphical charts provided by Forster (1984). It has been found that the water vapour thickness values were very small, without any important effect.

3.2.2 Analysis of satellite images

After the application of all the necessary pre-processing steps, spectral signature profiles were extracted for all the different materials during different acquisition dates of satellite images. Figure 7 shows the interrelation between Bands 1 and 4 for the different targets.

The results of the scatter plots indicated the scaling optimization of spectral separability of satellite imagery data from 0 to 23.7 mm of precipitation. Specifically, concerning 0 mm precipitation case, a spectral confusion was indicated between the "urban" targets (roof and tile) and chalk A and C targets. This conflict was outreached gradually as the precipitation level increased. The samples started to have different spectral behaviour, with the chalk samples (except chalk B) standing gradually away from the "urban" samples cluster in the scatter-plot. The same conclusions were derived from Table 3 where the Euclidean distance between all the bands of Landsat for all the different targets was calculated. A characteristic example is the
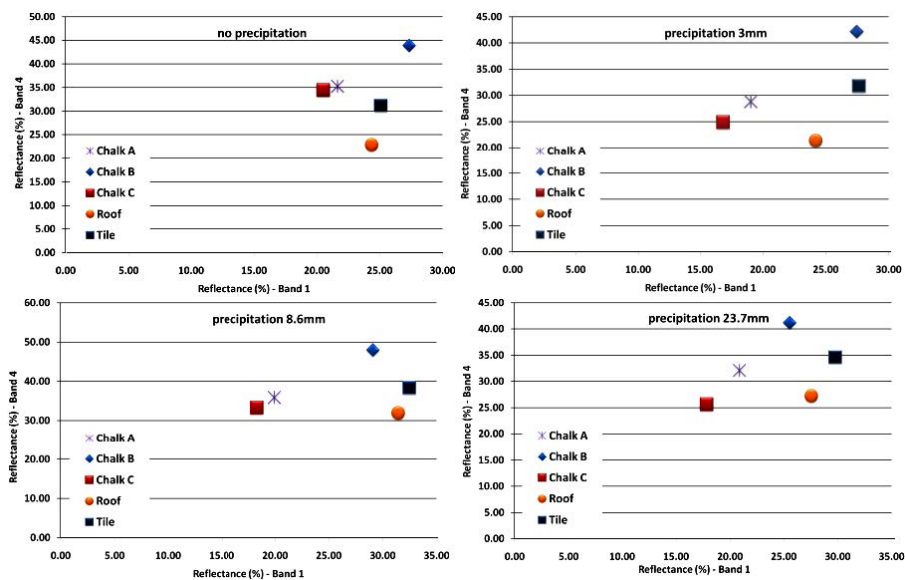

Fig. 7. Scatter-plots of the different targets examined in this studies for Bands 1-4 of Landsat images.

response of the chalk A sample compared to tile sample concerning Band 1. The initial distance of 3.43 for "dry" image is expanded to a value of 7.62 for the "23.7 mm precipitation" image.

Table 3

Euclidean distances for all the targets
for the first four bands (VNIR) of Landsat satellite imagery

Band 1 -23/07/2009	Chalk A	Chalk B	Chalk C	Roof	Tile	Band 2-23/07/2009	Chalk A	Chalk B	Chalk C	Roof	Tile
Chalk A		5.69	1.15	2.70	3.43	Chalk A		7.07	2.33	1.70	2.42
Chalk B			6.84	2.99	2.27	Chalk B			9.41	8.78	4.65
Chalk C				3.85	4.58	Chalk C				0.63	4.76
Roof					0.73	Roof					4.13
Tile						Tile					

Band 3-23/07/2009	Chalk A	Chalk B	Chalk C	Roof	Tile	Band 4-23/07/2009	Chalk A	Chalk B	Chalk C	Roof	Tile
Chalk A		8.01	1.66	5.32	0.24	Chalk A		8.65	0.83	12.40	4.06
Chalk B			9.67	13.33	7.78	Chalk B			9.48	21.06	12.71
Chalk C				3.66	1.90	Chalk C				11.58	3.24
Roof					5.55	Roof					8.34
Tile						Tile					

Band 1-02/06/2009	Chalk A	Chalk B	Chalk C	Roof	Tile	Band 2-02/06/2009	Chalk A	Chalk B	Chalk C	Roof	Tile
Chalk A		4.65	3.06	6.65	8.87	Chalk A		6.29	4.11	5.52	8.52
Chalk B			7.71	2.00	4.22	Chalk B			10.40	0.77	2.23
Chalk C				9.71	11.93	Chalk C				9.63	12.63
Roof					2.22	Roof					3.00
Tile						Tile					

Band 3-02/06/2005	Chalk A	Chalk B	Chalk C	Roof	Tile	Band 4-02/06/2009	Chalk A	Chalk B	Chalk C	Roof	Tile
Chalk A		7.27	5.10	2.53	7.62	Chalk A		9.09	6.47	4.87	2.52
Chalk B			12.37	4.73	0.35	Chalk B			15.56	13.96	6.57
Chalk C				7.64	12.72	Chalk C				1.60	8.99
Roof					5.09	Roof					7.39
Tile						Tile					

It is important to mention the quite different spectral response of chalk C sample in satellite images compared to its response to the laboratory specimens. This problem was occurred due to the medium spatial resolution of Landsat images (30 m pixel size) that increases the mixing pixel phenomenon which is highly common when trying to derive information from satellite imagery (Roosta *et al.* 2007). Regarding the mixed pixels they are frequently a combination of numerous disparate components of an area of interest. Not only a single ground-cover target but also two or more targets (categories) are contained in the instantaneous field of view of the sensor (Arai 1991).

4. RESULTS AND VERIFICATION

4.1 Per-pixel classification

The results from the laboratory and satellite imagery analysis methods high-lighted the different spectral response of materials to different levels of hu-midity. Although according to laboratory measurements the initial spectral response (dry) between artificial and natural targets is well defined, this does not always stand for the Landsat satellite images due to their low spatial resolution and the corresponding phenomenon of mixing pixels. However, the increase of humidity level to the different samples, either in laboratory conditions or due to precipitation concerning satellite images, increased sub-stantially the spectral interval between the different targets making it possi-ble for the end-user to optimize the accuracy of LULC maps. For the direct comparison of the classification accuracy between images, where different levels of precipitation have been recorded, two Landsat TM/ETM+ images acquired on 2 June 2005 (0 mm precipitation – A) and 23 July 2009 (23.7 mm precipitation – B) were classified and compared. Both unsupervised (ISODATA) and supervised classification algorithms (ML) were used. Kappa analysis was also performed to test if each classification was signifi-cantly better than a random classification and if any two classifications were significantly different. The Kappa coefficient is well suited for accuracy assessment of LULC maps (Van Vliet 2009). Concerning Kappa, a value of 0 corresponds to a total random classification, while a Kappa value of 1 represents a perfect agreement between the classification and reference data (Yang *et al.* 2011, Van Vliet *et al.* 2011).

Initially, the ISODATA classification technique was applied to both im-ages with 95% convergence threshold. The following 5 classes were used for both the supervised and unsupervised algorithms: (1) urban fabric, (2) marl-chalk formations, (3) vegetation, (4) bare soil, and (5) forest. The same clas-ses were created for the supervised technique in both images as well (Fig. 8).

Concerning the results of unsupervised algorithm for both dry and humid acquisition days they can be described as poor and cannot be evaluated ($K < 60\%$). On the other hand, the application of supervised algorithm to "rainy" image was effective, providing good accuracy results ($K = 0.75$) to the areas of no cloud cover in the image. The product of "dry" image was substantially better than that of unsupervised case but not accurate enough in order to be considered as credential. As shown in Fig. 8, in the "dry" image case there was a major fault in "urban" spectral class which seems to cover a vast area of the basin. On the other hand, the result of the application of supervised classification algorithm in "rainy" image is much more efficient with the final product to describe more precisely the real LULC regime of the area.
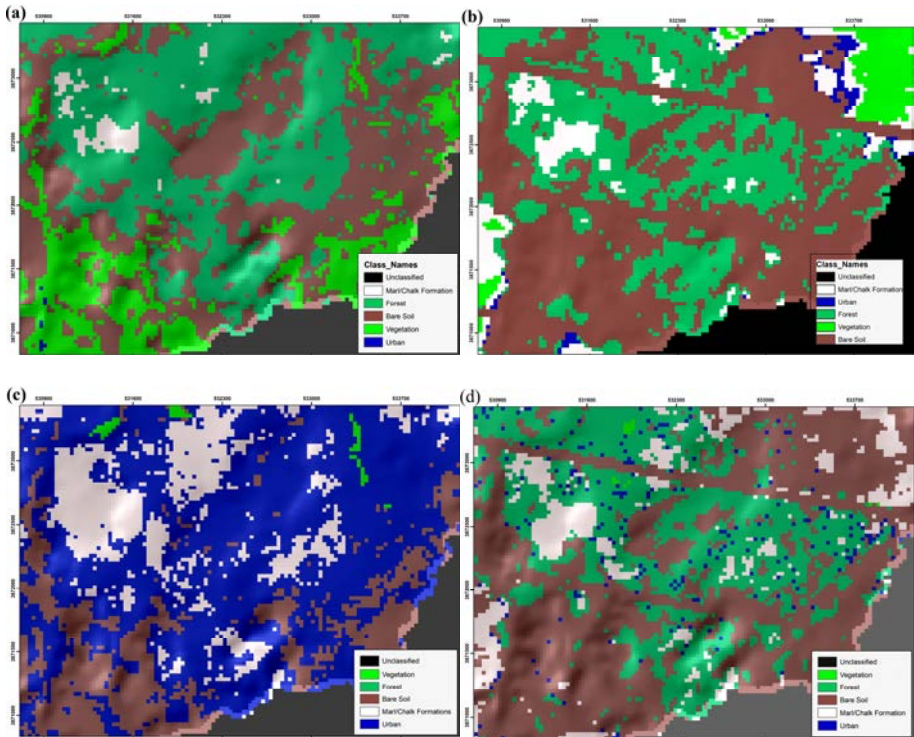
Fig. 8: (a) Detail of the "dry" satellite image after the application of unsupervised classification algorithm; (b) Detail of the "rainy" satellite image after the application of supervised classification algorithm; (c) Detail of the "dry" satellite image after the application of supervised classification algorithm; (d) Detail of the "rainy" satellite image after the application of supervised classification algorithm. Colour version of this figure is available in electronic edition only.

4.2 Object-based classification

After the application of the commonly used classification algorithms and the verification of the laboratory experimental results, the object-based classification process was implemented to the "rainy" Landsat image in order to optimize the final LULC map. The object-based classification is considered to be a contemporary classification technique where textural and contextual/relational information is used simultaneously with the spectral data for classification processing (Bhaskaran *et al*. 2010). The segmentation algorithm used in eCognition software is mainly a region-growing method based on the idea of collection of pixels whose attribute values represent a region. The segmentation can be realized as an optimization process where regions of minimum heterogeneity, given certain constraints, have to be detected. The
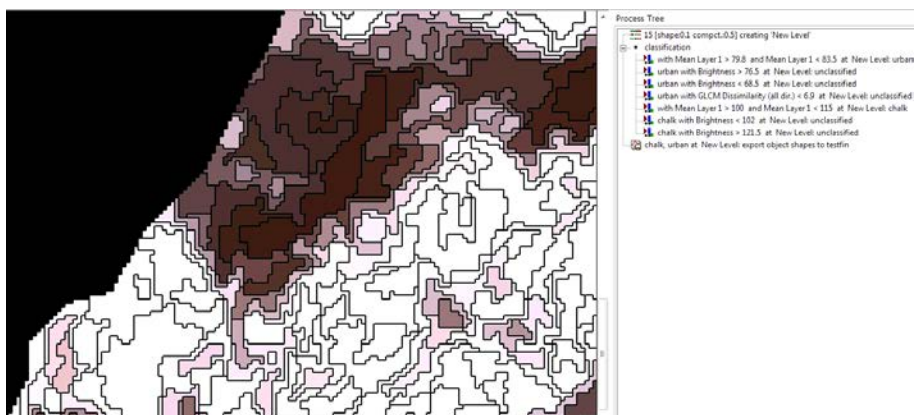
Fig. 9. Part of the Landsat ETM+ image after the implementation of segmentation process. At the right part of the image, the hierarchy rule used for the classification process is shown.

specific process allows an initial segmentation based on primary features (shape and gray tone) and then proceeds to more advanced classification-based segmentation (Benz *et al.* 2004). Moreover, segments are regions which are generated by one or more criteria of homogeneity in one or more dimensions (of a feature space, respectively). This is the reason why segments provide additional spectral information when compared to single pixels (Blaschke 2010).

In this study, the Landsat "rainy" image was segmented at one level using all the 6 bands with equal weighting. The shape parameter was adjusted to 0.1, the compactness to 0.5 and the scale factor to 15. At the next step concerning classification, mean pixel value, brightness and texture parameters were weighted according to the land cover to be classified. However, the settings of the shape parameter of this study did not provide clear indication for use with a certain type of land cover. In the specific case, hierarchy rules were used taking into account statistics concerning the mean pixel value of Landsat TM/ETM+ first band, the brightness, and dissimilarity texture index (Fig. 9).

At the end, the accuracy of the final classified product was substantially improved due to segmentation and knowledge based method of eCognition software. The value of Kappa coefficient ($K = 0.77$) denoted the potential of the specific classification method in optimizing classification results.

4.3 Application of maximum entropy in a one-class classification

The potential of the "rainy image" was finally evaluated with the use of maximum entropy approach (MaxEnt). Entropy is a fundamental concept in

information theory; it measures how much choice is involved in the selection of an event (Shannon 1948). The main principle of maximum entropy indicates that the distribution model that satisfies any given constraints should be as uniform as possible (Phillips *et al.* 2004). The specific approach has mainly been used for modeling species geographic distribution concerning epidemiological, biological, evolutionary, and ecological projects but has also been used in remote sensing classification projects, as mentioned in the introduction.

The following equation describes the MaxEnt modeling:

$$H(\pi) = -\sum \chi E \chi \times \pi(\chi) \times \ln \pi(\chi) , \tag{4}$$

where $H(\pi)$ is the entropy of π, while π is an unknown distribution over a finite set of χ. The distribution π assigns a probability $\pi(\chi)$ to each element of χ.

In the specific study, the MaxEnt algorithm was used (Jaynes 1957) which is ready to handle GIS raster data in the classification process (Phillips *et al.* 2004). For this reason, we used the "MaxEnt" software that is freely distributed. Concerning the inputs there were the positive raster values and their corresponding feature values. Approximately fifty training areas were selected from the original "rainy" Landsat image representing urban class. Moreover, ten layers were used as auxiliary for the image classification including six spectral bands of Landsat image. In addition, after the application of principal component analysis (PCA) to the satellite image the first principal component was used in order to create additional texture bands. The texture bands of mean value, contrast, homogeneity and second moment were calculated with the use of ENVI software version 4.8. At the final step regarding the results, the default output logistic gives a final estimate of probability between 0 and 1. Nevertheless it is important to mention that the output is proportional to the conditional probability of being positive (Fig. 10 top panel). As seen, the areas in red color have the greater possibility to belong to urban class. In Figure 10 (bottom) the sensitivity against specificity diagram indicates that the training data value is 0.995 which is very close to 1, a value that indicates optimum model performance.

Besides the image output representing the MaxEnt model for urban class in Yialias study area, an extra output of MaxEnt methodology is a table indicating analysis of different variables used in the model and the percent predictive contribution of each variable (Table 4). The higher the contribution the greater the impact that particular variable had on predicting the occurrence of that species. As it was proved, the variance texture band and the first band of Landsat TM/ETM+ images were the bands with the optimum contribution.
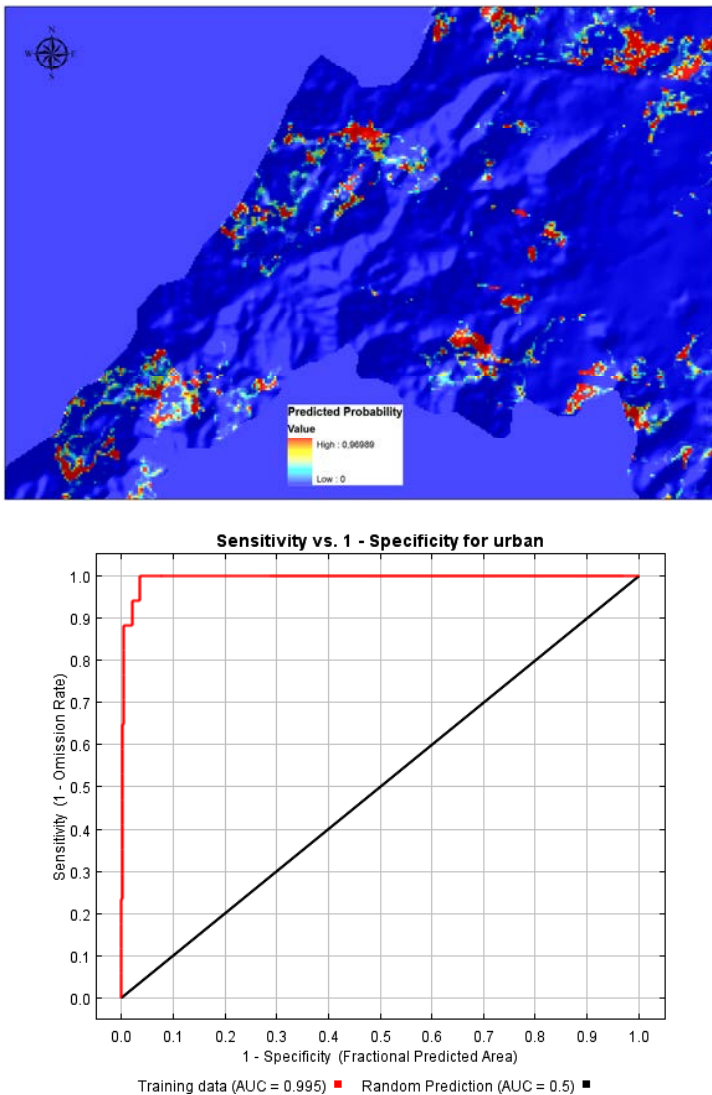
Fig. 10: (top) Detail of prediction probability image of the catchment area; (bottom) Graph displaying sensitivity *versus* specificity for urban class area. Colour version of this figure is available in electronic edition only.

While searching the final prediction results, it seemed that the final classified product was of medium accuracy concerning urban class cover. However, after the application of a threshold in value 0.9 (probability value) and concerning as appropriate only the pixels with values greater than 0.9, the Kappa coefficient reached a value of 0.78.

Table 4

Analysis of variable contributions

No.	Variable	Percent of contribution [%]
1	Variance	27.6
2	Layer 1	20.0
3	Homogeneity	17.9
4	Layer 6	16.5
5	Second Moment	12.9
6	Layer 3	3.1
7	Layer 2	1.0
8	Layer 4	0.7
9	Layer 5	0.2
10	Mean	0

5. CONCLUSIONS

During the last decades, satellite remote sensing has become an invaluable tool for monitoring and mapping land cover. The vast number of new and contemporary satellite sensors offer tremendous abilities to any possible end users of satellite imagery. However, although the spectral and spatial resolution of such a kind of imagery has been substantially increased, at the same time the cost of acquisition remains high in many cases. Thus, freely provided imagery, such as those of Landsat TM/ETM+, remains still a precious source of spectral data for all the satellite remote sensing community. This paper strived to denote an alternative methodology in order to exploit the classification abilities of Landsat TM/ETM+ imagery. As a case study, the catchment area of Yialias River in Cyprus (a typical Eastern Mediterranean setting) was selected where spectral mixing between marl/chalk geological formations and urban areas was observed. This mixing hindered the construction of efficient LULC maps with the use of traditional classification methods.

The results pointed to the importance of imagery acquisition date for optimization of classification results. Specifically, the overall accuracy of classification product was substantially increased (by more than 30% for supervised classification), especially for urban and marl/chalk areas, during days where high precipitation measurements were recorded in the broader study area. The results were established either by laboratory or satellite imagery analysis. At the end, the implementation of object-based classification method to the most potential Landsat TM/ETM+ image optimized the final results. In addition, the maximum entropy algorithm presented an alternative

methodology concerning one-class classification methodology and extracting crucial statistics about the contribution of different variables to the classification output. Both of these contemporary methodologies improved substantially the final classification products derived. Finally, the proposed methodology offers an alternative for the hydrologists (especially those interested in flood hydrological response of catchment areas in Eastern Mediterranean) to incorporate in their models data derived from satellite images of low cost and medium resolution. Specifically, models using GIS interface such as ArcSWAT need accurate LULC data in order to simulate flood events.

A constraint of the overall method can be considered the scarcity of rainy days in Cyprus and other areas in Eastern Mediterranean region and the possible cloud cover. The authors will continue the research in the field of classification optimization by using radar and high resolution images acquired during rainy days in Cyprus in order to overcome the drawback of potential cloud cover.

References

Agapiou, A., D.G. Hadjimitsis , C. Papoutsa, D.D. Alexakis, and G. Papadavid (2011), The importance of accounting for atmospheric effects in the application of NDVI and interpretation of satellite imagery for supporting archaeological research: The case studies of Palaepaphos and Nea Paphos sites in Cyprus, *Remote Sens.* **3**, 12, 2605-2629; DOI: 10.3390/rs3122605.

Alexakis, D.D., D.G. Hadjimitsis, A. Agapiou, K. Themistokleous, and A. Retalis (2011), Contribution of earth observation to flood risk assessment in Cyprus: the Yialias catchment area in Nicosia. **In:** *Proc. VI EWRA Int. Symp. "Water Engineering and Management in a Changing Environment", 29 June – 2 July 2011 Catania*.

Arai, K. (1991), Information extraction of inner pixel contents derived from satellite remote sensing imagery data, *J. Jpn. Soc. Photogramm. Remote Sens*. **30**, 4, 30-34.

Benz, U.C., P. Hofmann, G. Willhauck, I. Lingenfelder, and M. Heynen (2004), Multi-resolution, object-oriented fuzzy analysis of remote sensing data for

GIS-ready information, *ISPRS J. Photogramm. Remote Sens*. **58**, 3-4, 239-258, DOI: 10.1016/j.isprsjprs.2003.10.002.

Bhaskaran, S., S. Paramananda, and M. Ramnarayan (2010), Per-pixel and object-oriented classification methods for mapping urban features using Ikonos satellite data, *Appl. Geogr*. **30**, 4, 650-665, DOI: 10.1016/j.apgeog.2010.01.009.

Blaschke, T. (2010), Object based image analysis for remote sensing, *ISPRS J. Photogramm. Remote Sens*. **65**, 1, 2-16, DOI: 10.1016/j.isprsjprs.2009.06.004.

Blumberg, D.G., and G. Zhu (2007), Using a hierarchical multi-resolution mechanism for the classification and semantic extraction of land use maps for Beer-Sheva, Israel, *Int. J. Remote Sens*. **28**, 15, 3273-3289, DOI: 10.1080/01431160600993371.

Brown, D.G., B.C. Pijanowski, and J.D. Duh (2000), Modeling the relationships between land use and land cover on private lands in the Upper Midwest, USA, *J. Environ. Manage*. **59**, 4, 247-263, DOI: 10.1006/jema.2000.0369.

Congalton, R.G. (1991), A review of assessing the accuracy of classifications of remotely sensed data, *Remote Sens. Environ*. **37**, 1, 35-46, DOI: 10.1016/0034-4257(91)90048-B.

Congalton, R.G., and K. Green (1999), *Assessing the Accuracy of Remotely Sensed Data: Principles and Practices*, Lewis Publishers, Boca Raton, 137 pp.

De Kok, R., A. Buck, T. Schneider, and U. Ammer (2000), Analysis of image objects fromVHR imagery for forest GIS updating in the Bavarian Alps. **In:** *XIX Congress Int. Soc. for Photogrammetry and Remote Sensing (ISPRS), 16-23 July 2000, Amsterdam, Holland*, 222-229.

Du, P., X. Li, W. Cao, Y. Luo, and H. Zhang (2010), Monitoring urban land cover and vegetation change by multi-temporal remote sensing information, *Mining Sci. Technol*. **20**, 6, 922-932, DOI: 10.1016/S1674-5264.

Eggleton, R.A. (ed.), (2001), *The Regolith Glossary: Surficial Geology, Soils and Landscapes*, CRC LEME, Canberra, Australia, http://crcleme.org.au/ Pubs/Monographs/BookRegGloss.html.

Eiumnoh, A., and R.P. Shrestha (2000), Application of DEM data to Landsat image classification: Evaluation in a tropical wet-dry landscape of Thailand, *Photogramm. Eng. Remote Sens*. **66**, 3, 297-1304.

Foody, G.M. (2002), Status of land cover classification accuracy assessment, *Remote Sens. Environ*. **80**, 1, 185-201, DOI: 10.1016/S0034-4257(01)00295-4.

Forster, B.C. (1984), Derivation of atmospheric correction procedures for LANDSAT MSS with particular reference to urban data, *Int. J. Remote Sens.* **5**, 5, 799-817, DOI: 10.1080/01431168408948861.

Gamanya, R., P. De Maeyer, and M. De Dapper (2007), An automated satellite image classification design using object-oriented segmentation algorithms:

A move towards standardization, *Expert Syst. Appl.* **32**, 2, 616-624, DOI: 10.1016/j.eswa.2006.01.055.

Hadjimitsis, D.G. (2007), The use of satellite remote sensing and GIS for assisting flood risk assessment: a case study of the Agriokalamin Catchment area in Paphos-Cyprus, *Proc. SPIE* **6742**, 67420Z, DOI: 10.1117/12.751855.

Hadjimitsis, D.G. (2010), Determination of urban growth in catchment areas in Cyprus using multi-temporal remotely sensed data: risk assessment study, *Nat. Hazards Earth Syst. Sci.* **10**, 2235-2240, DOI: 10.5194/nhess-10-2235-2010.

Hadjimitsis, D.G., and C.R.I. Clayton (2008), The use of an improved atmospheric correction algorithm for removing atmospheric effects from remotely sensed images using an atmosphere-surface simulation and meteorological data, *Meteorol. Appl.* **15**, 3, 381-387, DOI: 10.1002/met.80.

Hadjimitsis, D.G., and C.R.I. Clayton (2007), The application of the covariance matrix statistical method for removing atmospheric effects from satellite remotely sensed data intended for environmental applications, *Proc. SPIE* 6749, 674936, DOI: 10.1117/12.751887.

Hadjimitsis, D.G., C.R.I. Clayton, and V.S. Hope (2004a), An assessment of the effectiveness of atmospheric correction algorithms through the remote sensing of some reservoirs, *Int. J. Remote Sens.* **25**, 18, 3651-3674, DOI: 10.1080/01431160310001647993.

Hadjimitsis, D.G., C.R.I. Clayton, and A. Retalis (2004b), On the darkest pixel atmospheric correction algorithm: a revised procedure applied over satellite remotely sensed images intended for environmental applications, *Proc. SPIE* **5239**, 464, DOI: 10.1117/12.511520.

Hjuler, M.L., and I.L. Fabricius (2009), Engineering properties of chalk related to diagenetic variations of Upper Cretaceous onshore and offshore chalk in the North Sea area, *J. Petrol. Sci. Eng.* **68**, 3-4, 151-170, DOI: 10.1016/j.petrol.2009.06.005.

Jaynes, E.T. (1957), Information theory and statistical mechanics, *Phys. Rev.* **106**, 4, 620-630, DOI: 10.1103/PhysRev.106.620.

Karl, J.W., and B.A. Maurer (2010), Multivariate correlations between imagery and field measurements across scales: comparing pixel aggregation and image segmentation, *Landscape Ecol.* **25**, 4, 591-605, DOI: 10.1007/s10980-009-9439-4.

Li, W., and Q. Guo (2010), A maximum entropy approach to one-class classification of remote sensing imagery, *Int. J. Remote Sens.* **31**, 8, 2227-2235, DOI: 10.1080/01431161003702245.

Liberti, M., T. Simoniello, M.T. Carone, R. Coppola, M. D'Emilio, and M. Macchiato (2009), Mapping badland areas using LANDSAT TM/ETM satellite imagery and morphological data, *Geomorphology* **106**, 3-4, 333-343, DOI: 10.1016/j.geomorph.2008.11.012.

Matikainen, L., and K. Karila (2011), Segment-based land cover mapping of a suburban area—comparison of high-resolution remotely sensed datasets

using classification trees and test field points, *Remote Sens*. **3**, 8, 1777-1804, DOI: 10.3390/rs3081777.

McLachlan, G.J. (1992), *Discriminant Analysis and Statistical Pattern Recognition*, John Wiley and Sons, New York.

Melgani, F., and S.B. Serpico (2002), A statistical approach to the fusion of spectral and spatio-temporal contextual information for the classification of remote-sensing images, *Pattern Recogn. Lett*. **23**, 9, 1053-1061, DOI: 10.1016/S0167-8655(02)00052-1.

Michaelides, S.C., F.S. Tymvios, and T. Michaelidou (2009), Spatial and temporal characteristics of the annual rainfall frequency distribution in Cyprus, *Atmos. Res.* **94**, 4, 606-615, DOI: 10.1016/j.atmosres.2009.04.008.

Mortier, F., S. Robin, S. Lassalvy, C. Baril, and A. Bar-Hen (2006), Prediction of Euclidean distances with discrete and continuous outcomes, *J. Multivariate Anal.* **97**, 8, 1799-1814, DOI: 10.1016/j.jmva.2005.06.010.

Moussa, R., and C. Bocquillon (2009), On the use of the diffusive wave for modelling extreme flood events with overbank flow in the floodplain, *J. Hydrol*. **374**, 1-2, 116-135, DOI: 10.1016/j.jhydrol.2009.06.006.

Peterson, A.T., and J. Shaw (2003), *Lutzomyia* vectors for cutaneous leishmaniasis in Southern Brazil: ecological niche models, predicted geographic distributions, and climate change effects, *Int. J. Parasitol*. **33**, 9, 919-931, DOI: 10.1016/S0020-7519(03)00094-8.

Phillips, S.J., M. Dudík, and R.E. Schapire (2004), A maximum entropy approach to species distribution modeling. **In:** *Proc. Twenty-First Int. Conf. on Machine Learning, Banff, Alberta, Canada*, ACM, New York, 655-662, DOI: 10.1145/1015330.1015412.

Phillips, S.J., R.P. Anderson, and R.E. Schapire (2006), Maximum entropy modeling of species geographic distributions, *Ecol. Model.* **190**, 3-4, 231-259, DOI: 10.1016/j.ecolmodel.2005.03.026.

Risnes, R., H. Haghighi, R.I. Korsnes, and O. Natvik (2003), Chalk-fluid interactions with glycol and brines, *Tectonophysics* **370**, 1-4, 213-226, DOI: 10.1016/S0040-1951(03)00187-2.

Risnes, R., M.V. Madland, M. Hole, and N.K. Kwabiah (2005), Water weakening of chalk – Mechanical effects of water-glycol mixtures, *J. Petrol. Sci. Eng.* **48**, 1-2, 21-36, DOI: 10.1016/j.petrol.2005.04.004.

Roosta, H., R. Farhoudi, and M. Roosta (2007), Multi temporal disaggregation of MODIS images using non-linear analysis. **In:** *Proc. of 5th WSEAS Int. Conf. on Environment, Ecosystems and Development, 14-16 December 2007, Tenerife, Spain*, 222-227.

Shafique, M., M. Van der Meijde, and S. Ullah (2011), Regolith modeling and its relation to earthquake induced building damage : A remote sensing approach, *J. Asian Earth Sci*. **42**, 1-2, 65-75, DOI: 10.1016/j.jseaes.2011.04.004.

Shankar, B.U., S.K. Meher, and A. Ghosh (2011), Wavelet-fuzzy hybridization: Feature-extraction and land-cover classification of remote sensing images, *Appl. Soft Comput.* **11**, 3, 2999-3011, DOI: 10.1016/j.asoc.2010.11.024.

Shannon, C.E. (1948), A mathematical theory of communication, *Bell Syst. Tech. J.* **27**, 379-423.

Takagi, T., T. Oguchi, J. Matsumoto, M.J. Grossman, M.H. Sarker, and M.A. Matin (2007), Channel braiding and stability of the Brahmaputra River, Bangladesh, since 1967: GIS and remote sensing analyses, *Geomorphology* **85**, 3-4, 294-305, DOI: 10.1016/j.geomorph.2006.03.028.

Van Vliet, J. (2009), Assessing the accuracy of changes in spatial explicit land use change models. **In:** *12th Annual AGILE Int. Conf. on Geographic Information Science 2009, Leibniz Universitat Hannover, Germany.*

Van Vliet, J., A.K. Bregt**,** and A. Hagen-Zanker (2011), Revisiting Kappa to account for change in the accuracy assessment of land-use change models, *Ecol. Model.* **222**, 8, 1367-1375, DOI: 10.1016/j.ecolmodel.2011.01.017.

Weng, Q. (2002), Land use change analysis in the Zhujiang Delta of China using satellite remote sensing, GIS and stochastic modelling, *J. Environ. Manage.* **64**, 3, 273-284, DOI: 10.1006/jema.2001.0509.

Wu, X., J.T. Sullivan, and A.K. Heidinger (2010), Operational calibration of the Advanced Very High Resolution Radiometer (AVHRR) visible and near-infrared channels, *Can. J. Remote Sens*. **36**, 5, 602-616, DOI: 10.5589/m10-080.

Yang, C., J.H. Everitt, and D. Murden (2011), Evaluating high resolution SPOT 5 satellite imagery for crop identification, *Comput. Electron. Agr.* **75**, 2, 347-354, DOI: 10.1016/j.compag.2010.12.012.

Zhang, R., and D. Zhu (2011), Study of land cover classification based on knowledge rules using high-resolution remote sensing images, *Expert Syst. Appl.* **38**, 4, 3647-3652, DOI: 10.1016/j.eswa.2010. 00.019.